COMPOSITE MATERIALS

Fatigue and Fracture

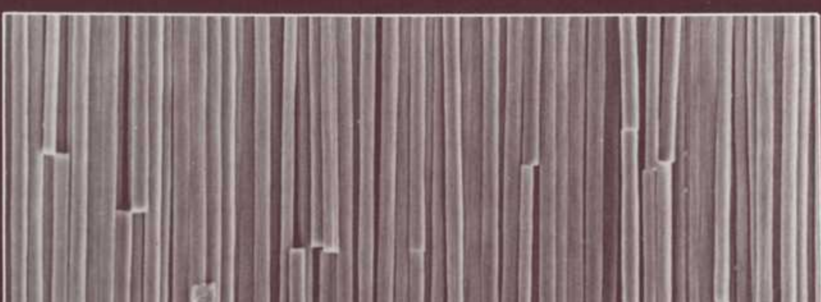

H. Thomas Hahn
editor

ASTM STP 907

COMPOSITE MATERIALS: FATIGUE AND FRACTURE

A symposium
sponsored by
ASTM Committee D-30
on High Modulus Fibers
and Their Composites
Dallas, TX, 24–25 Oct. 1984

ASTM SPECIAL TECHNICAL PUBLICATION 907
H. Thomas Hahn, Washington University,
editor

ASTM Publication Code Number (PCN)
04-907000-33

1916 Race Street, Philadelphia, PA 19103

Library of Congress Cataloging-in-Publication Data

Composite materials.

(ASTM special technical publication; 907)
"ASTM publication code number (PCN) 04-907000-33."
Includes bibliographies and index.
1. Composite materials—Fatigue—Congresses. 2. Composite materials—Fracture—Congresses. I. Hahn, H. Thomas. II. ASTM Committee D-30 on High Modulus Fibers and Their Composites. III. Series.
TA418.9.C6C57 1986 620.1'183 86-3509
ISBN 0-8031-0470-7

Library of Congress Catalog Card Number: 86-3509

NOTE

The Society is not responsible, as a body,
for the statements and opinions
advanced in this publication.

Printed in Baltimore, MD
June 1986

Foreword

The symposium on Composite Materials: Fatigue and Fracture was held in Dallas, Texas, 24–25 October 1984. ASTM Committee D-30 on High Modulus Fibers and Their Composites sponsored the symposium. H. Thomas Hahn, Washington University, presided as symposium chairman and editor of this publication.

Related ASTM Publications

Effects of Defects in Composite Materials, STP 836 (1984), 04-836000-33

Long Term Behavior of Composites, STP 813 (1983), 04-813000-33

Composites for Extreme Environments, STP 768 (1982), 04-768000-33

Nondestructive Evaluation and Flaw Criticality for Composite Materials, STP 696 (1979), 04-696000-33

Advanced Composite Materials–Environmental Effects, STP 658 (1978), 04-658000-33

A Note of Appreciation to Reviewers

The quality of the papers that appear in this publication reflects not only the obvious efforts of the authors but also the unheralded, though essential, work of the reviewers. On behalf of ASTM we acknowledge with appreciation their dedication to high professional standards and their sacrifice of time and effort.

ASTM Committee on Publications

ASTM Editorial Staff

Contents

Introduction

The ASTM Symposium on Composite Materials: Fatigue and Fracture was held on 24–25 October 1984 in Dallas/Ft. Worth, Texas. It was sponsored by ASTM Committee D-30 on High Modulus Fibers and Their Composites.

The main purpose of the symposium was to provide a forum for presentation and discussion on the recent developments in fatigue and fracture of composites. Specifically called for were papers describing experimental and analytical research in the following areas of composites technology: failure mechanisms and fractography, nondestructive evaluation, material improvement, environmental effects, time-dependent behavior, design implications, prediction methodology, and reliability aspects.

Not so long ago, one of the frequently asked questions was, "Is fracture mechanics applicable to composites?" Now we no longer ask the same question. We use the fracture mechanics methodology to analyze matrix/interface-controlled subcritical fracture such as ply cracking and delamination. The question we hear quite often these days is, "Composites have no fatigue problems. Why do we need to study fatigue of composites?" We only wish we could repeat the same question in the years to come.

The papers included in this volume address many of the important aspects of fatigue and fracture behavior of composite materials. Although most of the papers are on graphite/epoxy laminates, some discussion can be found on metal matrix composites as well as on unidirectional composites. There is an overall emphasis on the identification of damage mechanisms and on the development of prediction methodology for the formation and effect of damage based on the physics and mechanics of damage details. Such an emphasis will eventually point the way toward further material improvements and more efficient design for fatigue.

This symposium volume is the result of collective effort by many people involved. First of all, I would like to thank the symposium committee for their invaluable help in putting this program together. The members of the committee are Bob Badaliance of Naval Research Laboratory, Dave Glasgow of Air Force Office of Scientific Research, C. T. Sun of Purdue University, and Jerry Williams of NASA Langley Research Center. Grateful appreciation is also extended to the authors, the reviewers, and the ASTM staff for their generous contributions to this volume.

H. Thomas Hahn

Center for Composites Research, Washington University, St. Louis, MO; symposium chairman and editor.

Fracture

Joseph E. Grady[1] *and C. T. Sun*[1]

Dynamic Delamination Crack Propagation in a Graphite/Epoxy Laminate

REFERENCE: Grady, J. E. and Sun, C. T., "**Dynamic Delamination Crack Propagation in a Graphite/Epoxy Laminate,**" *Composite Materials: Fatigue and Fracture, ASTM STP 907,* H. T. Hahn, Ed., American Society for Testing and Materials, Philadelphia, 1986, pp. 5–31.

ABSTRACT: Ballistic impact tests of $[90/0]_{5s}$ T-300/934 graphite/epoxy laminates of beam-like dimension with embedded delamination cracks were conducted. High speed photography (16 000 frames/second) was used to record the impact response and subsequent crack propagation. From the photographic data, impact characteristics such as the contact duration and the dynamic response of the impact specimen were measured. In addition, the time of initiation of delamination propagation and measurements of the subsequent delamination length versus time were obtained. By changing the location of the embedded delamination in the specimens relative to the impact point, additional results were obtained on the variation of the threshold impact velocity necessary to cause crack propagation in the different specimen configurations. These data, together with the photographic results, suggest that the mode of crack propagation is dependent on the specimen geometry as well as the loading condition. The time dependent nature of the crack velocity and its variation with impact conditions was investigated.

A finite element program was used to calculate the dynamic strain energy release rate before the onset of crack propagation. This strain energy release rate was used to gage the instability of the delamination crack during impact.

KEY WORDS: composite materials, crack propagation, fracture (materials), dynamic fracture, crack velocity, crack arrest, dynamic toughness

Delamination, a mode of failure unique to composite laminates, can be produced by both static and dynamic loads. Great attention has been given to free-edge delamination in laminates subjected to in-plane static and fatigue loadings [*1–4*], and many attempts have been made to measure the fracture toughness with respect to delamination cracks [*5–9*]. To the authors' knowledge, however, no one has yet tried to determine the dynamic delamination fracture toughness.

It has been found that impact loading can cause severe delamination in composite laminates. In contrast to in-plane static loads, under which delamination

[1] Graduate student and professor, respectively, School of Aeronautics and Astronautics, Purdue University, West Lafayette, IN 47907.

often initiates from free edges, impact loading always results in interior delamination near the impact zone. Thus, the delamination mechanism cannot be explained by using the free edge singular stress concept. Moreover, due to the transient nature of the resulting deformation, the behavior of crack propagation is considerably different from that in the static case.

This paper presents the result of experiments conducted to observe dynamic delamination behavior. Threshold impact velocities above which delamination cracks become unstable were obtained for various impact specimen configurations. In addition, high speed photography was used to obtain estimates of delamination crack propagation velocities. Finite element analysis was used to calculate the dynamic strain energy release rate for a stationary crack. Critical values of strain energy release rate were obtained by comparing numerical results with experimental observation.

Experimental Apparatus and Procedure

Specimen Preparation

Impact specimens were cut from 20-ply $[90/0]_{5s}$ T-300/934 graphite/epoxy laminates of dimensions 0.25 by 30 by 46 cm. A delamination crack was embedded in the laminate by placing a 0.003 by 2.5 by 46-cm strip of trifluoroethylene resin between two plies during the layup process, thus preventing the two adjacent plies from bonding together in this area. A beam-like geometry was chosen for the impact specimen. Nominal dimensions are shown in Fig. 1. Thus, the initial delamination is a 2.54-cm-long, through-the-width crack. The location of the embedded crack in both the longitudinal and thickness directions was varied between laminates. This was done to study the effect of crack location on delamination characteristics.

Impact Cannon and Impactor

Silicon rubber balls 1.25 cm in diameter were used as impactors. These relatively soft impactors do not cause significant surface damage near the impact site, thus allowing crack extension to be the primary mode of impact damage. Nitrogen gas was used to fire the impactor through the cannon. A chamber pressure of 150 kPa could propel the 1-g rubber ball at approximately 150 m/s. The impact velocity was determined by two pairs of photoelectric diodes, placed on both sides of the path of the impactor, near the muzzle of the barrel. The travel time of the impactor between the diodes was measured to an accuracy of 1 μs.

Camera

A high-speed 16-mm FASTAX framing camera was used to record the crack propagation. It was mounted to give an edge-on view of the impact specimen, which was enclosed in a polymethylmethacrylate box to protect the camera lens

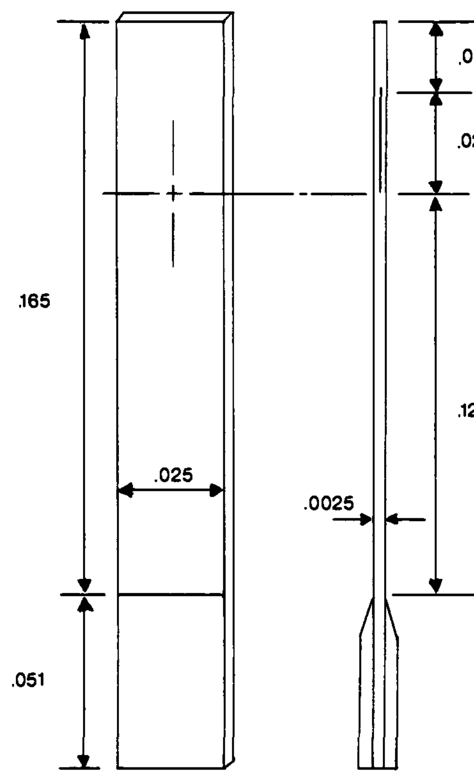

FIG. 1—*Nominal impact specimen dimensions.*

from the rebounding impactor. The peak framing rate of the camera is 8000 frames per second. This rate was effectively doubled by an internal rotating prism which made two exposures per frame, thus taking 16 000 pictures per second. Because of the high exposure rate of the film, very bright light was needed to adequately illuminate the impact specimen. This was provided by three 100-W floodlights.

The firing sequence was initiated from a control panel with timers set to trigger the camera and photo lights just before impact.

Experimental Results and Discussion

Threshold Impact Velocity

The dependence of delamination damage on impact velocity is of primary interest. Of particular importance is the threshold impact velocity, below which no delamination occurs. Figure 2 shows the geometry of six different specimen configurations tested. The location of the impact point varied slightly between

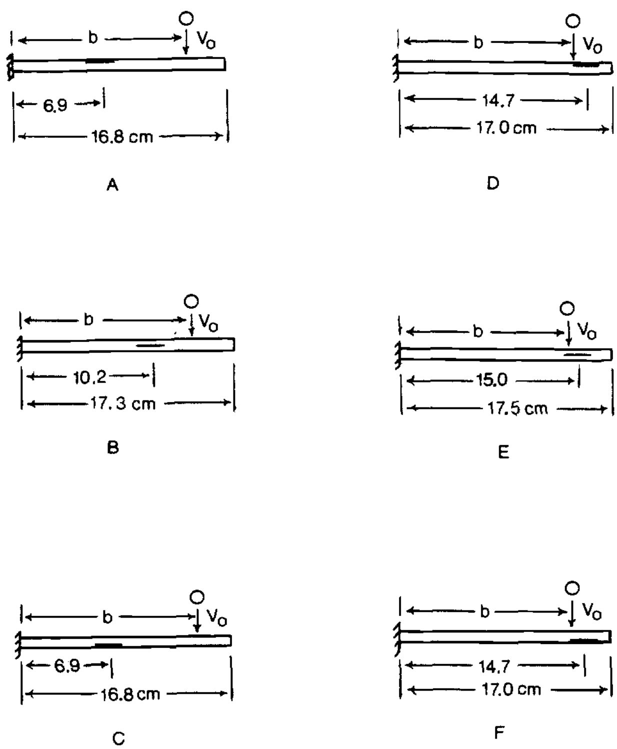

FIG. 2—*Impact specimen configurations.*

specimens due to small misalignments of the gun barrel. This is shown in Tables 1–6. The relation between impact velocity and total delaminated area for each specimen configuration is shown in Tables 1–6 and Fig. 3. Each specimen contains an initial (embedded) delamination of area 6.45 cm^2. For all cases considered, the existence of unambiguous threshold velocities is quite evident. Threshold velocities for each specimen configuration shown in Tables 1–6 were determined from graphs similar to that in Fig. 3. Among the three thickness locations tested, threshold velocity is greatest for the midplane crack (Table 2), and lowest for the lower off-midplane crack (Table 3). The distance between impact point and crack tip is also seen to affect threshold velocity. The results show that when impacted near the crack tip, the delamination crack becomes unstable at lower velocities. Tables 4 and 5 show that this phenomenon is more pronounced for cracks located near the top (impact) surface.

Midplane Delamination

A typical impact sequence is shown in Fig. 4. Characteristics such as duration of contact period and beam displacement response can be estimated from the

TABLE 1—*Variation of delaminated area with impact velocity for Specimen Configuration A.*

Specimen	Impact Velocity, V_0, m/s	Impact Distance, b, cm	[a]Delaminated Area, A, cm^2
A1	122	13.35	6.45
A2	130	13.10	6.45
A3	138	13.44	6.45
A4	142	13.20	12.70
A5	148	13.70	9.01
A6	148	14.00	6.45
A7	156	14.00	18.68
A8	173	13.92	22.99

[a]Initial delaminated area is 6.45 cm^2.

TABLE 2—*Variation of delaminated area with impact velocity for Specimen Configuration B.*

Specimen	Impact Velocity, V_0, m/s	Impact Distance, b, cm	[a]Delaminated Area, A, cm^2
B1	143	13.69	6.45
B2	144	13.89	6.45
B3	148	13.84	8.86
B4	148	12.77	6.45
B5	150	13.41	19.00
B6	155	12.90	41.94
B7	156	13.41	24.30
B8	158	13.03	40.56
B9	160	11.92	38.71
B10	161	13.71	44.77

[a]Initial delaminated area is 6.45 cm^2.

TABLE 3—*Variation of delaminated area with impact velocity for Specimen Configuration C.*

Specimen	Impact Velocity, V_0, m/s	Impact Distance, b, cm	[a]Delaminated Area, A, cm^2
C1	121	13.34	11.74
C2	138	13.59	16.72
C3	141	13.62	15.48
C4	142	13.58	13.27
C5	144	13.11	26.25
C6	144	13.36	21.60
C7	151	12.48	25.48
C8	151	12.93	30.10

[a]Initial delaminated area is 6.45 cm^2.

TABLE 4—*Variation of delaminated area with impact velocity for Specimen Configuration D.*

Specimen	Impact Velocity, V_0, m/s	Impact Distance, b, cm	[a]Delaminated Area, A, cm^2
D1	77	12.61	6.45
D2	102	13.24	6.45
D3	103	13.26	6.45
D4	111	13.87	14.88
D5	120	13.04	15.48
D6	133	13.04	25.10
D7	141	13.42	24.71

[a]Initial delaminated area is 6.45 cm^2.

TABLE 5—*Variation of delaminated area with impact velocity for Specimen Configuration E.*

Specimen	Impact Velocity, V_0, m/s	Impact Distance, b, cm	[a]Delaminated Area, A, cm^2
E1	122	12.92	6.45
E2	135	13.16	6.45
E3	141	13.00	6.45
E4	144	12.99	6.45
E5	145	13.13	10.67
E6	148	12.94	13.02
E7	149	13.10	9.82
E8	158	12.95	41.94
E9	162	13.41	19.23

[a]Initial delaminated area is 6.45 cm^2.

TABLE 6—*Variation of delaminated area with impact velocity for Specimen Configuration F.*

Specimen	Impact Velocity, V_0, m/s	Impact Distance, b, cm	[a]Delaminated Area, A, cm^2
F1	120	13.49	6.45
F2	122	12.82	6.45
F3	127	13.92	6.45
F4	138	13.29	26.88[b]
F5	140	13.69	6.45
F6	142	12.34	26.12[b]

[a]Initial delaminated area is 6.45 cm^2.
[b]Transverse cracking caused extensive spalling on back surface.

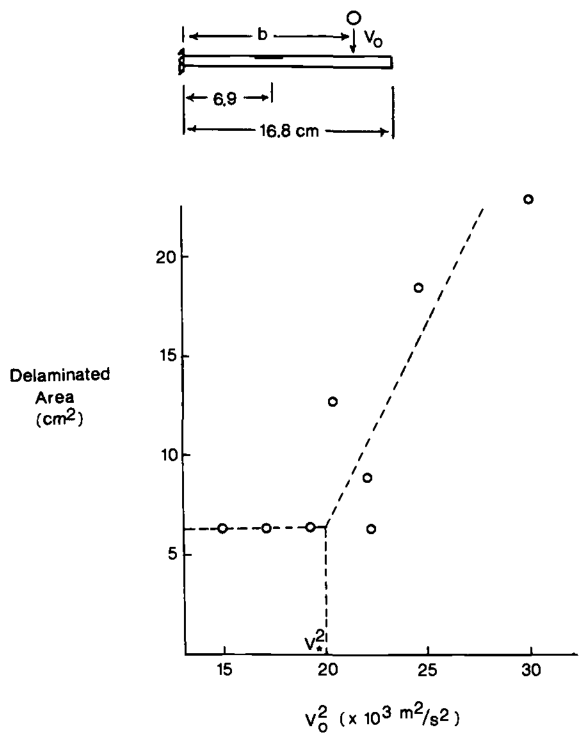

FIG. 3—*Delaminated area versus impact energy for Specimen Configuration A.*

figure. It should be noted that all measurements were taken from larger images projected on a screen. The figures shown here are primarily for illustration. In this case, the embedded crack lies along the specimen midplane and directly under the impact site, as shown in the figure. The resulting crack propagation is shown in Fig. 5. The crack arrest ($437.5 < t < 687.5$ μs) is apparently due to the nature of strain response near the propagating crack tip. A decrease in local curvature of the beam is accompanied by a decrease in available crack driving force. This correspondence is shown in Frames 9–11 of Fig. 4. Frames 12–14 ($687.5 < t < 812.5$ μs) show the subsequent increase in curvature, and the corresponding resumption of crack propagation.

Apparently, the geometry of the impact specimen can significantly affect crack propagation. Strain (curvature) will be affected by the arrival of flexural wave reflections from the boundaries, so the position of the crack relative to the boundaries will affect crack propagation. The time delay between impact and initial crack propagation observed in Figs. 4 and 5 is a result of the impact occurring directly on the embedded crack. The distributed compression on the crack faces caused by the deforming impactor ($62.5 < t < 375$ μs, Fig. 4) prevents any crack propagation from occurring during the contact interval.

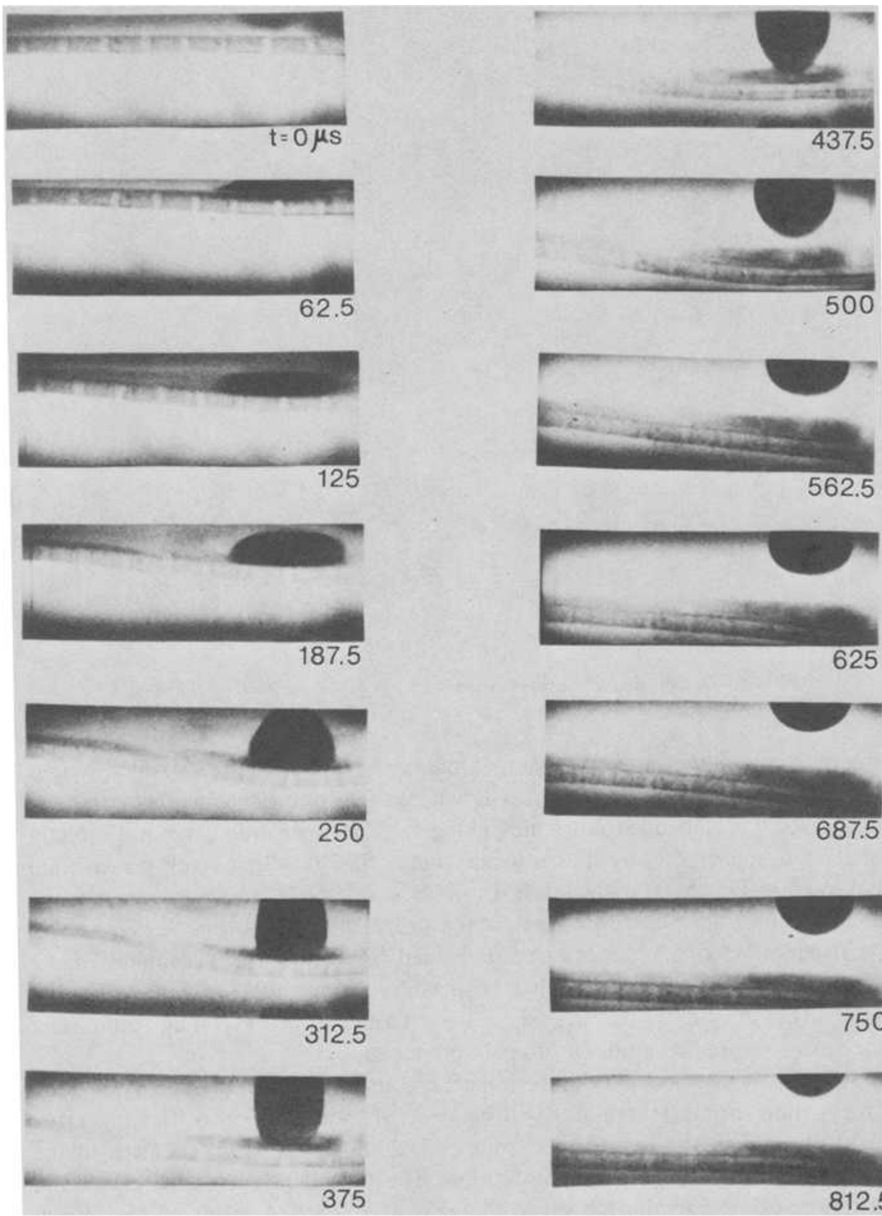

FIG. 4—*Impact response of Specimen No. E8.*

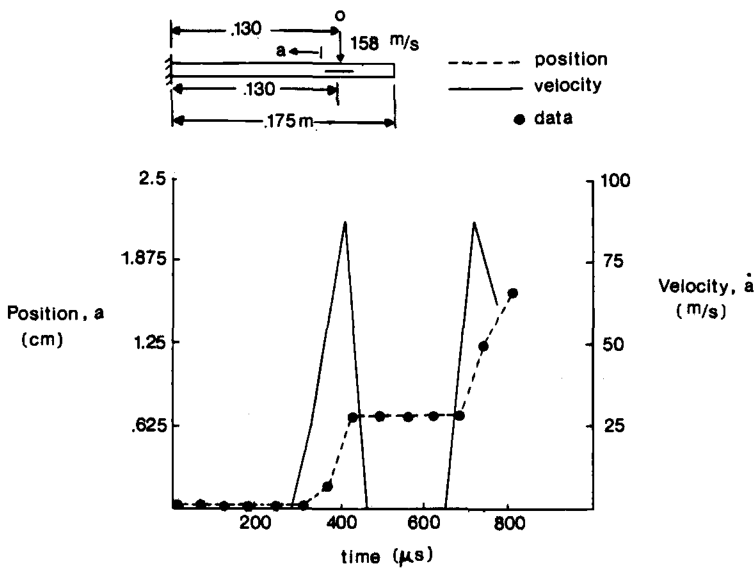

FIG. 5—*Crack-tip position and velocity in Specimen No. E8.*

Now, if the embedded crack is moved sufficiently away from the impact site, as depicted in Fig. 6, the interference of the impactor with crack propagation should be minimized. Compare Figs. 4 and 5 with Figs. 6 and 7. Both specimens show similar crack arrest characteristics as the wave reflections arrive. However, Figs. 6 and 7 show a significant difference in time between impact and onset of crack propagation.

Off-Midplane Delamination

All of the cases discussed so far involved delamination along the midplane of the beam. If the embedded crack is placed at a different through-the-thickness location, different crack propagation characteristics may be observed. In the following impact specimens, the embedded crack is halfway between the beam midplane and outer surface. Thus, five plies are on one side of the crack and 15 on the other. For these specimens, the camera was oriented to record the propagation of both crack tips simultaneously, instead of only a single crack tip, as in the previous cases.

Some distinctly different features of crack propagation in this case can be seen in Figs. 8–11. Onset of propagation is immediately preceded by a phenomenon similar to "buckling" of the delaminated plies. This is shown at 125, 812.5, and 875 μs in Fig. 8 and at 62.5, 812.5, and 875 μs in Fig. 10. This deformation is depicted schematically in Fig. 12*c*. The photographs suggest, then, that the onset of delamination is dominated by a Mode I (opening) rather than Mode II (shearing) type of action in this case.

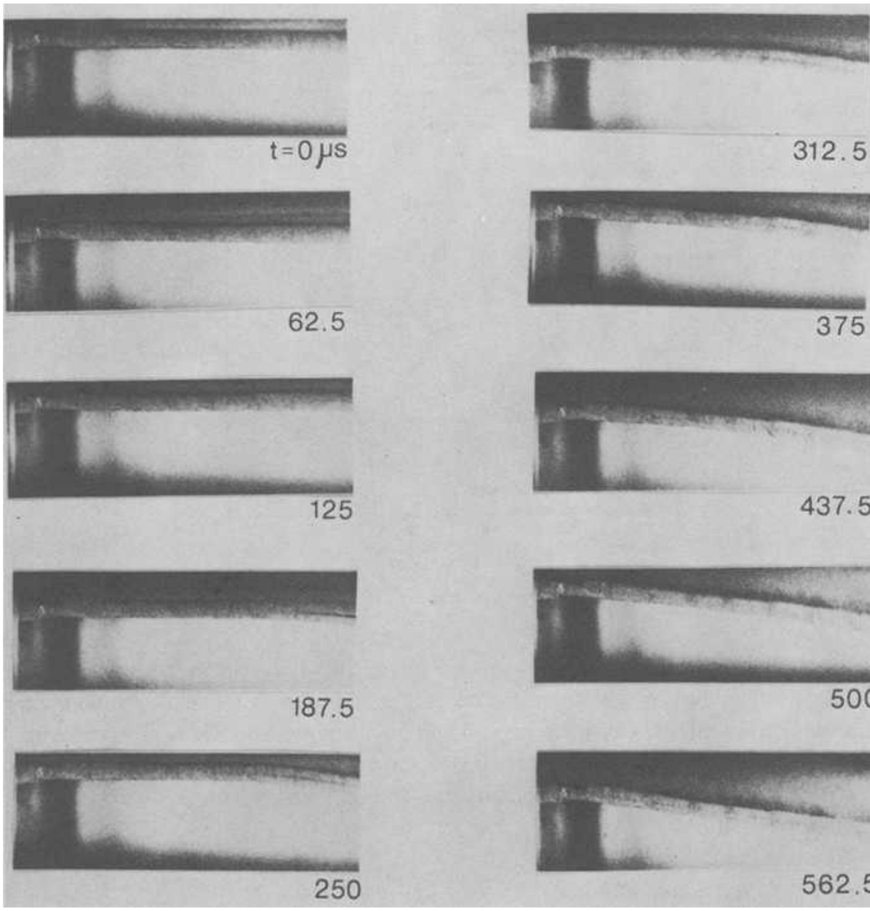

FIG. 6—*Impact response of Specimen No. B6.*

Tables 2 and 3 show that considerably greater impact energy is required to initiate crack propagation when the embedded crack lies along the midplane. The fact that no crack opening similar to that shown for off-midplane cracks is seen for midplane cracks (Figs. 4 and 6) suggests that considerably less Mode I action is involved when the crack lies on the midplane.

Because the initiation of crack extension is determined by the occurrence of the local ply buckling phenomenon, specimens of the configuration shown in Fig. 12 undergo no significant crack extension during the first half-cycle of their periodic motion after impact. Buckling can occur only when crack surfaces are in compression, as illustrated in Fig. 12*c*. As a result, the majority of crack propagation occurs during the second (compressive) half of the first cycle of motion for this specimen. This is in contrast to the specimen configurations shown in Figs. 8–11, in which plies neighboring the cracks are in compression immediately after impact.

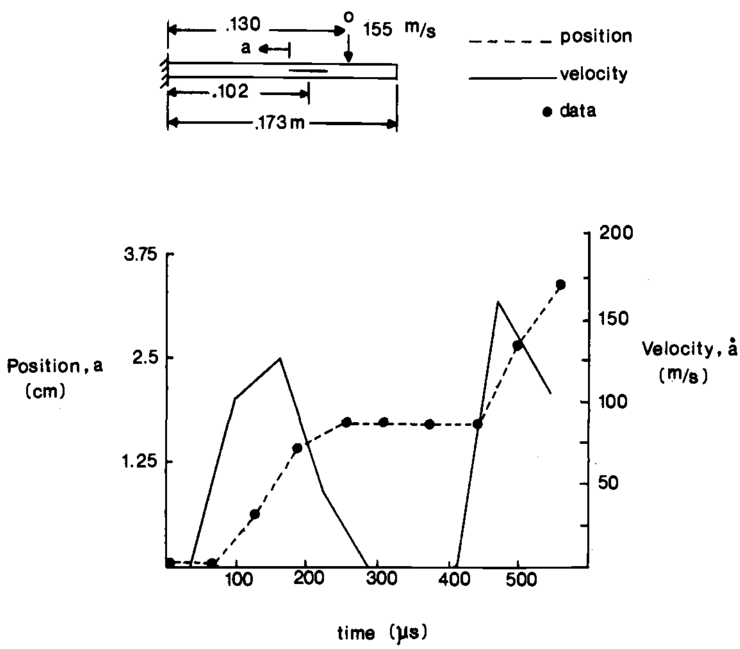

FIG. 7—*Crack-tip position and velocity in Specimen No. B6.*

The intermittent nature of the delamination process is illustrated in Figs. 8–11 after the onset of crack propagation has occurred. Flexural wave propagation through the delaminated plies causes them to exhibit a beam-like dynamic behavior independent of the gross deformation of the specimen. Reflection of the waves between crack tips causes alternating propagation arrest of the crack tips similar to that shown in Fig. 11 and to a lesser extent in Fig. 9.

It should be noted that the time scales used in plotting the experimental results can be used only as a relative base since a unique reference time frame cannot be set up. Thus, $t = 0$ cannot be regarded as the instant when the projectile comes in contact with the specimen.

Analysis

Finite Element Modeling

Strictly speaking, the impact problem concerned here is a three-dimensional problem. However, photographs taken by the high speed camera indicate that the impactor deformation covered almost the whole width of the specimen. Moreover, due to the small dimension in width, the specimen behaved like a beam except during the initial period of contact. In view of the foregoing, the laminate specimen was approximated as a two-dimensional body, and a two-dimensional linear elastic finite program was used to perform the dynamic analysis. The impact load was taken to be uniform across the width of the specimen,

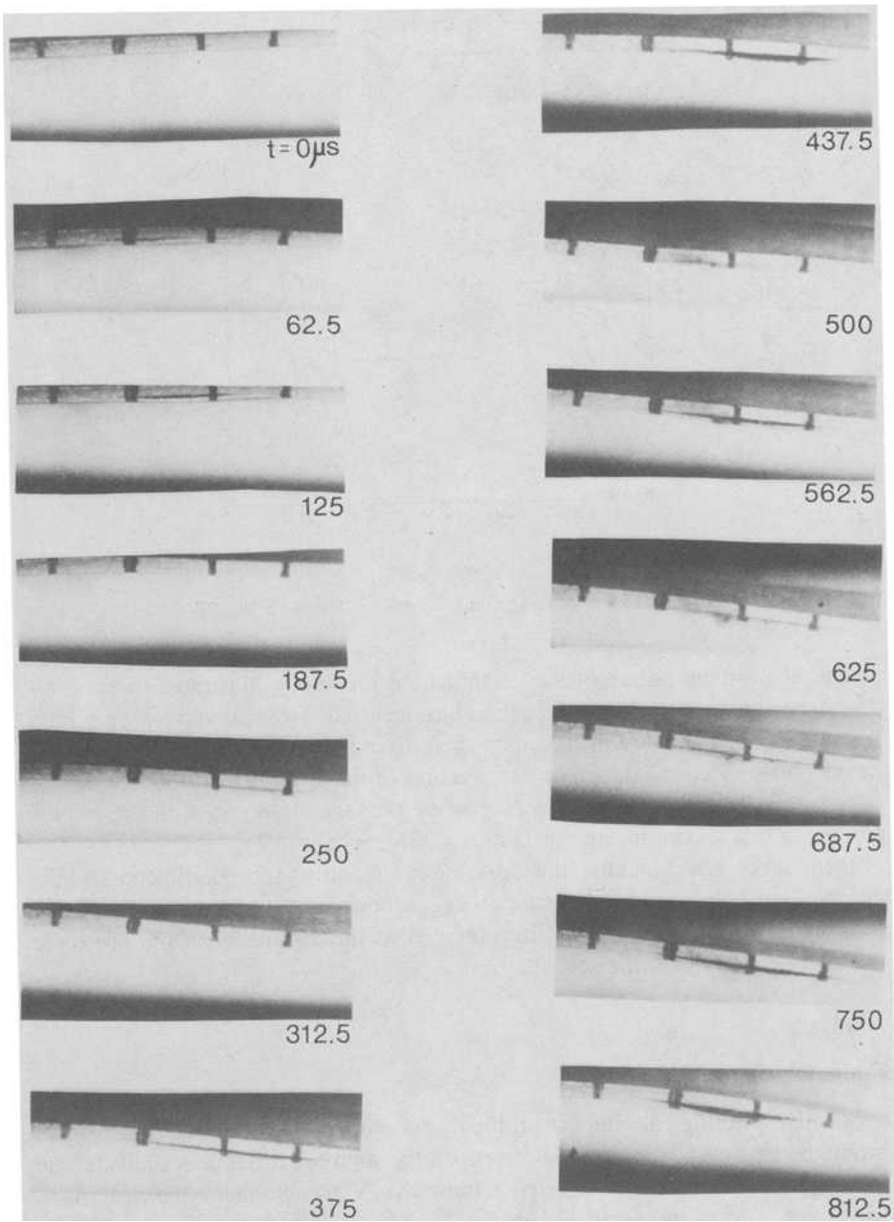

FIG. 8—*Impact response of Specimen No. C4.*

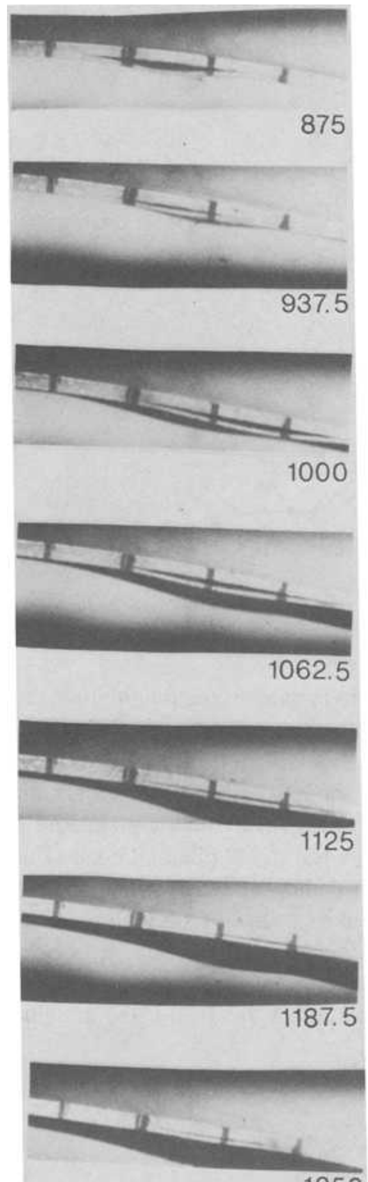

FIG. 8—*Continued.*

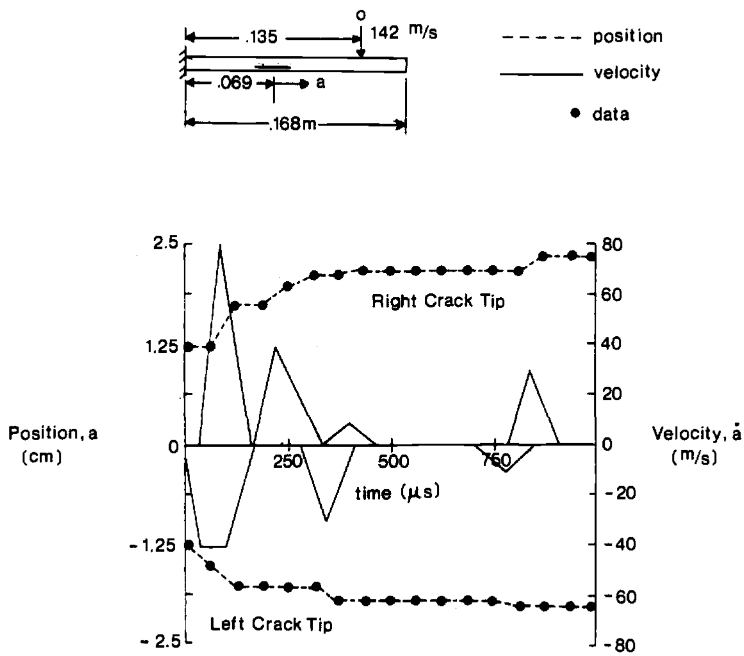

FIG. 9—*Crack-tip position and velocity in Specimen No. C4.*

and a state of plane strain parallel to the longitudinal cross section was assumed. This cross section was then modeled by regular four-node quadrilateral isoparametric finite elements.

Ideally, each lamina should be modeled with a number of finite elements to ensure the best accuracy. However, such a procedure may lead to a formidably large number of elements for the 20-plied laminate. For this reason, the $[90/0]_{5s}$ laminate was transformed into an equivalent homogeneous plate with a set of effective moduli obtained by using appropriate constant strain and constant stress assumptions [*10*]. For this special laminate, it is believed that these effective moduli are quite adequate for long wave motions.

The mechanical properties of the T-300/934 graphite/epoxy are given as

$$E_1 = 134.4 \text{ GPa}$$

$$E_2 = 10.3 \text{ GPa}$$

$$G_{12} = 5.0 \text{ GPa}$$

$$\nu_{12} = \nu_{13} = \nu_{23} = 0.33$$

In addition it was assumed that

$$G_{23} = G_{13} = G_{12}$$

in the numerical analysis. Corresponding effective moduli were

$$\bar{E}_1 = \bar{E}_2 = 72.4 \text{ GPa}$$

$$\bar{E}_3 = 10.3 \text{ GPa}$$

$$\bar{G}_{12} = 5.0 \text{ GPa}$$

$$\bar{\nu}_{13} = \bar{\nu}_{23} = 0.33, \quad \bar{\nu}_{12} = 0.025$$

$$\rho = 1.58 \times 10^{-5} \, N\text{-s}^2/\text{cm}^4$$

where directions 1, 2, and 3 indicate spanwise, width-wise, and thickness-wise directions, respectively. The finite element model was formulated using the above effective properties for the elastic constants of the elements.

Of interest to the present study is finding a parameter that can be used to gage the onset of dynamic delamination crack propagation. A natural choice is the use of dynamic strain energy release rate G, which can be calculated by using the crack-closure energy given by [*11*]

$$G = \lim_{\Delta a \to 0} \frac{1}{\Delta a} \int_0^{\Delta a} (\sigma_{yy} u_y + \sigma_{xy} u_x) dx \qquad (1)$$

where σ_{yy} and σ_{xy} are evaluated at the original crack size a, and u_x and u_y correspond to the extended crack of length $a + \Delta a$. Using the finite element method, the integral in Eq 1 can be carried out by using discrete nodal forces and displacements. Moreover, if a fine mesh is used, that is $\Delta a \ll a$, then crack opening displacements u_x and u_y can be approximated by those for a crack of length a.

The purpose of this analysis was to determine the critical value G_c at which the stationary crack becomes unstable. The time at which the crack starts its movement can be estimated from the high speed film. The corresponding calculated strain energy release rate at this time is taken as G_c.

Verification of the Crack Closure Method

A centrally cracked rectangular panel of homogeneous isotropic material subjected to a uniform tensile step function loading was analyzed by Chen using a finite difference method [*12*]. His solution was used in this study to validate the

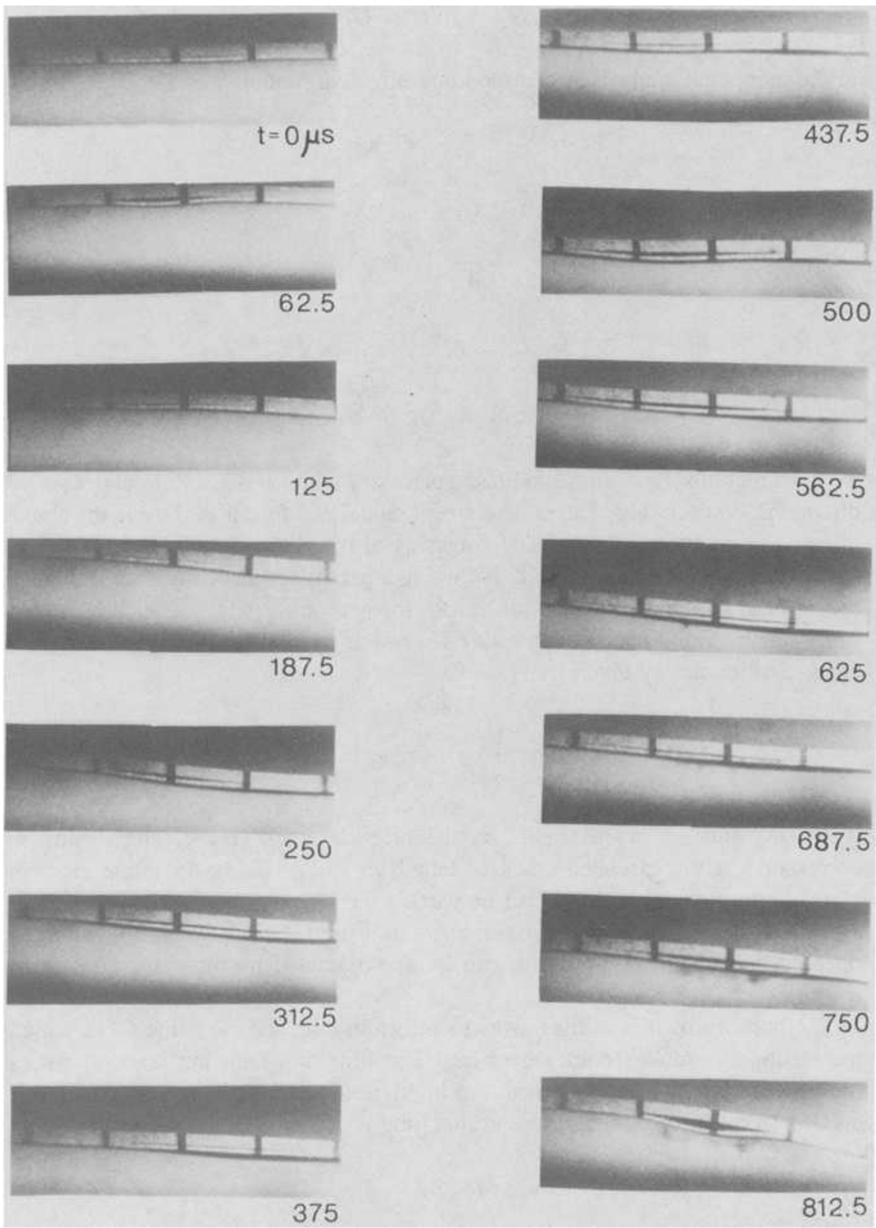

FIG. 10—*Impact response of Specimen No. C7.*

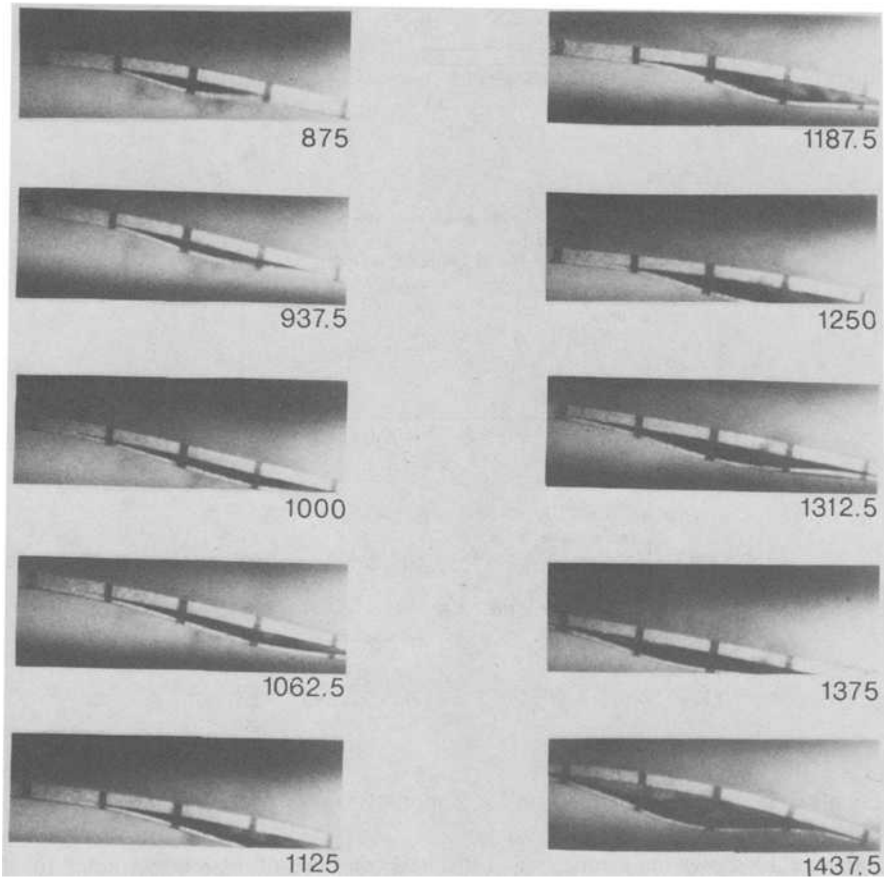

FIG. 10—*Continued.*

aforementioned finite element method in conjunction with the crack closure energy calculation. To compare with Chen's solution, which was presented in terms of stress intensity factors, the following relation for Mode I fracture

$$G_I(t) = \frac{\kappa + 1}{8\mu} K_I^2(t) \tag{2}$$

was used. In Eq 2, μ is the shear modulus, K_I is the Mode I stress intensity factor and

$$\kappa = \begin{cases} 3 - 4\nu & \text{for plane strain} \\ (3 - \nu)/(1 + \nu) & \text{for plane stress} \end{cases}$$

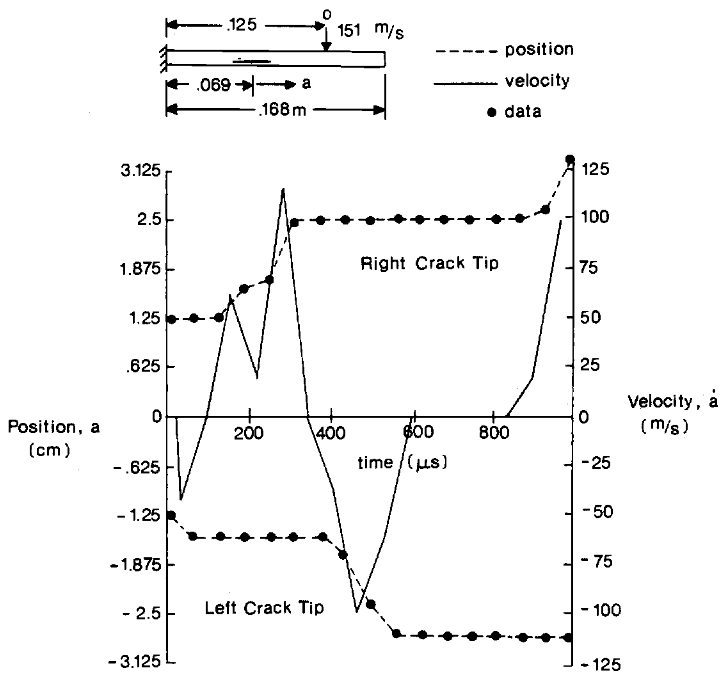

FIG. 11—*Crack-tip position and velocity in Specimen No. C7.*

Equation 2 was shown to be true for stationary cracks under dynamic loading [*13*].

Figure 13 shows the geometry and material constants of the model studied by Chen [*12*]. Due to symmetry, only a quadrant was modeled. Figure 14 shows the histories of the normalized stress intensity factor $\bar{K}_I$, given by

$$\bar{K}_I = \frac{K_I}{P\sqrt{\pi a}} \tag{3}$$

obtained by Ref *12* and by the present method.

Three finite-element meshes were used. The coarse mesh consists of 99 four-node quadrilateral plane strain elements and 221 degrees of freedom. In the critical area near the crack tip, the mesh size yields a ratio of $\Delta a/a = 1/4$. The finer mesh is composed of 323 elements with 682 degrees of freedom and a near-tip mesh size of $\Delta a/a = 1/8$. The third mesh has 841 elements, 1740 degrees of freedom and $\Delta a/a = 1/16$. The result from the third mesh was found to agree very well with that from the second mesh and thus can be considered a converged solution.

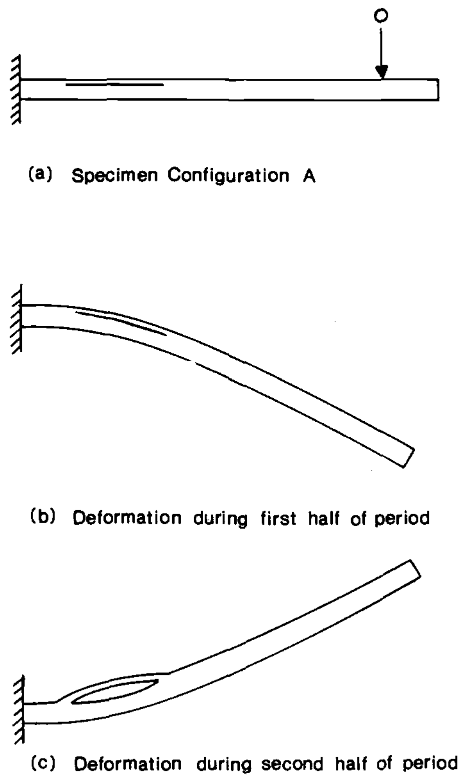

FIG. 12—*Delamination of impact Specimen Configuration A.*

The crack extension step Δa was taken to coincide with the size of the finite element near the crack tip. The integration time steps were $\Delta t = 0.1$ μs for the coarse mesh and $\Delta t = 0.05$ μs for the finer mesh. The comparison presented in Fig. 14 shows that the present method is quite acceptable.

Impact Force

The impact force history $F(t)$ must be specified in the dynamic finite element analysis. In lieu of a direct measurement of the contact force between the impactor and the target composite beam, a simple approximation was used.

Daniel et al *[14]* conducted an impact experiment on boron/epoxy and graphite/epoxy composite laminates using a 7.9-mm-diameter silicon rubber ball as impactor. Although the contact force was not measured, they were able to determine the contact area as a function of time. The contact area versus time curve could be well approximated by a sine function. Although the exact relation between the contact force and contact area is still unknown, it seems reasonable to assume

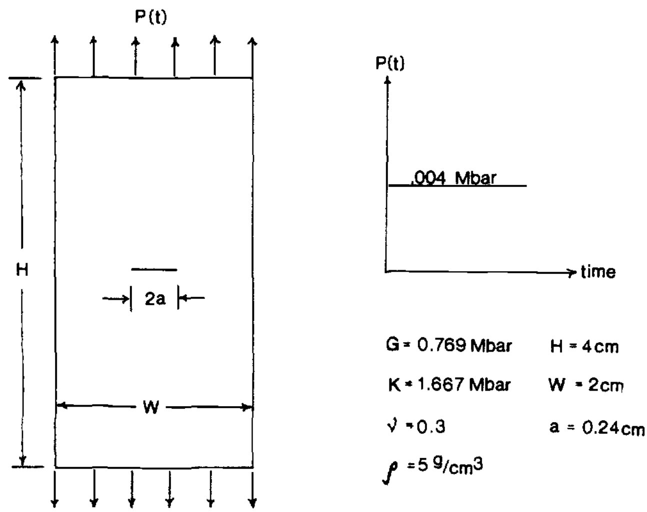

FIG. 13—*Center-cracked panel problem.*

that the contact force can also be approximated by a sine curve as

$$\begin{aligned} F(t) &= F_0 \sin\left(\frac{\pi t}{T}\right) \qquad & 0 < t < T \\ &= 0 & t > T \end{aligned} \tag{4}$$

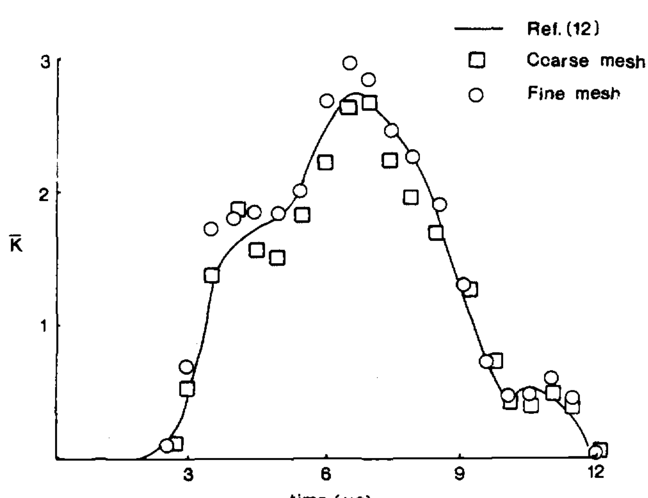

FIG. 14—*Stress-intensity factor for center-cracked panel.*

where T is the contact duration. To determine the unknown coefficients F_0 and T, the following experiment was performed.

An uncracked cantilever beam specimen, shown schematically in Fig. 15, was impacted with the silicon rubber ball at the velocity of 90 m/s. Two strain gages (Micro Measurements EA-06-250BG-120, S_g = 2.03) were mounted on the back side of the specimen to measure the bending strain history. One of the gages was mounted directly opposite the impact point, and the other gage was placed at 5.1 cm away from the first gage. The strain histories measured by these two gages are presented in Figs. 15 and 16.

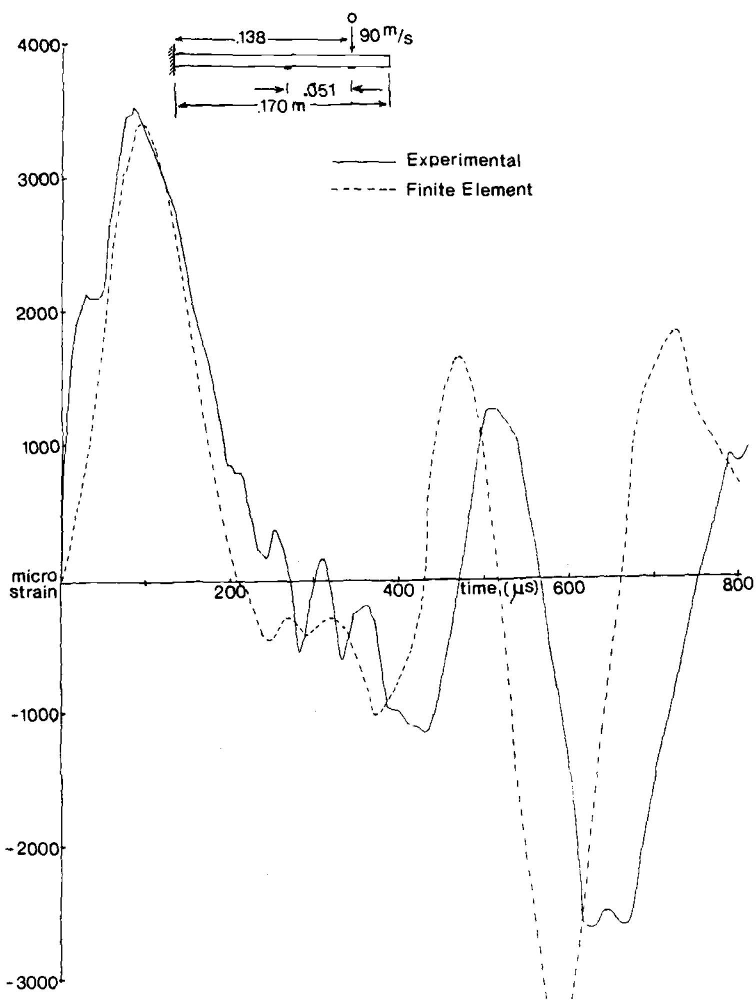

FIG. 15—*Strain history in uncracked beam at impact point.*

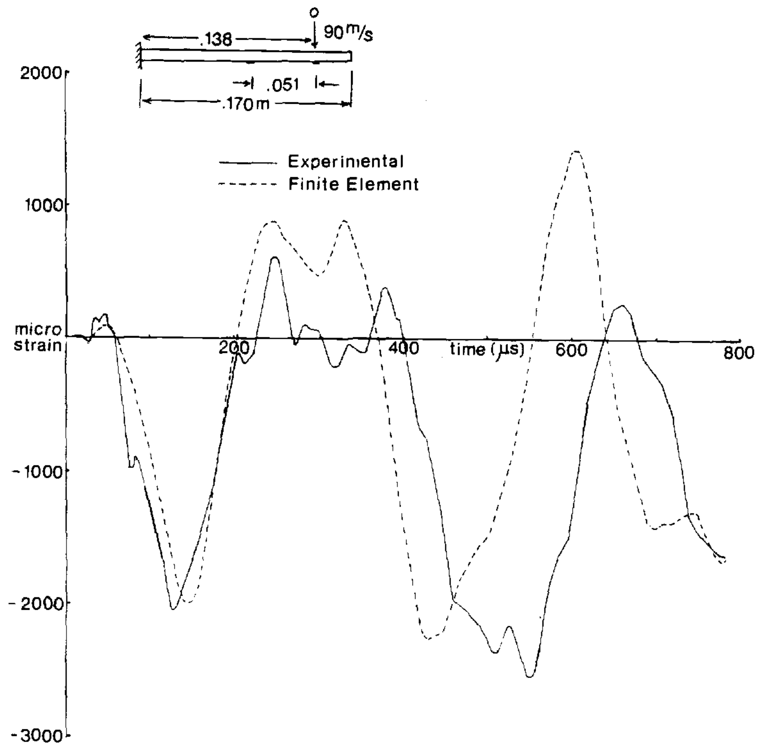

FIG. 16—*Strain history in uncracked beam 5.08 cm from impact.*

The four-node finite elements were then used to model the impacted beam and the strains at the two gage locations calculated. A uniform mesh of 400 elements was found to yield a converged solution and was used to find the values of T and F_0 that best matched the experimental results. The finite element results shown in Figs. 15 and 16 were obtained with $F_0 = 890$ N and $T = 125$ μs. In fitting these values, it was found more convenient to vary T to fit the time-phase and then determine the force amplitude F_0, as the strain is linearly proportional to the amplitude.

To extend the contact force model established for the impact velocity of 90 m/s, the result of a simple spring-mass system was used. In Ref *15*, relations were obtained for a mass impacting an elastic spring

$$F_0 = M_s V_s \sqrt{\frac{K}{M_s + M_T}} \tag{5}$$

and

$$T = \pi\sqrt{\frac{M_s + M_T}{K}}$$

where

F_0 = amplitude of force history,
T = contact duration,
M_s = mass of striker,
M_T = mass of target,
K = spring stiffness, and
V_s = impact velocity.

Thus, when a different impact velocity is used, contact duration is assumed unchanged while amplitude of contact force is assumed to be directly proportional to impact velocity.

Strain Energy Release Rate

As discussed earlier, the delamination crack could become unstable due to buckling of the delaminated plies if the embedded crack was placed near the top or bottom surfaces. In view of this, a midplane-cracked specimen was modeled to compute the strain energy release rate. The particular impact problem analyzed was Specimen No. B6, shown in Figs. 6 and 7. The impact velocity in this case is 155 m/s, which is slightly above the threshold velocity for this specimen configuration. Using Eqs 4–6, the impact force was obtained as

$$\begin{aligned} F(t) &= 1530 \sin\left(\frac{\pi t}{125\ \mu\text{s}}\right)\text{N} \qquad && 0 < t < 125\ \mu\text{s} \\ &= 0 && t > 125\ \mu\text{s} \end{aligned} \tag{6}$$

For this specimen, the camera was oriented to record the propagation of the left crack tip. The crack tip and the impact point were far apart, and only the left crack tip motion was filmed during impact. For this reason, the time at which the ball came in contact with the specimen could not be directly determined from the film. The indirect method described below was therefore used to match the reference time in the finite element analysis (where $t = 0$ measures the instant of initial contact) with that on the high speed film.

First, the finite element program was used to calculate the dynamic response of the specimen subjected to the impulsive force given by Eq 6. The calculated displacement of the left crack tip is plotted as a function of time in Fig. 17. The recorded deflections of part of the beam at a number of discrete times are shown

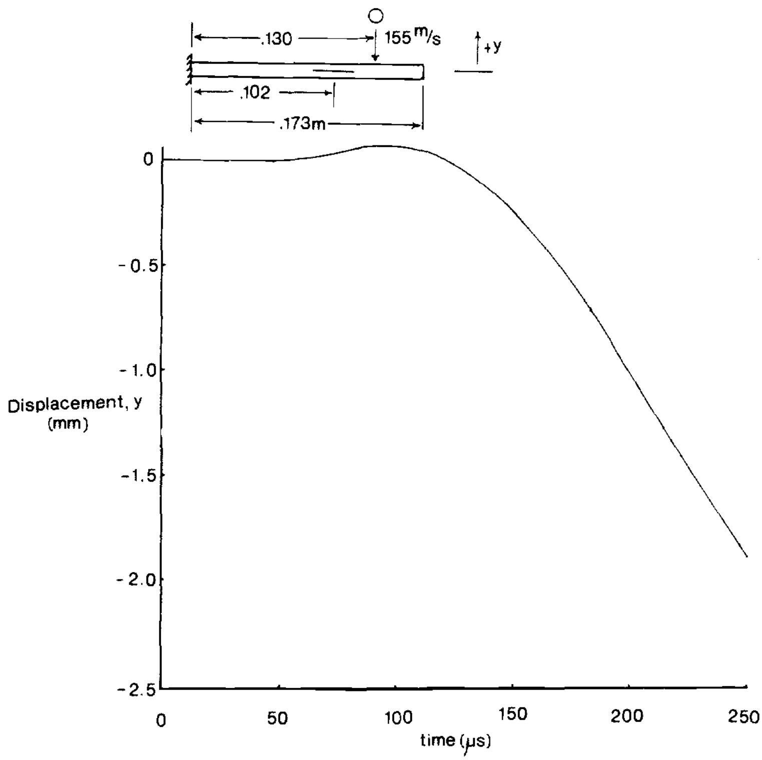

FIG. 17—*Flexural displacement at left crack tip of Specimen No. B6.*

in Fig. 6. From this figure, the displacement of the crack tip at $t = 125$ μs was found to be approximately 1.27 mm. The finite element solution predicts that this displacement would occur at $t = 210$ μs measured from the time of contact. Therefore, the time scale shown in Figs. 6 and 7 should be shifted by 85 μs if $t = 0$ is taken as the time of initial contact.

The finite element mesh used in the calculation of strain energy release rate consists of 648 elements and 1542 degrees of freedom. Near the crack tip of interest, the ratio of the element size to the crack length is $1/100$.

The calculated strain energy release rate is shown in Fig. 18 as a function of time. From the experimental result presented in Figs. 6 and 7, the onset of crack propagation was estimated to have occurred between 62.5 and 125 μs. When the time shift as discussed above is accounted for, this interval is from $t = 147.5$ μs to $t = 210$ μs, which contains the peak of the strain energy release rate versus time curve. It should be noted that, after the crack movement begins, the calculated strain energy release rate is no longer valid.

The precise instant of the onset of dynamic crack propagation cannot be de-

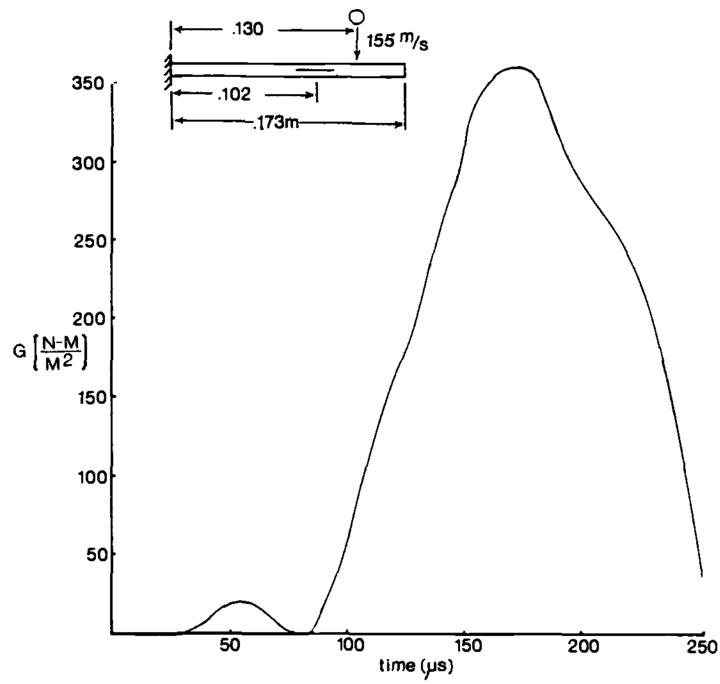

FIG. 18—*Strain energy release rate for Specimen No. B6.*

termined from the experimental results. Since the impact velocity considered is close to the threshold velocity, a good estimate of the critical value of strain energy release rate is the peak value that occurs in the time interval estimated from experimental data. Thus, we take

$$300 \leq G_c \leq 350 \text{ N/m} \tag{7}$$

It should be noted that the value of G calculated here is the total crack closure energy which, in general, includes both Mode I and Mode II contributions, that is

$$G(t) = G_{\text{I}}(t) + G_{\text{II}}(t) \tag{8}$$

In the present calculations, the Mode I contribution to the total crack closure energy, G_{I}, is negligibly small in comparison with the Mode II contribution. This supports the earlier experimental observation that the onset of crack propagation in the midplane-cracked specimens is dominated by a shearing rather than an opening action.

Summary

Dynamic delamination crack propagation behavior in a $[90/0]_{5s}$ graphite/epoxy laminate with an embedded interfacial crack was investigated experimentally using high speed photography. The dynamic motion was produced by impacting the beam-like laminate specimen with a silicon rubber ball. The threshold impact velocities required to initiate dynamic crack propagation in laminates with several delamination crack positions were determined. The crack propagation speeds were also estimated from the photographs.

Experimental results show that through-the-thickness position of the embedded crack can significantly affect the dominant mechanism and the threshold impact velocity for onset of crack movement. If the initial delamination crack is placed near the top or bottom surface of the laminate, local buckling of the delaminated plies may cause instability of the crack. If the precrack lies in the midplane and local buckling does not occur, then the initiation of crack propagation appears to be dominated by Mode II fracture. For Mode I dominated cracks, it was seen that the gross motion (that is, first bending mode) of the impact specimen determines when ply buckling, and hence initiation of fracture, will occur. The crack propagation and arrest observed were seen to be dependent on wave reflections from the boundaries, and on wave propagation within the delaminated region.

Ideally, once a suitable criterion for the initiation and propagation of delamination cracks is established, experimental results shown here could be duplicated by some analysis such as finite element modeling. It is apparent, however, that relatively few of the fracture mechanisms involved here are amenable to analysis by conventional finite element methods. Therefore, the most fundamental analysis of the data must necessarily be restricted to midplane crack geometries, which do not involve the buckling action associated with the remaining cases.

A simplified finite element analysis of the experimental data obtained from one of the midplane-cracked specimens was used to obtain a preliminary estimate of the critical strain energy release rate for this material. This parameter may determine the onset of unstable crack propagation.

Acknowledgment

This paper was prepared in the course of research sponsored by NASA Lewis Research Center under Grant No. NAG 3211.

References

[*1*] Sendeckyj, G. P., Stalnaker, H. D., and Kleismit, R. A. in *Fatigue of Filamentary Composite Materials, ASTM STP 636,* K. L. Reifsnider and K. N. Lauraitis, Eds., American Society for Testing and Materials, Philadelphia, 1977, pp. 123–140.

[*2*] Rodini, B. T. and Eisenmann, J. R. in *Fibrous Composites in Structural Design,* Plenum Press, New York, 1980, pp. 441–457.

[*3*] Raju, I. S. and Crews, J. H., Jr., *Computers and Structures,* Vol. 14, No. 1–2, 1981, pp. 21–28.

[4] Crossman, F. W. and Wang, A. S. D. in *Damage in Composite Materials, ASTM STP 775*, K. L. Reifsnider, Ed., American Society for Testing and Materials, Philadelphia, 1982, pp. 118–139.
[5] Roderick, G. L., Everett, R. A., and Crews, J. H. in *Fatigue of Composite Materials, ASTM STP 569*, American Society for Testing and Materials, Philadelphia, 1975, pp. 295–306.
[6] Rybicki, E. F., Schmueser, D. W., and Fox, J., *Journal of Composite Materials*, Vol. 11, 1977, pp. 470–487.
[7] Wang, A. S. D. and Crossman, F. W., *Journal of Composite Materials*, Supplementary Vol. 14, 1980, pp. 71–106.
[8] O'Brien, T. K. in *Damage in Composite Materials, ASTM STP 775*, K. L. Reifsnider, Ed., American Society for Testing and Materials, Philadelphia, 1982, pp. 140–167.
[9] Wilkins, D. J., Eisenmann, J. R., Camin, R. A., Margolis, W. S., and Benson, R. A. in *Damage in Composite Materials, ASTM STP 775*, K. L. Reifsnider, Ed., American Society for Testing and Materials, Philadelphia, 1982, pp. 168–183.
[10] Jones, R. M., *Mechanics of Composite Materials*, McGraw-Hill, New York, 1975, pp. 40–41.
[11] Erdogan, R. in *Fracture II*, H. Liebowitz, Ed., Academic Press, New York, 1968, pp. 498–592.
[12] Chen, Y. M., *Engineering Fracture Mechanics*, Vol. 7, 1975, pp. 653–660.
[13] Nilsson, F., *Journal of Elasticity*, Vol. 4, No. 1, 1974, pp. 73–75.
[14] Daniel, I. M., Liber, T., and LaBedz, R. H., *Experimental Mechanics*, Vol. 19, No. 1, 1979, pp. 9–16.
[15] Goldsmith, W., *Impact: The Theory and Physical Behaviour of Colliding Solids*, Edward Arnold Publishing, London, 1960.

C. David Shirrell[1] *and Mary G. Onachuk*[1]

Influence of Mold Coverage upon the Notch Strength of R25 Sheet Molding Compounds

REFERENCE: Shirrell, C. D. and Onachuk, M. G., "**Influence of Mold Coverage upon the Notch Strength of R25 Sheet Molding Compounds,**" *Composite Materials: Fatigue and Fracture, ASTM STP 907,* H. T. Hahn, Ed., American Society for Testing and Materials, Philadelphia, 1986, pp. 32–50.

ABSTRACT: The influence of a processing variable, mold coverage, upon two 25% by weight randomly oriented 2.54-cm-long glass fiber reinforced sheet molding compounds (R25 SMCs) was examined. Artificially created flaws, in the form of machined circular notches, were utilized to determine the effect of mold coverage upon the naturally occurring tensile flaw sites in these materials. The critical hole size (that size circular notch through which all specimens fail) was found to be 9.53 mm. Variations in mold coverage from 97.5 to 25% were observed to have virtually no effect upon this critical hole size. Thus, the most severe tensile critical flaw sites in R25 SMC appear to be unrelated to mold coverage. A comparison of the two R25 SMC's indicates that a rubber toughening agent reduces slightly the notch sensitivity of isophthalic polyester resin matrix sheet mold compounds. Within experimental error, the two-parameter notch strength model of Whitney-Nuismer was found to accurately describe the notch sensitivity of R25 SMC.

KEY WORDS: sheet molding compounds, random discontinuous composites, composites variability, notch strength of composites

The increasing use of sheet molding compounds (SMCs) in lightly loaded automotive structural components coupled with their potential application in more highly loaded structural elements has focused added attention upon the need to eliminate the substantial variability in mechanical properties of this polymeric composite material. Before this can be accomplished, it is first necessary to develop an understanding of the microstructural causes of this variability.

While the microstructural origins of flexural critical flaw sites in SMC have recently been investigated [*1*], only very little information about the tensile critical flaw sites in this material is available [*2*]. Furthermore, virtually no information

[1] Staff research engineer and senior science assistant, respectively, Polymers Department, General Motors Research Laboratories, General Motors Technical Center, Warren, MI 48090-9055. Mr. Shirrell is presently with the Polymer Systems Department of the Shell Development Co., Houston, TX 77001.

has been published relating processing variables and the microstructural origins of tensile failures in SMC [3]. In an attempt to begin to resolve this situation, we have initiated a study of the influence of SMC processing variables upon the microstructural origins of tensile failures in SMC.

One of the most important processing variables involved in the fabrication of SMC structures is the flow of this material during its compression molding cycle. Typically, during compression molding a selected amount of uncured SMC (that required to yield the exact volume of the cured component) is center-charged into a preheated compression mold. The mold is then closed and the curing SMC material is forced into the shape of the compression mold cavity.

Since it is well known that extensional flow of discontinuous composites affects the microstructure of these materials (and their resulting mechanical properties) [4–6], it is possible that flow of SMC during the compression molding process also affects the flaw sites in this material. The extent of flow (that is, the length of flow) of the SMC material in a compression mold is usually designated "mold coverage." Thus, 50% mold coverage implies that 50% of the surface area of the compression mold cavity (located in the center of the mold) was covered with uncured SMC before the mold was closed.

As the mold coverage increases, the extent of flow of the SMC decreases. Due to the complexity of SMC flow in compression molds, the actual distance that the SMC moved at any given point in the mold is not known with certainty.

This paper discusses the use of artificially created flaws, in the form of machined circular notches, to determine the effect of mold coverage upon the naturally occurring tensile flaw sites in two polyester resin based R25 SMCs.

Investigation

Material Fabrication

The R25 SMC materials used in this study came from two commercial sources. Material I utilized an isophthalic polyester as its resin matrix, while Material II was formulated with a rubber-toughened polyester resin. The details of the formulation of Material I can be found in Ref 7.

Both of these SMC materials were molded in the form of flat plaques with cured dimensions of 533 by 610 by approximately 3.4 mm (21 by 24 by 0.13 in.). The molding procedure consisted of charging approximately 2060 g (4.5 lb) of the uncured SMC material into a compression die preheated to 149°C (300°F) and applying a pressure of 6.9 MPa (1000 psi). The materials were held at their respective cure temperatures and pressures for 120 s. Both were center-charged in the mold cavity with the various mold coverage dimensions given in Table 1. To maintain an approximate plaque thickness of 3.4 mm (0.13 in.), it was necessary to use two layers of uncured SMC for 50% mold coverage and four layers for 25% mold coverage. After molding, all of the cured plaques were visually examined for defects. None were observed.

TABLE 1—*Mold coverages utilized.*

Mold Coverage, %	Charge Dimensions, mm	Material I	Material II
97.5	527 × 603	X	X
90	483 × 546	...	X
75	457 × 508	...	X
50	381 × 432	X	X
25	267 × 305	X	X

Specimen Fabrication

The cured SMC plaques were first cut into straight-sided tensile blanks using the template shown in Fig. 1 and then machined into their final dimensions using a Tensil-Kut router (Fig. 2). As shown in Fig. 1, no gage section of the tension specimens was within 20 mm (0.787 in.) of the edge of the SMC plaques. Thus, the extreme anisotropy often found near the edges of SMC plaques did not affect the results of this study. All specimens were numbered according to the plaque from which they were cut and their specific location on each plaque. Specimens from both of the SMC materials were sorted into the test matrix by means of a computer-generated list of random numbers. This procedure was utilized in order to eliminate the possibility of potential systematic plaque-to-plaque variations from influencing the results of the study.

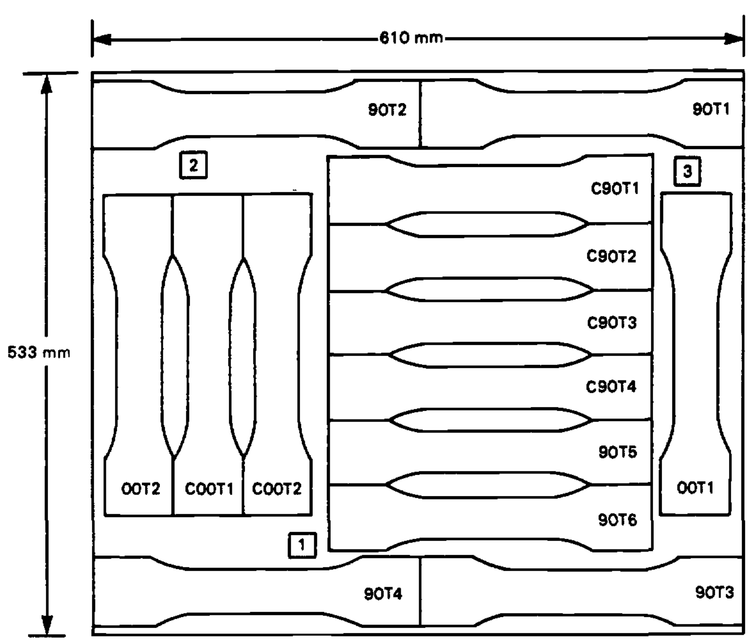

FIG. 1—*Plaque template used for R25 SMC mold coverage plaques.*

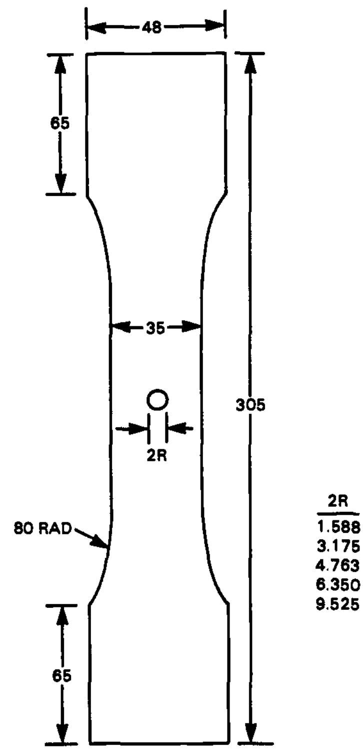

FIG. 2—*Circular notched tension specimen used for R25 SMC material (all dimensions in mm).*

The circular notches shown in Fig. 2 were machined in each specimen by initially drilling a starter hole of diameter 1.58 mm (1⁄16 in.) with a tungsten carbide bit. This hole was then carefully enlarged to its final dimensions by incremental grinding using diamond-edged tools. [The 1.58-mm (1⁄16 in.) circular notches used in this study were created by simply drilling.] As verified by visual inspection and burned-off specimens, this method for fabricating the circular notches prevented damage to the SMC test specimens larger than that of the created flaw (that is, the circular hole). After machining, the tension specimens were cleaned and sealed in polyethylene bags. The numbers of specimens tested with each combination of mold coverage and hole size used in this study are given in Table 2.

Chemical Testing Procedures

Density, resin, filler, fiber, and void contents of the SMC materials were determined for each of the panels used in the study. The details of these test procedures have been described previously [*8*] and the results are given in Table 3.

TABLE 2—*Number of specimens utilized in the test matrix.*

Mold Coverage, %	Circular Notch Diameter, mm						
	0	1.59	3.18	4.76	6.35	9.53	12.7
			MATERIAL I				
97.5	9	9	9	9	9	9	9
50	9	9	9	9	9	9	9
25	9	9	9	9	9	9	9
Total = 189							
			MATERIAL II				
97.5	8	4	3	5	4	4	...
90	5	5	5	5	4	4	...
75	5	5	5	5	4	4	...
50	5	5	5	5	4	4	...
25	5	4	5	5	5	4	...
Total = 140							

TABLE 3—*Chemical analysis of the R25 SMC panels.*

Mold Coverage, %	No. of Specimens Tested	Density, g/cm^3	Resin Content, weight %	Filler Content, weight %	Fiber Content, weight %	Calculated Void Content,[a] volume %
			MATERIAL I			
25	6	1.74(0.01)[b]	31.8(0.7)	44.1(1.1)	24.1(1.6)	3.6(0.4)
50	6	1.75(0.02)	32.4(0.8)	44.6(1.5)	23.1(1.8)	3.0(0.5)
75	6	1.74(0.01)	31.9(0.6)	44.6(0.9)	23.6(1.4)	4.1(0.5)
90	6	1.72(0.02)	32.5(0.4)	44.3(2.0)	23.2(2.3)	4.3(0.8)
97.5	6	1.75(0.01)	32.4(0.4)	45.2(0.8)	22.4(1.1)	2.9(0.3)
			MATERIAL II			
25	8	1.87(0.02)	28.1(1.0)	44.3(1.6)	27.6(1.9)	6.6(1.0)
50	8	1.88(0.02)	28.0(0.9)	42.1(2.0)	29.9(2.9)	5.9(0.3)
97.5	8	1.86(0.02)	28.6(0.5)	42.4(2.6)	29.0(2.6)	6.6(0.8)

[a]For these calculations, the following values were used: ρ(resin, Material I) = 1.06 g/cm^3; ρ(resin, Material II) = 1.21 g/cm^3; $\rho(CaCO_3)$ = 2.80 g/cm^3; and ρ(glass fiber) = 2.54 g/cm^3.

[b]This number is the average of the quantity; the value in parentheses is the estimated standard deviation of the quantity calculated by the N-1 method.

Mechanical Testing Procedures

Prior to mechanical testing, all specimens were maintained at 63°C (145°F)/ 0% relative humidity until they reached a constant weight (approximately 30 days). The circular notched tensile specimens were then tested at room temperature [21°C (70°F)] in uniaxial tension on an Instron Universal testing machine at a loading rate of 5 mm/min.

Results and Discussion

It is well known that notches reduce the tensile strength of continuous filament composite materials [*9–13*]. Several investigators [*14–19*] have also demonstrated that the tensile strength of SMC materials is influenced by the presence of this type of a stress concentrator. While the majority of the work in this area has emphasized the effect of notches upon the design of composite structures, the creation of machined circular flaws in SMC tension specimens can also be used to obtain an understanding of the naturally occurring tensile flaw sites in this material. Furthermore, this experimental technique can also be useful in determining the effect of processing variables such as mold coverage upon these SMC tensile flaw sites.

By creating a set of tension specimens, each with successively larger machined circular notches than its predecessor, information about the severity of the tensile flaw sites in a material can be obtained. Usually, the specimens with very small circular notches fracture at locations other than through these created flaws. This implies that the severity of the naturally occurring flaws in the material is greater than that of the artificially created flaw.

As the size of these created circular notches is increased, more and more of the specimens fracture through this artificial flaw. Eventually a "critical hole size" is reached where all of the specimens fracture through the created circular notch. The distribution in severity of the naturally occurring tensile flaw sites in the material can be determined by observing the rate of increase of specimen failure through the created flaw as a function of increasing circular notch size. The critical hole size provides experimental insight into the nature of the most severe tensile flaw site in a material.

By convention, in a set of specimens with step increases in hole sizes, the critical hole size is defined as the smallest hole through which all of the specimens failed. In reality, this type of testing procedure provides a range in which the critical hole size must lie. The conventional definition of critical hole size is used in this paper.

As shown in Table 4, the most severe tensile flaw sites in the two R25 SMC materials examined in this study appear to be relatively insensitive to mold coverage. Only Material II, with a 25% mold coverage, exhibited a critical hole size other than 9.53 mm (0.37 in.). These data show that flow of the uncured SMC material during molding (of center-charged flat panels) does not affect the tensile critical flaws in this type of random discontinuous composite. Thus, the

TABLE 4—*Observed critical hole sizes.*

Mold Coverage, %	Critical Hole Size, mm
MATERIAL I	
97.5	9.53
50	9.53
25	9.53
MATERIAL II	
97.5	9.53
90	9.53
75	9.53
50	9.53
25	>9.53

tensile critical flaws in these R25 SMC materials must have originated from other source(s) such as the curing process, thermal quenching after curing, or they may have existed in the uncured SMC before molding.

Notched Strength Models for Composite Materials

Two models have been developed to predict the effect of notches, either circular or slit, upon the tensile strength of composite materials. The first model, developed by Waddoups [9], employs the principle of linear elastic fracture mechanics (LEFM). It is based upon the premise that a material constant known as the "characteristic dimension," a, exists which governs the notch strength of composite materials. Recently, this assumption has been shown to be invalid [20].

The second model for predicting the effect of notches upon the tensile strength of composite materials was developed by Whitney and Nuismer [21,22] as an alternative to the LEFM model. This two-parameter model was essentially identical to the one proposed by Waddoups but requires the knowledge of the finite stress distribution in the vicinity of the notch. The specimen is assumed to fail when the stress at some characteristic distance (d_0) from the tip of the notch reaches the unnotched tensile strength of the laminate. In the Whitney-Nuismer model, d_0 is assumed to be a constant for all notch sizes. Recently, Wang et al [23] have shown that this characteristic length is not a constant in SMC materials. Thus, the use of this model to evaluate the notch strengths of R25 SMC may be questionable. Pipes et al [20] extended the Whitney-Nuismer model and introduced a three-parameter notch strength model which takes into consideration the effect of a stress concentration factor, K_T^∞ (important for predicting crack growth), the notch sensitivity factor C (a measure of the effect of K_T^∞ in reducing notch strength), and an exponential parameter, m (which describes the influence of notch size upon notch strength).

The influence of the radius, R, of an unloaded circular notch upon the strength of a composite laminate of infinite width is given by [20]

$$\sigma_R^{\infty}/\sigma_0 = 2\{2 + f(R)^{-2} + 3f(R)^{-4} - (K_T^{\infty} - 3)[5f(R)^{-6} + 7f(R)^{-8}]\}^{-1} \quad (1)$$

where

$$f(R) = [1 + R^{m-1} R_0^{-m} C^{-1}] \quad (2)$$

and

σ_0 = unnotched composite tensile strength,
σ_R^{∞} = notched composite tensile strength of a laminate of infinite width, and
R_0 = reference circular notch radius, 2.54 cm (1 in.).

The stress concentration factor K_T^{∞} can be expressed as a function of a material's orthotropic properties

$$K_T^{\infty} = 1 + \sqrt{2(\sqrt{E_y/E_x} - \nu_{yx} + E_y/G_{yx})} \quad (3)$$

where

E_x = transverse Young's modulus,
E_y = longitudinal Young's modulus,
ν_{yx} = Poisson's ratio,
G_{yx} = inplane shear modulus, and
y = loading axis of the material.

For isotropic materials [20]

$$K_T^{\infty} = 3 \quad (4)$$

and

$$\sigma_R^{\infty}/\sigma_0 = 2\{2 + f(R)^{-2} + 3f(R)^{-4}\}^{-1} \quad (5)$$

While SMC materials are not necessarily isotropic [18,24], a study of the anisotropy of the two R25 SMC panels used in this paper (see Refs *1* and *8*) demonstrated that they were isotropic. Thus, Eq 5 can be used to analyze the data collected in this study.

The relationship between the experimentally measured ratio of strengths from tension specimens and that ratio of strengths in a composite laminate of infinite width is

$$\sigma_R^{\infty}/\sigma_0 = (\mathrm{FWC})(\sigma_R/\sigma_0) \quad (6)$$

where FWC is the finite-width correction and σ_R the observed tensile strength of a specimen containing a circular notch of radius R. The value of FWC can be calculated from either of the following equations [*25,26*]

$$\mathrm{FWC} = 1 - 0.05\lambda + 1.5\,\lambda^2 \tag{7}$$

or

$$\mathrm{FWC} = \frac{2 + (1 - \lambda)^3}{3(1 - \lambda)} \tag{8}$$

where

$$\lambda = 2\,R/W \qquad (\lambda \leq 0.5) \tag{9}$$

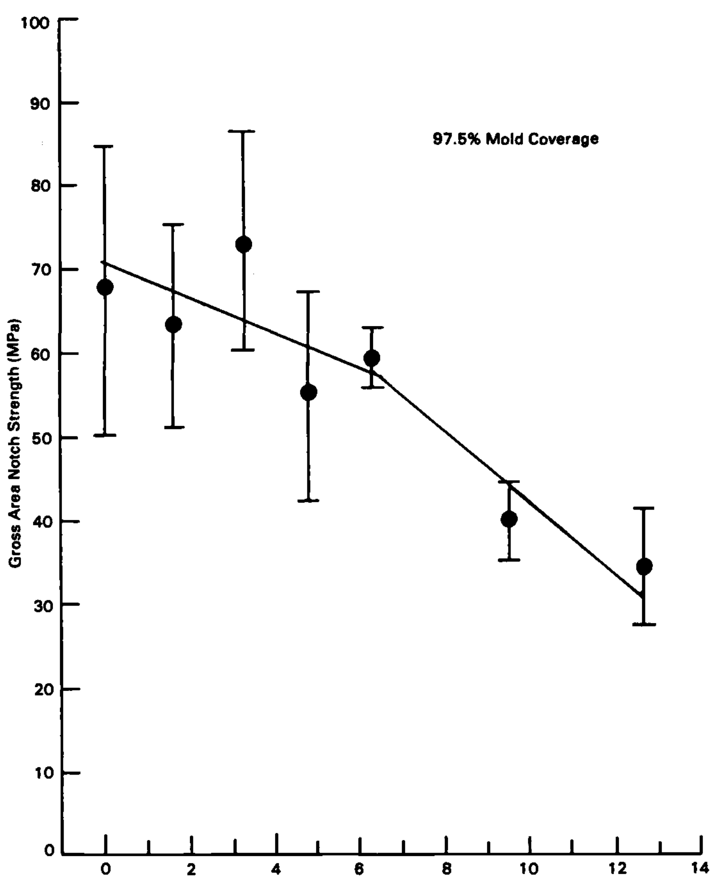

FIG. 3—*Effect of circular notched hole diameter upon gross area notch strength of Material I fabricated with 97.5% mold coverage.*

and W is the specimen width [2.54 cm (1 in.) for the specimens used in this study]. Equations 7 and 8 give virtually identical values of FWC for the values of λ used in this study.

It is possible to shift the notch strength relation given in Eq 1 to a master curve for all materials. The magnitude of this shift is a measure of the relative notch sensitivity for a particular material. The reference system that has been commonly chosen for the master curve is $m = 0.0$, $C = 25.4\ \text{mm}^{-1}$ and $R = 2.54$ mm [*17*]. The relative notch sensitivity factor, R_{ns}, can then be given by

$$R_{ns} = m + \log_{10} C \tag{10}$$

Influence of Mold Coverage upon Strength of R25 SMC Tension Specimens Containing Circular Notches

The effect of circular notches upon the gross area notched tensile strength of the R25 SMC materials (97.5% mold coverage) is shown in Figs. 3 and 4. (For brevity, only a small amount of the data collected are presented herein; unless otherwise noted, both of the SMC materials exhibited similar results.) The gross

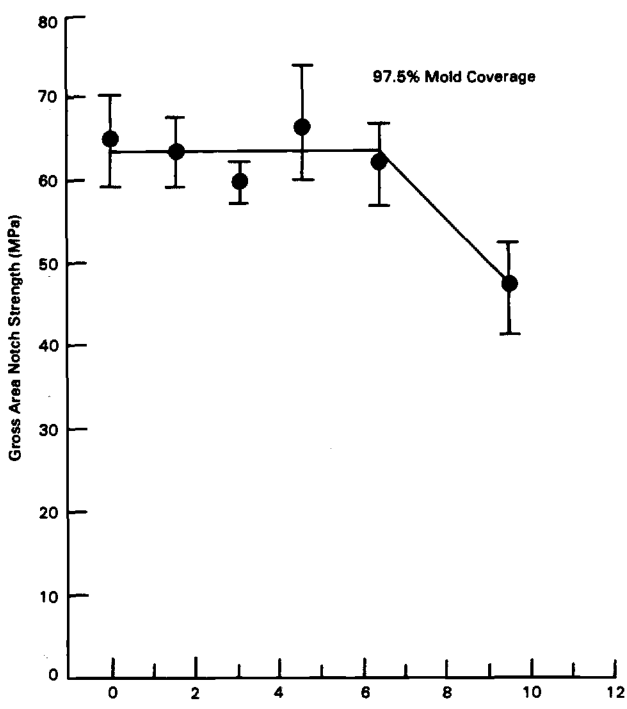

FIG. 4—*Effect of circular notched hole diameter upon gross area notch strength of Material II fabricated with 97.5% mold coverage.*

area notched strength values shown in these figures do not take into consideration the loss of specimen cross-sectional area due to the removal of the SMC material in the circular notch. In addition, the scatter bars in these figures represent one estimated standard deviation from the average value of each set of data.

The strength of Material I appears to decrease gradually with increasing hole size until the critical hole size is reached, 9.53 mm (0.37 in.), whereupon the strength decreases sharply. Due to the large scatter in the observed notched tensile strengths of this material, the gradual decrease in strength below the critical hole size may not be real. Figure 5 shows a representative set of fractured specimens. Upon examination, the failures in the test specimens with small machined holes were found to occur randomly throughout the test section. As the critical hole size was approached, more and more of the specimens fractured through the circular hole. The influence of mold coverage upon the percent of specimens fracturing through the hole is shown in Figs. 6 and 7.

The influence of mold coverage upon the percent of Material II specimens which fractured through their hole is shown in Figs. 8 and 9. No clear trends relating mold coverage and the severity of the flaw sites less than the critical

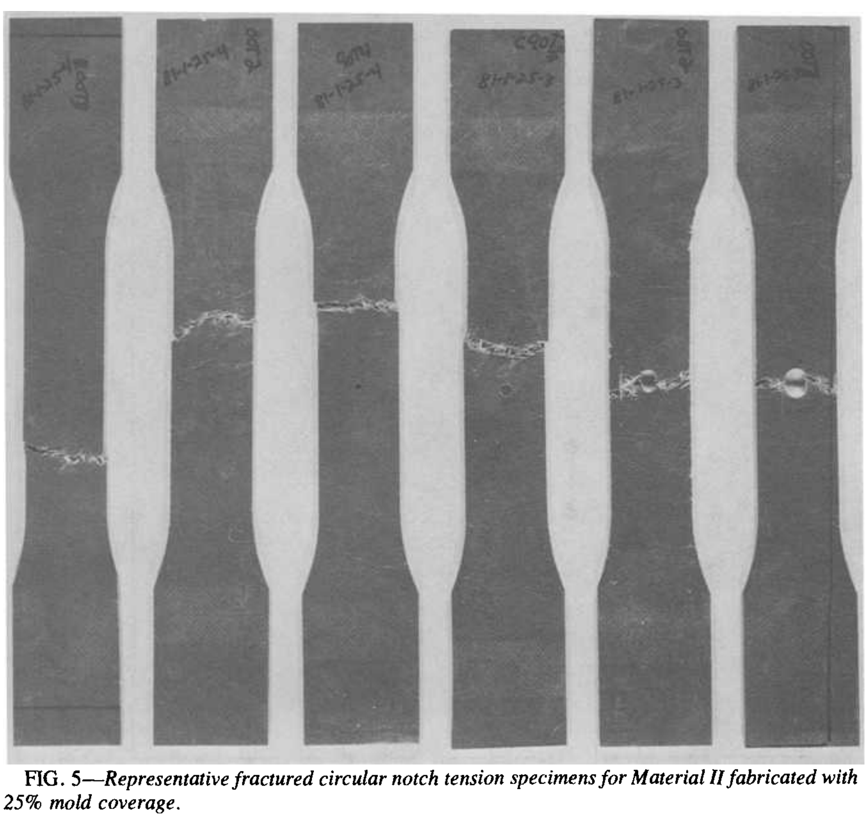

FIG. 5—*Representative fractured circular notch tension specimens for Material II fabricated with 25% mold coverage.*

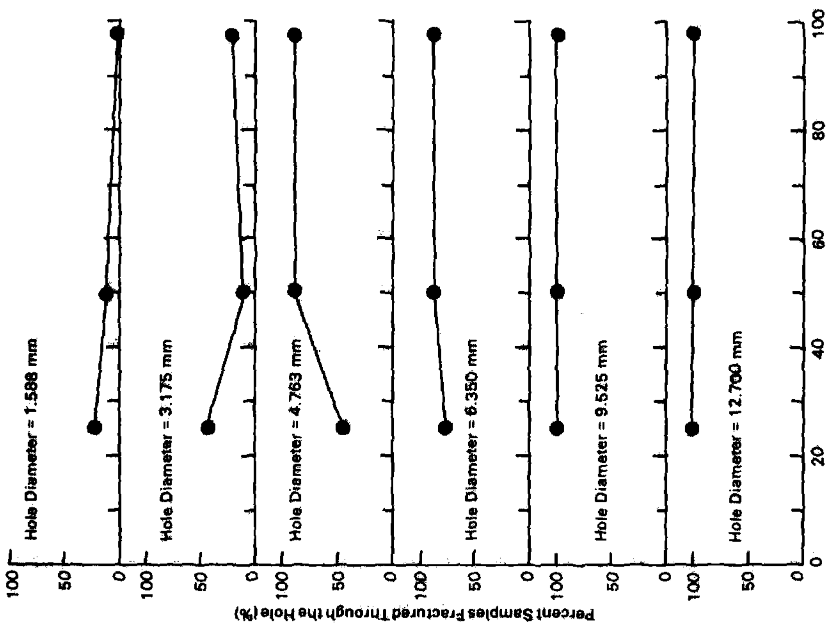

FIG. 7—*Effect of mold coverage upon percent of Material I tension specimens failing through various hole diameters.*

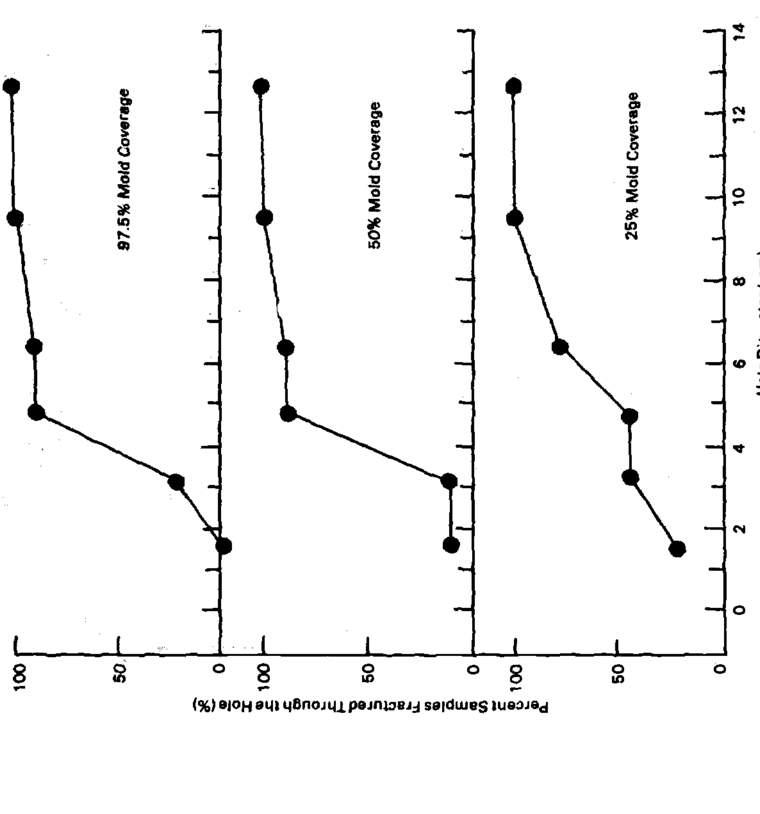

FIG. 6—*Effect of hole diameter upon percent of Material I tension specimens failing through holes of specimens fabricated with different mold coverages.*

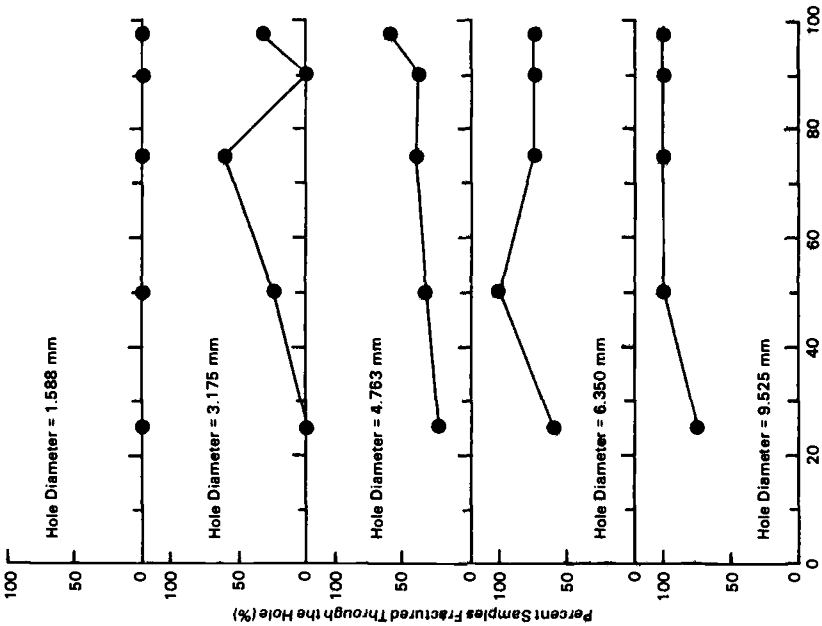

FIG. 9—*Effect of mold coverage upon percent of Material II tension specimens failing through various hole diameters.*

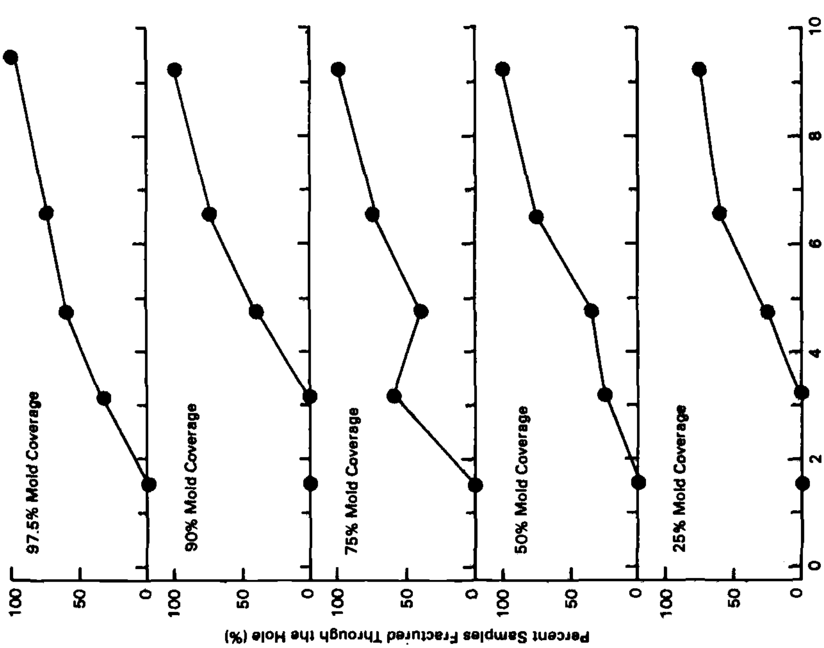

FIG. 8—*Effect of hole diameter upon percent of Material II tension specimens failing through holes of specimens fabricated with different mold coverages.*

hole size can be observed in Figs. 6 through 9. The number of test specimens at each mold coverage and hole size used in this study (Table 2) appears to be insufficient to accurately establish the existence or absence of any such relationship for the SMC materials examined. However, the most severe tensile flaw sites, that is, the ones identical to the critical hole size, were found to be unaffected by mold coverage.

Modeling the Notch Strength of R25 SMC Materials

To utilize Eq 5 to predict the notch strength of the two SMC materials examined, it is first necessary to obtain the values of m and C which yield the best fit to the experimental data, $(\overline{\sigma_R^{\infty}}/\overline{\sigma_0})_{\text{obs}}$, for each mold coverage. The values of $(\overline{\sigma_R^{\infty}}/\overline{\sigma_0})_{\text{obs}}$ can be calculated from Eq 6 given the observed values of the average gross area notch strengths, $\overline{\sigma_R}$, and the average value of the unnotched strength, $\overline{\sigma_0}$, for each set of mold coverage tension specimens. Equation 6 also requires a value for FWC which can be computed using both Eq 8 and Eq 9.

In addition, Eqs 5 and 2 can be employed to formulate an equation for $(\sigma_R^{\infty}/\sigma_0)_{\text{calc}}$ in terms of C and m. The values of C and m can then be numerically iterated to yield a value of $(\sigma_R^{\infty}/\sigma_0)_{\text{calc}}$ which minimizes the expression

$$\sum_{n=1}^{m} \left|(\sigma_R^{\infty}/\sigma_0)_{\text{calc},n} - (\overline{\sigma_R^{\infty}}/\overline{\sigma_0})_{\text{obs},n}\right| \tag{11}$$

where n is the running index number. Each value of n corresponds to a value of R utilized in the study. A digital computer program was employed to simplify the laborious calculations involved in this procedure.

The calculated values of m and C that gave the best fit to the experimental data observed are given in Table 5. Using these values, the calculated relationship between $(\sigma_R^{\infty}/\sigma_0)_{\text{calc}}$ and log radius along with the corresponding observed values of $(\overline{\sigma_R^{\infty}}/\overline{\sigma_0})_{\text{obs}}$ is plotted (for mold coverage of 50%) in Figs. 10 and 11.

Notch Sensitivity of R25 SMC

As demonstrated by these figures, the two R25 SMC materials examined in this study are relatively notch insensitive. This reduced notch sensitivity is a direct result of the large number and the severity of the naturally occurring tensile critical SMC flaw sites which are present in the material.

In the three-parameter model of Pipes et al [*20*], the effect of notch size upon the notch strength is apparent through both the notch sensitivity factor, C, and the exponential factor, m. The values of these parameters for the data collected herein plus two others in the literature are compared in Table 5. As is readily apparent from the results presented in this table, eight of the ten data sets have values of m equal to zero. Of the remaining two data sets, Material I at 97.5% mold coverage and Material II at 50% mold coverage both gave values of the

TABLE 5—*Computed values of* C *and* m.

Mold Coverage, %	m	$C(cm^{-1})$	R_{ns}
	MATERIAL I		
97.5	0.32	1.70	0.55
50	0	3.26	0.51
25	0	2.54	0.40
	MATERIAL II		
97.5	0	2.41	0.38
90	0	2.30	0.36
75	0	0.51	−0.29
50	0.5	0.46	0.16
25	0	0.51	−0.29
	OCF 920 [15]		
Unknown	0	0	0
	SOMMERVILLE INDUSTRIES LTD., G-1005-30 [16]		
Unknown	0	0	0

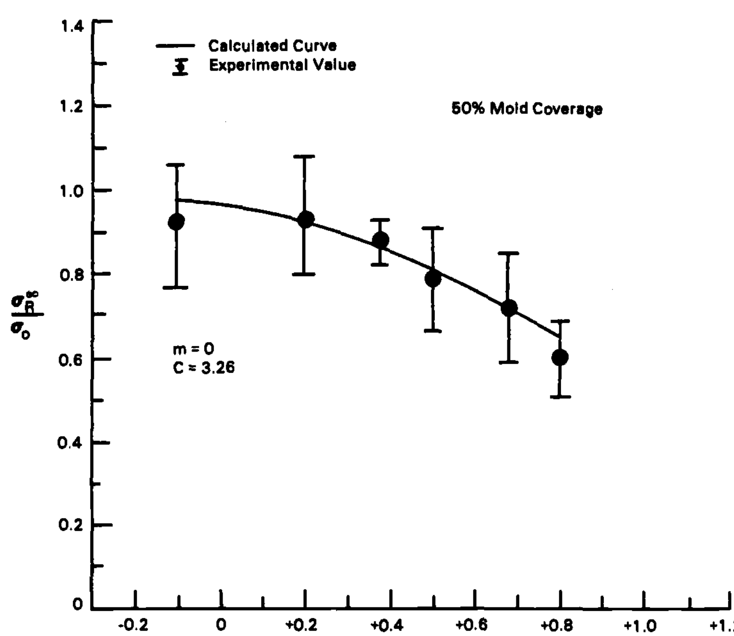

FIG. 10—*Comparison of experimental and calculated notched/unnotched strength ratios for 50% mold coverage Material I specimens.*

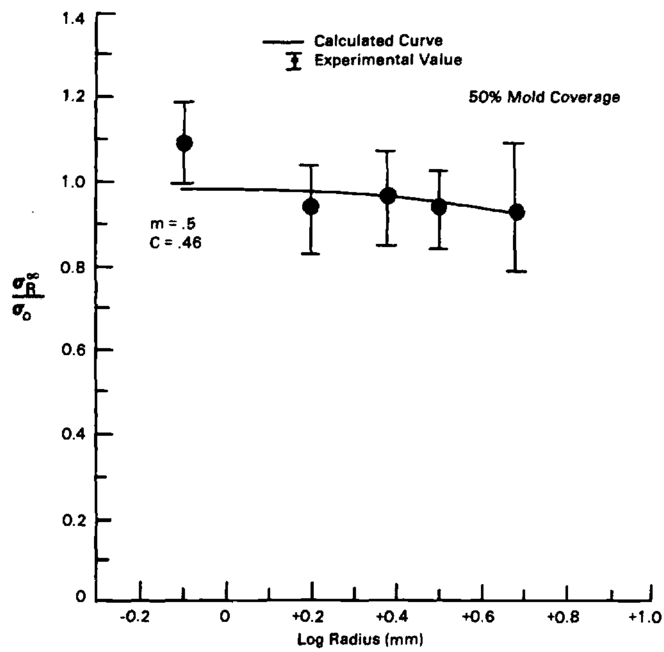

FIG. 11—*Comparison of experimental and calculated notched/unnotched strength ratios for 50% mold coverage Material II specimens.*

minimum sum of differences (Eq 11) that are within experimental error of those values where m is equal to zero, Table 6. Thus, all ten of the R25 SMC data sets can accurately be described by the Whitney-Nuismer two-parameter notch strength model [*21*].

A comparison of the notch strength sensitivities for Materials I and II indicates that Material I is slightly more notch sensitive than Material II. Since Material II is toughened by a rubber phase, its resin matrix should be less sensitive to microcrack growth than Material I's brittle polyester resin matrix. Thus, Material II should be more tolerant of stress concentrators.

Conclusions

Based on the results of this investigation, the following conclusions are made:

1. R25 SMC is relatively notch insensitive due to the large number of naturally occurring tensile critical flaws in this material.

2. The critical hole size (that size circular notch through which all specimens fail) of R25 SMC is 9.53 mm (0.37 in.). Variations in mold coverage from 97.5% to 25% were found to have virtually no effect upon the critical hole size in R25 SMC.

TABLE 6—*Effect of* m *upon minimum sum of differences* (*Eq 11*).

m	$C(\text{cm}^{-1})$	R_{ns}	Minimum Sum of Differences
	MATERIAL I/97.5% MOLD COVERAGE		
0.32	1.70	0.55	0.40
0	2.65	0.42	0.41
	MATERIAL II/50% MOLD COVERAGE		
0.50	0.46	0.16	0.17
0	1.49	0.17	0.20

3. There exists a wide spectrum of flaw sites in R25 SMC. The most severe of these are insensitive to mold coverage.
4. Within experimental error, the two-parameter notch strength model of Whitney-Nuismer can be used to accurately describe the notch sensitivity of R25 SMC.

Acknowledgments

The authors gratefully acknowledge the support of the following personnel: Mr. W. Todd and Mr. D. Hearn (currently with Chevrolet Motor Division) of General Motors Advanced Product and Manufacturing Engineering Staff for their aid in the fabrication of the SMC plaques; and Mr. R. Schuler, Polymers Department of General Motors Research Laboratories, for his diligence in mechanically testing the large number of specimens used.

References

[*1*] Shirrell, C. D. in *High Modulus Fiber Composites in Ground Transportation and High Volume Applications, ASTM STP 873*, American Society for Testing and Materials, Philadelphia, 1983, pp. 3–22.
[*2*] Kline, R. A. in *Composite Materials: Quality Assurance and Processing, ASTM STP 797*, American Society for Testing and Materials, Philadelphia, 1983, pp. 133–156.
[*3*] Burns, R., Gandhli, K. S., Hanken, A. G., and Lynskel, B. M., *Plastics and Polymers*, Dec. 1975, pp. 235–240.
[*4*] Bell, J. P., *Journal of Composite Materials*, Vol. 3, 1969, pp. 244–253.
[*5*] McNally, D., *Polymer-Plastics Technology Engineering*, Vol. 8, 1977, pp. 101–154.
[*6*] McCullough, R. L., Pipes, R. B., and Taggart, D. in *Composite Materials in the Automotive Industry*, American Society of Mechanical Engineers, New York, 1978, pp. 102–110.
[*7*] Shirrell, C. D., "The Effects of Absorbed Water Upon the Properties of a Sheet Molding Compound," SAE Paper No. 811340, Society of Automotive Engineers, Dec. 1981.
[*8*] Shirrell, C. D., *Polymer Composites*, Vol. 4, 1983, pp. 172–179.
[*9*] Waddoups, M. E., Eisenmann, J. R., and Kaminski, B. E., *Journal of Composite Materials*, Vol. 5, 1971, pp. 446–454.
[*10*] Whitesides, J. B., Daniel, I. M., and Rowlands, R. E., "The Behavior of Advanced Filamentary Composite Plates with Cutouts," Air Force Flight Dynamics Laboratory Technical Report AFFDL-TR-73-48, Wright-Patterson AFB, Dayton, OH, June 1973.
[*11*] Cruse, T. A., *Journal of Composite Materials*, Vol. 7, 1973, pp. 218–229.
[*12*] Waddoups, M. E. and Halpin, J. C., *Computers and Structures*, Vol. 4, 1974, pp. 659–673.
[*13*] Zweben, C., *Engineering Fracture Mechanics*, Vol. 6, 1974, pp. 1–10.

[*14*] Riegner, D. A., private communication, Aug. 16, 1979.
[*15*] Riegner, D. A. and Sanders, B. A., private communication, Nov. 1979.
[*16*] Hoa, S. V., *Polymer Composites*, Vol. 2, 1981, pp. 145–148.
[*17*] Pipes, R. B., Gillespie, J. W., Jr., and Wetherhold, R. C., *Polymer Engineering and Science*, Vol. 19, 1979, pp. 1151–1155.
[*18*] Pipes, R. B., McCullough, R. L., and Taggart, D. G., *Polymer Composites*, Vol. 3, 1982, pp. 34–38.
[*19*] Taggart, D. G., Pipes, R. B., Blake, R. A., Jr., Gillespie, J. W., Jr., Prabhakaran, R., and Whitney, J. M., "Properties of SMC Composites," Center for Composite Materials Report 79-01, University of Delaware, Newark, DL, 1979.
[*20*] Pipes, R. B., Wetherhold, R. C., and Gillespie, J. W., Jr., *Journal of Composite Materials*, Vol. 13, 1979, pp. 148–160.
[*21*] Whitney, J. M. and Nuismer, R. J., *Journal of Composite Materials*, Vol. 8, 1974, pp. 253–265.
[*22*] Nuismer, R. J. and Whitney, J. M. in *Fracture Mechanics of Composites, ASTM STP 593*, American Society for Testing and Materials, Philadelphia, 1975, pp. 117–142.
[*23*] Wang, S. S., Chim, E. S.-M., Yu, T. P., and Goetz, D. P., *Journal of Composite Materials*, Vol. 17, 1983, pp. 299–315.
[*24*] Denton, D. L., "Effects of Processing Variables on the Mechanical Properties of Structural SMC-R Composites" in *Proceedings*, 36th Annual Conference, Reinforced Plastic/Composites Institute, The Society of the Plastic Industry, Session 16-A, Feb. 16–20, 1981, pp. 1–8.
[*25*] Paris, P. C. and Sih, G. C. in *Fracture Toughness Testing and Its Applications, ASTM STP 381*, American Society for Testing and Materials, Philadelphia, 1965, pp. 84–113.
[*26*] Peterson, R. E., *Stress Concentration Factors*, Wiley, New York, 1974, pp. 110–111.

L.-J. Fu,[1] M. Schmerling,[1] and H. L. Marcus[1,2]

Interface Studies of Aluminum Metal Matrix Composites

REFERENCE: Fu, L.-J., Schmerling, M., and Marcus, H. L., "**Interface Studies of Aluminum Metal Matrix Composites,**" *Composite Materials: Fatigue and Fracture, ASTM STP 907*, H. T. Hahn, Ed., American Society for Testing and Materials, Philadelphia, 1986, pp. 51–72.

ABSTRACT: In both continuous- and discontinuous-fiber aluminum metal matrix composites (MMC) the interface plays a major role in fracture. The interface chemistry and crystallography of both graphite/aluminum continuous-fiber and silicon carbide/aluminum (SiC/Al) discontinuous-fiber MMCs were observed on ion beam thinned specimens in the transmission electron microscope (TEM). The fracture mode and fracture surface chemistry of SiC/Al MMCs were investigated with the scanning electron microscope (SEM) and Auger electron spectroscopy (AES) combined with inert ion sputtering. The materials investigated were representative of the discontinuous-fiber SiC/Al composite (ARCO, SILAG) and the particulate SiC/Al composites (DWA) at the time of the study.

The TEM results show that an oxide is present at some ot the SiC/Al interfaces, often in the form of γ-Al_2O_3 (along with $MgAl_2O_4$ when the aluminum matrix contains magnesium). The fracture path is not dominated by the interfacial failure but is primarily a matrix failure path. The more ductile the matrix, the less interfacial fracture. The large volume fraction of silicon carbide plays a major role in the fracture behavior by influencing the localized volume of material being deformed. Some of the fracture energy may have been reduced due to prior formation of dislocation networks due to thermal coefficient of expansion mismatch between the silicon carbide and the aluminum matrices. These networks were not apparent in the particulate SiC/Al MMC.

Both fine-grained γ-Al_2O_3 and small amounts of coarse-grained Al_4C_3 were found in the interfaces of the as-received graphite/aluminum composite specimens. During heat treatment, some of the Al_4C_3 phase grows into and along the graphite fiber surface.

KEY WORDS: aluminum, composite materials, fracture, heat treatment

Metal matrix composites (MMCs) have been investigated in recent years because they offer high performance and wide application as engineering materials. More than 100 different materials have been made as fibers or whiskers and used to strengthen the metal matrix materials. If the composite is exposed to high temperature, only high-melting-temperature fibers can be used [*1*]. This study reports results on carbon and silicon-carbide fibers in aluminum metal matrices.

[1] Department of Mechanical Engineering/Center for Materials Science and Engineering, The University of Texas, Austin, TX 78712.

[2] H. L. Kent, Jr., Professor of Mechanical Engineering.

Both continuous- and discontinuous-fiber composites and particulate composites were studied.

In general, the fiber-reinforced MMC is anisotropic. The degree of anisotropy depends primarily on the degree of fiber orientation. Fibers in metal matrix composites are used to carry the load, and the matrix serves to transfer and distribute the load to the fibers [*2*]. The interface is a region of significantly changed chemical composition and bonding between the matrix and the reinforcement [*3*], and it plays the role of transmitting shear stress in the composite systems. The interface must therefore be strong. The formation of brittle compounds at the interfaces must be controlled. The interfaces must be stable at the service temperature of the composite. The cross-sectional area of the interfacial reaction zone must be small compared with that of the fiber so that the fiber retains its original mechanical properties. The difference between the thermal expansion coefficients of the fiber and the matrix can lead to large induced residual stress [*4*]. The goal of minimizing thermal expansion mismatch to reduce residual stresses is seldom achieved because of the need to choose certain reinforcing phases which are sufficiently stable and of high modulus in the high-temperature-range applications. Graphite fibers and silicon carbide fibers are very often used. There is a large difference in the thermal expansion coefficient between the two types of fibers and the aluminum alloy metal matrices.

Recent MMC development has been primarily focused on the continuous-fiber composites because of their impressive mechanical properties both at room temperature and elevated temperature along the direction of the fiber [*5*]. Discontinuous fibers have seen a revival (they were first made during the 60's) [*6*] since these fibers can now be successfully immersed into aluminum alloys. The advantage in using a discontinuous-fiber reinforced MMC is that it can be processed in the more conventional ways, such as extrusion, rolling, forging, swaging and that it allows flexibility in making the required shapes and sizes [*7*].

Some high-strength whiskers, such as sapphire and silicon carbide, have been used in various metal matrices since the 1960s [*8*]. Many of these MMCs show very attractive mechanical properties, but the high cost of the whiskers inhibits their application. Relatively cheap β-silicon carbide whiskers were developed and successfully immersed into aluminum alloy matrices in the early 1970's [*6*]. This is one of the metal matrix composites discussed in this report.

Continuous-fiber composites have fibers that are continuous in length and uniformly dispersed through the whole composite section. It is generally assumed that the fibers are unidirectional [*3*]. A discontinuous-fiber composite means that the composite material includes reinforcing fibers of finite length and not unidirectionally dispersed in the composite. The longitudinal stress in a continuous-fiber composite usually can be approximated by the rule of mixtures. The stress behavior of discontinuous-fiber composites cannot be, unless the fiber length is much greater than some critical value [*3*].

In particulate-strengthened composite materials, the particles are more equiaxed than the whiskers, with sizes varying from 0.01 to 1.0 μm. The matrix is the major load-carrying constituent. The particles dispersed in the matrix are present to prohibit the motion of dislocations in the metal-matrix. Therefore, the reinforcement of metal matrix is primarily dependent on the effectiveness of the dislocation motion prohibiting mechanism (dispersion-hardening).

In the manufacturing of continuous-fiber composites, the graphite fibers are not wet spontaneously by liquid aluminum at temperatures near the melting point of aluminum [*9*]. It was found that the method to induce infiltration of bundles of fibers was to pretreat the graphite by chemical vapor deposition of titanium/boron on the surfaces of the fibers, which then allows molten aluminum to wet. This also prevents rapid attack of the fibers by aluminum [*10*]. After this titanium/boron treatment, the graphite-reinforced aluminum or aluminum alloys have useful longitudinal properties. However, a major problem is the poor transverse tensile strength. Previous research results on the graphite/aluminum composites have been reported by Tsai [*11*], Finello [*12*], and Lo [*13*]. They have shown that the interface structures present in the commercial graphite/aluminum composites are complex combinations of different glassy and crystalline phases, including TiB_2, Al_4C_3, γ-Al_2O_3, and $MgAl_2O_4$ [*11,13*]. Not all phases are present simultaneously in every case. Limited transverse strengthening of graphite/aluminum resulted from heat treatment to form aluminum carbide but only with a concurrent serious decrease in the longitudinal strength. Fiber degradation is used to explain this reduction in longitudinal strength. The graphite crystal orientation with heat treatment strongly influenced the aluminum carbide nucleation and growth [*12*]. With heat treatment the chemical composition of the fracture path is found to change.

Material Description

Silicon Carbide Discontinuous Fibers in Aluminum Alloys

The following are the six specimens of silicon carbide discontinuous fiber in aluminum matrice composites studied (see Table 1):

1. A6013Z: SXA 2024 + 22.45 weight % F-9 grade silicon carbide, flat, 12.7 by 127.0 by 47.6 mm (½ by 5 by 1⅞ in.), as extruded.

TABLE 1—*SiC/Al composites with matrix alloys and silicon carbide contents.*

Material	Metal Matrix	SiC
A6013Z	2024	22.45 weight %
C0115Z	6061	10 weight %
C0116Z	6061	30 weight %
D0026Z	7075	20 weight %
D0030Z-2	7075	5.7 weight %
E00197-2	Al-5Li	25 weight %
SiC particulate/Al	6061	25 volume %

2. C0115Z: SXA 6061 + 10 weight % F-9 grade silicon carbide, flat, 6.35 by 38.1 by 19.05 mm (¼ by 1½ by 1¾ in.), as extruded.
3. C0116Z: SXA 6061 + 30 weight % F-9 grade silicon carbide, flat, 3.175 by 58.737 by 39.687 mm (⅛ by 2$\frac{5}{16}$ by 1$\frac{9}{16}$ in.), as extruded.
4. D0026Z: SXA 7075 + 20 weight % F-9 grade silicon carbide, flat, 6.35 by 38.1 by 50.8 mm (¼ by 1½ by 2 in.), as extruded.
5. D0030Z-2: SXA 7075 + 5.7 weight % F-9 grade silicon carbide, rod, 15.875 by 44.45 mm (⅝ by 1¾ in.), as extruded.
6. E0019Z-2: SXA Al-5Li + 25 weight % F-9 grade silicon carbide, rod, 15.875 by 44.45 mm (⅝ by 1¾ in.), as extruded.

The particulate SiC/Al composite was 25 volume % silicon carbide powder blended in an Al 6061 metal-matrix. In order to evaluate both the silicon carbide discontinuous-fiber reinforced and silicon carbide particulate-reinforced aluminum MMC, Auger electron spectroscopy (AES) and scanning electron microscopy (SEM) fracture surface analyses, as well as transmission electron microscopy (TEM) microstructural analyses, were performed. In order to observe the silicon carbide fiber, SEM was used. Metallurgical specimens were etched in hydrochloric acid (Fig. 1). The metal matrix was etched away and the fibers were observed on the surface. The diameters of the fibers vary from 0.2 to 1 μm.

Continuous Graphite Fiber in Aluminum Alloy Composites

The material studied (G4924) contains P55 high-modulus fibers (titanium/boron processed) in an Al 6061 metal matrix. The as-received transverse strength is 32 MPa ±5. The graphite/aluminum MMC study observed the morphology of the interface by using TEM.

Experimental Approaches

AES Analysis of the Fracture Surfaces

Specimens from all of the silicon carbide discontinuous-fiber/aluminum composites and the 25 volume % silicon carbide particulate/aluminum composites were fractured inside the ultra-high-vacuum AES chamber. The discontinuous fibers and the particulate sizes are below the resolution of the Auger spectrometer used. Therefore, a square rastered beam of 3 μm at a TV scan rate was used to collect the average compositional AES information from the fracture surfaces. The quantitative AES analysis of the compositional ratio of aluminum to silicon in the spectrum was done by measuring the peak-to-peak heights of aluminum and silicon from a $dN(E)/dE$ curve and correcting by the relative sensitivity factors obtained from standards [*14*]. The studies were carried out in a Physical Electronics 590 SAM system using a nominal 1-μm electron beam size. Sputtering was accomplished using a differentially pumped argon ion gun with an approx-

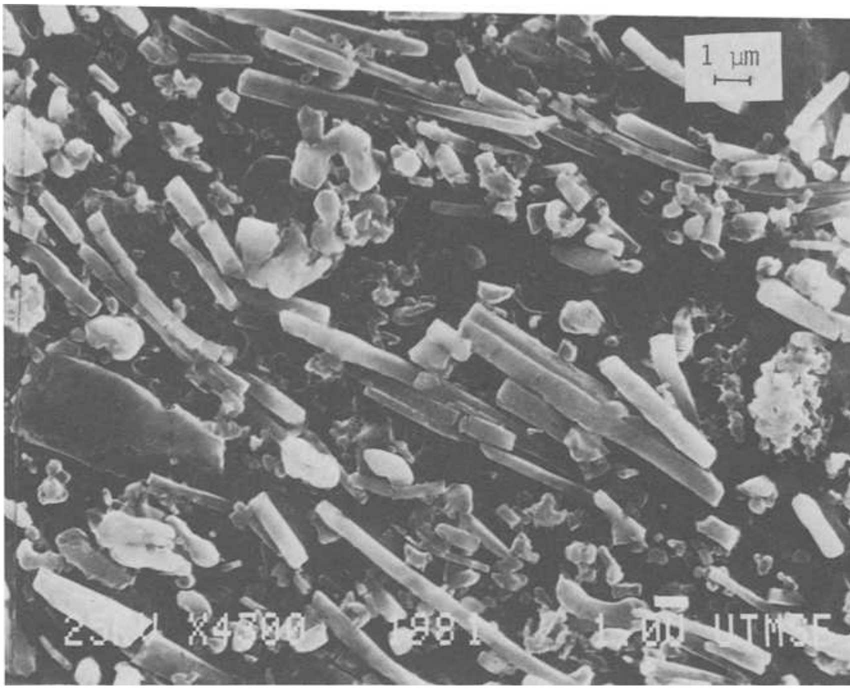

FIG. 1—*SEM micrograph of a silicon carbide discontinuous fiber/aluminum composite surface etched by hydrochloric acid. The diameters of the fibers are very small, varying from 0.2 to 1 µm.*

imately 1-mm-diameter beam size at the specimen. A 4-keV ion beam with a 25-mA current yielding an initial rate on the order of 10 nm/min was used.

SEM Investigation

The silicon carbide discontinuous fiber/aluminum composites and silicon carbide particulate/aluminum composites were fractured and quickly put into the SEM vacuum chamber to prevent the fracture surfaces from excessive oxidizing in air. A JEOL JSM-35C model SEM with a KEVEX energy dispersive spectroscopy system (EDS) was used for topological and chemical analysis.

TEM Analysis

For the TEM microstructural and interfacial studies, four kinds of silicon carbide discontinuous-fiber/aluminum composites were prepared by ion beam thinning and for one of them both ion beam thinning and jet poishing were used to get the thin regions (the as-received silicon carbide fiber/aluminum composite-A6013Z specimen). The jet polishing solution used was a mixture of 2% hydrochloric acid, 49% nitric acid, and 49% methanol. The as-received A6013Z prepared by the ion beam thinning technique was sliced in a transverse section. In an attempt to widen the interface region, the bulk A6013Z specimen was heat-treated by encapsulating the specimen at the diffusion-pumped rough vacuum condition (about 3×10^{-2} Pa) in a Vycor glass tube and heat-treated at 550°C for 24 h. The heat-treated specimen was then sliced in both transverse and longitudinal sections, followed by ion beam thinning.

Both the as-received and after tension test specimens of silicon carbide discontinuous-fiber/aluminum composite-C0116Z and 25 volume % silicon carbide particulate/aluminum composite were prepared by the ion beam thinning technique for TEM microstructural and interfacial studies.

The transverse sections of the as-received and heat-treated graphite/aluminum composite (G4924) were prepared by ion beam thinning for TEM interfacial studies. The heat treatment was done by encapsulating the specimen in the mechanical pump vacuum system (about 1 to 10^{-1} Pa) and was carried out at 550°C for 2 h [*12*].

The mechanical properties of graphite/aluminum MMC were observed in previous work [*5,12,13*], therefore only the morphology of the interfaces of this graphite/aluminum MMC was inspected in the present study.

The TEM work from the jet-polished A6013Z specimen was done using a JEOL JEM-150 while all the other TEM work was performed using a JEOL JEM-200CX.

The ion beam thinning technique is described in the Appendix.

Results and Discussion

SEM Analysis

SEM fractography on tension tested specimens showed a ductile-dimple fracture mode on the fracture surfaces of the silicon carbide discontinuous-fiber/aluminum and silicon carbide particulate/aluminum composites. It was rare to find fibers on the fracture surfaces of silicon carbide discontinuous-fiber/aluminum composites. A comparison of the fracture surfaces of D0026Z (Al 7075 + 20 weight % silicon carbide fiber), A6013Z (Al 2024 + 22.45 weight % silicon carbide fiber), and E0019Z-2 (Al-5Li + 25 weight % silicon carbide fiber) follows. Al 7075 is a more ductile matrix alloy than the Al 2024 and Al-5Li alloys. The three composites have about the same fiber content by weight. The SEM micrographs in Figs. 2*a*, 3, and 4 illustrate the limited number of fibers on the D0026Z fracture surface and the more predominant presence of fibers on the E0019Z-2 and A6013Z fracture surfaces. This was consistent with the results of AES quantitative analyses that follow.

It was very difficult to distinguish between the aluminum matrix and silicon carbide powder particles at the fracture surface of silicon carbide particulate/aluminum composites. As a result of SEM silicon-mapping, as shown in Fig. 5, it is evident that the size of the silicon carbide particles varies, with some as large as 10 μm. The spacing between the particles was not uniform.

AES Results

Auger electron spectra collected from the fracture surfaces of the silicon carbide discontinuous-fiber/aluminum alloy composites showed very small silicon peaks compared with the theoretical ratio of silicon to aluminum for the weight fraction of silicon carbide present. An extreme case is that of D0030Z-2, the ratio of aluminum to silicon is 88 to 1 which means that there is effectively no silicon at the fracture surface. After extensive inert ion sputtering (removal of about 0.5 to 1 μm) of the surfaces, increased silicon carbide was observed on most of the fracture surfaces. Figures 2*b* and 2*c* show the AES spectra of fracture surfaces of the D-0026Z before and after sputtering along with the SEM fracture surface picture in Fig. 2*a*. The results of the analysis of relative amounts of aluminum to silicon are listed in Table 2. The need to sputter the surface for long times to get the substantial silicon carbide spectra gives strong support for high interface strength in the silicon carbide discontinuous-fiber/aluminum composites.

Elemental maps of silicon using EDS in the SEM differed from the Auger studies. The silicon carbide particles or fibers were observed in the elemental mapping even though the AES results indicate a layer of interface and matrix aluminum alloy over them. This is because many of the characteristic X-rays escape from a deeper volume in the bulk material than Auger electrons.

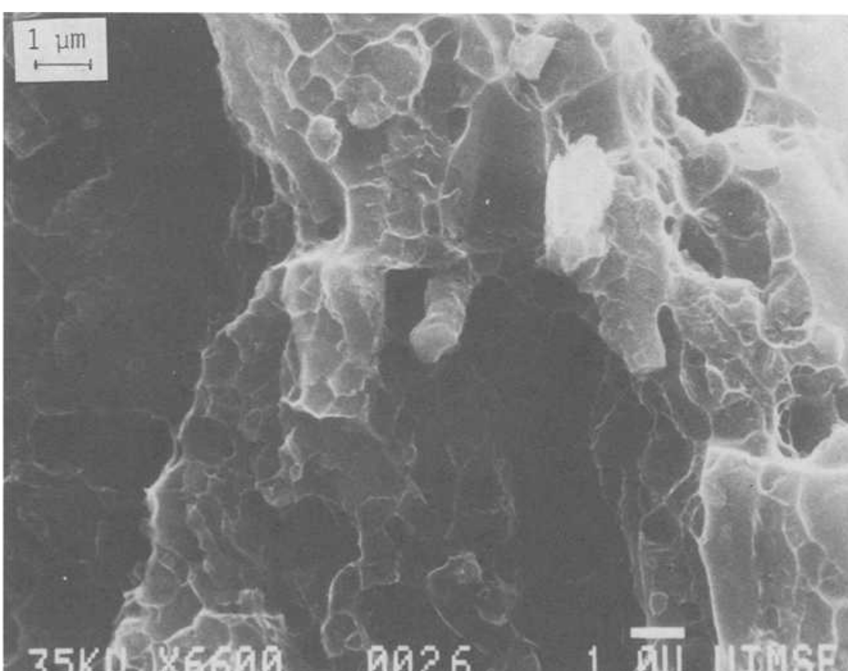

FIG. 2*a*—*SEM micrograph of specimen of fracture surface of D0026Z.*

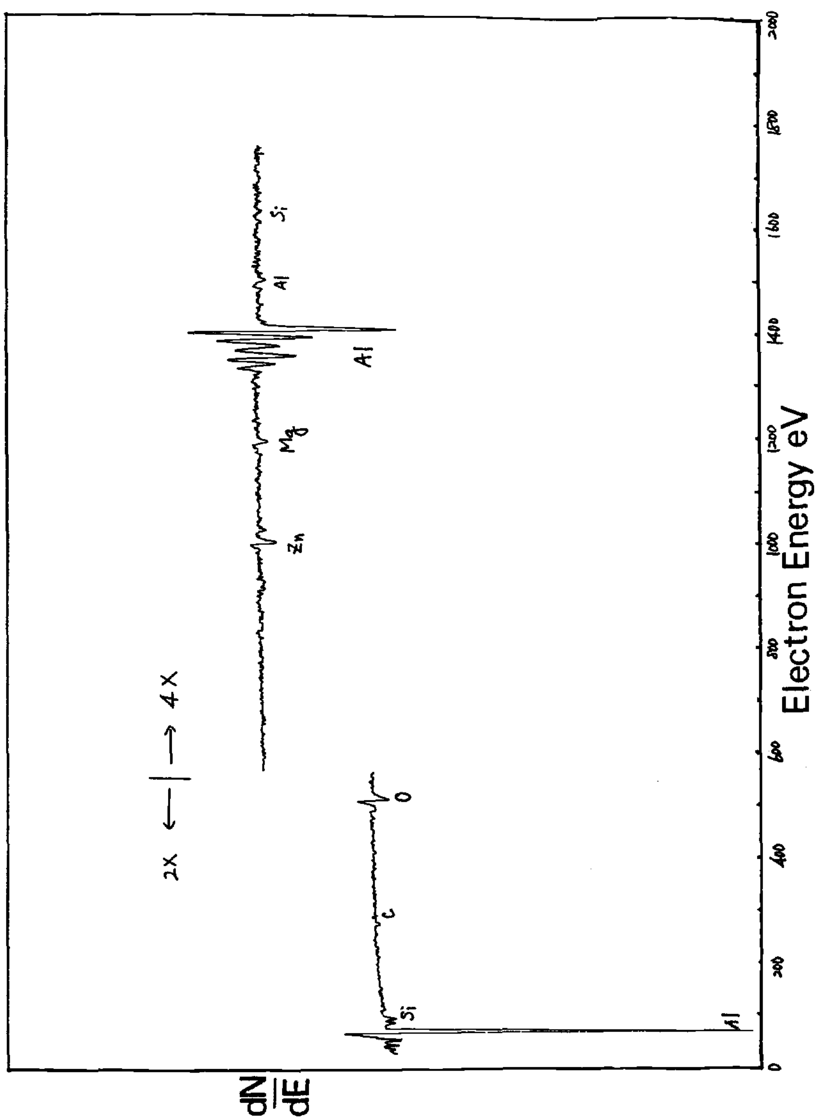

FIG. 2b—*AES of fracture surface of D0026Z before inert ion sputtering.*

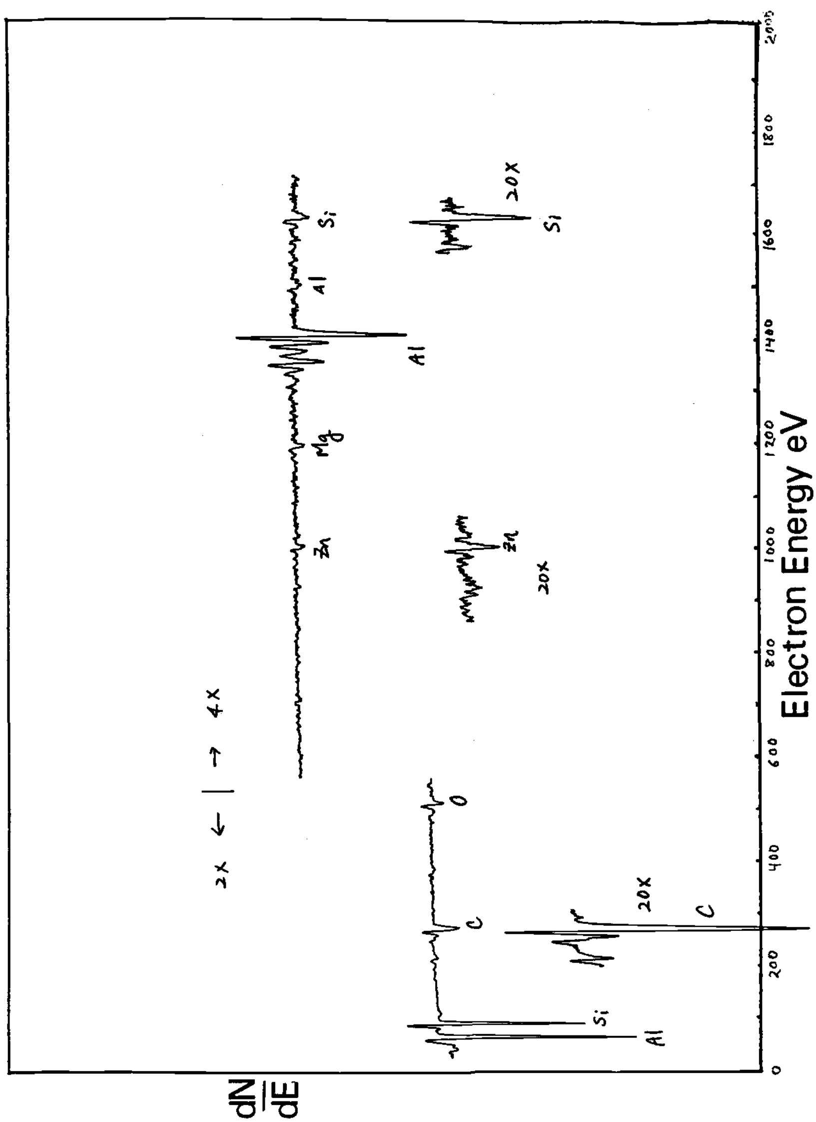

FIG. 2c—AES of fracture surface of D0026Z after inert ion sputtering (about 0.5 μm removed).

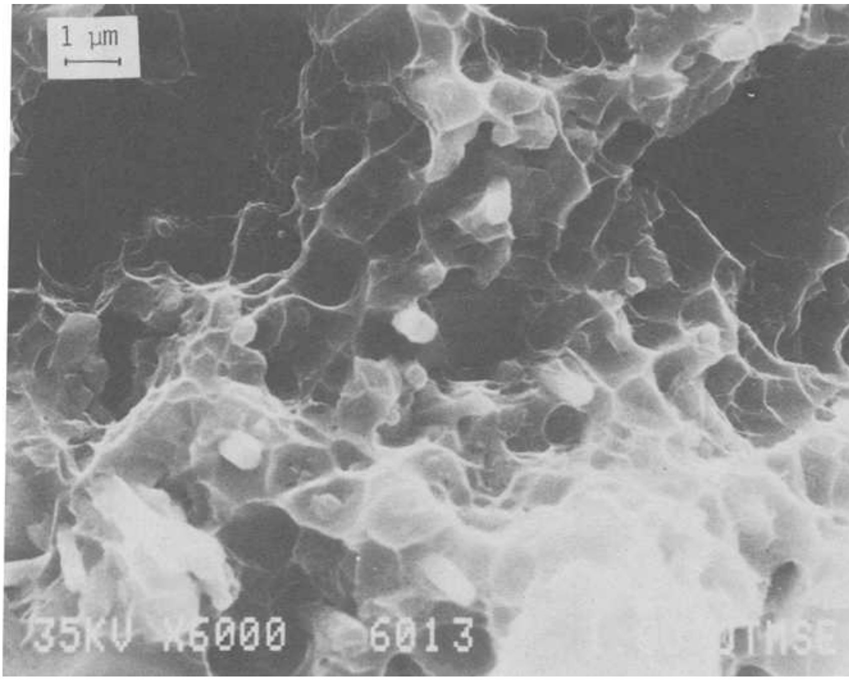

FIG. 3—*SEM micrograph of fracture surface of A6013Z.*

A comparison of the 25 volume % silicon carbide particulate/aluminum 6061 composite with C0116Z (Al 6061 + 30 weight % silicon carbide discontinuous fiber) showed that these two materials have the same metal matrix, and the C0116Z has larger silicon carbide content by volume than that of the 25 volume % silicon carbide particulate/aluminum composite. The quantitative AES results showed that the 25 volume % silicon carbide particulate/Al composite had a larger silicon concentration on the fracture surface. This indicates that more interface failure occurred in the silicon carbide particulate/aluminum composite than in the silicon carbide discontinuous fiber/aluminum composite.

TEM Results

Silicon Carbide/Aluminum Composites—A diffraction pattern taken from the interface of the jet-polished as-received A6013Z specimen was identified as γ-Al_2O_3. γ-Al_2O_3 was also identified in both interfaces of as-received C0116Z and a heat-treated A6013Z ion beam thinned longitudinal section. From the energy dispersive X-ray (EDS) analysis in a scanning transmission electron microscope (STEM), a small amount of magnesium is found in some interfaces. Therefore, at least some of the γ-Al_2O_3 is possibly $MgAl_2O_4$ (spinel), but their structures

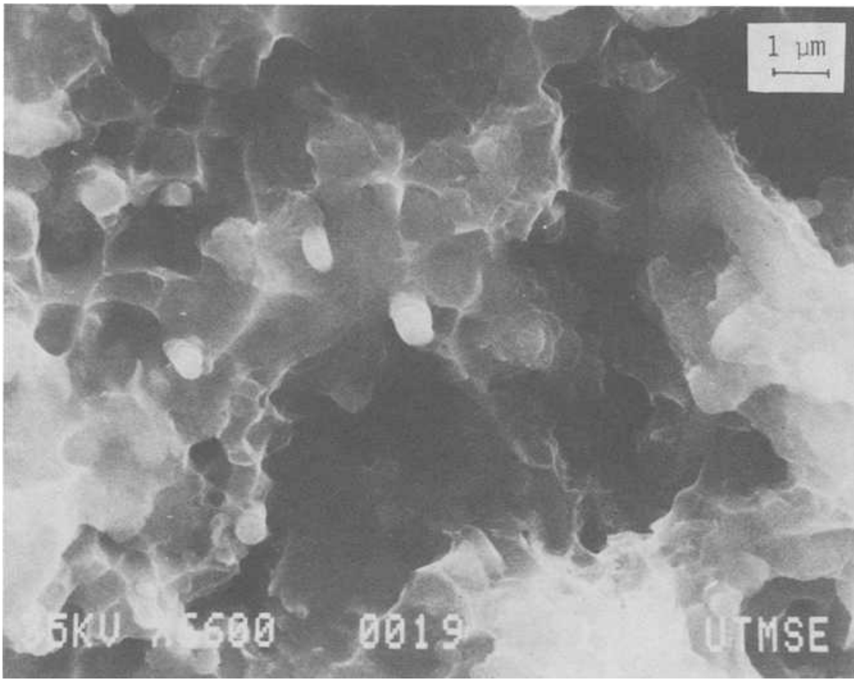

FIG. 4—*SEM micrograph of fracture surface of E0019Z-2.*

and lattice parameters differ by an amount too small to be resolved by electron diffraction from such a small area. Figures 6*a* and 6*b* are the TEM bright field and dark field micrographs of the interface of a heat-treated A6013Z longitudinal thinned section. The thickness of γ-Al_2O_3 phase is about 30 nm (only one variant of the γAl_2O_3 is seen in Fig. 6*b*). The crystalline oxide phase was not uniformly present at every interface. A comparison of microstructures of heat-treated and as-received transverse ion beam thinned A6013Z sections showed that there was no evidence of any significant reaction between silicon carbide fiber and aluminum metal matrix after annealing at 550°C in a diffusion-pumped rough vacuum (about 3×10^{-2} Pa) conditions for 24 h. A slight degradation was found by Kohara [*15*] at 600°C. γ-Al_2O_3 was not identified from a transverse thinned section. This may be due to the interface layer being too thin.

No interface phase was found in the silicon carbide particulate/aluminum composite. Presumably, the interface region was too thin to observe in the limited number of specimens prepared and may be amorphous.

In order to compare the distributions of dislocations before and after tension testing, the specimen C0116Z was chosen because it has the most silicon carbide content among the six types of as-received silicon carbide discontinuous-fiber/

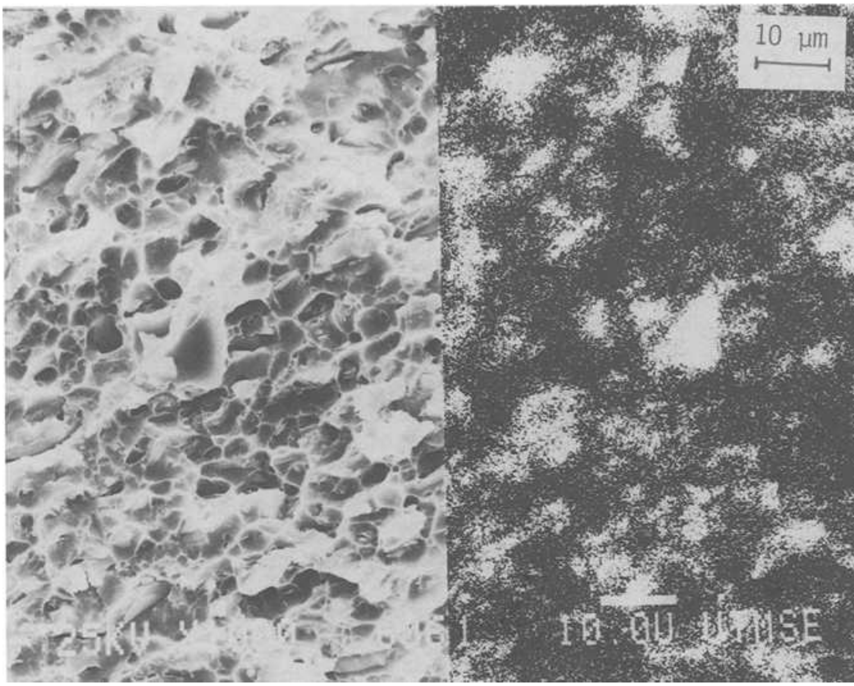

FIG. 5—*SEM silicon mapping* (right half) *with related fracture surface of the 25 volume % silicon carbide particulate/aluminum composite. The bright areas indicate the silicon carbide particles.*

TABLE 2—*Analysis of Auger spectra collected from fracture surfaces of silicon carbide fiber and silicon carbide particulate in aluminum alloy matrices composites.*

Material	Metal Matrix	SiC	Before Sputtering, C_{Al}/C_{Si}	After Sputtering, C_{Al}/C_{Si}	Theoretical Ratio for Known Weight % or Volume % of C_{Al}/C_{Si}
A6013Z	2024	22.45 weight %	10:1	3:1	3.45:1
C0115Z	6061	10 weight %	28:1	7:1	9:1
C0116Z	6061	30 weight %	7:1	3:1	2.33:1
D0026Z	7075	20 weight %	13:1	3:1	4:1
D0030Z-2	7075	5.7 weight %	88:1	11:1	16.45:1
E0019Z-2	Al-5Li	25 weight %	4:1	4:1	3:1
SiC particulate/Al	6061	25 volume %	5:1	5:1	3:1

aluminum composites. TEM microstructural analysis showed that there was not much difference between as-received and after tension testing ion beam thinned C0116Z sections. A large dislocation density was found in the aluminum metal matrix in the vicinity of the silicon carbide fibers in the as-received specimen (Figs. 7,8). A similar dislocation density appeared in both the transverse and the longitudinal ion beam thinned A6013Z sections. The reason for the heavy dislocation density is postulated to be associated with deformation due to the large difference in thermal expansion coefficient. This is complicated by any dislocation introduction associated with the ion thinning process. There was no heavy dislocation density observed in the as-received and after tension testing specimens of silicon carbide particulate/aluminum composite (Fig. 9). The few dislocations may be due to the small aspect ratio of the particulate material limiting the effects of differential thermal expansion.

Graphite/Aluminum Composite—All of the graphite/aluminum composite specimens in this study were prepared in transverse sections followed by ion beam thinning. Both fine-grained γ-Al_2O_3 and a small amount of coarse-grained Al_4C_3 were found in the interface of the as-received G4924 specimen. The diffraction patterns of γ-Al_2O_3 show continuous rings and the Al_4C_3 rings are spotty. The TEM dark-field picture (Fig. 10) showed that the γ-Al_2O_3 was next to the graphite fiber and the coarse-grained Al_4C_3 particles were outside the γ-Al_2O_3 phase. The Al_4C_3 particles extended into the aluminum matrix.

As in the previous work [*12*], the graphite/aluminum composite was aged at 550°C in a rough vacuum condition which promotes carbide formation. In the heat-treated specimens, it was easier to find Al_4C_3 in the interface than to find γ-Al_2O_3 phase. Perhaps during heat treatment the alumina goes from a thin layer structure to thicker islands that are statistically less easily observed in thin sections perpendicular to the layer. In the interface area without observable γ-Al_2O_3, Al_4C_3 seems to interlock through the porous sites of the graphite fiber surfaces as shown in Fig. 11. This mechanical locking could contribute to the transverse strengthening of graphite/aluminum composite after heat treatment [*12*]. The size of Al_4C_3 grains was about 0.2 μm and they were in polyhedral shape. Both the fine-grained and coarse-grained γ-Al_2O_3 were found in the interface of heat-treated G4924 specimens. The coarse-grained γ-Al_2O_3 did not have a regular shape, but was about 0.1 μm in diameter. The kinetics of carbide formation has the carbon from the graphite fiber surface diffusing through the interface to form Al_4C_3. This then formed the layered structure observed.

Conclusions

1. The more ductile the aluminum metal matrix, the less silicon carbide fiber appears on the SEM micrograph of the fracture surface, implying less interface

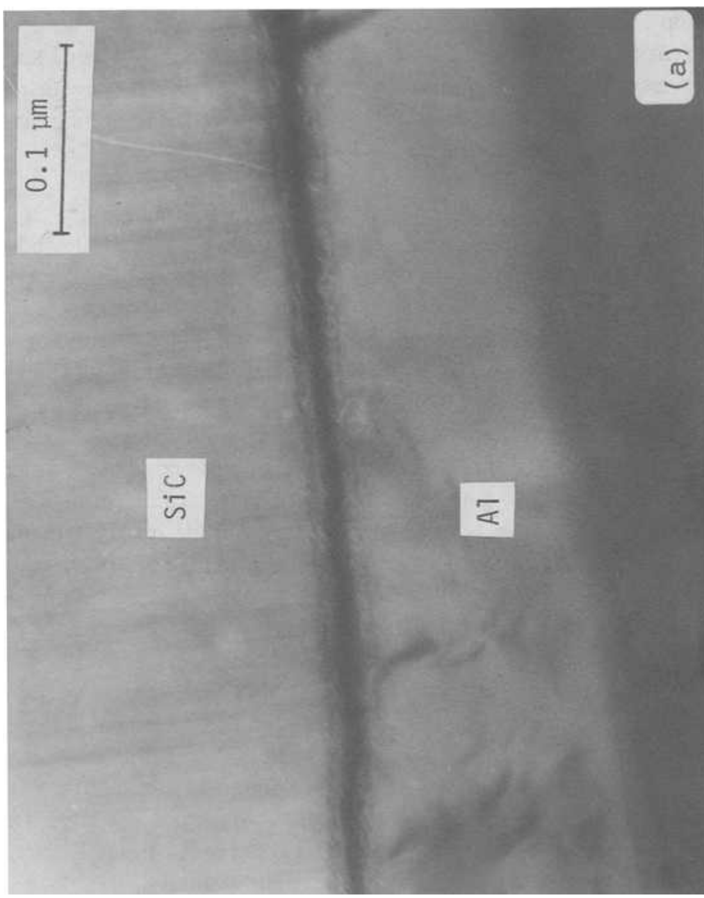
0.1 µm
(a)
SiC
Al

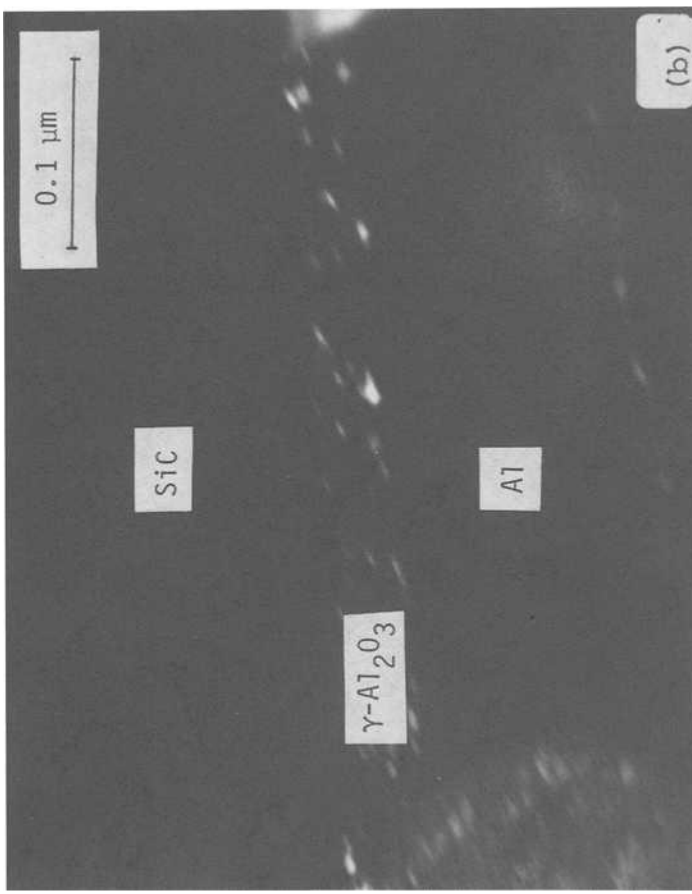

FIG. 6—*γ-Al_2O_3 was identified on the ion beam thinned longitudinal section of heat-treated A6013Z section:* (a) *bright-field microstructure;* (b) *dark-field microstructure.*

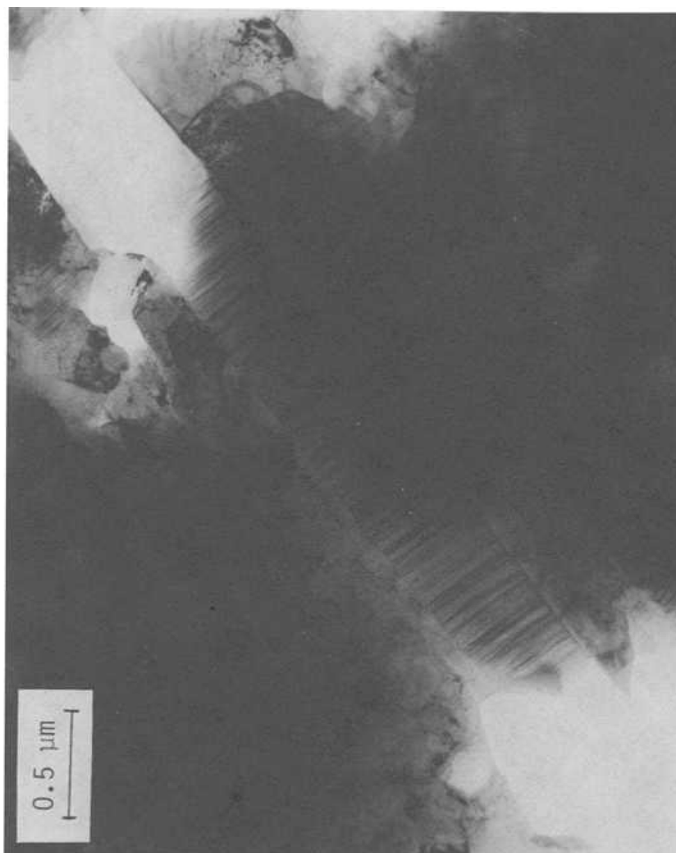

FIG. 7—Microstructure of as-received C0116Z specimen shows that the aluminum matrix in the vicinity of silicon carbide fiber has a large dislocation density.

FIG. 8—*Microstructure of C0116Z after tension testing. Both longitudinal and transverse direction fibers were in this type of specimen.*

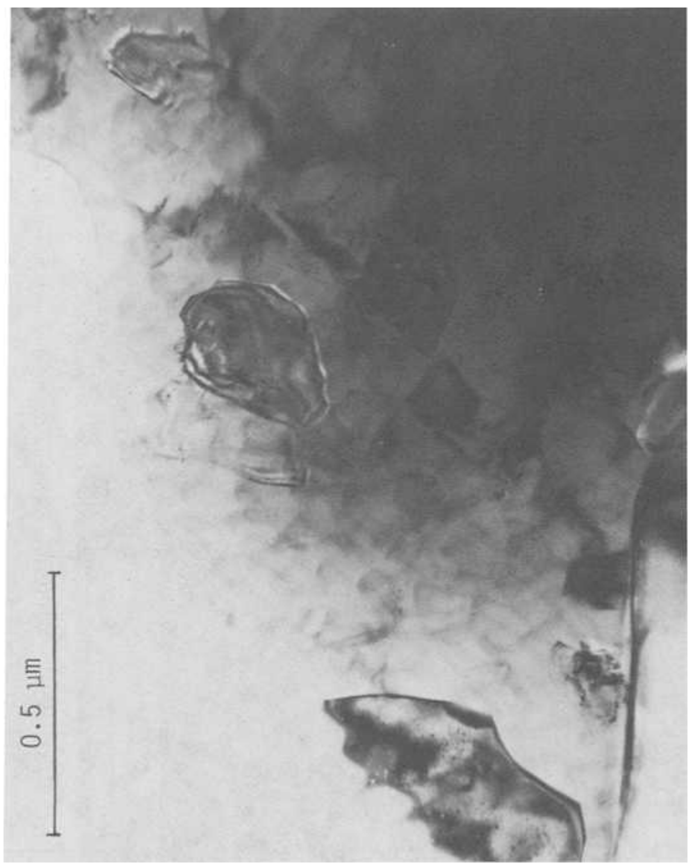

FIG. 9—*Microstructure of ion beam thinned as-received Al 6061 + 25 volume % silicon carbide powder specimen. Few dislocations occur around the silicon carbide particles.*

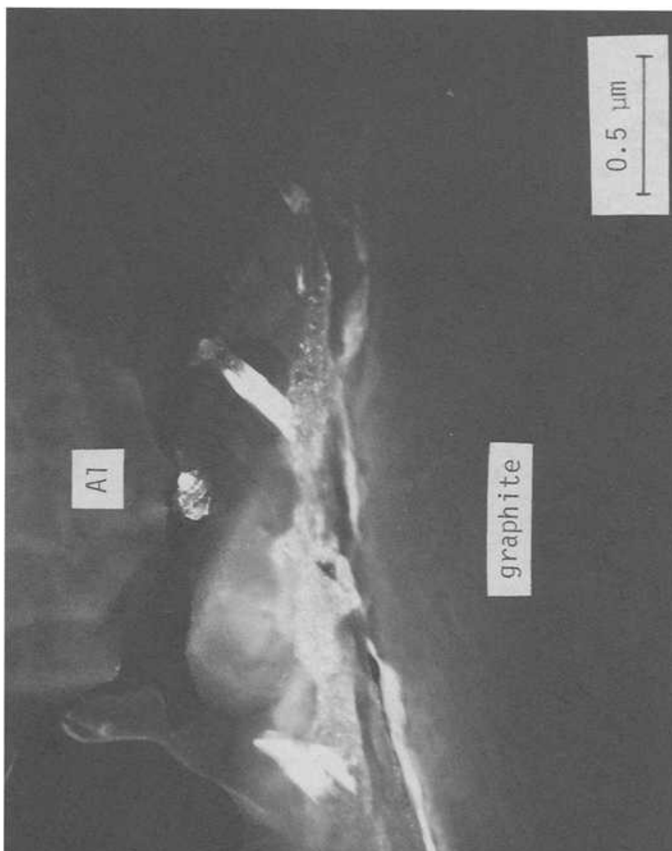

FIG. 10—*TEM dark-field microstructure of graphite/aluminum G4924 as-received specimen showing* γ-Al_2O_3 *along the graphite fiber surface and* Al_4C_3 *particles.*

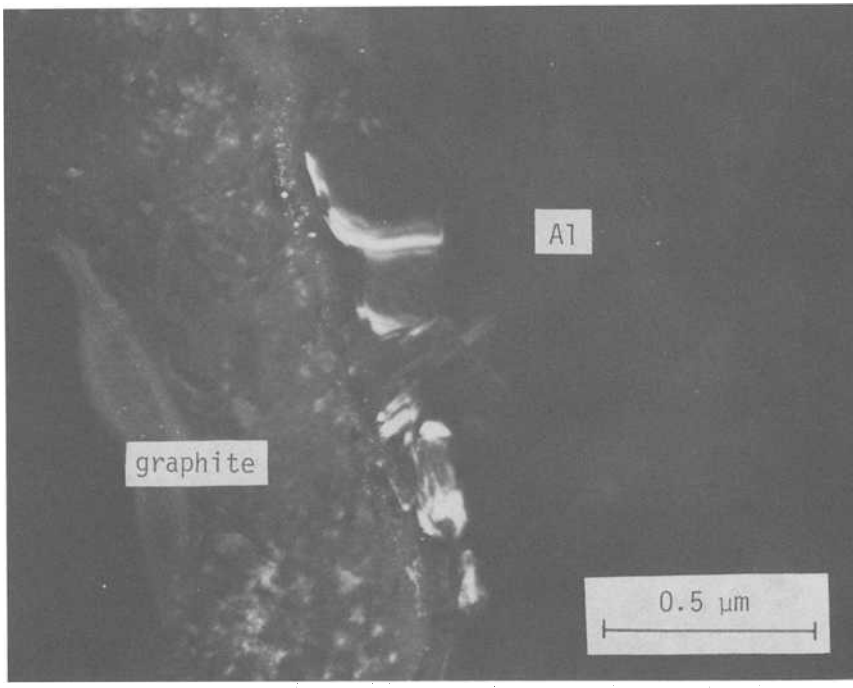

FIG. 11—*TEM dark-field microstructure of heat-treated G4924 specimen shows that Al_4C_3 particles grow into and along the graphite fiber surface.*

fracture in the silicon carbide discontinuous-fiber reinforced aluminum composites.

2. Very thin layers of γ-Al_2O_3 (along with $MgAl_2O_4$ when the aluminum matrix contains magnesium) are in some of the interfaces of the discontinuous-fiber SiC/Al composites.

3. Both fine-grained γ-Al_2O_3 and coarse-grained Al_4C_3 were found in the interfaces of the as-received graphite/aluminum composite specimens. During heat treatment, some of the Al_4C_3 phase grows into and along the porous sites of the graphite fiber surface. This mechanical locking could contribute to the transverse strengthening of graphite/aluminum composite after heat treatment.

Acknowledgment

This research was supported by the Office of Naval Research, Contract No. N00014-83-K-0143.

APPENDIX

Ion Beam Thinning of Composite Materials

In this research, most of the specimens for the TEM microstructural and interfacial studies were prepared by an ion beam thinning technique. There are several advantages to ion beam thinning. The technique gives a very clean surface. For specimens containing a finely divided second phase as in the composite materials, this is a good way to uniformly thin both phases simultaneously (which is very difficult to accomplish by chemical etching or electro-polishing). Therefore, it is especially good for observing transverse sections [*16*]. For the final preparation of highly reactive materials this technique avoids the dissolution of chemical etching or electro-polishing. This is especially important for the interface studies where certain phases might preferentially dissolve in the polishing solution [*13*].

An Edwards IBT 200 ion beam accessory was used to prepare the TEM specimens. It was found that a 4-keV accelerating argon ion beam voltage was perfect for thinning the aluminum metal matrix and the silicon carbide fibers or particulates simultaneously. Ion beam thinning for graphite/aluminum composites is more difficult than thinning of silicon carbide/aluminum composites. For the graphite/aluminum composite, using 4-keV or lower accelerating ion beam voltage, the graphite fibers were thinned faster than the aluminum metal matrix. If the voltage was 4.5 keV or higher, the aluminum metal matrix was thinned faster than the graphite fibers. Therefore, the thinning of graphite/aluminum composites was done in two steps. The 4.5-keV accelerating ion beam voltage was used to sputter the specimen to thin the aluminum and then the voltage was adjusted to 4 keV until both phases were thinned uniformly. During the thinning process, the graphite/aluminum specimens were taken out and examined by TEM or STEM stereo pair micrographs. Suitable adjustments of the ion beam voltage were then made to get both phases to a uniform thickness. The specimen tilt angle affects the sputtering rate. A 30-deg tilted angle was used at the beginning of the sputtering; in the later stages it was changed to 15 to 20-deg in order to slow down the sputtering rate and avoid ion beam damage to the very thin surfaces.

References

[*1*] Piatti, G. in *Advances in Composite Materials*, Applied Science Publishers, London, 1978.
[*2*] Kelly, A. and Nicholson, R. B. in *Strengthening Methods in Crystals*, Applied Science Publishers, London, 1971, pp. 331–403.
[*3*] Schoutens, J. E. and Tempo, K., *Introduction to Metal Matrix Composite Materials*, MMCIAC Tutorial Series, Santa Barbara, CA, June 1982.
[*4*] Scala, E. in *Composite Materials for Combined Functions*, Hayden Book Company, Rochelle Park, NJ, 1978, pp. 228–266.
[*5*] Kendall, E. G., *Composite Materials*, Vol. 4; also, *Metallic Matrix Composites*, K. G. Kreider, Ed., Academic Press, NY, 1974.
[*6*] Divecha, A. P., Fishman, S. G., and Karmarker, S. D., "Silicon Carbide Reinforced Aluminum—A Formable Composite," *Journal of Metals*, Sept. 1981, pp. 12–17.
[*7*] Divecha, A. P. and Fishman, S. G., *Mechanical Behavior of Materials*, Vol. 3, International Conference on Metals, K. J. Miller and R. F. Smith, Eds., Cambridge, U.K., Aug. 1979, pp. 351–361.
[*8*] Wolff, E. G., "Hydrodynamic Alignment of Discontinuous Fibers in a Metal Matrix" in *Fiber Science and Technology*, Elsevier, Essex, U.K., March 1969.
[*9*] Davis, L. W. and Sullivan, P. G. in *Failure Modes in Composites III*, T. T. Chiao and D. M. Schuster, Eds., American Institute of Mining, Metallurgical and Petroleum Engineers, 1976, pp. 212–225.
[*10*] Amateau, M. F., "Review of the Chemistry and Mechanisms of Graphite Reinforced Aluminum Matrices: Chemical and Mechanical Considerations" in *Proceedings*, Carbon Fiber Reinforced Metal Matrix Composites Conference, Pittsburgh, PA, 1975.
[*11*] Tsai, S. D., Ph.D. dissertation, The University of Texas at Austin, 1980.
[*12*] Finello, D., Ph.D. dissertation, The University of Texas at Austin, Aug. 1982.
[*13*] Lo, M. O., MSc. thesis, The University of Texas at Austin, Dec. 1981.

[14] Davis, L. E., MacDonald, N. C., Palmberg, P. W., Riach, G. E., and Weber, R. E., *Handbook of Auger Electron Spectroscopy*, 2nd ed., Physical Electronics Industries, Inc., Eden Prairie, MN, 1976.

[15] Kohara, S. in *Proceedings*, Japan-U.S. Conference on *Composite Materials*, K. Kawata and T. Akasaka, Eds., Tokyo, 1981, pp. 224–227.

[16] Hirsch, P., Howie, A., Nicholson, R. B., Pashley, D. W., and Whelan, M. J., *Electron Microscopy of Thin Crystals*, Robert E. Krieger Publishing Co., New York, 1977.

A. S. Krausz,[1] *K. Krausz,*[2] *and D. S. Necsulescu*[1]

Probabilistic Fracture Kinetics of "Natural" Composites

REFERENCE: Krausz, A. S., Krausz, K., and Necsulescu, D. S., **"Probabilistic Fracture Kinetics of "Natural" Composites,"** *Composite Materials: Fatigue and Fracture, ASTM STP 907,* H. T. Hahn, Ed., American Society for Testing and Materials, Philadelphia, 1986, pp. 73–83.

ABSTRACT: The behavior of crack propagation in "natural" composite materials (eutectics) was investigated. It was shown that the conditions of failure should be described by a probabilistic analysis that represents correctly the physical properties, rather than by the usual deterministic approach. It is considered that the method is applicable for the failure analysis of "artificial" composite materials as well.

The environment-enhanced subcritical crack velocity, v, is represented by the appropriate kinetics combination of the elementary rate constants, ℓ, as $v = f(\ell)$. The rate constants are described explicitly as

$$\ell = \frac{kT}{h} \exp\left(-\frac{\Delta G}{kT}\right) \text{ with } \Delta G = \Delta G^{+} - W(K)$$

where k is the Boltzmann constant, h is Planck's constant, T is the absolute temperature, ΔG^{+} is the appropriate atomic bond energy of the low- and high-strength components encountered, respectively, as the crack tip moves into the corresponding zone, W is the mechanical work in the corresponding zone, and K is the stress intensity factor.

The physical process is controlled by thermal activation; the consequence of this is that crack growth in a probabilistic process is controlled by the instantaneous state of the load-material-crack system. It is recognized that on the atomic scale, bond breaking as well as healing occurs—the equivalent of the birth-death Markovian processes of probability mathematics. The analysis defines the crack size distribution as a function of time: The expectation value of the probability distribution is the experimentally measurable average; the spread of the probability density function defines the failure time probability of the composite material. It is concluded that the probabilistic physical process leads to a significantly different, and often more dangerous, failure occurrence than what is expected from the usual deterministic analysis.

KEY WORDS: eutectic laminate, subcritical crack propagation, temperature dependence, probabilistic crack size distribution, Markovian process

The development of high-strength laminated composite materials requires an improved understanding of the physical mechanism of fracture (for example,

[1] Professor and associate professor, respectively, Faculty of Science and Engineering, University of Ottawa, Ottawa, Ont., Canada.

[2] Consultant, 300 The Driveway, Ottawa, Ont., Canada.

Refs *1–3*); better understanding of the effect of temperature and environment on the rate of crack propagation is of particular importance [*4*]. In previous studies it was shown that temperature-dependent subcritical crack propagation in a degrading environment is controlled by thermal activation and that the crack velocity in homogeneous materials, subject to sustained loading, is described well with the kinetics theory of fracture. It was also shown that the physical process of crack propagation is probabilistic and that this effect is superposed on the conventional Weibull statistical condition [*5*].

It is the purpose of this paper to report the results of a study in which the fracture kinetics method was developed further to consider the conditions of crack propagation in a composite material of regularly spaced soft-hard[3] components, subject to sustained loading in a degrading environment. The physical process of crack propagation is presented first, followed by a description of the mathematical technique and a discussion of the analytical results.

Physical Process of Crack Propagation in a Degrading Environment

The fundamental element of any crack propagation process is the breaking of atomic bonds; only the accumulation of these elementary events can be observed on the microscopic or macroscopic scale. An understanding of the basic processes that control the velocity has to be developed therefore from a physically rigorous theoretical model; testing the applicability of the conclusions derived from the study to the experimental results has to follow. Once the validity of the model is established, the conclusions can be extended to the description of the behavior outside the already measured range. This character of the physically based, rational theory is important and distinguishes it from the empirical descriptions. It becomes particularly significant for lifetime determination and for operation and maintenance schedule purposes.

Environment-assisted crack propagation occurs in two main steps: (1) The external or internal environment reacts with the solid at the crack tip and produces a region in which the bond strength of the chemically altered material is reduced. (2) Under the effect of the applied load the "weathered" bonds break and the crack moves across the degraded region. These two steps are repeated consecutively (Fig. 1).

While Step 1 of the environment-assisted crack propagation is very complex, it is often sufficient to describe the chemical degradation (cd) process by a single elementary rate constant, expressed as

$$\ell_{cd} \propto \frac{kT}{h} \exp\left(-\frac{\Delta G^{\ddagger}_{cd}}{kT}\right) \tag{1}$$

[3] It should be noted here that the soft-hard terms are used throughout this paper interchangeably with the concepts of low strength-high strength, although generally the two designations are not identical.

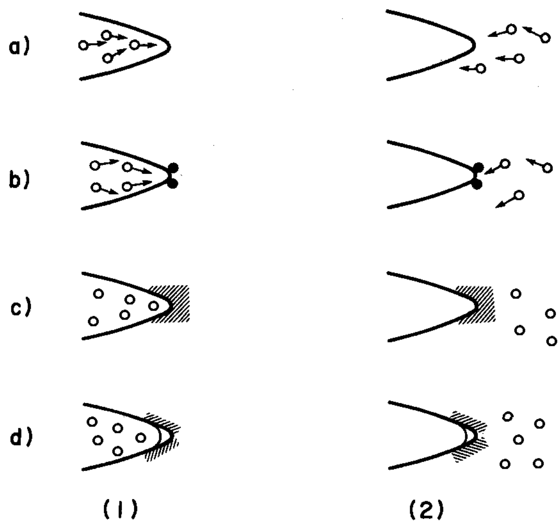

FIG. 1—*Progress of environment-assisted crack propagation:* (1) *external environment* (*liquid or gas*)*;* (2) *internal environment* (*for example, hydrogen diffusion*). *Open circles represent the reacting species transported to the tip; solid circles are the resultant species of the reaction between the solid and the environment; shading indicates the chemically altered zone.*

where

ℓ_{cd} = number of average activations per unit time, the measure of the chemical degradation step;
k, h = the Boltzmann and Planck's constants, respectively,
T = (absolute) temperature; and
$\Delta G^{\ddagger}_{cd}$ = an "activation free energy," the function of the chemical degradation.

The symbol $\ddagger$ signifies that the term is associated with the activated state. The meaning of Eq 1 is simply the statement that a corroded zone of a size sufficient for a crack propagation step develops ℓ_{cd}-times per second. This, of course, is a rather sweeping statement; for more detailed descriptions, see Refs *6–9*.

It is now well established [*10–11*] that Step 2 of the environment-assisted process, the actual subcritical (time and temperature dependent) crack propagation, is also controlled by the same type of behavior expressed by Eq 1. This is because crack propagation occurs by a sequence of atomic bond breaking steps and rearrangement of the atomic configuration in the crack tip zone—similar to the chemical reactions. Accordingly, the rate of the crack propagation (cp) steps is expressed rigorously as [*10*]

$$\ell_{cp} = \frac{kT}{h} \exp\left(-\frac{\Delta G^{\ddagger}_{cp} - W}{kT}\right) \tag{2}$$

where k_{cp} and $\Delta G^{\ddagger}_{cp}$ are, in analogy with Eq 1, the average rate of activation and the "activation free energy" of crack propagation. The applied mechanical work, W, represents the contribution of the external load and as such is considerably less than the Griffith surface energy.

Experimental evidence [12–14] and physical theoretical consideration [15] prove that, at least on the atomic scale, occasional atomic bond healing steps also occur. It is often important to consider this effect. The rate of crack healing steps k_{ch} is

$$k_{ch} = \frac{kT}{h} \exp\left(-\frac{\Delta G^{\ddagger}_{ch} + W}{kT}\right) \tag{3}$$

where the subscript "ch" denotes crack healing, and the other terms have their previously given meaning. Equations 1, 2, and 3 provide a powerful general description of environment-assisted crack propagation. The activation free energy terms, $\Delta G^{\ddagger}$, define quantitatively the atomic bond strength as the function of the chemical composition and structure of the region in which the crack tip finds itself: the degraded or nondegraded, low- or high-strength component of the composite. The contribution of the mechanical work, W, to the crack propagation process is usually described as

$$W = \alpha K \tag{4}$$

where α, the work factor, is also a function of the structure and the mechanism of the crack propagation process. The stress intensity factor K is a rigorous expression, derived from fracture mechanics concepts as

$$K = Y\sigma\,(a)^{1/2} \tag{5}$$

where

Y = geometrical factor of fracture mechanics,
σ = stress, and
a = crack size.

The system (Eqs 1 to 5) represents rigorously and fully the crack propagation process in composite materials subject to a hostile environment. It expresses quantitatively the effect of the chemical environment, the composition and microstructure of the material, the geometry of the specimen or structure element, the geometry of the crack, the mechanical load, and the temperature. For the purpose of this report the theory is presented in terms of linear elastic fracture mechanics. For a wide range of environment-assisted cracking this is a sufficiently good approximation: the extension to fracture, associated with a large plastic zone, is now in progress.

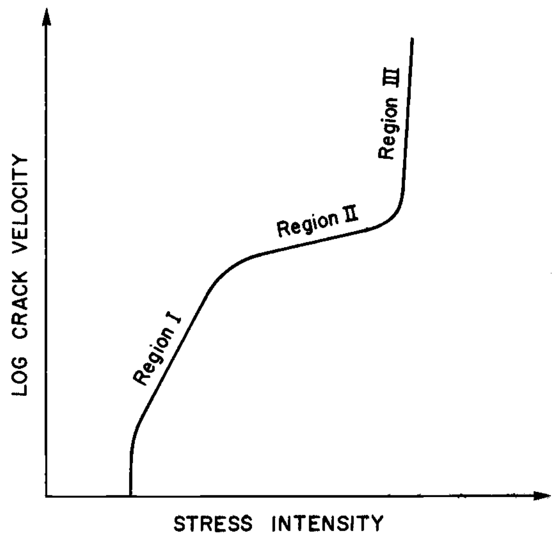

FIG. 2—*Typical environment-assisted crack propagation behavior in sustained loading.*

The mathematical formulation will be developed for the typical Region 1 condition of environment-assisted fracture (Fig. 2).

Environment-Assisted Crack Propagation in a Layered Composite

In Region I the chemical attack is much faster than the fracturing step in the corroded zone and consequently the crack propagation process is essentially controlled by these steps.

Consider a crack of size a_i; it has to wait a random time period, t, between two steps to move forward so that

$$t_{cp} = \frac{1}{k_{cp}} = \frac{h}{kT} \exp \frac{\Delta G_{cp}^{\ddagger} - W}{kT}$$

For the occasional healing step the waiting time is

$$t_{ch} = \frac{1}{k_{ch}} = \frac{h}{kT} \exp \frac{\Delta G_{ch}^{\ddagger} + W}{kT}$$

In each of the soft and hard layers the activation free energies, $\Delta G_{cp}^{\ddagger}$ and $\Delta G_{ch}^{\ddagger}$, and the mechanical work, W, have the corresponding specific value. The waiting time, t, is an exponentially distributed random variable because (as discussed in the following) the mathematical model of the probabilistic atomic bond breaking and healing mechanism of crack propagation is a Markov chain process.

If the healing effect is negligible the crack propagation time in a composite material is simply the sum of the two terms

$$t = (nt_{\mathrm{cp}})_{\mathrm{soft}} + (nt_{\mathrm{cp}})_{\mathrm{hard}}$$

where n is the number of steps in the corresponding element of the composite. When, however, the healing steps are not negligible, particularly in the important threshold zone, determination of the crack velocity is more complex.

Consider now a larger number of identical specimens ρ_i each having a crack size a_i. Figure 3 illustrates that the number of specimens ρ_i having a crack size a_i can change, for four reasons:

1. Cracks just one propagation step smaller than a_i grow to size a_i, and the rate of change is

$$\rho_{i-1}\, k_{\mathrm{cp}}$$

2. Cracks of a_i size grow to one step larger size at the rate of

$$\rho_i\, k_{\mathrm{cp}}$$

3. Cracks of a_i size shrink to one step size smaller dimension by healing at the rate of

$$\rho_i\, k_{\mathrm{ch}}$$

4. Cracks of one step larger than a_i heal back to a_i size at the rate of

$$\rho_{i+1}\, k_{\mathrm{ch}}$$

This behavior is illustrated in Fig. 3. The rate of change in the number of cracks ρ_i of size a_i can be expressed as the appropriate combination of the four

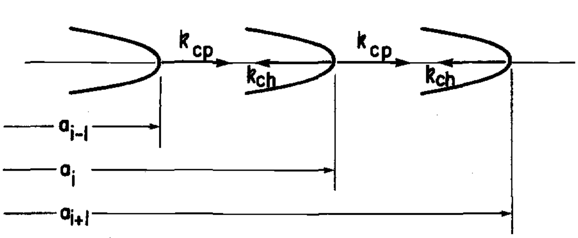

FIG. 3—*Schematic representation of the processes by which a crack size can change.*

possible rates

$$\frac{d\rho_i}{dt} = \rho_{i-1}\, k_{cp} - \rho_i(k_{cp} + k_{ch}) + \rho_{i+1}\, k_{ch} \tag{6}$$

It is, of course, necessary to consider the rate constant according to whether the corresponding crack size is in the soft or hard layer.

The mathematical formulation of Eq 6 is represented well by Fig. 4, the schematic equivalent of Fig. 3. It is clear from the figure and from Eq 6 as well that the model corresponds to a typical birth-death Markov chain process: The bond breaking and healing rates depend only on the conditions that exist at the instant of their occurrence; the rates are the averages of random atomic occurrences; the bond breaking (birth) and bond healing (death) rates do not interact, a specific condition that exists in the rate theory of thermally activated processes. Accordingly, a system of differential equations can be written for each crack size that is derived similarly to Eq 6. The crack sizes range from the initial microcrack size a_0 to the size that is the limit for the lifetime under consideration, the critical crack size a_c. The equation system is then

$$\begin{aligned}
\frac{da_0}{dt} &= -\rho_0\, k_{cp} + \rho_1\, k_{ch} \\
\frac{da_1}{dt} &= -\rho_0\, k_{cp} - \rho_1\,(k_{ch} + k_{cp}) + \rho_2\, k_{ch} \\
\frac{da_2}{dt} &= \rho_1\, k_{cp} - \rho_2\,(k_{ch} + k_{cp}) + \rho_3\, k_{ch} \\
&\vdots \\
\frac{da_i}{dt} &= \rho_{i-1}\, k_{cp} - \rho_i\,(k_{ch} + k_{cp}) + \rho_{i+1}\, k_{ch} \\
&\vdots \\
\frac{da_{c-1}}{dt} &= \rho_{c-2}\, k_{cp} - \rho_{c-1}\,(k_{ch} + k_{cp}) + \rho_c\, k_{ch} \\
\frac{da_c}{dt} &= \rho_{c-1}\, k_{cp} - \rho_c\,(k_{ch} + k_{cp})
\end{aligned} \tag{7}$$

Discussion

Analyses were carried out to investigate the crack propagation velocity in laminar composite materials of alternating soft-hard layers. The differential equation system (Eq 7) was converted into a computer program and numerical solutions

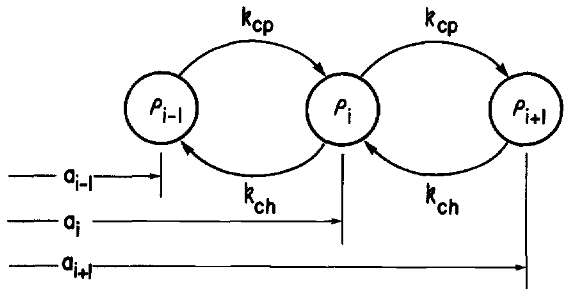

FIG. 4—*Markov chain representation of the crack propagation process.*

were obtained. The strength of the layers is expressed by the atomic bond strength, which is the function of composition and atomic structure. Accordingly, the activation energy of crack propagation, $\Delta G^{\ddagger}_{cp}$ varies periodically. Figure 5 illustrates the corresponding step function type used in the analysis.

The natural, physical, probabilistic behavior of the crack propagation process renders crack velocity a probabilistic quantity. Consequently, a distribution of crack velocities will be observed at any defined time, even under identical conditions. The crack size distribution is defined by the Eq 7 system as derived from the Markov chain condition of probability theory. The system was evaluated for a range of material and loading characteristics. A typical example is presented in Fig. 6. The figure shows the crack size distribution at subsequent times: Over the period illustrated here crack sizes vary already by several layers of thicknesses. The figure also illustrates that the average crack velocity fluctuates in the early times, but settles down to a steady probabilistic value that is significantly higher than the deterministic value [*16*] that would be considered by conventional analysis and design practices. Advanced technology applications of layered composites often require damage-tolerant design and maintenance practices. Because the basic assumption is that cracks do exist, it is their propagation rate that control the lifetime. Examination of the actual, physical, probabilistic crack propagation behavior demonstrates that conventionally deterministic tests and analyses, which

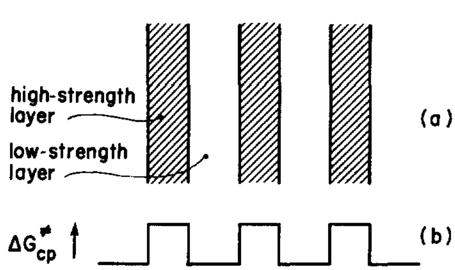

FIG. 5—*Schematic representation of the composite material* (a) *and the corresponding variation of the activation energy* (b).

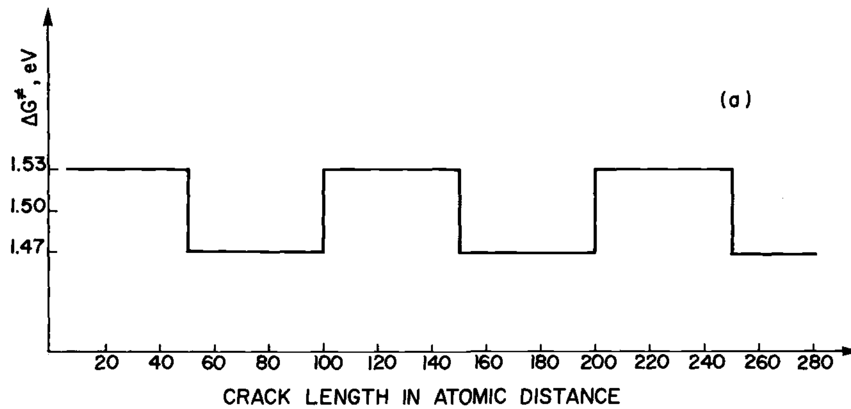

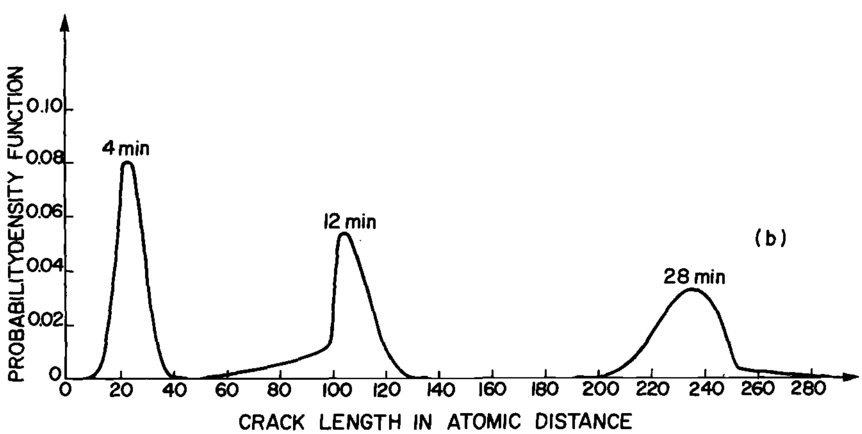

FIG. 6—*A typical example of crack size distribution in layered composites. The square wave strength variation was represented by an activation energy of* $\Delta G_{cp}^{\ddagger h} = 1.53$ *eV in the hard layer and* $\Delta G_{cp}^{\ddagger s} = 1.47$ *eV in the soft layer.*

$$\Delta G_{ch}^{\ddagger h} = \Delta G_{ch}^{\ddagger s} = 0; \quad W_{cp}^{h} = W_{cp}^{s} = 0.8 \text{ eV}; \quad T = 300 \text{ K}.$$

In the figure crack growth is defined by the random variable (crack size), X, associated with the expectation value. Accordingly, the instantaneous velocity is $v_{inst.} = (X_i - X_{i-1})/(t_i - t_{i-1})$, *where* $X_i - X_{i-1}$ = *interatomic distance, and* $t_i - t_{i-1}$ *is the time difference of the corresponding two locations of the expectation values. Similarly, the probabilistic average crack velocity is defined as* $v_{avg} = (X_i - X_0)/(t_i - t_0)$, *where* X_0 *and* t_0 *are the initial crack size and time. The deterministic crack velocity is defined as* $\bar{v} = a/\int_{a_0}^{a} v_{dx}^{-1}$, *where* a *is the crack size.*

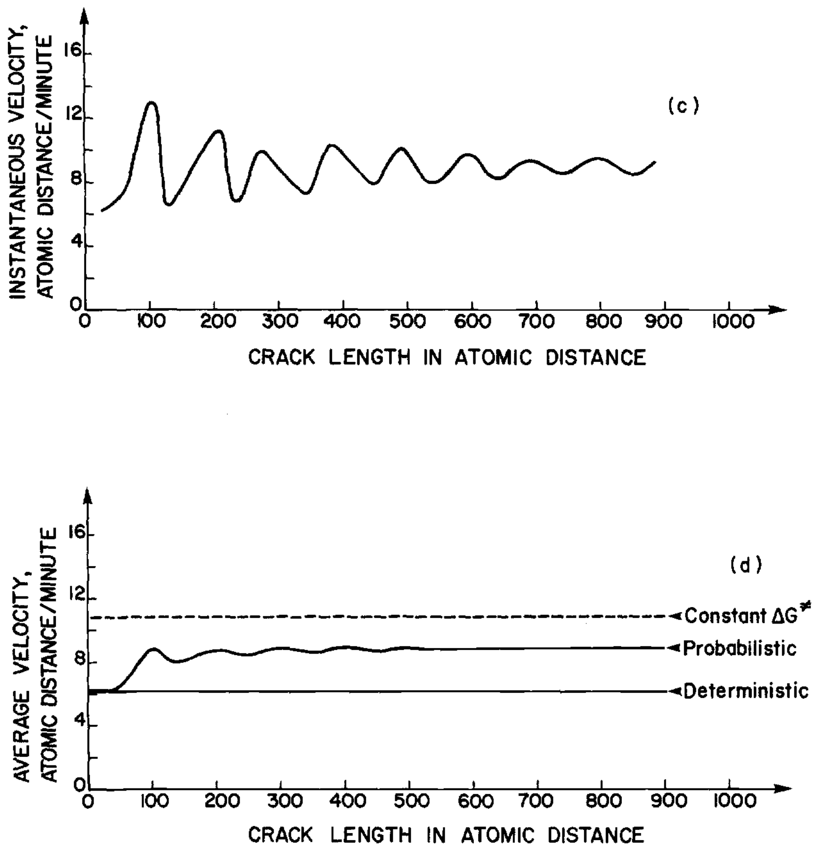

FIG. 6—*Continued.*

consider the crack velocities separately in soft and hard layers and approximate the combined (layered composite) behavior as the simple algebraic sum of crack propagation in each of the two layer types, result in low values of crack velocity. The probabilistic crack velocity analysis is, therefore, a more realistic and safer method of lifetime determination.

Computer capacity restricted the maximum number of crack propagation steps to about 1000 in this study. To obtain information from this relatively small number of steps, layer thicknesses were limited with respect to crack propagation step widths. Consequently, a realistic physical interpretation of the model, as imposed by the computational capacity, is given in terms of finely layered lamellar eutectic material, a natural composite. The results, however, are qualitatively valid for macroscopically layered (artificial) composites as well. The full results of the analyses will be published elsewhere.

References

[1] Underwood, J. H. in *Composite Materials: Testing and Design, ASTM STP 546,* American Society for Testing and Materials, Philadelphia, 1973, pp. 376–394.
[2] Morris, D. H. and Hahn, H. T. in *Composite Materials: Testing and Design, ASTM STP 617,* American Society for Testing and Materials, Philadelphia, 1976, pp. 5–17.
[3] Brinson, H. F. and Yeow, Y. T. in *Composite Materials: Testing and Design, ASTM STP 617,* American Society for Testing and Materials, Philadelphia, 1976, pp. 18–38.
[4] Thompson, J., *Metal Progress,* April 1984, pp. 41–46.
[5] Krausz, A. S., and Krausz, K. in *Proceedings,* Design Engineering Technical Conference, Hartford, CT, American Society of Mechanical Engineers, 1981, pp. 23–28.
[6] Hillig, W. B., and Charles, R. J., *High Strength Materials,* Wiley-Interscience, New York, 1965.
[7] Krausz, A. S., *International Journal of Fracture,* Vol. 14, 1978, pp. 5–15.
[8] Wiederhorn, S. M. in *Fracture Mechanics of Ceramics,* Vol. 4, R. C. Bradt, D. P. H. Hasselman, and F. F. Lange, Eds., Plenum Press, New York, 1978.
[9] Brown, S. D., *Journal of the American Ceramic Society,* Vol. 62, 1979, p. 515.
[10] Krausz, A. S., and Eyring, H., *Deformation Kinetics,* Wiley-Interscience, New York, 1975.
[11] Lawn, B. R., and Wilshaw, T. R., *Fracture of Brittle Solids,* Cambridge University Press, U.K., 1975.
[12] Obreimoff, J. W. in *Proceedings of the Royal Society of London,* Series A, Vol. 127, 1930, pp. 290–297.
[13] Forty, A. J., and Forwood, C. T., *Transactions,* British Ceramic Society, Vol. 62, 1963, pp. 715–724.
[14] Wiederhorn, S. M., and Townsend, P. R., *Journal of the American Ceramic Society,* Vol. 53, 1970, pp. 486–489.
[15] Glasstone, S., Laidler, K., and Eyring, H., *The Theory of Rate Processes,* McGraw-Hill, New York, 1941.
[16] Krausz, K., Krausz, A. S., and Necsulescu, D.-S., *International Journal of Fracture,* Vol. 23, 1983, pp. R155–R159.

P. W. M. Peters[1]

Constrained 90-Deg Ply Cracking in 0/90/0 and ±45/90/∓45 CFRP Laminates

REFERENCE: Peters, P. W. M., "**Constrained 90-Deg Ply Cracking in 0/90/0 and ±45/90/∓45 CFRP Laminates,**" *Composite Materials: Fatigue and Fracture, ASTM STP 907*, H. T. Hahn, Ed., American Society for Testing and Materials, Philadelphia, 1986, pp. 84–99.

ABSTRACT: The strength distribution of 90-deg plies in the laminates $(\pm\theta/90_n)_s$ with $\theta = 0$ deg and 45 deg and $n = 2$, 3, and 6 is described in the form of a two-parameter Weibull distribution. A common feature for both orientations of surface layers is that at decreasing 90-deg ply thickness the characteristic strength and shape parameter increase. The reason is that the surface layers suppress a growth of the defects in the 90-deg ply which are lying close to the interface with the surface layers. This causes the apparent shape parameter to increase from a value $a = 6.4$ for a thick 90-deg ply (which is comparable to the shape parameter determined on a unidirectional laminate) to a shape parameter of $a = 10.47$ for a thin 90-deg ply ($n = 2$) in case of the $(0_2/90_n)_s$ laminate. Further, it is shown that crack formation in the 90-deg plies of the $(\pm 45/90_n)_s$ laminates is strongly influenced by the severe edge stresses. This causes the applied one-dimensional fracture strain criterion to be inaccurate for the $(\pm 45/90_n)_s$ laminates.

KEY WORDS: composite materials, graphite composites, cross-ply cracking, Weibull strength distribution, edge effect, carbon fiber reinforced plastic (CFRP)

One of the first mechanisms of failure to occur in carbon fiber reinforced plastic (CFRP) laminates under static as well as fatigue loading is the development of cross-ply cracks. Often these cracks trigger other damage mechanisms (for example, delaminations) which finally can lead to total failure. For this reason many investigations have been done to study the phenomenon of cross-ply cracking [*1–9*]. Multiple 90-deg ply cracking has been studied as a function of 90-deg ply thickness [*1–7*] and as a function of the stacking sequence of the laminate [*2–3*]. In these cases the stacking sequence is normally chosen such that delaminations starting at the specimen edges occur at higher loads than cross-ply cracking.

The approaches for a 90-deg ply strength characterization are mainly based on (1) a fracture mechanical description of the strength [*1–5*] and (2) a description

[1] Scientist, DFVLR, Institute for Materials Research, Cologne, West Germany.

of the strength as influenced by the statistical distribution of defects in the 90-deg plies [*6–9*].

An energy criterion could be successfully applied for the description of the decreasing strength at increasing 90-deg ply thickness. The strength further was found to depend on the stacking sequence. An investigation of $(\pm\theta/90_n)_s$ laminates with $\theta = 0$, 30, and 60 deg showed that the 90-deg ply strength generally decreases at increasing angle θ [*2*]. This effect can also be explained by using an energy model [*5*]. It describes the tendency well, although at smaller 90-deg ply thickness the deviation between the theory and the experimental results of Ref *2* is large, especially for an increasing angle θ.

The statistical analyses are mainly based on a two-parameter Weibull distribution of the strength. The parameters for this Weibull distribution can be determined from the crack distance, as for example in Ref *6* on a glass-epoxy laminate. From the crack distributions it was found that the probability of crack formations close to existing cracks is lower. That is why in following investigations the inhomogeneous stress distribution in the cracked 90-deg ply was considered [*7,9*]. This was done for several CFRP cross-ply laminates assuming a constant value of the shape parameter. A direct determination of the Weibull strength distribution is possible using only one specimen, when the stress at every single occurring crack is measured [*9*]. From the determined strength distributions on $(0_2/90_n)_s$ laminates with $n = 2$, 3, and 6, it was found that the strength as well as the shape parameter increases at decreasing 90-deg ply thickness. In the present investigation the last-mentioned test procedure is applied to determine the strength of 90-deg plies in $(\pm45/90_n)_s$ laminates with $n = 2$, 3, and 6. As the test results seem to be influenced not only by the main stress, other stress components, especially at the specimen edges, are considered. In case of large edge stresses crack formation is expected to start mainly at the specimen edges. To study the effect of the edges on crack formation, some specimens out of the $(\pm45/90_2)_s$ laminate were immersed in water. In this way the main stress at the edge is reduced by swelling stresses and thus crack formation starting at the edge is suppressed.

Experimental Procedure

Angle-ply laminates with the orientation $(0_2/90_n)_s$ and $(\pm45/90_n)_s$ with $n =$ 2, 3, and 6 were produced from Fibredux 914C prepreg by the DFVLR Braunschweig. The curing sequence was 1 h at 175°C and 4 h at 190°C. Specimens of 16-mm width were cut by diamond wheel from the plates and stored in a dessicator. The specimens were loaded up to fracture in a displacement-controlled (2 mm/min) Instron testing machine with mechanical grips. In the gripping area the specimens were reinforced with 40-mm-long aluminum alloy tabs, leaving a free length of 115 mm. Four specimens out of the laminate $(\pm45/90_n)_s$ were covered with aluminum wrapping foil, leaving only the edges unprotected. After that they were immersed in distilled water for 126 h in order to saturate the specimens edges. Cracking of the 90-deg ply was detected in the investigated laminates by a piezoelectric load cell in connection with a high-speed recorder. Thus 90-deg ply cracking was registered as a function of time and of the applied strain up to final failure of the specimen.

Analysis

Stresses in the Separate Plies

For the balanced symmetric laminates, as investigated here, the state of stress of the 90-deg ply can be derived from lamination theory [*10*]. The in-plane constitutive equation is given by

$$N_i = A_{ij}\epsilon_j - N_i^t \qquad i,j = 1, 2, 6 \tag{1}$$

where

$$\begin{aligned} N_i^t &= \int Q_{ij} e_j^t \, dz \\ A_{ij} &= \int Q_{ij} \, dz \\ N_i &= \int \sigma_i \, dz \end{aligned} \tag{2}$$

with the integration from $z = -h/2$ to $z = h/2$

Now the in-plane stresses follow from

$$\epsilon_j = A_{ij}^{-1}(N_i + N_i^t) \tag{3}$$

The residual thermal strains are determined from Eq 3 in the absence of N_i

$$\epsilon_j^t = A_{ij}^{-1} N_i^t \tag{4}$$

After substitution of Eq 3 into the constitutive equation of the 90-deg ply

$$\sigma_i^{90} = Q_{ij}^{90}(\epsilon_j - \alpha_j \Delta T) \tag{5}$$

it follows

$$\sigma_i^{90} = Q_{ij}^{90}[A_{ik}^{-1}(N_k + N_k^t) - \alpha_j \Delta T] \tag{6}$$

In the case of the $(0_2/90_n)_s$ laminates the stresses perpendicular to the loading direction were neglected [9], leading to the thermal strain in the 90-deg ply being

$$\epsilon_1^{t,90} = \frac{\Delta T(\alpha_1^{90} - \alpha_1^{0})E_1^{0}}{n/2E_1^{90} + E_1^{0}} \tag{7}$$

TABLE 1—*Listing of investigated laminates indicating the 90-deg ply element length ℓ_0, the number of these elements* N *in the 115-mm free specimen length, the thermal strain in the 90-deg ply, and the total number of 90-deg ply cracks at specimen failure, respectively.*

Laminate	ℓ_0, mm	N	$\epsilon_1^{t,90}$, %	Number of Cracks
$(0_2/90_2)_s$	0.69	167	0.438	31 to 44
$(0_2/90_3)_s$	0.83	139	0.424	40 to 64
$(0_2/90_6)_s$	1.12	103	0.384	34 to 52
$(\pm45/90_2)_s$	0.59	195	0.325	38 to 46
$(\pm45/90_3)_s$	0.67	172	0.297	13 to 22
$(\pm45/90_6)_s$	0.80	144	0.236	1 to 6

The deviation from the two-dimensional approach according to Eq 4 was proven to be about +2%. The thermal strains in the 90-deg plies $\epsilon_1^{t,90}$ resulting from Eq 4 are indicated in Table 1.

As soon as 90-deg ply cracking occurs, the stresses in the 90-deg ply become inhomogeneous. At the crack the stress σ_1^{90} becomes 0, whereas farther from the crack the undisturbed stress, $\sigma_{1,\infty}^{90}$, is reached assymptotically. The stress distribution near the 90-deg ply cracks was determined using a shear lag analysis [*8*]. In this analysis only the stresses in Direction 1 are considered. The element of equilibrium of this analysis is presented in Fig. 1. The parameters a^0 and a^{90} represent the thickness of the surface layers and total thickness of the 90-deg ply, respectively, and b the thickness of the resin shear transfer layer. According to this analysis the stress distribution in the 90-deg ply is given by

$$\sigma_{1,x}^{90} = \sigma_{1,\infty}^{90}(1 - \exp - \gamma x) \tag{8}$$

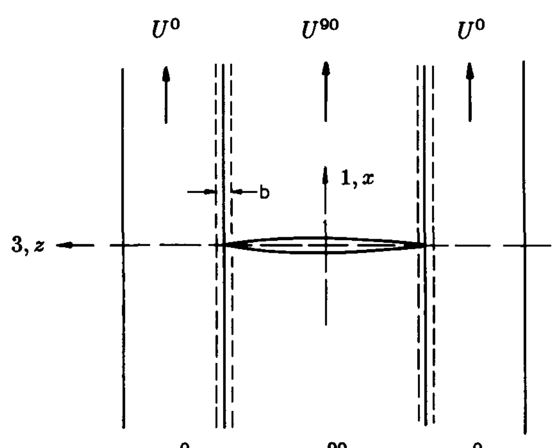

FIG. 1—*Element of applied shear lag analysis for which equations of equilibrium are solved.*

where

$$\gamma = \sqrt{\frac{G_m}{b}\left(\frac{1}{E_1{}^0 a^0} + \frac{2}{E_1{}^{90} a^{90}}\right)} \tag{9}$$

where $E_1{}^0$, $E_1{}^{90}$, G_m, and b represent the tensile modulus of the 0- and 90-deg layers (128 and 9.5 GPa, respectively), the matrix shear modulus (G_m = 1.48 GPa), and the thickness of the resin layer (b = 0.015 mm), respectively.

Weibull Strength Distribution

In this analysis fracture of the 90-deg ply is assumed to be the result of statistically distributed defects of different size. For this reason the strength of the 90-deg plies varies along the length. That is why on loading a specimen which contains a number of 90-deg plies, multiple cracking in the 90-deg ply will occur before final rupture. The occurrence of multiple 90-deg ply cracking makes it reasonable to consider the specimen as a chain of elements all of which can break. This number of elements should be equal to or larger than the number of cracks. A description of the strength of these elements can be made only when every element breaks only *once*. Thus the element has to be chosen sufficiently small.

The actual length of the element is chosen with the aid of the inhomogeneous stress distribution as given by Eq 8. It is clear that due to the low stress close to an existing crack here, no further crack formation will take place. For this reason the element length is somewht arbitrarily chosen as double the length in which 90% of the stress in the 90-deg ply is introduced again. This element length ℓ_0 is calculated using Eq 8 and the results for the laminates are presented in Table 1. It shows that the laminates investigated contain from 103 to 195 elements.

During the displacement-controlled tension test the piezoelectric load cell registers the dynamic load change (load drop) caused by the 90-deg ply cracking. The plot of the load drop as a function of the applied strain allows one to record the strain at which single elements fracture. The fracture strain of the elements is described by using a two-parameter Weibull fracture strain distribution with the probability of failure F at a strain ϵ_{f,ℓ_0} to be

$$F = 1 - \exp - (\epsilon_{f,\ell_0}/\hat{\epsilon}_{f,\ell_0})^a \tag{10}$$

with a being the shape parameter and $\hat{\epsilon}_{f,\ell_0}$ being the characteristic strength of the element with a length of ℓ_0. The probability of failure F is calculated using the median rank

$$F = \frac{j - 0.3}{N + 0.4} \tag{11}$$

where j represents the fracture order number (data listed in increasing order of strength) and N the number of elements ($N = 103$ to 195; see Table 1.) With the aid of Eqs 10 and 11 it is possible to find from the experimental results the Weibull parameters for each ply thickness. If the number of cracks in the 90-deg ply that develop before final specimen rupture is too small, the strength distribution cannot be determined from a single specimen. In this case the strength distribution is determined on 20 specimens by measuring the strain at the first occurring crack. This was done for all $(\pm 45/90_n)_s$ laminates.

In order to be able to compare the strength distributions determined on elements of different lengths, the strength for a uniform length has to be determined. This can be done applying

$$\hat{\epsilon}_{f,V_2}/\hat{\epsilon}_{f,V_1} = (V_1/V_2)^{1/a} \tag{12}$$

which describes the influence of the volume (V_1, V_2) on the strength according to the Weibull theory.

The applied fracture criterion neglects the influence of the stress perpendicular to the loading direction. This stress can—depending on the stacking sequence—differ substantially. Applying Eq 6 it is found that, for example, in the 90-deg plies of the $(0_2/90_2)_s$ and $(\pm 45/90_2)_s$ laminate the stresses σ_2^{90} are $\sigma_2^{90} = -54$ N/mm^2 and $\sigma_2^{90} = -135$ N/mm^2, respectively, at a total strain of $\epsilon_1^{90} = 1\%$ (Fig. 2*a*).

Probably more important for 90-deg ply crack formation is the complex stress situation at the edges. The tensile stresses in the thickness direction can especially have an influence on crack formation in the 90-deg ply. One reason for this is the multi-axial stress state at the edge and a second reason is that, by cutting the specimen, another class of defects is introduced. To find out how these stresses influence crack formation the edge stresses on four specimens out of the $(\pm 45/90_2)_s$ laminate were manipulated by introducing swelling stresses at the specimen edges only. This laminate was selected because the $(\pm 45/90_n)_s$ specimens have the most severe edge stresses. In particular, $n = 2$ was chosen because this laminate shows multiple 90-deg ply cracking which could be measured with the dynamic load cell.

The edge stresses in the thickness direction σ_3 were determined, following the simplified solution proposed by Pagano and Pipes [*11*]. According to this approach the shape of the stress distribution at the edge is as indicated in Fig. 2*b* with the maximum stress σ_3 at the edge given by

$$\sigma_{3,z} = \frac{90M(z)}{7h^2} \tag{13}$$

where

$M(z)$ = couple caused by stresses σ_2 with $M(z = 2h_0) = 4\sigma_2 h_0^2$,
h_0 = single ply thickness ($h_0 = 0.125$ mm), and
h = laminate thickness.

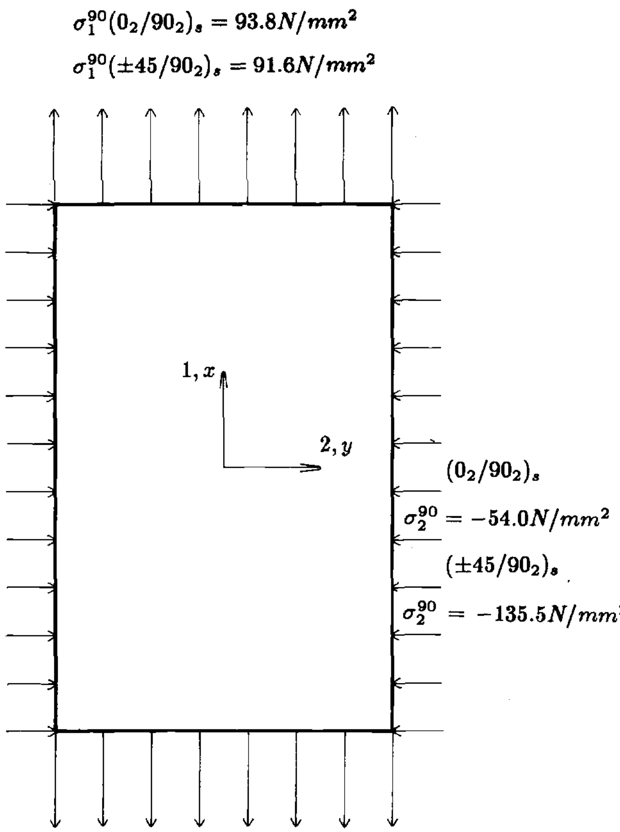

FIG. 2—*Stress components in 90-deg plies of* $(0_2/90_2)_s$ *and* $(\pm 45/90_2)_s$ *laminates at a total strain of* $\epsilon_1^{90} = 1\%$*:* (a) *in-plane stresses.*

In the present case $h = 1$ mm, so the range in which tensile edge stresses exist according to this approach is 0.333 mm. Next, a few specimens were immersed in distilled water, with only the edges unprotected, over such a period of time that in this range of 0.333 mm the thermal strain in the 90-deg plies $\epsilon_{1,y}^{r,90}$ was substantially reduced by swelling stresses. The residual strain near the specimens edges is given by

$$\epsilon_{1,y}^{r,90} = \epsilon_1^{t,90} + c_y^{90}\beta_1^{90} \tag{14}$$

where c_y^{90} is the moisture concentration as a function of y and β_1^{90} is the swelling coefficient. The swelling coefficient for the 90-deg plies was $\beta_1^{90} = 0.43$ and the moisture saturation contents measured 2.15% [12]. The moisture concentration after immersion in water for 126 h is calculated from

$$c/c_{\max} = 1 - \operatorname{erf}\left(\frac{|y - W/2|}{2\sqrt{Dt}}\right) \tag{15}$$

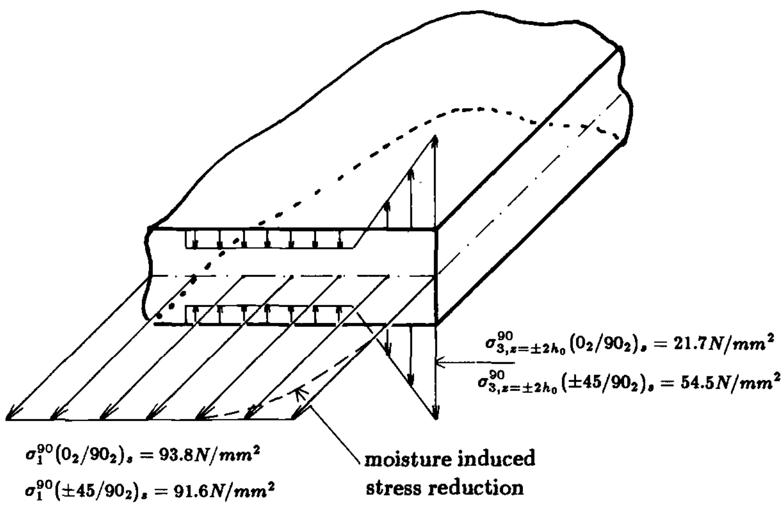

FIG. 2—*Continued.* (b) *edge stress in thickness direction* σ_3 *at* $z = \pm 2h_0$ *and moisture-induced stress reduction of stress* σ_1^{90} *at edge.*

with the diffusion coefficient being $D = 1.5 \times 10^{-4}$[mm²/h] [*12*] and t the time in hours. Thus at 0.333 mm from the specimen edges the moisture concentration reduces to $c/c_{max} = 0.087$. According to Eq 15 the residual strain in the 90-deg ply is reduced from $\epsilon_1^{t,90} = 0.325\%$ to $\epsilon_{1,y}^{r,90} = 0.245\%$ at $|y \pm W/2| = 0.333$ mm and to a compressive strain of $\epsilon_{1,y}^{r,90} = -0.60\%$ at the edges ($y = \pm W/2$).

Results

From the recording of the dynamic load the number of cracks is found and the respective strains at which they occur are determined. A record of the load drop against time is indicated in Fig. 3, from which the number of cracks can be found. It also shows that the load drop can be predicted reasonably well by the aid of the shear lag analysis, as shown before in Ref *8*. The Weibull strength distribution of the 90-deg plies as determined in Ref *9* is indicated in Fig. 4. This is the Weibull strength distribution for elements of length $\ell = 1$ mm, which was deduced from the Weibull strength distribution determined on four specimens of the respective laminates with $\ell = \ell_0$. Figure 5 presents the strength distribution determined on the 20 specimens of the $(\pm 45/90_n)_s$ laminates. The free length of the specimen was $\ell = 115$ mm. For both the $(0_2/90_n)_s$ and $(\pm 45/90_n)_s$ laminates an increasing shape parameter with decreasing 90-deg ply thickness can be found. This is also demonstrated in Fig. 6, where the shape parameter is shown as a function of the ply thickness.

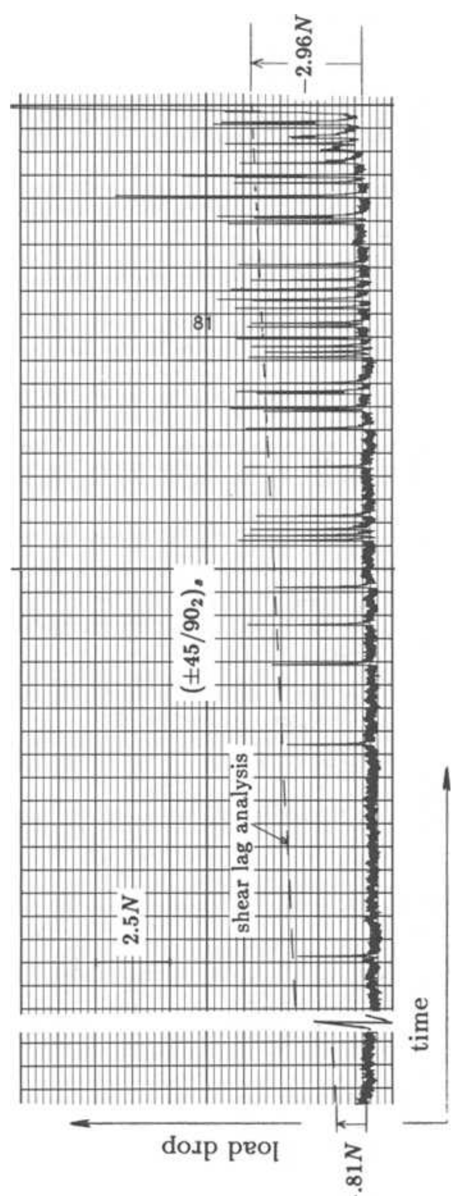

FIG. 3—Recording of measured load drop against time for a specimen out of the ($\pm45/90_2$)$_s$ *laminate showing multiple cracking and a reasonable agreement of measured load drop with theoretical calculation applying a shear lag analysis* [8].

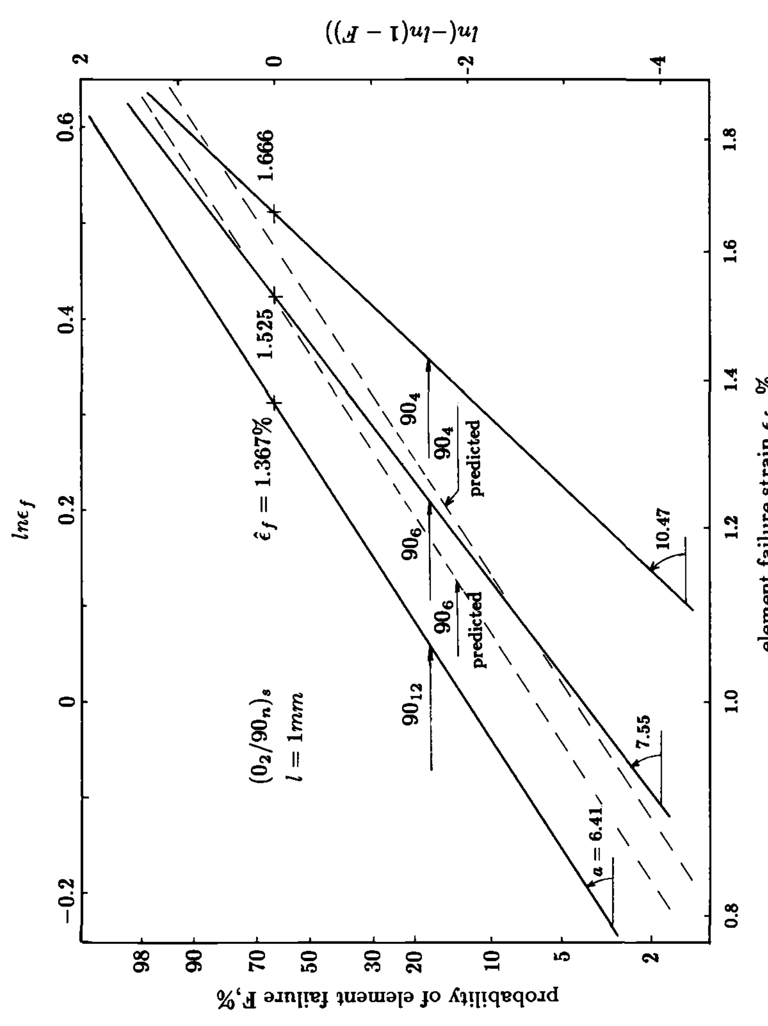

FIG. 4—*Weibull strength distribution for elements of a length l = 1 mm of 90-deg plies with a different thickness in $(0_2/90_n)_s$ laminates.*

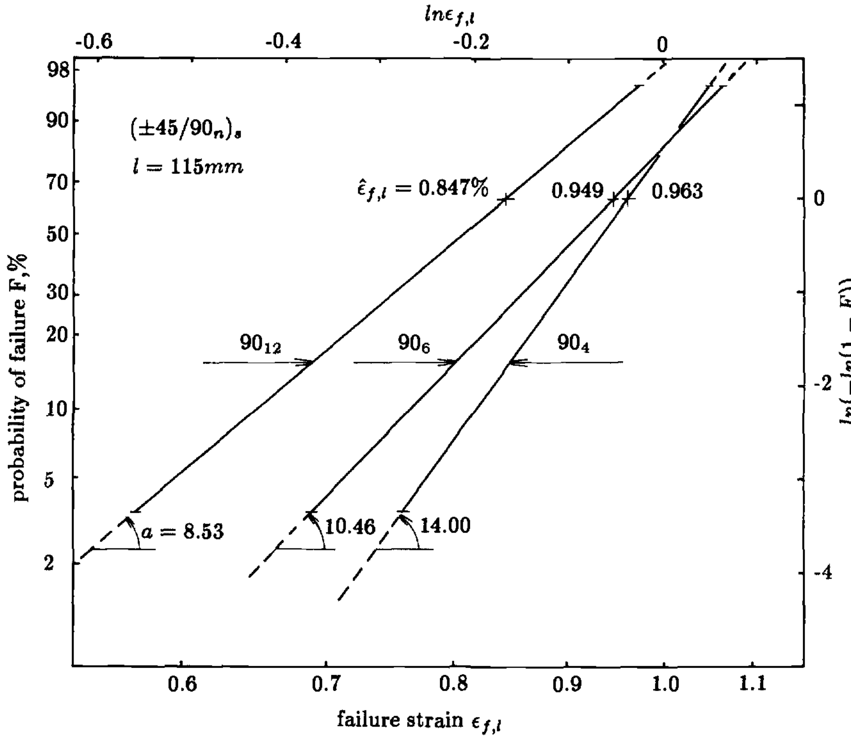

FIG. 5—*Weibull strength distribution for 90-deg plies with a length of ℓ = 115 mm in $(\pm45/90_n)_s$ laminates.*

The dependency of the 90-deg ply characteristic strength on the 90-deg ply thickness is given in Fig. 7. Indicated is the strength for specimens with a length of $\ell = 115$ mm. For the $(\pm45/90_n)_s$ laminate the measured test results are shown, whereas for the $(0_2/90_n)_s$ laminate the results are deduced from the element ($\ell = \ell_0$) strength distribution, making use of Eq 12. Both laminates show an increasing strength of the 90-deg ply with decreasing ply thickness. The strength in the $(\pm45/90_n)_s$ laminates levels off at approximately $t = 0.5$ mm ($n = 2$). For a larger 90-deg ply thickness the $(\pm45/90_n)_s$ laminates show a larger characteristic strength compared with those of the $(0_2/90_n)_s$ laminates.

The element ($\ell = \ell_0$) strength distribution of the 90-deg plies for both four specimens with wetted edges (by immersion in distilled water for 126 h) as well as for four dry specimens out of the $(\pm45/90_2)_s$ laminate is presented in Fig. 8. The mean results for both groups of specimens are indicated with a thick line: It clearly shows that by suppressing crack formation at the edge (by wetting the edges), the strength of the 90-deg ply is considerably increased. The shape parameter, however, seems not to be strongly affected by the suppression of edge crack formation.

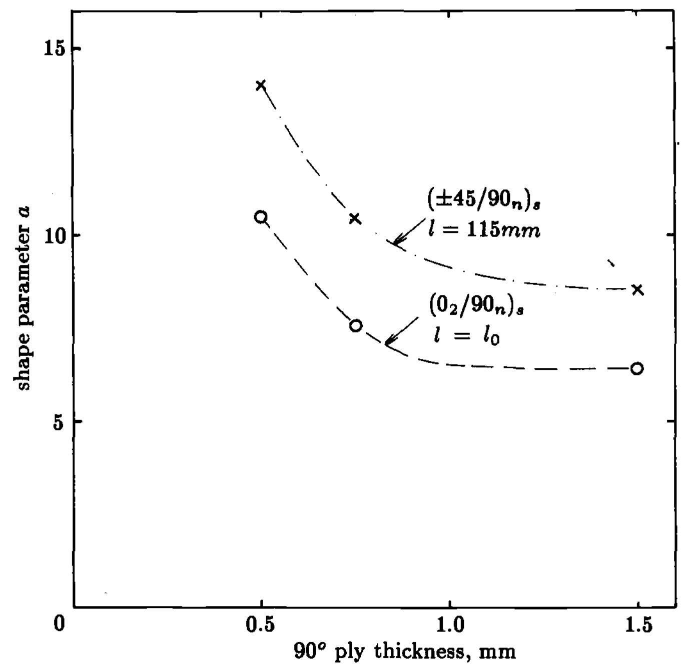

FIG. 6—*Shape parameter* a *of 90-deg ply Weibull strength distributions as a function of the 90-deg ply thickness for both* $(0_2/90_n)_s$ *and* $(\pm 45/90_n)_s$ *orientations.*

Discussion

Figure 4 shows the Weibull fracture strain distributions for the 90-deg layers in the $(0_2/90_n)_s$ laminates for a uniform element length of $\ell = 1$ mm. A prediction of the fracture strain distribution for the 90_6 and 90_4 layers based on the Weibull strength parameters of the 90_{12} layer, applying Eq 12, show too-conservative fracture strain distributions (intermittent lines). Thus the thickness effect of the 90-deg layer on the fracture strain distribution cannot be explained by the Weibull theory.

The actual fracture strain distributions indicate that the Weibull strength distribution for all 90-deg ply thicknesses approaches the same fracture strain for the probability of failure of F going to 1. From this it can be concluded that one out of 100 to 1000 elements with a length of 1 mm does not contain a defect and thus its strength is independent of thickness in the range of investigated 90-deg ply thicknesses (t = 0.5 to 1.5 mm). This fracture strain in the absence of defects is the maximum reachable fracture strain. Long specimens containing a number of elements fracture at a lower strain because of the distributed defects. Figure 4 shows that when defects are active, their influence is different when the 90-deg ply thickness is different. In Ref *9* it was concluded that this is the result of the 0-deg surface layers, which suppress defect growth in a range close to the

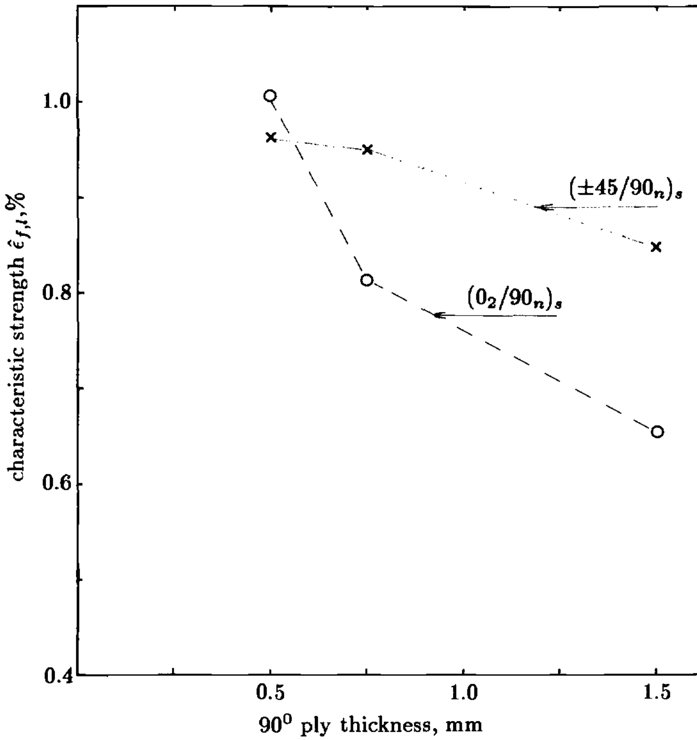

FIG. 7—*Characteristic strengths $\hat{\epsilon}_{f,l}$(ℓ = 115 mm) of 90-deg ply strength distributions for both $(0_2/90_n)_s$ and $(\pm45/90_n)_s$ orientations.*

0/90-deg ply interface. Suppression of defect growth is thus important for thin 90-deg plies and negligible for thick plies. For this reason the Weibull shape parameter for thick 90-deg plies between 0-deg surface layers is comparable to those determined in unidirectional laminates, for example, with a = 5.66 [*13*]. For thinner 90-deg plies between 0-deg surface layers the apparent shape parameter increases, although the defect distribution per unit of volume can be expected to remain unchanged. There exists an analogy with the phenomenon of a crack in a two-layer composite, with the crack in the weaker medium. When the crack approaches the interface with the stiffer medium the stress-intensity factor decreases [*14*]. Thus the interface can suppress crack growth as well as the growth of defects. The stiffer the second medium, the stronger is this effect.

For this reason it can be expected that the strength as well as the shape parameter of the 90-deg plies in between ±45-deg plies is smaller than that of the same thickness between 0-deg plies. The investigations of Flaggs and Kural [*2*] showed this effect on the strength using surface layers with 0, ±30, and ±60-deg orientations.

In the extreme case of thick 90-deg plies (with negligible influence of the

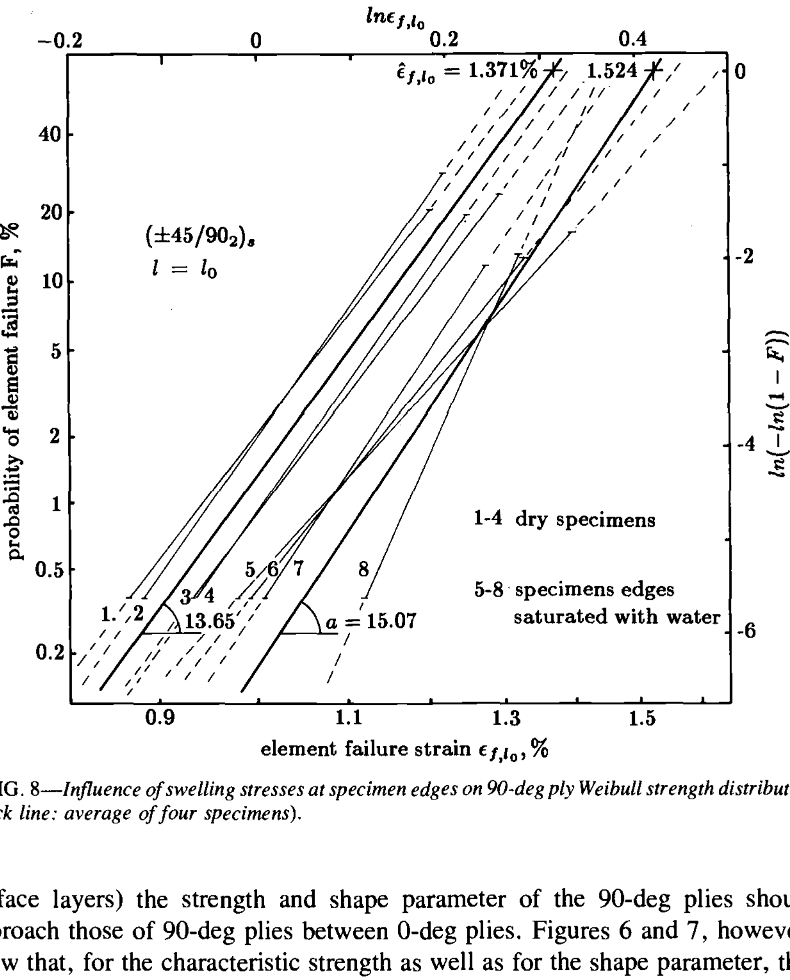

FIG. 8—*Influence of swelling stresses at specimen edges on 90-deg ply Weibull strength distribution (thick line: average of four specimens).*

surface layers) the strength and shape parameter of the 90-deg plies should approach those of 90-deg plies between 0-deg plies. Figures 6 and 7, however, show that, for the characteristic strength as well as for the shape parameter, this is not so, indicating that the 90-deg plies between the ±45-deg plies have a higher strength than those between the 0-deg plies. This is unexpected because both types of laminates were produced from the same prepreg batch, although the production date of the $(\pm 45/90_n)_s$ plates was nine months later than the other plates.

The general behavior of increasing characteristic strength and increasing shape parameter is, however, present. Another particular phenomenon in the strength distribution of the $(\pm 45/90_n)_s$ plies is visible in Fig. 5. There the strength distributions of the 90_6 and 90_4 plies intersect at a high probability of failure. This is unexpected, as the thinner ply should be stronger than the thicker ply. Now the question arises whether this can be caused by other stress components which are not considered in this one-dimensional stress (strain) fracture criterion. Suppression of crack formation at the specimen edges by introducing swelling strains at the edges increased the strength of the 90-deg ply (Fig. 8). This indicates that, when considerable edge stresses are present, a one-dimensional fracture criterion is inaccurate. Further investigations are necessary to describe the influence of the complex edge stresses on 90-deg ply cracking.

Conclusions

The strength distributions of the 90-deg plies between 0_2-deg as well as ± 45-deg surface layers show a similar phenomenon. At decreasing 90-deg ply thickness both the characteristic strength and the shape parameter increase. It was concluded that this is caused by a suppression of defect growth in a range close to the interface of the 90-deg ply with the surface layers. This effect is negligible for a large 90-deg ply thickness, resulting in a characteristic strength and shape parameter which is comparable to those determined on unidirectional material. At decreasing 90-deg ply thickness the influence of defect growth suppression is visible in the increasing strength and shape parameter. A quantitative comparison between the influence of both types of surface layers could not be made because:

1. The material properties of the 90-deg plies in the two types of orientations were different, although both types of orientations were produced from the same prepreg batch. Thus the properties seem to be influenced by (unknown) processing parameters other than cure temperature, time and pressure, which were identical for both orientations.
2. In case of the $(\pm 45/90_n)_s$ laminates, 90-deg ply cracking is strongly influenced by the edge stresses.

References

[1] Parvizi, A., Garrett, K. W., and Bailey, J. E., *Journal of Material Science*, Vol. 13, 1978, pp. 195–201.
[2] Flaggs, D. L., and Kural, M. H., *Journal of Composite Materials*, Vol. 16, March 1982, pp. 118–139.
[3] Crossman, F. W., and Wang, A. S. D., in *Damage in Composite Materials, ASTM STP 775*, American Society for Testing and Materials, Philadelphia, 1982, pp. 118–139.
[4] Wang, A. S. D., "Fracture Mechanics of Sublaminate Cracks in Composite Laminates" in *Characterisation, Analysis and Significance of Defects in Composite Materials, Proceedings*, Advisory Group for Aerospace Research and Development Conference, No. 355, London, 1983.
[5] Nuismer, R. J., and Tan, S. C., "The Role of Matrix Cracking in the Continuum Constitutive Behaviour of a Damaged Composite Ply" in *Mechanics of Composite Materials, Proceedings*, International Union of Theoretical and Applied Mechanics Symposium on Mechanics of Composite Materials, Virginia Polytechnic Institute and State University, Blacksburg, VA, 1982.
[6] Manders, P. W., Chou, T. W., Jones, F. R., and Rock, J. W., *Journal of Material Science*, Vol. 18, 1983, pp. 2876–2889.
[7] Fukunaga, H., Chou, T. W., Peters, P. W. M., and Schulte, K., *Journal of Composite Materials*, Vol. 18, July 1984, pp. 339–357.
[8] Peters, P. W. M., "The Strength of 0/90 Graphite-Epoxy Laminates with Cracked 90° Layers," Poster paper presented at Conference on Testing Evaluation and Quality Control of Composites, University of Surrey, Guildford, U.K., 13–14 Sept. 1983.

[9] Peters, P. W. M., *Journal of Composite Materials*, Vol. 18, Nov. 1984, pp. 545–557.
[10] Tsai, S. W., and Hahn, H. T., "*Introduction to Composite Materials*," Technomic Publishing Co., Stamford, CT, 1980.
[11] Pagano, N. J., and Pipes, R. B., *International Journal of Mechanical Science*, Vol. 15, 1973, pp. 679–688.
[12] Niederstadt, G., and Nitsch, P., "Diffusion, Wärmedehnung und Quellung von CFK (Zusammenfassende Darstellung)," I.B. 131-84/6, Institut für Strukturmechanik, DFVLR Braunschweig, Germany, 1984.
[13] Sun, C. T., and Yamada, S.E., *Journal of Composite Materials*, Vol. 12, 1978, pp. 169–176.
[14] Sih, G.C., and Chen, E. P., "Cracks in Composite Materials," *Mechanics of Fracture*, Vol. 6, Martinus Nijhoff, The Hague, the Netherlands, 1981.

Charles E. Harris[1] *and Don H. Morris*[2]

Fracture of Thick Graphite/Epoxy Laminates with Part-Through Surface Flaws

REFERENCE: Harris, C. E. and Morris, D. H., "**Fracture of Thick Graphite/Epoxy Laminates with Part-Through Surface Flaws,**" *Composite Materials: Fatigue and Fracture, ASTM STP 907,* H. T. Hahn, Ed., American Society for Testing and Materials, Philadelphia, 1986, pp. 100–114.

ABSTRACT: An experimental investigation of the fracture behavior of tension specimens containing part-through semi-elliptic surface flaws was conducted utilizing T300/5208 graphite/epoxy laminates with a $[0/\pm45/90]_{10s}$ stacking sequence. The notched strength of the specimens was found to be influenced by the flaw aspect ratio as well as flaw depth. Using a value of fracture toughness previously obtained for this material system, linear elastic isotropic fracture mechanics predicted the influence of the flaw shape and size on the notched strength.

KEY WORDS: fracture of composites, thick laminates, part-through surface flaws, graphite/epoxy laminate

Notch sensitivity and damage tolerance are subjects of considerable interest in the design of laminated structures fabricated from high-modulus fiber reinforced composite materials. A number of design approaches currently being utilized are either based on strength of materials [*1*] or fracture mechanics concepts [*2,3*]. These design approaches were based on the experimental observations of the fracture behavior of thin laminates. The fracture of thick graphite/epoxy laminates with through-the-thickness cracks has been the subject of recent research by the authors [*4*]. The primary result from this study was that laminate thickness significantly influenced notched strength (or fracture toughness). However, notched strength (or fracture toughness) asymptotically approached a constant value with increasing laminate thickness. In order to more fully explore the possibility that the constant value of fracture toughness is a "material property,"

[1] Assistant professor, Aerospace Engineering Department, Texas A&M University, College Station, TX 77843; formerly with the Engineering Science and Mechanics Department, Virginia Polytechnic Institute and State University, Blacksburg, VA 24061.

[2] Professor, Engineering Science and Mechanics Department, Virginia Polytechnic Institute and State University, Blacksburg, VA 24061.

thick laminates with semi-elliptic part-through surface flaws have been studied. That study is the subject of this paper.

There have been several investigations of surface flaws in laminated composites [*5–8*]. These studies considered flaw profiles that were straight cuts partially or completely across the specimen width, or semicircular. The flaws were typically cut through only a few of the surface plies. The investigators generally used strength-of-materials concepts to interpret the test results. In the subject investigation 80-ply quasi-isotropic laminates prepared from T300/5208 graphite/epoxy were notched with semi-elliptic surface flaws at a variety of flaw depths and flaw aspect ratios. The fracture toughness of the material was established in a previous research program [*4*] and will be utilized along with isotropic fracture mechanics concepts to interpret the test results.

Experimental Program

A quasi-isotropic $[0/\pm45/90]_{10s}$ laminate was chosen for this study so that some of the existing fracture mechanics solutions developed for surface flaws in isotropic materials could be utilized. The 0-deg fiber direction was parallel to the direction of the applied load and perpendicular to the machined center flaw. The laminate panels were cured at 179°C (355°F) in an autoclave under 0.69 MPa (100 psi) pressure for 2 h. After cooldown, there was no postcure. The approximate per-ply thickness was 0.127 mm (0.005 in.). Finally, it should be noted that one of the four panels was fabricated with an incorrect stacking sequence. The resulting stacking sequence, $[0/\pm45/90]_{18T}$, produced a nonsymmetric laminate that was about 10% thinner than the other three $[0/\pm45/90]_{10s}$ panels.

The lamina and laminate strength and stiffness properties for this material system are documented in Ref *4*. The unnotched strength of the laminate, 556 MPa (80.6 ksi), was established primarily for the $[0/\pm45/90]_s$ laminate. It will be assumed that this value of unnotched strength is appropriate for the thick laminate. (Unnotched strength is utilized herein only to normalize notched strength for ease of interpretation of the test results.) The asymptotically approached value of fracture toughness, 1043 MPa $\sqrt{\text{mm}}$ (30.0 ksi $\sqrt{\text{in.}}$), was reached at 64 plies and was constant beyond this thickness [*4*]. This value of fracture toughness was determined by standard fracture toughness tests using center-cracked tension, compact tension, and three-point specimens at a variety of machined crack lengths and laminate thicknesses, for through-the-thickness cracks.

The configuration of the test specimens and the geometric parameters that define the semi-elliptic flaw shape are shown in Fig. 1. The test matrix consists of seven combinations of flaw depth (a/t) and flaw aspect (a/c) ratios. These test conditions are listed in Table 1. The surface flaws were cut by an ultrasonic cutting tool using a 0.406-mm (0.016 in.) blade prepared with the appropriate elliptic profile. No attempt was made to further sharpen the machined flaws.

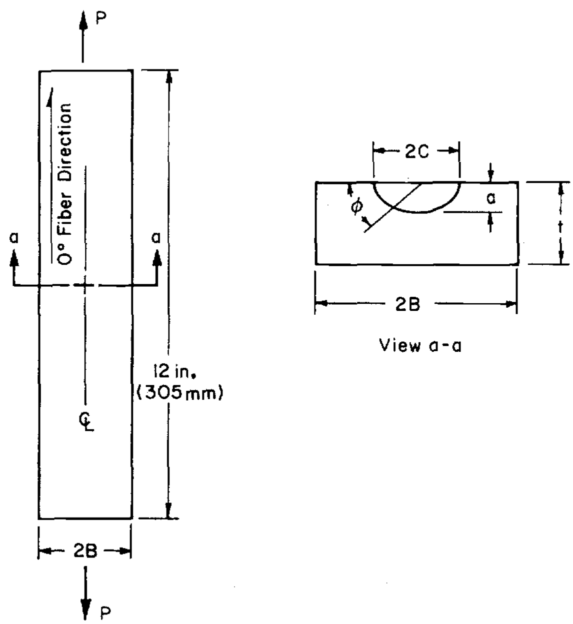

FIG. 1—*Specimen configuration.*

TABLE 1—*Specimen geometry and notched strength data.*

				Symmetric Laminates[a]		Unsymmetric Laminate[b]	
2*B*, in. (mm)	*a*, in. (mm)	*c*, in. (mm)	*a*/*c*	*t*, in. (mm)	Notched Strength, ksi (MPa)	*t*, in. (mm)	Notched Strength, ksi (MPa)
1.00 (25.4)	0.094 (2.39)	0.047 (1.19)	2.0	0.392 (9.96)	65.0 (448)	0.362 (9.19)	52.5 (362)
1.00 (25.4)	0.188 (4.78)	0.094 (2.39)	2.0	0.392 (9.96)	61.5 (424)	0.365 (9.27)	58.0 (400)
1.00 (25.4)	0.250 (6.35)	0.125 (3.18)	2.0	0.392 (9.96)	51.0 (352)	0.365 (9.27)	48.2 (332)
1.00 (25.4)	0.313 (7.95)	0.157 (3.99)	2.0	0.392 (9.96)	42.7 (294)	0.366 (9.30)	46.4 (320)
1.00 (25.4)	0.125 (3.18)	0.125 (3.18)	1.0	0.392 (9.96)	56.9 (392)	0.365 (9.27)	58.1 (401)
1.00 (25.4)	0.250 (6.35)	0.250 (6.35)	1.0	0.392 (9.96)	36.1 (249)	0.364 (9.25)	31.7 (219)
2.00 (50.8)	0.129 (3.28)	0.500 (12.7)	0.26	0.392 (9.96)	40.0 (276)	0.365 (9.27)	39.9 (275)

[a]Average of four or five tests.
[b]Average of one or two tests.

This resulted in a notch root radius that was consistent with the center-cracked tension specimens from which the value of fracture toughness [1043 MPa $\sqrt{\text{mm}}$ (30 ksi $\sqrt{\text{in.}}$)] was obtained.

Quasi-static tension tests were conducted at a constant crosshead displacement rate of 0.02 mm/s (0.05 in./min). Crack-opening displacement (COD) and applied load were recorded during each test [*4*]. There were six replicate test specimens for each test condition.

In order to more fully understand the fracture processes, damage development prior to rupture of the specimen was extensively studied. Using damage indications in the load-COD record [*4*], zinc iodide enhanced X-ray radiography was employed to study and document the progression of damage prior to complete failure. Radiographs were taken of the face view and edge view of the specimens. To more fully study the development of damage through the thickness, selected specimens were destructively deplied. The deply procedure involved a partial pyrolysis of the laminate which allowed the individual plies to be separated and examined [*9*]. A gold chloride marking agent was used to permanently mark regions of delamination.

Experimental Results

The experimentally determined values of notched strength are tabulated in Table 1. The notched strength is defined as the far-field stress at failure which is calculated by $P/2Bt$, where the symbols are defined in Fig. 1. Six replicate specimens at each flaw configuration were obtained from four laminate panels. One of these panels was layed up incorrectly. Two layers of the repeated stacking sequence (eight plies) were left off the outside surface on one side of the midplane. This resulted in an unsymmetric laminate about 10% thinner than the other five panels. Therefore, the notched strength values in Table 1 under "Symmetric Laminates" are the average of four or five replicate tests, depending on flaw configuration. Likewise, the notched strength values reported for the "Unsymmetric Laminate" are one test or the average of two tests. Notched strength was normalized by the unnotched strength 556 MPa (80.6 ksi) and is displayed graphically in Fig. 2 as a function of flaw depth (a/t) and aspect (a/c) ratios. (The fracture mechanics prediction curves also plotted in Fig. 2 are discussed in the next section.) The symbol in Fig. 2 represents the average value while the bar drawn through the symbol provides the high and low value in each data set. Also note that the data from both the symmetric and unsymmetric laminates are displayed in Fig. 2. Because the unsymmetric laminate is thinner than the other panels, values of a/t are slightly higher.

The experimentally determined stresses ($P/2Bt$) shown in Fig. 2 were calculated using the load when the notched layer failed (see next paragraph for a discussion of failure modes). In one case [$a/c = 2$, $a = 2.39$ mm (0.094 in.)] the stress was calculated using the load at catastrophic failure; the specimen did not fail at the flaw.

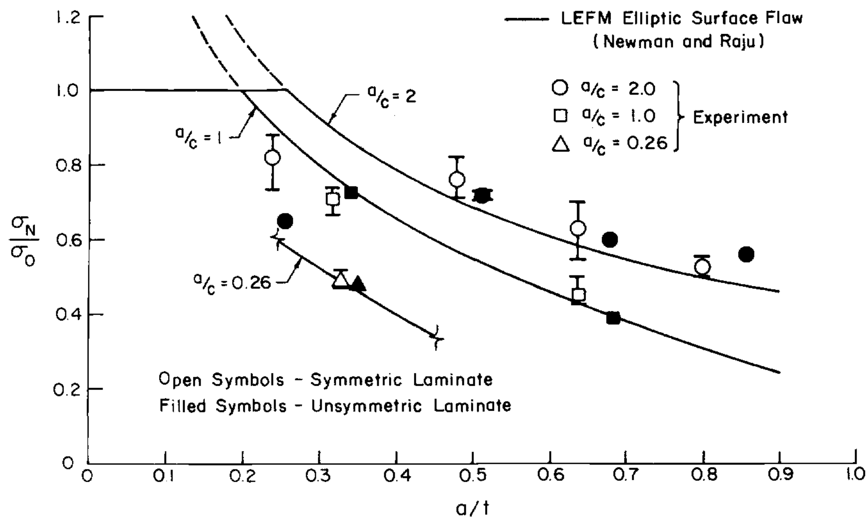

FIG. 2—*Comparison of experimental data with isotopic LEFM predictions.*

The specimens with the smallest flaw [a/c = 2, a = 2.39 mm (0.094 in.)] failed away from the flaw and exhibited very little notch sensitivity. The deeper-flawed specimens typically exhibited a two-part fracture consisting of the fracture of the layer containing the surface flaw (notched layer) followed by fracture of the layer below the bottom of the flaw (unnotched layer), as shown in Fig. 3. The notched layer separated from the unnotched layer at the first fracture because of a long delamination that opened at the bottom of the flaw and extended completely across the specimen width and several inches in each direction along the specimen length. The notched layer also fractured across the specimen width. The notched layer fracture was accompanied by a reduction in the applied load which allowed for examinations of the specimen. X-ray and deply examinations did not reveal any damage in the unnotched layer below the delamination that separated the two layers. Upon reloading those specimens that were not deplied, the unnotched layer fractured in a manner generally independent of the notched layer fracture.

The appearance of the fracture surfaces of the notched layers was quite different from that of the unnotched layers (Fig. 3). The notched layer exhibited a fracture surface that was relatively uniform and coplanar with the plane of the machined flaw. The fracture surface greatly resembled the fracture surfaces of thick quasi-isotropic center-cracked tension specimens [*4*]. On the other hand, the fracture of the unnotched layer was nonuniform and splintered similar to the typical fracture exhibited by an unnotched tension coupon.

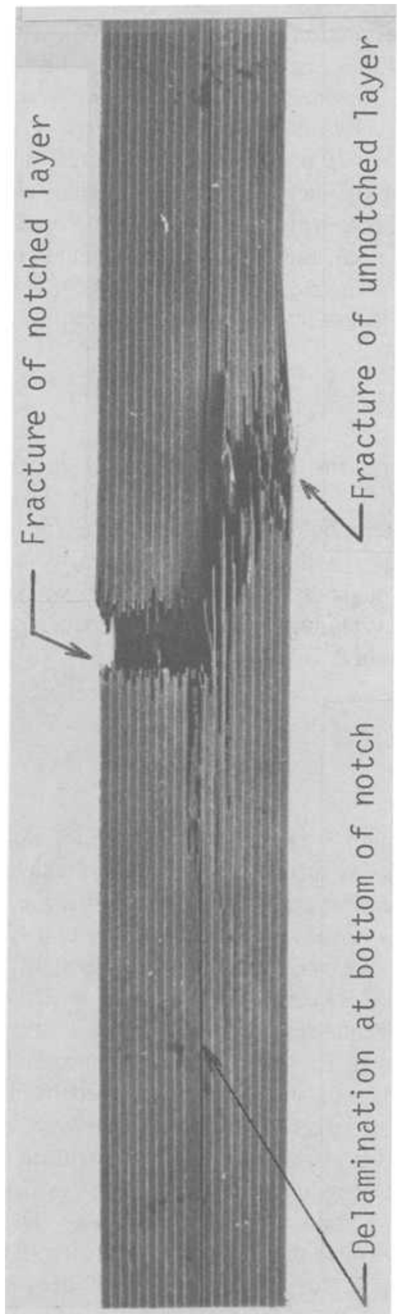

FIG. 3—*Photograph of fractured specimen (edge view).*

Interpretation and Discussion of Results

The analytical isotropic solution for the semi-elliptic surface crack generated by Newman and Raju [*10*] is used herein to aid in the interpretation of the experimental results. The Newman and Raju solutions were used because they account for the influence of finite specimen geometry on the stress-intensity factor expression. Reference *10* provides empirical stress-intensity factor equations calculated using a three-dimensional finite-element analysis of the cracked-body geometry. The stress-intensity factor equations are a function of the parametric angle of the ellipse (ϕ), flaw depth (a), flaw length ($2c$), plate thickness (t), and plate width ($2B$). The meaning of the symbols is depicted in Fig. 1. Written symbolically, the stress-intensity factor is given by [*10*]

$$K_{\mathrm{I}} = S\left(\frac{\pi a}{Q}\right)^{1/2} F_s\left(\frac{a}{c}, \frac{a}{t}, \frac{c}{B}, \phi\right) \tag{1}$$

where S is the remote uniform tensile stress and Q the ellipse shape factor, $Q = Q(a/c)$.

In fracture mechanics terminology, the value of the stress-intensity factor at fracture is typically referred to as the critical stress-intensity factor (K_Q) or fracture toughness. If the fracture toughness of the material is known, Eq 1 can be rewritten to provide the remote stress at failure (notched strength) for a given flaw geometry. The predicted notched strength is then given by

$$\sigma_N = \frac{K_Q}{\left(\frac{\pi a}{Q}\right)^{1/2} \dot{F}_s} \tag{2}$$

Values of notched strength were predicted using Eq 2 along with a K_Q-value of 1043 MPa $\sqrt{\text{mm}}$ (30 ksi $\sqrt{\text{in.}}$) [*4*]. The ratios of predicted notched strength to unnotched strength [556 MPa (80.6 ksi)] are shown in Fig. 2 as the solid lines. The solid horizontal line drawn at a stress ratio of 1 simply indicates that the notched strength cannot exceed the unnotched strength. With the exception of the smallest flaw [a = 2.39 mm (0.094 in.), a/c = 2], there is close agreement between the experimental results and the linear elastic fracture mechanics (LEFM) isotropic solutions. The smallest flaw is apparently in the transition region between the fracture of small flaws governed by net section ultimate strength and the fracture of larger flaws governed by fracture mechanics. (Additional experimental work is planned to more fully define this transition region.)

As Eq 1 indicates, the stress-intensity factor varies in magnitude around the perimeter of the semi-elliptic flaw (F_s is a function of ϕ). The schematics in Fig. 4 provide a comparison between the stress-intensity factor at the surface (ϕ = 0 deg) and at the deepest point along the flaw (ϕ = 90 deg) for a/t = 0.30. For a/c values of 2.0 and 1.0, the maximum stress-intensity factor occurs at the

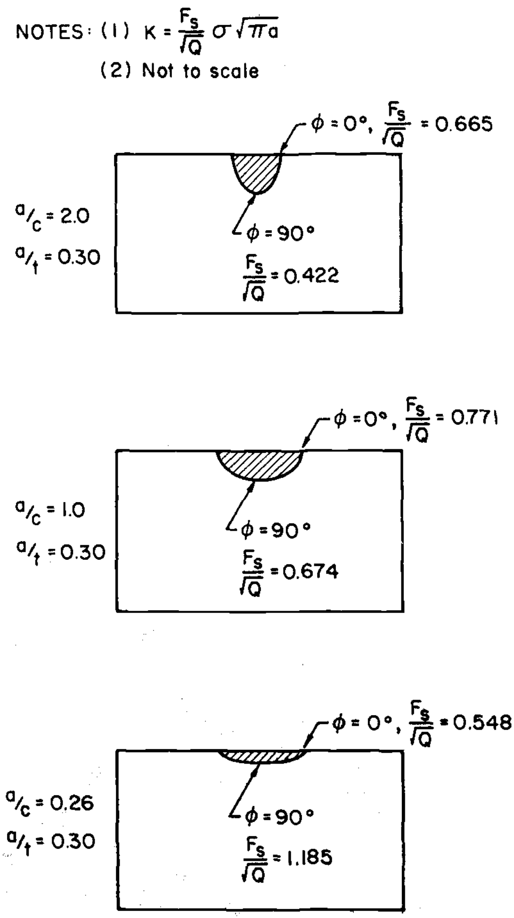

FIG. 4—*Variation in stress-intensity factor.*

surface. However, for $a/c = 0.26$ the maximum value is at the deepest point. The prediction curves shown in Fig. 2 were calculated based on the maximum stress-intensity factor. This provided the best comparison with the experimental results.

The development of flaw-related damage prior to notched layer fracture was also closely related to the variation in stress-intensity factor around the flaw perimeter. In the case of the four flaw geometries with an aspect ratio 2.0, the stress-intensity factor at the surface was 50% higher than at the deepest point. The damage that developed prior to notched layer fracture was concentrated near the surface. Figure 5 shows a face and edge view radiograph of the specimen with a flaw depth of 7.95 mm (0.313 in.). The delaminations visible in the face

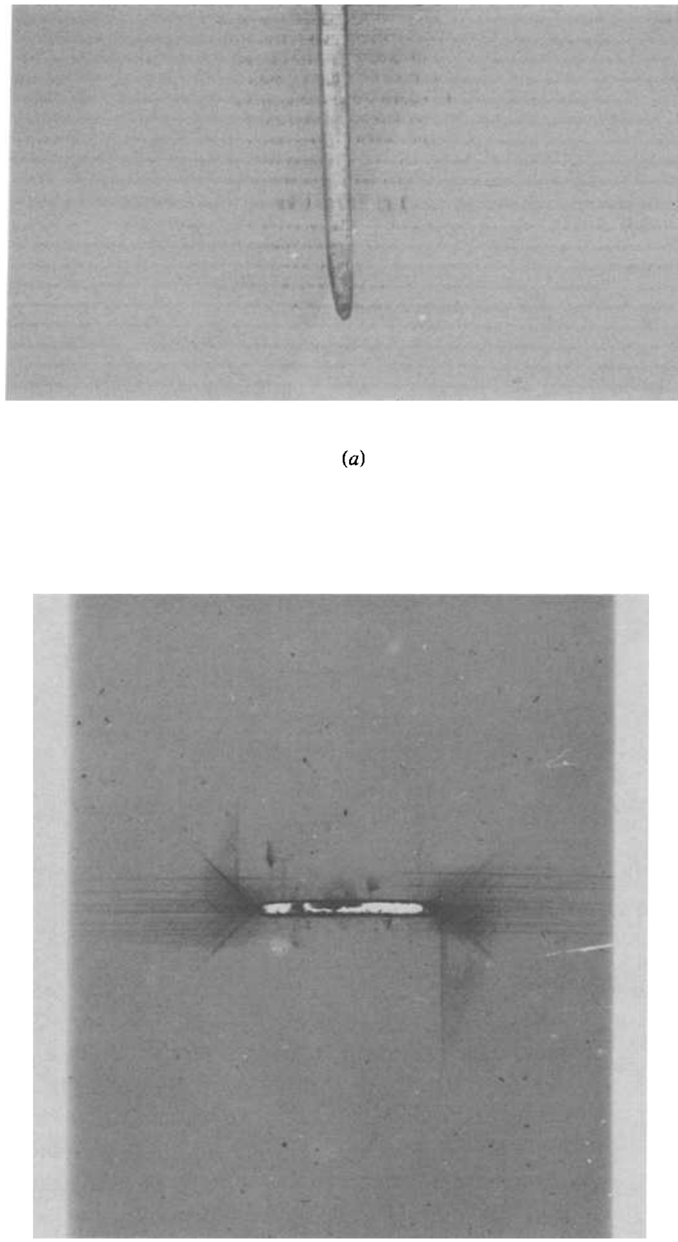

(*a*)

(*b*)

FIG. 5—*X-ray radiographs showing* (a) *edge view and* (b) *face view of specimen with maximum stress-intensity factor at surface* (a/c = *2.0*).

view radiograph are seen in the edge view radiograph to be concentrated near the surface. Likewise the transverse cracks in the 90-deg plies also diminish toward the bottom of the flaw.

The two flaw geometries with an aspect ratio of 1.0 are characterized by a stress-intensity factor that is somewhat more uniform. A typical damage state is illustrated by the radiographs shown in Fig. 6 of a specimen with a flaw depth of 3.18 mm (0.125 in.). The transverse cracks and delaminations are distributed relatively uniformly through the thickness of the notched layer. Finally, the stress-intensity factor variation for the flaw aspect ratio of 0.26 is in stark contrast to those of the high-aspect-ratio geometries. The stress-intensity factor at the deepest point was more than twice as high as the surface value. The damage state illustrated by the radiographs of Fig. 7 exhibits a similar variation. The damage clearly increases throughout the notched layer with major delaminations present at the bottom of the flaw.

Summary and Conclusions

The notched strength of quasi-isotropic T300/5208 graphite/epoxy tension specimens with semi-elliptic surface flaws was found to be a function of the flaw depth (a/t) and flaw aspect (a/c) ratios. The variations in notched strength were predicted quite accurately by linear elastic isotropic fracture mechanics for large values of a/t. Predictions were generated by using a previously established value of fracture toughness that exhibited an asymptotically approached constant value [1043 MPa $\sqrt{\text{mm}}$ (30 ksi $\sqrt{\text{in.}}$)] for thick laminates with through-the-thickness cracks. The close correlation between the variation in stress-intensity factor around the perimeter of the flaw and the development of damage through the thickness of the notched layer provided additional evidence of the usefulness of fracture mechanics for predicting the notched strength of the thick quasi-isotropic laminate.

Specimen failure for one value of a/t was notch insensitive; that is, failure did not originate at the flaw. There appeared to be a transition region between the small and large values of a/t. Further work is needed to characterize the behavior in the transition region, and for small values of a/t.

The results of this program indicate that conventional LEFM together with an appropriate value of fracture toughness may be useful in addressing the damage tolerance of thick laminated composites, at least for larger values of a/t. (This general conclusion must be tempered with the realization that only the quasi-isotropic graphite/epoxy laminate has been extensively investigated.)

Acknowledgments

The authors wish to acknowledge the financial support provided by a grant from the NASA-Langley Research Center. In addition, the authors wish to acknowledge the helpful discussions and suggestions provided by the contract monitor, C. C. Poe, Jr.

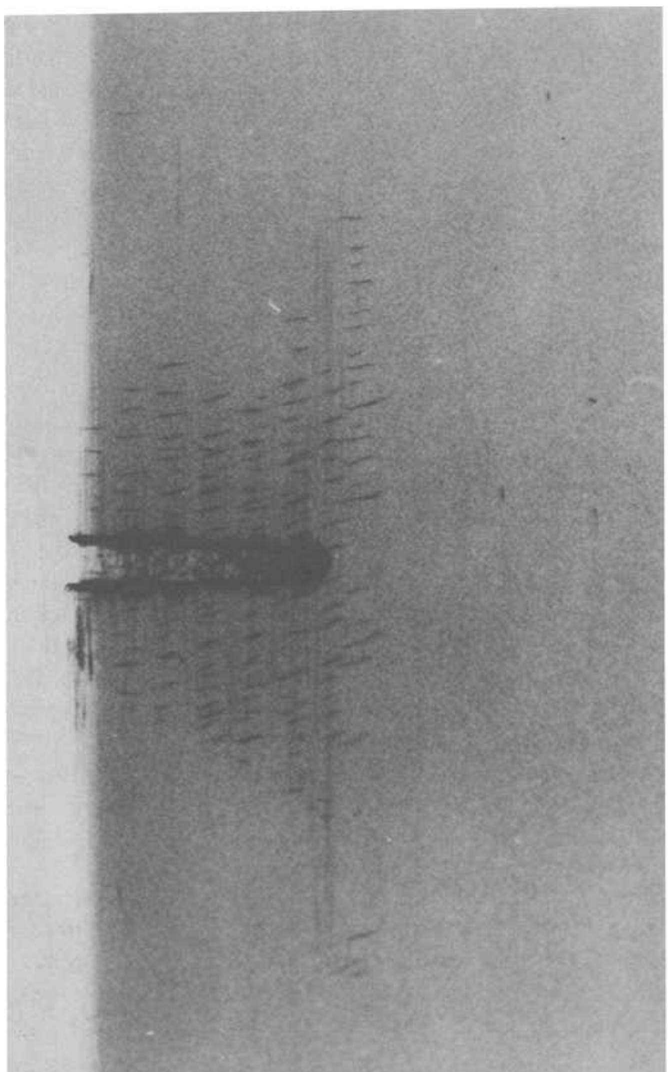

(a)

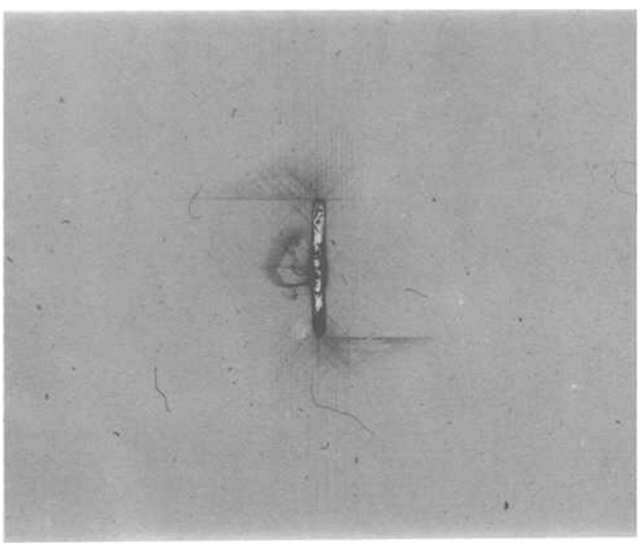

(b)

FIG. 6—*X-ray radiographs showing* (a) *edge view and* (b) *face view of specimen with approximately uniform stress-intensity factor* (a/c = *1.0*).

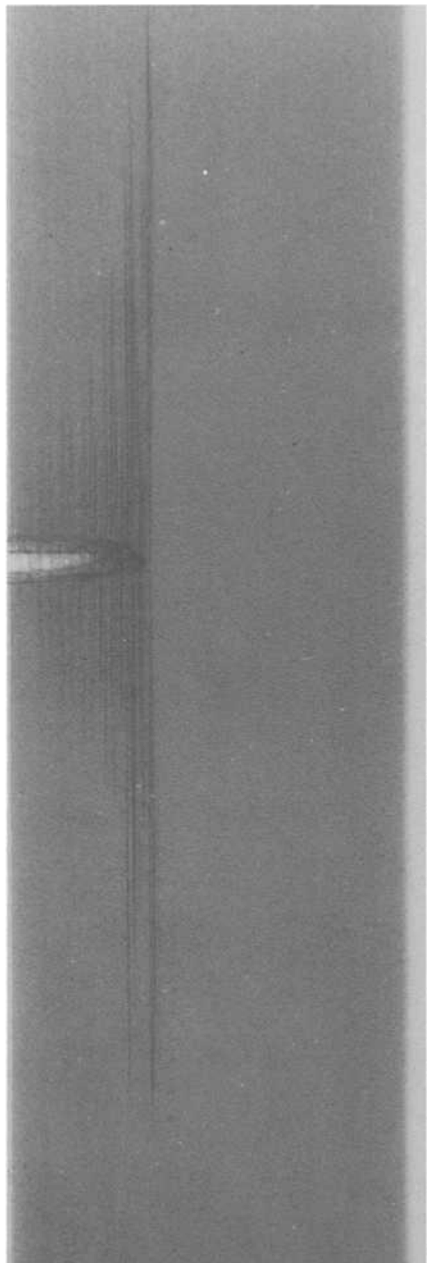

(a)

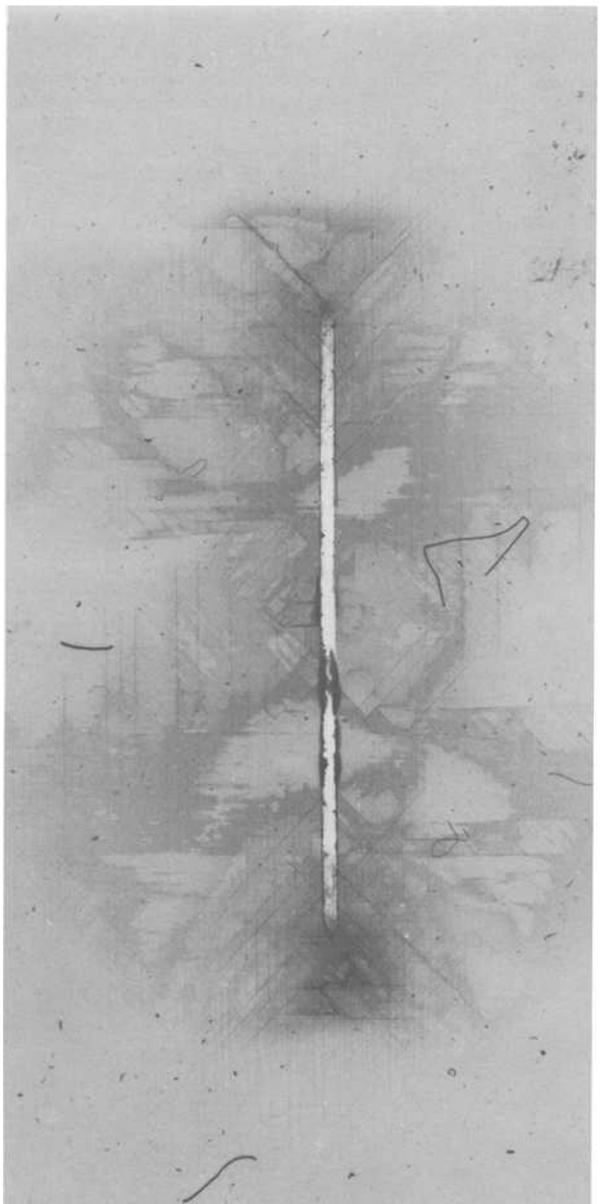

(*b*)

FIG. 7—*X-ray radiographs showing* (a) *edge view and* (b) *face view of specimen with maximum stress-intensity factor at bottom of flaw* (a/c = *0.26*).

References

[*1*] Whitney, J. M. and Nuismer, R. J., *Journal of Composite Materials*, Vol. 8, July 1974, pp. 253–265.
[*2*] Waddoups, E. M., Eisenmann, J. R., and Kaminski, B. E., *Journal of Composite Materials*, Vol. 5, Oct. 1971, pp. 446–454.
[*3*] Poe, C. C., Jr., *Engineering Fracture Mechanics*, Vol. 17, 1983, pp. 153–171.
[*4*] Harris, C. E. and Morris, D. H., "Fracture Behavior of Thick, Laminated Graphite/Epoxy Composites," NASA CR-3784, National Aeronautics and Space Administration, Washington, DC, 1984.
[*5*] Lo, K. H. and Wu, E. M., "Serviceability of Composites Surface Damage," *Fibrous Composites in Structural Design*, E. M. Lenoe, D. W. Oplinger, and J. J. Burke, Eds., Plenum Press, New York, 1978.
[*6*] Sendeckyj, G. P. in *Proceedings*, 12th Annual Meeting of the Society of Engineering Science, University of Texas at Austin Press, 1975, pp. 625–634.
[*7*] Wang, S. S. and Mandell, J. F., "Analysis of Delamination in Unidirectional and Crossplied Fiber-Composites Containing Surface Cracks," NASA CR-135248, National Aeronautics and Space Administration, Washington, DC, May 1977.
[*8*] Sendeckyj, G. P. in *Fracture of Composite Materials*, G. C. Sih and V. P. Tamuzs, Eds., Martinus Nijhoff Publishers, Boston, 1981, pp. 115–127.
[*9*] Freeman, S. M. in *Composite Materials: Testing and Design (Sixth Conference), ASTM STP 787*, I. M. Daniel, Ed., American Society for Testing and Materials, Philadelphia, 1982, pp. 50–62.
[*10*] Newman, J. C., Jr. and Raju, I. S. in *Fracture Mechanics: Fourteenth Symposium—Volume I: Theory and Analysis, ASTM STP 791*, J. C. Lewis and G. Sines, Eds., American Society for Testing and Materials, Philadelphia, 1983, pp. I-238-I-265.

J. H. Crews, Jr.,[1] *and R. V. A. Naik*[2]

Failure Analysis of a Graphite/Epoxy Laminate Subjected to Bolt-Bearing Loads

REFERENCE: Crews, J. H., Jr., and Naik, R.V.A., **Failure Analysis of a Graphite/Epoxy Laminate Subjected to Bolt-Bearing Loads,"** *Composite Materials: Fatigue and Fracture, ASTM STP 907,* H. T. Hahn, Ed., American Society for Testing and Materials, Philadelphia, 1986, pp. 115–133.

ABSTRACT: Quasi-isotropic graphite/epoxy laminates (T300/5208) were tested under bolt-bearing loads to study failure modes, strengths, and failure energy. Specimens had a range of configurations to produce failures by the three nominal failure modes: tension, shearout, and bearing. Radiographs were made after damage onset and after ultimate load to examine the failure modes. Also, the laminate stresses near the bolt hole were calculated for each test specimen configuration, and then used with a failure criterion to analyze the test data.

Failures involving extensive bearing damage were found to dissipate significantly more energy than tension-dominated failures. The specimen configuration influenced the failure modes and therefore also influenced the failure energy. In the width-to-diameter ratio range of 4 to 6, which is typical of structural joints, a transition from the tension mode to the bearing mode was shown to cause a large increase in failure energy.

The failure modes associated with ultimate strength were usually different from those associated with the damage onset. Typical damage sequences involved bearing damage onset at the hole boundary followed by tension damage progressing from the hole boundary. Ultimate failures involved shearout beyond the clampup washer for specimens with small edge distances and involved bearing damage beyond the washer for larger specimens. Strength predictions indicated that the damage corresponding to ultimate strength was governed by the maximum stress near the hole.

KEY WORDS: laminate, bolt, bearing, graphite/epoxy, strength, damage, stress analysis, composites

Nomenclature

- C bolt-hole clearance, m
- C_b coefficient for bearing damage onset prediction
- C_t coefficient for tension damage onset prediction
- d hole diameter, m

[1] Senior engineer, National Aeronautics and Space Administration, Langley Research Center, Hampton, VA 23665.

[2] Graduate student, Old Dominion University, Norfolk, VA.

e specimen edge distance, m
K_{bb} bearing stress concentration factor
K_{tb} tension stress concentration factor
P bolt load, N
r, θ polar coordinates, m, deg
r_{ob} characteristic dimension for bearing failure prediction, m
r_{ot} characteristic dimension for tensile failure prediction, m
S_b nominal bearing stress, MPa
S_{bo} damage onset strength, MPa
S_{bu} ultimate strength, MPa
t laminate thickness, m
w specimen width, m
x,y Cartesian coordinates, m
δ hole elongation, m
θ_c bolt-hole contact half-angle, deg
σ laminate stress, MPa
σ_{cu} laminate compressive ultimate strength, MPa
σ_{rr} radial stress component, MPa
σ_{tu} laminate tensile ultimate strength, MPa
$\sigma_{\theta\theta}$ circumferential stress component, MPa

Bolt loads can produce failures by one of three basic failure modes—tension, shearout, or bearing. However, joints are usually designed with little regard for failure modes and typically are optimized for maximum ultimate strength. For current graphite/epoxy composites, this approach usually leads to joints that fail in the tension mode. Unfortunately, such tension failures can develop with little advance warning in a rather catastrophic manner.

The objective of the present study was to analyze and compare laminate failures for each of the three basic failure modes. Toward this end, tests were conducted to measure damage onset strength, ultimate strength, and failure energy for specimens subjected to bolt-bearing loads. Specimens were 16-ply quasi-isotropic T300/5208 graphite/epoxy laminates in various configurations that were designed to produce the different failure modes. Radiographs, enhanced with a dye penetrant, were used to observe the local damage. A finite-element stress analysis was conducted for each specimen configuration to determine how the configuration influenced the local stresses near the loaded hole. The computed stresses were also used with laminate failure criteria to predict failure modes and strengths. All of the damage analyses and failure predictions were performed on a laminate (two-dimensional) level; ply-by-ply analyses were beyond the scope of this study.

Tests results are presented in terms of strength and failure energy plotted for the range of specimen configurations. Failure modes and sequences are identified and discussed. Stress results are presented as stress distributions and stress concentration factors. Failure predictions based on the stresses are discussed and compared with observed test results.

Test Procedures

Test specimen configuration and loading are shown in Fig. 1. All specimens were made from the same $(0/45/90/-45)_{2s}$ T300/5208 graphite/epoxy laminate which had a nominal thickness of 2.24 mm. Bolt holes were ultrasonically drilled with a diameter of 6.37 mm. The steel bolts had a nominal diameter of 6.35 mm, but their actual diameter was 6.32 mm. This produced a hole clearance C of 0.05 mm. The specimen width-to-hole diameter ratio, w/d, ranged from 2 to 8. The edge distance-to-hole-diameter ratio, e/d, ranged from 1.5 to 4.0. These specimen configurations were selected to produce failures by the three basic failure modes shown in Fig. 2*b*, *c*, and *d*. The other failure modes in Fig. 2 are discussed later.

The bolt-loading apparatus is shown in Fig. 3. A pair of steel clevis straps loaded the bolt in double shear; a friction grip reacted the load. The washers (12.7 mm diameter) between the clevis straps and the specimen (see Fig. 3*c*) distributed the clampup torque load over an area around the bolt hole. All bolts were torqued to 5.65 N·m, a moderate clampup torque for a 6.35-mm bolt.

Inductive displacement transducers were used to measure bolt-hole elongation. The apparatus shown in Fig. 3*d* measured the relative displacement between the clevis and a small, stiff wire that rested against the edge of the hole under the bolt. To provide clearance for the wire, the bolt and the washers were slotted. The measured displacements were approximately equal to hole elongation because the clevis and bolt deflections were found to be relatively small.

The curve of nominal bearing stress, S_b ($S_b = P/td$), versus hole elongation,

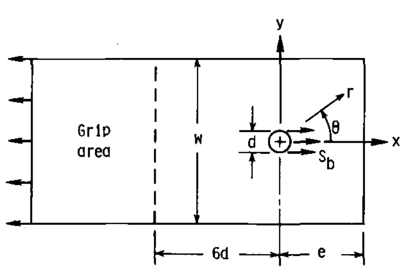

(a) Specimen configuration and loading

w/d	2	3	4	6	8	8	8	8	8
e/d	4	4	4	4	4	3	2.5	2	1.5

(b) Test specimen configurations

FIG. 1—*Test specimen configurations and loading.*

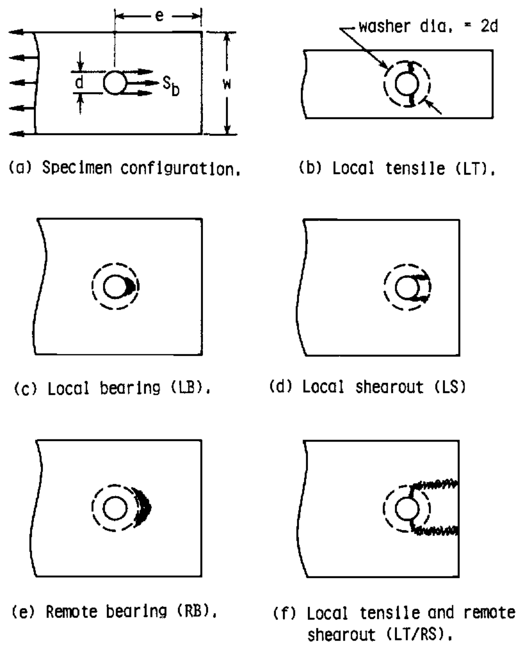

FIG. 2—*Failure modes for loaded holes.*

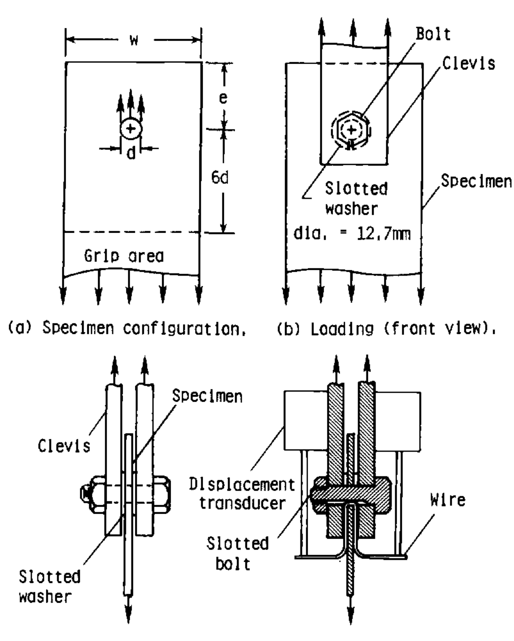

FIG. 3—*Specimen and test apparatus.*

δ, was recorded throughout each test. The tests were conducted using hole elongation as the servo control variable. The hole elongation was increased at a very slow rate (0.002 mm/s) until the ultimate strength was reached. This procedure produced load-displacement records that were very sensitive to any localized damage near the bolt hole; it also allowed the specimens to be unloaded after ultimate strength was reached. The unloading prevented the failure mode information (that is, local damage) corresponding to ultimate strength from being masked by the gross damage caused by complete specimen failure. A typical recording of bearing stress against hole elongation (S_b versus δ) is shown in Fig. 4. The nonlinearity near the origin is due to clampup friction between the washers and the specimen. Results in Ref *1* with a similar test apparatus showed that the friction force was only about 50 N for the clampup torque used in the present study. For higher load levels, the $S_b - \delta$ curves were essentially linear despite the nonlinear contact that developed between the hole and the clearance-fit bolt. This contact behavior is discussed later in the stress analysis section.

The damage onset strength, S_{bo}, was determined using three independent methods. The start of nonlinearity in the $S_b - \delta$ curve was the first evidence of damage and was used to indicate damage onset, as shown in Fig. 4. At slightly higher loads, snapping and popping noises were heard. The first such audible noise was taken as the second indication of damage onset, and the corresponding point was marked on each $S_b - \delta$ record. As the loading progressed, abrupt drops or jumps would occur in the curve, also indicating sudden damage development. The first such drop was used for the third S_{bo} measurement. In some tests, specimens were unloaded immediately after the first audible noise was

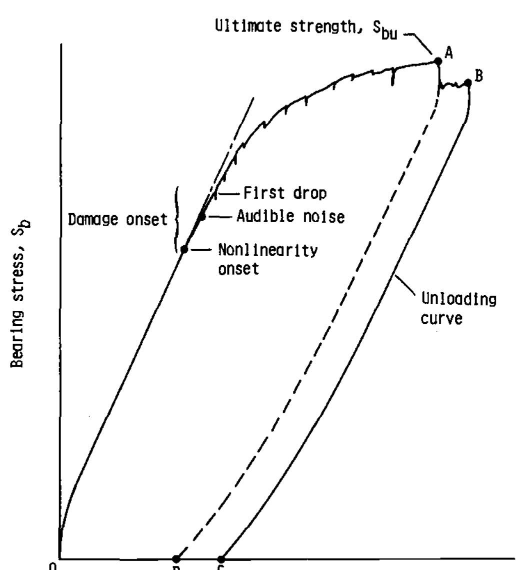

FIG. 4—*Typical recording of bearing stress against hole elongation.*

detected and then radiographed using an X-ray opaque dye penetrant to determine the location, mode, and extent of damage. These specimens were not tested further. Most specimens were loaded to ultimate strength before they were unloaded and radiographed.

Specimens could not be unloaded precisely after ultimate load (Point A) was reached; testing had to continue slightly beyond this point to be certain that it was the peak value for that curve. For example, the curve in Fig. 4 extends beyond Point A to Point B before unloading to Point C. However, the unloading curve from Point A was needed to calculate the failure energy. The failure energy was calculated from the area enclosed by the curve OAD. The desired unloading curve from Point A was approximated, as shown in Fig. 4, by shifting the BC curve to get the AD curve.

Analytical Procedures

Stress Analysis

Laminate stresses near the fastener hole were calculated using the NASTRAN finite-element program with isoparametric elements. The finite-element model shown in Fig. 5 corresponds to the largest test specimen ($w/d = 8$ with $e/d = 4$). Other specimen configurations were modeled by eliminating elements to change the w/d or e/d ratio as required. As a result, the mesh refinement near the hole was identical for all configurations. The mesh in this area consisted of small triangular elements, each subtending 0.9375 deg as shown in Fig. 5. The distance to the grip line end of the model was $6d$ for all cases. A Young's modulus of 58.89 GPa and a Poisson's ratio of 0.31 were used to represent the quasi-isotropic T300/5208 laminate. These properties were obtained using lamination theory and the T300/5208 ply properties from Ref *2*.

As previously mentioned, the case of a laminate with a clearance-fit, loaded hole is a nonlinear problem. The contact area between the bolt and the hole increases nonlinearly as a function of the bolt bearing stress, producing a changing boundary condition at the hole boundary. An analytical approach similar to that in Ref *3* was used here to determine the nonlinear relationship between the bearing stress, S_b, and the contact angle, θ_c. The bolt was assumed to be frictionless, rigid, and fixed and the grip-line end of the model was subjected to a uniform displacement, u_o, in the negative x-direction. Within a specified contact arc, θ_c, the nodes on the hole boundary were constrained to lie on a circular arc having the bolt radius. The bearing stress, σ_{rr}, at the end of the contact arc ($\theta = \theta_c$) should be zero when the proper combination of θ_c and u_o is found. The procedure started by assuming values of θ_c and u_o and then calculating σ_{rr} at $\theta = \theta_c$. A second u_o-value was used with the same θ_c value and a second σ_{rr} was calculated at $\theta = \theta_c$. A linear extrapolation (or interpolation) was used to find the u_o-value corresponding to $\sigma_{rr} = 0$. This u_o-value along with the assumed θ_c-value defined a point on a $u_c - \theta_c$ curve. The procedure was repeated to develop a $u_o - \theta_c$ curve for each specimen configuration. A similar procedure led to $S_b - \theta_c$ curves.

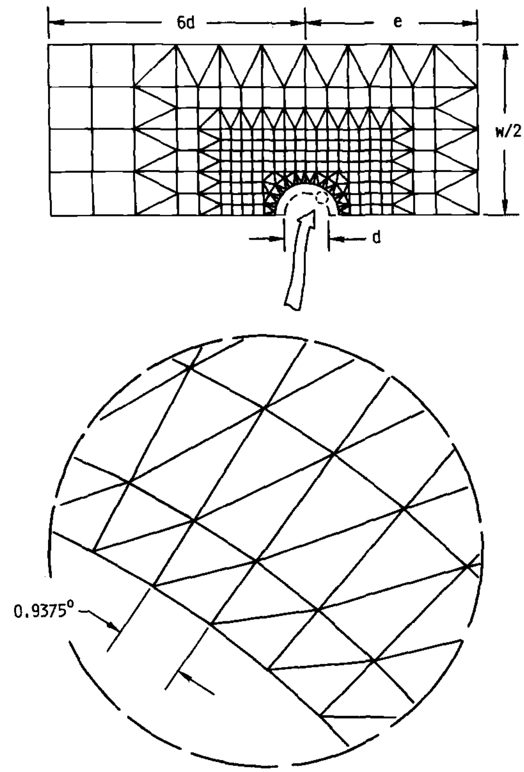

FIG. 5—*Finite-element model.*

After these nonlinear curves were established, the proper θ_c- and u_o-values could be found for any S_b-value.

Failure Predictions

Damage initiation was assumed to be governed by the peak stresses at the hole boundary. Accordingly, tension damage onset was predicted by setting the peak tensile stress at the hole equal to the ultimate tensile strength, σ_{tu}, for the laminate. Using the tensile stress concentration factor, K_{tb}, produced the following equation:

$$C_t S_{bo} K_{tb} = \sigma_{tu} \tag{1}$$

The C_t coefficient was introduced to account for the local stress gradient near the hole. Whereas the σ_{tu}-value was obtained from coupons where a relatively large volume of material was subjected to a uniform stress, the material near the hole is subjected to a stress gradient and the peak stress exists only over a small volume. As a result, the hole boundary strength exceeds σ_{tu}. The coefficient C_t

attempts to account for this stress gradient effect and was computed by solving Eq 1 for C_t using test data involving tension damage. To predict tension damage onset, Eq 1 was rewritten using this C_t-value

$$S_{bo} = \sigma_{tu}/(C_t K_{tb}) \tag{2}$$

This empirical relationship is similar to that proposed in Ref *4* to predict the ultimate strength of loaded holes.

A similar expression was found for bearing damage onset using the bearing stress concentration factor, K_{bb}, and the laminate compressive strength, σ_{cu}

$$S_{bo} = \sigma_{cu}/(C_b K_{bb}) \tag{3}$$

For a given case, both Eqs 2 and 3 were used to predict S_{bo}-values for the two different damage onset modes. The lower S_{bo}-value was taken as the damage onset strength prediction and it also indicated the predicted failure mode.

Although the damage onset was predicted using hole boundary stresses, the ultimate strength S_{bu} was predicted using the well-known Whitney–Nuismer point-stress approach [*5*]. According to this approach, failure is predicted when the computed laminate stress (or stresses) satisfies a failure criterion at a characteristic distance from the hole boundary. The maximum stress failure criterion was used with the point-stress approach. For tensile failures, the characteristic dimension r_{ot} was found by fitting the strength prediction procedure to a measured S_{bu}-value corresponding to an observed tensile failure. This r_{ot}-value was then used to predict failure for other cases by using the stress distributions computed for these cases. This procedure is discussed further when the predictions are compared with test results.

Results and Discussion

Test Results

Test results are presented for ranges of w/d-values and then for e/d-values. In each case, the damage onset strengths and failure modes are presented and discussed. Next, the ultimate strengths and failure modes are addressed. Finally, the measured failure energies are compared and discussed for the various failure modes. Throughout this section, data points typically represent the average of three or more test values.

Width Effects—Damage onset results are presented in Fig. 6 for w/d values ranging from 2 to 8 with e/d = 4. Data from the three damage onset detection techniques (nonlinearity onset, audible noise, and first drop) are compared in Fig. 6*a*. For w/d = 2 and 3, the damage onset was in the local tension mode. ("Local" refers to damage that was confined to the region under the washer.

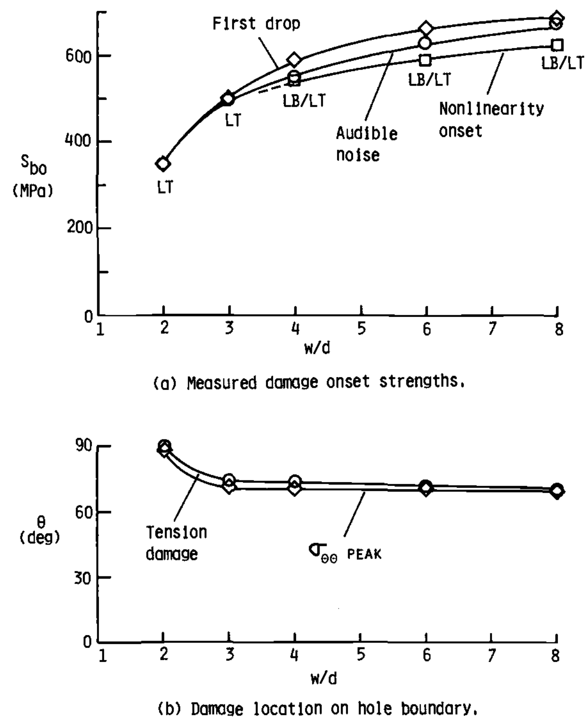

FIG. 6—*Damage onset results for* w/d *range,* e/d = *4.*

Damage beyond this region will be referred to as "remote" damage.) Notice that for the small w/d-values, nonlinearity was not observed. For larger w/d-values, nonlinearity developed before audible noises and two modes of damage were detected, local bearing (LB) and local tension (LT). This suggests that LB damage caused the nonlinearity and LT damage caused the audible noise. The subsequent damage that caused the first drop in the $S_b - \delta$ curve could have been caused by larger-scale abrupt damage in either the LT or LB modes.

The damage onset locations are shown in Fig. 6*b*. Except for $w/d = 2$, the LT damage occurred in the range of θ from 71 to 74 deg. The LT damage appeared to consist of lamina splitting and was concentrated in a small region extending transversely from the hole, as shown in Fig. 2*b*. In contrast, the bearing damage appeared to be mostly delamination and was spread over a large arc centered about $\theta = 0$ deg on the hole boundary. The curve labeled "$\sigma_{\theta\theta}$ peak" is discussed later.

Ultimate strength results are compared with damage onset results in Fig. 7. Except for the $w/d = 2$ case, which failed abruptly in a net-section tension (NT) mode, the failure mode data for the ultimate strengths were found by unloading the specimens after the maximum test load was reached, as previously explained. Consequently, the failure modes associated with the post-ultimate response, cul-

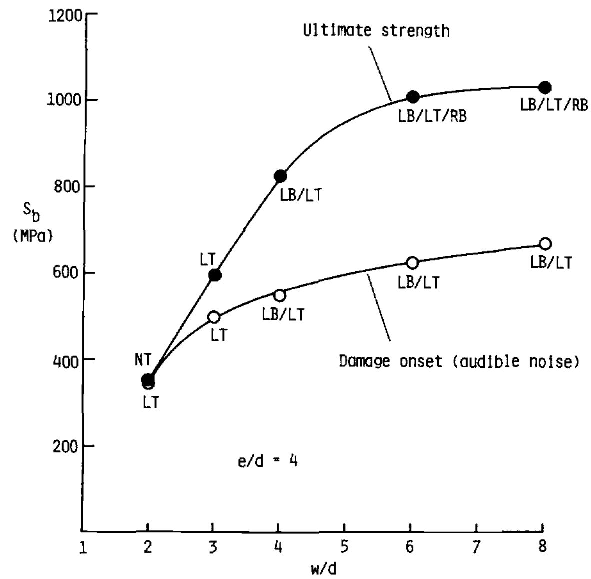

FIG. 7—*Damage onset and ultimate strength for a range of* w/d *values.*

minating in complete specimen failure, may be different from those indicated in Fig. 7. Comparison of the failure modes for damage onset and for ultimate strength indicates failure sequences. For small *w/d*-values, damage initiated in the LT mode and progressed in the tensile mode until specimen failure. As previously discussed, for $w/d \geq 3$, the damage apparently initiated in the LB mode, followed by LT damage which produced the audible noise. As the load was further increased, the damage progressed in both modes in a stable manner until the ultimate strength was reached. For $w/d \geq 5$, remote bearing (RB) failure mode was found after ultimate strength was reached and the specimen was unloaded; see Fig. 2*b*. It is doubtful that this RB damage developed in a stable manner because it occurred beyond the clampup washer where the laminate had no lateral support. It probably developed abruptly at ultimate load. Notice that in Fig. 7 the transition from LT to RB failures occurred for $4 \leq w/d \leq 6$, the range commonly used in composite joints. Also for this important *w/d* range, notice that damage initiates at stress levels that are as small as 61% of the ultimate strength.

Failure energy data are presented in Fig. 8. As expected, the tension-dominant failures (small *w/d*-values) dissipated very little energy. Significantly higher energy levels were measured for the larger *w/d* cases. Part of this increase is due to the higher ultimate strengths for large *w/d*-values. However, a significant part of the increase is believed to be attributable to the LB failure mode observed for the larger *w/d* cases. The lateral support provided by the bolt clampup allowed the local bearing deformation to progress in a somewhat stable manner. This stable LB damage progressed until the specimen reached its ultimate strength.

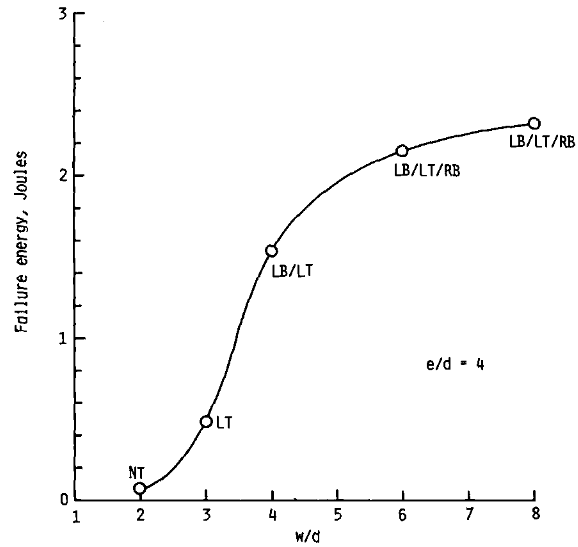

FIG. 8—*Failure energy for range of* w/d*-values.*

Although damage also grew in the LT mode, this damage did not appear to dissipate much energy, as shown by the results for *w/d* = 3 in Figs. 7 and 8. If this is the correct interpretation of the dramatic increase in failure energy shown in Fig. 8 for the large *w/d* cases, it indicates that failure mode can have a strong influence on the toughness of composite joints. For some joint applications, the increase in failure energy for $4 \leq w/d \leq 6$ may be more important than the increase in strength in that w/d range.

Edge Distance Effects—Damage onset results for *w/d* = 8 and a range of *e/d*-values are presented in Fig. 9. Damage initiated either in the LT or LB modes. For the smallest *e/d*-value, when the specimens were radiographed after an audible noise, only the LT mode was observed. This is further evidence that the audible noise was caused by LT damage. Notice that even for the smallest *e/d*-value, the expected shearout mode was not observed. For large *e/d*-values, nonlinearity developed before the first audible noise and both LB and LT damage was found when the specimens were unloaded. Consequently, as with the *w/d* data, these results suggest that LB damage caused the nonlinearity onset and that LB damage preceded the LT damage. Figure 9*b* shows that LT damage developed near θ = 71 deg for the entire range of *e/d*-values. The radiographs showed this damage in rather narrow radial bands extending from the hole, as shown in Fig. 2*f*.

Figure 10 shows ultimate strength results for the *e/d*-values tested. For the smallest *e/d*-value, the specimens failed by the sequence of LT damage followed by remote shearout (RS) to the specimen edge; see Fig. 2*f*. For the intermediate *e/d*-values, the damage started with local bearing, followed by local tension, and ended with remote shearout, shown as LB/LT/RS in Fig. 10. For the larger *e/d*-

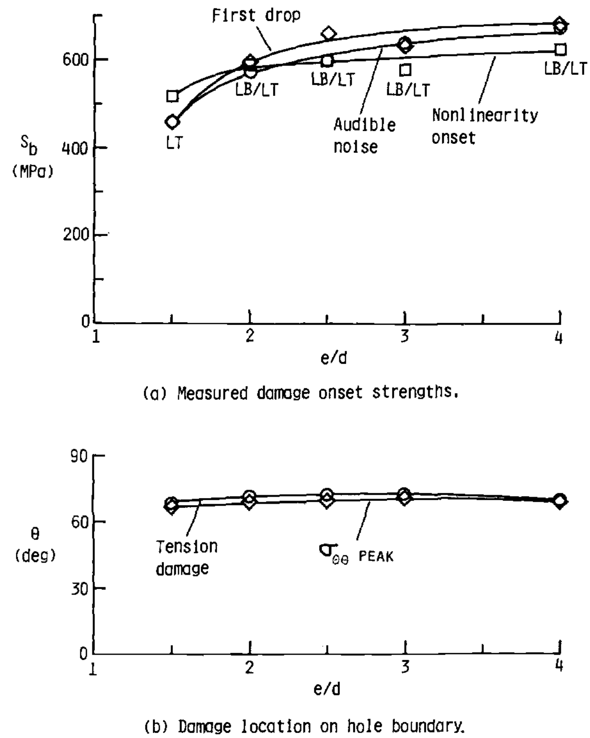

FIG. 9—*Damage onset results for* e/d *range,* w/d = *8.*

values, the failure sequences culminated in RB failures. Note that the $e/d = 4$ case in this figure corresponds to the $w/d = 8$ case shown previously in Fig. 7.

The failure energy results in Fig. 11 show the same trend as discussed earlier for the *w/d* cases. Although the radiographs showed that the RS mode resulted in considerable delamination, this mode apparently dissipated little energy. The larger failure energy measurements appear to correlate with the presence of bearing damage.

Local Stress Evaluation

Stresses computed around the hole boundary are plotted in Fig. 12 for three different cases. These stresses, the $\sigma_{\theta\theta}$ tangential stress and the σ_{rr} bearing stress, have been normalized by S_b for comparison. The dashed curves correspond to the stresses for an infinite laminate with a snug-fitting ($C = 0$) rigid bolt. This case provides good reference stress distributions because the contact angle does not change with applied bearing stress. Therefore, the contact angle ($\theta_c = 82$ deg) and the stress distributions shown as dashed curves apply for any level of bearing stress. The peak value of $\sigma_{\theta\theta}/S_b$ is 0.92, which agrees with the values of

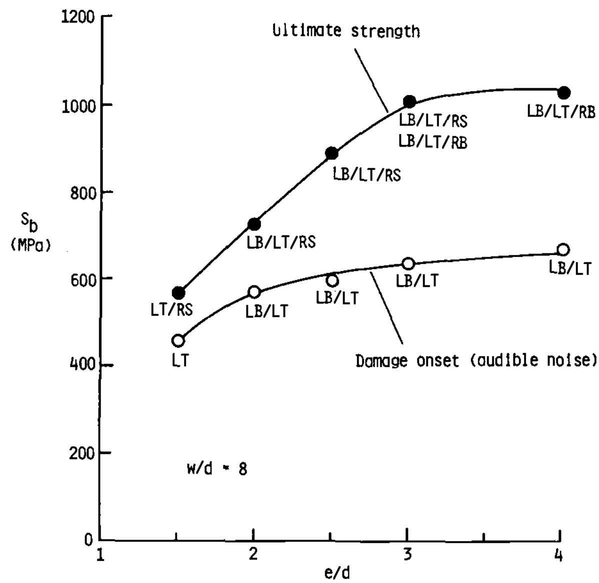

FIG. 10—*Damage onset and ultimate strength for a range of* e/d*-values.*

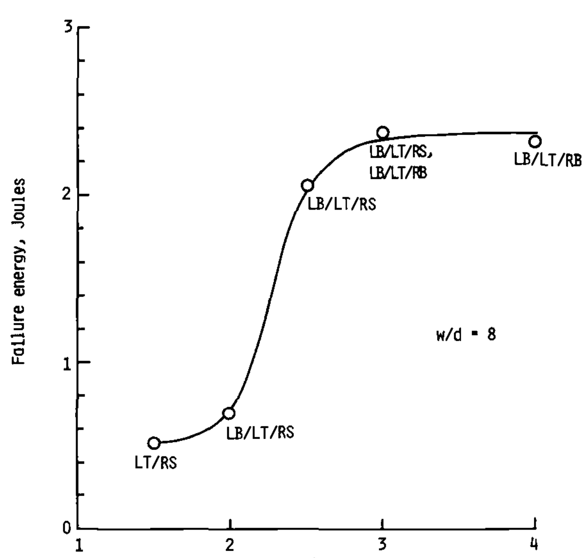

FIG. 11—*Failure energy for range of* e/d*-values.*

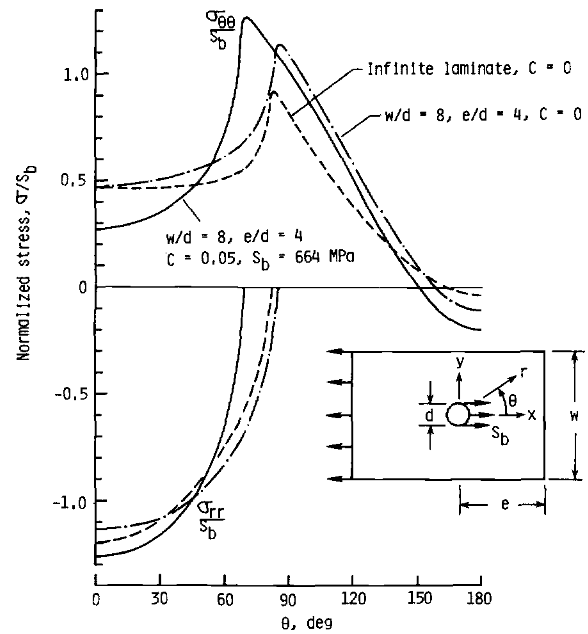

FIG. 12—*Stress distribution along hole boundary.*

0.91 and 0.92 from Refs *6* and *7*, respectively. This agreement verifies the finite-element modeling used in the present study.

The dash-dot curves in Fig. 12 represent stress distributions for the largest test specimen ($w/d = 8$ with $e/d = 4$) with a snug-fitting ($C = 0$) bolt. The contact angle of 85 deg is only slightly higher than for the infinite laminate case, but the $\sigma_{\theta\theta}/S_b$ peak value was 1.14, more than 20% larger than the reference case. This shows that even the largest specimen used in the present study only roughly approximated the infinite laminate behavior.

The solid curves in Fig. 12 show the stress distributions for the largest test specimen with a 0.05-mm clearance fit. In this case, as discussed earlier, the contact angle increases with applied bearing stress. The results shown correspond to $S_b = 664$ MPa (the measured damage onset stress for this test configuration); the contact angle was found to be about 70 deg. The solid curve has a peak $\sigma_{\theta\theta}/S_b$-value of 1.27. Comparison with the dash-dot curve shows that clearance fit increased the $\sigma_{\theta\theta}$ peak by more than 10% and shifted its location by 15 deg. This emphasizes the importance of modeling the clearance fit in the present stress analyses.

The peak values of $\sigma_{\theta\theta}/S_b$ and σ_{rr}/S_b, expressed as stress concentration factors K_{tb} and K_{bb}, respectively, were calculated for the w/d and e/d ranges used in the test program. The applied bearing stress levels used in these calculations correspond to the damage onset strengths presented earlier in Figs. 7 and 10. The

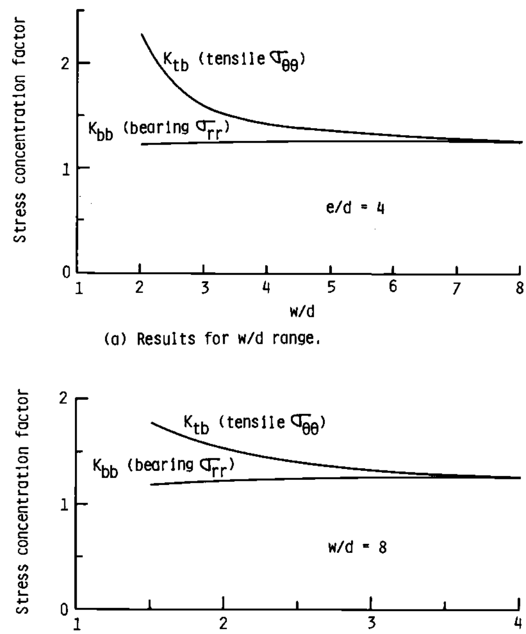

(a) Results for w/d range.

(b) Results for e/d range.

FIG. 13—*Stress concentration factors for test specimens.*

computed K_{tb} and K_{bb} results are plotted in Fig. 13. As expected, the small w/d cases had high K_{tb}-values. The locations of $\sigma_{\theta\theta}$ peaks on the hole boundary are shown in Fig. 6*b*. These locations agree well with the observed locations for tension damage onset as shown in Fig. 6*b*. In contrast to the K_{tb} results, the K_{bb}-values in Fig. 13*a* are virtually unaffected by the w/d ratio.

The K_{tb}-values in Fig. 13*b* are elevated for smaller e/d ratios. This trend is probably responsible for the local tension damage previously observed for the test cases with small e/d-values. This is further discussed when strength predictions are presented in the next section. The locations for the $\sigma_{\theta\theta}$ peaks, corresponding to the K_{tb} results, are shown in Fig. 9*b*. Again, the locations for $\sigma_{\theta\theta}$ peaks agree very closely with the measured locations for tension damage onset.

Failure Predictions

The dashed curves in Fig. 14 are predictions for damage onset, obtained by using the calculated K_{tb}- and K_{bb}-values in Eqs 2 and 3. The laminate strengths used in these predictions were 414 and 455 MPa for the tension and compression, respectively [2]. The value of the C_t coefficient was determined from Eq 1 using the S_{bo} data for the w/d = 2 case, which involved only tension damage. Tension damage predictions agreed reasonably well with the test data shown by open

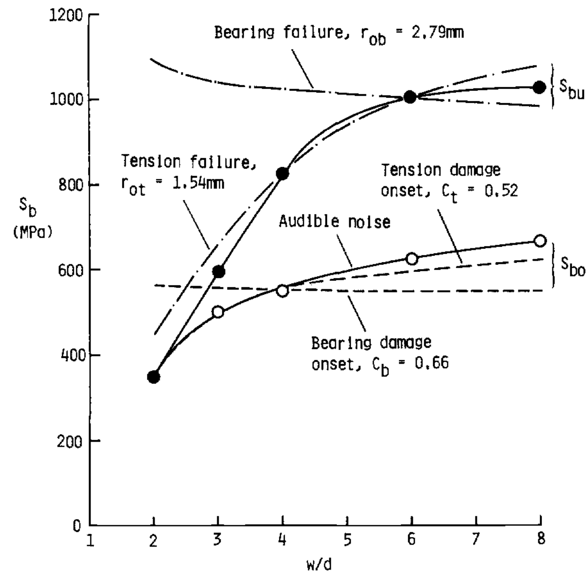

FIG. 14—*Strength predictions for* w/d *range.*

symbols. For the bearing predictions, C_b was found using S_{bo} data for the w/d = 4 case. For the small w/d ratios, the tension-damage curve lies below the bearing curve, indicating tension as the predicted damage onset mode. For w/d-values greater than 4, bearing is the predicted mode. These trends agree with the observed failure modes discussed earlier.

The dot-dash curves in Fig. 14 are predictions for ultimate strength. The point-stress procedure was used with the σ_{xx} stress distributions and the maximum-stress failure criterion to calculate these curves. The σ_{xx} distributions used in this procedure were those calculated along the observed direction of damage growth. For tension predictions, the growth directions were transverse lines that intersected the hole boundary at the observed damage onset locations, shown earlier in Fig. 6*b*. The characteristic dimension r_{ot} for tension was found to be 1.54 mm, based on the w/d = 4 data, and that value was used to predict tension failure strengths for the other w/d-values. The procedure was applied in a similar manner to obtain the predicted curve for bearing failure strengths. The bearing predictions were all based on σ_{xx} distributions along the x-axis. The characteristic bearing dimension r_{ob} was found to be 2.79 mm based on data from the w/d = 6 case. Comparison of the two dash-dot curves shows that bearing damage is predicted for $w/d \geq 6$, which agrees with the failure mode data shown in Fig. 7. Furthermore, the strength predictions agree reasonably well with the test results (solid symbols) in Fig. 14.

Figure 15 shows strength predictions for the e/d-values. The damage onset predictions (dashed curves) were calculated using C_t- and C_b-values determined

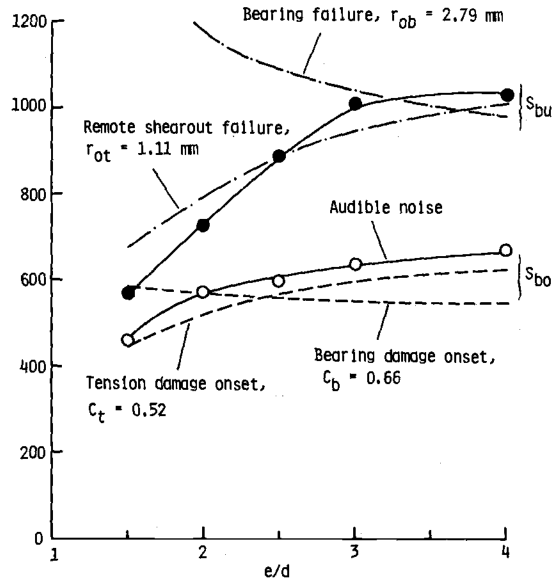

FIG. 15—*Strength predictions for* e/d *range.*

from the w/d results. For this reason these curves are not as accurate as for w/d predictions. Nevertheless, these curves predict the damage onset modes correctly and also predict the proper damage sequence for the large e/d cases. Because local shearout (see Fig. 2*b*) was a viable failure mode for small e/d-values, the shear stresses along the shearout plane ($y = d/2$) were determined for applied bearing stresses equal to the measured S_{bo}-values. Even for the rather extreme case of $e/d = 1.5$, the maximum shear stress on this plane was slightly below the laminate shear strength (310 MPa [*2*]). In contrast, the corresponding σ_{xx} stresses along the observed damage path (a radial line at $\theta = 71$ deg) exceeded the tensile ultimate strength by as much as 70%. This explains why the damage initiated in tension and propagated along the $\theta = 71$ deg radial line rather than in the shear mode along the local shearout plane.

The predicted curve for remote shearout failures was calculated using the σ_{xx} distribution along the $\theta = 71$ deg direction. As previously discussed, the failure sequence for the smaller e/d cases started as a tension failure along the $\theta = 71$ deg path followed by remote shearout failure along the $y = d$ plane; see Fig. 2*f*. The predicted dash-dot curve in Fig. 15 indicates the data trends, but the predicted strengths have errors as large as 20%. Comparison of the two predicted dash-dot curves indicates the proper failure mode trends, but not with as much accuracy as shown for the w/d cases.

The strength prediction procedures were repeated with several failure criteria in addition to the maximum stress criterion. These other criteria were the Tsai–Hill [*8*], Tsai–Wu [*9*], Hoffman [*10*], Yamada–Sun [*11*], and the maximum strain criteria. The results based on the maximum strain criterion were almost as good as those based on maximum stress. However, none of the other criteria produced satisfactory predictions. Note that all of these other criteria involve multi-axial stress components. This suggests that the failures were influenced primarily by the maximum stress, which in all cases was the x-axis stress component.

Concluding Remarks

Quasi-isotropic graphite/epoxy laminates (T300/5208) were tested under bolt-bearing loads using a simple fixture with a 6.35-mm steel bolt. Test specimens had a range of widths and edge distances to produce failures by several different modes. Radiographs were made after damage onset and after ultimate load to examine the failure modes and the failure sequences. The laminate stresses near the bolt hole were calculated for each test specimen configuration using a finite-element procedure. These stresses were then used in a failure prediction procedure to analyze the test results.

Damage onset was found to develop at stress levels that were as low as 62% of specimen ultimate strength. This damage developed in either the bearing mode or the tension mode. Even specimens with small edge distances developed damage in the tension mode rather than the shearout mode. Except for specimens with very small widths or edge distances, the first damage usually developed in the bearing mode and consisted mainly of ply delamination. At slightly higher stress levels, however, tension damage appeared in the form of ply cracks. The location of tension damage on the hole boundary correlated very well with the location of the computed maximum tensile stress. The stress analysis showed that both the location and magnitude of this maximum stress are strongly influenced by the bolt clearance.

The failure modes associated with ultimate strength were usually different from the damage onset mode. Only for the case of tensile failures in narrow specimens did the damage initiate and grow to failure in the same mode. When wide specimens were tested to ultimate strength, they first developed damage in the local bearing mode at the hole boundary, then local tension damage (also at the hole boundary), and finally developed remote bearing immediately beyond the clampup washer. Specimens with moderately small edge distances also failed in a sequence involving three modes: Damage appeared first in the local bearing mode, then in the local tension mode, which led to the remote shearout mode extending from the edge of the washer.

Failures involving extensive bearing damage were found to dissipate significantly more energy than tension-dominated failures. Because the specimen configuration influenced the failure mode, it therefore influenced the failure energy also. With increasing w/d-values, for example, the transition from tension failure to bearing failure that occurred in the range of $4 \leq w/d \leq 6$ caused a very large increase in failure energy. For some applications, this increase in failure energy for $4 \leq w/d \leq 6$ may be more important than the increase in strength in that range. The failure energy for bearing-loaded holes is a material response that should be given additional emphasis in joint design procedures as well as in material development activities.

References

[1] Crews, J. H., Jr. in *Joining of Composite Materials, ASTM STP 749*, K. T. Kedward, Ed., American Society for Testing and Materials, Philadelphia, 1981, pp. 131–144.
[2] "DOD/NASA Advanced Composites Design Guide, Vol. IV-A: Materials, First Edition," Contract No. F33615-78-C-3203, Air Force Wright Aeronautical Laboratories, Dayton, OH, July 1983, (available as NASA CR-173407 and from DTIC as AD B080 184L).
[3] Mangalgiri, P. D., Dattaguru, B., and Rao, A. K. in *Proceedings*, Seventh International Seminar on Computational Aspects of the Finite-Element Method (CAFEM-7), Chicago, IL, Aug. 29–30, 1983, pp. 123–157.
[4] Hart-Smith, L. J., "Bolted Joints in Graphite-Epoxy Composites," NASA CR-144899, National Aeronautics and Space Administration, Jan. 1977.
[5] Whitney, J. M., and Nuismer, R. J., *Journal of Composite Materials*, Vol. 8, July 1974, pp. 253–265.
[6] DeJong, Theo, *Journal of Composite Materials*, Vol. 11, July 1977, pp. 313–331.
[7] Eshwar, V. A., Dattaguru, B., and Rao, A. K., "Partial Contact and Friction in Pin Joints," Report No. ARDB-STR-5010, Department of Aeronautical Engineering Indian Institute of Science, Bangalore, India, Dec. 1977.
[8] Tsai, S. W. in *Fundamental Aspects of Fiber Reinforced Plastic Composites*, R. T. Schwartz and H. S. Schwartz, Eds., Wiley Interscience, New York, 1968, pp. 3–11.
[9] Tsai, S. W. and Wu, E. M., *Journal of Composite Materials*, Vol. 5, Jan. 1971, pp. 58–80.
[10] Hoffman, O., *Journal of Composite Materials*, Vol. 1, 1967, pp. 200–206.
[11] Yamada, S. E. and Sun, C. T., *Journal of Composite Materials*, Vol. 12, July 1978, pp. 275–284.

Carl-Gustaf Aronsson[1] *and Jan Bäcklund*[1]

Damage Mechanics Analysis of Matrix Effects in Notched Laminates

REFERENCE: Aronsson, C.-G. and Bäcklund, J., "**Damage Mechanics Analysis of Matrix Effects in Notched Laminates,**" *Composite Materials: Fatigue and Fracture, ASTM STP 907,* H. T. Hahn, Ed., American Society for Testing and Materials, Philadelphia, 1986, pp. 134–157.

ABSTRACT: The main objective of this study was to investigate the matrix influence on the fracture behavior of carbon/epoxy three-point bend specimens. The matrices investigated were a brittle Fiberite 1034 and a more ductile Fiberdux 914C epoxy matrix. For the analysis of strength and load versus displacement behavior of the specimens, a damage zone model (DZM) was used. The damage is represented by a Dugdale/Barenblatt cohesive zone, where the cohesive stresses are assumed to decrease linearly with an increased crack opening.

Excellent agreement is obtained between predicted and measured fracture loads of the specimens. Also the nonlinear load versus displacement curves are accurately reproduced by the analysis. The present model is compared with previous models, such as the inherent flaw and the point stress criteria. The damage zone extension in the brittle and ductile matrix specimens was studied and compared with the DZM calculations, as an attempt to explain the difference in fracture behavior between the brittle and ductile matrix specimens.

KEY WORDS: composite materials, carbon/epoxy, predictions, radiography, damage, stiffness change

Relatively few investigations of the matrix influence on the fracture behavior of continuous fiber composites are found in the literature. Some work has, however, been reported on the fracture of randomly oriented short fiber composites [*1–3*]. Agarwal and Giare [*1*] studied the fracture toughness of short glass fiber-reinforced epoxy composites. Epoxy of different moduli and strengths were employed to investigate the influence of the matrix properties on the fracture behavior. By the use of crack growth resistance method (K_R-curves) they found a significant influence of the modulus and strength of the matrix materials on the fracture toughness. Gaggar and Broutman [*2,3*] have studied the fracture toughness of random glass fiber epoxy and polyester composites using the K_R-

[1] Research associate and professor, respectively, Department of Aeronautical Structure and Materials, The Royal Institute of Technology, S-100 44, Stockholm, Sweden. Coauthor Bäcklund is currently visiting professor, Center for Composite Materials, University of Delaware, Newark, DE 19716.

curve approach, and showed that the fracture behavior was different in the two matrix systems.

In order to predict the static strength of notched laminates with continuous fiber, Waddoups et al [4] applied linear elastic fracture mechanics (LEFM) and proposed a model denoted the inherent-flaw model (IFM). Whitney and Nuismer [5,6] introduced two fracture models, the point stress criterion (PSC) and the average stress criterion (ASC), which are based on the exact stress distribution in the vicinity of the notch. Each model is based on the unnotched tensile strength and a characteristic length, which was assumed to be a material parameter for a given composite material system and layup. However, a basic problem with these methods is that they require different values of the characteristic length for various sizes of the notch in the same type of laminate [7–11].

A more general model [12], requiring only basic properties of the laminate such as laminate stiffnesses, unnotched strength, and apparent fracture energy, is here used to predict the fracture behavior of the brittle and ductile three-point bend (TPB) specimens. In the model, called the damage zone model (DZM), the damage zone is approximated by a crack with cohesive stresses acting on its surfaces. Damage in the material is taken into account by reducing the cohesive stresses with increased crack opening, which in turn corresponds to increased separation of the material.

Results from load predictions based on the DZM, IFM, and PSC are compared with experimental results obtained from the brittle and ductile matrix TPB specimens. It might be pointed out that the brittle matrix should be considered as a reference, and the load data presented here are taken from Ref *13*.

Analysis

Damage Zone Model

During increasing external load on a laminate with a notch, a damage zone will form and grow in the stress-intense region at the notch. The damage is represented along, or projected onto, two adjacent crack surfaces and treated by a Dugdale/Barenblatt-type analysis [14–18], Figs. 1, 2. On the crack surfaces, cohesive stresses σ are assumed to act, Fig. 2*a*. Damage growth results in increased crack opening v and a reduction of the cohesive stresses σ.

A linear relationship between crack opening and cohesive stress, Fig. 2*b*, has proven to give good results [13,19] and is used in the calculations here. It is important to note that the area below the σ-v curve is equal to the apparent fracture energy G_c^* and that the maximum value σ_0 of the stress is the unnotched tensile strength of the laminate. G_c^* represents the sum of all energies dissipated in the various fracture mechanisms.

In the virgin, unloaded material there is no damage and hence no equivalent crack in the model. When the load is increased such that the stress at a Point A in Fig. 1 reaches σ_0, the equivalent crack is assumed to form. Upon further

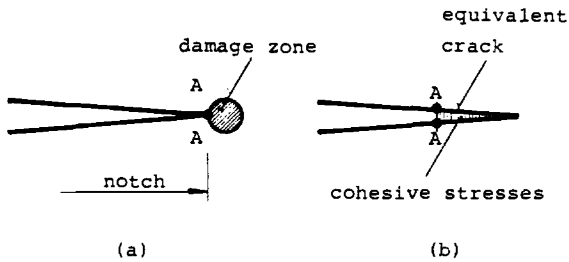

FIG. 1—*Damage zone at a notch and equivalent crack used in the analysis:* (a) *damage zone;* (b) *equivalent crack.*

loading, this crack opens and grows into the laminate. The stress σ at Point A is then assumed to be reduced according to the linear relationship shown in Fig. 2*b*. The stress $\sigma(x)$ at Points *P*, Fig. 2*a*, along an *a priori*-determined crack path is treated in the same way. Through this procedure, nucleation, stable growth, and unstable growth of the crack are modeled for increased external loading in a series of calculations using a condensed finite-element model (FEM) stiffness matrix of the structure. Moreover, redistribution of stress and change in stiffness is accounted for in the model. The numerical technique used is described in Refs *19* and *20*.

Inherent-Flaw Model

The IFM was originally developed for predicting the strength of notched laminates with infinite width, but has been extended to be used for finite geometry by introducing the geometric correction factor [*21*,*22*]. For a TPB specimen with a crack of length a and an inherent flaw of length c_0, the notched strength P_N^{IFM} is given by [*13*]

$$P_N^{\mathrm{IFM}} = \frac{P_0}{Y} \sqrt{\frac{c_0}{a + c_0}} \tag{1}$$

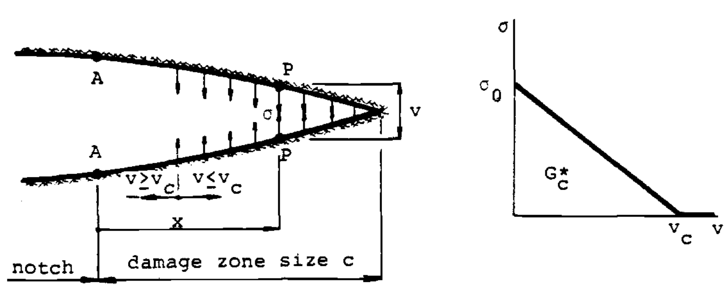

FIG. 2—*Dugdale/Barenblatt cohesive zone:* (a) *crack opening* v(x), *cohesive stress* σ(x) *and length* c; (b) *assumed linear relation between* σ *and* v.

where P_0 is a reference load (see Tables 4*a* and 4*b*) and Y is the geometric correction factor based on the original crack length a [22].

The geometric correction factor used in the calculations was obtained from [23]

$$Y\left(\frac{a}{w}\right) = 1.09 - 1.73\left(\frac{a}{w}\right) + 8.2\left(\frac{a}{w}\right)^2 - 14.2\left(\frac{a}{w}\right)^3 + 14.6\left(\frac{a}{w}\right)^4$$

This factor is derived for an isotropic material and can be used for the quasi-isotropic laminates considered.

While the material is considered homogeneous, orthotropic, and linear elastic, the following relationship between P_N^{IFM} and the fracture energy G_c is obtained [13]

$$P_N^{\mathrm{IFM}} = \frac{P_0}{Y\sqrt{1 + (\pi a \sigma_0^2/CG_c)}} \tag{2}$$

where

$$C = \left[\frac{A_{11}A_{22}}{2}\left(\sqrt{\frac{A_{22}}{A_{11}}} + \frac{2A_{12} + A_{66}}{2A_{11}}\right)\right]^{-1/2} \tag{3}$$

A_{ij} are the in-plane laminate flexibilities as determined from laminated plate theory [24].

A linear relationship between c_0 and G_c may further be obtained by studying a tension coupon [13]

$$c_0 = \frac{C}{\pi\sigma_0^2} G_c \tag{4}$$

Point Stress Criterion

The PSC has been derived by considering the exact elasticity solution for the normal stress ahead of a notch. The requirement of an exact expression of the normal stress restricts, however, the use of the model. By approximating the exact solution of the normal stress ahead of a crack with the asymptotic solution, the model can be extended to the use on cracked laminates with finite geometry. This is justified if the crack length is sufficiently large compared with the size of the damage zone d_0 [1,25].

For the TPB specimen, an approximate expression for the notched strength according to the PSC is given by [13]

$$P_N^{\mathrm{PSC}} = \frac{P_0}{Y}\sqrt{\frac{2d_0}{a}} \tag{5}$$

where d_0 is the characteristic length defined in the PSC [5,6]. Note that Eq 5 is valid only if $d_0 \ll a$. A more accurate expression for P_N^{PSC} is given by Eq 6 [5,6,26]

$$P_N^{PSC} = \frac{P_0}{Y} \sqrt{\frac{(2a + d_0)d_0}{(a + d_0)^2}} \tag{6}$$

It is easy to show that the value of P_N^{PSC} obtained from Eq 6 will be identical to that from the IFM (Eq 2) if the quotient d_0/a is small enough.

Material Selection and Experiments

Two different epoxy matrices were investigated. They were a Fiberite Hy-E-1034 and Fiberdux 914C. Since 1034 is the more brittle (lower G_c^*) and 914 is the more ductile (higher G_c^*) of the two, they are referred to as the "brittle" and the "ductile" matrix, respectively, below. The matrices were reinforced with Thornel 300 carbon fibers and hand laid up for the desired $[0/90/\pm45]_{ns}$ stacking sequences, where $n = 4$, 8, and 10 for the ductile matrix and $n = 6$ for the brittle matrix. The panels were cured according to the manufacturer's recommended procedure and the thicker laminates ($n \geq 6$) were compacted before final cure in order to minimize the void content. The void content was less than 0.5%. The fiber volume fraction was approximately 65%. TPB specimens were machined from the panels and the cracks were machined with a thin (0.13 mm) diamond-coated disk, whereafter the tips were sharpened with a razor blade. Geometry and dimensions of the specimens are shown in Fig. 3.

The unnotched tensile strengths σ_0 for the brittle and the ductile matrix materials were determined from tension tests on coupon-type specimens of length 120 mm, width 22 mm, and thickness 2.05 mm.

All specimens were loaded statically in a 300-kN MTS testing machine under displacement control with a displacement rate of 1 mm/min. Curves of load versus grip displacement δ_p were recorded for each specimen. The environmental conditions in the laboratory were approximately constant at 20°C and 40% relative humidity.

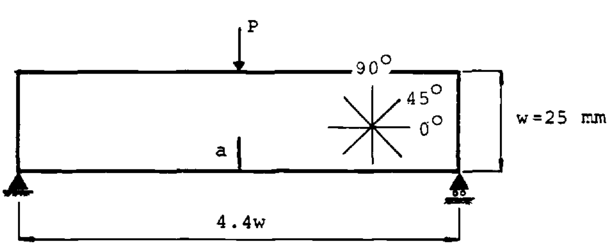

FIG. 3—*Geometry and dimensions in mm for TPB specimens:* a = *6, 9, 12, 15 and 18 mm.*

The formation of damage in some specimens was at certain load levels examined by using the TBE-enhanced X-ray technique [27]. For detection of failed fibers some specimens were deplied [*19*] after the maximum load was reached and the plies were grouped in 0, 45, and −45-deg layers. The damage zone ahead of the crack tip was then inspected in a Rekhert MeF2 microscope.

Experimental Results

In Table 1 the average experimental unnotched tensile strength σ_0 and the variation from the average value for each matrix material are given. It is noted that the difference in the unnotched strength between the brittle and ductile matrix specimens is negligible.

Table 2 gives the average experimental bending strength and the variation from the average value in percent for specimens with various initial crack lengths. The strength values are normalized with the unnotched bending strength P_0, which is calculated according to the expression given in Table 2. No systematic influence of thickness on strength is noted for the ductile matrix specimens at a given crack length, and the data for the ductile matrix were taken from the 8s specimens. For each crack length the strength of the ductile matrix specimens is larger than the strength of brittle matrix specimens. No tendency of out-of-plane instabilities was found at the tests, and local indentations at rollers introducing load and support forces were negligible.

Damage in some specimens at different load levels was detected by the TBE-enhanced X-ray technique [27]. For a brittle matrix specimen, loaded to about 80% of the fracture load, a small damage zone ahead of the crack tip in the form of extensive matrix cracking is observed in Fig. 4*a*. Immediately after the maximum load is reached the crack-tip damage is mainly colinear with the crack, but matrix cracks occur in the 90 and 45-deg plies. In the ductile matrix specimen a similar damage extension occurs. However, the size of the damage zone at the failure load is larger than in the brittle matrix specimen; see Figs. 4*b* and 5*b*.

In order to detect any failed fibers in the damage zone, a brittle and a ductile matrix specimen with the same crack length were deplied. The specimens were unloaded immediately after reaching maximum load. The same type of damage was observed through the thickness for plies with the same fiber direction. In Fig. 6*a*, fiber fractures are observed close to the crack tip in a 0-deg ply of the brittle matrix specimen, while unbroken fibers are observed at small distances

TABLE 1—*Unnotched tensile strengths σ_0 for brittle and ductile specimens.*

Matrix Material	No. of Specimens	σ_0, MPa	Variation, %
Brittle	10	581	+4 −5
Ductile	10	580	+2 −3

TABLE 2—*Experimental strengths for brittle and ductile matrix specimens.*

	No. of Specimens	a/w	P_N^{EXP}/P_0	Variation, %
[a]Brittle matrix specimens $[0/90/\pm45]_{6S}$	5	0.24	0.463	+5 −6
	5	0.36	0.347	+5 −2
	5	0.48	0.247	+3 −5
	5	0.60	0.158	+3 −3
	4	0.72	0.089	+4 −5
[b]Ductile matrix specimens $[0/90/\pm45]_{4S}$	4	0.36	0.449	+3 −2
	3	0.48	0.308	+6 −6
	4	0.60	0.202	+3 −5
	4	0.72	0.104	+6 −5
$[0/90/\pm45]_{8S}$	4	0.24	0.588	+2 −4
	5	0.36	0.436	+4 −5
	5	0.48	0.312	+5 −3
	5	0.60	0.187	+5 −6
	4	0.72	0.108	+5 −6
$[0/90/\pm45]_{10S}$	4	0.24	0.598	+2 −1
	4	0.36	0.420	+3 −2
	5	0.48	0.312	+3 −4
	5	0.60	0.202	+3 −4
	4	0.72	0.108	+3 −7

[a]Where $P_0 = \frac{2w^2}{3s}\sigma_0 = 2201$ N/mm.

[b]Where $P_0 = \frac{2w^2}{3s}\sigma_0 = 2197$ N/mm.

ahead of the crack tip. It is noted that the damage extends mainly colinear with the crack. The damage in the 45-deg ply, shown in Fig. 6*b*, extends in form of bundles of failed fibers which show a hackled fracture pattern, and the damage extension is not colinear with the crack. It was observed that the same failure behavior occurred in the −45-deg plies as for the 45-deg plies.

The damage extension in the 0-deg ply from the ductile matrix specimen, Fig. 7, is similar to the brittle matrix specimen. On the other hand, the hackles in the 45-deg ply, shown in Fig. 7*b*, are larger than in the brittle matrix specimen and are not initiated at the crack tip but at a small distance in the front of it.

Figure 8 shows typical $P - \delta_p$ curves recorded experimentally (dashed curves) and $P - \delta_p$ curves calculated from the DZM (solid curves) for a brittle and a ductile matrix specimen with $a/w = 0.24$. Initially the curves show a linear behavior and become nonlinear at higher load levels. Good agreement is noted for both the rising and falling branches of the curves.

Numerical Results

To predict the notched strengths P_N^{DZM} from the DZM, a value of the apparent fracture energy G_c^* for each material system must be determined. This was done in the following way: For each material system, the notched to unnotched strength P_N/P_0 versus the apparent fracture energy G_c^* is calculated from the DZM by using the FE mesh shown in Fig. 9, and the results are plotted versus the apparent fracture energy G_c^*. The value of G_c^* which gives the fracture load equal to the experimental average for some crack length ($a/w = 0.24$ is chosen) is then taken as the adequate G_c^* for each material system. For the brittle and ductile matrix material $G_c^* = 35$ kJ/m^2 and $G_c^* = 70$ kJ/m^2, respectively, are obtained. These values of G_c^* are then used in all DZM computations presented in this study; see also Table 3.

In order to calculate the notched bending strengths from the IFM and the PSC using Eqs 1 and 5, 6, respectively, values of c_0 and d_0 for each material were determined from the strength of the specimens used for determining the apparent fracture energy discussed above. The values obtained for the brittle and the ductile matrix material are given in Table 4.

Strengths calculated from the DZM, IFM, and PSC are given in Tables 4*a* and 4*b* together with the variations in percent from the average experimental strengths. The primary input data used in the calculations are also given. In Tables 4*a* and 4*b* it is noted that the agreement between the experimental and the predicted values obtained from the DZM is very good in all cases. On the other hand, the variations for the IFM and the PSC (Eq 6) increase with increased a/w and this is particularly pronounced for the ductile specimens. For the two largest crack lengths also, the PSC (Eq 5) gives relatively poor agreement. It is noteworthy that the PSC according to Eq 5 gives better agreement with the average experimental values than the strengths calculated from Eq 6.

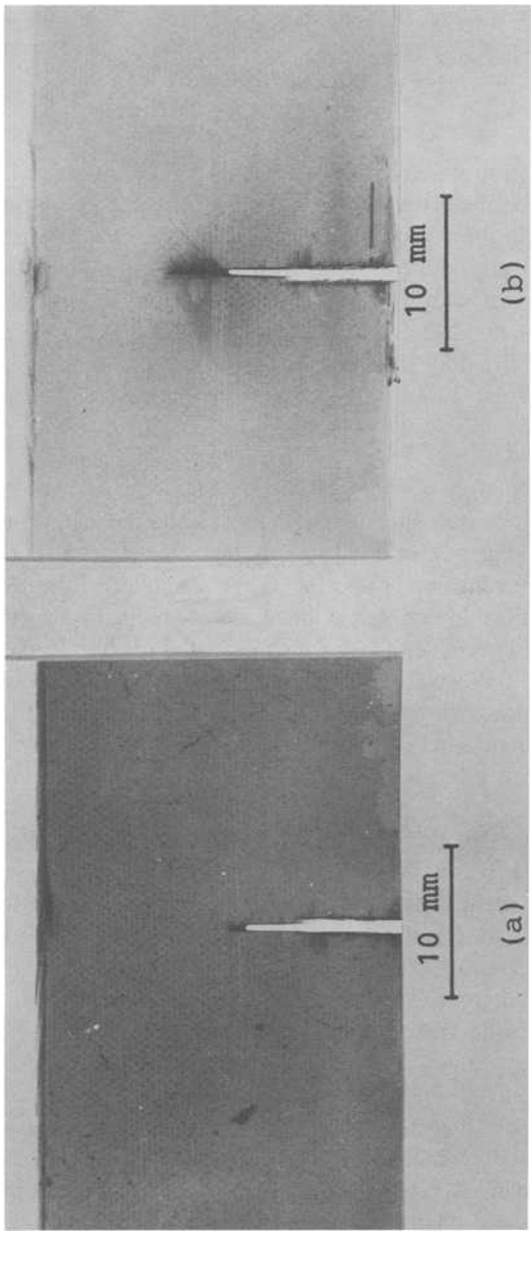

FIG. 4—*X-ray pictures for a brittle matrix specimen with* a/w = *0.48 at about* (a) *80% of the average fracture load;* (b) *100% of the average fracture load.*

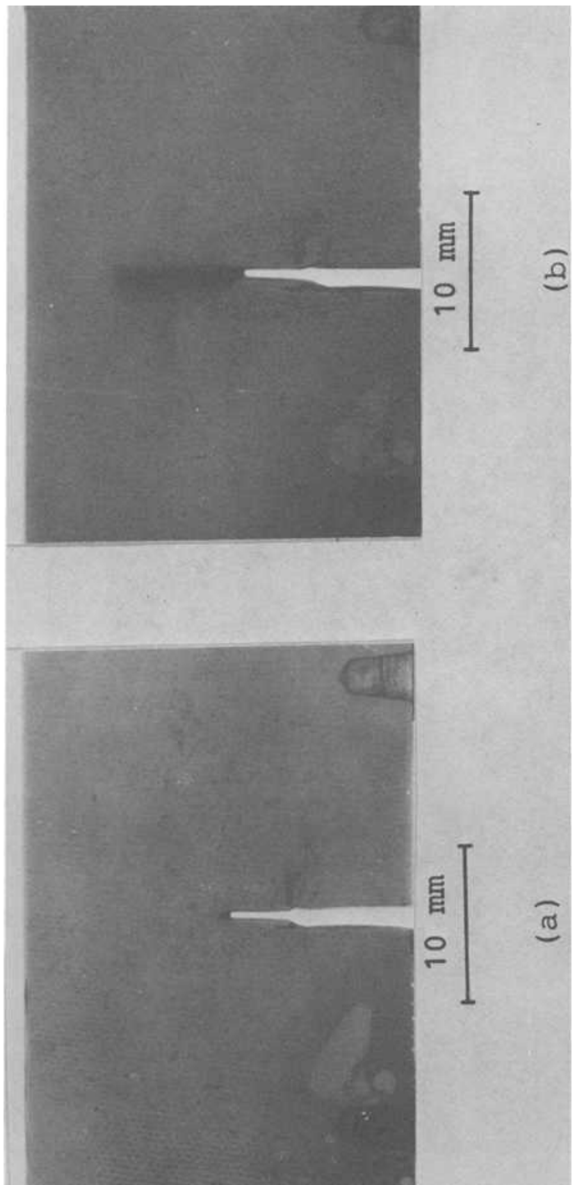

FIG. 5—*X-ray pictures for a ductile matrix specimen with a/w = 0.48 at about (a) 60% of the average fracture load; (b) 100% of the average fracture load.*

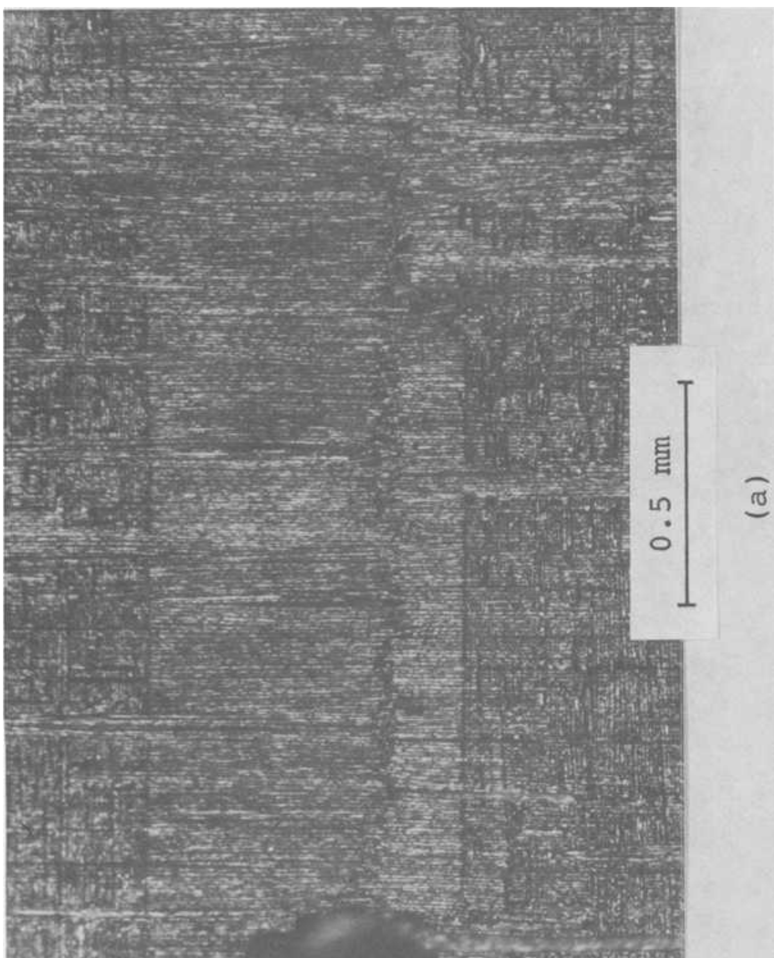
0.5 mm
(a)

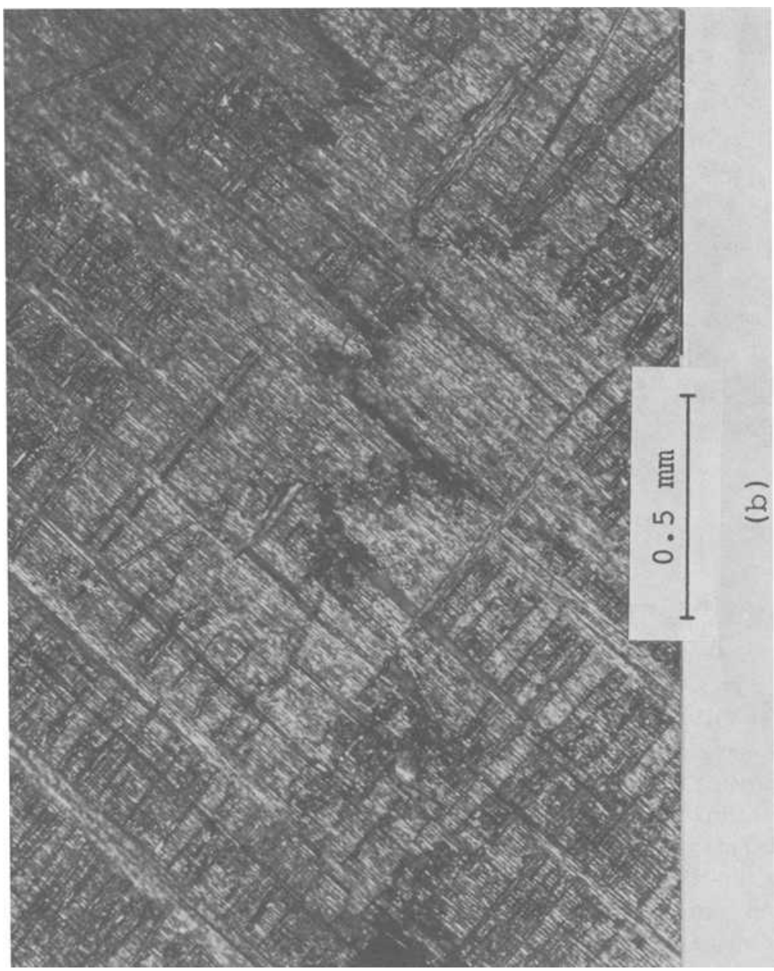

FIG. 6—*Failure pattern ahead of the crack tip in a brittle matrix specimen with* a/w = *0.36:* (a) *0-deg ply;* (b) *45-deg ply.*

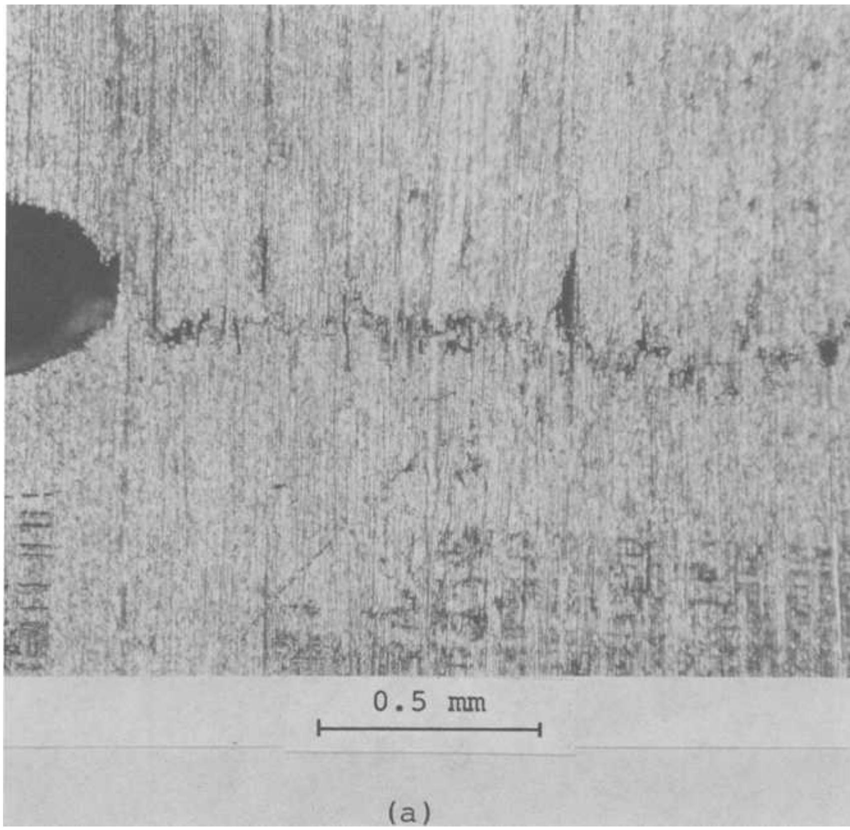

FIG. 7—*Failure pattern ahead of crack tip in a ductile matrix specimen with* a/w = *0.36:* (a) *0-deg ply;* (b) *45-deg ply.*

In Fig. 10 the nondimensional notched strength as predicted by DZM for various input data values of the apparent fracture energy G_c^* is plotted. Each solid curve is calculated from the DZM and represents both the brittle and the ductile matrix specimens. The notched strength obtained from the IFM (Eq 2) is plotted in Fig. 10 versus the fracture energy G_c (dashed curves). Both methods show a similar behavior, and the strength predicted from both methods should approach zero as G_c^* and $G_c \rightarrow 0$. This is obtained with reduced element size at the damage zone with the DZM.

A way to illustrate the variation in G_c^* and G_c with crack length for the brittle and the ductile matrix specimens is shown in Fig. 11. For each crack length (a/w) the plotted values of G_c^* and G_c give the predicted load equal to the average experimental value. Small variation in G_c^* with a/w is noted in Fig. 11*a* for the brittle matrix, while a larger variation is obtained for G_c. The same tendency is

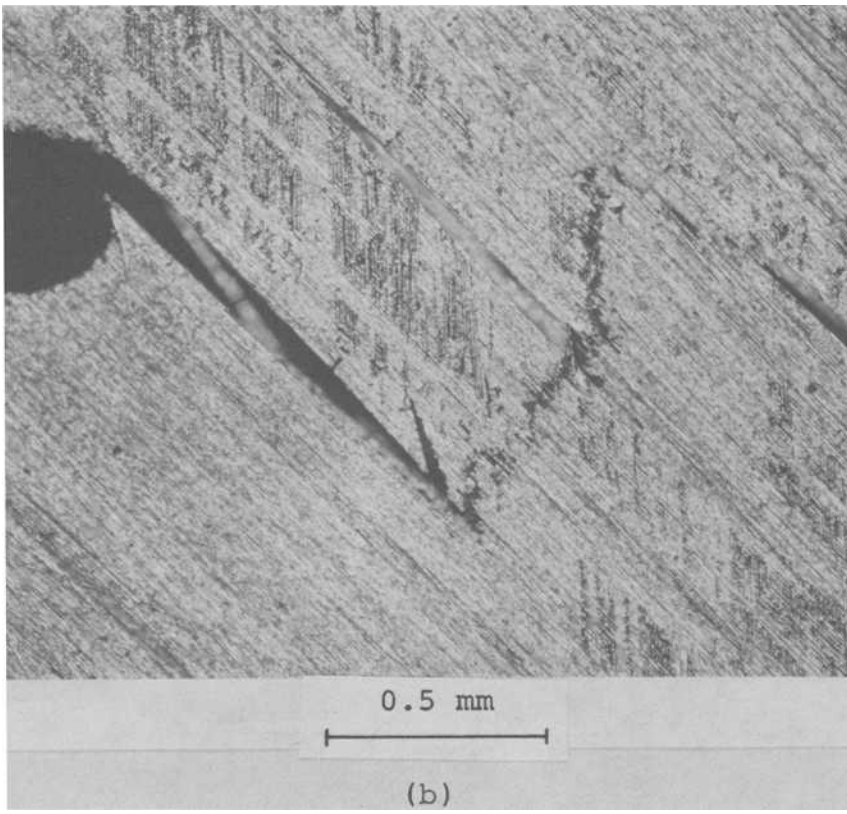

FIG. 7—*Continued.*

obtained for the ductile matrix, but the variation in G_c with a/w is larger than for the brittle matrix. Since there is a relationship between G_c and the parameter c_0 (see Eq 4), the large variations in G_c with a/w imply that c_0 is not a material constant.

In Fig. 12 the applied load normalized with the unnotched strength P/P_0 is plotted versus the extension c of the damage zone for various crack lengths. With increasing external load all curves show a stable damage growth, until the load has reached its maximum value, illustrated by squares, whereafter the damage growth becomes unstable. Since the crack causes a singularity in the stress field, the results with respect to initiation of damage are entirely related to the size of the finite elements at the crack tip. The results with respect to failure load (maximum load) are, however, not significantly affected by the error in modeling damage initiation.

The stress distribution ahead of the crack tip corresponding to the DZM and

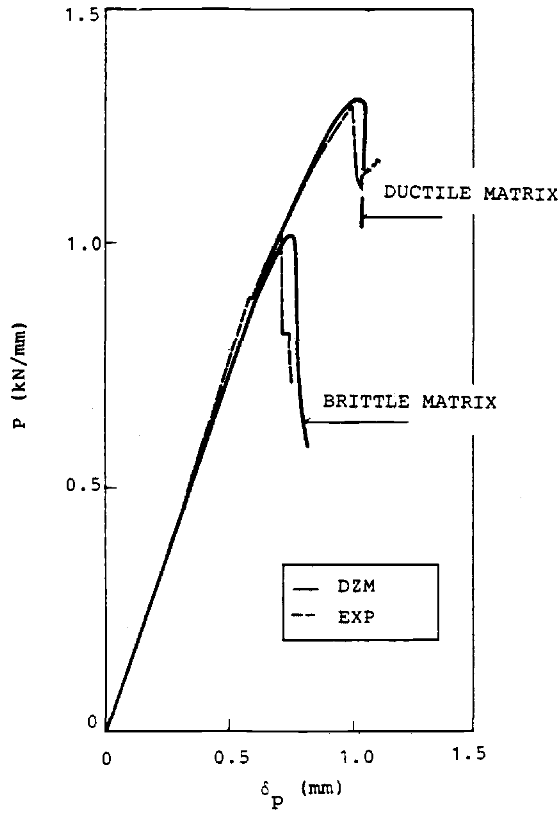

FIG. 8—*Predicted and experimental load versus displacement curves for a brittle and a ductile matrix specimen with* a/w = *0.24.*

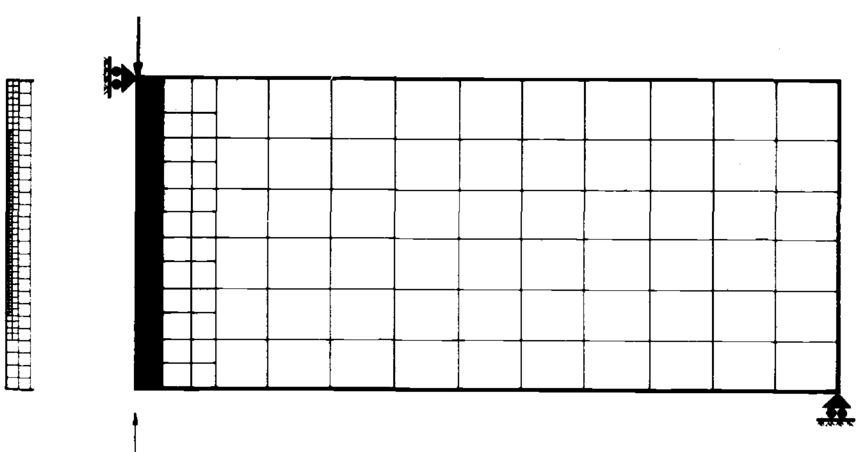

FIG. 9—*FE mesh for one half of a TPB specimen. Length of smallest element = 0.25 mm.*

TABLE 3—*Input data used in the DZM calculations.*

Brittle Matrix Laminate		Ductile Matrix Laminate	
Ply Data	Laminate Data	Ply Data	Laminate Data
E_{11} = 138 GPa	σ_0 = 581 MPa	E_{11} = 138 GPa	σ_0 = 580 MPa
E_{22} = 11 GPa	G_c^* = 35 kJ/m^2	E_{22} = 11 GPa	G_c^* = 70 kJ/m^2
G_{12} = 4 GPa	...	G_{12} = 5.6 GPa	...
ν_{12} = 0.35	...	ν_{12} = 0.35	...

the IFM as well as that obtained from LEFM for a brittle matrix specimen with $a/w = 0.24$ loaded to the fracture load is shown in Fig. 13. The stress σ_y normalized with the unnotched tensile strength σ_0 is plotted versus the distance x ahead of the crack tip. The more accurate curve calculated by FEM is given for comparison with the approximative curve obtained by LEFM. The curve representing LEFM is calculated from $\sigma = K/\sqrt{2\pi x}$ [28], where K is the Mode I stress-intensity factor.

It is noted that the curves obtained from the models show quite different behavior near the crack tip and that the size of the critical damage zones is different for the different models. The stress σ_y, in the region between the crack tip and d_0, is not likely to increase with decreasing distance to the crack tip as obtained by LEFM. From a physical point of view a more probable stress distribution is assumed in the IFM, which gives a constant stress within the distance c_0.

With increased external load, partial material separation occurs in the extending damage zone, resulting in a more compliant material close to the crack tip. This leads to a reduced stress σ_y, and such a behavior is assumed in the DZM calculations. Moreover, the critical damage zone sizes c calculated from the DZM are in agreement with those estimated in the experiments. This is not the case for the other models. Similar results were obtained for the ductile matrix specimens loaded to the fracture load.

Discussion and Conclusions

The influence of a brittle and a ductile matrix on the fracture behavior of notched $[0/90/\pm45]_{ns}$ carbon/epoxy composites has been studied by the use of a damage zone model, where the damage zone is modeled as a crack with cohesive forces acting on the crack surfaces.

The strengths predicted from the DZM and the PSC agree in general very well with the experimental values for the brittle and the ductile matrix TPB specimens. Also, the load versus displacement behavior for the brittle and the ductile matrix specimens calculated from the DZM is in good agreement with the experimental results. The results from the IFM show a variation which for all specimens increases with increasing crack length and reaches an unacceptable level for the

TABLE 4a—*Predicted strengths for brittle matrix specimens.*[a]

a/w	P_N^{DZM}/P_0	P_N^{IFM}/P_0	P_N^{PSC}/P_0 (Eq 5)	P_N^{PSC}/P_0 (Eq 6)	Δ^{DZM}, %	Δ^{IFM}, %	Δ^{PSC}, % (Eq 5)	Δ^{PSC}, % (Eq 6)
0.24	0.463*	0.463*	0.463*	0.463*	0.0	0.0	0.0	0.0
0.36	0.341	0.353	0.336	0.350	−1.8	1.7	−3.1	0.9
0.48	0.241	0.256	0.239	0.253	−2.2	3.6	−3.1	2.4
0.60	0.159	0.172	0.158	0.169	0.6	8.9	0.3	7.0
0.72	0.093	0.106	0.097	0.104	4.6	19.1	8.7	16.9

[a] Where $P_0 = \frac{2w^2}{3s}\sigma_0 = 2201$ N/mm.

$\Delta^x = (P_N^x/P_N^{EXP} - 1) \cdot 100\%$; x = DZM, IFM, PSC.

[b] Used for determination of parameters of the models.

Input data:

DMZ: $\sigma_0 = 581$ MPa, $G_c^* = 35$ kJ/m^2.

IFM: $\sigma_0 = 581$ MPa; $c_0 = 1.64$ mm or $G_c = 33.3$ kJ/m^2.

PSC: $\sigma_0 = 581$ MPa; $d_0 = 0.63$ mm (Eq 5).

PSC: $\sigma_0 = 581$ MPa; $d_0 = 0.77$ mm (Eq 6).

TABLE 4b—*Predicted strengths for ductile matrix specimens* $[0/90/\pm45]_{8s}$.[a]

a/w	P_N^{DZM}/P_0	P_N^{IFM}/P_0	P_N^{PSC}/P_0 (Eq 5)	P_N^{PSC}/P_0 (Eq 6)	Δ^{DZM}, %	Δ^{IFM}, %	Δ^{PSC}, % (Eq 5)	Δ^{PSC}, % (Eq 6)
0.24	0.588[b]	0.588[b]	0.588[b]	0.588[b]	0.0	0.0	0.0	0.0
0.36	0.435	0.459	0.432	0.453	−0.4	5.3	−1.0	3.9
0.48	0.306	0.338	0.307	0.331	−2.0	8.3	−1.5	6.1
0.60	0.199	0.229	0.203	0.222	6.3	22.5	8.5	18.7
0.72	0.116	0.142	0.125	0.138	7.4	31.5	15.7	27.8

[a] Where $P_0 = \frac{2w^2}{3s}\sigma_0 = 2197$ N/mm.

$\Delta^x = (P_N^x/P_N^{EXP} - 1) \cdot 100\%$; x = DZM, IFM, PSC.

[b] Used for determination of parameters of the models.

Input data:

DMZ: $\sigma_0 = 580$ MPa, $G_c^* = 70$ kJ/m^2.

IFM: $\sigma_0 = 580$ MPa; $c_0 = 3.18$ mm or $G_c = 64.6$ kJ/m^2.

PSC: $\sigma_0 = 580$ MPa; $d_0 = 1.04$ mm (Eq 5).

PSC: $\sigma_0 = 580$ MPa; $d_0 = 1.42$ mm (Eq 6).

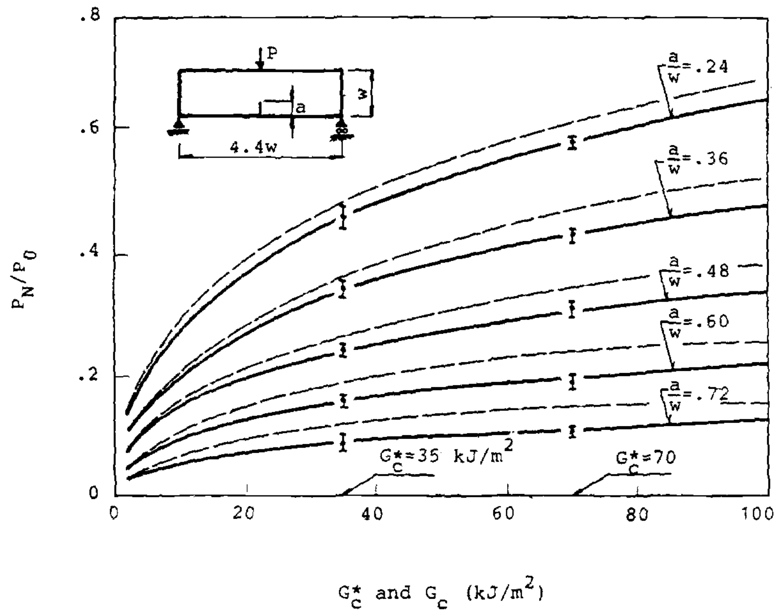

FIG. 10—*Notched to unnotched strength* P_N/P_0 *versus apparent fracture energy* G_c* (solid lines) *and fracture energy* G_c (dashed lines) *for brittle and ductile matrix specimens.*

larger cracks. This means that the parameter c_0 or the fracture energy G_c should not be considered as a material constant.

For both the brittle and the ductile matrix materials, it is noted that the fracture energies used in the DZM and the IFM are of the same order of magnitude. The DZM predictions are, however, in closer agreement with the experiments than those from the IFM. This might be explained by the fact that the stress distribution in the damage zone calculated from the DZM is more realistic. Moreover, a consequence of different stress distributions is that the critical damage zone sizes are different for the two models.

It is noted that a change in the value of G_c^* is sufficient to adequately predict the different fracture behavior for the brittle and the ductile matrix specimens. All other input data are the same for the two material systems except the shear modulus G_{12}. However, the small difference in G_{12} has negligible influence on the results for the stacking sequence used here.

From the DZM calculations it is noted that the critical size of the damage zone for both material systems varies with the crack length. It is also noted that the critical size of the damage zone is larger for the ductile than for the brittle matrix specimens in quantitative agreement with the nondestructive examination.

The results from all DZM calculations show that cohesive stresses act on the entire crack surfaces up to the maximum load. Immediately after the maximum load is reached, however, only small parts of the crack surfaces become unloaded.

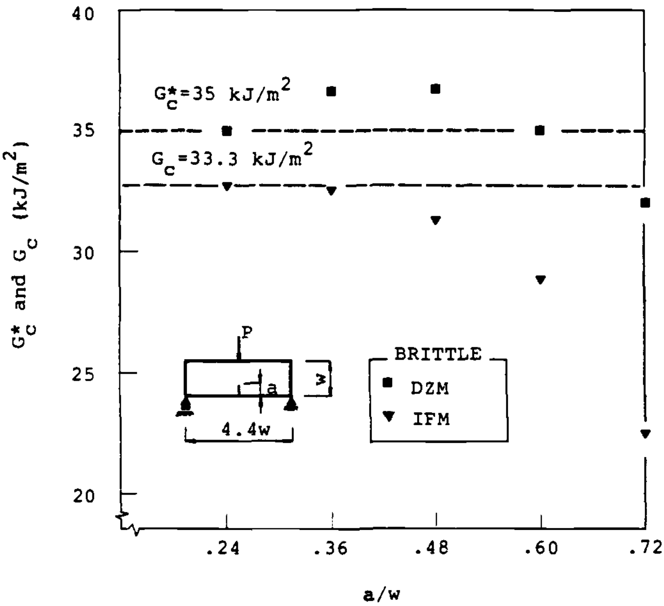

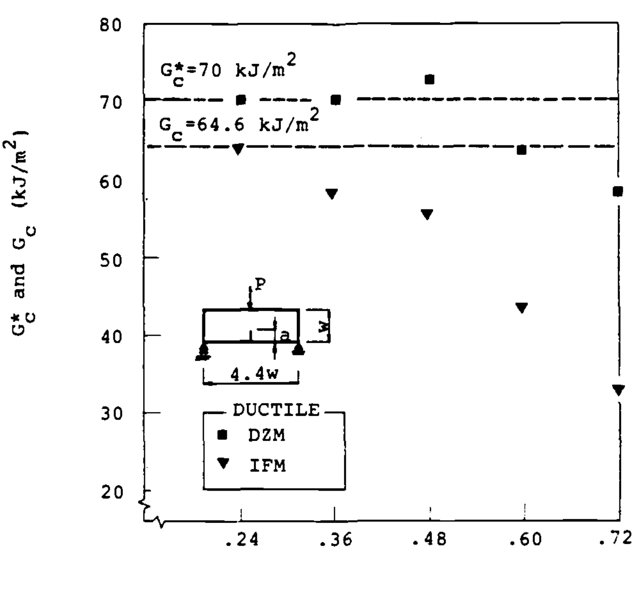

FIG. 11—*Apparent fracture energy* G_c* *and fracture energy* G_c *versus initial crack length to specimen width ratio* a/w *for* (a) *brittle matrix specimens;* (b) *ductile matrix specimens.*

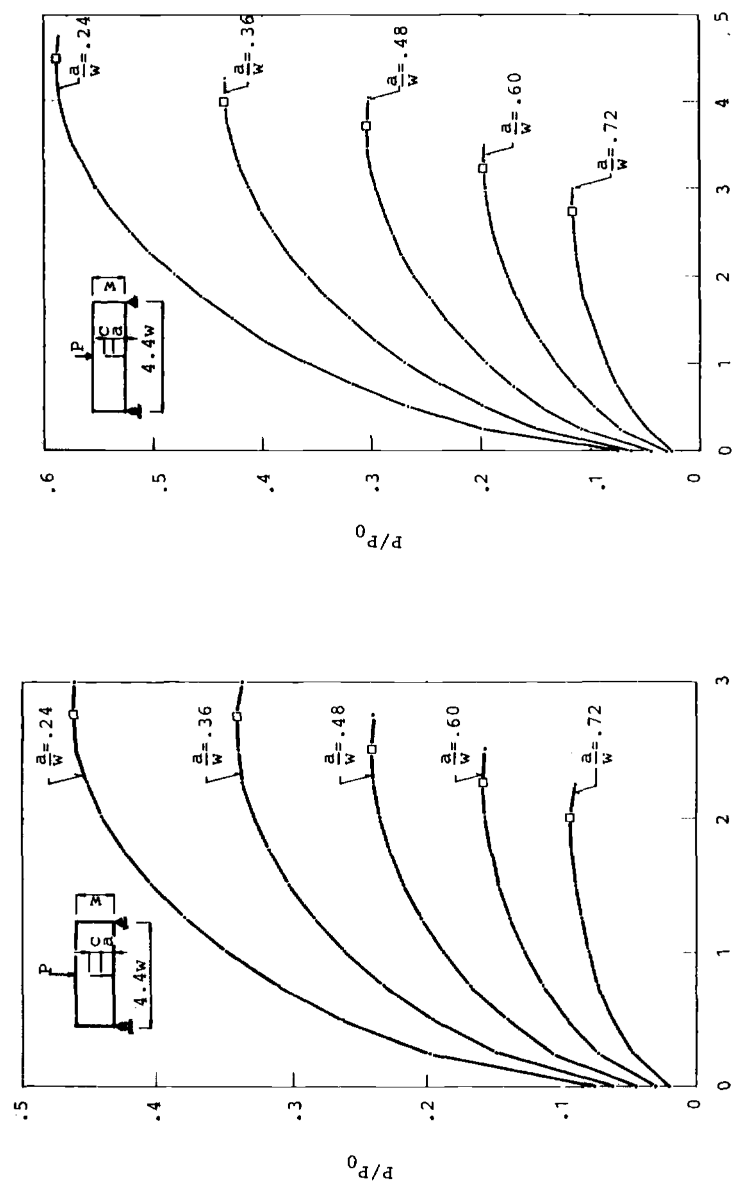

FIG. 12—*Normalized load* P/P_0 *versus damage zone size* c *for* (a) *brittle matrix specimens;* (b) *ductile matrix specimens.*

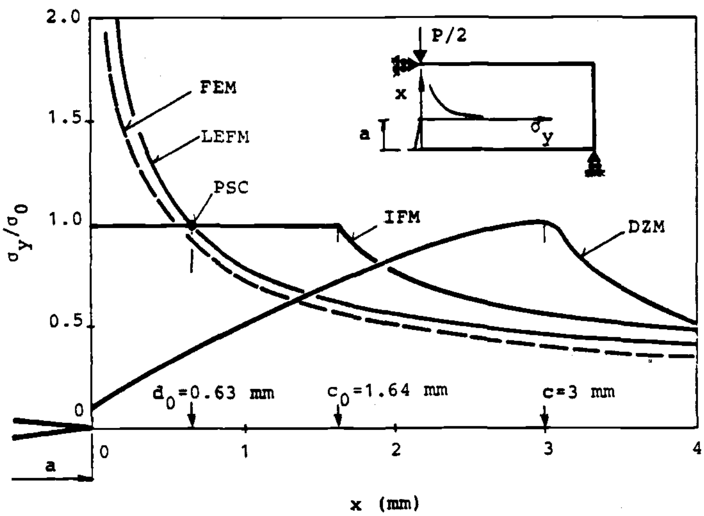

FIG. 13—*Normalized stress* σ_y/σ_0 *versus distance ahead of crack tip,* x, *obtained from* DZM, IFM, LEFM, *and* FEM *for a brittle matrix specimen with* a/w = *0.24.*

This means that complete material separation does not occur in the damage zone, which is in agreement with the damage observed in the plies for the brittle and ductile specimens immediately after the maximum load was reached. The different fracture behavior observed in the plies and the different sizes of the critical damage zone for the two matrix systems may explain the large difference in G_c*. However, a more detailed study of various fracture mechanisms and their contribution to the energy dissipated in the damage zone is required.

Acknowledgments

This study was supported financially by the Swedish Board for Technical Development under Contract No 83-3566. The authors would also like to thank the SAAB-SCANIA Co. for supplying the material used in the study.

References

[*1*] Agarwal, B. D. and Giare, G. S., *Materials Science and Engineering*, Vol. 52, 1982, pp.139–145.

[2] Gaggar, S. K. and Broutman, L. J., *Materials Science and Engineering*, Vol. 21, 1975, p. 177.

[*3*] Gaggar, S. K. and Broutman, L. J., *Journal of Composite Materials*, Vol. 9, 1975, pp. 216–227.

[*4*] Waddoups, M. E., Eisenmann, J. R., and Kaminski, B. E., *Journal of Composite Materials*, Vol. 5, 1971, pp. 446–454.

[*5*] Whitney, J. M. and Nuismer, R. J., *Journal of Composite Materials*, Vol. 8, 1974, pp. 253–265.

[*6*] Nuismer, R. J. and Whitney, J. M. in *Fracture Mechanics of Composites, ASTM STP 593*, American Society for Testing and Materials, Philadelphia, 1975, pp. 117–142.

[7] Pipes, R. B., Wetherhold, R. C., and Gillespie, J. M., *Materials Science and Engineering,* Vol. 45, 1980, pp. 247–253.
[8] Karlak, R. F. in *Proceedings,* 4th Joint ASM-Metallurgical Society of AIME Symposium on Failure Modes in Composites, Chicago, 1977, The Metallurgical Society of the American Institute of Mining, Metallurgical and Petroleum Engineers, Warrendale, PA, 1979, pp. 105–117.
[9] Prabhakaran, R., *Materials Science and Engineering,* Vol. 41, 1979, pp. 121–125.
[10] Peters, P. W. M., *Composites,* Vol. 14, 1983, pp. 365–369.
[11] Yeow, Y. T., Morris, D. H., and Brinson, H. F., *Journal of Testing and Evaluation,* Vol. 7, 1979, pp. 117–125.
[12] Bäcklund, J., *Computers and Structures,* Vol. 13, 1981, pp. 145–154.
[13] Aronsson, C.-G., "Tensile Fracture of Laminates With Cracks," to be published.
[14] Barenblatt, G. I., *Advance in Applied Mechanics,* Vol. 7, 1962, pp. 55–129.
[15] Hillerborg, A., Modeer, M., and Petersson, P. E., *Cement and Concrete Research,* Vol. 6, 1976, pp. 773–782.
[16] Hillerborg, A. in *Proceedings,* International Conference on Fracture Mechanics in Engineering Applications, Bangalore, India, March 1979.
[17] Modeer, M., "A Fracture Mechanics Approach to Failure Analysis of Concrete Materials," Report TVBM-1001 (thesis), Division of Building Materials, University of Lund, Sweden, 1979.
[18] Petersson, P. E., "Crack Growth and Development of Fracture Zones in Plain Concrete and Similar Materials," Report TVBM-1006 (thesis), Division of Building Materials, University of Lund, Sweden, 1981.
[19] Bäcklund, J. and Aronsson, C.-G., "Tensile Fracture of Laminates With Holes," to be published.
[20] Aronsson, C.-G. and Bäcklund, J., "Sensitivity Analysis of The Damage Zone Model," to be published.
[21] Morris, D. H. and Hahn, H. T., *Journal of Composite Materials,* Vol. 11, 1977, pp. 124–138.
[22] Awerbuch, J. and Hahn, H. T., *Journal of Composite Materials,* Vol. 13, 1979, pp. 82–107.
[23] Brown, W. F. in *Review of Developments in Plane Strain Fracture Toughness Testing, ASTM STP 463,* American Society for Testing and Materials, Philadelphia, 1970, p. 249.
[24] Ashton, J. E. and Whitney, J. M., *Theory of Laminated Plates,* Technomic Publishing Co., Stamford, CT, 1970.
[25] Zweben, C. in *Analysis of the Test Methods for High Modulus Fibers and Composites, ASTM STP 521,* American Society for Testing and Materials, Philadelphia, 1973, pp. 65–97.
[26] Lekhnitskii, S. G., *Anisotropic Plates,* 2nd ed., Translated from the Russian by S. W. Tsai and T. Cheron, Gordon and Breach, New York, 1968.
[27] Sendeckyj, G. P., Maddox, G. E., and Tracy, N. A. in *Proceedings,* Second International Conference on Composite Materials (ICCM/2), B. Norton, R. Signorelli, K. Street, and L. Phillips, Eds., American Institute of Mining, Metallurgical, and Petroleum Engineers, 1978, p. 1037.
[28] Sih, G. C., Paris, P. C., and Irwin, G. R., *International Journal of Fracture Mechanics,* Vol. 1, 1965, pp. 189–203.

DISCUSSION

J. H. Underwood[1] *(written discussion)*—The work by Aronsson and Bäcklund is significant because it uses a prominent model in fracture behavior of materials, the Dugdale model, to describe frequently observed behavior[2] in composite ma-

[1] U.S. Army Armament Research and Development Center, Watervliet, NY.

[2] Underwood, J. H. and Kendall, D. P. in *Proceedings,* 1975 International Conference on Composite Materials, American Institute of Mining, Metallurgical and Petroleum Engineers, Vol. 2, 1976, pp. 1122–1147.

terials—damage zone formation. However, since the Dugdale model is best known for its application to metals, which are relatively homogeneous materials, its application to composite materials may be subject to criticism. Sure enough, some criticism, including the above point, was presented during the oral discussion period of the paper at the symposium. Dr. C. C. Chamis questioned whether the Dugdale model would result in any useful descriptions of composite material behavior since it does not take into account the local inhomogeneities of the material.

Dr. Chamis's question is worth considering, and the answer is clear. Fracture analysis, even though generally limited to a continuum, has been a resounding success in describing and predicting the deformation and failure behavior of a wide variety of materials, many of which are quite inhomogeneous. So there should be no resistance to informed application of fracture analysis to composite materials, application in which certain limits that have been shown to work with other materials are used with composite materials. Such a limit, related to the Aronsson and Bäcklund work, is consideration of only those damage zones which are considerably larger in size than the characteristic fiber and layer dimensions.

Within limits, continuum fracture analysis of composite materials will give useful, quantitative descriptions of damage and failure. Therefore, work such as the Aronsson and Bäcklund paper, which properly and critically interrelates experiment and theory, should be applauded, not criticized.

Fatigue

W. S. Johnson[1] *and R. R. Wallis*[2]

Fatigue Behavior of Continuous-Fiber Silicon Carbide/Aluminum Composites

REFERENCE: Johnson, W. S. and Wallis, R. R., "**Fatigue Behavior of Continuous-Fiber Silicon Carbide/Aluminum Composites,**" *Composite Materials: Fatigue and Fracture, ASTM STP 907,* H. T. Hahn, Ed., American Society for Testing and Materials, Philadelphia, 1986, pp. 161–175.

ABSTRACT: Four layups of continuous-fiber silicon carbide (SCS_2) fiber/aluminum matrix composites were tested to assess fatigue mechanisms, including stiffness loss, when cycled below their respective fatigue limits. The layups were $[0]_8$, $[0_2/\pm45]_s$, $[0/90]_{2s}$, and $[0/\pm45/90]_s$. The data were compared with predictions from the first author's previously published shakedown model which predicts fatigue-induced stiffness loss in metal matrix composites. A fifth layup, $[\pm45]_{2s}$, was tested to compare the shakedown and fatigue limits. The particular batch of silicon carbide fibers tested in this program had a somewhat lower modulus (340 GPa) than expected and displayed poor bonding to the aluminum matrix. Good agreement was obtained between the stiffness loss model and the test data. The fatigue damage below the fatigue limit was primarily in the form of matrix cracking. The fatigue limit corresponded to the laminate shakedown limit for the $[\pm45]_{2s}$ laminate.

KEY WORDS: silicon carbide fibers, aluminum matrix, metal matrix composite, fatigue, stiffness loss

Nomenclature

E^f	Fiber elastic modulus, MPa
E^m	Matrix elastic modulus, MPa
$E_{\text{eff}}{}^m$	Effective modulus of matrix in loading direction, MPa
E_0	Initial elastic modulus of first cycle (modulus of undamaged laminate), MPa
E_s	Secant modulus, MPa
E_{SDS}	Laminate modulus assuming damaged matrix material, MPa
R	Stress ratio, $S_{\min}/S_{\max}$
$S_{\max}$	Maximum laminate stress, MPa
$S_{\min}$	Minimum laminate stress, MPa
Y	Maximum cyclic yield stress, MPa
$\Delta\epsilon$	Laminate strain range

[1] Senior research engineer, NASA Langley Research Center, Hampton, VA 23665.
[2] Engineer, Foster-Miller, Inc., Waltham, MA. Coauthor Wallis was a co-op student at Virginia Polytechnic and State University, Blacksburg, VA, working at NASA during this research.

$\Delta\epsilon_{comp}{}^m$ Compressive strain range of matrix material in loading direction
ΔS Laminate stress range, MPa
ΔS_{sh} Maximum laminate stress range that causes no fatigue damage (shakedown stress range), MPa
σ^f Axial stress in fiber in loading direction, MPa
σ^m Axial stress in matrix in loading direction, MPa
$\sigma_{sh}{}^m$ Stress in matrix material in loading direction at laminate shakedown limit, MPa

Metal matrix composites (MMC) are currently being considered for use on missiles, aircraft and other high-performance vehicles where low weight and high stiffness are important. Continuous-fiber MMC exhibit high directional stiffness and strength-to-weight ratios. However these composites are expensive. A commercially available continuous silicon carbide fiber, designated SCS_2, has been developed by AVCO Specialty Materials Division of Lowell, MA, and is expected to be much more economical to produce than the most commonly used continuous fiber for MMC, boron. Therefore, silicon carbide/aluminum (SCS_2/Al) composites are expected to be more cost competitive with metals and epoxy resin composites. The purpose of this paper is to examine the stiffness loss behavior of five layups of SCS_2/Al composites and assess the applicability of the stiffness loss model previously proposed for boron/aluminum [*1*].

Previous research on the fatigue behavior of boron/aluminum composites [*1–5*] has shown that boron/aluminum can develop significant internal matrix cracking even when cycled below the fatigue limit. This results in laminate modulus loss. In quasi-isotropic laminates, matrix cracks reduce stiffness as much as 40%. Because most MMC structural components are expected to be stiffness critical, even a small drop in component stiffness may render the part useless or cause failure of the structure. Therefore this paper focuses on the stiffness loss in the SCS_2/Al composites as a function of cyclic loading and not on final laminate failure. Only the $[\pm 45]_{2s}$ laminate will be examined by establishing the fatigue limit and comparing it with the calculated shakedown limit.

Experimental Procedure

Composite Laminate

The material tested was unnotched silicon carbide composite with a 6061 aluminum matrix and 0.14-mm-diameter SCS_2 fibers provided by the manufacturer. Table 1 presents material properties for the SCS_2 and aluminum constituents. The specimens were straight-sided with a width of 19.0 mm and a thickness of 1.6 mm. Each laminate had a fiber volume fraction of approximately 0.44. All the specimens were annealed before testing. All the specimens were fatigue loaded at 10 Hz except when the stress-strain response of the material was recorded on an *X-Y* plotter. The stress-strain data were taken under quasi-static

TABLE 1—*Composite constituent mechanical properties.*

	SCS_2 Fiber, 0.14 mm diameter	6061-TO Aluminum
Elastic modulus, GPa	340	72.5
Poisson's ratio	0.25	0.33

conditions at 1, 2, 3, 4, 5, 10, 50, 100, 500, 1000, 5000, 50 000, 100 000, and 500 000 cycles for each stress level. The strain was measured with a 25.4-mm gage length extensometer. Except for the $[\pm 45]_{2s}$ laminates, all the specimens were cycled at constant-amplitude stress levels below stress levels which would cause failure in 500 000 cycles. The stress ratio, R, was constant for each test. All tests were conducted at $R = 0.1$ except for a few specimens of $[0_2/\pm 45]_s$ which were also tested at a $R = 0.3$.

In the present study, the tests were conducted at a constant cyclic stress range for 500 000 cycles (time enough for a saturation damage state to develop), and then the stress-strain response was recorded. The stress range was then increased to a new desired level, and another 500 000 cycles applied. The resulting stress-strain response was recorded. This process was repeated up to as many as five different stress levels per specimen. Saturation fatigue damage at each level depends only on the applied stress range and, therefore, is not influenced by the prior cycling at lower stress ranges as shown in Ref *2*. This test method was also used with success to generate data in Ref *1*. The $[\pm 45]_{2s}$ laminates were cycled to failure or 2 million cycles (whichever occurred first) to determine their fatigue limit.

Fibers

Individual SCS_2 fibers were pulled in tension to determine their elastic modulus. The fibers were obtained by leaching away the aluminum matrix of a $[0/90]_{2s}$ and $[0]_8$ laminate using a hydrochloric acid solution. Since the fiber cross section is round, the diameters were easily measured with a micrometer in order to calculate cross-sectional area. The individual fibers were bonded and aligned between thin aluminum tabs to facilitate gripping. Three fiber lengths were tested: 51, 76, and 102 mm.

The specimens were then loaded in a tabletop screw-driven machine where the crosshead displacement and load were recorded. The elastic modulus of the fiber was calculated from the load-displacement curve.

Analysis

If fatigue damage in general is to be avoided, the cyclic loading must produce only elastic strains in the constituents. Even so, local plastic straining can be permitted in the composite during the first few load cycles, provided that the composite "shakes down" during these few cycles. The shakedown state is reached if the matrix cyclically hardens to a cyclic yield stress, Y, such that, subsequently, only elastic deformation occurs under load cycles. The shakedown limit for the composite containing 0-deg fibers is considerably below the composite's fatigue limit [*4*]. Previous tests have shown that the matrix fatigue limit coincides with the maximum stable cyclic yield stress for annealed aluminum [*4,6*] and steels [*6*]. The value of Y is 70 MPa for the annealed 6061 aluminum [*4*].

The shakedown stress range for a unidirectionally loaded laminate can be found by using laminate theory to determine the yield surfaces for individual plies in the laminate. For the experimental program reported herein, the shakedown stress range, ΔS_{sh}, is the width of the overall yield surface in the direction of the applied uniaxial loading. The value of ΔS_{sh} can be calculated easily with the computer program AGLPLY [*7*]. The AGLPLY program incorporates a modified materials model, and not a straight series model, to determine lamina transverse properties. Input for the AGLPLY program consists of the following: the fiber elastic modulus and Poisson's ratio; the matrix elastic modulus, Poisson's ratio, and cyclic yield stress; the fiber volume fraction of each ply; the fiber angle orientation of each ply; and the relative thickness of each ply. The laminate stress that causes first yielding in the matrix of any ply is printed out. This laminate stress is half of the shakedown stress range. More details on this procedure can be found in Refs *3*, *4*, and *7*.

The shakedown stress range is used in conjunction with the stiffness loss model [*1*] to develop a cyclic strain versus cyclic stress relationship for a given laminate. As shown in Fig. 1, when the cyclic stress range ΔS exceeds the shakedown

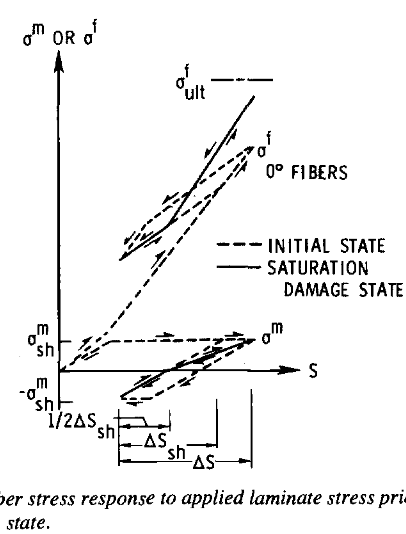

FIG. 1—*Matrix and fiber stress response to applied laminate stress prior to and after development of the saturation damage state.*

range, ΔS_{sh}, the matrix is assumed to respond as an elastic-perfectly plastic material along the dotted line for the first few cycles. The matrix stress cycles between $+\sigma_{sh}{}^m$ and $-\sigma_{sh}{}^m$ where $\sigma_{sh}{}^m$ equals half the shakedown strain range times the undamaged matrix modulus E^m. That is

$$\sigma_{sh}{}^m = (\Delta S_{sh}/2E_0)E^m$$

With continued load cycling, cracks form in the matrix. The cracks open on tensile excursions and close on compressive excursions of the matrix stress, leading to the behavior represented by the solid line in Fig. 1. For a given total strain range $\Delta\epsilon$, as shown in Fig. 2, the effective tensile modulus of the matrix $E_{eff}{}^m$ can be written

$$E_{eff}{}^m = \sigma_{sh}{}^m/(\Delta\epsilon - \Delta\epsilon_{comp}{}^m)$$

where

$$\Delta\epsilon_{comp}{}^m = \Delta S_{sh}/2E_0$$

which is the compressive strain range of the matrix. This modulus is entered into a laminate analysis to obtain the laminate tensile modulus, E_{SDS}, which is then used to estimate the secant modulus for the damaged laminate. The laminate stress-strain relation is stated as

$$\Delta S = (\Delta\epsilon_{comp}{}^m)E_0 + (\Delta\epsilon - \Delta\epsilon_{comp}{}^m)E_{SDS}$$

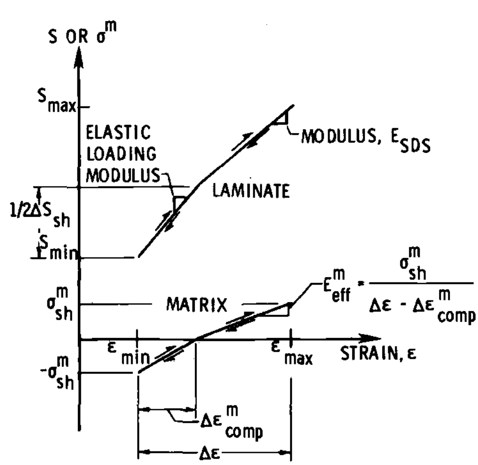

FIG. 2—*Composite laminate and matrix stress-strain response for a saturation damage state.*

from which ΔS is calculated for strain-controlled tests. The laminate secant modulus prediction is then

$$E_S = \Delta S/\Delta\epsilon$$

Results and Discussion

Fiber Modulus

Initial laminate elastic moduli measurements were considerably less than predicted by laminate analysis. Since the predictions were excellent in an earlier study on boron/aluminum [*4*], this large discrepancy needed to be resolved. The original moduli predictions were made using a fiber modulus of 390 GPa as suggested by the manufacturer. Since the aluminum modulus is 72.5 GPa and the fiber volume fraction is easily measured, the fiber modulus is the only uncertain parameter.

Individual fibers were tested to determine the modulus used in the current work. Table 2 lists the fiber moduli for the two laminates and three fiber lengths. The $[0/90]_{2s}$ fibers show average moduli slightly lower than the $[0]_8$ fibers. Further, the 51-mm fiber gage length showed a lower average modulus than the 76- and 102-mm gage length. This indicated some sensitivity to gage length tested probably due to slippage of the fibers. The variation of modulus is proportional to the amount of slippage divided by the measured displacement. The longer the specimen, the greater is the measured displacement, while the amount of slippage is almost constant. Therefore, the longer the fiber, the less is the effect of slippage. The results of the 76- and 102-mm gage lengths were very close to each other. A modulus value of 340 GPa was chosen to represent the fiber. According to Ref *8*, production process problems (carbon-rich deposition zones) that were occurring when these fibers were produced may have resulted in lower than normal fiber strength and modulus. The production process problems have been resolved since then and fiber moduli of approximately 400 GPa are being achieved routinely [*9*].

Laminate Properties

The shakedown stress range, ΔS_{sh}, and E_0 were calculated using the fiber modulus of 340 GPa as shown in Table 3. Figure 3 shows the predicted initial

TABLE 2—*Average SCS_2 fiber modulus, GPa.*

	Gage Length, mm		
Layup	51	76	102
$[0]_8$	313	343	342
$[0/90]_{2s}$	307	332	. . .

TABLE 3—*Calculated and experimental elastic moduli and calculated shakedown stress range.*

Laminate	Experimental, E_0, GPa	Calculated	
		E_0, GPa	ΔS_{sh}, MPa
$[0]_8$	191	190	368
$[0_2/\pm45]_s$	158	154	199
$[0/90]_{2s}$	128	153	204
$[0/\pm45/90]_s$	123	137	179
$[\pm45]_{2s}$	101	118	150

elastic modulus using 340 GPa versus the experimental. The predictions are quite good with the largest error of 15% for the $[\pm45]_{2s}$ laminate. This can be due to even lower fiber moduli than the 340 GPa measured or due to bad fiber matrix interface, as will be discussed next.

Fiber-Matrix Interface

The fiber-matrix interface was noticeably weaker for these SCS_2/Al composites than for the previously tested boron/aluminum. This was evident by more fiber pull out during static strength tests of the SCS_2/Al laminates than previously observed for boron/aluminum laminates and by the separation of the matrix and fiber during fatigue tests of the $[0_2/\pm45]_s$ layup. Figure 4 shows a micrograph of early fiber/matrix separation. After continued cycling at a higher stress level, these separations join together to form an edge delamination as shown in Figs. 4 and 5. Figure 6 shows the extent of the edge delamination into the specimen. The $[0_2/\pm45]_s$ layup was the only laminate tested that showed the edge delam-

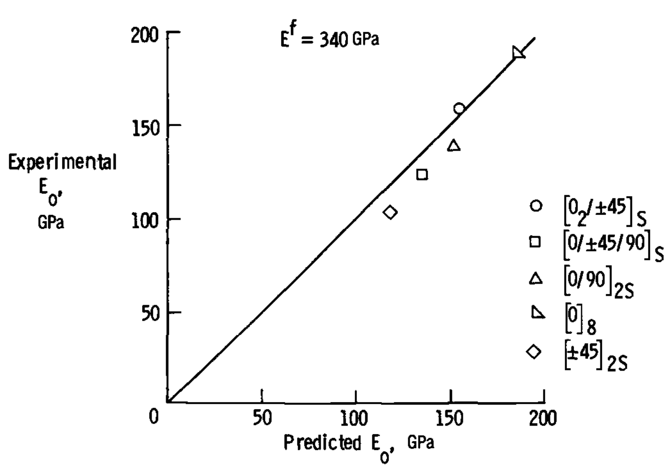

FIG. 3—*Predicted versus experimental laminate elastic modulus.*

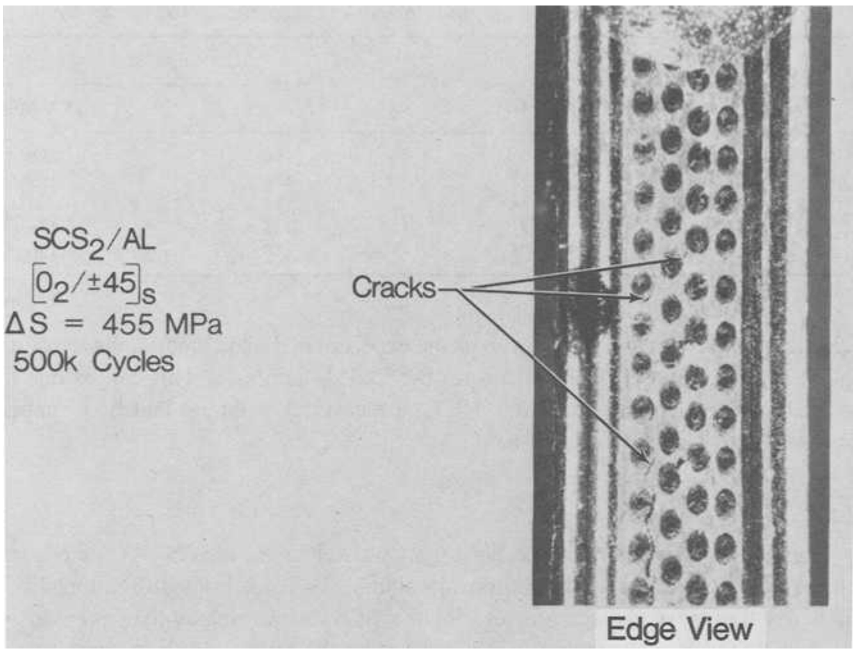

FIG. 4—*Edge view of fiber-matrix separation.*

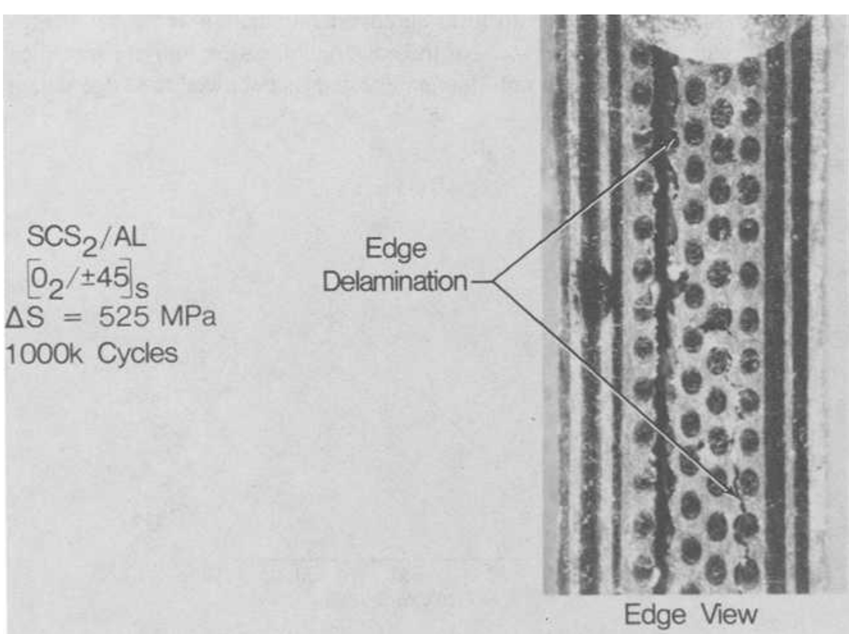

FIG. 5—*Edge view of edge delamination due to weak fiber-matrix bonding.*

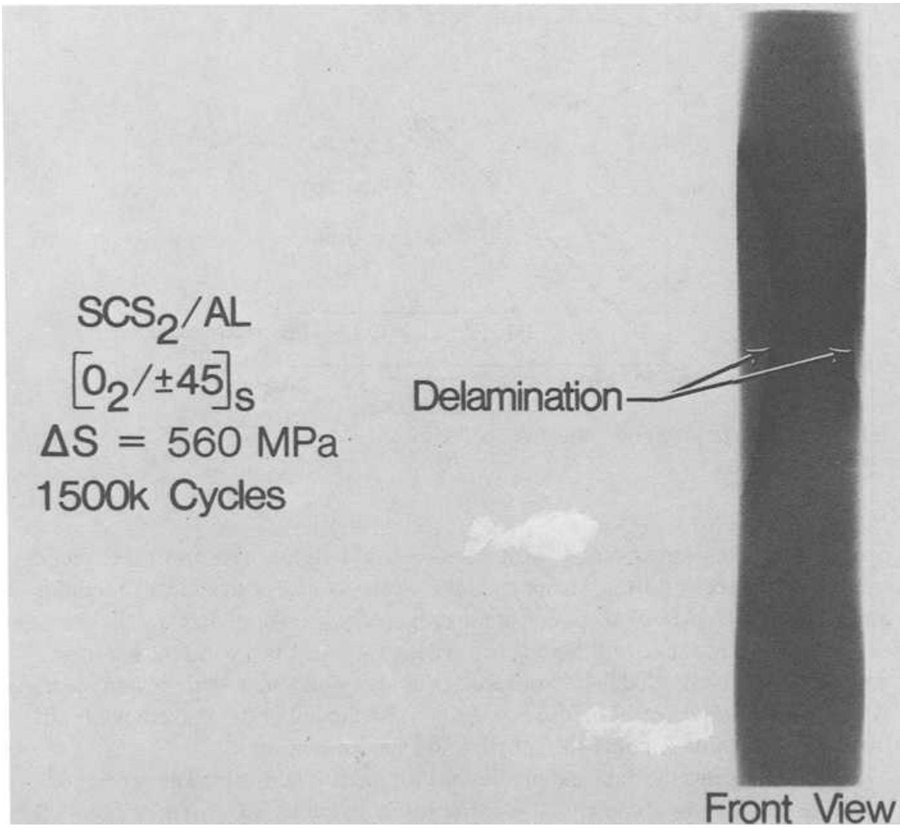

FIG. 6—*Radiograph of edge delamination.*

ination as described, indicating that this plate must have had poorer quality bonding between the fiber and matrix than the others tested. If this edge delamination was due to high interlaminar stresses (as common in graphite/epoxy composites), it would be expected that delamination would have occurred in the $[0/\pm45/90]_s$ laminate since that layup has the highest interlaminar stresses of those tested.

Stiffness Loss and Predictions

The predicted cyclic stress-strain response after 500 000 cycles and its associated secant modulus are presented in this subsection and compared with measured experimental results. The predictions are shown as solid lines (see Fig. 7 as an example). For reference, the dashed line is the undamaged elastic modulus of the laminate. The secant modulus scale can be read in two ways. First, entering on the ΔS axis, crossing to the solid prediction line and down to the secant modulus scale gives the predicted secant modulus of a laminate after 500 000

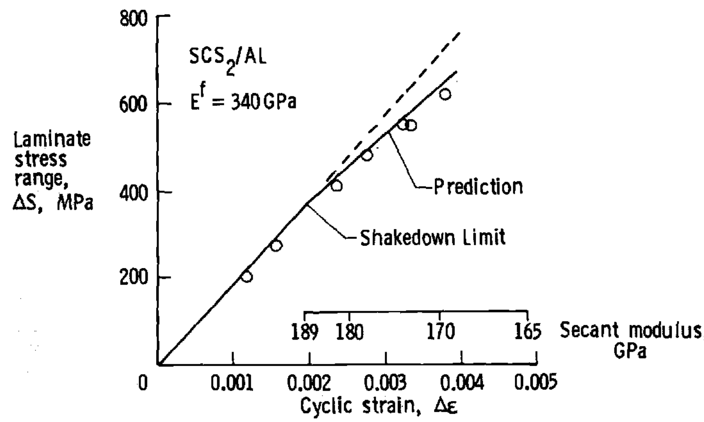

FIG. 7—*Correlation of experimental and model prediction for $[0]_s$ laminates after 500 000 Hz fatigue.*

cycles at a given stress range. Second, one could simply rise from the cyclic strain scale directly to the secant modulus scale to assess the secant modulus after 500 000 cycles of a given strain range. As shown in Ref *1*, the same saturation damage state will be reached whether the test is a constant stress or a constant strain controlled test. Notice that the secant modulus scale is nonlinear. Also notice that the secant modulus scale ends on the left at the shakedown limit; the secant modulus is equal to E_0 below the shakedown limit.

Figure 7 presents the data and predictions for the $[0]_8$ laminate. The predictions are quite good. Approximately 10% of the secant modulus was lost after 500 000 cycles at a cyclic strain range of 0.004.

The $[0_2/\pm45]_s$ data are shown in Fig. 8. Both the $R = 0.1$ and 0.3 data behave the same when cyclic stress range is plotted versus resulting cyclic strain range,

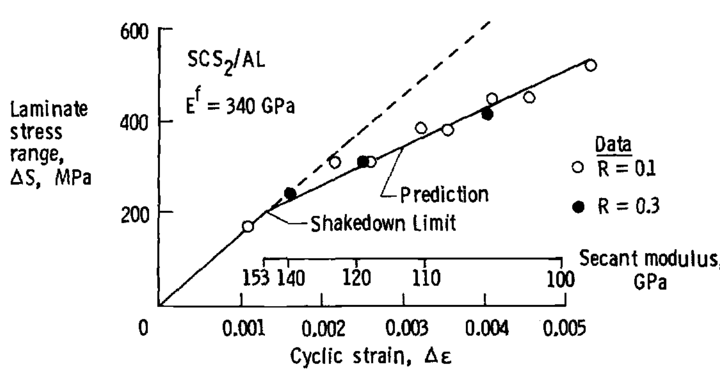

FIG. 8—*Correlation of experimental and model predictions for $[0_2/\pm45]_s$ laminates after 500 000 Hz fatigue.*

indicating once again [2,4] that the matrix damage described herein is a function of stress range and not mean stress. There is very good agreement between predictions and data. The previously discussed delamination apparently does not decrease the stiffness beyond that due to the predicted matrix cracking. The $[0_2/\pm45]_s$ laminate had a 30% loss in secant modulus at $\Delta\epsilon = 0.004$.

The $[0/90]_{2s}$ predictions as shown in Fig. 9 were not very good compared with the other laminates. Approximately 25% of the 90-deg fibers were observed to be longitudinally cracked after fatigue. The lamination theory would predict a loss of 15% in stiffness by eliminating the 90-deg fibers. Perhaps the split fibers account for some of the discrepancy between test and prediction. A 35% loss in stiffness was predicted to occur at $\Delta\epsilon = 0.004$, whereas the experimental results showed a 45% loss.

The predictions agree well with the data for the $[0/\pm45/90]_s$ laminate as shown in Fig. 10. This laminate is subject to a 40% loss in secant modulus when cycled at $\Delta\epsilon = 0.004$.

Behavior of $[\pm45]_{2s}$ *Laminate*

The $[\pm45]_{2s}$ laminate is unique among the laminates tested in that it has no 0-deg fibers to pick up the load from the damaged matrix as suggested in the previously discussed shakedown stiffness loss model. The 0-deg fibers also serve to limit axial strain. Since the $[\pm45]_{2s}$ laminate has no 0-deg fibers to limit axial deformation, large plastic deformations occurred in the specimen upon yielding. This can result in rotation of the ±45-deg fibers to approximately ±39 deg.

The following is a description of observed behavior as a function of cyclic stress range: Below the shakedown stress range (Fig. 11) of 150 MPa the specimen underwent large plastic deformation (as much as 0.08 strain). During cyclic

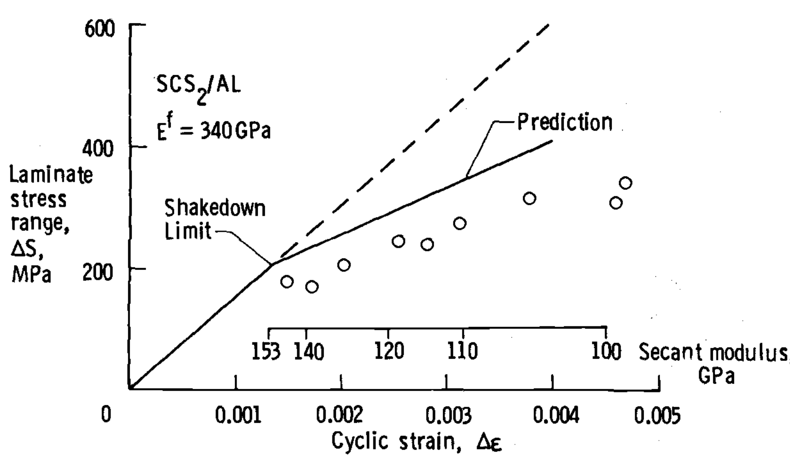

FIG. 9—*Correlation of experimental and model predictions for* $[0/90]_{2s}$ *laminate after 500 000 Hz fatigue.*

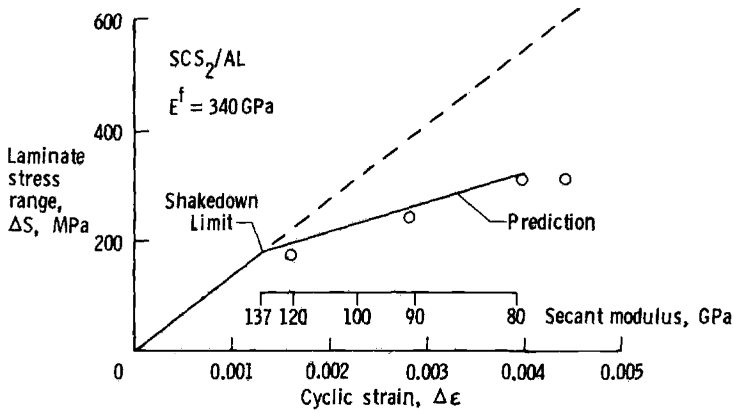

FIG. 10—*Correlation of experimental and model predictions for* $[0/\pm45/90]_s$ *laminate after 500 000 Hz fatigue.*

loading, the matrix yield stress changed from its initial value of 40 MPa to a fully hardened, stabilized value of 150 MPa. The rotation of the fibers (to approximately ±41 deg) actually causes the elastic modulus and secant modulus to increase slightly. The cross-sectional area of the specimen decreased by approximately 8% during a cyclic stress range of 138 MPa. The stress-strain behavior of the laminate stabilized. No fatigue damage was noticed. Above the shakedown stress range, fatigue damage developed in the form of many matrix cracks growing into the specimen from the edge. Under these conditions the elastic modulus and the secant modulus of the laminate decrease. At $\Delta S = 172$ MPa the fibers rotated to ±39 deg.

The exact values of the moduli were somewhat difficult to obtain because of the large-scale plastic deformation and accompanying decrease in cross-sectional area. Figure 11 shows an *S-N* curve of the tests in terms of engineering stress (that is, load/original area). The figure shows the predicted shakedown limit based on the original cross-sectional area and ±45-deg fiber orientation. The data indicate that the fatigue endurance limit at 2×10^6 Hz is approximately

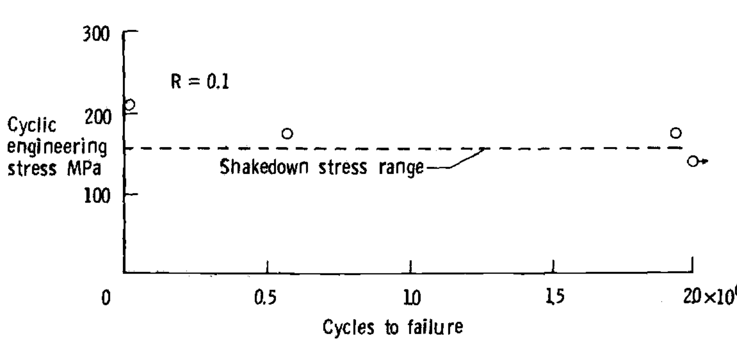

FIG. 11—S-N *curve for* $[\pm45]_{2s}$ *laminates.*

equal to the shakedown stress range. Once fatigue damage initiates in the matrix it will eventually grow to cause laminate failure since there are no 0-deg fibers to pick up the load in a strain control fashion. Thus, the fatigue limit of laminates with no continuous 0-deg fibers may be predicted by the shakedown stress range. These type laminates do, however, undergo large plastic deformations below the shakedown down range, which may make them impractical for structural application at high stress levels. Perhaps some of this plasticity problem could be eliminated by heat-treating the matrix to a -T4 or -T6 condition.

SCS_2/Al Versus Boron/Aluminum Behavior

The stiffness loss of eight different layups of boron/aluminum composites was presented in Ref *1*. Many of these layups had the same fiber volume fraction and stacking sequence as the SCS_2/Al composites tested in the current work. The manufacturer's suggested fiber modulus for SCS_2 (390 GPa) is the same as the boron fiber (although, as previously discussed, the actual SCS_2 modulus was closer to 340 GPa for the tested laminates). The SCS_2/Al has been suggested to be a more economical alternative to boron/aluminum; therefore it is appropriate to directly compare the behavior of the two systems.

The boron/aluminum showed superior fiber/matrix bonding. This was evident from less fiber pullout at failure surfaces (that is, exposed matrix-free fibers extending from the failure surface). Also, none of the previously tested boron/aluminum laminates showed any signs of the delamination behavior illustrated in Figs. 4–6.

Because the boron fiber modulus is higher than for SCS_2, the boron/aluminum laminate's modulus is higher than the SCS_2/Al for equivalent fiber volume fraction and stacking sequence. The higher boron fiber modulus also results in a higher shakedown stress and higher stiffness above the shakedown stress. A typical example is shown in Fig. 12 for the $[0_2/\pm45]_s$ layup. It is expected that

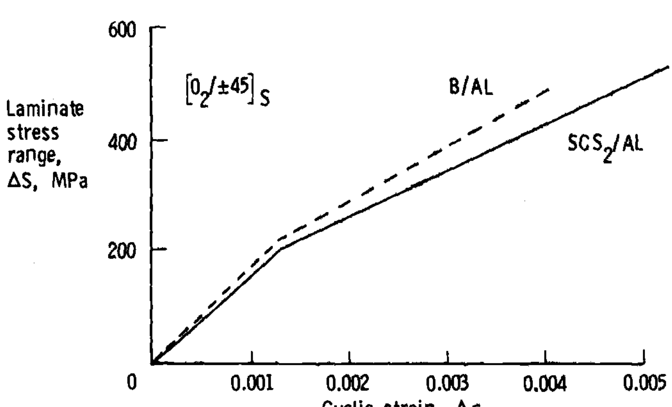

FIG. 12—*Comparison of boron/aluminum and SCS_2/Al composite stiffness loss behavior after 500 000 Hz load.*

the latest SCS_2 fibers [9] would result in laminates with comparable performance to boron/aluminum.

The shakedown stiffness loss model predicts the behavior of SCS_2/Al as well as it did for boron/aluminum in spite of the poor SCS_2 fiber/matrix bonds.

Summary and Conclusions

Four layups of continuous fiber silicon carbide SCS_2 fiber/aluminum matrix composites were tested to assess stiffness loss when cycled below their respective fatigue limits. The layups were $[0]_8$, $[0_2/\pm45]_s$, $[0/90]_{2s}$, and $[0/\pm45/90]_s$. The data were compared with predictions from the first author's previously published shakedown model which predicts fatigue-induced stiffness loss in metal matrix composites. A fifth layup, $[\pm45]_{2s}$, was tested to compare the shakedown and fatigue limits. The following observations were made:

1. With the exception of the $[\pm45]_{2s}$ laminate, the SCS_2/Al laminates exhibited significant stiffness loss when cycled below the fatigue limit. As an example, the quasi-isotropic laminate lost over 40% of the original stiffness after 500 000 cycles.
2. Most of the stiffness loss was attributed to fatigue cracks in the matrix material.
3. The stiffness loss model predictions compared well with the data.
4. The SCS_2 fibers were poorly bonded to the matrix in several laminates. This poor fiber/matrix bonding resulted in edge delaminations in one layup ($[0_2/\pm45]_s$).
5. The fatigue limit corresponds to the shakedown limit for the $[\pm45]_{2s}$ laminate.
6. The modulus of the SCS_2 fiber was found to be lower than reported by the manufacturer. The modulus was found to be approximately 340 GPa.

References

[1] Johnson, W. S., "Modeling Stiffness Loss in Boron/Aluminum Laminates Below the Fatigue Limit" in *Long-Term Behavior of Composites, ASTM STP 813*, American Society of Testing and Materials, Philadelphia, 1983, pp. 160–176.

[2] Johnson, W. S., "Mechanisms of Fatigue Damage in Boron/Aluminum Composites," NASA TM-81926, National Aeronautics and Space Administration, Washington, DC, Dec. 1980; also *Damage in Composite Materials, ASTM STP 775*, American Society for Testing and Materials, Philadelphia, pp. 83–102.

[3] Dvorak, G. J. and Johnson, W. S., "Fatigue of Metal Matrix Composites," *International Journal of Fracture*, Vol. 16, No. 6, Dec. 1980, pp. 585–607.

[4] Johnson, W. S., "Characterization of Fatigue Damage Mechanisms in Continuous Fiber Reinforced Metal Matrix Composites," Ph.D. thesis, Duke University, Durham, NC, Dec. 1979.

[5] Dvorak, G. J. and Johnson, W. S., "Fatigue Mechanisms in Metal Matrix Composite Laminates" in *Advances in Aerospace Structures and Materials*, ASME AD-01, American Society of Mechanical Engineers, New York, 1981, pp. 21–34.

[6] Weng, M. T., "Some Aspects of Fatigue Relative to Cyclic Yield Stress," *International Journal of Fatigue*, Vol. 3, No. 3, Oct. 1981, pp. 187–193.

[7] Bahei-El-Din, Y. A., "Plastic Analysis of Metal-Matrix Composite Laminates," Ph.D. thesis, Duke University, Durham, NC, July 1979.
[8] Wawner, F. E., Teng, A. Y., and Nutt, S. R., "Microstructural Characterization of SiC(SCS) Filaments" in *Metal Matrix, Carbon, and SiC Composites*, NASA Conference Publication 2291, Nov. 1983.
[9] Suplinskas, R. J., "Development of Low Cost Methods of Fiber Manufacture," 4th Monthly Technical Report (Submitted to U.S. Army Materials and Mechanics Research Center) Contract DAAG46-82-C-0033, 24 Sept. 1984.

Wen S. Chan[1]

Delamination Arrester—An Adhesive Inner Layer in Laminated Composites

REFERENCE: Chan, W. S., "**Delamination Arrester—An Adhesive Inner Layer in Laminated Composites,**" *Composite Materials: Fatigue and Fracture, ASTM STP 907*, H. T. Hahn, Ed., American Society for Testing and Materials, Philadelphia, 1986, pp. 176–196.

ABSTRACT: Delamination arrestment in laminated composites has been achieved by using tough adhesive strips embedded in the interior of the laminate. For $(\pm 30_2/90_3/\mp 30_2)_T$ and $(\pm 35/0/90)_s$ laminates, edge delamination was arrested under both static and fatigue tension loadings. For the $(\pm 30_2/90_3/\mp 30_2)_T$ laminates, delamination was delayed and fatigue life was significantly increased. These results are attributed to the G_I component of the total strain-energy release rate decreasing as delamination approaches the adhesive strip region. It is suggested that the initiation of delamination for both static and fatigue loadings is mainly due to the highest G_I component in the laminate, not the total G. A characterization of fatigue behavior is discussed. It was found that delamination growth rate decreases as the number of fatigue cycles increases.

KEY WORDS: adhesive strip, composite materials, crack arrester, damage tolerance, delamination, fatigue, graphite/epoxy, strain-energy release rate

Designing for improved damage tolerance and durability of composite structures has become a critical issue over the past decade. Delamination is one of the most frequently occurring types of damage during the service life of composite components. It is a life-limiting failure mode in composite structures. The presence and growth of delamination cause a reduction in stiffness and a degradation of the composite material due to exposure of the interior to adverse environmental attack. Hence, design concepts for suppressing or arresting delamination are of considerable interest. Efforts have been directed toward the development of delamination resistance by improving both materials and laminate construction.

Damage arrestment in laminated composite structure applications has been under investigation for some time. In Ref *1*, Sendeckyj reviews various crack-arrestment concepts using softening buffer strips for a through-crack. These concepts use stiffness variations in the load-carrying ply of laminates to achieve

[1] Senior engineering specialist, Research Group, Bell Helicopter Textron Inc., Fort Worth, TX 76101.

the crack arrestment. For a crack running between two laminae, such as in a delamination, crack arrestment has not been studied.

The major part of this paper is devoted to the development of a method of delamination arrestment that could be used in a fail-safe approach to damage-tolerant design. This method concerns the extension of the use of adhesive inner layers to suppress delamination. Both static and fatigue cases were considered. A characterization of fatigue growth in both fiber- and matrix-dominated laminates is discussed, and the effect of adhesive strips on delamination growth is investigated.

Adhesive Inner Layer

The fracture toughness variations in a structural panel play an important role in crack arrestment. Experience in metal fracture mechanics indicates that the more ductile materials have a higher degree of crack resistance than the brittle materials and consequently a higher fracture toughness. With this in mind, Chan et al established a design concept to improve interlaminar fracture toughness by placing a ductile adhesive layer in a laminate at the delamination-prone interface [*2*]. Similar concepts have been studied by Browning and Schwartz [*3*]. Browning et al examined the failure surface of their double-cantilever beam specimens, which had an adhesive layer in the delamination plane, and found that the delamination growth took place in the adhesive. Chan et al successfully demonstrated that a mixed-mode edge delamination can be effectively suppressed by placing a layer or strip of adhesive film along the edges of a specimen. This effect was attributed to the lower modulus of the adhesive film, which caused a reduction in the interlaminar stress and G_{I} component of the total strain-energy release rate. Since the total strain-energy release rate is the principal energy source for delamination growth, it is suggested that as delamination grows into the adhesive region, the energy available to drive the delamination growth will be reduced. As a result, delamination growth will be retarded.

Experimental Program

Experiments were conducted to investigate the delamination arrestment capability of adhesive strips, under both static and fatigue loadings, and to characterize the fatigue damage behavior. Such a characterization would help to establish a damage model for analytical study. Coupons of AS4/3501-6 graphite/epoxy laminates with adhesive strips along the free edges and at a distance away from the free edges were tested. Coupons without adhesive strips were fatigue-tested to understand the fatigue characteristics. Both fiber- and matrix-dominated laminates were studied. The overall test program is outlined in Table 1. The adhesive strips used in this study were FM1000, an American Cyanamid product. This adhesive has a weight of 0.15 kg/m^2 (0.03 lb/ft^2) and an uncured thickness of 0.13 mm (0.005 in.), approximately.

TABLE 1—*Design of test program.*

Laminate Type	Coupon Type	Test Conditions	No. of Tests
$(\pm 35/0/90)_s$	adhesive strips	static	Ref 2
		fatigue	5
	adhesive strips along the free edges	static	Ref 2
		fatigue	5
	adhesive strips interior to free edges	static	4
		fatigue	5
$(\pm 30_2/90_3/\mp 30_2)_T$	no adhesive	static	Ref 2
		fatigue	5
	adhesive strips interior to free edges	static	4
		fatigue	6

Coupon Preparations and Configurations

Panels measuring 254 mm (10 in.) on the side were fabricated of all laminates. Some panels contained no adhesive strips, some had 6.35-mm-wide (0.25 in.) strips of adhesive, and some had 12.7-mm (0.5 in.) strips of adhesive. The 6.35-mm-wide (0.25 in.) strips of adhesive were placed 25.4 mm (1 in.) apart in the direction of the 0-deg ply at the 0/90 interface of the $(\pm 35/0/90)_s$ laminates and at the $-30/90$ interface of the $(\pm 30_2/90_3/\mp 30_2)_T$ laminates. These layups were chosen to minimize the applied strain required to measure delamination before final failure [*4*]. These panels were cut so as to form coupons with the adhesive strips located 6.35 mm (0.25 in.) away from the free edges. The 12.7-mm-wide (0.5 in.) strips were placed 25.4 mm (1 in.) apart at the same interfaces and were cut along the centerline of the strips so that each coupon had a 6.35-mm-wide (0.25 in.) strip of adhesive along its free edges. All panels were cured by the procedure described in Appendix A of Ref *2*. Before cutting, the panels were checked by C-scan for any imperfections that might have occurred during fabrication.

The coupon configurations for the laminates used in the test program are shown in Fig. 1. All coupons were approximately 38 mm (1.5 in.) wide and 254 mm (10 in.) long. Because the adhesive strips were unconstrained during curing, two strips in the thickness direction were not exactly located at the same distance from the free edge. Glass-laminate end tabs were used for all panels. Before running the tests, the coupons were checked by X-radiographic inspection for any induced delamination during curing.

Static Tests

Only coupons with interior adhesive strips were tested under static loading. The coupons were loaded in tension and monitored by a 10-cm (4 in.) extensiometer coupled to an *X-Y* plotter that recorded the load-versus-elongation curve. During the test, coupons were periodically removed from the testing machine,

2b = 38.1 mm (1.5 in)
ℓ = 254 mm (10 in)
W = 6.35 mm (0.25 in)
d = 6.35 mm (0.25 in)
h = 0.137 mm (0.0054 in)

Adhesive strip - FM1000

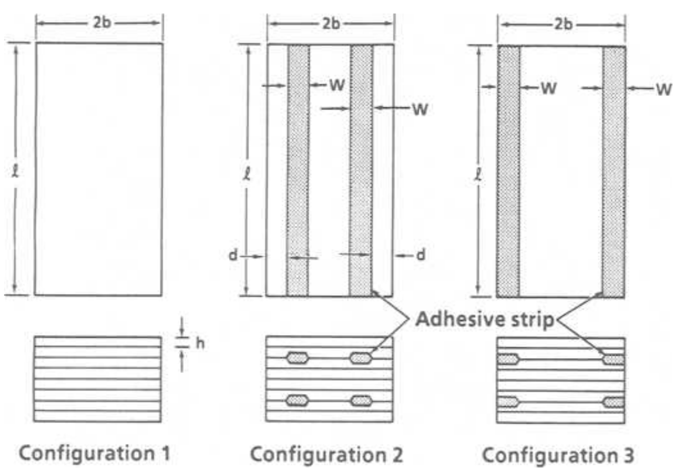

FIG. 1—*Coupon configurations.*

treated with a zinc iodide solution, and examined along the free edges by both microscope and X-ray. X-radiographs and microphotographs were taken to document the delamination. These inspection records were used to construct a load-damage relationship for the laminates. Delamination was measured from X-radiographs by a planimeter over a 114 mm (4.5 in.) length of coupon at each load level.

Delamination damage developed along the free edge of the laminate and grew into the width of the coupon. As it approached the region of the adhesive, growth in the delamination was arrested. Higher loads were required to extend the delamination process.

Plane-view X-radiographs were taken to show damage modes in fiber-dominated and matrix-dominated laminates, with and without adhesive strips. Figure 2 shows the fiber-dominated laminates at 98% of ultimate for the coupon without adhesive strips and at 96% of ultimate for the coupon with adhesive strips. Figure 3 shows the matrix-dominated laminates at 97% of ultimate for both coupons. As can be seen, delaminations develop at the free edges and grow into the width of the coupon. Figure 4 illustrates a comparison of a typical load-damage relationship. It clearly indicates that the delamination is arrested at the boundary of the adhesive strips until further loading drives the delamination through the

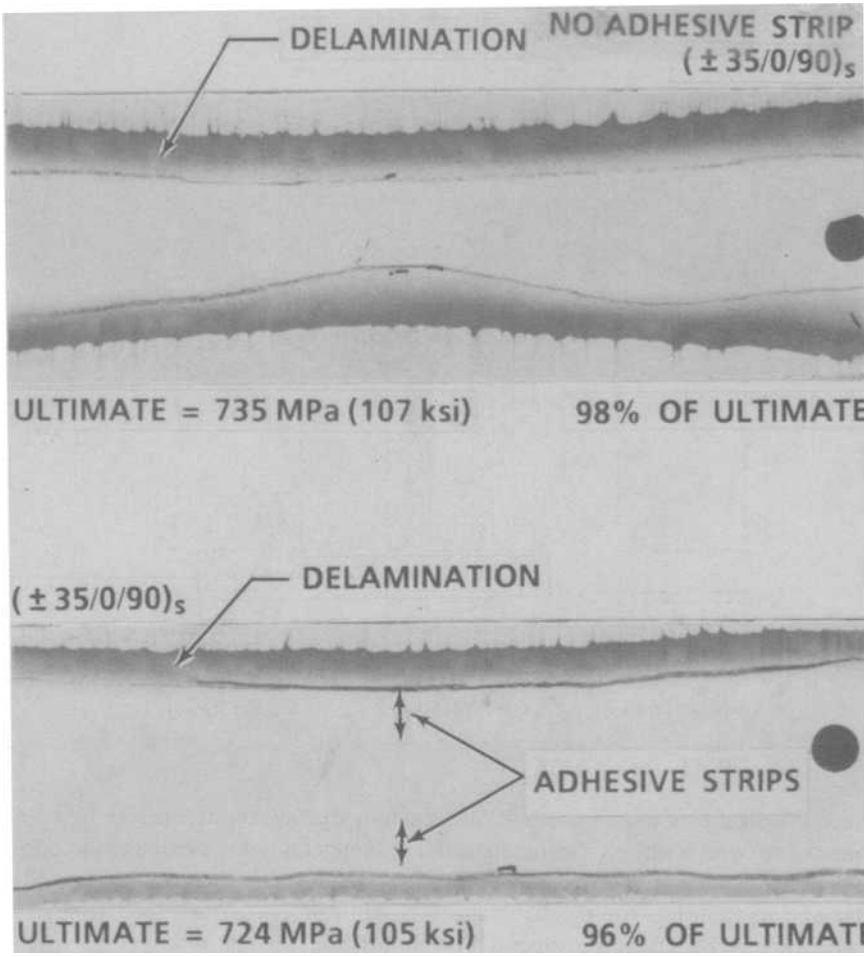

FIG. 2—*Static delamination of fiber-dominated laminates.*

adhesive zone. For the laminates with the adhesive strip along the free edge, delamination is effectively suppressed until final failure [2].

Chou et al [5] suggest that by examining the load-damage curve, the onset-of-delamination strength can be determined by extrapolating the curve to $a = 0$. The result, shown in Fig. 5, is an average of four test coupons. As expected, the onset-of-delamination strength for the laminates with interior adhesive strips is the same as that for laminates without adhesive strips.

Fatigue Test

In the fatigue test, all the coupons were subjected to load-controlled, tension-tension conditions with R (ratio of minimum stress to maximum stress) = 0.1. The maximum test load level was approximately 90% of the static delamination

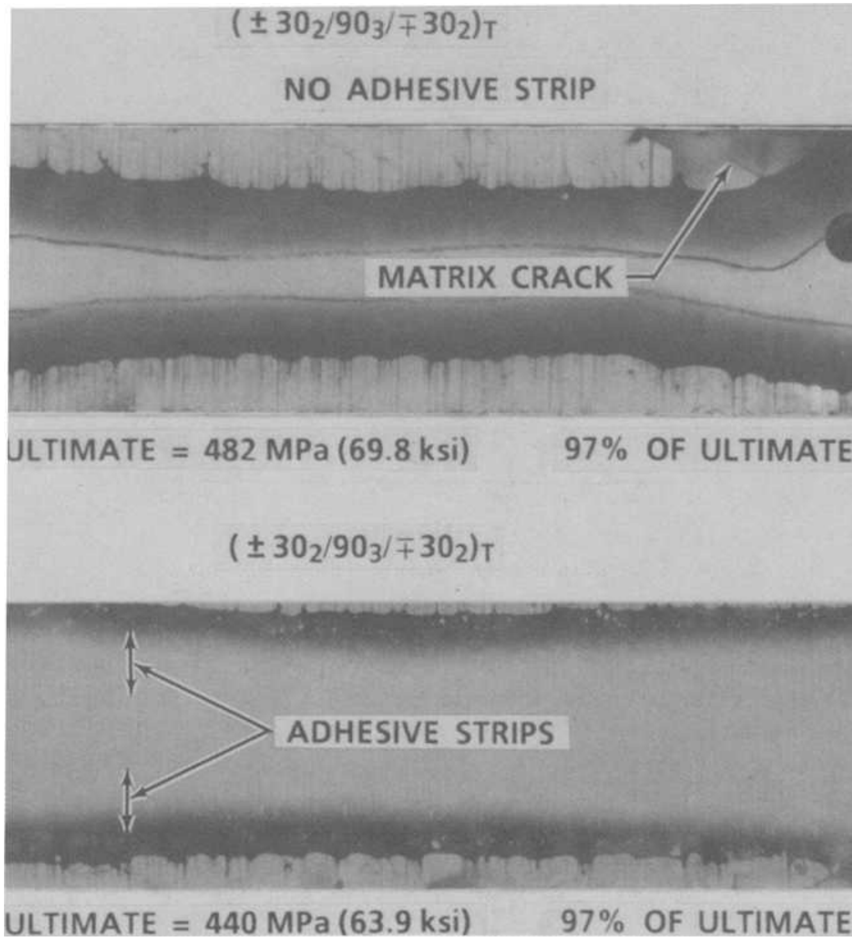

FIG. 3—*Static delamination of matrix-dominated laminates.*

strength (shaded value in Fig. 5) of the corresponding laminate without any adhesive strips. Three coupons of the adhesive-stripped $(\pm 30_2/90_3/\mp 30_2)_T$ laminates were tested at 70% of static delamination strength to investigate the effect of loading on the onset of delamination during the fatigue cycle.

During the course of the fatigue tests, each coupon was periodically removed from the machine and examined for fatigue damage by the method described in static tests. The results were also documented as in the static tests.

Test results and load conditions are summarized in Table 2. A discussion of the test results and test observations is given below.

Damage Mode—Figure 6 shows a fatigue delamination at the 0/90 interface of the $(\pm 35/0/90)_s$ laminate in an edge-view photograph. This is identical to that observed in the static case. An X-radiographic comparison of transverse

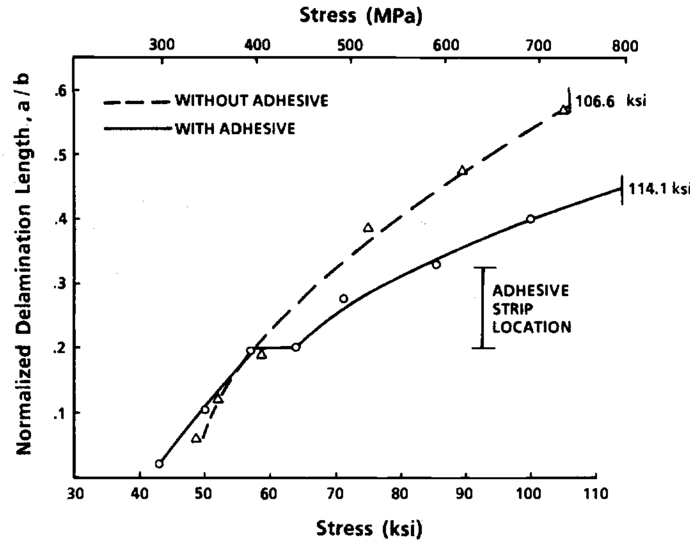

FIG. 4—*Typical load-damage relationship for* ($\pm 35/0/90$)$_s$ *laminates.*

cracking and delamination for the laminate with and without the delamination arrester (adhesive strips) is shown in Fig. 7. It is observed that delamination reaches the boundary of the adhesive strip near 5×10^5 cycles. There is no further delamination growth at 4×10^6 cycles when the test is halted for a residual strength test. For the Configuration 3 test coupons, in which the adhesive strips were placed along the free edge, no delamination was observed at 10^6 cycles, as shown in Fig. 8. Delamination is initiated at 4×10^6 cycles and grows through the adhesive strip regions at 5×10^6 cycles (see Fig. 8). The delamination occurs

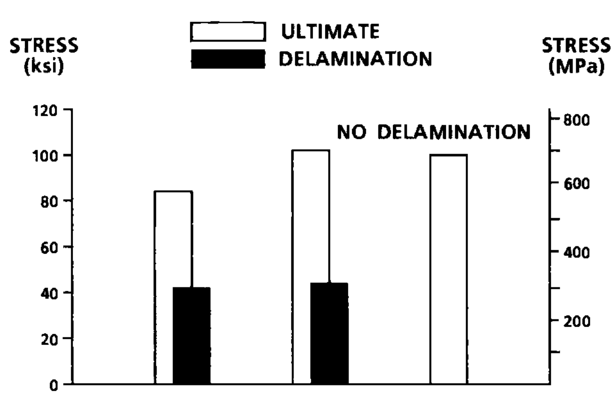

FIG. 5—*Comparison of static strength of coupon configurations.*

at the adhesive/90-deg-ply interface, as can be seen in Fig. 9. This is unlike the static case where delamination did not occur until final failure. This observation can be explained by the strain-energy release rate concept discussed later in the paper. For the matrix-dominated laminates with an arrester, the primary delamination began at the $-30/90$ interface, reached the arrester around 1×10^5 cycles, and then stopped growing until 1×10^6 cycles. At 2×10^6 cycles, this primary delamination grew into the interface between the adhesive strip and 90-deg ply (see Fig. 10). In the meantime, a secondary delamination at the interface between $-30/90$ plies was observed, as shown in Fig. 11. Figure 12, a cross-sectional view photograph, confirms these observations. A typical final failure surface of the laminate is shown in Fig. 13.

Delamination Growth—Typical delamination growth patterns for laminates with and without adhesive strips are presented in Figs. 14 and 15. As can be seen in the figures, delamination grows as the number of cycles increases. For the laminate with interior adhesive strips, delamination stops growing at the boundary of the adhesive regions. The delamination-versus-cycle data were used to determine da/dN information. Results shown in Figs. 16 and 17 indicate that the delamination growth rate (da/dN) tends to be a monotonically decreasing function of the number of fatigue cycles. This suggests that delamination growth slows down as the number of cycles increases. This phenomenon was also observed in Ref *6*.

Fatigue Life and Residual Strength—As shown in Table 2, the residual strength for fiber-dominated laminates seems not to depend upon the number of cycles applied and is perhaps dependent on the unidirectional ply properties. The mean value of residual strength for these laminates is slightly higher than the static strength. This is perhaps due to relaxation of edge stresses of fatigue delamination. For a matrix-dominated laminate, the fatigue life is significantly increased when delamination is arrested.

Analytical Study

Fracture mechanics and finite-element analyses served as analytical tools to investigate the effect of the interior adhesive strips of the laminates on delamination growth. The strain-energy release rate used in fracture mechanics, which measures the strain energy required to extend delamination, was applied in this study. The strain-energy release rates, G_I, G_{II}, G_{III}, corresponding to Modes I, II, and III of the fracture modes, are due to interlaminar stresses σ_z, τ_{yz}, and τ_{xz}, respectively, in the edge-delamination problem. In computing the strain-energy release rate, both closed-form solutions [*6*] and the finite-element method [*2,6,7*] are used. The finite-element method used in Ref *2* was also applied in this study.

In the finite-element computation, the strain-energy release rate is calculated as the amount of work done to close up a new crack [*8*]. Among the closed-

TABLE 2—*Summary of fatigue test conditions and results.*

Laminate Type	Coupon Type	Maximum Fatigue Load MPa	Maximum Fatigue Load ksi	Number of Cycles Completed (10^6)	Residual Strength MPa	Residual Strength ksi	Static Strength MPa	Static Strength ksi
$(\pm 30_2/90_3/\mp 30_2)_T$	Configuration 1	192.0	[a]27.84	1.06				
				1.31				
				1.75	failure		460.7	66.81
				2.34				
				2.58				
				avg 1.81				
	Configuration 2	192.0	[a]27.84	3.81	failure			
				4	380.6	55.2	445.4	64.60
				4	391.0	56.71		
					avg 385.8	avg 55.96		
		149.3	[b]21.65	4	514.6	74.63		
				4	503.1	72.97	445.4	64.60
				4	491.5	71.29		
					avg 503.1	avg 72.96		

(±35/0/90)$_s$	Configuration 1	259.8	[a]37.68	9	...	...		
				9	683.6	99.15		
				9	656.5	95.21	584.4	84.76
				4	643.1	93.27		
				4	655.9	95.13		
					avg 659.8	avg 95.69		
	Configuration 2	259.8	[a]37.68	5.71	failure			
				9	...	...		
				9	617.5	89.56	773.6	112.2
				4	709.7	102.93		
				4	679.9	98.61		
					avg 669.0	avg 97.03		
	Configuration 3	259.8	[a]37.68	6	725.9	105.28		
				6	690.0	100.07		
				6	539.3	78.21	679.4	98.54
				4	670.0	97.17		
				4	685.5	99.42		
					avg 662.1	avg 96.03		

[a] 90% of static delamination strength.
[b] 70% of static delamination strength.

FIG. 6—*Typical edge delamination of a* $(\pm 35/0/90)_s$ *laminate under fatigue loading.*

form solutions, O'Brien [*6*] derived an equation for laminates subjected to a constant strain. In his derivation, the laminate stiffness was assumed to be linearly dependent on the delamination size. Therefore, the expression for G is independent of a/b. For laminates subjected to a constant load, an expression for strain energy release can be derived by a method similar to that in Ref *6*.

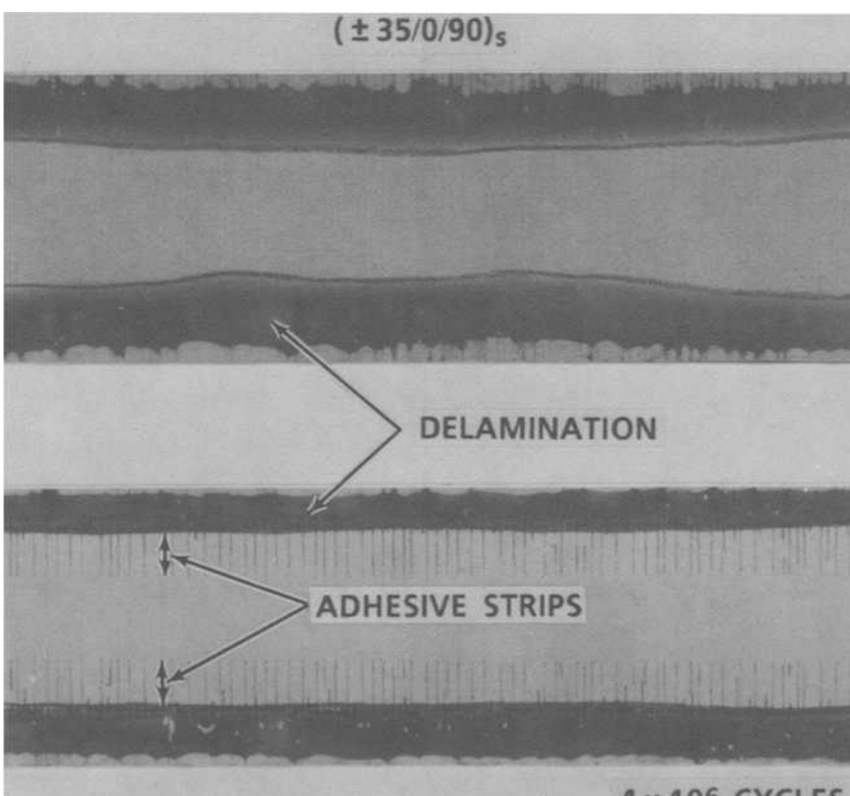

FIG. 7—*Delamination of* $(\pm 35/0/90)_s$ *laminates with and without adhesive strips.*

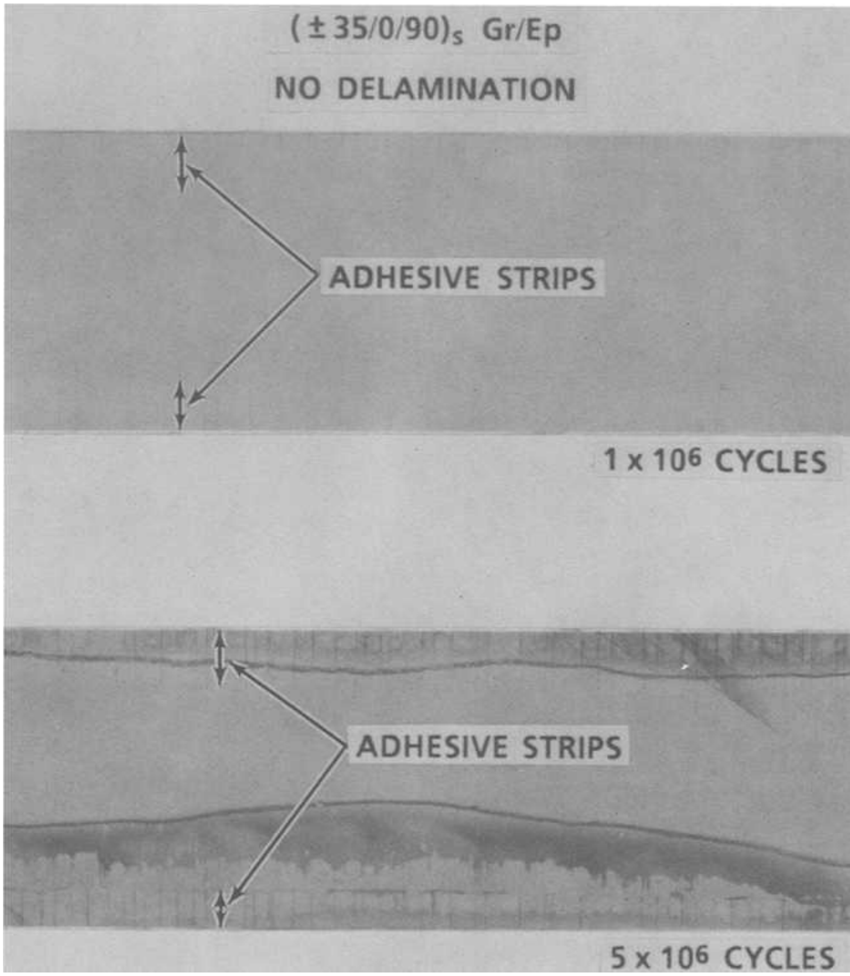

FIG. 8—*X-radiograph of edge-stripped* $(\pm 35/0/90)_s$ *laminates.*

Strain-Energy Release Rate for a Constant Loading

Considering a laminate containing a delamination area A, the strain-energy release rate G can be defined as

$$G = \frac{\partial W}{\partial A} - \frac{\partial U}{\partial A} \tag{1}$$

where W is the work done by external loads and U is the strain energy stored in the laminate. For the laminate subjected to a constant load, the term W can be

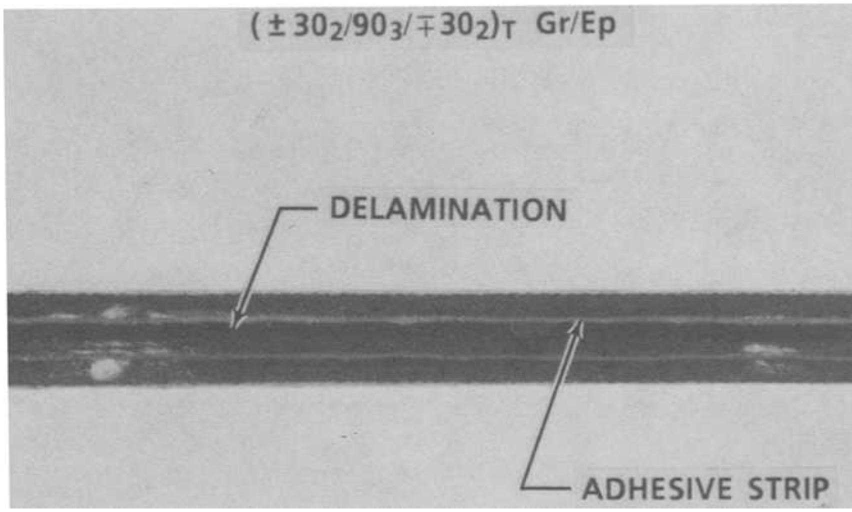

FIG. 9—*Delamination of laminates with edge-stripped adhesives: edge view.*

written as

$$W = 2U \tag{2}$$

Then Eq 1 becomes

$$G = \frac{\partial U}{\partial A} \tag{3}$$

since

$$U = \frac{\sigma^2}{2E}V \tag{4}$$

Combining Eqs 3 and 4 yields

$$G = -V\frac{\sigma^2}{2E^2}\frac{dE}{dA} \tag{5}$$

This expression is similar to O'Brien's equation for a constant strain condition [*6*]. Substituting the equations

$$\begin{aligned} V &= 2b \cdot \ell \cdot t \\ A &= \ell \cdot 2a \end{aligned} \tag{6}$$

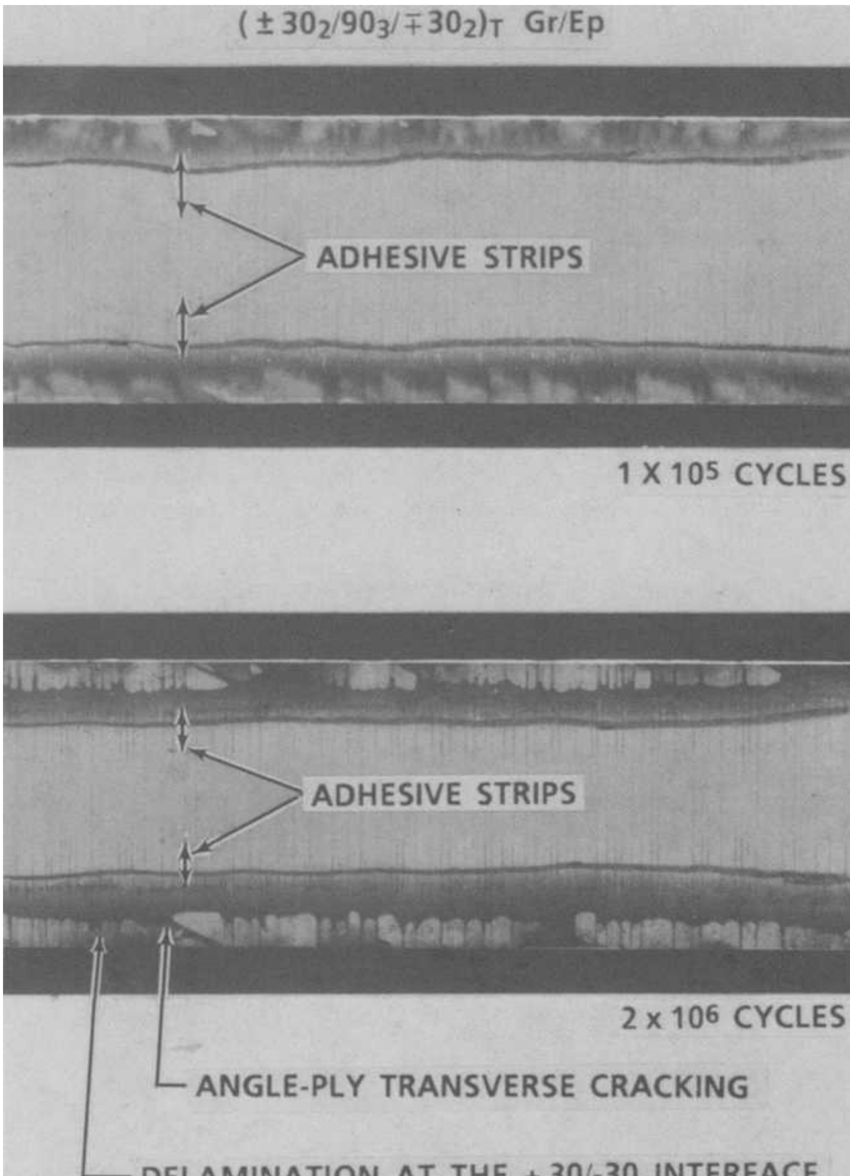

FIG. 10—*Primary and secondary delamination of a* $(\pm 30_2/90_3/\mp 30_2)_T$ *laminate: plane view.*

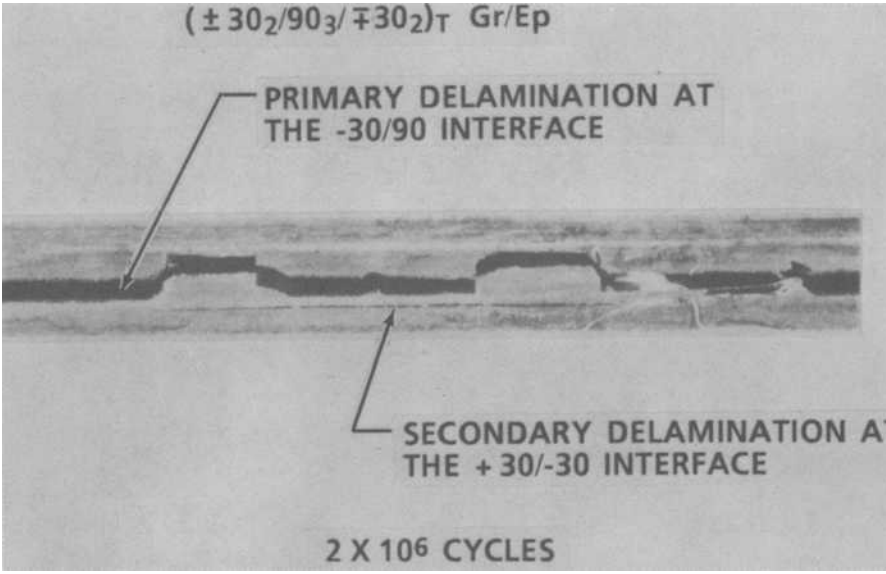

FIG. 11—*Primary and secondary delamination of a* $(\pm 30_2/90_3/\mp 30_2)_T$ *laminate: edge view.*

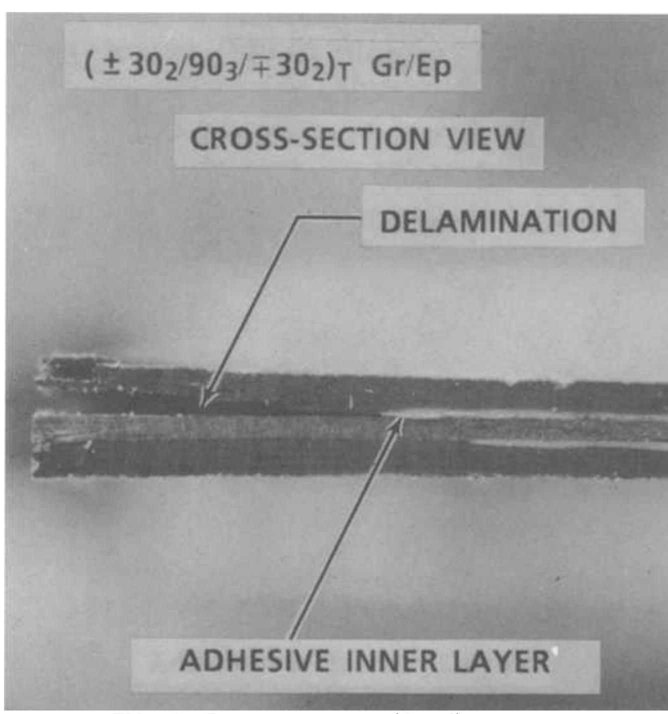

FIG. 12—*Delamination arrested by adhesive strips.*

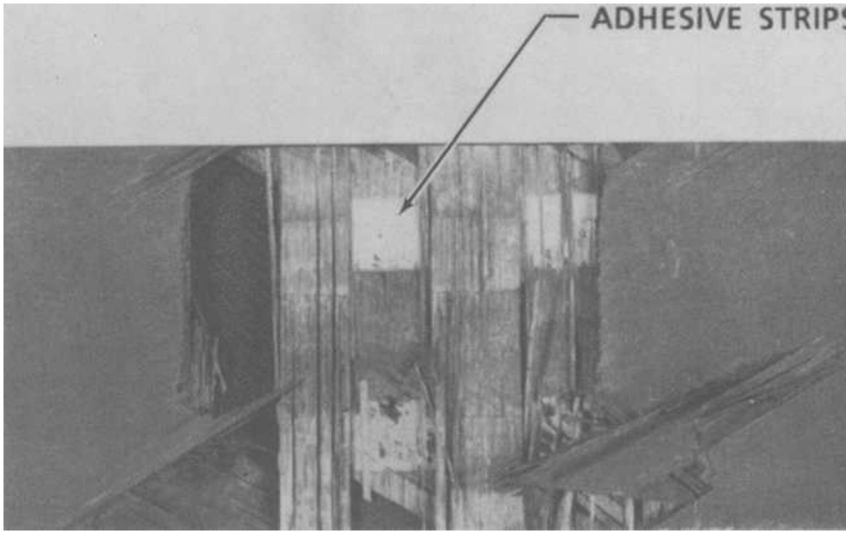

FIG. 13—*Final failure of a* $(\pm 30_2/90_3/\mp 30_2)_T$ *laminate.*

into Eq 5 yields

$$G = -\frac{\sigma^2}{2E^2}\,t\,\frac{dE}{d(a/b)} \tag{7}$$

The term $dE/d(a/b)$ can be either determined from an E-versus-a/b curve of test coupons or calculated from an equation such as the one shown in Ref *6* (Eq

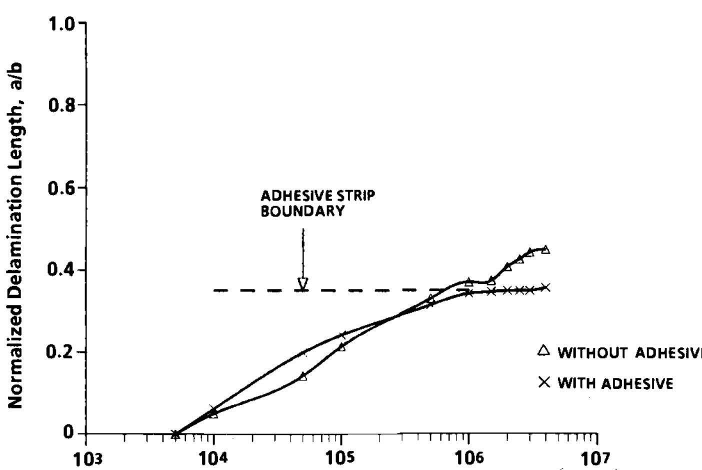

FIG. 14—*Delamination-cycle relationship for* $(\pm 35/0/90)_s$ *laminates, with and without adhesive.*

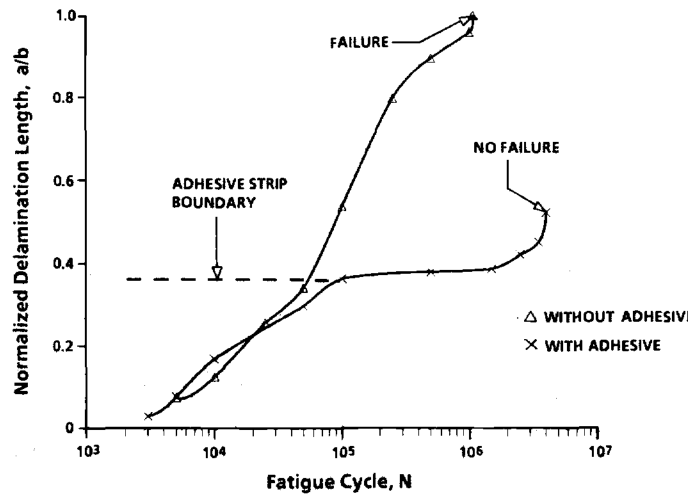

FIG. 15—*Delamination-cycle relationship for* $(\pm 30_2/90_3/\mp 30_2)_T$ *laminates, with and without adhesive.*

4 to Ref *6*). The expression for G indicates that G increases as E decreases. Hence, for a constant load, G is not independent of a/b.

Mixed-Mode Delamination Initiation and Growth

Configurations 1 and 3 of the $(\pm 35/0/90)_s$ laminate were used to investigate the strain-energy release rate variations at each different interface. The delamination length in the finite-element model was three times the thickness of the

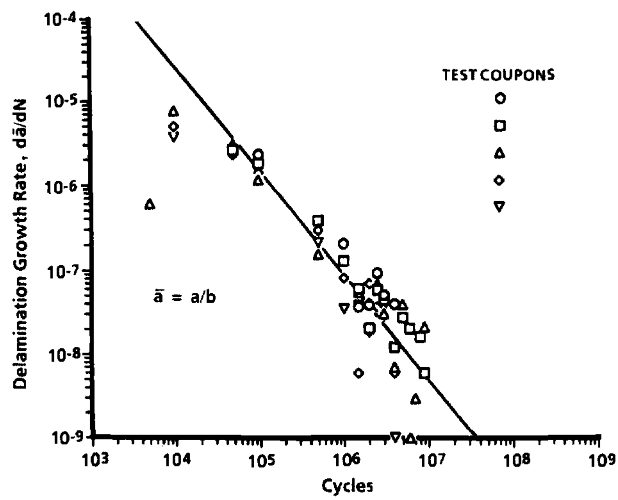

FIG. 16—*Fatigue delamination growth rate versus cycles for* $(\pm 35/0/90)_s$ *AS4/3501-6.*

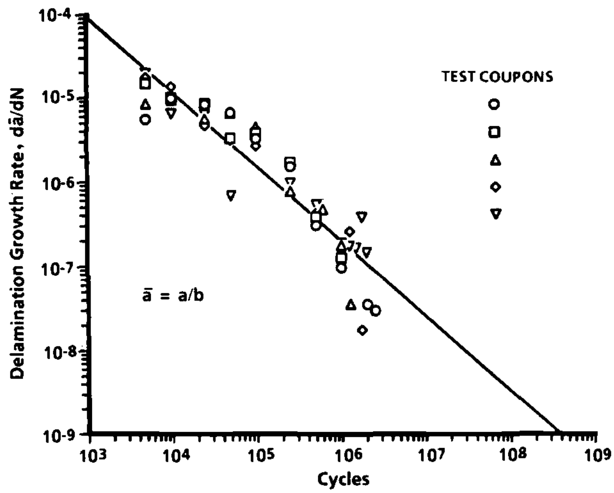

FIG. 17—*Fatigue delamination growth rate versus cycles for* $(\pm 30_2/90_3/\mp 30_2)_T$ *AS4/3501-6.*

ply, and the laminate width was approximately six times the thickness of the laminate. The material constants used in this study were as follows:

AS4/3501-6, Graphite/Epoxy	Adhesive Layer, FM1000
E_1 = 133 GPa (19.3 Msi)	E_1 = 1.45 GPa (0.210 Msi)
E_2 = 11.2 GPa (1.62 Msi)	$E_2 = E_1$
G_{12} = 7.03 GPa (1.02 Msi)	$G_{12} = E_1/2(1 + \nu)$
ν_{12} = 0.288	ν = 0.425
t_{ply} = 0.137 mm (0.0054 in.)	t = 0.137 mm (0.0054 in.)

For analysis purposes, the adhesive strip thickness was assumed to be the same as a ply thickness of graphite/epoxy. In the finite-element model, the adhesive strip was modeled as two layers of elements.

The results, shown in Fig. 18, indicate that the highest G_I component for both the $(\pm 35/0/90)_s$ and $(\pm 35/0/\text{adhesive}/90)_s$ laminates occurs at the 0/90 and adhesive/90 interfaces, respectively. The highest total strain-energy release rate is at the $+35/-35$ interface for both laminates. From the test, as shown in Fig. 9, the delamination is located at the 0/90 and adhesive/90 interfaces for Configurations 1 and 3, respectively. It is suggested, therefore, that the G_I component controls the start of delamination, not the total G, for both static and fatigue loading. Mall et al [9] showed that while the debond growth rate was controlled by total G, the debond location was determined by maximum G_I. However, the exact physical mechanism is still far from known.

Effect of Adhesive Strips in Laminates

In this section, Configuration 2, which has an interior strip, is discussed. Delamination was placed at the interface between the 0 and 90-deg plies in accordance with the test observation. The results of Mode-I strain-energy release

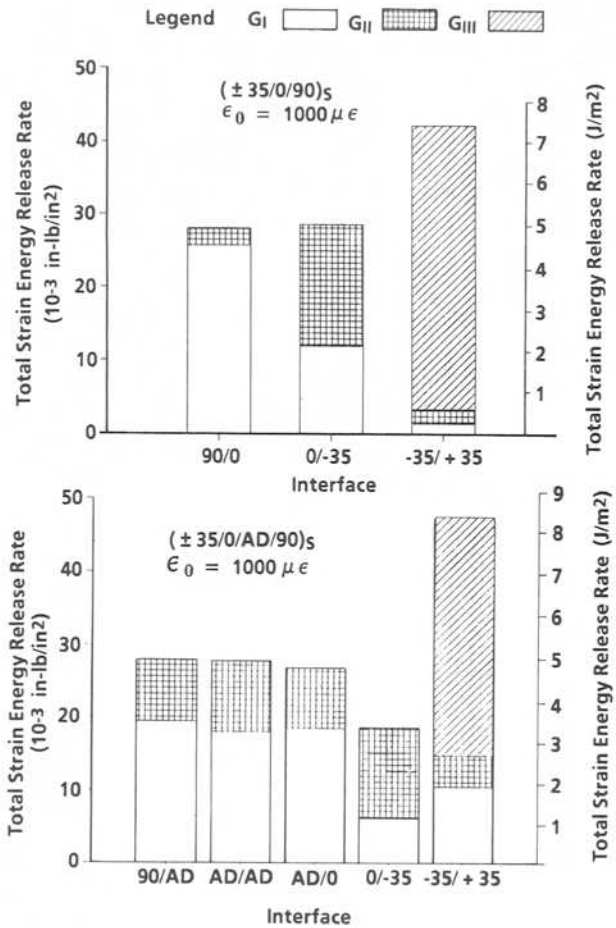

FIG. 18—*Strain-energy release rate at various interfaces of* $(\pm 30/0/90)_s$ *and* $(\pm 35/0/AD/90)_s$ *laminates.*

rate (G_I), normalized by the total strain-energy release rate (G_T), are depicted in Fig. 19. It is shown that there is no difference in G_I/G_T for laminates either with or without adhesive strips, except when the delamination approaches to within approximately four ply thicknesses away from the adhesive strip, at which point G_I/G_T is decreased. In addition, the G_T is fairly constant for the laminates with and without adhesive strips. The reduction in G_I/G_T is due primarily to the presence of the low-modulus adhesive strip. This should explain the retardation of the delamination growth.

Conclusions

Adhesive strips have been successfully demonstrated to be effective delamination arresters for both matrix-dominated and fiber-dominated laminates. De-

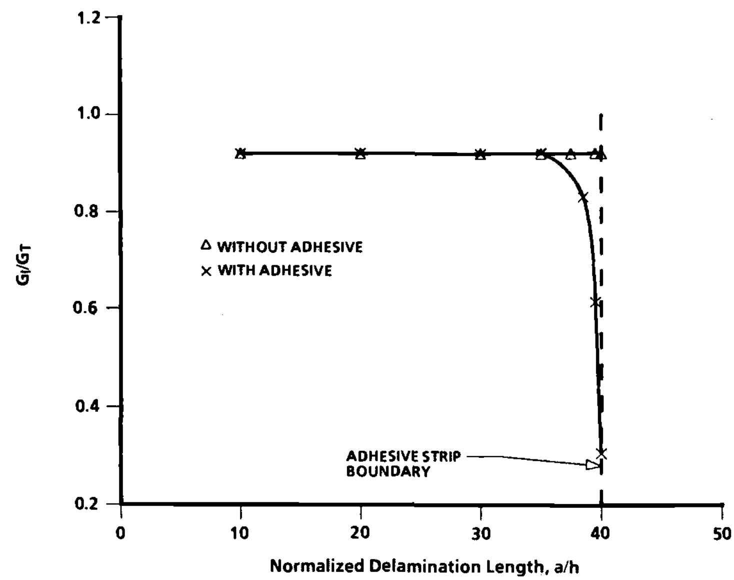

FIG. 19—*Effect of strain-energy release rate for laminates with and without adhesive.*

lamination arrestment depends upon reducing the percentages of the G_I component in the total strain-energy release. The delay in delamination growth results in a significant increase in fatigue life for matrix-dominated laminates. For both $(\pm 30_2/90_3/\mp 30_2)_T$ and $(\pm 35/0/90)_s$ graphite/epoxy laminates, the delamination growth rate decreases as the number of fatigue cycles increases. From test observation, it is suggested that the start of delamination for both static and fatigue loadings is due to the highest G_I in the laminate, not the total G. In fact, there is no real delamination arrest, but only a reduction in the delamination growth rate. However, if the delay of delamination propagation is sufficiently long, the use of delamination arrester strips will provide a degree of fail-safety capability and meet the damage tolerance and durability requirement.

Acknowledgments

This work was supported under the IR&D Program of Bell Helicopter Textron Inc., Fort Worth, Texas. The author is grateful to Mr. C. Rogers of Bell Helicopter and Dr. T. K. O'Brien of the Army Structures Laboratory at NASA Langley for their fruitful discussions. Thanks are also due to Mr. J. Jensen of The Methods and Materials Laboratory of Bell Helicopter for his assistance in conducting the tests.

References

[1] Sendeckyj, G. P. in *Fracture Mechanics of Composites, ASTM STP 593*, American Society for Testing and Materials, Philadelphia, 1975, pp. 215–226.

[2] Chan, W. S., Rogers, C., and Aker, S. in *Composite Materials: Testing and Design (Seventh Conference), ASTM STP 893*, American Society for Testing and Materials, Philadelphia, 1986, pp. 266–285.
[3] Browning, C. E. and Schwartz, H. S. in *Composite Materials: Testing and Design (Seventh Conference), ASTM STP 893*, American Society for Testing and Materials, Philadelphia, 1986, pp. 256–265.
[4] O'Brien, T. K. in *Effects of Defects in Composite Materials, ASTM STP 836*, American Society for Testing and Materials, Philadelphia, 1983, pp. 125–142.
[5] Chou, P. C., Wang, A. S. D., and Miller, H., "Cumulative Damage Model for Advanced Composite Materials," AFWAL-TR-82-4083, Sept. 1982
[6] O'Brien, T. K., in *Damage in Composite Materials, ASTM STP 775*, American Society for Testing and Materials, Philadelphia, 1982, pp. 140–167.
[7] Wang, A. S. D., Slomiana, M., and Bucinell, R. B., in *Delamination and Debonding of Materials, ASTM STP 876*, American Society for Testing and Materials, Philadelphia, 1985, pp. 135–167.
[8] Rybicki, E. F. and Kanninen, M. F., "A Finite Element Calculation of Stress Intensity Factors by a Modified Crack Closure Integral," *Engineering Fracture Mechanics*, Vol. 9, 1977.
[9] Mall, S., Johnson, W. S., and Everett, R. A., "Cyclic Debonding of Adhesively Bonded Composites," in *Adhesive Joints: Their Formation, Characterization, and Testing*, K. L. Mittal, Ed., Plenum Press, New York, 1984; also NASA TM 84577, Nov. 1982.

P. K. Mallick, [1] *R. E. Little,* [1] *and J. Thomas* [1]

Fatigue Damage in Notched Pultruded Composite Rods

REFERENCE: Mallick, P. K., Little, R. E., and Thomas, J., "**Fatigue Damage in Notched Pultruded Composite Rods,**" *Composite Materials: Fatigue and Fracture, ASTM STP 907,* H. T. Hahn, Ed., American Society for Testing and Materials, Philadelphia, 1986, pp. 197–209.

ABSTRACT: The primary damage mode in a notched pultruded composite rod in rotating bending fatigue was found to be fiber-matrix debonding which originated at the notch root and extended along the length of the specimen. At stress amplitudes equal to or greater than 35% of the tensile strength of the material, debonding was followed by tensile rupture of the fibers at or near the notch, resulting in catastrophic failures of the specimens. At lower stress amplitudes, the slow growth in debonding resulted in a gradual increase in the dynamic deflection of the specimen. The static flexural stiffness ratio of a fatigue-damaged specimen to that of an undamaged specimen was found to be a reasonable measure of damage due to fiber-matrix debonding.

KEY WORDS: pultruded rod, unidirectional composite, rotating bending fatigue, damage mechanism, debonding, catastrophic failure, dynamic deflection, static stiffness ratio

Pultrusion is a continuous molding process used in the production of fiber-reinforced composite structural shapes. Since the major constituent in a pultruded composite is longitudinal, continuous fibers, its tensile strength-to-weight ratio (specific tensile strength) is comparable to or even higher than many steels and aluminum alloys. For this reason, pultruded composites are finding use in many high-volume structural applications, such as ladder rails, light poles, beams, and joists.

Static tensile properties of pultruded composite materials are routinely reported in the product literature published by the manufacturers [*1*]. Halsey et al [*2*] have evaluated the static tensile strength, modulus of elasticity, flexural modulus, and stress rupture properties of various pultruded rod materials in relation to their use in guy lines and insulating rods for large communication towers and antenna arrays. In these as well as many other structural applications, fatigue behavior of the pultruded composites must be known for their safe design.

In long-life fatigue tests (say, greater than 10^5 cycles), fiber-reinforced com-

[1] Associate professor, professor, and student, respectively, Department of Mechanical Engineering, University of Michigan-Dearborn, Dearborn, MI 48128.

posite materials are known to fail in a progressive manner through gradual deterioration (damage development) in the material [3,4]. Similar behavior was observed in preliminary fatigue tests with commercially available pultruded composite rods. For these materials, it is better to establish an S-N curve by defining fatigue life (failure) in terms of some specific measure of damage growth. In the present work, dynamic deflection during the fatigue test and residual static stiffness after the fatigue test are considered as measures of fatigue damage in pultruded composite rods containing continuous unidirectional fibers. Relationships between these two measurable quantities and fatigue damage are explored.

Procedure

Test Specimen

The 12-mm-diameter pultruded rods contain continuous E-glass fibers, 75% by weight, in a thermosetting polyester matrix. The tensile strength of the rod material is approximately 690 MPa [5]. Test specimens were 102 mm long with a sharp V-notch ($K_t \approx 5$) machined at the midlength. Specimen dimensions appear in Fig. 1.

Test Method

Cyclic fatigue tests were performed on a rotating bending fatigue machine. A schematic of the fatigue machine and the loading arrangement is shown in Fig. 2. In this arrangement, the length of the specimen between the collets plus the length of the tailstock form a 241-mm-long cantilever beam. Thus, when a load is applied at the end of the tailstock, there is a linear variation of bending moment along the ungripped length of the specimen, Fig. 3. Since the ungripped length is only 42 mm, the difference in bending moments at the two ends of the specimen is 20%. At the onset of each fatigue test, the position of a poise weight is adjusted on the calibrated loading arm to obtain the desired maximum bending stress level at the minimum cross section of the specimen. As the specimen is rotated by the drive spindle in the headstock, every point on each conceptual cross section on the specimen experiences an alternating cyclic stress ($R = -1$); however, the

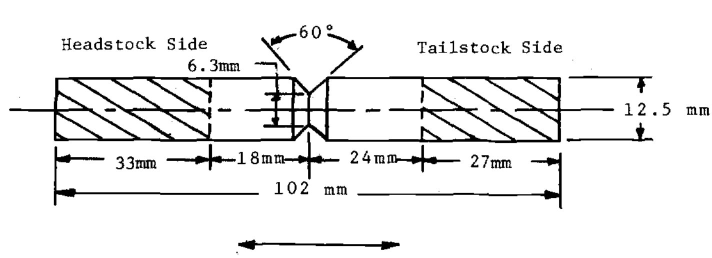

FIG. 1—*Notched fatigue specimen.*

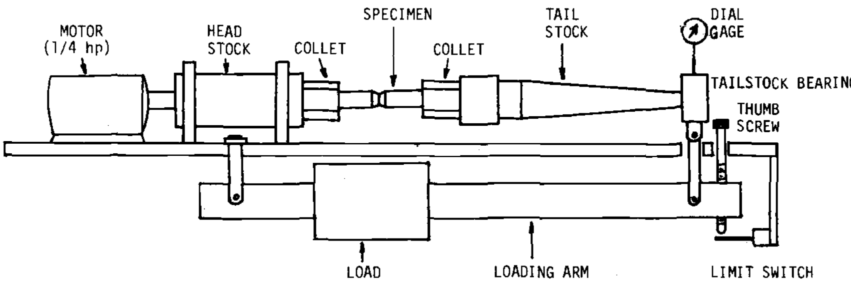

FIG. 2—*Schematic of a rotating bending machine.*

magnitude of this stress amplitude depends linearly on the distance from the neutral axis.

Nominal stress amplitudes at the notch root ranged from 72 to 290 MPa (approximately 10% to 42% of the tensile strength). Cyclic frequency was 10 Hz. In all fatigue tests, stress cycling was accompanied by a gradual increase in deflection of the specimen. In preliminary fatigue tests at long lives involving approximately ten specimens (S_a = 72, 96, and 121 MPa) this deflection limit was preset by adjusting the position of a calibrated screw attached to the tailstock. As the predetermined limit of deflection was reached, the lower end of the screw

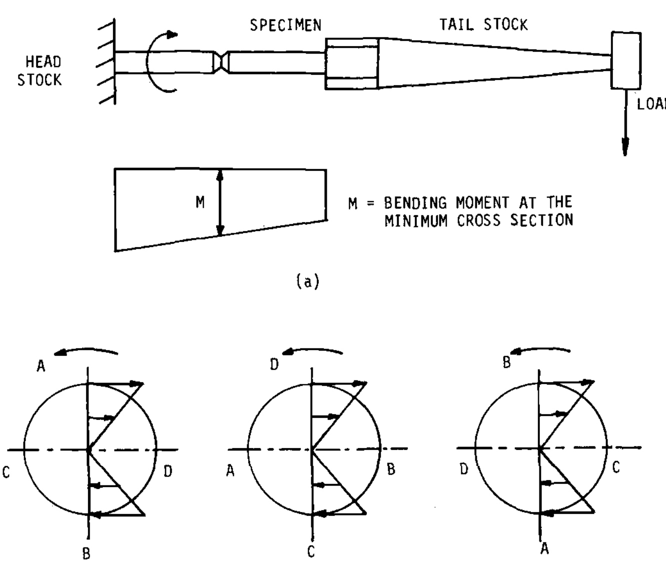

FIG. 3—*Bending moment and stress distribution in the specimen:* (a) *bending moment;* (b) *stress distribution.*

contacted a cutoff switch which stopped the machine. The test was then continued by resetting the screw to a new limit.

In subsequent fatigue damage tests at S_a = 145, 193, 241, and 290 MPa, the deflection at the end of the tailstock was continuously measured by means of a dial indicator (with a minimum division of 0.025 mm) positioned vertically above the tailstock bearing. A second dial indicator was used to measure the horizontal runout. Each test in this series (which included approximately 40 specimens) was conducted for a predetermined number of cycles. The deflection at the tailstock bearing and the vertical runout were recorded periodically. After unloading the specimen at the end of cycling, the specimen was slowly reloaded in five steps up to a maximum static stress level of 99 MPa. Static deflections at these stress levels were recorded. The slope of a least-squares fit straight line through the deflection points was compared with the slope of a similar line for the undamaged specimen. The ratio of the slopes of these two lines is defined herein as the static stiffness ratio.

The fatigued specimens were then sectioned longitudinally using a diamond saw. The crack lengths on both sides of the V-notch were measured using a stereomicroscope at a $\times 7$ magnification.

Results

Fatigue Damage Mechanism

The first visible sign of fatigue damage was a circumferential crack at the notch root. When the fatigued specimens were sectioned longitudinally, internal debonding cracks were evident. These debonding cracks originated from the root of the circumferential crack and proceeded toward each collet along the length of the specimen, Figs. 4 and 5. Sectioning across the cross section revealed that debonding occurred around a core of material approximately of the same diameter as that at the notch root; however, from uneven crack lengths on either side of the notch in Figs. 4 and 5, it is clear that crack growth is not uniform across the periphery of the core.

Debonding cracks were found even at the end of the first cycle at all four stress amplitudes ranging from 145 to 290 MPa. Crack length measurements for various stages of cycling revealed that the debonding crack growth was progressive, Figs. 6 and 7. For any given cycle, however, the crack length on the headstock side of the specimen was greater than that on the tailstock side. This difference in crack lengths is due to higher bending stresses on the headstock side of the specimen.

The debonding cracks in the specimens are followed by a number of longitudinal cracks in the shell surrounding the debonded core, due to differential flexing of the core against the shell. These secondary cracks also originated at the root of the circumferential crack and progressed toward the grips, as schematically shown in Fig. 8. The density of these cracks was a function of the stress amplitude, while their length depended on the number of cycles endured.

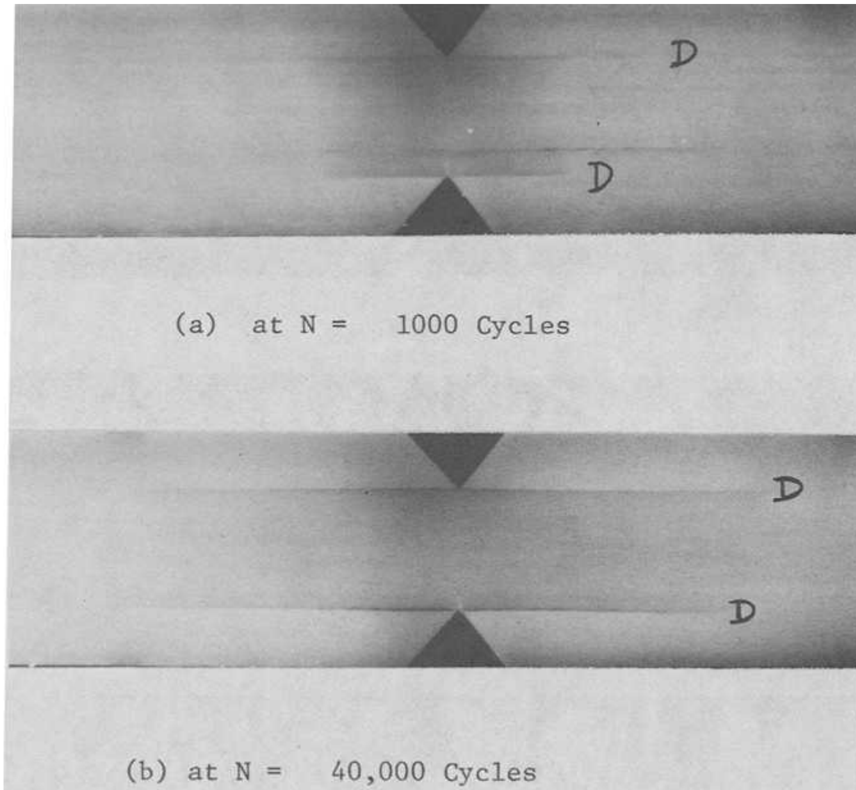

FIG. 4—*Internal debonding cracks* (D) *at 193 MPa.*

At S_a = 240 and 290 MPa, the debonding and secondary cracks are followed with catastrophic tensile rupture of the longitudinal fibers near the V-notch; however, the transverse cracks did not always originate at the tip of the V-notch, Fig. 5. At 290 MPa, catastrophic failure was observed at as low as 425 cycles; however, the variability in this material is evident in that three other specimens failed in a similar manner at 950, 2050, and 2250 cycles, respectively. At 240 MPa, catastrophic failure was observed in three specimens at 2650, 4300, and 6700 cycles, respectively; however, two other specimens tested for 5000 and 6000 cycles did not fail catastrophically. Another specimen tested at 240 MPa ran for more than 5×10^6 cycles in the preliminary fatigue test without catastrophic failure; in this case, however, the debonding crack extended well into the gripped area.

Dynamic Deflection

At low stress amplitudes (S_a = 72, 96.5, and 121 MPa), no appreciable increase in dynamic deflection occurred in tests conducted as long as 5×10^6

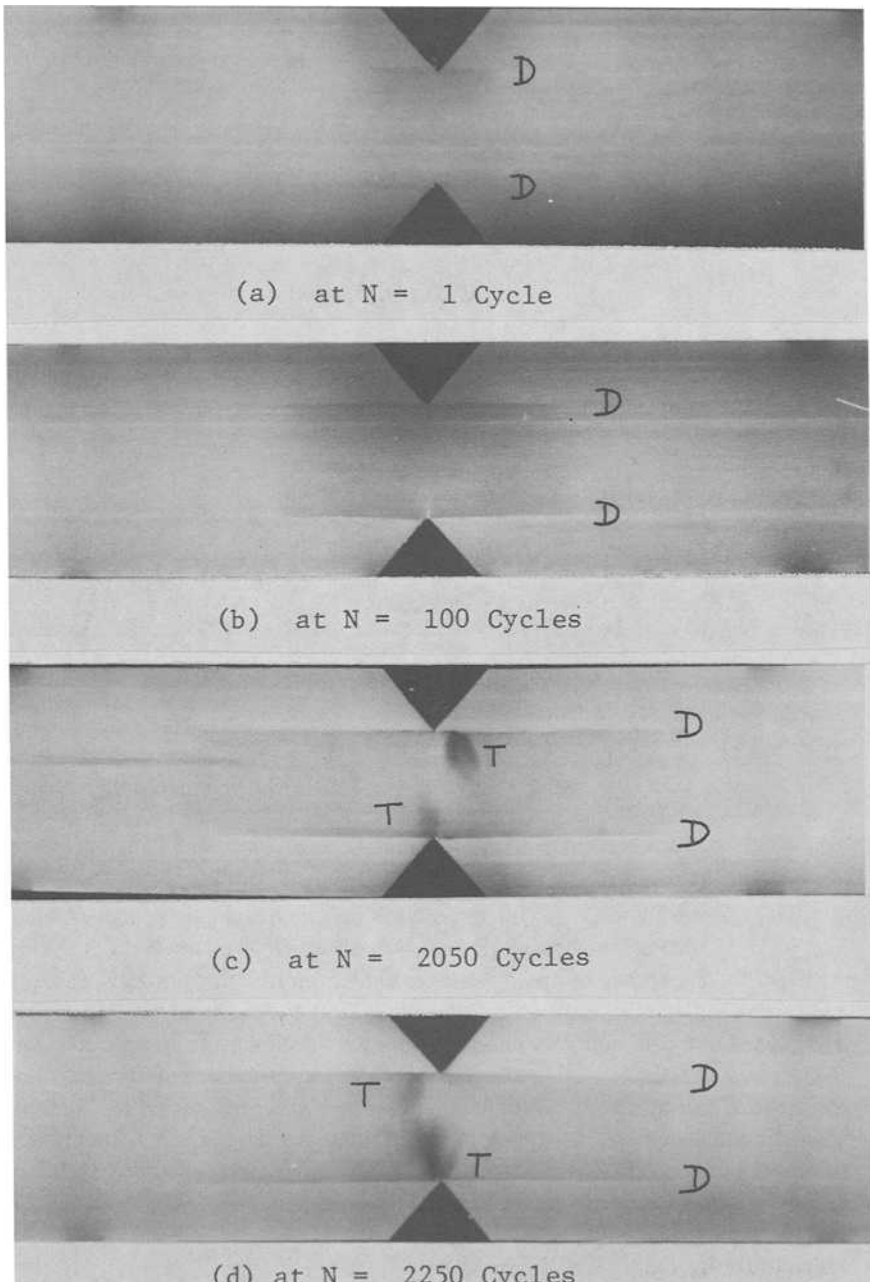

FIG. 5—*Internal debonding cracks* (D) *and transverse cracks* (T) *at 290 MPa.*

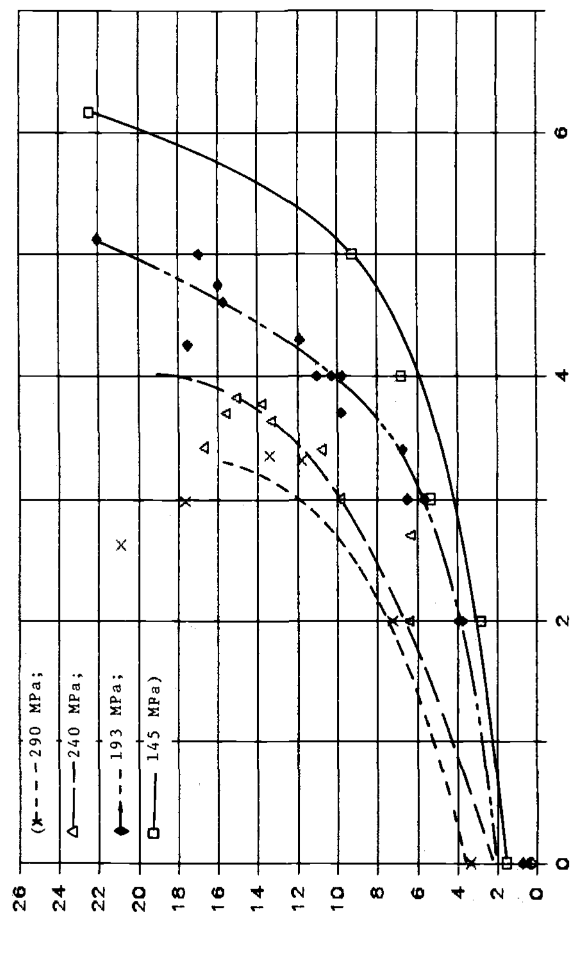

FIG. 6—*Mean crack length on the headstock side versus log cycles.*

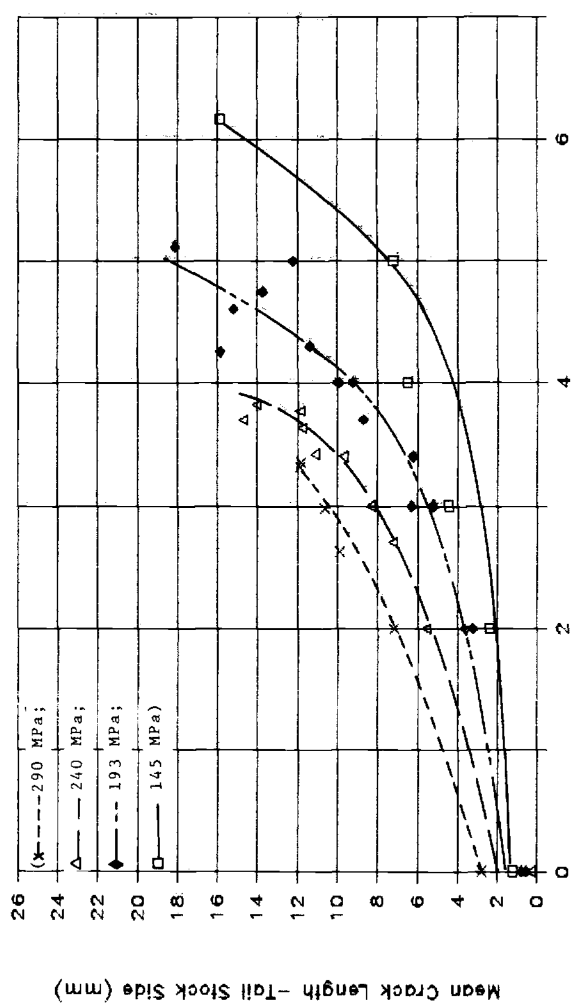

FIG. 7—*Mean crack length on the tailstock side versus log cycles.*

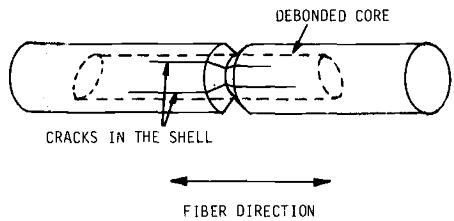

FIG. 8—*Schematic representation of cracks in notched pultruded specimen in rotating bending fatigue.*

cycles. For example, one specimen tested at 72 MPa showed a deflection of only 0.4 mm in the preliminary fatigue test even after 121×10^6 cycles. At higher stress amplitudes, the rate of increase in deflection increased as the stress amplitude was increased. Figure 9 shows the deflection at the bearing of the tailstock as a function of log (fatigue cycles). For convenience, data in this figure represent the deflection at the last cycle in each test; however, deflection data collected periodically during the cycling of each specimen indicate the same trend. At 240 and 290 MPa, the deflection increased at an accelerated rate after 100 to 1000 cycles and failed in a catastrophic manner with a sudden increase in deflection. At 145 and 193 MPa, no catastrophic failure was observed in tests conducted as long as 10^7 cycles. In these tests, the deflections continued to increase gradually.

Static Stiffness Ratio

The static flexural stiffness ratio of fatigued specimens to that of undamaged specimens is plotted in Fig. 10 as a function of log (cycles). For stress amplitudes of 241 and 290 MPa, the stiffness ratio could be determined only for those specimens which did not fail catastrophically. The stiffness ratio decreases continuously with increasing number of cycles, indicating a continuous growth of overall damage in the specimen. For a given cycle, the fatigue damage, as measured by the debonded crack length, is greater at higher stress amplitudes. This has resulted in the lower static stiffness ratio with increasing stress amplitudes.

The static stiffness ratio is also plotted as a function of percent debonded crack length in Fig. 11. Percent debonded crack length is the percentage ratio of the total mean debonded crack length to the total length of the specimen between the grips. As mentioned earlier, the stiffness ratio decreases with increasing debonded crack length. It is also evident from this figure that the stiffness ratio, when related to the debonded crack length, is independent of the stress amplitude for practical purposes. Apparently, at all stress amplitudes, internal debonding is the primary mode of damage which caused the reduction in static stiffness.

Conclusion

The present study has shown that progressive changes in the dynamic deflection and the static stiffness ratio are related to fatigue damage in pultruded composite

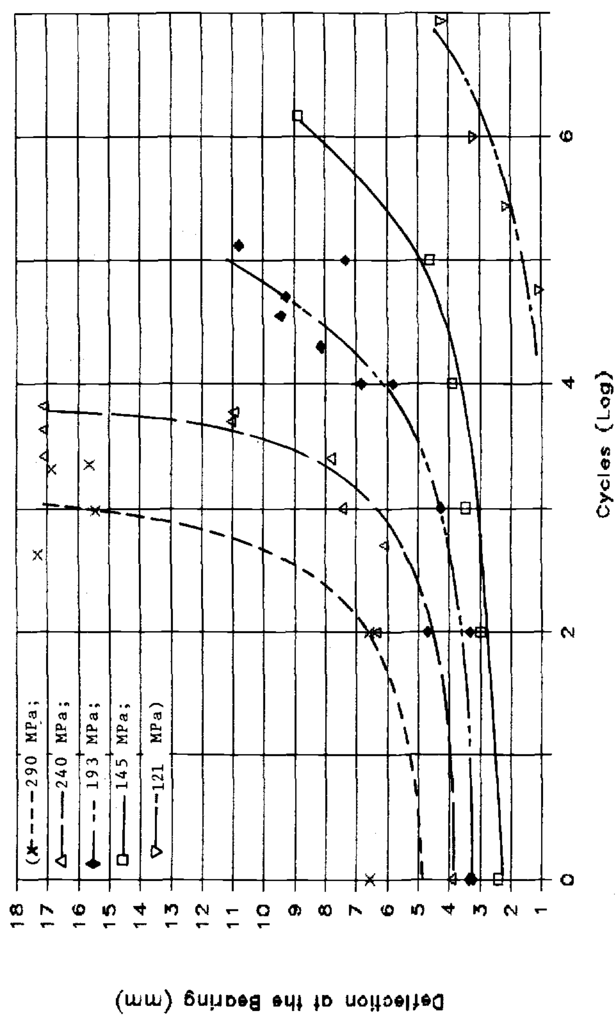

FIG. 9—*Deflection at the bearing versus log cycles.*

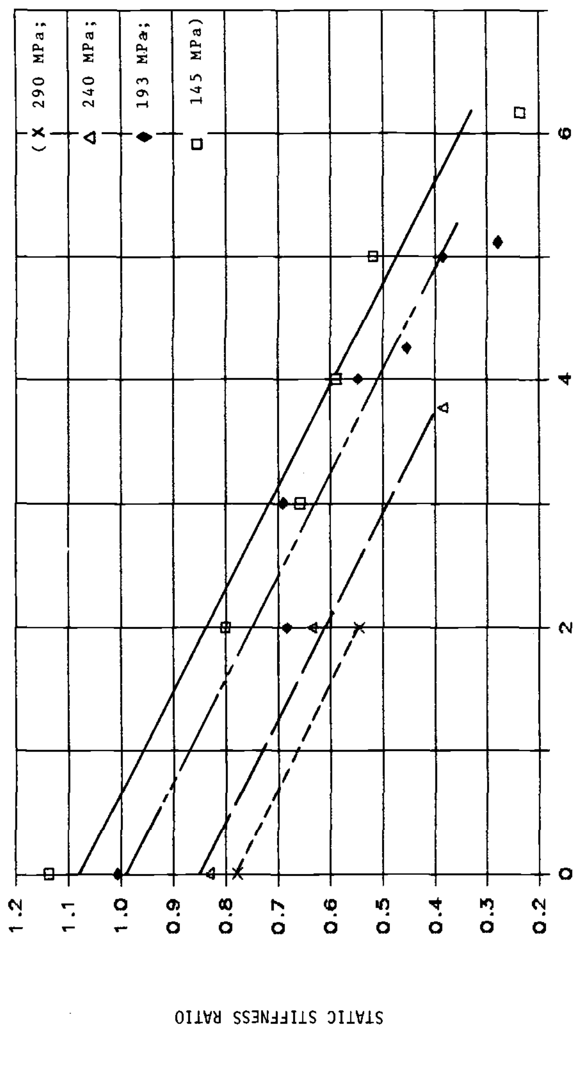

FIG. 10—*Static stiffness ratio versus log cycles.*

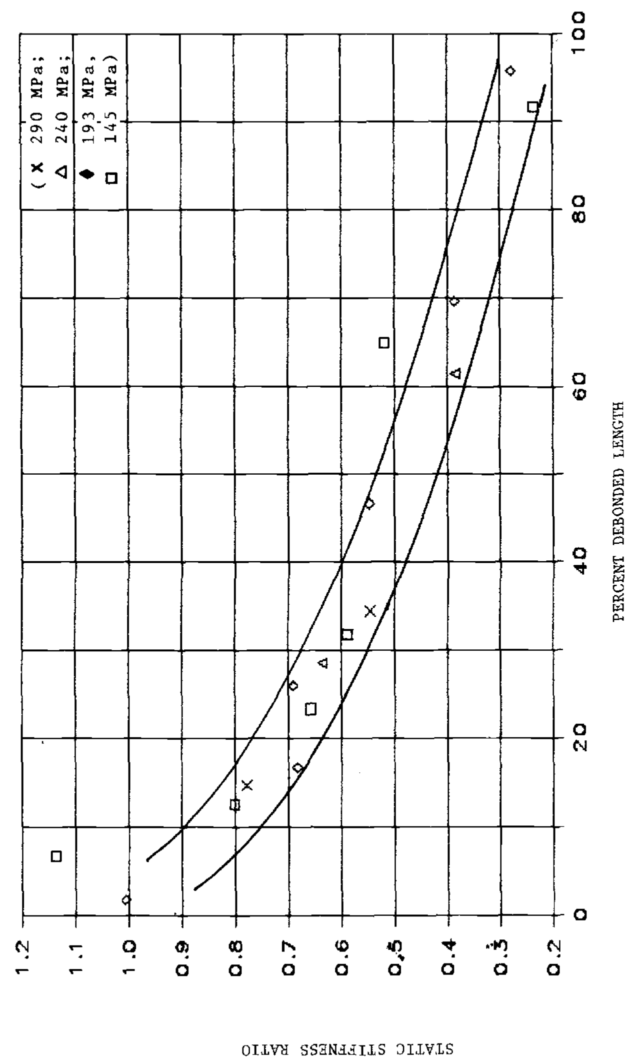

FIG. 11—*Static stiffness ratio versus percent debonded length.*

rods. However, the static stiffness ratio, as defined herein, is subject to considerable experimental scatter, apparently due to variability in the material as well as in the cracking configuration. Thus, although classical *S-N* curves can be drawn for various fixed levels of static stiffness ratio, extensive testing is required to establish these *S-N* curves. From the results of the present tests, it is observed that there exists a threshold stress amplitude differentiating progressive failure (progressive damage) from catastrophic failure. In the case of pultruded composite rods, this threshold stress amplitude is between 193 and 240 MPa. If the load-carrying capacity of a structure is important in design, any stress level above this threshold stress amplitude must be avoided.

The static stiffness ratio decreases to very low values (approximately 0.25) at long lives even at moderate stress amplitudes ($S_a/S_u = 0.3$). Thus, if deflection is an important parameter in design, it appears that S_a must be kept well below 145 MPa.

Acknowledgment

The authors wish to thank the Morrison Molded Fiberglass Co., Bristol, VA, for supplying the pultruded rods used in this study.

References

[1] "Extren: Fiber Glass Structural Shapes," Morrison Molded Fiberglass Co., Bristol, VA, 1971.
[2] Halsey, N., Mitchell, R. A., and Mordfin, L., "Evaluation of GRP Rod and Rope Materials and Associated End Fittings," Technical Report NBSIR 73-129, National Bureau of Standards, Washington, D.C., Dec. 1982.
[3] Talreja, R., "Fatigue of Composite Materials: Damage Mechanisms and Fatigue Life Diagrams," *Proceedings of the Royal Society of London*, Series A, Vol. 378, 1981.
[4] Mallick, P. K., "A Fatigue Failure Warning Method for Fiber Reinforced Composite Structures" in *Failure Prevention and Reliability*, American Society of Mechanical Engineers, 1983.
[5] Mallick, P. K., Little, R. E., and Haupt, E., "Tensile Failure Modes in Notched Pultruded Rods" (in preparation).

Luis Lorenzo[1] *and H. Thomas Hahn*[1]

Fatigue Failure Mechanisms in Unidirectional Composites

REFERENCE: Lorenzo, L. and Hahn, H. T., "**Fatigue Failure Mechanisms in Unidirectional Composites,**" *Composite Materials: Fatigue and Fracture, ASTM STP 907,* H. T. Hahn, Ed., American Society for Testing and Materials, Philadelphia, 1986, pp. 210–232.

ABSTRACT: The tension fatigue behavior of unidirectional composites has been studied using model composites where bundles of E-glass and T300 graphite fibers were combined with ductile and brittle epoxies. Model specimens allowed one to monitor and identify the basic failure mechanisms which are difficult to detect in real composite coupons. Fatigue failure modes and the sequence of damage accumulation depended on the stress level. Matrix microcracks between fibers normal to the applied load were subcritical failure mechanisms which occurred early during fatigue in both glass and graphite bundles. In graphite fiber bundle, they were initiated at the interface along the fibers and were rather isolated. These microcracks were not deleterious in that they neither triggered fiber failures nor grew bridging the fibers. At medium and high cyclic stresses, degradation of the glass as well as the graphite bundle in the form of fiber failures was observed. In glass specimens, extensive interfacial failure and matrix cracking followed while in graphite bundles matrix cracking occurred close to the zones of accumulation of fiber breaks. At low stress levels, only matrix microcracking and few scattered fiber failures were seen.

KEY WORDS: unidirectional composites, glass/epoxy, graphite/epoxy, fatigue failure mechanisms, failure modes, damage accumulation, fiber bundles

Several recent works addressed differences in damage accumulation between glass/epoxy and graphite/epoxy composites [*1–5*]. In both materials, failure in low-cycle fatigue resembles static fracture. In high-cycle fatigue, however, fatigue failure modes are different from static ones because of the higher fatigue sensitivity of matrix and interface [*6–9*]. The observation of transverse matrix cracks and a fatigue limit strain of composite being approximately equal to that of the matrix suggests a matrix-dominated failure in glass/epoxy [*1,2*]. On the other hand, the similar fatigue degradation of dry and impregnated glass bundles indicates a fiber-dominated failure [*3*]. Thus, it is not clear yet which constituent triggers failure of unidirectional composites in fatigue.

Fatigue ratios of graphite/epoxy composites are higher than those of glass/epoxy composites as a result of lower strain capability of graphite fibers [*4–6*].

[1] Research assistant and professor, respectively, Center for Composites Research, Washington University, St. Louis, MO 63130.

In the former, fracture is sudden with most of the damage accumulating in the last few loading cycles [*4,5*]. The difference in damage accumulation between these two materials is also evidenced by differences in stiffness and strength reductions in fatigue [*1,5,10*].

The objective of the present study was to identify subcritical and critical failure mechanisms and damage accumulation during fatigue of unidirectional glass and graphite composites. The study was accomplished by using model specimens which enabled the progressive accumulation of individual failure modes to be monitored, eliminating edge effects and tab failures usually encountered in fatigue testing of real composites. Specimens included a single bundle and a single layer of bundles embedded in either a ductile or a brittle epoxy resin. The static behavior was previously determined to have available baseline information regarding the failure mechanisms. During fatigue, failure modes were identified and correlated with material behavior. Permanent strains were measured during testing in order to assess the character of constituent fatigue failure. Fractographic analysis of fracture surfaces was carried out to locate fracture sources and to study the fracture propagation pattern.

Experimental Procedure

Materials

Two Diglycidyl ether of bisphenol A based epoxy systems were used as matrix materials. The Epon 815/Versamid 140 (60/40 by weight) formulation presents higher ductility than the Epon 828/Epon Z (80/20 by weight) formulation. However, the latter shows an ultimate strength almost twice as high as that of the former. Table 1 shows neat resin data from tension tests of the ASTM Test Method for Tensile Properties of Plastics (D 638-76) dogbone Type I specimens run at 5 mm/min. A more detailed characterization of the mechanical behavior of the resins in static and fatigue environments has been reported elsewhere [*11,12*].

Two different fibers were used. The first was E-glass 433-AE133 bundles supplied by Owens Corning Co. This has a surface finish compatible with polyester resins. The other choice was T300 graphite fibers supplied by Union

TABLE 1—*Mechanical properties of resin systems* [11,12].

Property	815/V140	828/Z
Young's modulus, GPa	2.130	3.450
Ultimate point		
stress, MPa	45.490	85.370
strain, %	4.000	5.000
Failure point		
stress, MPa	36.200	82.900
strain, %	14.000	9.000
Poisson's ratio	0.390	0.400

Carbide Co. Thus, differences in fatigue behavior between glass and graphite could be delineated and the effect of the weaker interfacial strength of the glass fibers could be assessed.

The glass bundle contains 204 fibers of nominal diameter 13 μm. It has a rectangular cross section approximately 1 mm wide and 0.2 mm thick. The graphite strand has a cylindrical cross section with a diameter of about 1.2 mm. This consisted of 3000 filaments of nominal diameter 7 μm. The bundles were used as received.

Specimens

Two different types of specimens were fabricated. One consisted of a single bundle (E-G1, SB and T300, SB) of fibers embedded in the matrix material. The other had a single layer of bundles with spacing between them approximately equal to a bundle diameter. Glass layer specimens accommodated ten bundles (E-G1, 10B) while graphite layer specimens had seven bundles (T300, 7B) due to the larger size of the graphite strand.

Dogbone Type I specimens 4 mm thick were used for single-bundle model composites. For single-layer composites, a new dogbone was designed in accordance with the recommendations of the ASTM Recommended Practice for Constant Amplitude Axial Fatigue Tests of Metallic Materials (E 466-72T). This had a gage section 30 mm long by 12 mm wide with a grip-to-gage width ratio of 3 to prevent grip failures. The bundles were centered at specimen cross section (Fig. 1).

Preparation of the single-bundle specimens was reported in Ref *13*. Single-

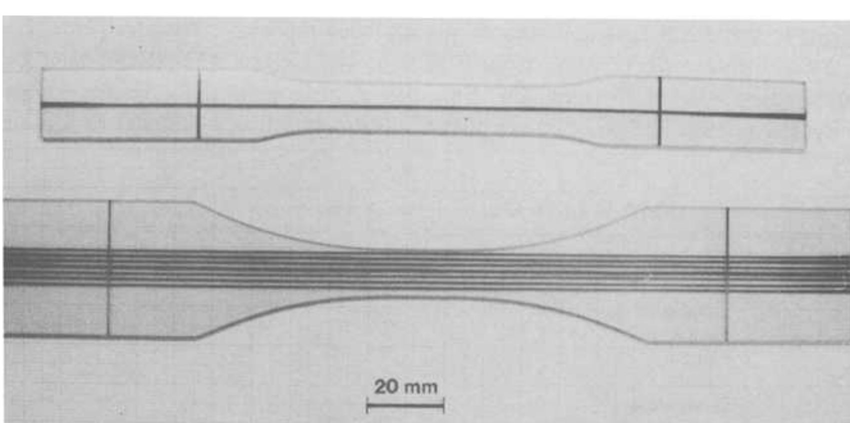

FIG. 1—*Bundle and layer model specimens of graphite fibers in ductile epoxy.*

layer specimens were similarly fabricated [14]. After preparation, specimens were stored in the laboratory environment until testing.

Test Methods

Static tests were run on an Instron machine while fatigue tests were performed on a 2000-lb (900 kg) MTS hydraulic testing machine.

Static tests were run at a crosshead speed of 5 mm/min (initial loading rate = 20 MPa/s). Load-controlled tension-tension fatigue tests were run at a constant loading rate of 100 MPa/s. The applied load had a sinusoidal waveform. The frequency was adjusted in order to maintain the same loading rate at different maximum fatigue stresses. All fatigue tests were run at a stress ratio $R = 0.1$. During testing, ambient temperature was kept constant at 24°C.

Longitudinal strains were measured by an Instron extensometer model G-51-11 with 25.4-mm gage length and 10% maximum strain. Residual elongations during fatigue were measured from the output of the linear variable differential transformer (LVDT) of the MTS machine. At regular intervals fatigue testing was stopped and the residual displacement upon complete unloading was recorded after a short recovery (2 to 4 s). This deformation was then converted to strain within the gage length by using a calibration curve established separately. Dynamic elongations were monitored throughout the test on a HP 1740A oscilloscope.

Instron grips with fine teeth were used for static tests of Type I dogbones. They were also used in fatigue tests of ductile matrix specimens. With brittle epoxy specimens, however, Instron grips with ductile aluminum plates glued on were used to prevent grip failures [12]. Single-layer specimens were tested using specially designed holders with V-wedge grips. In this case, the surface of the grips was filed down to prevent early grip failures.

During testing, specimens were monitored through a plane polariscope using white light. This helped monitor the deformation process, identify zones of accumulation of fiber failures, and detect crack initiation. Also, a portable Zeiss stereo optical microscope ($\times 8 - \times 100$) was used for microscopic inspection with normal and polarized lights. Tested specimens were microscopically inspected under normal and polarized lights on the Zeiss stereomicroscope and a Leitz optical microscope ($\times 50 - \times 200$). Fracture surfaces were examined also by a scanning electron microscope (SEM).

Different angles between the light beam and the fiber bundle were used on the stereomicroscope in order to distinguish fiber breaks, matrix cracks, and interfacial failure. Illumination along the fiber bundle allowed identification of fiber breaks, while the light beam normal to the bundle enhanced detection of interfacial damage. Microcracking of the matrix between fibers could be detected by using various angles of incidence between these two extreme positions.

Results

Bundle Specimens

Figure 2 shows typical stress-strain relations for single-bundle specimens. The static fracture process has been reported elsewhere [*13*] and will only be briefly summarized here. Results applicable to both resin systems have been condensed in Table 2. Note that static fracture of glass specimens resulted from the overload of the matrix due to bundle failure. On the other hand, in graphite specimens, fracture was the result of the bundle failure.

Fatigue tests were run at different stress levels until specimen failure or runout (completion of the first million cycles). In those cases in which imminent failure was detected, tests were interrupted before specimen fracture. Figure 3 shows

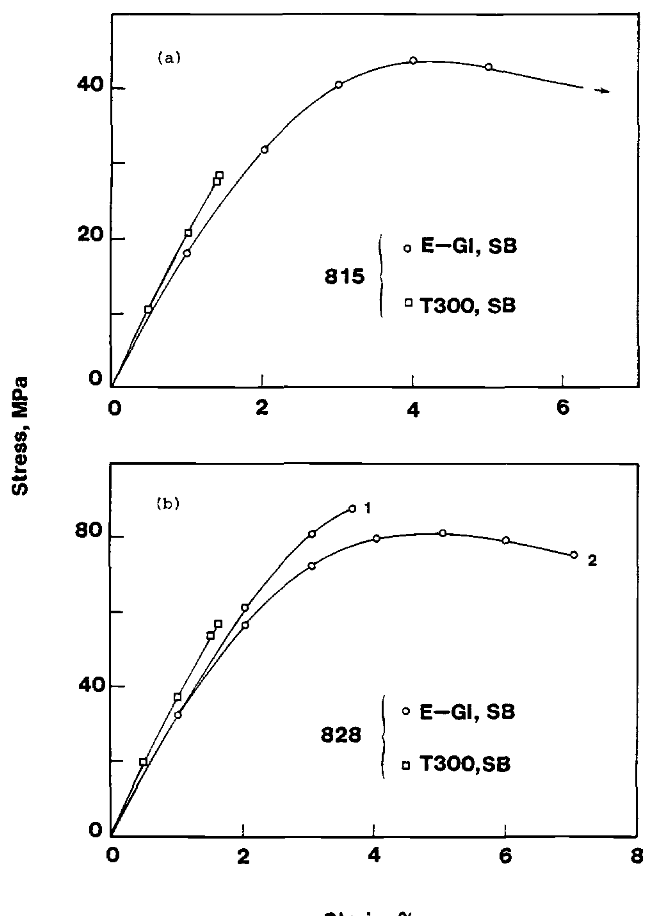

FIG. 2—*Static stress-strain relations for bundle specimens:* (a) *ductile resin;* (b) *brittle resin.*

TABLE 2—*Static failure processes of single-bundle composites.*

Fiber	Strain Level	Failure Mode
E-glass	below 2%	no fiber breaks or matrix damage
	2% to 3%	matrix microcracks among fibers normal to applied load
		isolated fiber breaks followed by interfacial failure
	3% to 3.5%	isolated zones of transverse accumulation of fiber breaks
	3.5% to 5%	transverse accumulation of fiber breaks followed by interfacial failure and matrix cracking
	above 5%	complete failure of bundle at one or more zones of clustered fiber breaks
		extensive interfacial failure and matrix cracking among fibers growing from bundle failure
		fracture of specimen by a transverse matrix nucleated in matrix
		bundle pullout and no flow of matrix
T300	below 0.8%	no fiber breaks or matrix damage
	0.8% to 1.3%	small matrix cracks along fiber/matrix interface
		scattered fiber failures
	above 1.3%	sudden transverse accumulation of fiber breaks that lead to specimen failure
		fracture source at bundle failure
		no plastic deformation of matrix
		no bundle pullout

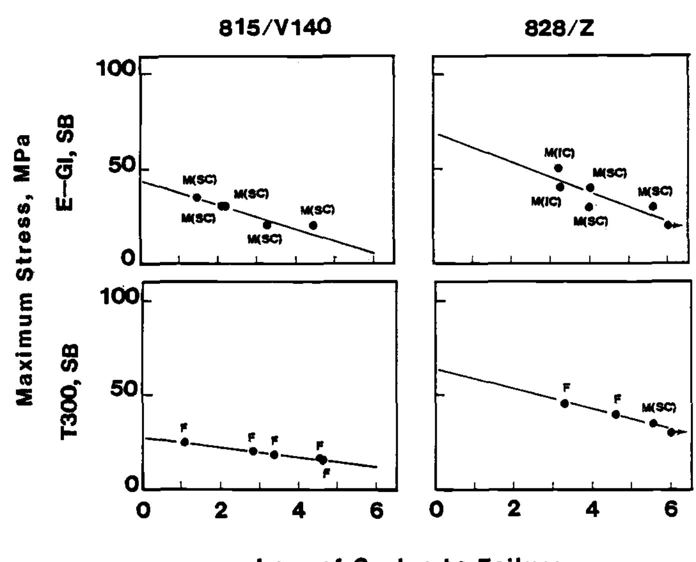

FIG. 3—*S-N relations of bundle specimens.*

S-N relations for the different materials. Also indicated in each case is the straight-line fit

$$S = S' - S'' (\log N) \tag{1}$$

where S and N are the maximum fatigue stress applied to the specimen and the number of cycles to failure, respectively, and S' and S'' are constants.

An F or an M next to each data point indicates whether specimen fracture resulted from bundle failure or a transverse crack growth in the matrix. In the latter case, initials SC and IC further stand for crack initiation at a specimen surface and within the specimen, respectively.

Table 3 summarizes the least-square estimators of S' and S''. Mean values of static strength are included for comparison as well as the fatigue stress at runout given by Eq 1 as percentages of S'.

In 815/E-G1, SB and 815/T300, SB specimens, large cycle-dependent creep strains were recorded even at low applied stresses (Fig. 4). These combined with the cyclic components exceeded the failure strain of the fibers. Pure epoxy specimens under similar loading conditions showed creep strains as high as 6% depending on applied loads [*12*]. In graphite specimens, creep strains were below these values; however, glass specimens presented larger permanent strains. Large creep strains were the result of resin necking at the point of bundle failure.

The *S-N* relation of 815/E-G1, SB specimens showed a larger rate of degradation than that of pure epoxy specimens tested at similar loading conditions [*12*]. In 815/T300, SB specimens—even though the rate of degradation is lower than that of pure epoxy specimens—there was only a very slight reinforcing effect due to the incorporation of the graphite bundle. No runouts were observed with single-bundle specimens of ductile resin while the epoxy itself was run out at a cyclic stress of about 20 MPa [*12*].

In 815/E-G1, SB specimens, fibers started to fail during cycling because of the increasing applied strain. Accumulation of fiber breaks occurred rapidly, leading finally to complete bundle failure as in the static case. Failure was not the effect of fatigue degradation of the glass fibers but rather their static overload. Final fracture of the specimens occurred at a section where the bundle had failed. At that section, matrix overload accelerated the initiation and growth of a crack

TABLE 3—*Parameters of* S-N *curves of model composites.*

Specimen	X_s, MPa	S', MPa	S'', MPa	$S(10^6)/S'$ %
815/E-G1, SB	43.25	43.48	6.40	11.68
815/T300, SB	28.02	27.35	2.60	42.96
828/E-G1, SB	80.97	68.62	7.83	31.54
828/T300, SB	57.07	62.82	5.24	49.95

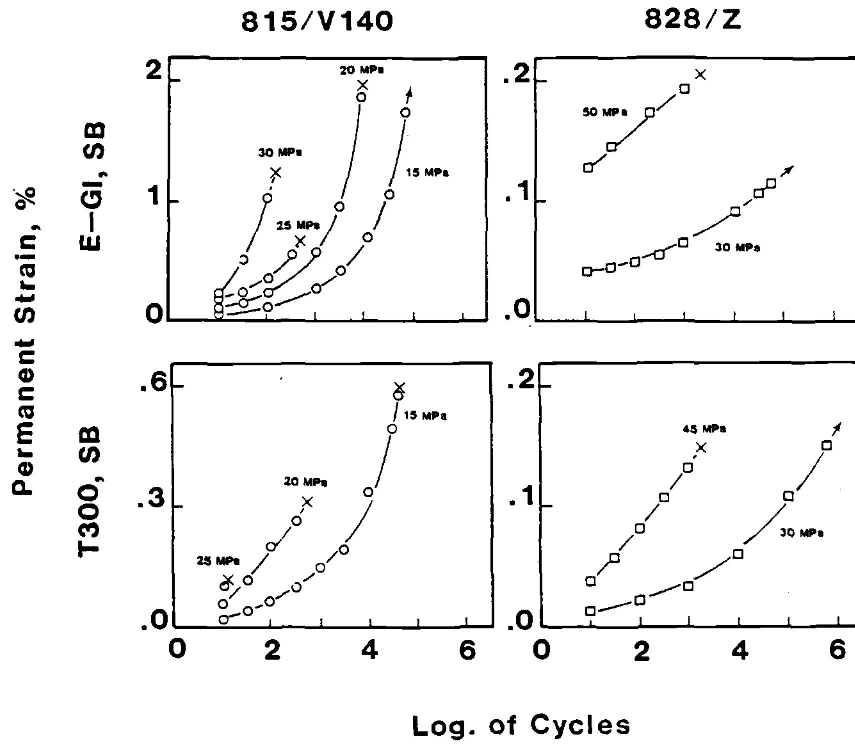

FIG. 4—*Permanent strain versus number of cycles in bundle specimens.*

normal to the applied load. As previously mentioned, localized necking was observed near the fracture region.

In 815/T300, SB, failure was also the result of static fiber breaks. In this case, lower fatigue stresses were registered in both low- and high-cycle regions due to the lower strain capability of graphite fibers compared with glass fibers. As in glass specimens, fiber breaks accumulated very suddenly in a cross section, leading to specimen fracture, the broken bundle being the fracture source. However, small zones of accumulation of fiber breaks were also observed along the bundle. It should be noted that in specimens statically tested, fiber breaks were localized only at the fracture section.

In both types of specimens, matrix cracks appeared between the fibers after the first load cycle. They were normal to the applied load and nucleated in regions of densely packed fibers. Comparative inspection under the stereomicroscope showed that the size and density of cracks were larger in glass specimens. Furthermore, in graphite specimens microcracks were preferentially at the fiber/matrix interface. In no case did these cracks grow either to fracture or to bridge the fibers.

In graphite specimens shear-assisted matrix cracks appeared at medium and low stresses next to the zones of accumulation of fiber breaks and grew from them along the fibers [9]. This type of cracking was not observed in static specimens, however.

The lack of appreciable creep in the brittle resin resulted in different failure modes. Here, creep strains were lower than those of the ductile resin specimens (Fig. 4) and close to those of pure epoxy specimens [12].

The *S-N* relation of 828/E-G1, SB followed closely that of the brittle epoxy since the addition of the glass bundle had negligible effect on specimen fracture. Specimen failure was the result of a transverse crack in the matrix that propagated cutting the bundle.

On the other hand, in 828/T300, SB specimens a reinforcing effect appeared mainly because graphite fibers reduce the load carried by the matrix, prolonging its life. In this case, failure was fiber-controlled in low-cycle specimens while a high-cycle specimen failed as a result of a matrix crack. Isolated fiber breaks were observed mostly along the graphite bundle with no zones of transverse accumulation.

Matrix microcracking was also observed in brittle resin specimens. Cracking was extensive in glass specimens while it could hardly be detected along graphite bundles. Furthermore, for a given material combination, matrix cracking was more extensive in specimens tested in the low-cycle region.

Layer Specimens

Figure 5 shows the static stress-strain relations for layer specimens. Static fracture processes are summarized in Table 4. Note that even in glass specimens creep of the matrix has disappeared, Fig. 6. As in single-bundle specimens, final

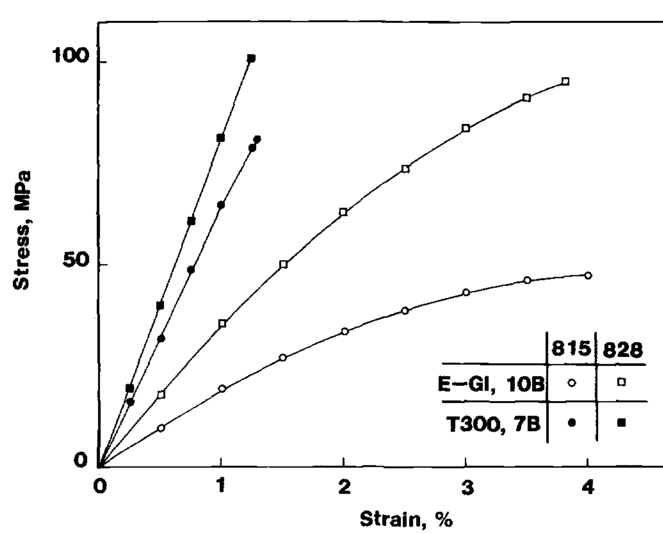

FIG. 5—*Static stress-strain relations for layer specimens.*

TABLE 4—*Static failure processes of single-layer composites.*

Fiber	Strain Level	Failure Mode
E-glass	below 1.2%	no fiber breaks or matrix damage
	1.2% to 2.5%	matrix microcracks among fibers normal to applied load
		isolated fiber breaks followed by interfacial failure
	2.5% to 3.6%	isolated zones of transverse accumulation of fiber breaks followed by interfacial failure and matrix cracking
	3.6% to fracture	transverse accumulation of fiber breaks followed by interfacial failure and matrix cracking
		complete failure of bundle at this location
		initiation of a transverse matrix crack that propagated, cutting remaining unfailed bundles, and led to specimen fracture
		bundle pullout; pullout length shorter than in single-bundle specimens
		no plastic flow of matrix
T300	below 0.8%	no fiber breaks or matrix damage
	0.8% to 1.2%	matrix microcracks along fibers
		scattered fiber breaks with no interfacial damage
		transverse accumulation of fiber breaks at several positions along bundles with no matrix cracking or interfacial failure
	1.2% to fracture	sudden transverse accumulation of fiber breaks that led to bundle failure at one location in one bundle
		initiation of unstable matrix crack with failed bundle as fracture source
		fracture of remaining bundles and specimen failure
		no plastic deformation of matrix
		no bundle pullout

fracture was the result of a crack growth in the resin accelerated by failure of a bundle. However, in layer specimens bundle failure occurred only at one section. In graphite specimens, failure of one of the bundles triggered the failure of the specimen. Here, a matrix crack originating at a failed bundle cut the remaining unfailed bundles. The aforementioned failure behavior was independent of the type of the resin.

Figure 7 shows the *S-N* relations for the different layer combinations where the straight-line fits given by Eq 1 are included. Linear regression estimators for layer specimens are listed in Table 5. The same convention used for bundle specimens was also applied in this case to identify fracture sources.

Fracture of glass specimens was the result of a transverse crack propagation in the matrix. The crack nucleated on an external surface at a section where fiber breaks started to accumulate, overloading the matrix. A region of stable crack growth surrounded the fracture source. This was limited by a boundary defining the initiation of unstable growth.

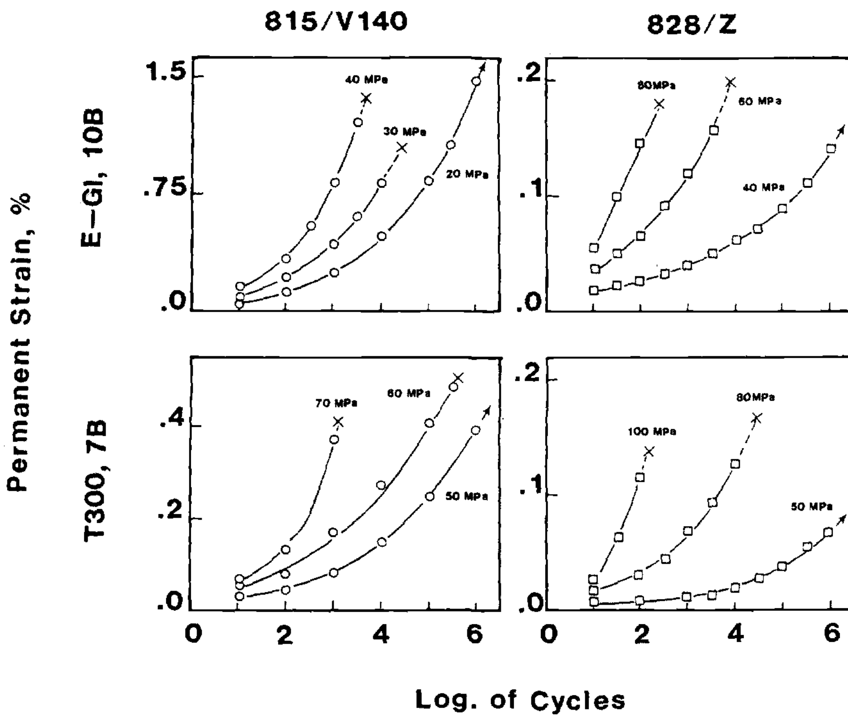

FIG. 6—*Permanent strain versus number of cycles in layer specimens.*

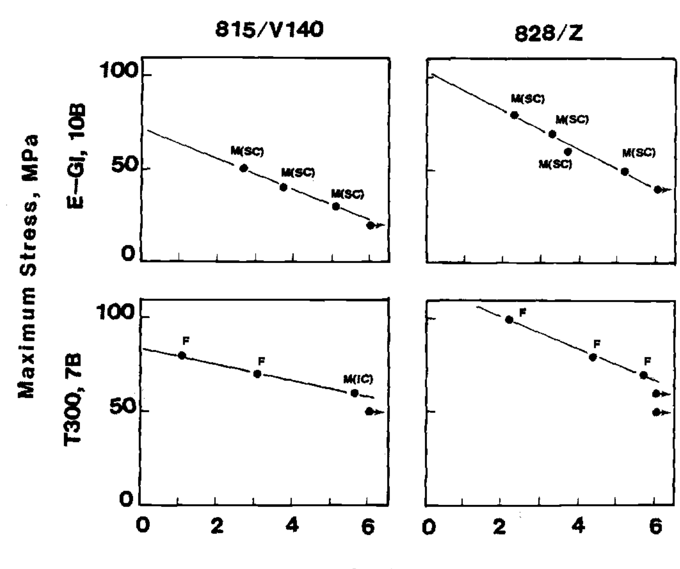

FIG. 7—S-N *relations of layer specimens.*

TABLE 5—*Parameters of* S-N *curves of model composites.*

Specimen	X_s, MPa	S', MPa	S'', MPa	$S(10^6)/S'$, %
815/E-G1, 10B	51.86	71.27	8.16	31.30
815/T300, 7B	80.96	84.36	4.39	68.79
828/E-G1, 10B	93.98	102.77	10.43	39.08
828/T300, 7B	97.56	118.08	8.52	56.71

On the other hand, fracture of graphite specimens was due to a matrix crack originating at a bundle break. As in static specimens, the stress concentration on the matrix surrounding a bundle break initiated a matrix crack that cut the remaining bundles. The fracture surface revealed no stable crack growth. The only exception to this behavior was found in one 815/T300, 7B specimen cycled at 60 MPa for 420 000 cycles. A microscopic inspection of its fracture surface revealed that a matrix crack originated at an impurity within the matrix next to a zone of accumulation of fiber breaks.

Fiber breaks were detected along the glass and graphite bundles in ductile and brittle resin specimens. For a given reinforcement, the ductile resin specimen presented a larger number of fiber breaks than the brittle resin specimen cycled at the same initial strain level. This was also the case in specimens statically tested where fewer fiber breaks resulted in fewer acoustic emissions [*14*].

In 815/E-G1, 10B specimens tested at 40 and 50 MPa, isolated fiber breaks appeared during the first load cycle. Upon further cycling, more fibers failed randomly along the bundle and zones of transverse accumulation of fiber breaks appeared. Figure 8 shows such a zone where it is also possible to distinguish the interfacial damage that extended away from the fiber failures. The interfacial yielding grew along the fibers during cycling.

Similar specimens tested at 20 and 30 MPa showed only a few isolated fiber breaks that appeared during cycling. No fiber breaks were detected after the first load cycle in these specimens. Also, interfacial damage was not so extensive as in the specimens cycled at higher stresses.

In 828/E-G1, 10B specimens, a similar fracture sequence was observed. Fiber breaks started to accumulate during the first load cycle in specimens tested at high stresses (70 and 80 MPa). Thereafter, fiber breaks accumulated at one or more sections, and the specimen fracture followed. At medium stresses (60 and 50 MPa), isolated fiber breaks appeared during cycling. In the runout specimen, no fiber breaks were detected along the bundles.

Brittle resin specimens cycled at medium and high stresses showed interfacial damage in the form of debonding extending from the broken fiber ends. This was more extensive at higher stresses. However, debonding did not grow much during cycling.

Matrix microcracks were observed between the glass fibers in ductile and brittle-resin specimens at all stress levels. More extensive microcracking occurred

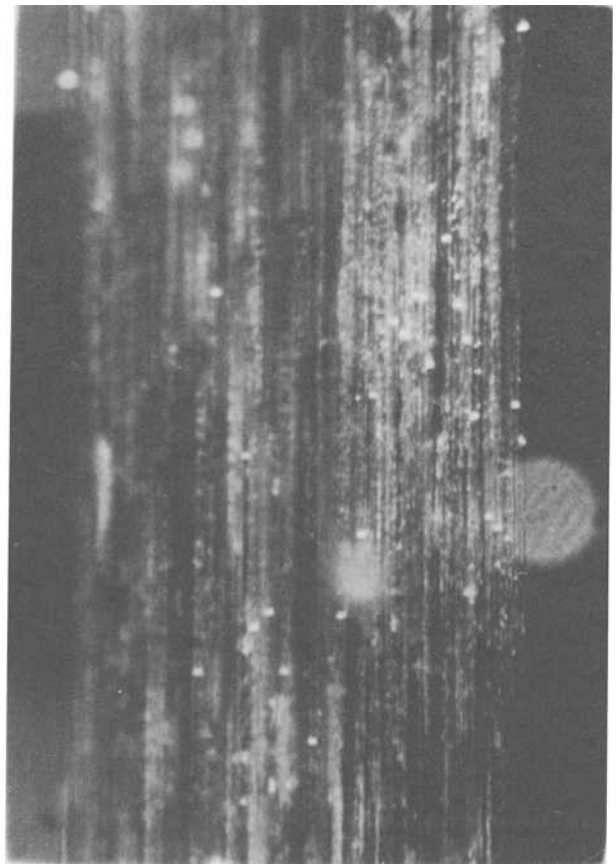

FIG. 8—*Accumulation of fiber failures in 815/E-G1, 10B specimen cycled at 40 MPa. White dots are fiber breaks. Note interfacial damage growing from the zone of accumulation of fiber failures.*

in the specimens tested at medium cyclic stresses. Microcracks appeared normal to the applied load in regions where fibers were closely packed. They were similar to those observed in static specimens. No growth or coalescence of these cracks into a main crack was observed. Rather, they remained stable or, unlike the static case, grew by Mode II in the matrix along the fibers. Figure 9 shows a microcrack lying in a polished cross section of a static 828/E-G1, 10B specimen, Here, the crack surface is normal to the fibers. On the other hand, Fig. 10 shows a side view of a polished bundle in an 828/E-G1, 10B specimen cycled at 50 MPa. Here, the microcrack nucleated at the fiber/matrix interface, and has turned and started to grow in the matrix along the fibers.

Graphite specimens also presented fiber breaks along the bundles. As in glass specimens, the graphite bundles embedded in the ductile resin showed more fiber breaks at the same strain level than those embedded in the brittle resin.

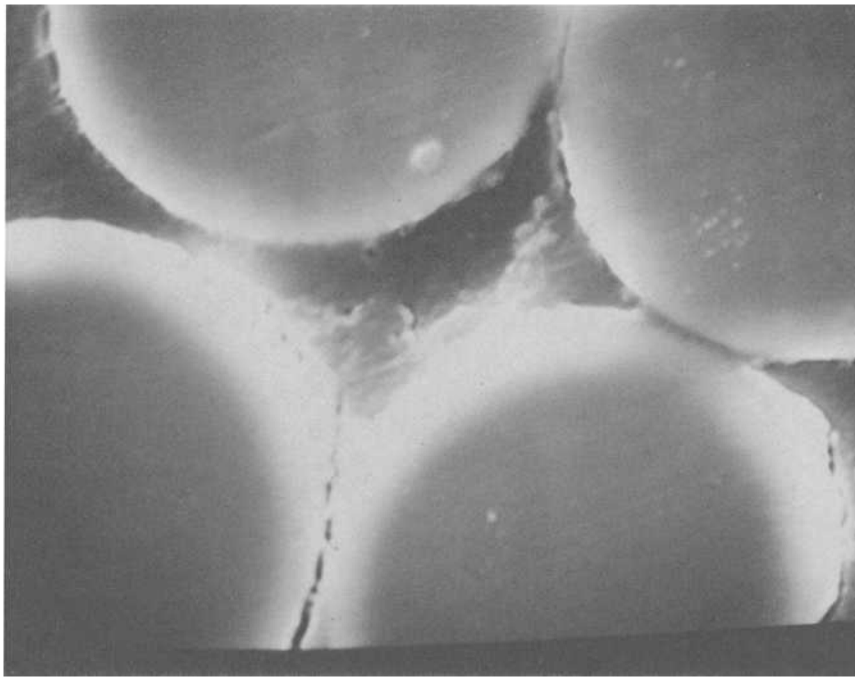

FIG. 9—*Scanning electron microscope (SEM) photomicrograph of a matrix microcrack in a polished cross section of statically tested 828/E-G1, 10B. The plane of the crack is normal to the fibers and the applied load* (×*5000*).

At high stress levels, zones of transverse accumulation of fiber breaks were observed in both ductile- and brittle-resin specimens. The accumulation occurred rapidly, and the specimen fracture followed in a few loading cycles. Figure 11 shows localized zones of fiber breaks along the graphite bundles in these specimens.

At medium stresses, isolated fiber breaks appeared during cycling. Upon further cycling fiber breaks accumulated at several points along the bundles. Figure 12 shows two zones of fiber breaks in graphite bundles embedded in the ductile resin. Unlike Fig. 11*a*, the matrix cracking here has progressed along the fibers away from the broken ends. This type of cracking was seen to originate at the larger zones of fiber breaks probably because of the high shear stresses imposed on the matrix. At points where only a few fiber breaks were close together, no matrix cracking was observed.

Brittle-resin specimens tested at medium stress levels showed only isolated fiber breaks without large zones of accumulation. Also, no shear-assisted matrix cracking, as observed in the ductile matrix, could be found along the bundles.

Runout specimens of both resins showed a few isolated fiber breaks without any accumulation across the bundles.

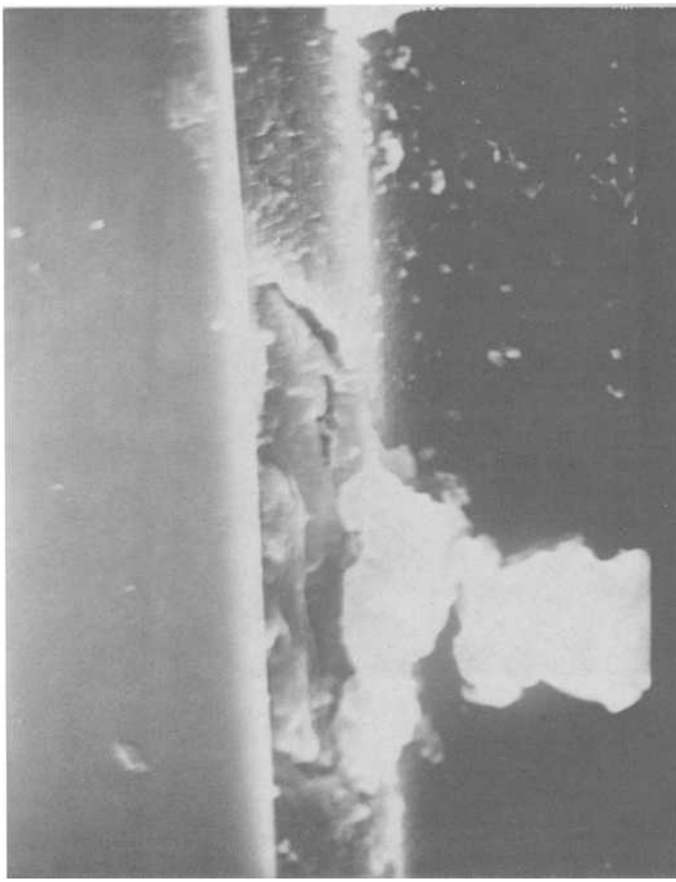

FIG. 10—*SEM photomicrograph of shear growth of a microcrack in an 828/E-G1, 10B specimen cycled at 50 MPa (×3500).*

Matrix microcracking was also present between graphite fibers. Figure 13 shows glass and graphite bundles where microcracks can be seen. As in glass specimens, microcracking was more extensive at medium stress levels. Comparison of the cracks in glass and graphite bundles under the stereomicroscope indicated larger crack size in glass specimens.

Discussion

In order to compare the behavior of the different specimens tested, a strain-life diagram was obtained (Fig. 14). Here, the maximum strains were obtained by dividing the maximum cyclic stresses by the corresponding longitudinal moduli obtained in static tests [*14*]. Since the effect of loading rate was neglected [*11,12*],

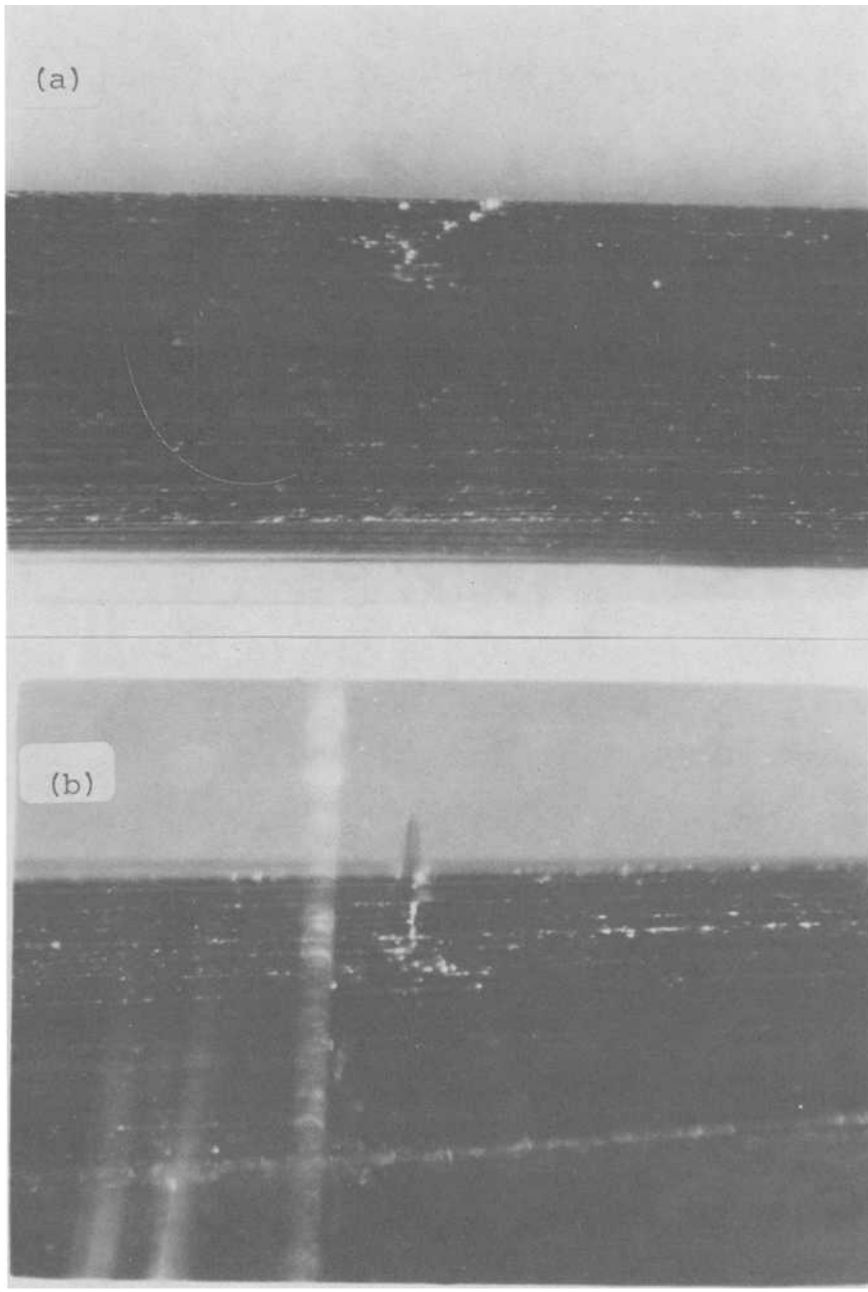

FIG. 11—*Accumulation of fiber breaks in graphite bundles at high stress levels.* (a) *815/T300, 7B:* S = *80 MPa,* N = *12 cycles* (×*100*). (b) *828/T300, 7B:* S = *100 MPa,* N = *144 cycles* (×*100*).

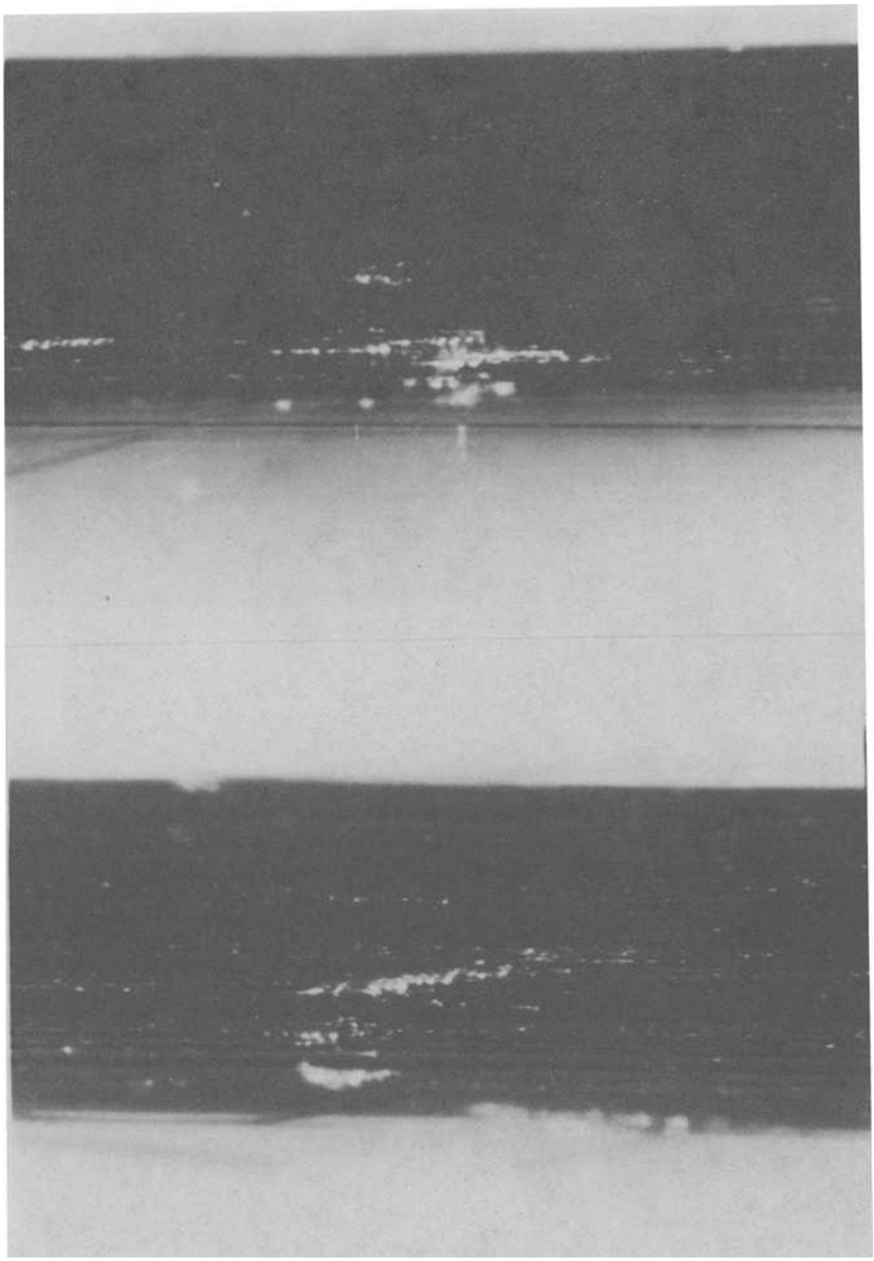

FIG. 12—*Accumulation of fiber breaks in graphite bundles embedded in ductile resin at medium stress level* S = *60 MPa* (×*100*). *Note matrix cracking growing from the fiber failures.*

the calculated strains overestimate the actual strains applied. Only layer specimens have been considered in this diagram because the failure of bundle specimens involved considerable creep.

Strain-life relations for each fiber type follow closely the same trend independent of the matrix material. Straight-line fits of the data are indicated in the figure for each fiber type. Based on the linear fits, a fatigue degradation of 67% over one million cycles is registered in the glass specimens while only 35% occurs in graphite specimens over the same number of cycles.

In Fig. 14 three regions are indicated which characterize the failure behavior previously described. In Region I, with strains larger than 2% and 1.1% in glass and graphite specimens, respectively, fatigue failure resembles static failure. Fiber breaks appear during the first loading cycle and accumulate very rapidly leading to specimen fracture.

In Region II the failure process is progressive. A few fiber breaks and matrix microcracks appear initially but they are not critical. Upon further cycling, damage accumulates slowly; more microcracks, isolated fiber failures, and zones of transverse accumulation of fiber breaks across the bundles appear. The amount of damage suffered by the fibers depends on the applied strain: the higher the strain, the more microcracks and fiber breaks. Brittle-resin specimens show fewer isolated fiber breaks and fewer zones of fiber break accumulation with less interfacial degradation. Thus, stress concentration is more effective in breaking neighboring fibers in the brittle resin.

Region III corresponds to runouts. Only a few scattered fiber breaks are seen with little matrix microcracking. During cycling damage progression is very slow.

Restrictions imposed by the fibers to the matrix deformation are suspected to be one of the reasons why matrix cracks occur at lower strains than would be expected from the bulk behavior. In uniaxial testing of neat ductile epoxy specimens, cracks nucleated around a strain of 14%. In that case, the state of stress is almost uniaxial with a triaxial state of strain due to Poisson's effect. However, the matrix between fibers in a composite is subjected to a highly triaxial state of stress which results in a more uniaxial state of strain in the direction of fibers than in the neat resin. The components of strain in a cross section normal to the fibers are on average only about 10% of the longitudinal strain.

To investigate the effect of the state of strain upon epoxy failure strains, ductile epoxy specimens with a gage section 12 mm long by 71 mm wide were prepared with three different thicknesses. The epoxy specimens were glued to steel plates which were connected by one pin to the testing machine. Tension load was transmitted to the specimen mainly by shear stresses through the adhesive layer with no transverse pressure at the grips. Tests were run at a loading rate of 5 mm/min. Results in Fig. 15 show that failure strains are reduced considerably as the uniaxial state of strain is approached. For the largest thickness tested, the failure strain amounts to only 0.70%.

Total strains during fatigue exceeded at least 0.80% for all material combi-

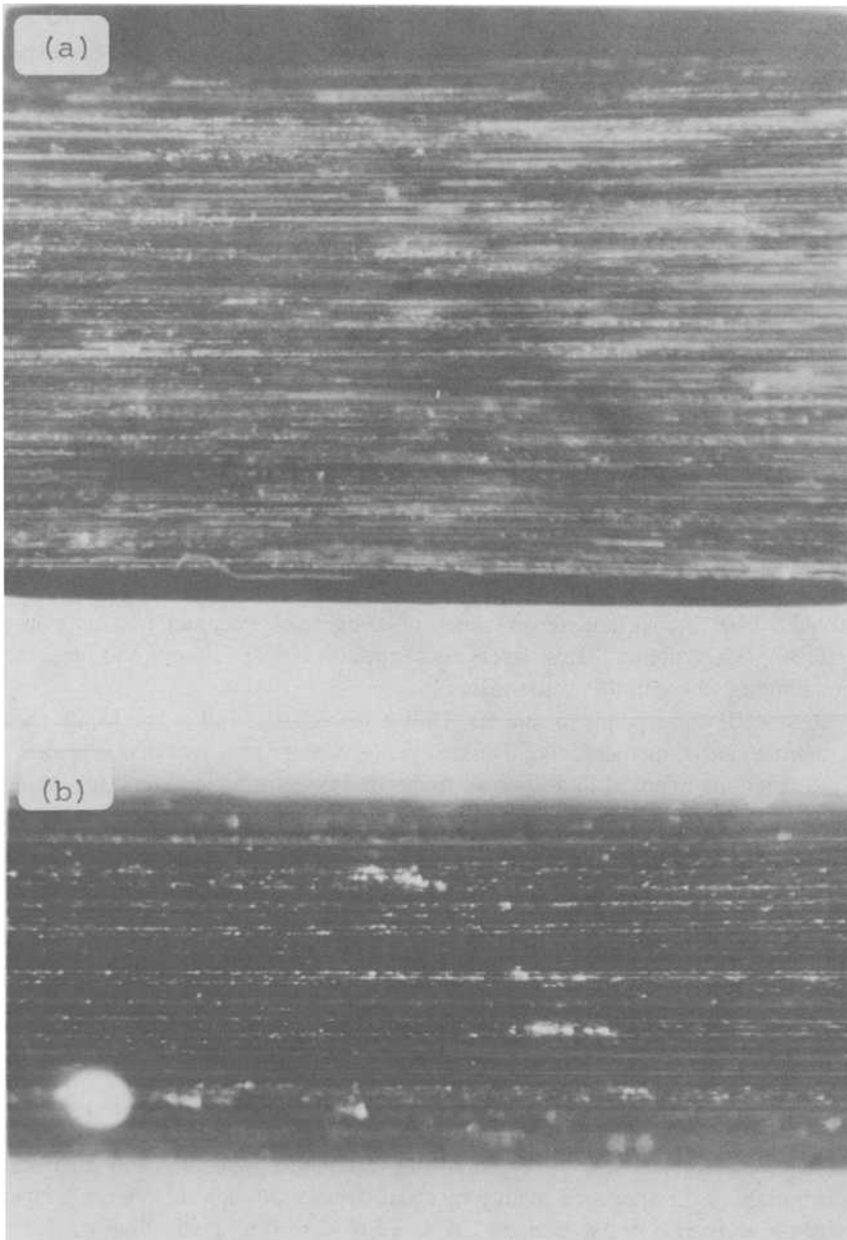

FIG. 13—*Matrix microcracks in layer specimens.* (a) *815/E-G1, 10B:* S = *30 MPa,* N = *28 000 cycles* (×*100*). (b) *815/T300, 7B:* S = *60 MPa,* N = *417 353 cycles* (×*100*). (c) *828/T300, 7B:* S = *80 MPa,* N = *23 607 cycles* (×*100*).

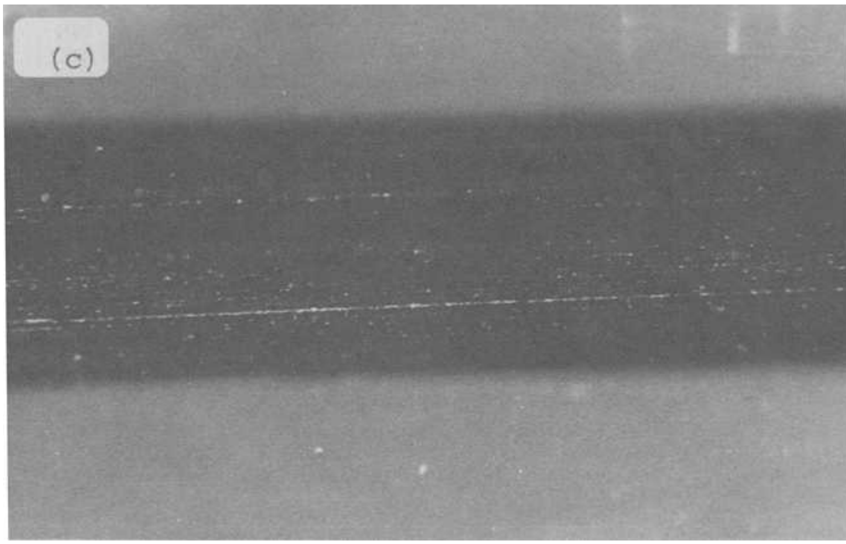

FIG. 13—*Continued.*

nations [*14*]. Thus, uniaxial strain conditions promoting matrix cracking between fibers are believed to exist in composites.

Despite the incorporation of several bundles, none of the layer specimens show stable growth of matrix cracks between bundles. As suggested in Ref *8*, the maximum microcrack dimension is of the order of a fiber diameter. The reason is that since the crack opening displacement is constrained by the fibers, there is not much driving force to extend microcracks. Moreover, the higher stiffness of graphite fiber allows lower stresses to be carried by the matrix, and hence smaller cracks are observed in graphite specimens.

The lack of matrix cracks on the external surfaces of actual composite specimens under fatigue [*8,10*] can be explained by the difference between the state of stress inside the composite and that in the surface layer. As explained previously, a uniaxial state of strain exists in the matrix between the fibers inside the composite. However, the surface layer is two to three fiber diameters thick and is primarily under a uniaxial state of stress. Thus, a larger stress is required to nucleate a crack on the external surface than inside the composite.

Conclusions

The following conclusions can be drawn from the present study:

1. Fatigue failure of glass and graphite fibers was observed with a larger fatigue degradation in glass. Fewer fiber breaks and fewer zones of transverse

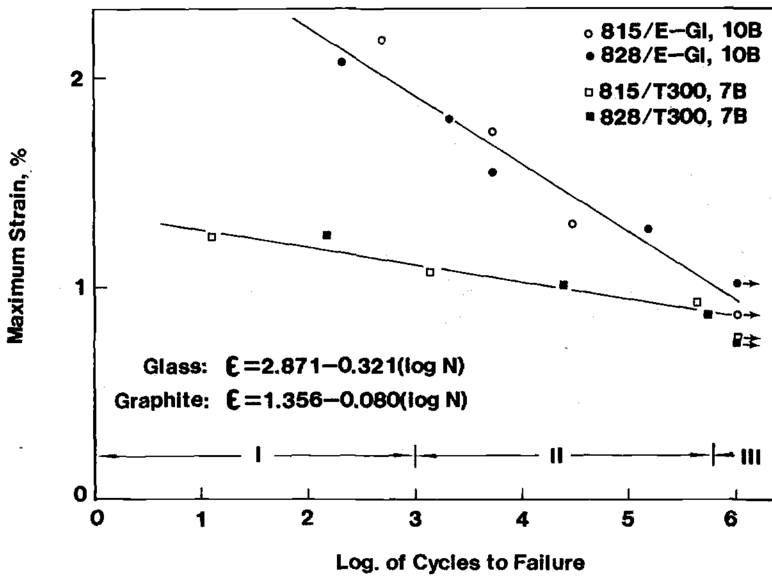

FIG. 14—*Strain versus life relations of layer specimens. Data points are based on static longitudinal moduli.*

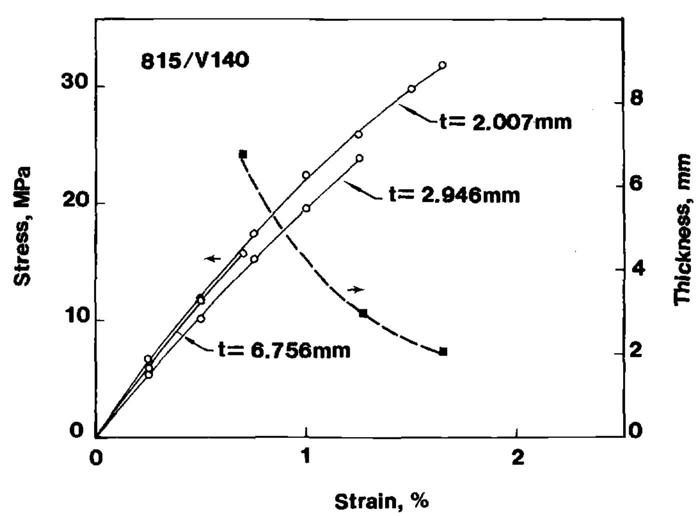

FIG. 15—*Static stress-strain relations of ductile epoxy specimens of different thicknesses resembling uniaxial strain loading conditions.*

accumulation of fiber breaks appeared in brittle-resin specimens. Yet, the ductility of the resin has negligible effect on the fatigue degradation of the fibers.

2. Extensive matrix cracking normal to fibers appeared along glass and graphite bundles as a result of the lower strain capability of the resin under the state of stress prevalent between the fibers. In ductile-resin specimens matrix cracking was more extensive. The growth of matrix damage along the fibers was induced by high shear stresses and was more extensive in ductile-resin specimens because of the lower strength of the matrix. In graphite specimens matrix cracks grew only from large zones of accumulation of fiber breaks. In glass bundles, microcracks joined with interfacial failure to grow in a shear mode.

3. No matrix cracks grew normal to the applied load because the crack opening displacement was limited by the fibers. Yet, the effect of these cracks on fracture of the adjacent fibers needs to be better understood.

4. In unidirectional composites, fiber break and matrix cracking will be the dominant failure mechanisms during fatigue. Since matrix cracks are not deleterious to the fibers, a fiber-dominated fracture is prone in both glass and graphite composites. In high-strain composite systems such as glass composites, however, extensive longitudinal splitting is likely due to the growth of microcracks along the fibers.

Acknowledgments

This paper is based on work supported by the National Science Foundation through Grant No. MEA-8110777 with Clifford J. Astill as program director.

References

[1] Dharan, C. K. H. in *Fatigue of Composite Materials, ASTM STP 569*, American Society for Testing and Materials, Philadelphia, 1975, pp. 171–188.
[2] Dharan, C. K. H., *Journal of Materials Science*, Vol. 10, 1975, pp. 1665–1670.
[3] Mandell, J. F., Huang, D. D., and McGarry, F. J., *Composite Technology Review*, Vol. 3, 1981, pp. 96–102.
[4] Sturgeon, J. B. in *Proceedings*, 28th Annual Technical Conference, The Society of the Plastics Industry, 1973, Section 12-B, pp. 12–13.
[5] Awerbuch, J. and Hahn, H. T. in *Fatigue of Filamentary Composite Materials, ASTM STP 636*, American Society for Testing and Materials, Philadelphia, 1977, pp. 248–266.
[6] Hahn, H. T. in *Composite Materials: Testing and Design (Fifth Conference), ASTM STP 674*, American Society for Testing and Materials, Philadelphia, 1979, pp. 383–417.
[7] Talreja, R., *Proceedings of the Royal Society of London*, Series A, Vol. 378, 1981, pp. 461–475.
[8] Hahn, H. T., "A Synergistic Effect in Fatigue of Composites," presented at the American Society of Mechanical Engineers Winter Annual Meeting, 1983, unpublished.
[9] Hahn, H. T. and Lorenzo, L. in *Proceedings*, Sixth International Conference on Fracture, New Delhi, India, 1984, Vol. 1, pp. 549–568.
[10] Hahn, H. T., Hwang, D. G., Chin, W. K., and Lo, S. Y., "Mechanical Properties of a Filament-Wound S2-Glass/Epoxy Composites for Flywheel Application," UCRL-15635, Lawrence Livermore Laboratory, Livermore, CA, March 1982.
[11] Hollmann, K., "Acoustic Emission Behavior of Epoxies During Tensile Loading," M.Sc. Thesis, Department of Mechanical Engineering, Washington University, St. Louis, MO, Dec. 1983.

[*12*] Lorenzo, L. and Hahn, H. T., "Effect of Ductility on the Fatigue Behavior of Epoxy Resins," to be published in *Polymer Engineering and Science*.
[*13*] Lorenzo, L. and Hahn, H. T. in *Proceedings*, First International Symposium on Acoustic Emission from Reinforced Plastics, The Society of the Plastics Industry, 1983, Session 2, pp. 1–13.
[*14*] Lorenzo, L., "Fatigue Failure of Unidirectional Composites and its Acoustic Emission Characterization," D.Sc. Thesis, Department of Mechanical Engineering, Washington University, St. Louis, MO, May 1985.

Alton L. Highsmith[1] *and Kenneth L. Reifsnider*[2]

Internal Load Distribution Effects During Fatigue Loading of Composite Laminates

REFERENCE: Highsmith, A. L. and Reifsnider, K. L., "**Internal Load Distribution Effects During Fatigue Loading of Composite Laminates,**" *Composite Materials: Fatigue and Fracture, ASTM STP 907,* H. T. Hahn, Ed., American Society for Testing and Materials, Philadelphia, 1986, pp. 233–251.

ABSTRACT: Two fundamental processes govern the reduction of strength and stiffness of composite laminates caused by cyclic loading, commonly called the "fatigue effect." One process is the reduction of the strength and stiffness of the individual constituent materials in the composite, caused by events such as localized nonconservative deformation, microcrack formation, and substructure variations. This process is essentially the source of the "fatigue effect" homogeneous materials, except that macrocrack formation and fracture dominated by a single crack generally does not occur as a consequence of this process in composite materials. In laminated composites there is another fundamental process which plays a major role in determining residual properties. That process is the damage-dependent redistribution of load sharing among the plies of the laminate caused by the continuous variation of the elastic stiffness properties of each ply induced by microdamage development in those plies. Experience suggests that this process is critical and, in some cases, dominant in the determination of the residual strength and life of a laminate under cyclic loading. This paper addresses the experimental and analytical aspects of this fundamental process. The results of the present work indicate that strain (and stress) redistributions in regions of highly localized damage are large and significant. The general nature of these redistributions has been established, which provides the first firm foundation for the formulation of the philosophy needed to interpret these physical damage states in terms of residual strength and life.

KEY WORDS: composite materials, laminates, fatigue, localization process, transverse (matrix) cracking, delamination, stress redistribution, characteristic damage state

The rate of growth of the use of composite materials in engineering components has exceeded the predictions of nearly everyone. The breadth of applications is equally surprising, ranging from medical prosthetic devices to sports equipment to automotive parts, including heavy-duty springs and pistons, to high-performance aircraft structures. The safety and reliability of these components depends

[1] Assistant professor of aerospace engineering, Texas A&M University, College Station, TX 77843.
[2] Reynolds Metals professor of engineering science and mechanics, Materials Response Group, Virginia Polytechnic Institute and State University, Blacksburg, VA 24061-4899.

on the long-term strength, stiffness, and life of the composite materials from which they are made under conditions which usually involve loads that vary in time. Despite this fact, there is no general model or even a cogent philosophy based on physical observations of microdamage that can be used to predict the residual strength of such materials under long-term fatigue loading. Such a mechanistic model must be based on a well-defined generic damage pattern which controls the initiation of the final fracture event. The authors, and their colleagues in the Materials Response Laboratory at Virginia Tech, have identified what is believed to be one such pattern which is thought to control the local stress state that initiates the final fracture event under tension loading for many common polymeric matrix multiaxial composite laminates subjected to fatigue damage caused by tension and compression loading [*1*]. A fundamental mechanics problem associated with this problem is discussed in this paper. It is the problem of two cracks, one in each of two orthotropic plies of a laminate, which cross at a point on the interface between the plies as a result of the difference in orientation of the two plies. The question of the nature of the stress state in the region of the intersection is addressed in this paper.

Analysis

The analysis used in this investigation is based on a structural theory developed by Pagano [*2*]. This structural theory was developed by assuming that the in-plane stresses for a layer of material vary linearly through the thickness of the layer. Equilibrium considerations determine the order of the variations through the thickness of the remaining stress components. Substitution of these functional forms for the stresses in Reissner's variational principle yields a system of 23 algebraic and linear first-order partial differential equations in the two in-plane coordinates that describe the constitutive behavior, equilibrium conditions, and interlaminar continuity conditions for a single layer. In addition, the seven conjugate pairs of boundary conditions that must be specified at each edge are determined. The dependent variables are force, moment, and shear resultants, interlaminar stresses, and through-the-thickness weighted averages of displacements for a layer. A brief description of the crossed-crack problem and the solution technique is presented below. A more detailed description will appear in another paper.

The specific problem under consideration here is that of a $[0,90_2]_s$ graphite/epoxy laminate with uniformly distributed transverse cracks in the 90-deg plies and uniformly distributed longitudinal splits in the 0-deg plies subjected to a unidirectional tension load. Both sets of matrix cracks are assumed to be infinite in length in the fiber directions of their respective plies. The transverse cracks are spaced every $2a$ units, while the longitudinal splits are spaced every $2b$ units. For simplicity, the cracking is assumed symmetric about the midplane. The laminate stress state can be characterized by one quadrant of the volume bounded by planes through two adjacent transverse cracks and two adjacent longitudinal splits. One such quadrant is shown schematically in Fig. 1. In the analysis, only half of the quadrant, which is symmetric about the midplane, was considered.

One half of the $[0,90_2]_s$ laminate was modeled as two layers—an interior 90-deg ply of thickness $2h$, and an exterior 0-deg ply of thickness h. The application of stress-free conditions at the outer surface, stress and displacement continuity of the interface, and symmetry about the midplane reduces the number of equations to 38. The elimination of algebraic equations further reduces the governing equations to a system of 32 linear first-order partial differential equations and 32 unknowns. This system can be written in matrix form as

$$\left([X]\frac{\partial}{\partial x} + [Y]\frac{\partial}{\partial y} + [C]\right)\{u\} = \{0\} \tag{1}$$

where $\{u\}$ represents the set of dependent variables. By applying the coordinate transformations

$$r = \frac{2x}{a} - 1$$

$$s = \frac{2y}{b} - 1$$

Eq 1 becomes

$$\left([X]\,(2/a)\frac{\partial}{\partial r} + [Y]\,(2/b)\frac{\partial}{\partial s} + [C]\right)\{u\} = \{0\} \tag{2}$$

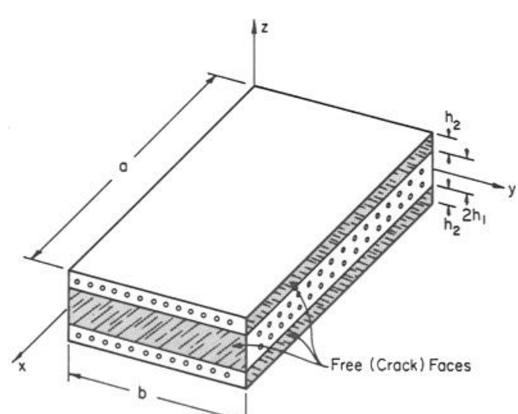

FIG. 1—*Schematic representation of the idealized crossed crack problem.*

In addition, a total of 44 edge-type boundary conditions must be satisfied.

In order to obtain an approximate solution to the problem described above, the following for m for $\{u\}$

$$\{u\} = \sum_{i=0}^{m} \sum_{j=0}^{n} [\{u\}_{ij} \, T_i(r) \, T_j(j)] \tag{3}$$

where $T_k(q)$ is a Chebyshev polynomial in q of order k, is substituted into Eq 2 and into the boundary conditions. Here a few comments about Chebyshev polynomials are in order. The Chebyshev polynomials are a set of orthogonal polynomials on the interval $[-1,1]$ with respect to the weight function $[1 - q^2]^{-1/2}$. That is

$$\int_{-1}^{1} [1 - q^2]^{-1/2} \, T_i(q) T_j(q) \, dq = 0 \text{ if } i \neq j$$

The effect of the term $[1 - q^2]^{-1/2}$ is then to bias the inner product so that the boundary regions are given extra importance. This feature is ideal for the solution of boundary-layer problems, as is the one under consideration here. The first five Chebyshev polynomials are

$$T_0(q) = 1$$

$$T_1(q) = q$$

$$T_2(q) = 2q^2 - 1$$

$$T_3(q) = 4q^3 - 3q$$

$$T_4(q) = 8q^4 - 8q^2 + 1$$

The derivative of a Chebyshev polynomial can be expressed in terms of lower-order Chebyshev polynomials. Upon substitution of Eq 3 into Eq 2, grouping terms involving identical-order polynomials are both r and s, and setting each of these coefficients to zero simultaneously, a set of $32(m + 1)(n + 1)$ algebraic equations is obtained. Upon substituting Eq 3 into the boundary conditions, a set of $22(m + n + 2)$ algebraic equations is obtained. Since there are only $32(m + 1)(n + 1)$ coefficients in the expansion for $\{u\}$, this complete system of algebraic equations is overdetermined.

What remains is to solve a linear least-squares problem in order to get a "best approximation" to the coefficients in the expansion for $\{u\}$. In order to insure that the boundary conditions are satisfied, the algebraic equations developed from the boundary conditions are multiplied by a large constant. The solution technique uses a series of orthogonal transformations to transform the overdetermined system of equations into an upper triangular form. The solution of this set of upper triangular equations is in fact the least-squares solution for the overdetermined system [3].

The material under consideration was graphite/epoxy. The following material properties were used:

$$E_{11} = 130 \text{ GPa} \qquad E_{22} = 9.72 \text{ GPa} \qquad E_{33} = 9.72 \text{ GPa}$$

$$\nu_{12} = 0.308 \qquad \nu_{13} = 0.308 \qquad \nu_{23} = 0.492$$

$$G_{12} = 5.39 \text{ GPa} \qquad G_{13} = 5.39 \text{ GPa} \qquad G_{23} = 3.25 \text{ GPa}$$

The lamina thickness used was $h = 0.127$ mm. The crack spacing in the 90-deg plies was $2a = 0.635$ mm and in the 0-deg plies, $2b = 1.59$ mm. The applied axial strain was 1.0%. Chebyshev polynomials of order 5 and higher were dropped from the series expansion (that is, $m = n = 4$ in Eq 3).

Experimental Procedure

A panel of $[0,90_2]_s$ graphite/epoxy was fabricated from Hercules A5/3501-6 prepreg tape. The scrim cloth ordinarily used as a mild release leaves a cloth-textured impression in the surface of the cured panel. Such a surface is not well suited to the application of a diffraction grating and subsequent moiré measurements. In order to obtain a smooth surface, a sheet of trifluoroethylene was used as a mold release on one side of the panel. Specimens 254 mm long and 25.4 mm wide were cut from the panel. The nominal thickness was 0.81 mm.

Tension-tension fatigue loading was used to develop damage in the specimens. Specimens were cycled at 10 Hz with a maximum stress of $0.8\sigma_{ult}$ [$\sigma_{ult} = 634$ MPa] and a stress ratio of $R = 0.1$. A 50.8-mm clip-on type extensometer was attached to the specimen and, during cycling, a microcomputer was used to monitor dynamic secant modulus. Jamison [4] has observed that the secant stiffness history of a $[0,90_2]_s$ laminate provides a good indication of the damage development within the laminate. Secant stiffness was used as a control parameter such that when a specified decrease in stiffness was achieved, the test was halted. Penetrant-enhanced X-ray radiography was then used to verify that the desired damage state had in fact been attained.

After cyclic loading, a diffraction grating was applied to the smooth surface of each specimen. The diffraction gratings used here were crossed gratings, and had a frequency of 1200 lines/mm. These gratings were produced by exposing a photographic plate to two beams of collimated coherent light that intersect at a particular angle [5]. The two beams of light interfere with each other such that exposed and unexposed regions of the photographic plate effectively form a grating of the desired frequency. Two such patterns at right angles to each other constitute a crossed grating. After the photographic plate is developed, the different shrinkage properties of exposed and unexposed photographic emulsion results in a set of ridges furrows in the surface which form a phase grating. This surface is treated with a Kodak Photo-Flo 200 solution, sputter-coated with aluminum, and then used as a mold for a plate grating. The specimen is "bonded" to the grating using an epoxy adhesive. After the epoxy has cured, the photographic plate is removed, and an impression of the surface is left in the epoxy which is attached to the specimen. The aluminum is transferred with the epoxy and increases the reflectivity of the grating.

Moiré interferometry was then used to measure nonuniform deformation near damage events. The moiré technique involves interfering two collimated, coherent beams of light that are diffracted by a grating on the specimen [*5*]. Deforming the specimen changes the frequency of the grating, and thus the orientation of the two diffracted beams. The interference of these two beams results in a fringe pattern, where the fringes are contours of constant relative displacement. The moiré apparatus used in this investigation is shown schematically in Fig. 2. The series of elements up to the collimating mirror (6) provides a beam of collimated, coherent light. A beamsplitter (7) is used to divide this beam into two parts. Part of the beam passes through the beamsplitter and is reflected by a mirror (8H) and is directed toward the specimen-mirror assembly. Part of this beam is diffracted by the specimen (10) directly, and part of this beam is reflected onto the specimen by a mirror (9H). These two diffracted beams are collected by the camera lens (11). The associated interference pattern provides contours of transverse displacements. The beamsplitter (7) also directs a beam of light to an identical collection of elements (8V, 9V, and 10). This second light path is used to determine longitudinal displacement contours. Thus, the system shown is capable of measuring both in-plane displacements. For this particular configuration, resolution is 2400 fringes per millimetre of displacement.

Results and Discussion

During the fatigue life of a $[0,90_2]_s$ graphite/epoxy laminate, several stages of damage development can be identified. The first stage is the development of the characteristic damage state (CDS). For this relatively simple laminate, the CDS consists of a set of uniformly spaced transverse cracks in the 90-deg plies. These cracks extend through the thickness of all four interior plies. The next stage of interest is the development of longitudinal splits in the 0-deg plies. (We will ignore the development of fiber fractures for the purpose of this discussion.) The first of these splits develop near the specimen edge. Small strips of 0-deg material near the edge break away from the bulk of the laminate, and effectively carry no load. This process is reflected by a sudden decrease in specimen stiffness. Eventually, longitudinal splits also develop in the interior of the laminate, and grow along the laminate length. After sufficient growth of these longitudinal splits, small interior delaminations develop near crossing points of longitudinal splits and transverse cracks [*4*]. These internal delaminations grow with continued

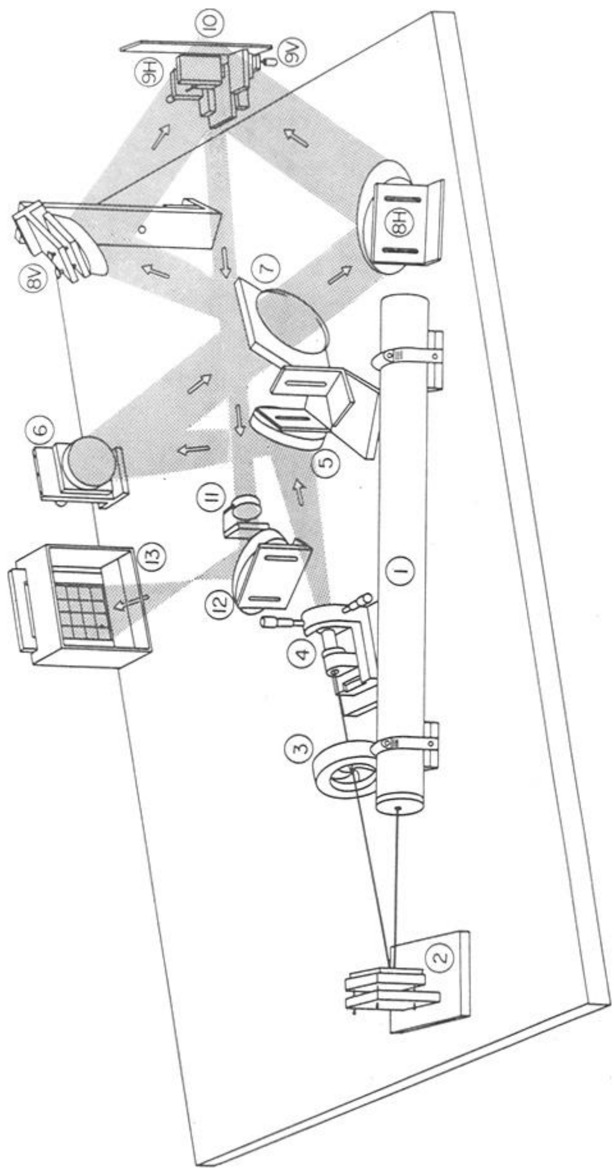

FIG. 2—*Schematic diagram of the moiré apparatus.*

cyclic loading, and this delamination growth is also reflected by decreasing laminate stiffness. A section of a radiograph of a severely damaged $[0,90_2]_s$ specimen is shown in Fig. 3. Note that there are several relatively uniformly spaced transverse cracks in the 90-deg plies, as well as two longitudinal splits in the zero-deg plies. Examination of a stereo pair of radiographs revealed that

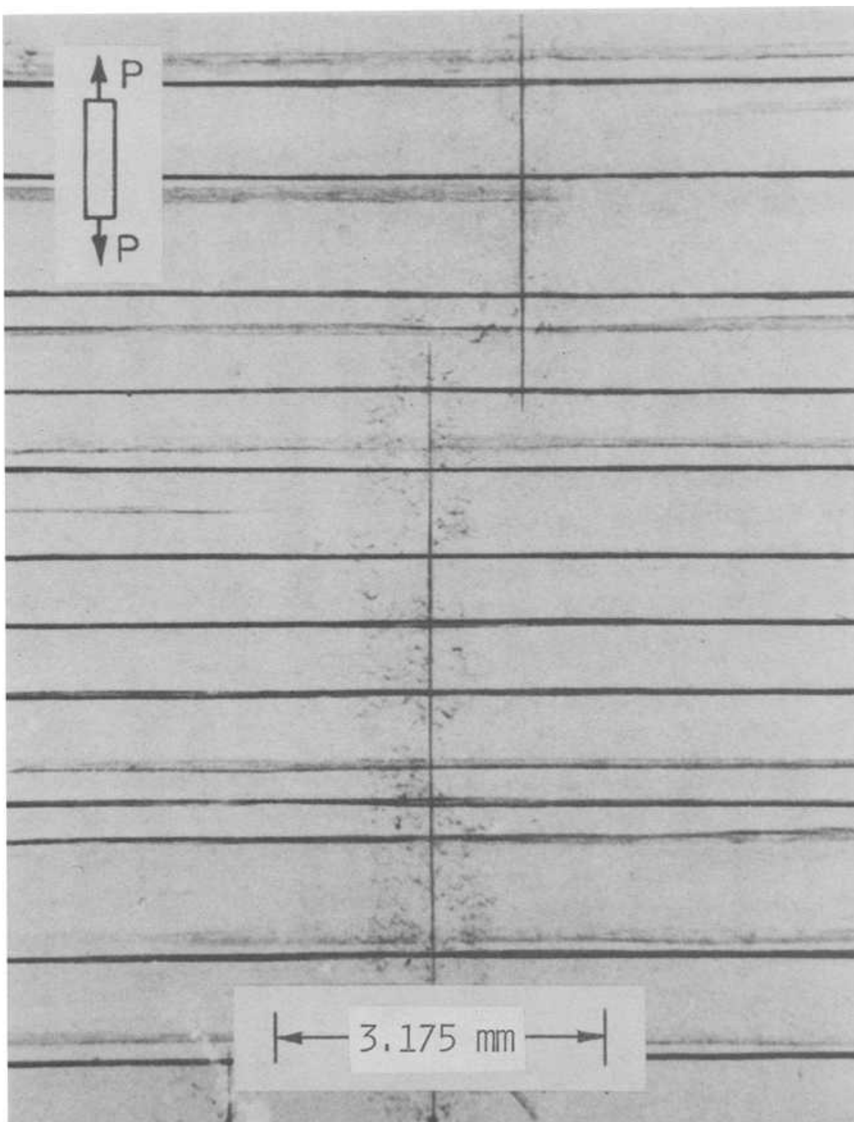

FIG. 3—*A section of an X-radiograph from a* $[0,90_2]_s$ *laminate exhibiting advanced damage development.*

the larger split was on the smooth side of the specimen which was studied via moiré interferometry. Deformations in this region were studied and compared to predicted deformation.

Figure 4 is a longitudinal moiré fringe pattern observed in the central part of the region depicted by Fig. 3. The fringes represent contours of the longitudinal moiré displacement field resulting from the application of a net stress of 173

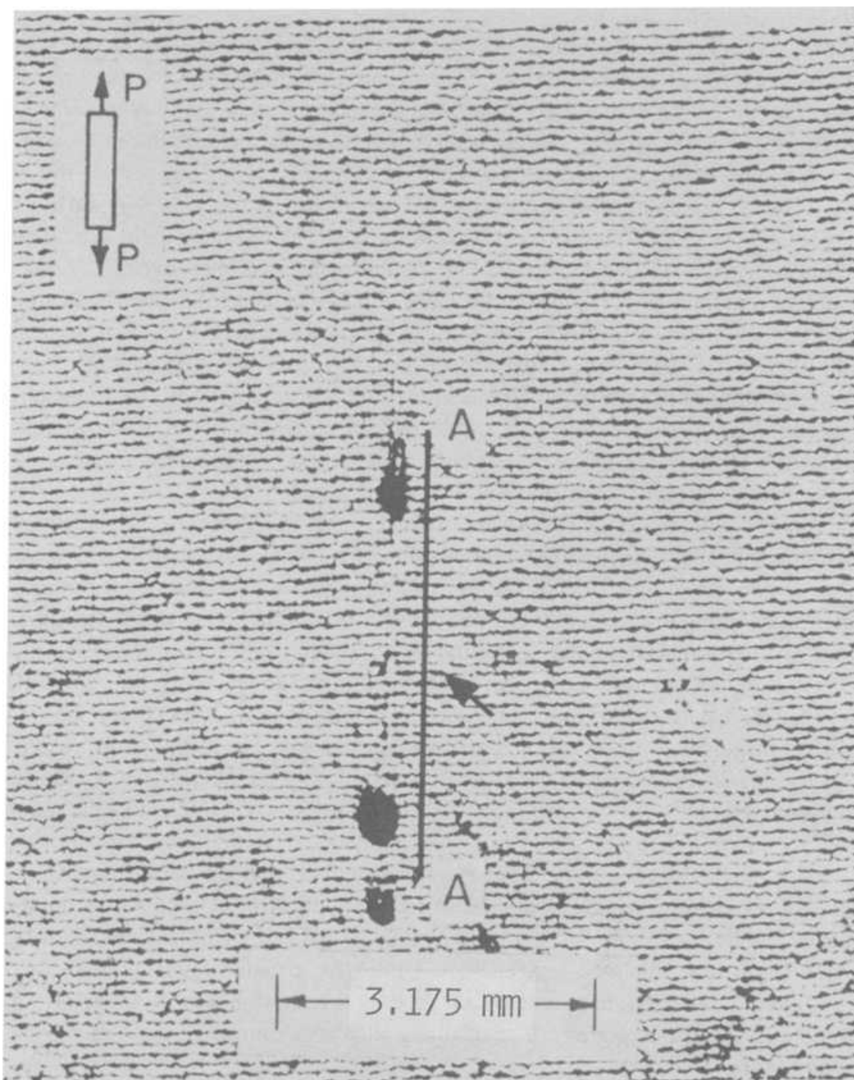

FIG. 4—*Longitudinal moiré pattern obtained from a region of advanced damage development in a* $[0.90_2]_s$ *laminate.*

MPa. The fringes are relatively uniformly spaced, and give little indication of the damage state of the specimen. One disturbance in the fringe pattern, a band of fringes that are apparently more closely spaced than the surrounding fringes, is indicated by an arrow. It was subsequently determined that this disturbance was in fact associated with a transverse crack in the interior plies. Note that there is no significant irregularity in the fringes near the longitudinal split. Figure 5 is the distribution of longitudinal displacement determined from the fringe pattern along the section marked A-A in Fig. 5. This section crosses several transverse cracks. The displacement varies nearly linearly with position, though the plot exhibits several slight irregularities. One of these irregularities, indicated by an arrow, is associated with the disturbance in the fringe pattern that was mentioned previously. The data in Fig. 5 were used to determine the net longitudinal strain. The laminate stiffness was found to be 43.4 GPa. A similar analysis of moiré data from an undamaged specimen yielded a stiffness of 52.5 GPa. A stiffness reduction of 17.4% is indicated. The longitudinal displacement field predicted by the analysis is shown in Fig. 6. The displacement is plotted over one representative quadrant of the laminate (see Fig. 1). Note that the displacement distribution is essentially uniform. The analysis predicts that neither the longitudinal split (at $y/b = 1.0$) nor the transverse (at $x/a = 1.0$) has a significant effect on the longitudinal displacement. This is consistent with the experimental results.

Figure 7 is a transverse moiré fringe pattern, again observed in the region depicted by Fig. 3. In this case, the fringes represent contours of the longitudinal displacement resulting from the application of a net stress of 338 MPa. Two comments about this fringe pattern are in order. First, the transverse displacement is discontinuous across the longitudinal split. This can be determined by considering fringes on either side of the split. The apparent fringe order difference determined along a section that crosses the split is different from that determined along a section ahead of the split tip. To accurately assign fringe orders, the initial assignment must be done ahead of the split tip. The remaining fringe orders can then be easily determined. The second comment is that the transverse deformation indicated by the fringe pattern is quite large. Using the moiré results directly, a Poisson's ratio of 0.15 is calculated. Using a biaxial strain rosette, a Poisson's ratio of 0.031 is measured. This second value is consistent with laminate analysis predictions. The discrepancy is a result of a rotation of the mirror assembly (9H in Fig. 2.) about the load axis upon load application. The transverse field is very sensitive to such a rotation. A rotation of 0.001 rad induces a fictitious transverse strain of 0.083% [*6*]. A direct analysis of Fig. 7 indicates a strain of −0.12%. It was assumed that Poisson's ratio for the damaged laminate was 0.031, and the uniform excess strain induced by the rotation was subtracted from the data in the fringe pattern. The resulting displacement distribution along the section marked A-A in Fig. 7 is present in Fig. 8. The split is located at approximately the zero position. Note that near the split, where the 0-deg ply is free to contract, the transverse strain is relatively large. These regions of large

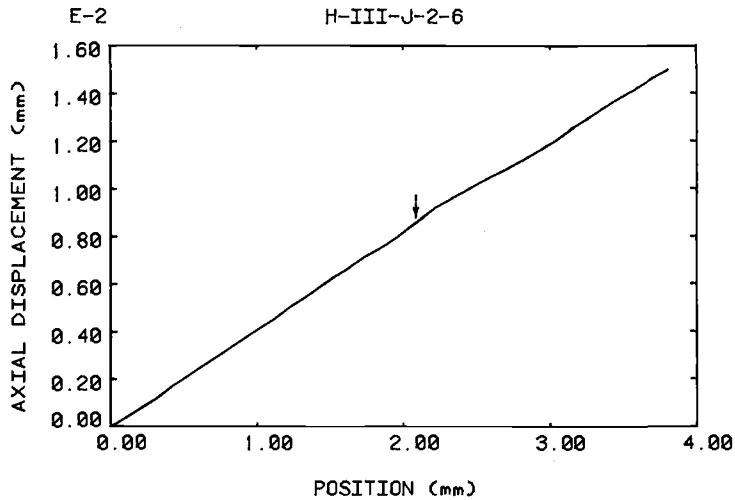

FIG. 5—*Longitudinal displacement distribution determined along a section of the longitudinal moiré pattern.*

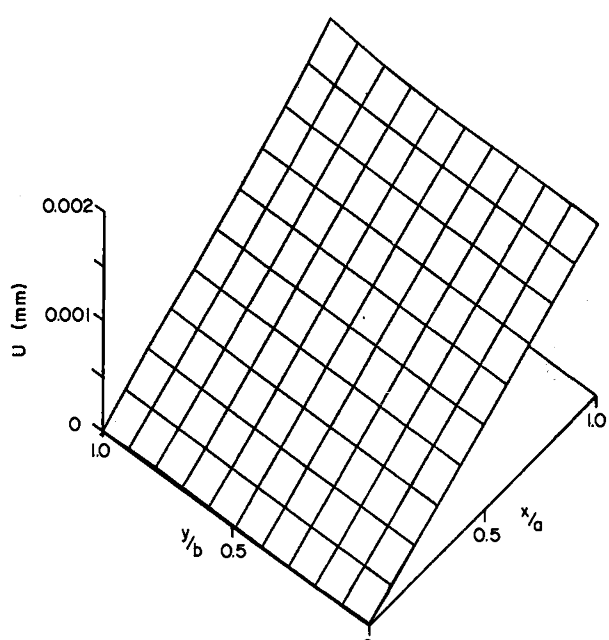

FIG. 6—*Predicted distribution of longitudinal surface displacement over a representative quadrant.*

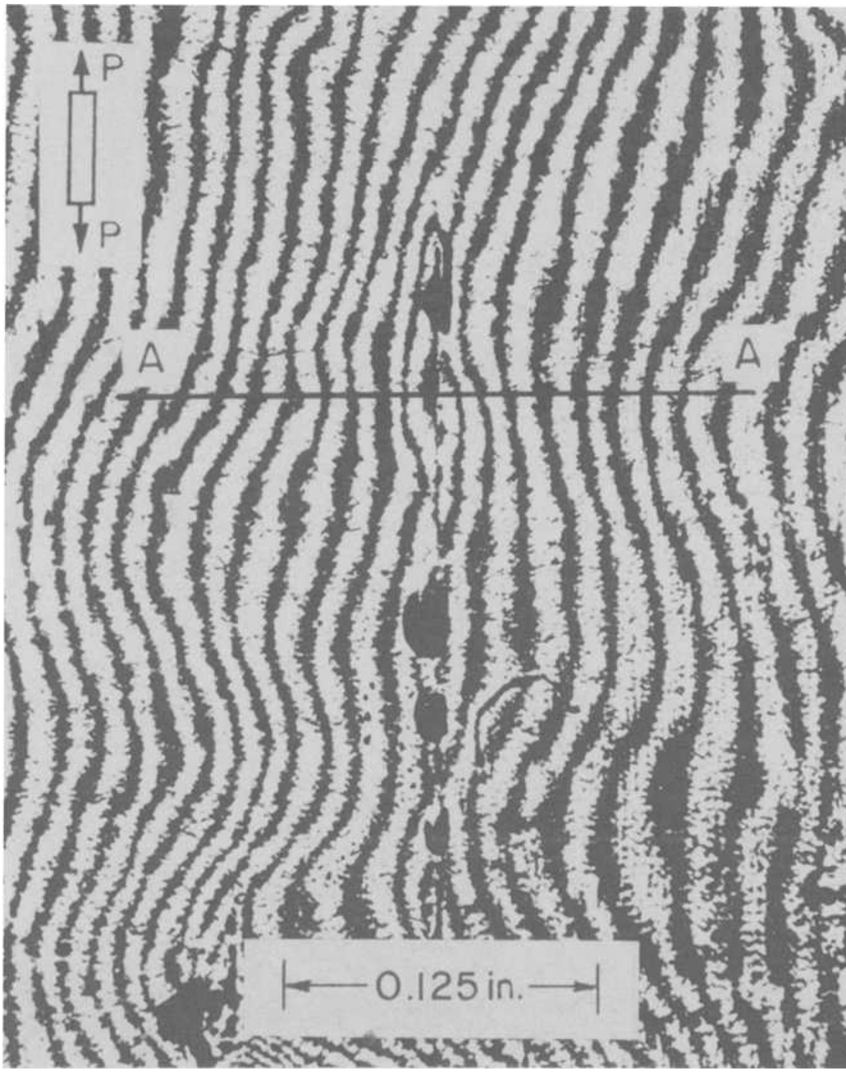

FIG. 7—*Transverse moiré pattern obtained from a region of advanced development in a* $[0,90_2]_s$ *laminate.*

transverse strains occur over zones within about 0.5 mm of the split. The predicted displacement field is shown in Fig. 9. The total contraction across this section exceeds the net laminate contraction, which indicates that the transverse displacement is discontinuous across the longitudinal split. A large displacement gradient is predicted in the region within about 0.35 mm of the longitudinal split. This dimension is comparable to that determined via moiré interferometry. Virtually all of the transverse contraction is predicted to occur within this zone, and

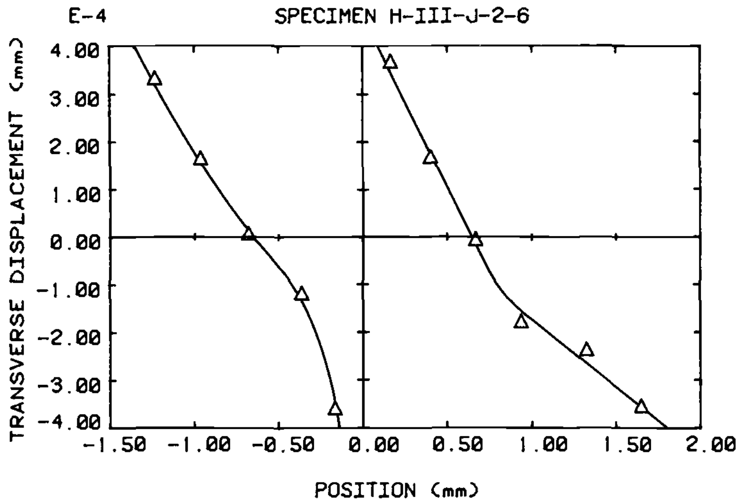

FIG. 8—*Transverse displacement distribution determined along a section of the transverse moiré pattern.*

in a region beyond this zone, small tensile transverse strains are predicted. This feature of the predicted displacement field was not observed experimentally. However, this discrepancy may be a result of the somewhat imprecise method used to account for the rotation of the mirror assembly. Generally the agreement between theory and experiment is quite reasonable, especially in light of the

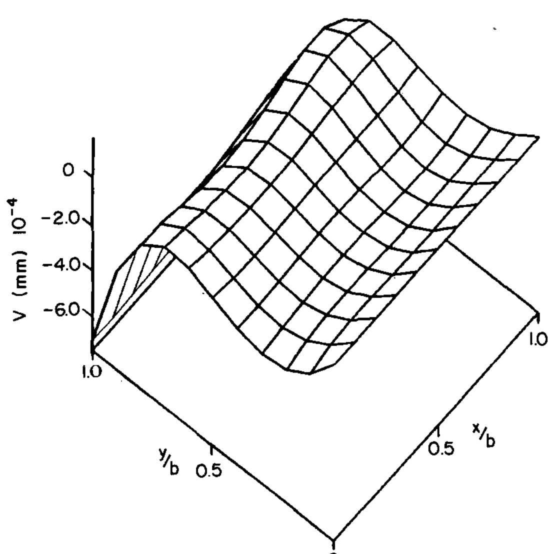

FIG. 9—*Predicted distribution of transverse surface displacement over a representative quadrant.*

relatively simple two-layer model for a symmetric half of the laminate used in the analysis.

We have seen so far that the analysis provides reasonable predictions of the in-plane surface displacements near the crossing point of a transverse crack and a longitudinal split. With this verification of the analysis, we consider now some of the internal stresses predicted by the analysis. Of particular interest are those stresses that influence the subsequent development of fiber breaks in the 0-deg ply and delamination at the 0/90 interface. The distribution of longitudinal stress σ_x in the 0-deg ply near the 0/90 interface is shown in Fig. 10. This stress is increased by about 8% near the line at the transverse crack in the adjacent 90's. Such a concentration of stress would influence the breaking of fibers by causing fibers to break preferentially along transverse crack lines in the adjacent ply. This is in agreement with experimental data obtained by Jamison [*4*]. Note that the predicted distribution of longitudinal stress shows little sensitivity to the longitudinal split. Figure 11 is a plot of the predicted distribution of interlaminar normal stress σ_z in the damaged material. The interlaminar normal stress is seen to reach a large tensile value near the transverse crack line. While the transverse crack dominated the geometry of the distribution, the longitudinal split causes a 70% increase in σ_z along the line of the transverse crack. Here, some interaction between the two damage events is indicated. The predicted distribution of the interlaminar shear stress τ_{xz} is shown in Fig. 12. Again, the geometry of the distribution shows that the strongest influence on this stress is that of the transverse crack. A maximum value is reached at a small distance from the crack line. There does appear to be an increased value of τ_{xz} at a small distance from the longitudinal split, but this interaction is not a strong one. The distribution of the interlaminar shear stress τ_{yz} is shown in Fig. 13. This stress reaches its maximum absolute value at the point $x/a = 0.7$, $y/b = 0.8$, which is slightly displaced from the crossing point of the longitudinal split and the transverse crack. Here, considerable interaction of the two damage events is seen, and the two events seem to have nearly equal influence on the distribution. The three interlaminar stress distributions all have extrema near the crossing point, which suggest that such crossing points are preferred sites for internal delamination development. This is consistent with Jamison's observations [*4*].

One final experimental result is considered. The transverse moiré fringe pattern from an area containing an internal delamination is shown in Fig. 14. The corresponding applied axial strain is 0.4%. The delamination is a thumbnail-shaped region near a longitudinal split, and is indicated by rather closely spaced curved fringes. The fringes are most closely spaced near the delamination front, which indicates that transverse strains are particularly large there. An analysis of the fringe pattern (again, rotation of the mirror assembly must be taken into account) reveals that the net transverse strain across the delamination is about -0.135%, while the remote strain is about -0.012%. The ratio of these strains is very nearly the same as the ratio of the Poisson's ratio of the 0-deg ply ($\nu_{12} = 0.308$) to the Poisson's ratio of the laminate ($\nu_{xy} = 0.031$). The delam-

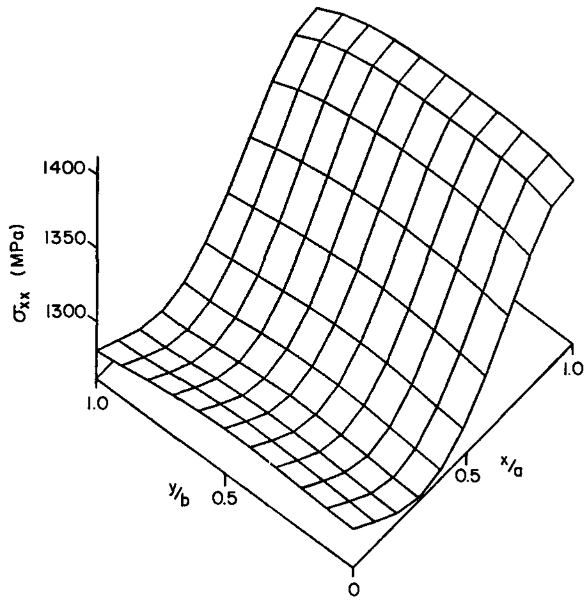

FIG. 10—*Predicted distribution of axial normal stress σ_x in the 0-deg ply near the 0/90 interface near crossing cracks.*

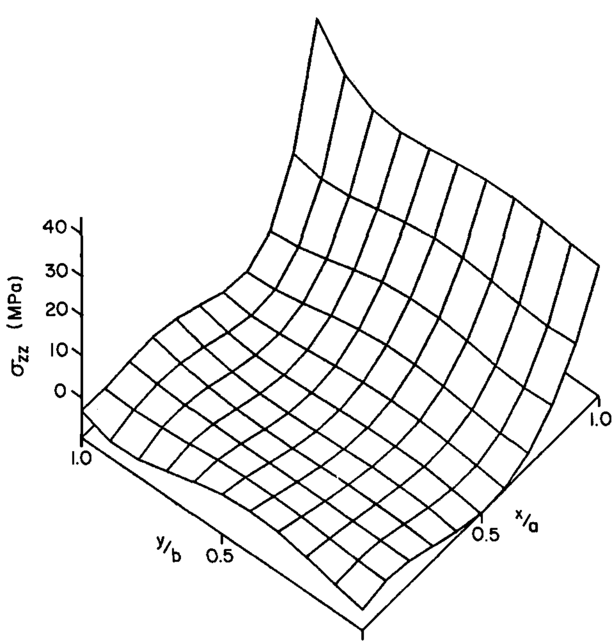

FIG. 11—*Predicted distribution of interlaminar normal stress σ_z at the 0/90 interface near crossing cracks.*

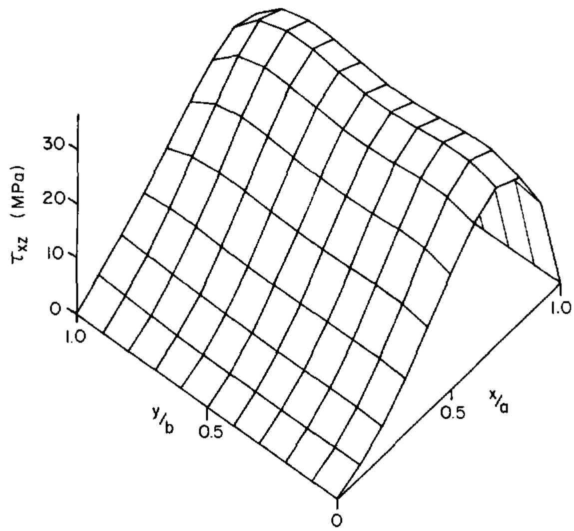

FIG. 12—*Predicted distribution of the interlaminar shear stress τ_{xz} at the 0/90 interface near crossing cracks.*

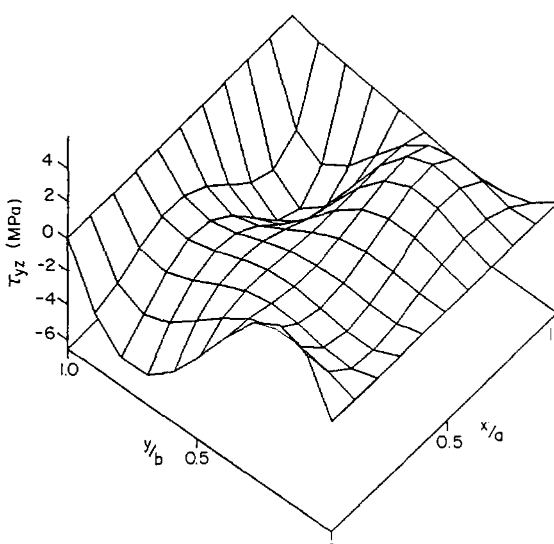

FIG. 13—*Predicted distribution of the interlaminar shear stress τ_{yz} at the 0/90 interface near crossing cracks.*

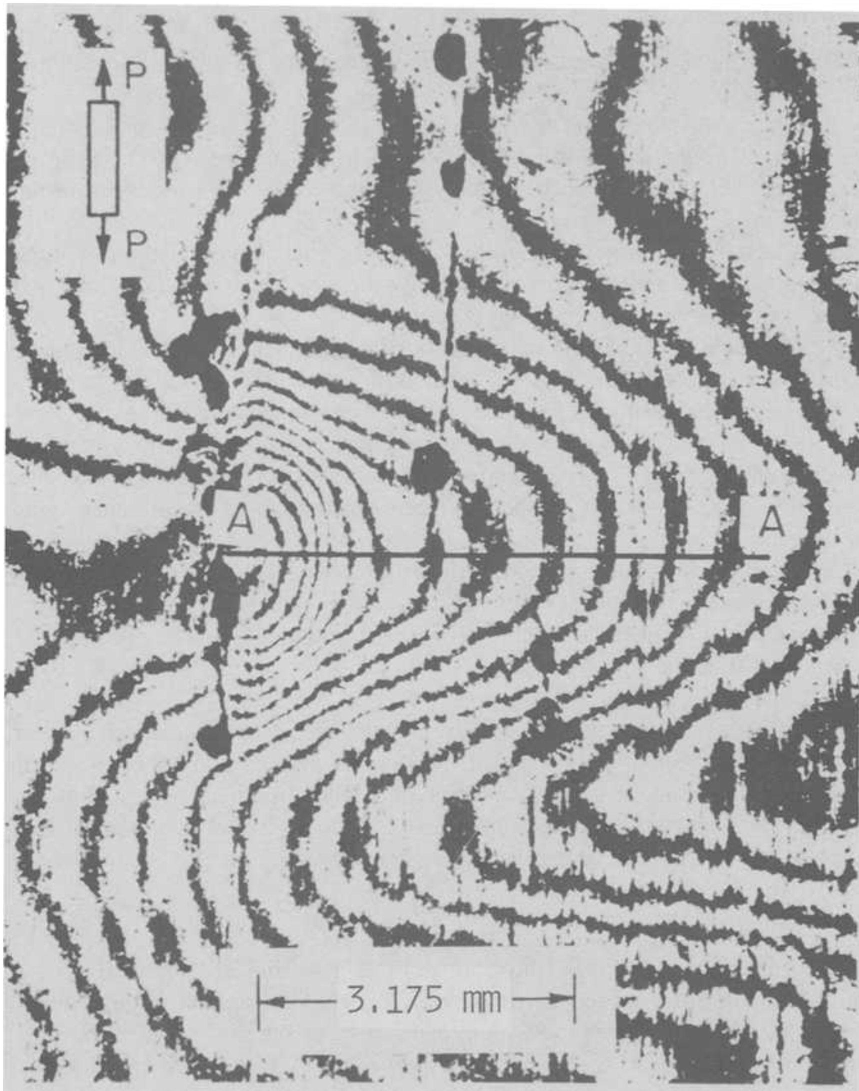

FIG. 14—*Transverse moiré pattern near an internal delamination in a* $[0,90_2]_s$.

ination is a region where the transverse constraint ordinarily imposed on the 0-deg ply by the interior 90-deg plies is relaxed. It is especially important to note that without the longitudinal split and the discontinuity in transverse displacement that it affords, such a relaxation of the transverse constraints would not be possible.

Conclusions

Based on the specific results cited above, we make the following observations.

1. The approximate laminate analysis suggested by Pagano based on Reissner's variational theorem can be used to analyze micro-damage patterns in composite laminates. The results of such an analysis have been verified by experimental measurements.
2. Matrix cracks in adjacent plies of different orientation which cross at the ply interface create a region of significantly increased interlaminar normal and shear stress around the intersection point.
3. The stress fields of the two intersecting cracks appear to interact to produce a disturbance greater than the superposition of the two effects.
4. Local delamination at the crack intersection further redistributes the local stresses by relaxing the constraint of the deformation in one ply by the resistance of differently oriented fibers in an adjacent ply (formerly bonded to it). This relaxation is made possible by the presence of matrix cracks (longitudinal splits in the present case).
5. The present findings are consistent with the idea that the region of crossed cracks becomes a region of highly localized and increased stress during the development of damage, and could provide the initiation point for specimen or component fracture.

Many issues are yet unresolved, even with respect to the damage pattern addressed here. But it is hoped that the present analysis and experience will provide one more stone in the foundation on which a mechanistic model of the strength of damaged laminates will be built. Indeed, the authors believe that some of the architecture of that structure is suggested by the present results.

Acknowledgments

The authors wish to thank the College of Engineering at Virginia Tech for partial support of the present investigation. The technical support of other members of the Materials Response Group, and former members—especially Dr. R. Jamison (now at the U.S. Naval Academy)—is also gratefully acknowledged. Our thanks to Professor Daniel Post and Mr. Robert Czarnek for providing valuable and essential assistance and guidance for the optical experiments, and to Ms. Barbara Wengert for typing the manuscript.

References

[1] Highsmith, A. L., Stinchcomb, W. W., and Reifsnider, K. L. in *Effects of Defects in Composites, ASTM STP 836*, D. J. Wilkins, Ed., American Society for Testing and Materials, 1984, pp. 194–216.
[2] Pagano, N. J., *International Journal of Solids and Structures*, Vol. 14, 1978, pp. 385–400.
[3] Stewart, G. W., *Introduction to Matrix Computations*, Academic Press, Orlando, FL, 1973.

[4] Jamison, R. D., "Advanced Fatigue Damage Development in Graphite Epoxy Laminates," Ph.D. dissertation, College of Engineering, Virginia Polytechnic Institute and State University, Blacksburg, VA, Aug. 1982.
[5] Post, D., in *Mechanics of Nondestructive Testing*, W. W. Stinchcomb, Ed., Plenum Press, New York, 1980, pp. 1–53.
[6] Post, D., "Moiré Interferometry," Chapter 7 of *SESA Handbook on Experimental Mechanics*, A. S. Kobayashi, Ed., Prentice Hall, Englewood Cliffs, NJ, to be published.

Russell D. Jamison[1]

On the Interrelationship Between Fiber Fracture and Ply Cracking in Graphite/Epoxy Laminates

REFERENCE: Jamison, R. D., "**On the Interrelationship Between Fiber Fracture and Ply Cracking in Graphite/Epoxy Laminates,**" *Composite Materials: Fatigue and Fracture, ASTM STP 907,* H. T. Hahn, Ed., American Society for Testing and Materials, Philadelphia, 1986, pp. 252–273.

ABSTRACT: The present work examines in a systematic way the development of microdamage in several laminates of graphite/epoxy material subjected to both quasi-static tensile loading and tension-tension fatigue. Emphasis is placed upon discriminating and quantifying matrix and fiber microdamage. Penetrant-enhanced standard- and stereo X-ray radiography were used along with edge replication to follow the progression of matrix damage. The recently developed technique of laminate deply was used to map the development of fiber fracture.

The most significant result, confirmed in both the quasi-static and fatigue tests, was the dominant role played by off-axis ply cracks in the fracture of fibers in adjacent load-bearing plies. By direct observation of fiber fractures *in situ*, it was established in both cases that fiber fractures do not occur in a random pattern at elevated loads/cycles, but instead occur in narrow bands adjacent to off-axis ply cracks. It is the action of these crack tips upon adjacent fibers which may govern the wearout or overload of laminates under these conditions.

By direct accounting of fiber fractures in deplied laminae taken from damaged but unfailed laminates, the relationship between the density of fiber fractures and the number of cycles at one cyclic stress level is reported. The relationship between fiber fracture density and quasi-static stress level is reported as well.

For the quasi-statically loaded specimens, efforts to characterize and discriminate between fiber fracture and transverse ply cracking on the basis of acoustic emission (AE) amplitude distribution are described. Correlations between attributes of the AE amplitude distribution and the established damage extent and chronology are reported. Common assumptions regarding the contributions of these distinct damage modes to acoustic emission from laminates under tensile loading are discussed in terms of the present evidence.

Finally, in comparing damage resulting from quasi-static tension loading of cross-ply laminates with that observed in tension-tension cyclic loading of laminates of similar graphite/epoxy material, microdamage modes unique to fatigue are identified and discussed.

KEY WORDS: composite materials, laminates, graphite/epoxy, fatigue, tensile failure, damage, ply cracking, fiber fracture, edge replication, stereoradiography, deply, acoustic emission

[1] Assistant professor, Mechanical Engineering Department, United States Naval Academy, Annapolis, MD 21402.

Fiber-reinforced composite materials may be unique among the classes of materials in their complexity of failure. In seeking to understand failure and thereby predict residual properties of strength, stiffness, and fatigue lifetime it is necessary to confront the complexity of the prefailure damage state. Specifically, it is necessary to follow the incipience, growth, and coalescence of discrete damage modes in order to define the functional relationships between observed damage and residual properties. The present work examines in a systematic way the development of microdamage in several laminates of graphite/epoxy material subjected to both quasi-static tension loading and tension-tension fatigue. Emphasis is placed upon discriminating and quantifying matrix and fiber microdamage by both physical and nondestructive evaluation (NDE) techniques.

Procedure

Specimens for fatigue testing were fabricated from NARMCO T300/5208 prepreg material. Specimens for static testing were fabricated from Fothergill and Harvey T300/Code 91 prepreg. The Code 91 resin is similar in composition and properties to the 5208 resin but has a lower cure temperature. Specimens measuring 203 mm long and 25 mm wide with stacking sequences $[0,0]_s$ and $[0,90_2]_s$ were used for both fatigue and static test series. Fiber volume fractions were approximately 61% for both layups, and specimen thicknesses were approximately 0.6 and 0.9 mm, respectively. Fatigue testing was performed only on the $[0,90_2]_s$ laminates in a tension-tension mode at 10 Hz in a sinusoidal form and at a stress ratio $R = 0.1$. Maximum stress amplitude was 70% of the mean static ultimate strength ($\bar{S}_{ult}$). Static tension testing was accomplished on both $[0,90_2]_s$ and $[0,0]_s$ laminates in a displacement-controlled mode at a strain rate of $1.7 \times 10^{-4}\ s^{-1}$.

Fatigue specimens were cyclically loaded to various stages of their anticipated fatigue lifetime based upon a reduction in stiffness damage analog described in a previous paper [*1*]. Static specimens were loaded to various fractions of the mean ultimate strength and unloaded immediately. In both cases damage was characterized by the nondestructive techniques of X-ray radiography and edge replication and the destructive techniques of sectioning and deply. These methods are described in detail in Refs *2*,*3*, and *4*.

For the static testing of both unidirectional and cross-ply specimens, acoustic emissions were monitored. The system consisted of a wide-band piezoelectric (PZT) transducer having a contact diameter of 25.4 mm. The transducer output passed through a 60-dB preamplifier which contained a 100-Khz to 1-Mhz band-pass filter into a modified AETC Model 203 amplitude analyzer. This system covered an amplitude range from 20 μV to 20 mV at the sensor (26 to 86 dB with respect to 1 μV at the sensor). The analyzer divided this range equally into 50 channels each of amplitude width 1.2 dB. The threshold of the instrument could be raised above 20 μV and channels eliminated to filter some low-amplitude noise. In the present work channels 0–3 were excluded in this way, giving an effective threshold of approximately 30 μV at the sensor.

The AETC system operated also as an event counter capable of distinguishing one event from another provided there existed a dead time of at least 100 μs between successive events. For a typical pulse of 400 μs the system as modified was intrinsically capable of registering 2000 events per second. Static testing was accomplished at a low strain rate to stay within this limitation and avoid the loss of information near failure when large count rates are generally observed.

Results and Discussion

Fatigue Damage Assessment

The assessment of damage development in $[0,90_2]_s$ laminates of T300/5208 material under tension-tension cyclic loading has been the subject of a previous paper by the author [*5*]. Those results which specifically relate to transverse ply cracking and fiber fracture will be repeated here as a basis for comparison with static results to be presented in a following section.

The first damage which occurs during cyclic loading is cracking of the 90-deg plies. For a stress amplitude of 70% $\bar{S}_{ult}$, approximately one half of the transverse cracks which ultimately form in these laminates do so in the first half-cycle. Cracks continue to occur at a diminishing rate with increasing cycles until a saturation crack density is achieved. Beyond this point, additional cycles do not produce additional transverse ply cracks. The development of cracks in the off-axis plies of laminates subjected to tensile loading has been studied extensively [*6–10*]. The development of a saturation spacing of cracks has been predicted and observed [*11*]. This condition which imposes an upper bound on crack density has been termed the "characteristic damage state" (CDS) [*12*]. It has been shown to be dependent upon the properties of each ply, the ply thickness, and the stacking sequence, but independent of the load history [*13*]. Figure 1 shows the development of 90-deg ply cracks as a function of cycles for a typical $[0,90_2]_s$ specimen. This figure also shows the associated reduction in the longitudinal stiffness resulting directly from the formation of these cracks.

With continued cycling, longitudinal cracks develop in the 0-deg plies. By following the initiation and growth of this damage through stereo X-ray radiography of progressively damaged laminates, these longitudinal cracks were seen to initiate at existing transverse cracks and to grow along the 0-deg ply fiber direction very slowly in a fatigue fashion. This is in contrast to the development of transverse ply cracks, which initiate and extend across the full specimen width almost instantaneously. The existence of such longitudinal cracks has previously been predicted and observed in glass/epoxy laminates [*6*]. They are particularly likely to occur in tension loading of cross-ply laminates in which the large Poisson mismatch between 0- and 90-deg plies produces large tensile transverse stresses in the 0-deg plies. The role of the 90-deg ply cracks in initiating longitudinal cracks in graphite/epoxy cross-ply laminates has not, to the author's knowledge,

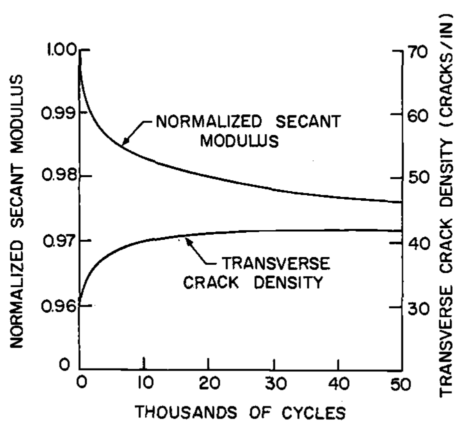

FIG. 1—*Transverse crack density and normalized secant modulus versus fatigue cycles for a* $[0,90_2]_s$ *laminate.*

been previously described. Consideration of the stresses at the transverse ply crack tips provides the explanation for this apparent damage coupling. For tensile longitudinal loads on the laminate, the crack-tip stress parallel to the transverse cracks are tensile. It is these local Poisson-related σ_y stresses produced at the 0/90-deg interfaces which add to the global σ_y stresses in the 0-deg plies to produce the initiation sites for longitudinal crack initiation. Longitudinal crack-tip stresses normal to the ply are also tensile under tension loading of the laminate. Hence at crossing points between transverse cracks in the 90-deg plies and longitudinal cracks in the 0-deg plies the local out-of-plane stresses are additive and maximum. Stereoscopic examination of $[0,90_2]_s$ specimens in advanced stages of fatigue damage development revealed that at some of these crossing points interior delaminations had occurred. These delaminations could be attributed only to local stresses since global out-of-plane stresses do not exist in the interior of the laminate. This coupling of transverse and longitudinal cracks to produce interior delamination is an important feature of fatigue in these laminates. Figure 2 is an enlargement of a penetrant-enhanced radiograph of a $[0,90_2]_s$ in an advanced state of fatigue showing these dominant modes of matrix damage. An arrow points to one interior delamination. Figure 3 is a schematic representation of the way in which matrix damage is developed about the transverse ply cracks. The important role of these cracks in initiating and localizing other modes of matrix damage characterizes the matrix-related process of fatigue in these laminates. Their influence upon fiber fracture in fatigue will be considered in a following section.

Static Damage Assessment

Matrix damage in quasi-static tension loading of $[0,90_2]_s$ is by appearance a somewhat simpler matter than that associated with fatigue loading. Transverse

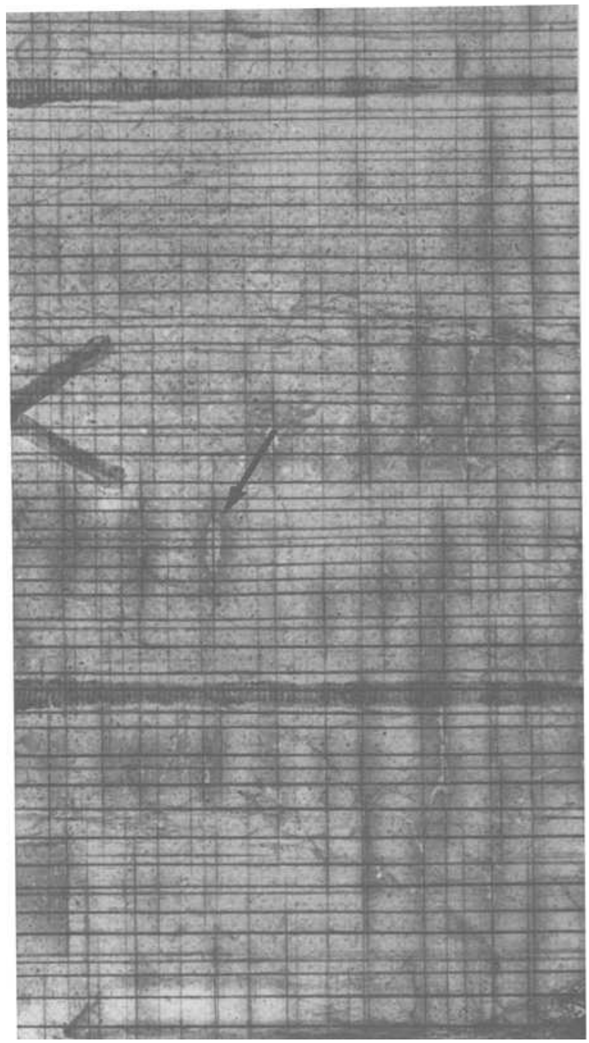

FIG. 2—*Radiograph enlargement of a fatigue damaged* $[0,90_2]_s$ *laminate.*

ply cracks were the first damage observed with the first cracks developing at loads above 30% of the mean ultimate strength. Figure 4 shows the relationship between tension load and the observed density of cracks in $[0,90_2]_s$ specimens. These are instantaneous measurements at specified loads. Measured crack densities did not achieve the equilibrium saturation spacing associated with the characteristic damage state. The crack density at 100% $\bar{S}_{ult}$ was 38% lower on average than the CDS prediction based on a one-dimensional shear lag analysis [*14*]. This difference is attributable to the viscoelastic behavior of the resin matrix.

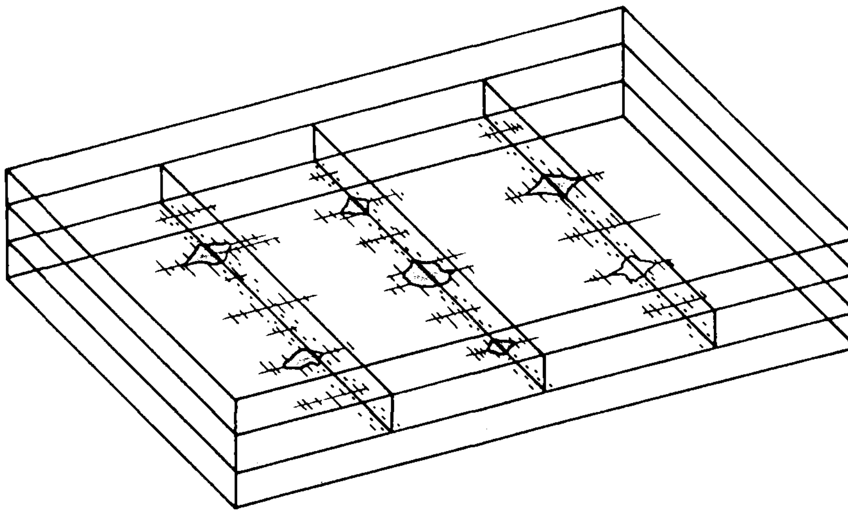

FIG. 3—*Schematic of damage localization pattern.*

Even at very low strain rates there was insufficient time for complete crack development to occur at a given load. At a constant load of 70% $\bar{S}_{ult}$, for example, approximately 30 s was required for a stable crack density to develop. Because one goal of the present work was to establish a correlation between transverse ply cracking and acoustic emission measured during quasi-static tension loading, the power-law relationship shown in Fig. 4 was taken to represent real-time crack development under tension loading of these laminates.

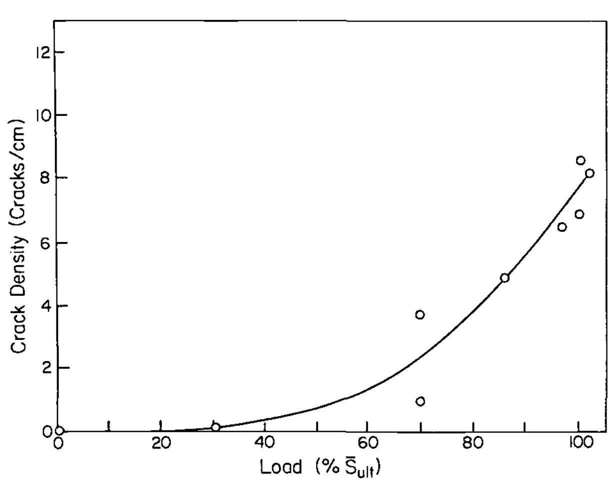

FIG. 4—*Transverse crack density versus static tension load for* $[0,90_2]_s$ *laminates.*

Sections, both transverse and longitudinal, were prepared from specimens and examined microscopically for evidence of resin cracking or disbonding in the transverse plies as well as in the 0-deg plies. Even for specimens loaded above 100% $\bar{S}_{ult}$ no evidence of microcracking or disbonding was observed. The overall state of resin damage resulting from quasi-static tension loading is provided by a penetrant-enhanced radiograph shown enlarged in Fig. 5. This radiograph of a specimen loaded to 100% $\bar{S}_{ult}$ exhibits only transverse ply cracks without the accompanying longitudinal cracking or interior delamination seen previously to be associated with fatigue loading of similar $[0,90_2]_s$ specimens.

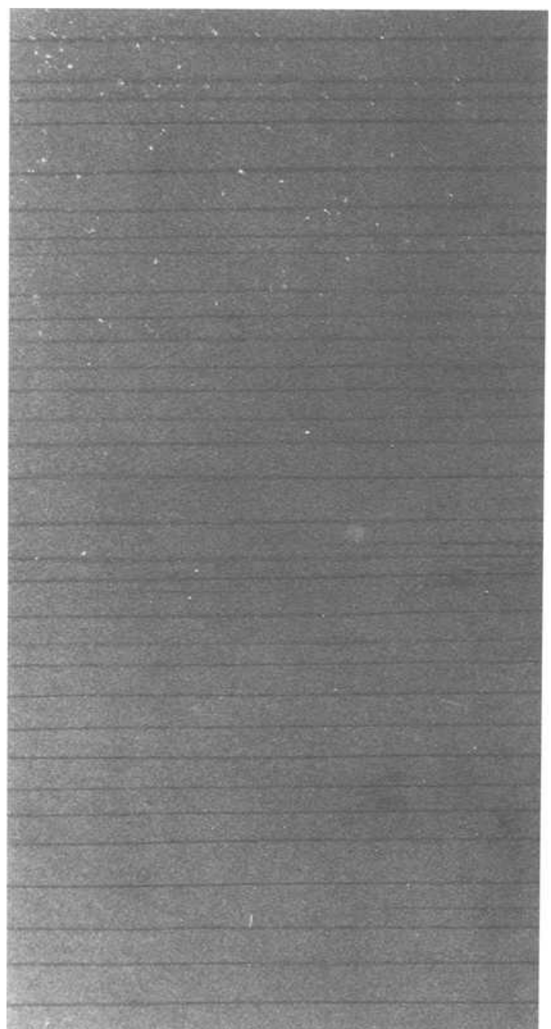

FIG. 5—*Radiograph enlargement of a statically damaged* $[0,90_2]_s$ *laminate.*

Fiber Fracture

The state of fiber fracture in fatigue and quasi-static tension loading was examined next. The method of laminate deply [4] was used to "unstack" the 0-deg plies from laminates loaded cyclically for various fractions of anticipated fatigue lifetimes, or statically to specified fractions of the mean ultimate stress. Portions of these plies were examined in a scanning electron microscope (SEM) and the average fiber fracture density was calculated by counting broken fibers in a number of randomly chosen representative areas of dimensions approximately 3.5 by 4.9 mm. The process of deplying, if done with care, produces very few fiber fractures. Average fiber fracture densities for virgin specimens were calculated and used as a basis from which the true relationship between load or cycles and fiber fracture could be determined.

Figure 6 shows this relationship for tension fatigue loading of $[0,90_2]_s$ laminates at a stress amplitude of 70% $\bar{S}_{ult}$. Fiber fracture density is seen to increase rapidly during early cycles. Fiber fracture continues to occur with increasing cycles but at a substantially diminished rate. Although the available data were not sufficient to completely characterize this relationship, the existence of a plateau as shown in Fig. 6 was suggested by examination of post-failure specimens. In these specimens the fiber fracture density away from the fracture site was not observed to be significantly larger than in prefailure measurements of similar specimens at advanced life. While at the failure site rapid growth of fiber fractures must occur, there is no evidence at this time to suggest that such a phenomenon occurs on a global scale.

Fiber fracture density in quasi-static tension loading is shown in Fig. 7. At loads below 70% $\bar{S}_{ult}$ there are essentially no broken fibers in excess of those found in virgin specimens. At loads above this level, however, fiber fracture density increases rapidly in an approximate power-law form. Thus, while a load of 70% $\bar{S}_{ult}$ is not sufficient to produce a significant number of fiber fractures in

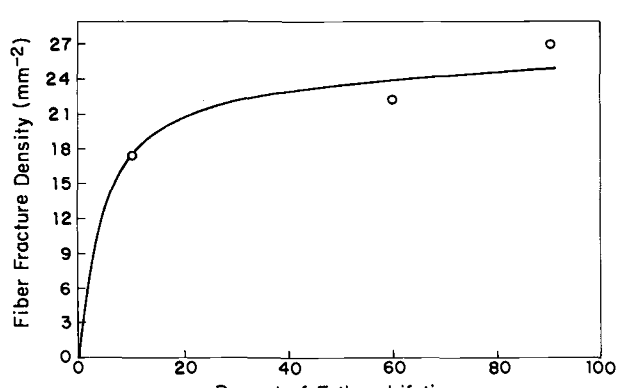

FIG. 6—*Fiber fracture density versus fatigue cycles for* $[0,90_2]_s$ *laminates.*

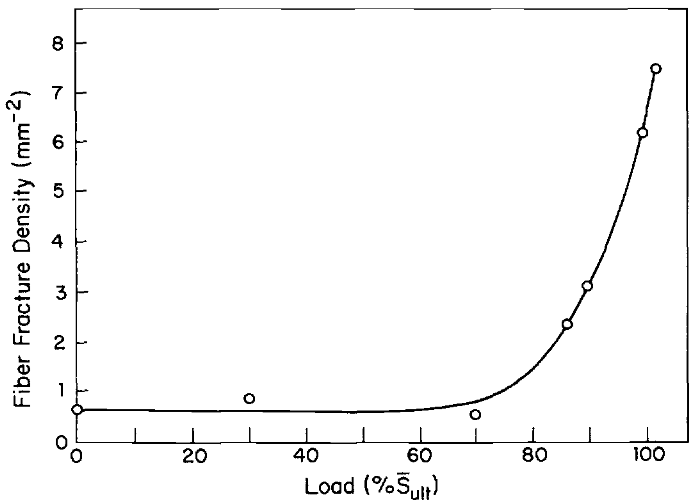

FIG. 7—*Fiber fracture density versus static tension load for* $[0,90_2]_s$ *laminates.*

a quasi-static tension loading environment, repeated application of that load is sufficient to produce a substantial number of broken fibers in a tension fatigue environment. Accepting the general assumption that graphite fibers themselves are not subject to fatigue failure [*19*], one is left with evidence of the important role of matrix microdamage and damage coupling in elevating the fiber stress to a level sufficient to cause static fiber fracture in the fatigue case.

In the course of counting broken fibers in the load-bearing plies of fatigue or statically damaged specimens, it was observed that fiber breaks in these cross-ply laminates did not occur in a random pattern. They instead were localized into distinct bands. Outside of these bands very few fiber fractures were observed. This was true of both fatigue and statically loaded specimens. Measurement of the distance between adjacent bands revealed that the mean spacing corresponded to the measured spacing between adjacent 90-deg ply cracks measured from replicas and confirmed in radiographs. By the use of gold chloride as a marking medium for transverse cracks in a procedure described fully in Ref *2*, this association between the location of ply cracks and the location of zones of fiber fractures was confirmed. Figures 8 and 9 are SEM micrographs showing typical examples of these fiber fracture patterns in fatigue-damaged and statically damaged $[0,90_2]_s$ laminates, respectively. Figure 10 is a schematic representation of the same patterns.

Related work [*5*] on fatigue-damaged $[0, \pm 45]_s$ and $[0,90, \pm 45]_s$ graphite/epoxy laminates exhibited the same phenomenon. In all cases examined, fiber fractures which occurred in any ply were localized and corresponded to the location of cracks in adjacent plies. This localization and segregation of fiber fractures reflect the strong and perhaps dominant role of off-axis ply cracks and

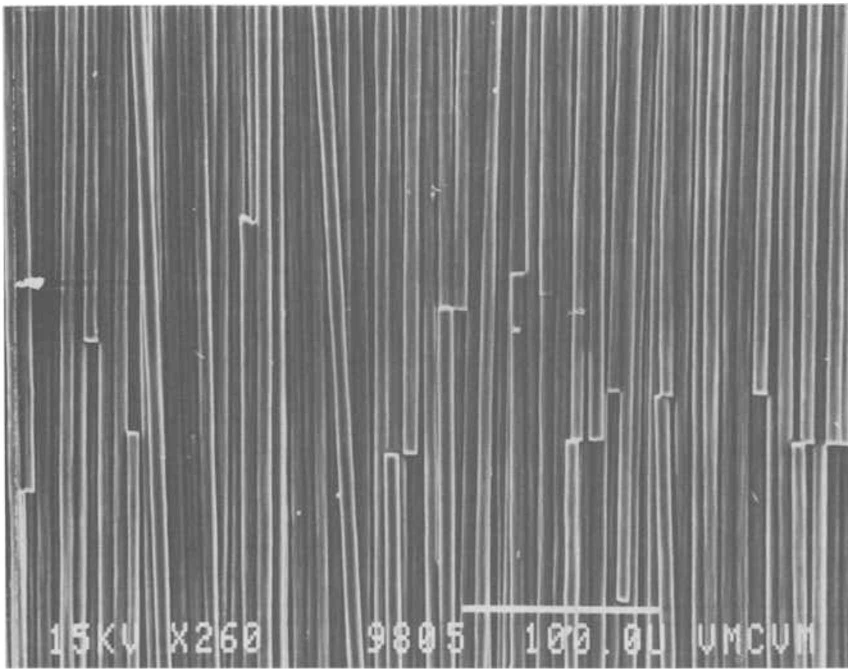

FIG. 8—*Micrograph of fiber fractures in a fatigue-damaged* $[0,90_2]_s$ *laminate.*

their associated resin damage zones in controlling fiber fracture. It is the combination of global stress and local stress concentration due to adjacent ply cracks which dictates the density and distribution of fiber fractures in the load-bearing plies of these laminates.

Fiber fractures in $[0,0]_s$ laminates subjected to static tension loading were also examined. In this case the fiber breaks which occurred were distributed in an apparently random pattern. The density of these fiber breaks as a function of load is shown in Fig. 11. Results for the statically loaded $[0,90_2]_s$ laminates are repeated for comparison. Significant numbers of fiber fractures did not occur at loads below approximately 70% $\bar{S}_{ult}$. The fiber fracture density then increased rapidly with increasing load through laminate failure.

Inspection of Fig. 11 would suggest that the density of fiber fractures near failure is substantially higher in the cross-ply laminate. While this may in fact be true, the difference would be less than that shown. The method of counting fiber fractures has undoubtedly exaggerated whatever real difference there may be. In the cross-ply laminates fiber fractures were counted in the fiber layer adjacent to the 0/90-deg interface and hence nearest to the crack tip. It has been shown by the author in previous work [*2,5*] that the density of fiber fractures is markedly diminished in fiber layers away from the 0/90-deg interface—70% fewer only one fiber diameter removed from the interface in the case of fatigue.

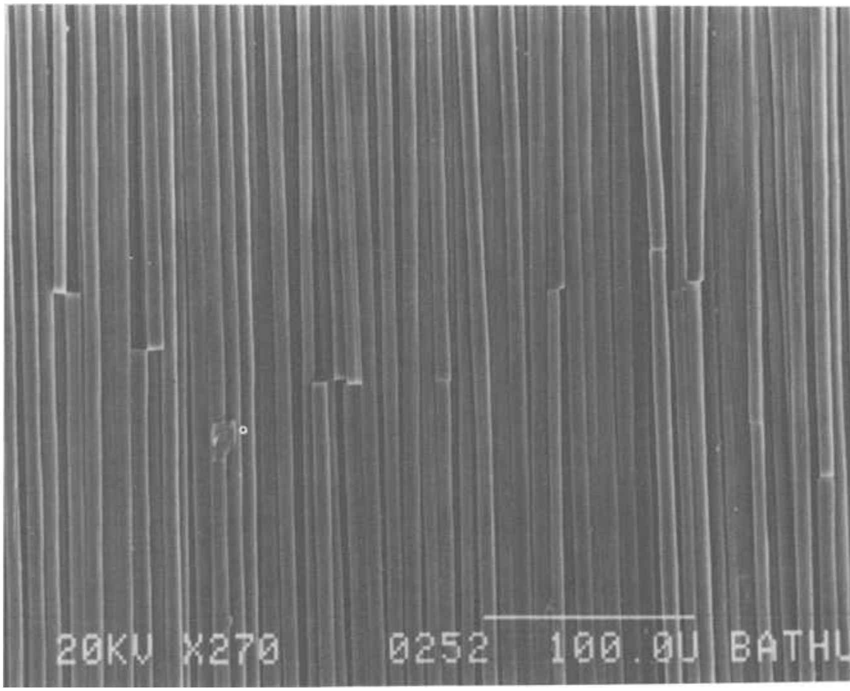

FIG. 9—*Micrograph of fiber fractures in a statically damaged* $[0,90_2]_s$ *laminate.*

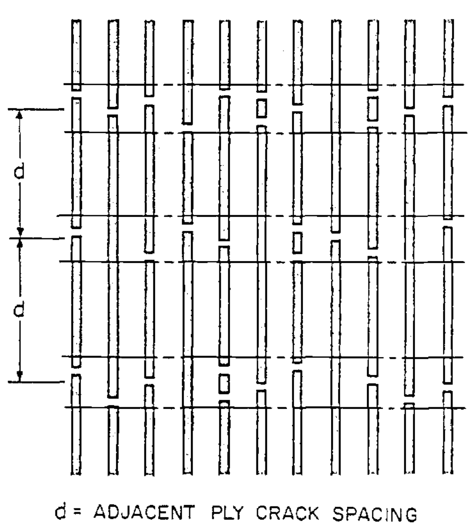

FIG. 10—*Schematic of the localized pattern of fiber fractures.*

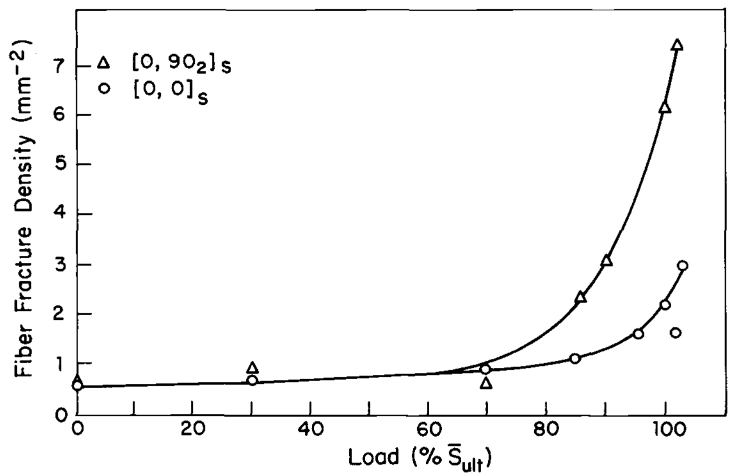

FIG. 11—*Fiber fracture density versus static tension load for* $[0,0]_s$ *and* $[0,90_2]_s$ *laminates.*

Although it is possible to remove fiber layers from the deplied laminae by the application and careful removal of pressure-sensitive tape, the number of observations required to produce meaningful fracture density statistics precluded through-thickness accounting. It is possible to conclude from this evidence only that fiber fracture density observed at the interface is higher in cross-ply laminates than in unidirectional laminates.

The potential significance of the ply cracking-fiber fracture relationship in laminate failure and the obvious importance of fiber fracture in fiber-dominated laminates poses an experimental challenge: Is there a nondestructive way in which to characterize the onset and development of fiber fracture during tension loading of laminates having stacking sequences and ply orientations not already characterized by the tedious procedure of deply and fiber fracture accounting used in the present work? The effectiveness of such an NDE technique ultimately would hinge upon its ability to discriminate fiber fracture from the resin-related damage modes which occur. In the present instance of $[0,90_2]_s$ laminates of graphite/epoxy, this would mean discriminating between transverse ply cracking and fiber fracture.

Acoustic Emission Analysis

One NDE method which would seem to hold promise for such a purpose is acoustic emission. Therefore, acoustic emissions recorded during tension loading of $[0,90_2]_s$, and $[0,0]_s$ laminates were analyzed to seek correlations between attributes of the AE pulses and the physical picture of damage development described in the previous sections.

Figure 12 shows the cumulative acoustic emissions recorded during the tension

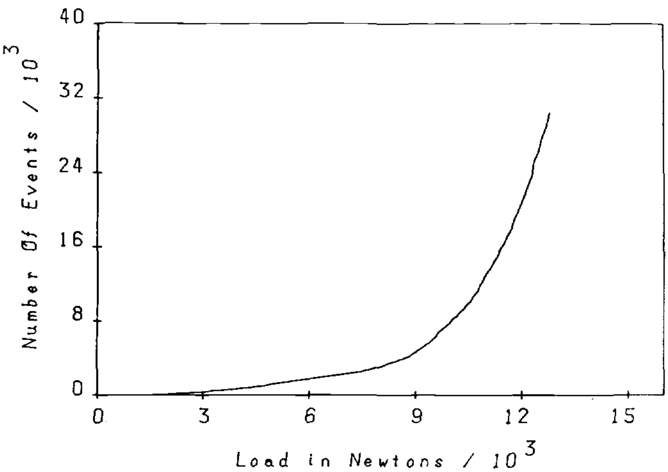

FIG. 12—*Cumulative AE counts versus load for a* $[0,90_2]_s$ *laminate.*

loading of a typical $[0,90_2]_s$ laminate to failure. The functional relationship is suggestive of the damage relationships of Figs. 4 and 7. The absence of evident fine structure, however, diminishes the usefulness of such a curve in discriminating between the principal damage modes which have been seen to occur in this laminate.

Figure 13 shows the amplitude distribution of the acoustic emission in each of six load ranges for a typical specimen. The load ranges used as a basis for comparison of the AE amplitudes were defined as follows:

LOAD RANGE INDEX	LOAD RANGE (% $\bar{S}_{ult}$)
1	0–30
2	30–60
3	60–70
4	70–80
5	80–90
6	90–prefailure

These load range references will be used throughout the succeeding discussion of results. In load ranges 1 and 2, which together extend from no load to 60% $\bar{S}_{ult}$, the amplitude distribution is inclusive of channels 4–20. These are the load ranges in which cracks are occurring prior to a significant amount of fiber fracture. In load range 3 (60–70% $\bar{S}_{ult}$), ply cracking activity has increased and remains the predominant active damage mode. The amplitude distribution for this load range includes a small but significant number of events in channels 20–30. In load range 4 (70–80% $\bar{S}_{ult}$), where cracking continues and fiber fracture begins, the amplitude distribution exhibits a small shift toward the channels in the range between 15 and 30. With increasing load in ranges 5 and 6 (80% $\bar{S}_{ult}$–failure), the amplitude distribution remains essentially unchanged. This is the load range over which both damage mechanisms are operating simultaneously. (It should be noted that range 6 includes events which occur prior to fracture but does not include events which occur during the actual fracture process. This acoustic emission of "rending" has been excluded in the present analysis.)

These patterns, which were observed when the acoustic emission was examined by load range—although subtle—were highly repeatable. In the range of loading over which transverse ply cracking is the dominant active damage mechanism (30–70% $\bar{S}_{ult}$), the amplitude distribution is clearly not shifted to lower amplitudes with respect to the distribution of amplitudes over the load range 70% $\bar{S}_{ult}$–failure when fiber fractures begin to occur. This phenonmenon is perhaps better seen in a slightly different presentation of the same data used to produce the amplitude histograms of Fig. 13. Figure 14 shows the relative distribution of events which occurred in selected channel ranges as a function of load. The channel ranges were chosen arbitrarily to be

RANGE NUMBER	CHANNELS INCLUDED
1	4– 9
2	10–15
3	16–21
4	22–27
5	28–33
6	34–50

At low loads there are few total counts and the interpretation is not meaningful. But as the first significant damage begins to occur at loads between 4 and 6 kN, the share of events in the lowest channel range begins to diminish. In this range (channels 4–9) are included spurious, low-amplitude background events which occur independently of the load as well as a sizable number of the actual damage-generated acoustic events. As channel range 1 decreases its share of the total, channel ranges 2–5 increase their relative share of the total cumulative events. This trend becomes significant at loads around 8 kN (approximately 65% $\bar{S}_{ult}$) when ply cracking becomes increasingly active. Significantly, the proportion of events in the highest channel range is seen to begin to diminish at loads above 10 kN and to continue to diminish through failure. This is the load range over which nearly all fiber fractures are occurring.

Such behavior is inconsistent with the assumption that fiber fracture is the source of higher-amplitude acoustic emissions. Indeed as the rate of fiber fracture is greater than the rate of ply cracking in the higher load ranges, it could be concluded that transverse ply cracking is the principal contributor of the higher-amplitude events and, in becoming proportionately a smaller fraction of the total cumulative damage as load is increased, its higher-amplitude contributions to the cumulative acoustic emission would likewise become proportionately smaller.

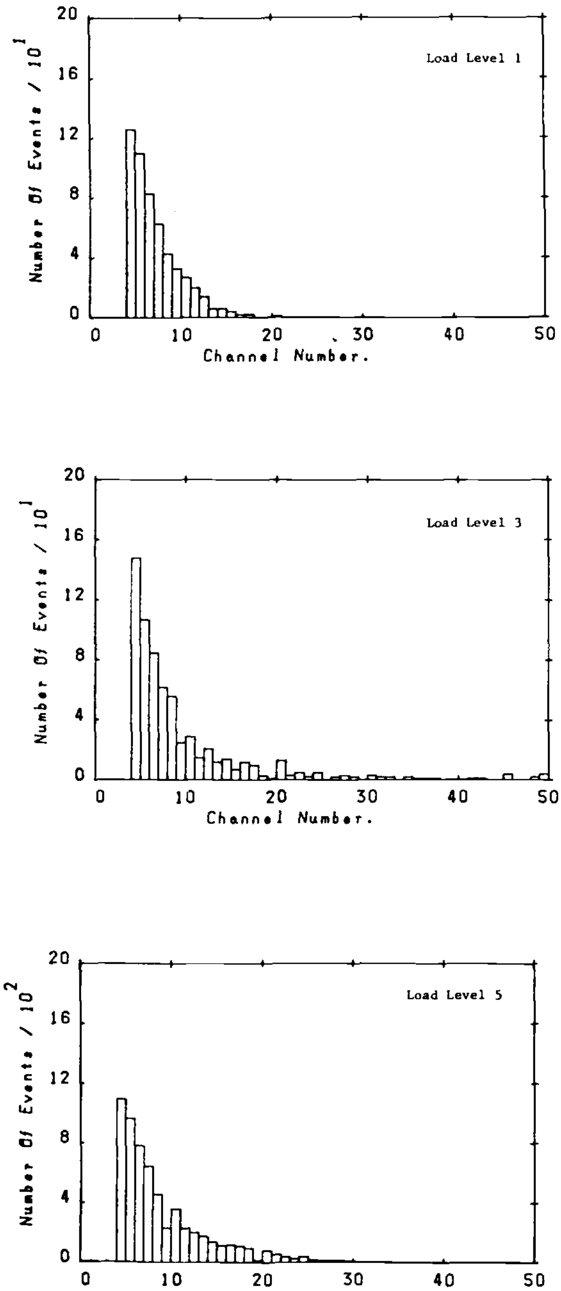

FIG. 13—*Amplitude distribution of AE events by load range for a* $[0,90_2]_s$ *laminate.*

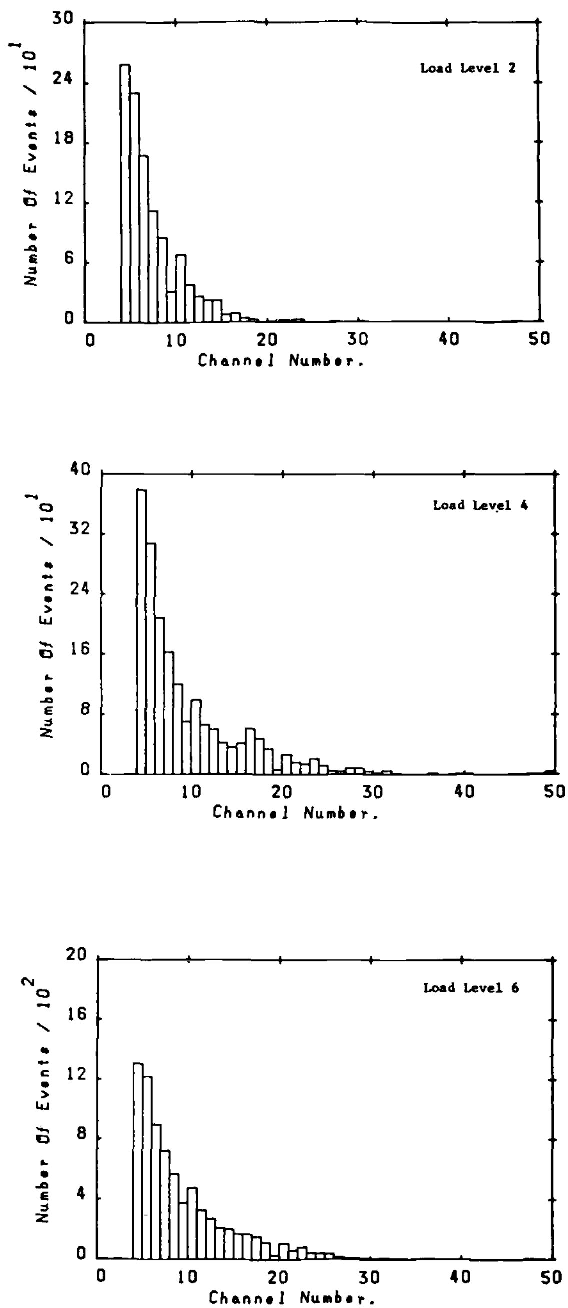

FIG. 13—*Continued.*

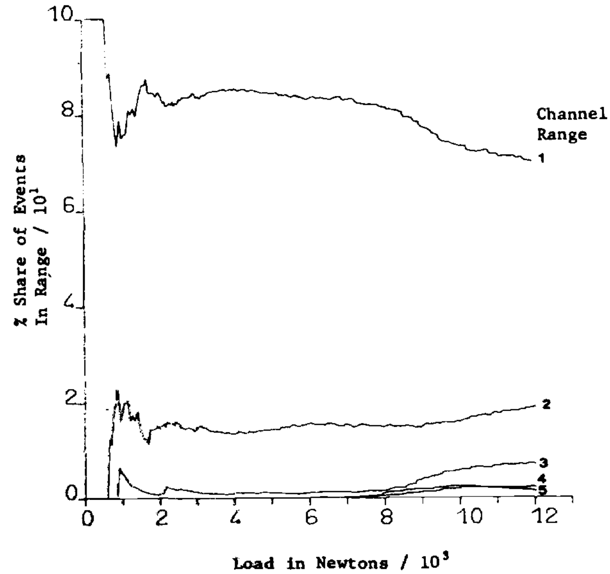

(a)

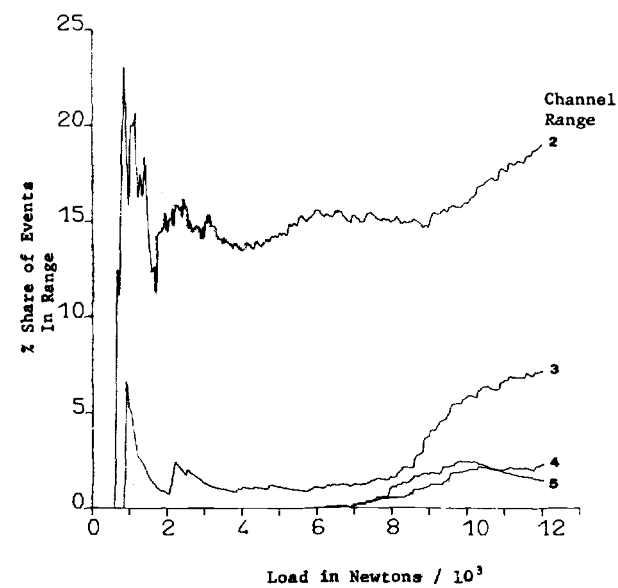

(b)

FIG. 14—*Percent share of AE events in range for a* $[0,90_2]_s$ *laminate.* (a) *Including channel range 1;* (b) *excluding channel range 1.*

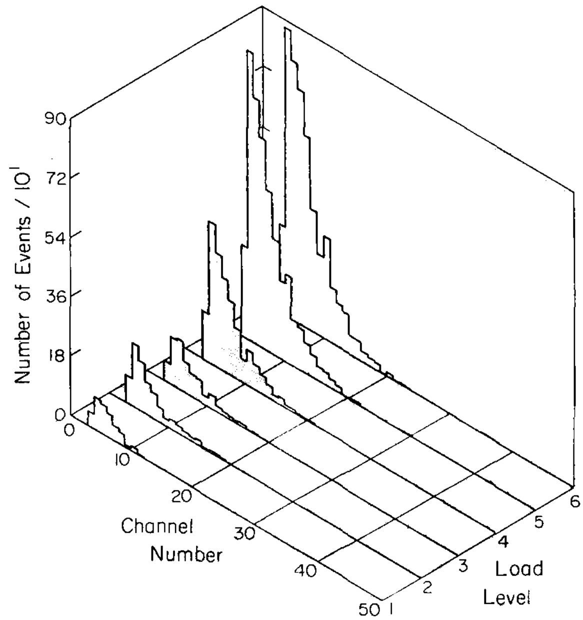

FIG. 15—*Amplitude distributions by load level for a* $[0,0]_s$ *laminate.*

These patterns were identified repeatedly in similar plots for other specimens tested. In all cases, without exception, the proportion of events occurring in the highest-amplitude range recorded during tension loading to failure of $[0,90_2]_s$ laminates diminished as the specimen neared failure.

Figure 15 presents the amplitude distribution data for a typical $[0,0]_s$ specimen. The load ranges are the same as previously defined. Events occurring at low load ranges are seen to principally populate channels in the range 4 to 22. In fact for this and all other unidirectional specimens loaded to failure, event amplitudes were generally below channel 25 for all load ranges. The shape of the distributions showed little change with increasing load, and no shift to higher amplitudes was observed. In comparison with the evolution of the amplitude distributions of cross-ply laminates with increasing load (Fig. 13), the results for the unidirectional specimens are seen to be more stationary. Whereas the cross-ply amplitude distribution shifts to higher-amplitude channels with increasing load and then retreats slightly to lower channels at loads near failure, the unidirectional specimens can be characterized by a single, low-amplitude-dominated distribution across the load-to-failure spectrum. Such a result is consistent with the operation of two damage mechanisms in the cross-ply laminate and only one in the unidirectional.

Figure 16 shows the cumulative percentage share of events in various channel ranges as defined previously. The virtual absence of events in channels 22–50 is notable. The fraction of events in channels 16–21 is essentially unchanged

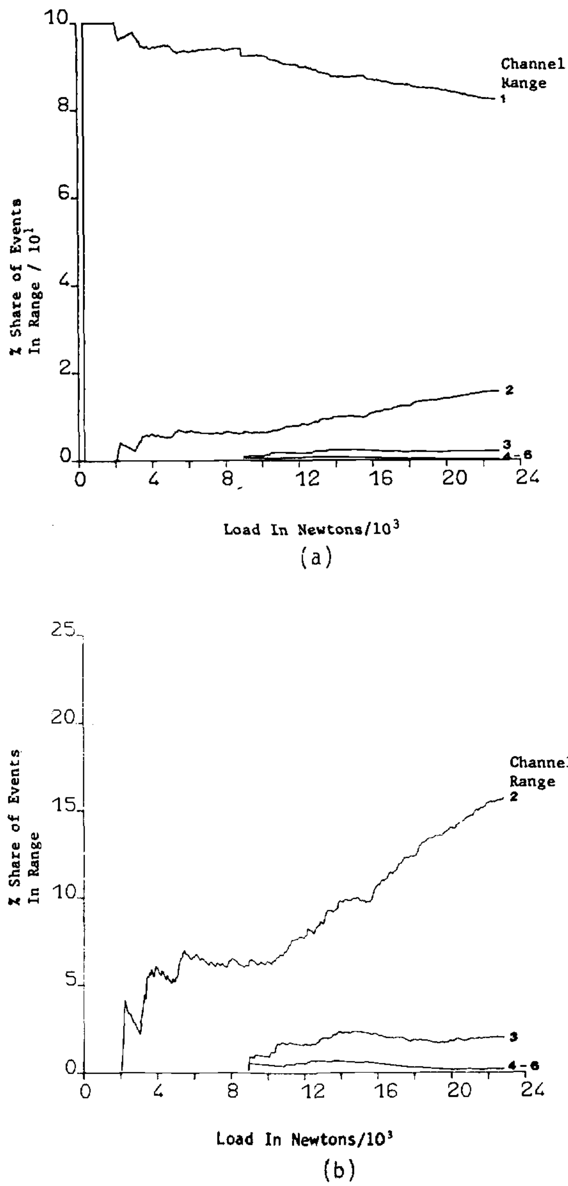

FIG. 16—*Percent share of events in range for a* $[0,0]_s$ *laminate.* (a) *Including channel range 1;* (b) *excluding channel range 1.*

through failure. The share of events in channels 10–15 increases at loads near failure. Inasmuch as fiber fractures are the dominant source of acoustic emission near failure, this channel range may best characterize the associated acoustic emission. It is significant that this pattern observed in the amplitude distribution of unidirectional laminates and attributable to fiber fracture alone is consistent with the conclusion reached for fiber fracture in cross-ply laminates: For this material system, fiber fracture is on average a lower-amplitude AE event than transverse ply cracking.

The association of fiber fracture with low-amplitude acoustic emission is counter to much of the conventional wisdom for acoustic emission in composite materials. It is frequently assumed that fiber fracture in any material system will release large amounts of strain energy relative to other damage mechanisms and will therefore be the source of the highest-amplitude acoustic emissions. This assumption is so common, perhaps because it seems so intuitive, that the lack of substantiating evidence of its general validity is sometimes unquestioned. It is indeed possible that for a particular fiber/resin system and a particular laminate type, fiber fracture may be the source of high-amplitude acoustic emission. However, as with nearly all aspects of AE analysis, the association of an attribute of the acoustic emission pulse, such as amplitude, with an attribute of the source of the pulse, such as energy, is complicated. First, given the dispersive nature of the composite media, there is no assurance that pulses originating with given relative amplitudes will arrive at the transducer with the same relative amplitudes. Second, fiber fracture occurring in surface plies may yield fundamentally different AE pulses at the receiver than the same fractures occurring in imbedded plies; that is, the laminate geometry and stacking sequence have an important influence on the characteristics of the received pulse. Third, and perhaps most important in the present context, the average energy released by a particular event is intimately related to the environment in which that event occurs. In the case of fiber fractures for example, it is commonly assumed that because they occur typically at elevated loads, the strain energy released must be greater than for events occurring at lower loads. By invoking this violin string analogy, the reality of fiber fracture is obscured. When fibers which are imbedded in moderately ductile resin matrices break at elevated loads, the strain energy released per unit volume is relatively large. However, the volume of fibers from which this energy is released is quite small if the fiber-matrix interface remains intact away from the fracture site. It has been shown in woven glass-reinforced plastic laminates for example that the energy released by the fracture of a fiber disbonded over a length of 2 mm is approximately 200 times greater than the fracture energy for an undisbonded fracture [*15*]. The present results for unidirectional graphite/epoxy laminates and prior work reported by other investigators [*16,17*] indicate that fiber-matrix disbonding in this system is minimal or nonexistent. It would not be unexpected then that the net energy released by a single fiber fracture, even at loads near failure, might be small relative to transverse ply cracking.

Discrimination between ply cracking and fiber fracture based on analysis of the amplitude produced requires that quite subtle distinctions be made. These distinctions in the evolution of the amplitude distribution with increasing load are nonetheless clear and repeatable. Identification of damage modes based solely upon attributes of the amplitude distribution of the associated acoustic emission is difficult. And when several modes are occurring simultaneously (albeit at different rates) the discrimination problem is formidable. In the present instance, discrimination between ply cracking and fiber fracture, perhaps the most physically distinguishable pair imaginable, requires a conclusion that ply cracking is a slightly higher-amplitude event on average than fiber fracture. Recent work on a similar graphite/epoxy system by other investigators [*18*] yielded the same conclusion.

Proper interpretation of AE data depends strongly upon knowledge of the details of damage at the microstructural level. Without such characterization plausible misinterpretations can obscure the real potential benefits of the technique for damage mode discrimination.

Acknowledgments

Portions of this work were supported by the Air Force Office of Scientific Research under Contract No. F33615-81-K-3225, the Defense Advanced Research Projects Agency under Contract No. DAAG29-82-K-0190, and by the School of Materials Science, University of Bath, England.

References

[*1*] Reifsnider, K. L. and Jamison, R. D. in *International Journal of Fatigue*, Vol. 4, 1982, pp. 187–197.

[*2*] Jamison, R. D., "Advanced Fatigue Damage Development in Graphite/Epoxy Laminates," Ph.D. dissertation, Virginia Polytechnic Institute and State University, Blacksburg, VA, 1982.

[*3*] Stalnaker, D. O. and Stinchcomb, W. W. in *Composite Materials: Testing and Design (Fifth Conference), ASTM STP 674*, American Society for Testing and Materials, Philadelphia, 1979, pp. 620–641.

[*4*] Freeman, S. M. in *Composite Materials: Testing and Design (Sixth Conference), ASTM STP 787*, American Society for Testing and Materials, Philadelphia, 1982, pp. 50–62.

[*5*] Jamison, R. D., Schulte, K., Reifsnider, K. L., and Stinchcomb, W. W. in *Effects of Defects in Composite Materials, ASTM STP 836*, American Society for Testing and Materials, Philadelphia, 1984, pp. 21–55.

[*6*] Kelly, A. in *Fracture of Composite Materials*, G. Sih, Ed., 1978, pp. 193–202.

[*7*] Wang, A. S. D., "Fracture Mechanics of Sublaminate Cracks," presented at the Advisory Group for Aerospace Research and Development Meeting, London, 1983.

[*8*] Bader, M. G., Bailey, J. E., Curtis, P. T. and Parvizi, A. in *Mechanical Behavior of Materials: Proceedings of the Third International Conference*, 1979, Vol. 3, pp. 227–239.

[*9*] Korcznskyj, J. and Morley, J. G., *Journal of Materials Science*, Vol. 16, 1981, pp. 1785–1795.

[*10*] Harris, B., *Metal Science*, Vol. 8, 1980, pp. 351–363.

[*11*] Masters, J. E. and Reifsnider, K. L. in *Damage in Composite Materials, ASTM STP 775*, American Society for Testing and Materials, Philadelphia, 1982, pp. 40–62.

[*12*] Reifsnider, K. L., Henneke, E. G. and Stinchcomb, W. W., "Defect-Property Relationships in Composite Materials" in *Proceedings*, 14th Annual Society of Engineering Science Meeting, Lehigh University, Bethlehem, PA, 1977.

[*13*] Reifsnider, K. L. and Highsmith, A. L., "Characteristic Damage States: A New Approach to Representing Fatigue Damage" in *Composite Laminates Materials: Experimental and Design in Fatigue*, Westbury House, Guildford, England, 1981.
[*14*] Highsmith, A. L. and Reifsnider, K. L. in *Damage in Composite Materials, ASTM STP 775*, American Society for Testing and Materials, Philadelphia, 1982, pp. 103–117.
[*15*] Guild, F. J., Phillips, M. G. and Harris, B., *NDE International*, Oct. 1980, pp. 209–218.
[*16*] Lorenzo, L. and Hahn, H. T., "Acoustic Emission Study of Fracture of Fibers Embedded in Epoxy Matrix" in *Proceedings*, First International Symposium on Acoustic Emission from Reinforced Composites, Los Angeles, July 1983.
[*17*] Fuwa, M., Bunsell, A. R. and Harris, B., "Acoustic Emission and Fatigue of Reinforced Plastics," *Composites—Standards, Testing and Design*, University of Sussex, Brighton, U.K.
[*18*] Valentin, D., Bonniou, Ph., and Bunsell, A. R., "Failure Mechanism Discrimination in Carbon-Reinforced Epoxy Composites," *Composites*, Vol. 14, No. 4, 1983.
[*19*] Harris, B., *Composites*, Oct. 1977, pp. 214–220.

Alain Charewicz[1] *and Isaac M. Daniel*[1]

Damage Mechanisms and Accumulation in Graphite/Epoxy Laminates

REFERENCE: Charewicz, A. and Daniel, I. M., "**Damage Mechanisms and Accumulation in Graphite/Epoxy Laminates,**" *Composite Materials: Fatigue and Fracture, ASTM STP 907,* H. T. Hahn, Ed., American Society for Testing and Materials, Philadelphia, 1986, pp. 274–297.

ABSTRACT: Damage mechanisms and accumulation, and associated stiffness and residual strength reductions, were studied in cross-ply graphite/epoxy laminates under cyclic tensile loading. Stress-life data were fitted by straight lines on a log-log scale. The fatigue sensitivity decreases with the number of contiguous 90-deg plies. Five different damage mechanisms were observed: transverse matrix cracking, dispersed longitudinal cracking, localized longitudinal cracking, delaminations along transverse cracks, and local delaminations at the intersections of longitudinal and transverse cracks. Variations of residual modulus and residual strength were measured as a function of cyclic stress level and number of cycles. The residual modulus shows a sharp reduction initially, followed by a more gradual decrease up to failure. The residual strength showed some characteristic features: a sharp decrease initially then a near plateau in the middle part of the fatigue life, and a rapid decrease in the last part of the fatigue life. A cumulative damage model is proposed based on residual strength and the concept of equal damage curves.

KEY WORDS: composite materials, graphite/epoxy, fatigue, damage mechanisms, damage accumulation, radiography, residual stiffness, residual strength, cumulative damage modeling

Damage mechanisms and damage accumulation have been the subject of many recent investigations [*1–12*]. The basic failure mechanisms in a composite laminate are matrix cracking, which can be intralaminar or interlaminar (delamination), interface failure (fiber-matrix debonding), and fiber fracture, splitting, or buckling. Damage development consists of three stages—initiation, growth, and localization—leading to ultimate failure.

The predominant mechanism in the initiation stage is the formation of intralaminar matrix cracks in the off-axis plies. These cracks extend up to the adjacent plies and they are either arrested or they cause interface failures leading to delamination and longitudinal cracking. The damage state of a ply within the laminate is characteristic of the layup and the loading direction.

[1] Graduate student and professor/director, respectively, Mechanics of Materials Laboratory, Illinois Institute of Technology, Chicago, IL 60616.

Further increase in load or number of fatigue cycles causes crack coupling with interfacial cracks, leading to local delamination and random fiber failures. It is assumed that such fiber failures are promoted by the stress concentration at the ends of the transverse cracks. This random fiber breakage leads to matrix cracking in the load-carrying plies, for example, 0-deg plies, in the loading direction, which can be distributed or localized. This leads to isolation of the 0-deg plies and bundles within those plies, with a concomitant increase in the local strain level. The criterion for ultimate failure is the maximum strain in the 0-deg plies. When the local strain reaches the ultimate strain for the ply, with the appropriate statistical distribution, failure occurs. In many cases most of the fiber failures and damage localization occur in the last 10% of the life of the laminate. The damage mechanisms above influence the overall mechanical behavior of the laminate. As the damage develops and grows, the stiffness of the damaged ply as well as that of the laminate is reduced. Analytical procedures have been developed for relating stiffness degradation to the damage state [*7,8,11*]. Stiffness reduction can be related to intralaminar crack density, delamination area, and a combination of both which leads to ply isolation. Ultimate failure is determined by the manner in which the load is redistributed and transferred into the load-carrying plies. The increase in strain in these plies is directly related to stiffness reduction. A rapid stiffness reduction precedes failure. Residual strength, like stiffness, is related to the damage state but in a less deterministic way. The various failure mechanisms affect residual strength in different ways from residual stiffness, although qualitatively both properties exhibit the same trends. Both residual stiffness and residual strength ultimately are related to residual life, although in an even less deterministic way.

The ultimate objective of the ongoing investigations is to understand and relate damage state, stiffness, residual strength, and fatigue life and thereby to develop models for predicting residual properties of a laminate that has undergone a known loading and environmental history. The several analysis methods developed in recent years can be categorized as follows:

1. lamina-based analyses,
2. dispersed defects/fracture mechanics analyses,
3. phenomenological or macromechanical analyses, and
4. hybrid analyses.

An example of a lamina-based analysis is described by Rotem [*13*]. The dispersed defects/fracture mechanics approach has been followed by Wilkins et al [*14*], Chou et al [*5*], and Wang and Slomiana [*15*]. Phenomenological theories have been proposed by Hashin and Rotem [*16*] and Poursartip et al [*17*]. An example of the hybrid approach is given by Reifsnider and co-workers [*4*].

All of the preceding work is quite general, although some specific examples have been discussed. The amount of relevant experimental data available for model verification is still limited. The primary experimental input into the models is modulus. It is recognized by most investigators that no approach followed to date is entirely satisfactory and there is need for continued investigation.

The present work deals with one specific aspect of the problem. An investigation is described of damage mechanisms and associated stiffness and residual strength reductions in crossply graphite/epoxy laminates under tension-tension fatigue loading, with the objective of developing a cumulative damage model.

Experimental Procedures

The material used in this investigation was AS-4/3501-6 graphite/epoxy obtained from Hercules Corp. in prepreg form. The unidirectional material was fully characterized under static loading.

Laminates of layups $[0/90_2]_s$, $[90_2/0]_s$, $[0/90_4]_s$, and $[90_4/0]_s$ were fabricated. Coupons 22.9 by 2.54 cm (9 by 1 in.) with 3.81-cm-long (1.5 in.) glass/epoxy end tabs were prepared from these plates. The straight-edge coupon was chosen, although there may be some questions about its validity. Most of the fatigue data to date have been obtained using such specimens. Proposed alternatives, such as the "streamlined" specimen, would create additional problems, especially for 0-deg specimens.

Fatigue testing was conducted with an electrohydraulic system using a sinusoidal tension-tension cyclic load with a stress ratio of $R = 0.1$ at a frequency of 10 Hz. This frequency is commonly used in fatigue testing of graphite/epoxy composites. Measurements during fatigue have indicated a temperature rise of the order of 2°C (3°F), which is considered small. This would affect, in a small way, only the comparison between fatigue and static results. A few coupons in each group were tested at a frequency of 1 or 2.5 Hz to determine more precisely failure occurring before 500 cycles. The first task was to determine stress versus number of cycles to failure (*S-N* curves) for the following layups: $[0_6]$, $[90_{16}]$, $[0/90_2]_s$, $[90_2/0]_s$, $[0/90_4]_s$, and $[90_4/0]_s$. Thirty to fifty specimens of each layup were tested to failure or runout at 10^6 cycles. Specimens that did not fail at 10^6 cycles were unloaded and their residual strength was measured.

A second task was undertaken to monitor internal damage during fatigue loading by means of X-radiography enhanced with a penetrant opaque to X-rays. As such, a nontoxic solution of zinc iodide, Kodak photoflow 200, isopropyl alcohol, and distilled water was used. The penetrant was applied to the specimen through the edges after loading to various levels. Within 45 min of the penetrant application the specimens were exposed to X-rays for 16 to 20 s at 7 kV and 3 mA in a Torr Radifluor 150 X-radiographic chamber. Kodak Type M Direct Exposure X-ray film was used. Two sets of tests were conducted, one at stresses below the fatigue limit at 10^6 cycles and one at stresses above it. The first set of specimens was tested at stress levels ranging from 69 MPa (10 ksi) up to the fatigue limit (at 10^6 cycles), in steps of 69 MPa (10 ksi). This gave seven stress levels for the first two layups and four for the last two layups. Two coupons were tested at each stress level. Cycling was interrupted and X-ray photographs taken, first at 100 cycles, then at increments of one decade up to 10^5 cycles, and finally at 5×10^5 cycles. In the second set of tests two specimens of each type were tested at each of two stress levels above the endurance limit. X-ray photographs were taken at intervals sufficient to yield five inspections before failure.

Residual modulus measurements were conducted for the $[0/90_2]_s$ and $[0/90_4]_s$ laminates on five specimens at each of two stress levels above the endurance limit. Stiffness measurements were made using a 2.54-cm-long (1 in.) strain gage extensometer mounted near the center of the specimen gage length. Obviously, the measured stiffness is representative of the damage within the gage length of the extensometer and is more truly representative in the cases of uniformly distributed damage. In the more general cases the results become more representative of the overall damage as the number of specimens increases. Stiffness was measured during cycling in a few cases; however, most of the measurements were made quasi-statically after interrupting the cyclic loading. Results from both types of measurement were the same.

Residual strength was measured for the following layups: $[0/90_2]_s$, $[90_2/0]_s$, $[90_4/0]_s$. Twenty to thirty specimens of each layup were cycled at each of two different cyclic stress levels above the endurance limit. The cyclic tests were interrupted at various preselected numbers of cycles and the specimens were then loaded statically to failure to determine residual strength. Thus, residual stength curves were obtained as a function of number of fatigue cycles at which cyclic loading was interrupted. Since appreciable scatter was found, three to four sets of specimens were used for each curve. The coupons from each set came from the same plate and each set was tested over the full range of the curve, from static to fatigue failure. This was done so that each residual strength curve would represent the average of the properties of the four plates used.

Results

S-N *Curves*

Experimental results showed that the $[90_2/0]_s$ laminate, although approximately 10% stronger than the $[0/90_2]_s$ laminate in quasi-static tension, is more fatigue-sensitive and has a lower residual strength at high numbers of cycles. A similar trend holds true for the $[0/90_4]_s$ and $[90_4/0]_s$ laminates.

All data above were fitted by straight lines on a log-log scale as follows:

$$\log S = \log F_e - \frac{1}{m} \log N \tag{1}$$

where

S = applied cyclic stress amplitude,
F_e = equivalent static strength,
N = number of cycles to failure, and
m = exponent.

TABLE 1—S-N *Curve parameters.*

Layup	Equivalent Static Strength F_e, MPa (ksi)	Exponent, m
$[90_{16}]$	64 (9.28)	57.67
$[0/90_2]_s$	779 (113)	25.42
$[90_2/0]_s$	822 (119)	22.99
$[0/90_4]_s$	456 (66)	50.25
$[90_4/0]_s$	427 (62)	31.00

The equivalent static strength, as defined by Sendeckyj [*18*], is uniquely related to the fatigue life and residual strength of the material. Following the fitting procedures described in this reference, the parameters were determined for the *S-N* curves of the various laminates as given in Table 1. Results of this curve-fitting are shown in Fig. 1 along with additional results from a more complex fitting for the $[0_6]$ lamina. The fatigue sensitivity, as evidenced by the slope of the *S-N* curve, decreases with increasing number of 90-deg plies.

Damage Development

Damage mechanisms and development are strongly dependent on laminate layup and stacking sequence. They also depend, in some cases, on the level of

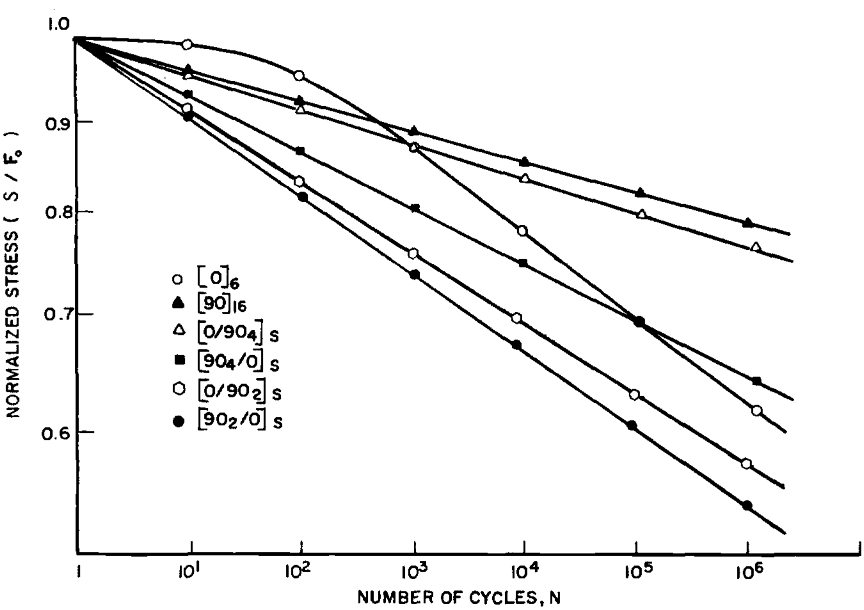

FIG. 1—*Stress-life* (S-N) *curves for unidirectional and cross-ply graphite/epoxy laminates.*

cyclic stress and the number of cycles to failure. Five different damage mechanisms were observed:

1. transverse matrix cracking in the 90-deg plies,
2. dispersed longitudinal cracking in the 0-deg plies, randomly distributed throughout the specimen,
3. localized (major) longitudinal cracking,
4. delamination in the 0/90-deg interface along transverse cracks, and
5. small local delaminations at the intersection of longitudinal and transverse cracks.

No edge delamination was observed in any of the laminates, except for a few broken fibers and fiber-debonding at the very edge.

The first type of mechanism is illustrated in Fig. 2 for a $[90_2/0]_s$ laminate cycled at a peak stress of 207 MPa (30 ksi). The multiplication of transverse cracks with number of cycles at different cyclic stress levels is illustrated in Fig. 3 for the same laminate. The number of cracks reaches a limiting value, or characteristic damage state (CDS), in every case. The maximum transverse crack densities measured in the four laminates tested are

$[0/90_2]_s$	1.81 cracks/mm (46.1 cracks/in.)
$[90_2/0]_s$	1.60 cracks/mm (40.7 cracks/in.)
$[0/90_4]_s$	1.35 cracks/mm (34.4 cracks/in.)
$[90_4/0]_s$	0.85 cracks/mm (21.6 cracks/in.)

Only the results for the $[0/90_4]_s$ laminate are in good agreement with quasi-static results. In the case of the $[90_2/0]_s$ and $[90_4/0]_s$ laminates it was observed that, when the cyclic stress is low enough, a limiting value lower than the CDS can be reached. The last four types of the above damage mechanisms are illustrated in Fig. 4.

In the $[0/90_2]_s$ laminate dispersed longitudinal cracking is observed mainly at low loads [below 550 MPa (80 ksi)] and increases with number of cycles up to failure. At higher stresses [above 580 MPa (84 ksi)] localized longitudinal cracking appears to be the main damage mechanism prior to failure. A sequence of radiographs of the first type of failure is shown in Fig. 5. The two types of longitudinal damage prior to failure are illustrated in Fig. 6. Ultimate failure patterns show the variation of the dominant failure mechanisms as we move from quasi-static loading to short-life (high stress) fatigue, to long-life (low stress) fatigue (Fig. 7). Static and short-life failure patterns tend to be straight transverse failures, whereas long-life patterns are brush-like.

The $[90_2/0]_s$ laminate exhibits dispersed longitudinal cracking, more extensive than the $[0/90_2]_s$ laminate, and some major localized longitudinal cracking. When a major longitudinal crack appears it is accompanied by local delamination at

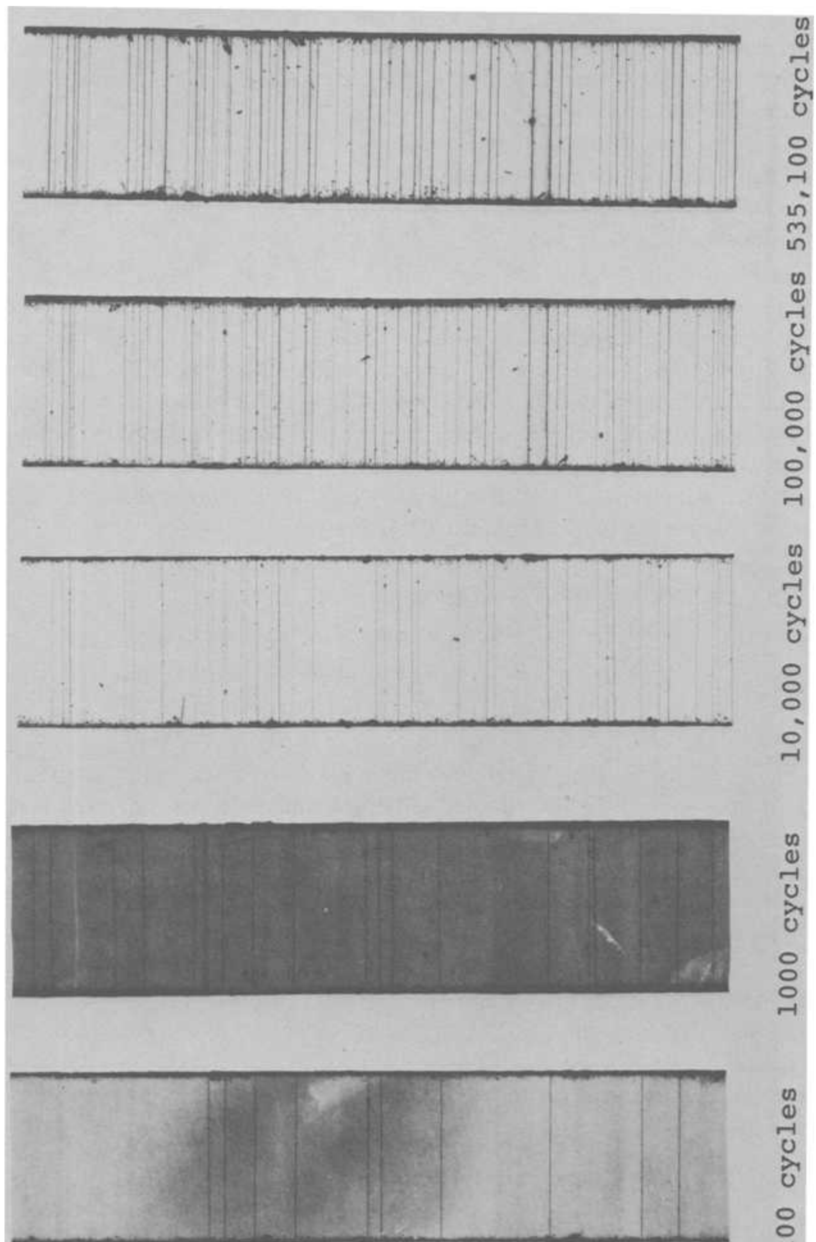

FIG. 2—*X-Radiographs of a* $[90_2/0]_S$ *graphite/epoxy laminate subjected to fatigue loading at 207 MPa (30 ksi).*

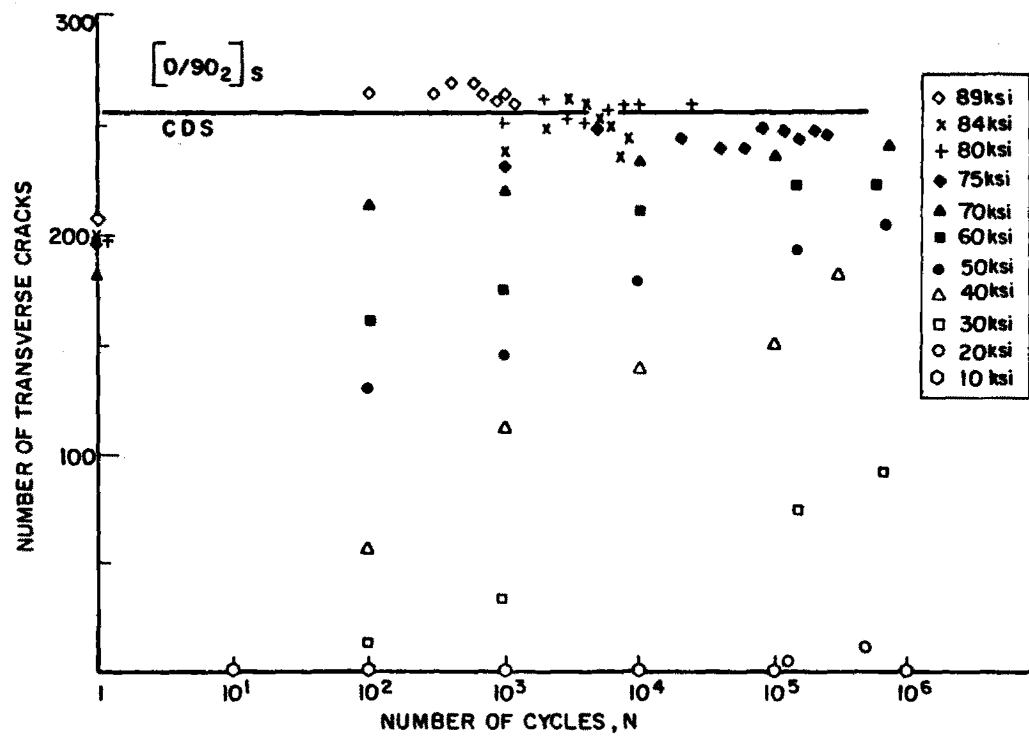

FIG. 3—*Number of transverse cracks over a 14-cm (5.5 in.) length in* $[0/90_2]_s$ *graphite/epoxy laminate as a function of number of cycles and applied stress.*

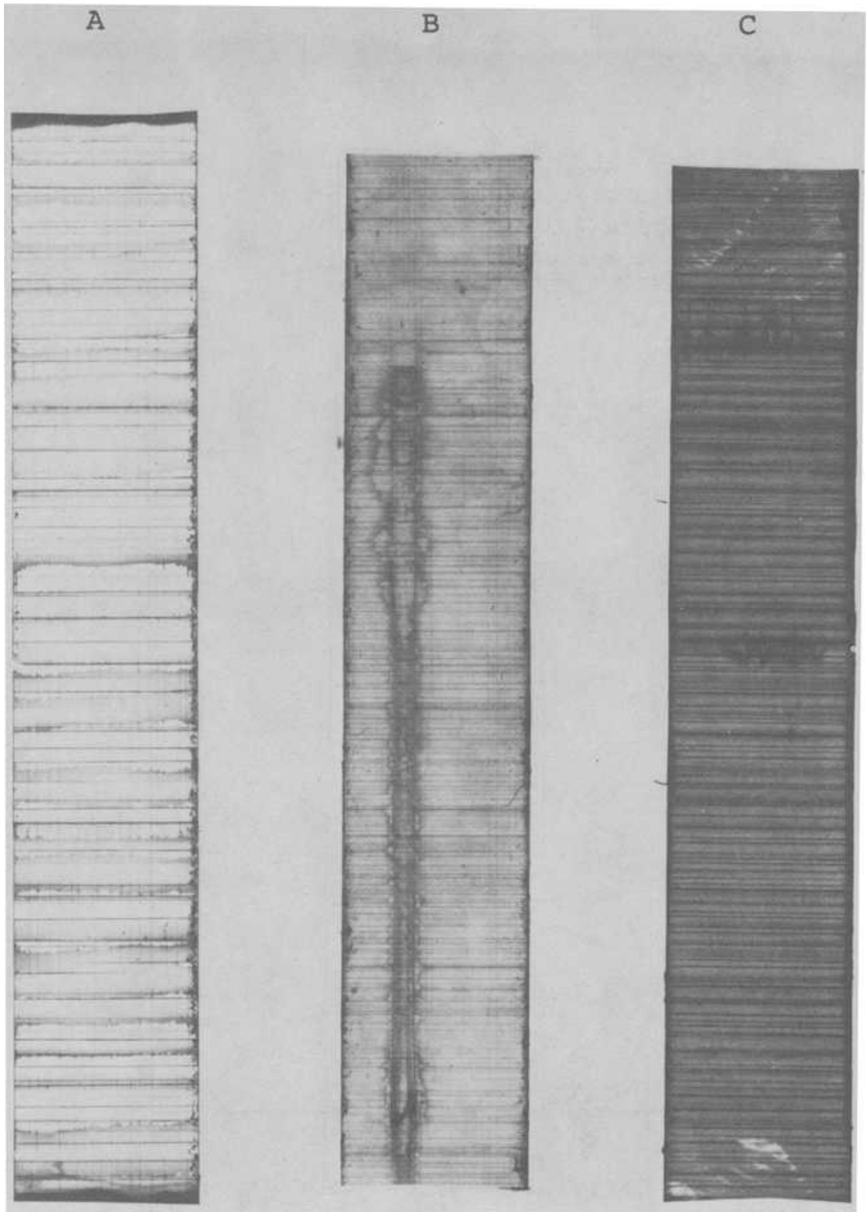

FIG. 4—*Illustration of five different types of damage mechanisms:* (a) *transverse cracking, dispersed longitudinal cracking, and delamination along transverse cracks in* $[90_4/0]_s$ *laminate;* (b) *transverse cracking and localized longitudinal cracking in* $[90_2/0]_s$ *laminate; and* (c) *transverse cracking and local delamination at intersection of transverse and longitudinal cracks in* $[0/90_4]_s$ *laminate.*

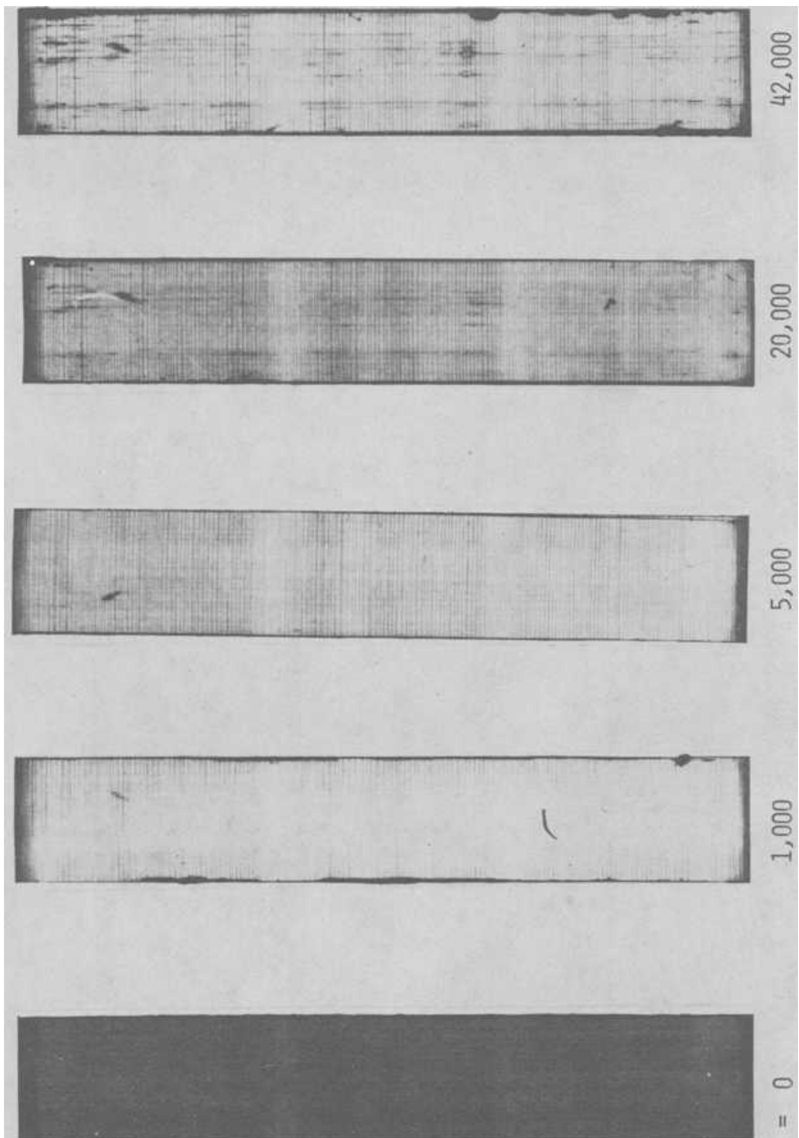

FIG. 5—*X-Radiographs of* $[0/90_2]_s$ *graphite/epoxy specimen tested under fatigue loading with* R = *0.1*, σ_{max} = *518 MPa (75 ksi), for various number of cycles.*

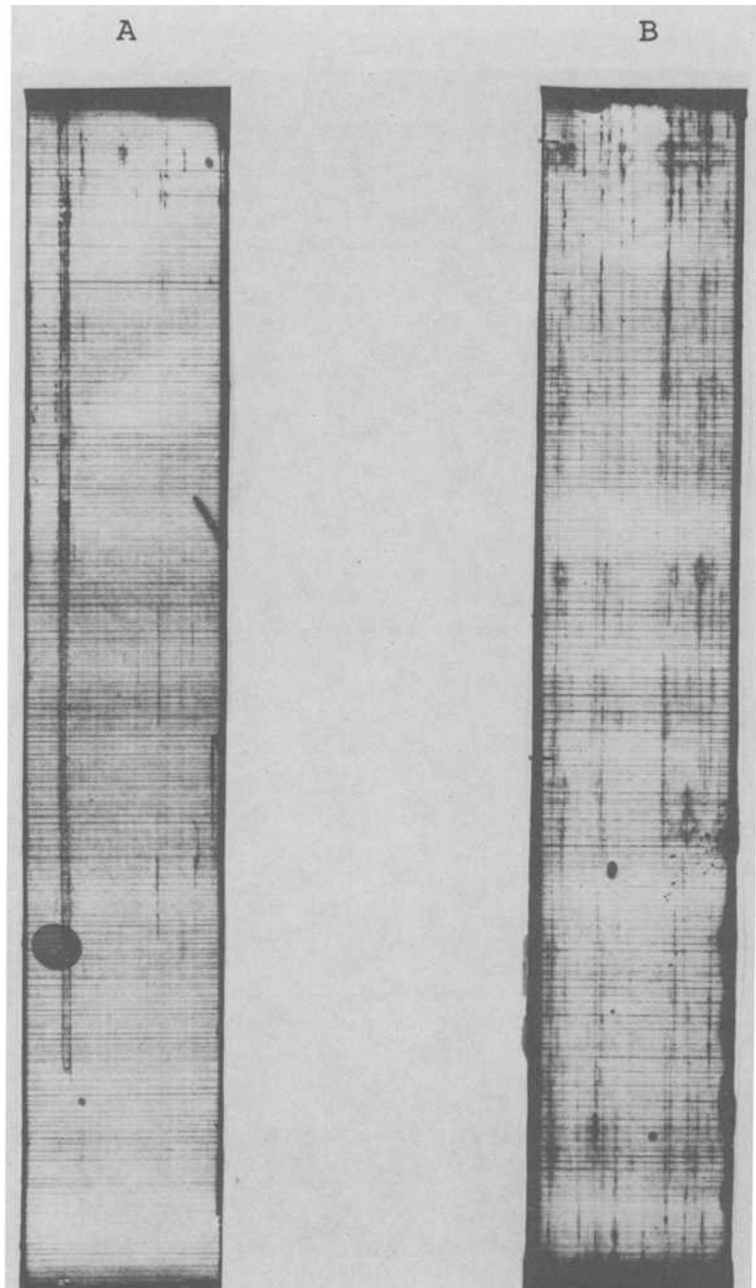

FIG. 6—*Damage mechanisms in* $[0/90_2]_s$ *graphite/epoxy laminate:* (a) *localized longitudinal cracking at high stress (short life);* (b) *dispersed longitudinal cracking at low stress (long life).*

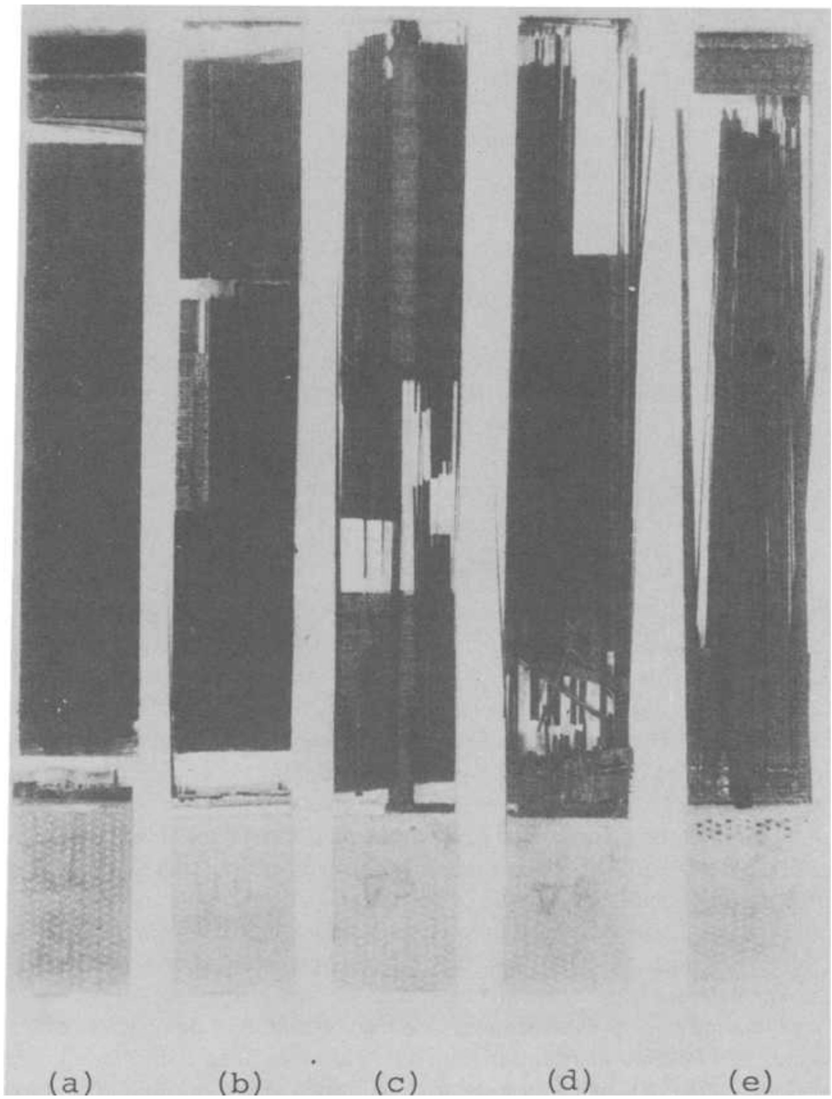

(a) *static test*, σ_u = *616 MPa (89 ksi);*
(b) *fatigue test*, R = 0.1, σ_{max} = *606 MPa (88 ksi)*, N = *370 cycles;*
(c) *fatigue test*, R = 0.1, σ_{max} = *548 MPa (79 ksi)*, N = *2140 cycles;*
(d) *fatigue test*, R = 0.1, σ_{max} = *531 MPa (77 ksi)*, N = *12 357;*
(e) *fatigue test*, R = 0.1, σ_{max} = *495 MPa (72 ksi)*, N = *349 529.*

FIG. 7—*Failure patterns of* $[0/90_2]_s$ *graphite/epoxy specimens tested under static and fatigue loading conditions.*

the intersections with transverse cracks, as shown in Fig. 8. The dominant damage mechanism prior to failure is either an increase in the number of dispersed longitudinal cracks or the growth of major longitudinal damage following dispersed longitudinal cracking.

No major localized damage appears in the $[0/90_4]_s$ laminate before failure. Some dispersed longitudinal cracking and local delamination appear, but to a lesser extent than in the $[0/90_2]_s$ laminate. The absence of any major damage in this laminate may account for the large scatter in fatigue life (three to four decades).

The $[90_4/0]_s$ laminate behaves in a way similar to the $[90_2/0]_s$ laminate, except for the presence of delaminations between the 0- and 90-deg plies along the transverse cracks, (Fig. 9). The mechanism controlling failure appears to be an increase in dispersed longitudinal cracking, which is more intense than in the case of the $[90_2/0]_s$ laminate. Dispersed longitudinal crack density increases with number of cycles and reaches a critical value at failure [0.59 cracks/mm (15 cracks/in.)]. A correlation appears to exist between transverse and longitudinal cracking as shown in Fig. 10.

Stiffness Variations

Stiffness changes occur throughout the fatigue life of the specimens and are related to the damage development. The largest change occurs during the first loading cycle as illustrated by the stress-strain curve for a typical $[0/90_4]_s$ specimen (Fig. 11). The initial part of the curve is linear up to an applied stress of 166 MPa (24 ksi) or a strain of approximately 0.005. No cracking appears up to this level. Beyond this threshold level, transverse matrix cracking increases rapidly through the second stage of deformation up to a stress level of approximately 228 MPa (33 ksi). The third stage of deformation with an increase in stiffness corresponds to a leveling off of the crack density, that is, to the CDS of the laminate. The first unloading curve for this laminate starts with a slope slightly lower than the initial slope of the loading curve and ends with a slope approximately equal to the terminal slope of the first loading curve.

As the number of cycles increases, the loading and unloading curves tend to coincide and become more linear (Fig. 11). However, they exhibit in all cases a stiffening effect at higher stresses, a phenomenon which must be related to a similar effect in 0-deg unidirectional laminates.

The residual (initial) modulus was measured for the $[0/90_2]_s$ and $[0/90_4]_s$ laminates at two cyclic stress levels as a function of loading cycles. The modulus was normalized by dividing it by the initial value, and the number of cycles by dividing it by the life of each individual specimen. Results for the $[0/90_4]_s$ laminate are shown in Fig. 12. Results for the $[0/90_2]_s$ laminate are similar. The normalized modulus shows a sharp drop initially, followed by a more gradual decrease up to failure.

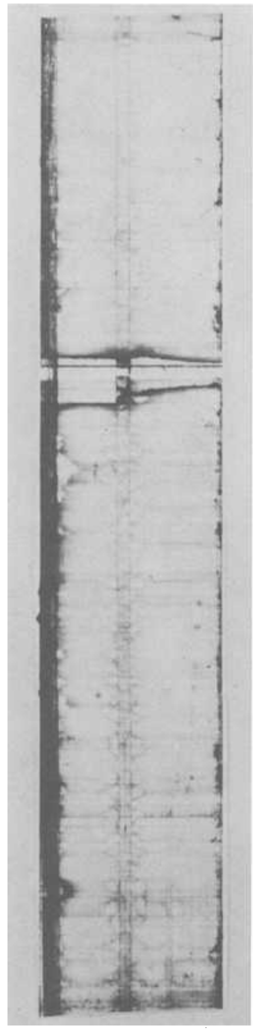

FIG. 8—*Fatigue damage in* $[90_2/0]_s$ *graphite/epoxy laminate [localized longitudinal crack with delaminations at intersections with transverse cracks; 99.9% of fatigue life at 517 MPa (75 ksi)].*

Residual Strength

Residual strength results showed a very large scatter in both strength and number of cycles. An averaging scheme was devised to take into account failure points of specimens that failed during fatigue loading. To reduce the scatter somewhat, data obtained at various cyclic stress levels were pooled together by assuming that the normalized residual strength as a function of the normalized

FIG. 9—*Fatigue damage in* $[90_4/0]_s$ *graphite/epoxy laminate [dispersed longitudinal cracking and delaminations along transverse cracks; 94% of fatigue life at 310 MPa (45 ksi)].*

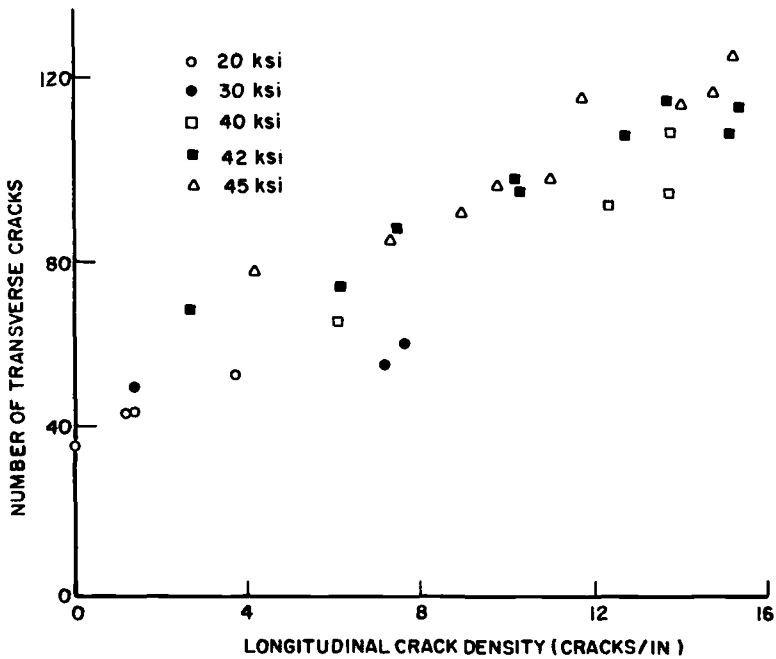

FIG. 10—*Correlation between transverse and longitudinal matrix cracking in* $[90_4/0]_s$ *graphite/epoxy laminate [transverse cracks measured over a 14-cm (0.546 in.) length].*

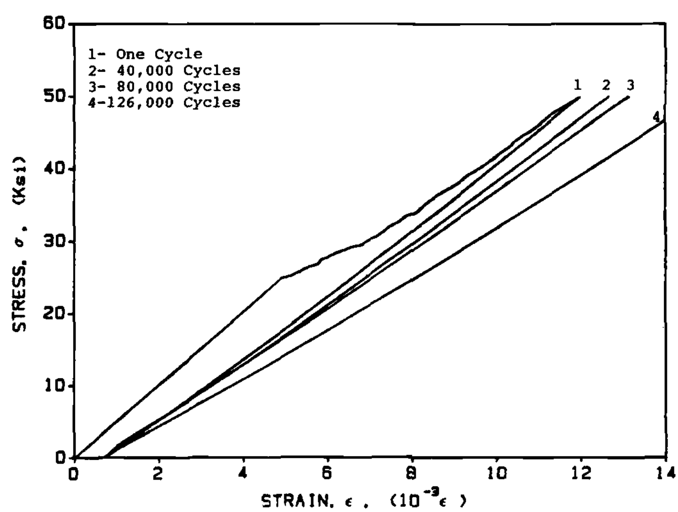

FIG. 11—*Stress-strain curves for* $[0/90_4]_s$ *graphite/epoxy specimen at various stages of fatigue life (R = 0.1).*

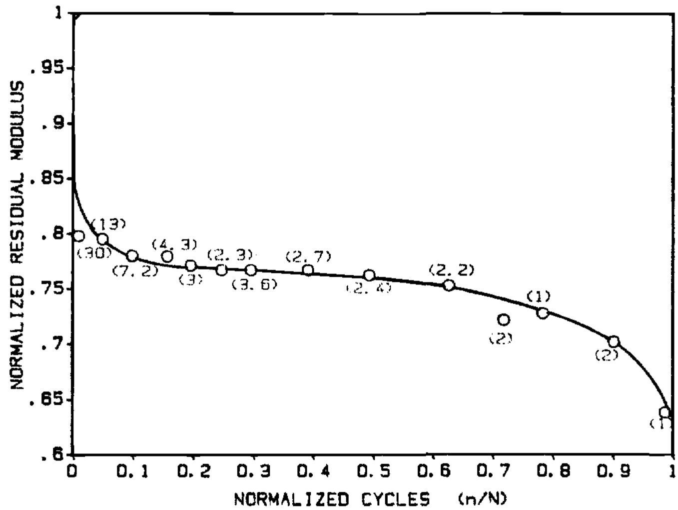

FIG. 12—*Normalized residual modulus for* $[0/90_4]_s$ *graphite/epoxy specimen under fatigue loading at* R $= 0.1$ *and* $\sigma_{max} = 345$ *MPa (50 ksi).*

number of cycles is independent of the applied stress. Thus

$$\frac{F_r - \sigma_a}{F_0 - \sigma_a} = g\left(\frac{n}{N}\right) \tag{2}$$

where

F_r = residual strength after n cycles,
F_0 = mean static strength (used as a normalizing factor),
σ_a = applied cyclic stress,
N = number of cycles to failure at stress σ_a, and
$g\left(\frac{n}{N}\right)$ = function of normalized number of cycles.

Equation 2 can be written as

$$\frac{f_r - s}{1 - s} = g\left(\frac{n}{N}\right) \tag{3}$$

where

$f_r = F_r/F_0$ = normalized residual strength and
$s = \frac{\sigma_a}{F_0}$ = normalized applied cyclic stress.

From the definitions above it follows that the function $g(n/N)$ must satisfy the conditions

$$g(0) = 1$$
$$g(1) = 0 \tag{4}$$

Normalized residual strength data for the $[0/90_2]_s$ and $[90_2/0]_s$ laminates are shown in Figs. 13 and 14, respectively. Curves have been drawn having the same characteristic features as the residual modulus curves, that is, a sharp decrease initially, then a near plateau in the middle part of the fatigue life, and a rapid decrease in the last part of the fatigue life. The existence of the plateau is only conjectured at this point. In fact, the experimental data show a local minimum in residual strength in the first quarter of the fatigue life and a local maximum in the middle of the fatigue life. The paradox of increasing residual strength with number of cycles is not totally inconceivable. The following is a plausible explanation. In the beginning, as the specimen is cycled, damage sites are created which reduce its strength. As the specimen is cycled further, more damage sites are created and dispersed, blunting the severity of the early ones, and thus actually increasing the residual strength. A better characterization of the residual strength curve for various laminates merits further investigation.

Cumulative Damage Modeling

An approach to a cumulative damage model is proposed based on residual strength and the concept of equal damage curves. For a specimen cycled at a

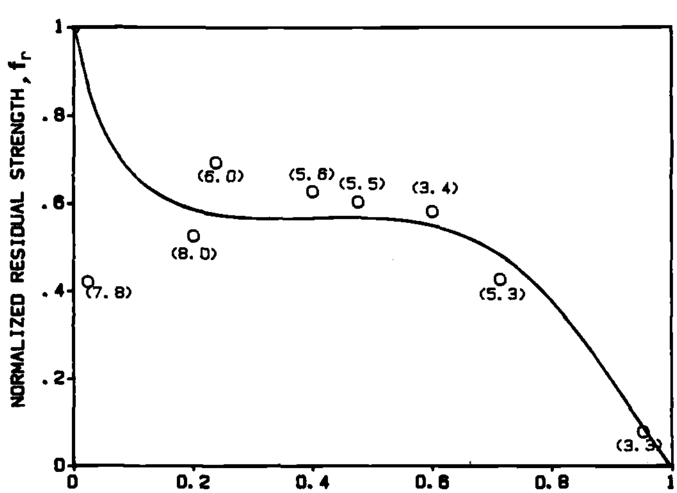

FIG. 13—*Normalized residual strength versus normalized number of cycles for* $[0/90_2]_s$ *graphite/epoxy laminate (numbers in parentheses refer to number of specimens weighted).*

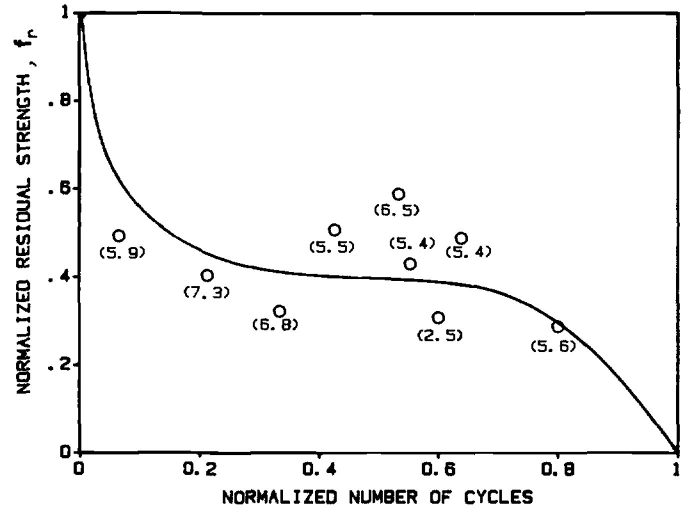

FIG. 14—*Normalized residual strength versus normalized number of cycles for* $[90_2/0]_s$ *graphite/epoxy laminate (numbers in parentheses refer to number of specimens weighted).*

stress level σ for n cycles the residual strength can be expressed as

$$F_r = f(\sigma,n) \tag{5}$$

satisfying the conditions at $n = 1$ and $n = N$

$$F_0 = f(\sigma,1) \tag{6}$$

$$\sigma = f(\sigma,N) = S \tag{7}$$

where N is the number of cycles to failure at stress σ.

The definition of damage as a function of residual strength only allows the determination of equal damage curves in the (σ,n) plane. Thus, a specimen cycled at a stress σ_1 for n_1 cycles has the same damage as a specimen cycled at a stress σ_2 for n_2 cycles if

$$f(\sigma_1,n_1) = f(\sigma_2,n_2) \tag{8}$$

Thus, points (σ_1,n_1) and (σ_2,n_2) lie on a damage curve defined by the value of residual strength of all points along this curve. Since all points on the S-N curve correspond to a residual strength S, the equal damage curve of residual strength S starts at point (S,N) on the S-N curve as shown in Fig. 15. This figure illustrates the method of obtaining the damage curve of residual strength S from the residual strength curves at different cyclic stress levels. Residual life predictions can be

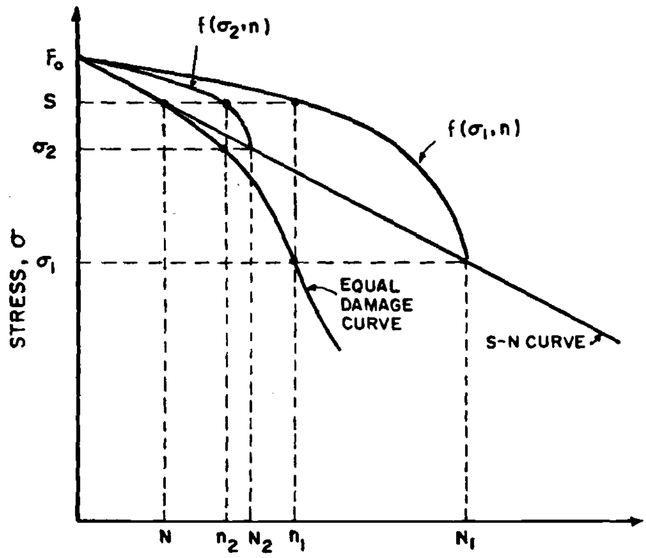

FIG. 15—*Prediction of residual life for two-step loading by means of equal damage curve.*

made once the equal damage curves are determined. To determine, for example, the residual number of cycles at a cyclic stress σ_2, after the specimen has been cycled at stress σ_1 for n_1 cycles, one has to follow the damage curve passing through point (σ_1,n_1) up to $\sigma = \sigma_2$. Residual life then is equal to $N_2 - n_2$ as shown in Fig. 15.

An experimental determination of residual life was conducted on the $[90_2/0]_s$ laminate. Seven specimens were cycled at 552 MPa (80 ksi) for 3000 cycles and then at 587 MPa (85 ksi) up to failure. The average residual number of cycles obtained at 587 MPa (85 ksi) was found to be 326 cycles for the geometric mean (average of log n) and 995 cycles for the arithmetic mean. From the *S-N* curve (Fig. 1) and the residual strength curve (Fig. 14) determined for this laminate one can predict a residual life of 450 cycles, which is quite good in view of the scatter in the number of cycles.

To generalize the approach, a damage function D must be defined having the values 0 and 1 at the beginning and end of the life, respectively. The normalized change in residual strength, obtained from Eq 3, can be defined as one particular form of the damage function

$$\frac{1 - f_r}{1 - s} = 1 - g\left(\frac{n}{N}\right) = D\left(\frac{n}{N}\right) \tag{9}$$

In this particular case the damage function is only a function of the normalized number of cycles and independent of the cyclic stress level.

In order to take into account the variation of damage mechanisms with stress level a more general form of the damage function, or of residual strength, is necessary. One approach would be to define a damage rate function of the normalized number of cycles, cyclic stress level, and the damage itself

$$\frac{dD}{dn} = F\left(\frac{n}{N}, s, D\right) \tag{10}$$

The number of cycles N_f required to increase the damage from an initial value D_i to a final value D_f is

$$N_f = \int_{D_i}^{D_f} \frac{dD}{F\left(\frac{n}{N}, s, D\right)} \tag{11}$$

In the case of spectrum fatigue loading, the damage produced after the kth block of loading is expressed as

$$D_k = \sum_{i=1}^{k} \int_0^{n_i} F\left(\frac{n_i}{N}, s_i, D_i\right) dn \tag{12}$$

which is a form of Miner's rule. A more general form of function F above, which is sensitive to block loading sequence, is obtained by replacing n/N with $\log n/\log N$ [*19*].

Although the prediction obtained in the example discussed before is fairly close to the experimental value of residual life, considering the scatter in the number of cycles, the proposed model is far from satisfactory. The main drawback is the complete reliance on experimental determination of the residual strength curve, which apparently has a plateau. This fact creates many problems since there is no single-valued correspondence between residual strength and number of cycles over this plateau. This also implies that since residual strength is assumed to be a single-valued function of damage, the latter should not change over the entire plateau, a fact which is contrary to the X-ray observations. Thus, residual strength alone does not seem to be a very good parameter to represent damage, since it appears insensitive to damage variations over the entire length of the plateau.

Summary and Conclusions

Damage mechanisms and accumulation, and associated stiffness and residual strength reductions, were studied in cross-ply graphite/epoxy laminates under cyclic tensile loading.

Stress-life data were fitted by straight lines on a log-log scale. The fatigue sensitivity decreases with increasing number of contiguous 90-deg plies. Laminates such as the $[0/90_2]_s$ have lower static strength but longer fatigue life than their stacking sequence variation $[90_2/0]_s$. Five different damage mechanisms were observed: transverse matrix cracking, dispersed longitudinal cracking, major localized longitudinal cracking, delaminations along transverse cracks, and local delaminations at the intersection of longitudinal and transverse cracks. The first type of damage is a low-level type and develops early in the fatigue life. It reaches the CDS level long before laminate failure. However, the CDS level is not always attained if the cyclic stress is too low. Longitudinal cracking, dispersed or localized, is a particularly active form of damage. The higher fatigue sensitivity observed in the $[90_n/0]_s$ laminates corresponds to a larger extent of longitudinal cracking, as compared with the $[0/90_n]_s$ laminates.

Failure patterns vary with stress level and number of cycles to failure. Under monotonic loading failure is brittle-like and concentrated. At high stresses and short fatigue lives failure results from few localized flaws, whereas at lower stresses and longer fatigue lives failure results from more dispersed flaws. These observations cast doubts on the validity of accelerated testing as a means of life prediction.

The residual modulus shows a sharp reduction initially, followed by a more gradual decrease up to failure. The residual strength showed a very large scatter in both strength and number of cycles. To minimize the effects of large scatter, all data for a given laminate were pooled together and a normalized residual strength, independent of stress level, was expressed as a function of normalized number of cycles. The characteristic features of residual strength are a sharp decrease initially, then a near plateau in the middle part of the fatigue life, and a rapid decrease in the last part of the fatigue life. The existence of the plateau is not certain in view of the large scatter. In fact, there is evidence of nonmonotonic change in residual strength. This could be rationalized by the dominance of localized flaws in the early part of the fatigue life, causing a sharp decrease in residual strength. Later on in the fatigue life, flaws become more dispersed and somewhat less severe, possibly causing an increase in residual strength.

A tentative cumulative damage model is proposed based on residual strength and the concept of equal damage curves. Although a reasonable prediction based on this model was demonstrated, the application of the model relies on a good definition of the residual strength curve. The latter is very difficult to obtain in view of the scatter. The characteristic plateau, if indeed it exists, poses a great problem as there is no single-valued correspondence between residual strength and number of cycles over this plateau. Thus, residual strength alone, as it is measured now, does not seem to be a very discriminating measure of damage. Furthermore, the proposed model, based on pooling of normalized strength data, does not account for damage dependence on actual load level and life. More sophisticated and complex models are needed to account for the various damage mechanisms and their relationship to load level and life.

Acknowledgment

The work described here was sponsored by the Office of Naval Research (ONR). We are grateful to Dr. Yapa Rajapakse of ONR for his encouragement and cooperation. Thanks are due Dr. G. Yaniv, Messrs. H. C. Soo, J. W. Lee, and P. Draper for their assistance, and Mrs. Dorthy Howard for typing the manuscript.

References

[*1*] Reifsnider, K. L., Henneke, E. G., II, and Stinchcomb, W. W., "Defect Property Relationships in Composite Materials," AFML-TR-76-81, Air Force Materials Laboratory, Wright-Patterson AFB, Dayton, OH, Part IV, 1979.

[*2*] Wang, A. S. D. and Crossman, F. W., "Initiation and Growth of Transverse Cracks and Edge Delamination in Composite Laminates—Part I—An Energy Method," *Journal of Composite Materials,* June 1980.

[*3*] Crossman, F. W., Warren, W. J., Wang, A. S. D., and Law, G. L., "Initiation and Growth of Transverse Cracks and Edge Delamination in Composite Laminates—Part II—Experimental Correlation," *Journal of Composite Materials,* June 1980.

[*4*] Liechti, K. M., Reifsnider, K. L., Stinchcomb, W. W., and Ulman, D. A., "Cumulative Damage Model for Advanced Composite Materials," AFWAL TR-82-4094, July 1982.

[*5*] Chou, P. C., Wang, A. S. D., and Miller, H., "Cumulative Damage Model for Advanced Composite Materials," Air Force Wright Aeronautical Laboratories, Dayton, OH, TR-82-4083, Sept. 1982.

[*6*] Nuismer, R. J. and Tan, S. C. in *Mechanics of Composite Materials, Recent Advances (Proceedings,* IUTAM Symposium on Mechanics of Composite Materials), Z. Hashin and C. T. Herakovich, Eds., Pergamon Press, New York, 1983, pp. 437–448.

[*7*] Ryder, J. T. and Crossman, F. W., "A Study of Stiffness, Residual Strength and Fatigue Life Relationships for Composite Laminates," NASA CR-172211, National Aeronautics and Space Administration, Oct. 1983.

[*8*] Talreja, R., "Residual Stiffness Properties of Cracked Composite Laminates," The Danish Center for Applied Mathematics and Mechanics, Lyngby, Denmark, Report No. 277, Feb. 1984.

[*9*] Reifsnider, K. L. and Masters, J. E. in *Damage in Composite Materials, ASTM STP 775,* K. L. Reifsnider, Ed., American Society for Testing and Materials, Philadelphia, 1982, pp. 40–62.

[*10*] Reifsnider, K. L., Henneke, E. G., Stinchcomb, W. W., and Duke, J. C. in *Mechanics of Composite Materials, Recent Advances (Proceedings,* IUTAM Symposium on Mechanics of Composite Materials), Z. Hashin and C. T. Herakovich, Eds., Pergamon Press, New York, 1983, pp. 399–420.

[*11*] O'Brien, T. K. in *Damage in Composite Materials, ASTM STP 775,* K. L. Reifsnider, Ed., American Society for Testing and Materials, Philadelphia, 1982, pp. 140–167.

[*12*] Reifsnider, K. L., "Some Fundamental Aspects of the Fatigue and Fracture Response of Composite Materials," in *Proceedings,* 14th Annual Meeting of Society of Engineering Science, Lehigh University, Bethlehem, PA, 14–16 Nov. 1977.

[*13*] Rotem, A. in *Mechanics of Composite Materials, Recent Advances,* Z. Hashin and C. T. Herakovich, Eds., Pergamon Press, New York, 1983, pp. 421–436.

[*14*] Wilkins, D. J., Eisenman, J. R., Camin, R. A., Margolis, W. S., and Benson, R. A. in *Damage in Composite Materials, ASTM STP 775,* American Society for Testing and Materials, Philadelphia, 1982, pp. 168–183.

[*15*] Wang, A. S. D. and Slomiana, M., "Fracture Mechanics of Delamination-Initiation and Growth," NADC-TR-79056-60, Naval Air Development Center, 1982.

[*16*] Hashin, Z. and Rotem, A. in *Materials Science and Engineering,* Elsevier-Sequoia, Lausanne, Switzerland, 1978, pp. 147–160.

[17] Poursartip, A., Ashby, M. F., and Beaumont, P. R. W. in *Fatigue and Creep of Composite Materials* (Third RISØ International Symposium on Metallurgy and Materials Science), H. Lilholt and R. Talreja, Eds., Denmark, 1982, pp. 279–284.

[18] Sendeckyj, G. P. in *Test Methods and Design Allowables for Fibrous Composites, ASTM STP 734,* C. C. Chamis, Ed., American Society for Testing and Materials, Philadelphia, 1981, pp. 245–260.

[19] Hashin, Z., private communication, 1985.

Kenneth L. Reifsnider[1] *and W. W. Stinchcomb*[1]

A Critical-Element Model of the Residual Strength and Life of Fatigue-Loaded Composite Coupons

REFERENCE: Reifsnider, K. L. and Stinchcomb, W. W., **"A Critical-Element Model of the Residual Strength and Life of Fatigue-Loaded Composite Coupons,"** *Composite Materials: Fatigue and Fracture, ASTM STP 907,* H. T. Hahn, Ed., American Society for Testing and Materials, Philadelphia, 1986, pp. 298–313.

ABSTRACT: This paper addresses the basic question of how to develop a mechanistic cumulative damage model that has the capability of describing and predicting the strength and life of high-modulus continuous-fiber composite laminates subjected to general cyclic loading. The paper is a first step in philosophy from phenomenological descriptions of composite laminate fatigue behavior to mechanistic modeling based on the physics and mechanics of the details of the laminate response during cyclic loading. The major point of departure of the present effort from prior modeling activities is the mechanistic approach.

KEY WORDS: critical element, residual strength, composite laminates, fatigue life

The history of the development of models of the effect of cumulative damage in composite materials is diverse, diffuse, and largely phenomenological. A review of the major elements is provided by the authors in Ref *1*. Early work is anchored by the research of Broutman and Sahu, who introduced a linear equation for residual strength as a function of fatigue cycles, and compared it with a large set of data developed from tests of 13-ply E-glass reinforced epoxy cross-ply specimens [*2,3*]. At about the same time a "wearout" concept was introduced by Halpin and Waddoups [*4*]. The association between quasi-static strength and life distributions was suggested by the concept of the "equal rank assumption" introduced by Hahn and Kim a few years later [*5,6*]. This concept is used in virtually all of the current models that deal with the statistical character of composite material strength and life [*7*].

Among the newer approaches to cumulative damage is the approach taken by Hashin [*8*]. He introduces the concept of "damage curves" which "define" equal damage contours in the sense that any loading to that curve (in *S-N* space)

[1] Reynolds Metals professor of engineering science and mechanics and professor, Materials Response Group, respectively, Virginia Polytechnic Institute and State University, Blacksburg, VA 24061-4899.

will result in equal residual life, regardless of the loading history or internal damage modes. The concept of "equivalent damage" is based on the requirement of "equal life."

All of the foregoing are essentially phenomenological. While it is certainly true that many of the formulations were motivated by various damage characteristics, no explicit dependence on mechanics is included in the models. The present modeling effort is mechanistic and uses the concept of equivalent damage based on equal residual strength to develop a systematic and rational (albeit incomplete) cumulative damage model for damage development in high-modulus fibrous multiaxial composite laminates subjected to cyclic loading in tension and compression.

General Problem Definition

The scope of the present work is intentionally broad; it addresses the residual strength and life of several types of composite laminates in unnotched coupon (plate) specimen form subjected to tension-tension, compression-compression, tension-compression, and spectral cyclic loading. The present work attempts to construct a framework, a lattice of rational rigor and sound physical philosophy, into which intricacies of precise representations, physical insights, and mathematical sophistication can be interwoven as understandings of the physical phenomena involved are developed and analytical representations achieved. The modeling effort described herein is entirely a result of this commitment to a general approach. Since the scientific and engineering community is at a very early stage of development of an understanding of the behavior of composite laminates under cyclic loading, and a great number of questions regarding the strength, stiffness, and life of laminates under those conditions are presently unanswered, the penalty of initial inprecision of such an approach will certainly be evident in our results. However, if we are successful in establishing a valid, general approach to the mechanistic description of cumulative damage under the arbitrary cyclic loading modes and loading histories mentioned above, then it is reasonable to expect that a sound foundation has been laid for the construction of a rigorous general philosophy for the anticipation of residual response of such laminates under a variety of practical situations with an acceptable amount of precision.

Hence, we concentrate our present attention on an effort to develop an engineering model in such a way that a minimum amount of phenomenological characterization of material systems can be used to anticipate the behavior of various laminate configurations under arbitrary loading conditions. We require that the model be based on measurable parameters which can be used to characterize the development and current state of damage in a composite laminate so that an assessment of the current condition and anticipated behavior of a given specimen can be made based on measurements of immediate physical characteristics (in contrast to statistical predictions of group behavior based on statistical sample characterization). We further require that a definition of "equivalent damage states" be established so that cumulative damage under arbitrary load spectra can be correctly assessed. Finally, we require that the model provide a framework into which representations of individual events (damage modes, etc.) can be removed and inserted as understandings of those events allow, and that the framework be constructed in such a way that it can easily be translated into operational codes which allow engineers to use the philosophy in a straightforward way for initial design and subsequent inspection interpretations.

In the present paper we will attempt only to provide a thorough basic presentation and development of the critical-element model of residual strength and life. Although the model has been applied to a full range of tension, compression, and block loading and the results compared with data from an extensive test program, only a demonstrative single example will be provided herein. The presentational format consists of four sections which address the fundamental problems of how to deal with complex damage, how to incorporate cycle-dependent damage accumulation, how to predict residual properties, and a brief comparison with experimental data.

Complex Damage: What Problem to Solve?

The first fundamental problem to be dealt with is the complexity of damage in composite laminates. In the presence of a myriad of combinations of matrix and fiber damage, delaminations, debonding, and (in some cases) discontinuous microdeformations, what (mechanics) problem should be solved? This difficulty is overcome by a two-step process. The first step achieves an appropriate representation of the complex damage state, and the second step identifies the associated mechanics problem that controls laminate behavior.

A substantial amount of information has been reported which describes the nature of damage development in composite laminates [*1*]. It is clear that a wide range of damage modes normally operates and that damage events are usually distributed throughout the material. This situation presents a special challenge to any effort to model such damage states. Our approach to this problem is best illustrated by briefly examining the generic nature of damage development commonly observed in high-modulus continuous-fiber reinforced multiaxial laminates subjected to combinations of cyclic tension and compression loading.

We consider a simple coupon under cyclic loading as shown in Fig. 1. We assume that the laminate consists of plies having at least two orientations, only 0 and 90-deg in our example. We further assume that the applied load levels are sufficiently large so that the strength of the specimen is reduced with cycles, and the life of the specimen is finite. Finally, we assume that the loading spectrum contains, on the average, similar amounts of tensile and compressive loading. We examine the resulting damage state by the thought process of "looking inside" the damaged laminate as suggested by Fig. 1. Our purpose is served by opening a small section of the interior interface between the 90-deg plies and one of the

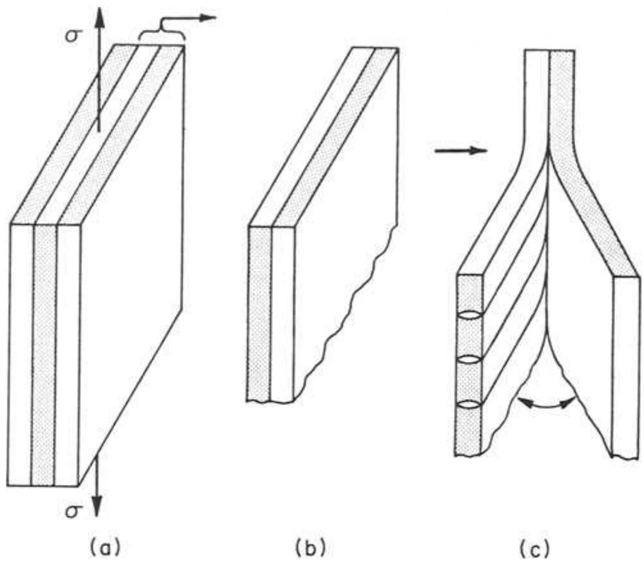

FIG. 1—*Schematic diagram showing location of damage states to be discussed.*

exterior 0-deg plies, as suggested by Fig. 1*c*. The first, and most common, damage mode that normally forms is matrix cracking along fiber directions in the off-axis plies. These cracks generally form through the ply thickness and across the width of the specimen, and continue to nucleate until a stable regular array of cracks typical of the laminate has formed. This stable crack pattern has been called the "characteristic damage state" (CDS) for matrix cracking [*10*–*13*]. It is a laminate property independent of loading history, and can be reliably predicted [*11*].

As cyclic loading continues, our interior view would resolve additional events, as suggested by Fig. 2. Shortly after the primary cracks (described above) begin

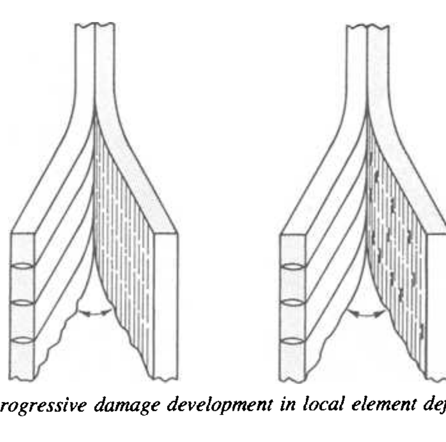

FIG. 2—*Progressive damage development in local element defined in Fig. 1.*

to form, fibers begin to break in the adjacent plies in the regions of high stress associated with the cracks, near the interface as sketched in Fig. 2*a*. These fiber breaks occur exclusively in those regions; usually about two thirds of the total number of breaks to fracture occur in the first one third of the cyclic life of the component under constant-amplitude loading. As cycling continues, secondary cracks begin to form as sketched in Fig. 2*b*. These cracks are limited in extent to regions near the primary crack tips at the ply interfaces. They usually extend only short distances into the adjacent plies in both the ply thickness and in-plane directions. However, the numbers of these cracks are generally quite large [*14*]. The details of this development process are distinct and essential, and have been reported elsewhere [*14,15*].

Now we must answer the question of what problem to solve, given the complex details alluded to above, knowing that various combinations of degree of development of those details may occur for different load histories. The first step we take is to choose a representative volume for our analysis. This approach is a common one in the field of effective property analysis [*16,17*]. It assumes that one can identify a volume element that is typical of the total volume of the specimen in the sense that the mechanical response of that element will be the same as the bulk material. In the present case we choose a representative volume as sketched in Fig. 3. As we discussed earlier in our brief outline of generic damage development, damage development in composite laminates under general loading usually concentrates around primary cracks near the interface between plies. This process can be viewed as a progressive localization of damage which may include local delamination at the intersection of primary and secondary cracks (as sketched in Fig. 3), and is believed to culminate in local fracture initiation which propagates in an unstable way to cause specimen (or component) fracture [*10*].

The second step is to decide what problem to set and solve using the repre-

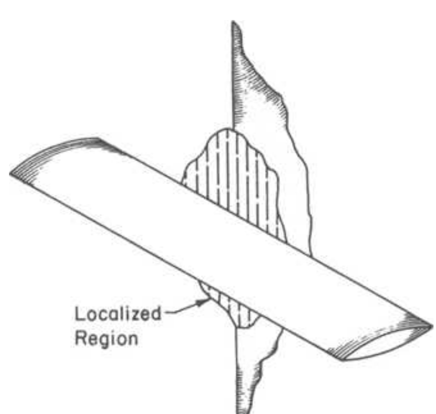

FIG. 3—*Damage features in a representative volume used for model analysis.*

sentative volume shown in Fig. 3. We make the claim that such a choice must be made on the basis of the mechanism that produces the response which we wish to describe. For the present we choose to be concerned with strength; hence, we ask "What is the mechanism that causes fracture?" Although the number of fracture modes is much smaller than the number of common damage modes, several possibilities present themselves. Since we are attempting to add formalism to the description of composite laminate behavior, we choose not to be concerned in this paper with structural failure modes such as buckling. (The model has been applied to such situations, and the results will be described in another setting.) Instead we concern ourselves with failure caused by a tensile load excursion in a loading spectrum which may include both tension and compression cyclic load amplitudes. Hence, we shall attempt to describe failure of the load-direction fibers in our representative volume in Fig. 3.

Damage Accumulation: How to Set the Problem as a Function of *n*

Having decided what is to be done, we must now formulate the problem in such a way that the essential mechanics can be described at any number of applied cycles, n. Our approach to this situation is, in fact, the principal defining feature of our model. We divide our representative volume into critical and subcritical elements, based on their contribution to the response, and handle each of them separately, and quite differently. The manner in which they are chosen and handled follows.

In order to predict residual properties at any number of applied cycles, two things must be known: the state of stress and the state of the material. For composite laminates of the types considered, the introduction of damage changes both of those states. When matrix cracks form, for example, load distribution among the plies of the laminate changes so that the microstress state in all elements of the laminate is a function of the number of applied cycles. We group together the material elements involved in these types of changes and call them "subcritical elements" in the sense that their failure does not cause laminate failure, but does cause changes in internal stress states that are important to (and indeed are a major part of) the fatigue damage "process" that we call cumulative damage. The subcritical elements participate in our model as representations of internal stress redistribution. The nature of that redistribution is defined by local geometry changes as described by the progressive damage events in our representative volume. The magnitude of the redistribution is determined from a measurable parameter. However, the choice of such a parameter is difficult. If we were attempting to solve this problem in homogeneous metals, we would choose the length of a single dominant crack as input to a fracture mechanics analysis. It is not common for such a crack to appear in composite laminates, except for special cases where a single dominant edge delamination grows in a self-similar way. Our experience, and that of others, has shown that stiffness changes are directly related to microdamage and attendant reduction in strength [*18–20*]. Moreover,

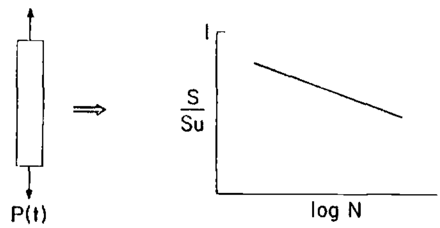

$$\Longrightarrow \frac{S}{Su} = A - \frac{B}{(\log N)^x}$$

FIG. 4—*"Critical element" (fibers) illustration.*

stiffness changes are excellent quantitative indicators of internal stress redistributions since the same damage events produce both effects in proportion. Hence, we choose stiffness change as our measurable parameter. For our present example, the off-axis plies that form matrix cracks will be the subcritical elements in our model. The internal state of stress is continuously recalculated as a function of cycles according to the amount of damage which occurs in the subcritical elements as indicated by the measured (or predicted) stiffness changes.

Having discussed the state of stress as a function of cycles, we now turn our attention to the state of the material. For that purpose we define "critical elements" in our laminate to be those parts which control fracture strength directly. The state of these elements will define the "state of the material." That state will be characterized on the basis of the physical constitutive characteristics of the critical elements under cyclic loading. For our illustrative example, we take the critical elements to be the zero-degree plies and introduce a phenomenological representation of their constitutive behavior (life, in this case) as a function of the normal stress range in the fiber direction and the number of applied cycles, the simplest possible case. Figures 4 and 5 indicate the choices of critical and subcritical elements. At the risk of introducing confusion at this point, it should be noted that various other constitutive characterizations of the 0-deg plies could be introduced if the data and understandings were available. Multiaxial *S-N* data, models of fiber fracture under cyclic loading, or even more formal (if less

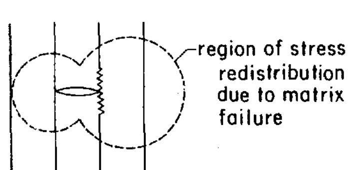

⇒ State of stress, rate of degradation changes in unbroken Plies.

FIG. 5—*"Subcritical element" (matrix) illustration.*

physical) kinetic theories could be introduced as critical-element response representations [21]. In any case, the stress state which drives any of these models will be described as a function of n by the subcritical-element response as mentioned earlier. Hence, we have settled the question of how to determine the state of stress and state of material as a function of the number of applied cycles in general, and have specified the particular nature of the process for our present example.

Residual Property Prediction: How to Apply the Model

In order to apply the model we need only calculate strength as a function of n since the occasion of coincidence between that value and the applied load level will define the life of the laminate. To this end we construct a generalized equation expressed in normalized form which computes the reduction in residual strength as a function of increments of applied cyclic loading. The rationale behind the generation of that equation can be demonstrated by the following discussion.

We begin with Fig. 6, which is a schematic representation of some of the basic relationships for laminate fatigue behavior. We imagine that this representation is essentially one-dimensional, that is, that the residual strength, S_r, and the life locus represent laminate values determined from unidirectional loading. The residual strength curve can be written in terms of the applied stress, S_a, as shown in Eq 1 where i is a parameter introduced to accommodate the nonlinearity in the residual strength reduction curve

$$S_r(n) = 1 - \left[1 - \frac{S_a}{S_u}\right]\left[\frac{n}{N}\right]^i \tag{1}$$

where n/N is the life fraction.

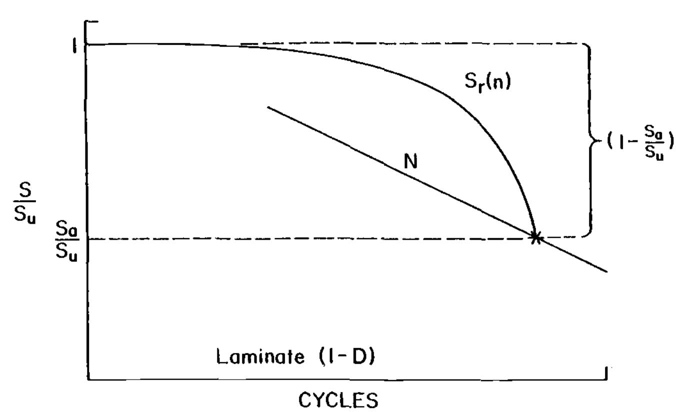

FIG. 6—*Schematic diagram of laminate strength reduction-life relationship.*

It is further assumed that the applied stress amplitude, S_a, is constant throughout the test. The residual strength, S_r, is a function of the number of applied cycles.

We have indicated that the modeling approach we have taken is based on a phenomenological characterization of the critical elements in the laminate, and not on the laminate itself. Hence, the next step in the construction of our generalized summation equation is to consider the fatigue behavior of the critical elements, as schematically indicated in Fig. 7. Since these critical elements are imbedded within a laminate, and since, as we have emphasized, the internal stress state is constantly changing as damage develops in the subcritical elements causing internal stress redistribution, the applied stress, S_a, is no longer constant as a function of the number of cycles. Since it is a variable, we cannot simply multiply all of our terms in a degradation equation by the ratio of applied cycles to life, the so-called life fraction. Instead, an equation such as Eq 2 is more appropriate

$$S_r(n) = 1 - \int_0^{\gamma} \left[1 - \frac{S_a(n)}{S_u}\right] i \left[\frac{n}{N(n)}\right]^{i-1} d\left[\frac{n}{N(n)}\right] \tag{2}$$

where γ is a specific value of n/N.

Here it should be noted that the integrand is a function of the number of applied cycles, not only because of the variation of the applied stress on the critical element, S_a, but also because of the fact that the life calculated from a given applied stress (from the equation which fits the phenomenological data for the critical element) is also a function of the number of applied cycles; that is, N is a function of n.

The last major item to be added to our development incorporates the reality

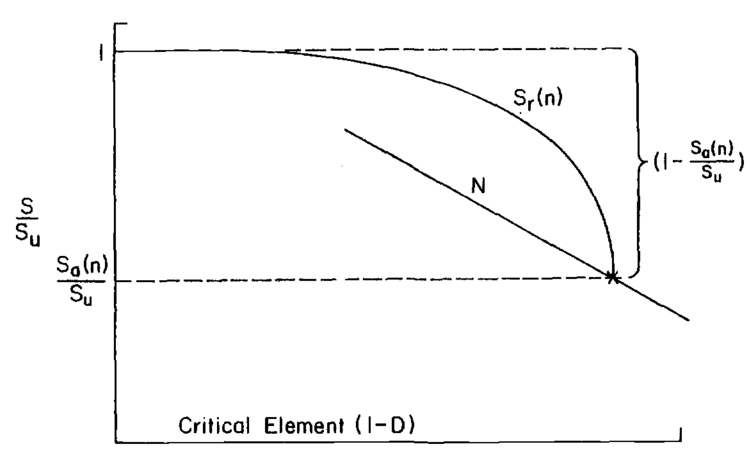

FIG. 7—*Schematic diagram of critical-element strength-life relationship.*

that the stress state of the critical element is almost never one-dimensional. Since it is imbedded in a laminate, the internal stresses are generally predominantly two-dimensional, and occasionally three-dimensional. In order to correct our model for that fact, we introduce a local failure function, F_L, to replace the local applied stress ratio, S/S_u. This local failure function is unspecified at this point, except to the extent that it must represent the tendency for the internal stress state in the critical elements to cause failure of those elements (see Fig. 8). There is an obvious relationship between the concept behind the local failure function and the familiar "failure theories" introduced by a variety of investigators such as Tsai-Hill, Tsai-Wu, and others. For this refinement, Eq 2 becomes Eq 3, the final form of our residual strength equation

$$\Delta S(n) = \int_0^{\gamma} [1 - F_L(n)]\, i \left[\frac{n}{N(n)}\right]^{i-1} d\left[\frac{n}{N(n)}\right] \tag{3}$$

This equation functions by producing a normalized change in residual strength estimate (a fraction of the static ultimate strength) as a continuous function of loading history indicated by the number of cycles of load application, n. The equation produces that estimate by integrating and convoluting the influence of two fundamental types of microdamage development consequences associated with microevents which occur in "noncritical" elements of the laminate (events that influence the degradation of the laminate primarily by internal stress redistribution and adjustment of geometry), and microevents which act directly on "critical elements" (elements which control the final fracture of the laminate). Rather than attempt to provide an elaborate and complex discussion of the various

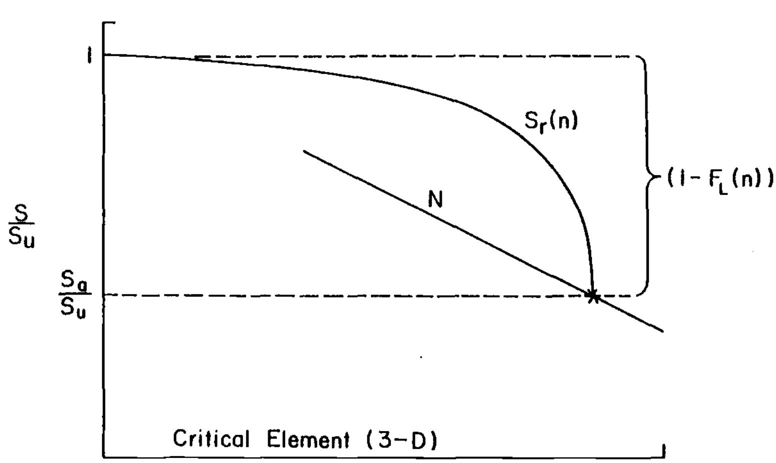

FIG. 8—*Schematic diagram of critical-element strength-life relationship for three-dimensional formulation.*

nuances of this equation in this document, we provide an example application for cyclic tensile loading.

This scenario is based on tension-tension fatigue loading of an angle-ply laminate which is constructed in such a way that no significant edge delamination occurs. The various terms in Eq 3 are identified in Fig. 9. We will discuss the figure from right to left. The life locus described by the function N is a phenomenological representation of the life of the critical element, taken to be the 0-deg plies in this case. The equation is written as a function of the applied unidirectional stress, $S(n)$, normalized by the ultimate strength of the element, S_u. The material constants, A, B, and C, are determined by fitting the data obtained from fatigue testing of unidirectional material of the type from which the laminate was constructed. Since, in this case, we are concerned only with the unidirectional performance of the 0-deg plies (the critical elements), one such relationship will suffice for all laminates regardless of their construction (stacking sequence, etc.). Since it is recognized that the 0-deg plies in the laminate may carry different amounts of the total load as the damage development in noncritical elements redistributes stress and alters internal geometry, the applied stress on the critical element, $S(n)$, is stated as a continuous function of the number of applied cycles, n. It should also be mentioned that the local internal applied stress, $S(n)$, can be determined from measurements of changes in laminate stiffness which the authors

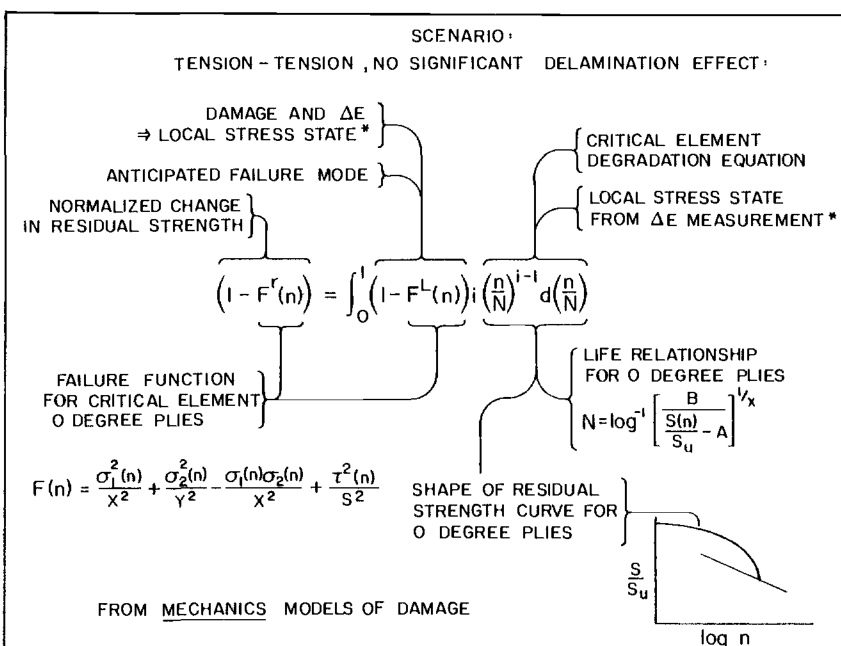

FIG. 9—*Schematic diagram of interpretation of terms in Eq 3.*

have found, by experience and through a number of mechanics models [*11,12,18,19*], to be related to internal stress redistributions.

The choice of variable of integration, n/N, is important since that variable is a continuous function, even in circumstances when the applied loading spectrum is continuously varying in time. Hence, the damage accumulation Eq 3 can be used to determine the effect of cumulative damage under spectrum loading. The parameter i in Eq 3 is a material parameter which is associated with the nonlinearity of degradation (sometimes referred to as a tendency for sudden death) in composite laminates, and is also obtained from curve-fitting of data. However, that constant generally has a value close to unity and does not appear, at this writing, to be a function of the construction of the laminate.

Continuing to move to the left in Fig. 9, the term in parentheses determines the total amplitude of allowable strength reduction, in the sense that the laminate is expected to fail when the laminate strength (determined from the computation achieved by the equation) is reduced to the level of the normalized failure function, $F_L(n)$. The failure function for the critical element, the 0-deg plies in this case, can be taken to be any of the typical phenomenological characterizations of strength computed at that load level. However, it is especially important that the stresses that enter into such an equation may be functions of n since internal stress redistribution will generally change the local stresses that cause failure of the critical element. Hence, the first term in parentheses in Eq 3 is also altered by the microdamage that occurs in subcritical elements causing internal stress redistributions and changes in internal geometry. Those changes are, as mentioned earlier, detected and interpreted based on stiffness changes in the scenario described. The choice of the failure function (and indeed a choice of the critical element) is dependent upon an anticipated failure mode of the laminate itself. This anticipation must be based on prior experience or guiding experiments. When the integral is performed, a normalized change in residual strength is produced as a function of the applied cycles, n, as indicated on the left of the equation shown in Fig. 9.

For load spectra which include compression excursions, other micromechanical models are used to provide input to the damage accumulation equation. The choice of approach in each case is controlled by the failure mode that is appropriate for the dominant damage development mode or modes. When failure involves buckling (as a consequence of delamination for example) the failure function may take the form of stiffness ratios. Since stiffness is the only material property which appears in stability equations, it is not surprising that such a parameter seems to provide a good representation of the compression-controlled behavior. Regardless of the micromechanical model that is used to represent the prefracture damage patterns, the scheme for application of the residual strength equation is unchanged, a fact that makes application in computer-coded form very convenient. A conceptual flow chart of such a code appears in Fig. 10. Figure 11 shows an example of the results obtained from the model for tension-tension ($R = 0.1$) loading of 48-ply coupon specimens made from AS1/3502 having the stacking

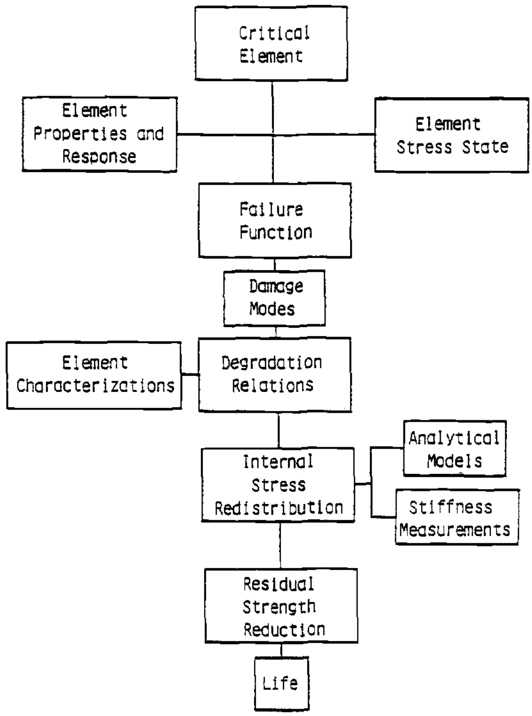

FIG. 10—*Flow chart of cumulative damage model.*

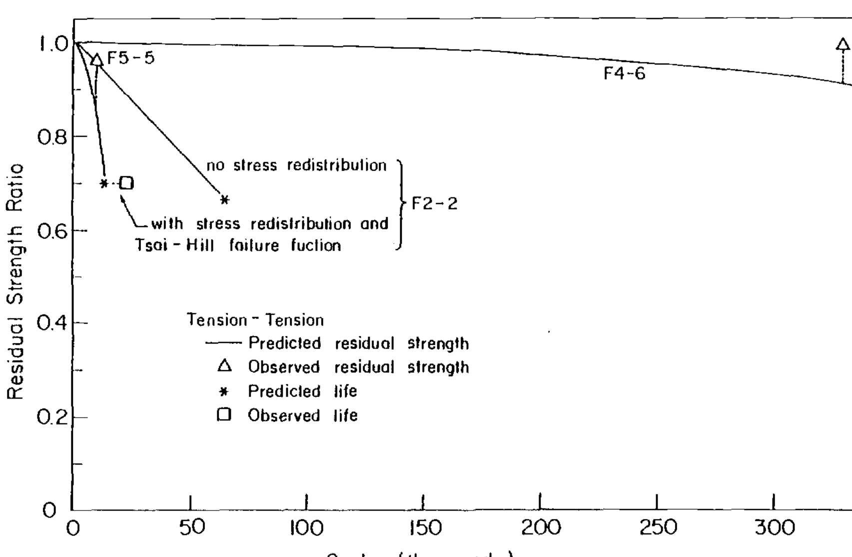

FIG. 11—*Example of application of model to T-T loading and failure, showing the effect of stress redistribution.*

sequence $[(0,\pm45)_3]_{4s}$. The maximum stiffness changes observed for this laminate were in the 10% to 15% range. The phenomenological input for all laminates modeled and tested was

$$S/S_u = 1 - 0.07 \log n \tag{4}$$

as the one-dimensional response of the zero-degree plies. The parameter i was taken to be 1.2 for all cases considered. If the failure function, $F_L(n)$, is taken to be the equal to the ratio of the fiber-direction stress in the zero-degree plies compared to the ultimate tensile stress in that direction, an example of the predicted results is shown in Fig. 11. If internal stress redistribution is ignored, the prediction is seen to be very poor compared to the data, indicating the essential nature of internal stress redistribution for this highly fiber-dominated laminate. If the local failure function, $F_L(a)$, is corrected for two-dimensional stress in the zero-degree plies using a correction derived from the Tsai-Hill failure theory, the predictions become quite close to observed values as shown for several cases in Fig. 12. Further details of the application and development of the model can be found in Ref *22*.

Closure

In the space available, we have been able to present only the fundamental concepts and the simplest possible example of the critical-element model, a

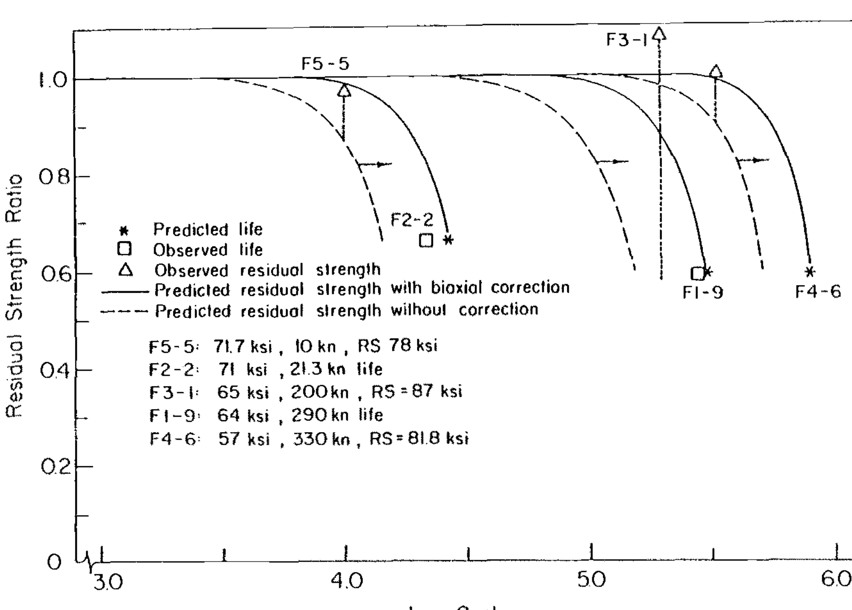

FIG. 12—*Several calculations for the model with biaxial correction added compared with experimental data.*

mechanistic model which can be used to predict the residual strength and life of composite laminates under arbitrary cyclic loading. While we believe this is a significant first step, and agreement with data has been satisfactory for a variety of situations, it should be emphasized that the model is still in very primitive form. There is great need for better understanding (and analysis) of the internal stress states associated with critical damage patterns, the nature of (synergistic) damage development under combined tension-compression loading, the implications of this approach for notched components, the influence of material system constituent properties, and the influence of time-dependent response (to name a few) as inputs to the model. Nevertheless, we believe that the approach and basic concepts are useful, and offer the model in the hope of at least providing a stimulus for further work.

Acknowledgments

The authors gratefully acknowledge the support of the U.S. Air Force, Wright Patterson AFB, under Contract No. F33615-81-C-5049 monitored by M. Knight, and the support of the General Dynamics Corp. in the developmental effort. Our thanks also go to B. Wengert for typing the manuscript.

References

[*1*] "Cumulative Damage Model for Advanced Composite Materials," Semi-annual Progress Report No. 3, FZfM-7070, General Dynamics Corp., Forth Worth, TX, Oct. 1982.

[*2*] Broutman, L. J. and Sahu, S., "Progressive Damage of a Glass-Reinforced Plastic During Fatigue" in *Proceedings*, 24th Annual Technical Conference, Reinforced Plastics and Composites Division, Society of the Plastics Industry, 1969.

[*3*] Broutman, L. J. and Sahu, S. in *Composite Materials: Testing & Design Second Conference, ASTM STP 497*, American Society for Testing and Materials, Philadelphia, 1972, pp. 170–188.

[*4*] Halpin, J. C., Johnson, T. A. and Waddoups, M. R., *International Journal of Fracture Mechanics*, Vol. 8, 1972, pp. 465–472.

[*5*] Hahn, H. T. and Kim, R. Y., *Journal of Composite Materials*, Vol. 9, 1975, pp. 297–311.

[*6*] Hahn, H. T. and Kim, R. Y., *Journal of Composite Materials*, Vol. 10, 1976, pp. 156–179.

[*7*] Chou, P. C. and Croman, R., *Journal of Composite Materials*, Vol. 12, 1978, pp. 177–194.

[*8*] Hashin, Z. and Rotem, A., *Materials Science and Engineering*, Vol. 34, 1978, pp. 147–160.

[*9*] *Damage in Composite Materials, ASTM STP 775*, K. L. Reifsnider, Ed., American Society for Testing and Materials, Philadelphia, 1982.

[*10*] Reifsnider, K. L. in *Proceedings*, 14th Annual Meeting of Society of Engineering Science, Lehigh University, Bethlehem, PA, Nov. 14–16, 1977, pp. 373–384.

[*11*] Reifsnider, K. L., Stinchcomb, W. W., and Henneke, E. G. II, "Defect-Property Relationships in Composite Laminates," AFML-Technical Report 76–81, Part III, Air Force Materials Laboratory, Wright-Patterson AFB, Dayton, OH, April 1979.

[*12*] Reifsnider, K. L. and Highsmith, A. L. in *Materials, Experimentation and Design in Fatigue*, Westbury House, Guildford, U.K., 1981, pp. 246–260.

[*13*] Kriz, R. N., Stinchcomb, W. W., and Tenney, D. R., "Effects of Moisture, Residual Thermal Curing Stresses and Mechanical Load on the Damage Development in Quasi-Isotropic Laminates," VPI-E-80-5, College of Engineering, Virginia Polytechnic Institute and State University, Blacksburg, VA, Feb. 1980.

[*14*] Jamison, R. D., "Advanced Fatigue Damage Development in Graphite Epoxy Laminates," Ph.D. dissertation, College of Engineering, Virginia Polytechnic Institute and State University, Blacksburg, VA, Aug. 1982.

[15] Reifsnider, K. L. and Jamison, R. D., *International Journal of Fatigue*, Vol. 4, No. 4, 1982.
[16] Krajcinovic, D. and Fosenka, G. U., *Transactions, American Society of Mechanical Engineers, ASME, Journal of Applied Mechanics*, Vol. 48, 1981, p. 809.
[17] Christensen, R. M. *Mechanics of Composite Materials*, Chapters 2 and 3, Wiley, New York, 1979.
[18] Highsmith, A. L. and Reifsnider, K. L. in *Damage in Composite Laminates, ASTM STP 775*, K. L. Reifsnider, Ed., American Society for Testing and Materials, Philadelphia, 1982, pp. 103–117.
[19] Reifsnider, K. L., Henneke, E. G. II, and Stinchcomb, W. W., "Defect-Property Relationships in Composite Materials," AFML-TR-76-81, Part IV, Air Force Materials Laboratory, Wright-Patterson AFB, Dayton, OH, June 1979.
[20] O-Brien, T. K. in *Mechanics of Nondestructive Testing*, W. W. Stinchcomb, Ed., Plenum Press, New York, 1980, pp. 101–121.
[21] Christensen, R. M., "Residual Strength Determination in Polymeric Materials," UCRL-84532, Lawrence Livermore Laboratory, Stanford, CA, 1980.
[22] "Cumulative Damage Model for Advanced Composite Materials," Phase II Final Report, General Dynamics Corp., Forth Worth, TX, May 1984.

Charles E. Bakis[1] and Wayne W. Stinchcomb[1]

Response of Thick, Notched Laminates Subjected to Tension-Compression Cyclic Loads

REFERENCE: Bakis, C. E. and Stinchcomb, W. W., "**Response of Thick, Notched Laminates Subjected to Tension-Compression Cyclic Loads,**" *Composite Materials: Fatigue and Fracture, ASTM STP 907*, H. T. Hahn, Ed., American Society for Testing and Materials, Philadelphia, 1986, pp. 314–334.

ASBTRACT: The fatigue response of a $[(0/45/90/-45)_s]_4$ T300-5208 graphite/epoxy laminate with a drilled center hole subjected to constant-amplitude, fully reversed tension-compression loading was investigated. Damage evaluation techniques such as stiffness monitoring, penetrant-enhanced X-ray radiography, C-scan, laminate deply, and residual strength were used to establish the mechanisms of damage development as well as the relations between this damage and the stiffness, strength, and life of the laminate. Two load levels provided for fatigue lives of 10^5 to 10^6 cycles and significant stiffness reductions. Damage initiated at the hole as matrix cracking parallel to the fibers in all plies. Matrix cracks had a significant effect on delamination initiation and growth. Delaminations initiated near the surface in the densely cracked region at the hole and grew along major matrix cracks. Delaminations of smaller extent developed later throughout the interior of the laminate and followed similar growth patterns as those closer to the surface. Compressive properties degraded more rapidly than tensile properties. At the stress levels used in this investigation, residual tensile strength increased early in the fatigue life and remained approximately constant to near the end of life, when failure was precipitated by excessive laminate instability during the compressive portion of the loading.

KEY WORDS: composite materials, graphite/epoxy, fatigue, damage, delamination, strength, stiffness, life, nondestructive evaluation, notched laminate, tension, compression

Fatigue behavior of fiber-reinforced composite laminates has been the subject of much research in recent years due to the need for a better understanding of the long-term behavior of structures containing stress concentrations such as notches and cutouts. Adhesive bonding, stitching and cocuring have shown great potential for certain joining applications, but drilling and bolting still remains a common method of joining composite structures today, especially where disassembly is required. Unloaded circular holes are studied frequently because they

[1] Graduate research assistant and professor, respectively, Materials Response Group, Virginia Polytechnic Institute and State University, Blacksburg, VA 24061-4899.

represent a simple starting point for investigations of the stress state and nature of damage development in the vicinity of a notch or cutout.

Analytical modeling of the mechanical behavior of composite materials is quite complex when changes in the state of the material are considered. During static or cyclic loading, graphite/epoxy composites commonly develop matrix cracks parallel to the fibers, disbonds along fiber-matrix interfaces, matrix crazing, delamination of adjacent laminae, and fiber fracture or microbuckling. Collectively, these events that affect laminate life, stiffness, and strength are called "damage." While the location of some forms of damage initiation can be predicted at a notch from interlaminar stress distributions, the subsequent direction and extent of propagation cannot be predicted by analysis of the undamaged laminate [*1,2*]. This is due to an extensive redistribution of stress in the damaged material. As a further complication in analytical schemes, initiation and accumulation of damage are dependent on load history, load rate, method of load introduction, environmental conditions, laminate material, stacking sequence, specimen constraint and geometry, and the nature of stress concentrations [*3–7*]. To help address these issues, careful experimental investigations are often required.

It is widely believed that compression-induced damage is of a different nature in notched graphite/epoxy laminates than tension-induced damage [*7*]. The rate of damage development has been observed to be highest for tension-compression (T-C) fatigue loading when compared to equal peak amplitudes or stress ranges of T-T or C-C or both [*8*]. Stress reversal during the load cycle is generally considered to represent the most severe load case for composite laminates since both tensile and compressive damage mechanisms are active [*5,8–11*]. This is partly due to the coupling of damage modes induced separately in the compression and tension load excursions. Matrix cracking induced during the tensile portion of the load may act as a delamination catalyst during compression in some laminates.

Experiments (such as the present one) involving compression load components are very sensitive to alignment and constraint conditions. Misalignment of the load axis with respect to the material axis of elastic symmetry causes out-of-plane deflection, unsymmetric damage development through the test specimen thickness or premature specimen failure. An increased amount of constraint (as in antibuckling supports) can delay the onset of out-of-plane deflection, but some form of out-of-plane stresses are consequently induced in the material. These stresses could bias damage development and ultimately the test results.

In the case of compression-dominated loading, experimental results suggest that failure is primarily matrix-related [*6*]. This implies matrix cracking, fiber-matrix debonding, delamination, and fiber buckling in regions of degraded matrix, which reduce the laminate's ability to sustain compression load [*8–10,12,13*]. Compressive residual strength tests, however, are subject to buckling effects, making definitive conclusions on this material parameter elusive [*10,12,13*]. Several investigators have found that the tensile strength of some notched graphite/epoxy laminates increases by up to 40% after some period of cyclic loading [2,4,10]. This type of behavior is not thoroughly understood, but has been suggested to be due to a reduction of the stress concentration by material "softening" in the damaged area around the notch.

Objectives

The objectives of this study are to evaluate the initiation, progression and interaction of damage modes in a thick, notched graphite/epoxy laminate subjected to fully reversed tension-compression cyclic loading and to determine relationships between the damage state and the strength, stiffness, and life of the laminate.

Experimental Test Program

The material system evaluated in this study was Narmco T300-5208 graphite/epoxy prepreg arranged in a quasi-isotopic laminate with a stacking sequence of $[(0/45/90/-45)_s]_4$. The panels were cured at 179°C (355°F) in an autoclave with 0.69 MPa (100 psi)[2] pressure for two hours (no post-cure). The mean coupon thickness was 4.17 mm (0.164 in.). The zero-degree direction coincides with the loading axis, and positive angles of ply orientation are measured clockwise from zero. Test coupon dimensions (Fig. 1) were 38.1 mm (1.5 in.) wide by 121 mm (4.75 in.) long, with a 9.53-mm-diameter (0.375 in.) hole core-drilled through the center. A slight amount of damage caused by the drilling process consisted of a small delamination at the last ply interface encountered by the drill. All coupons were nondestructively inspected before testing to document machining defects such as these. There was no biasing of damage development due to initial defects.

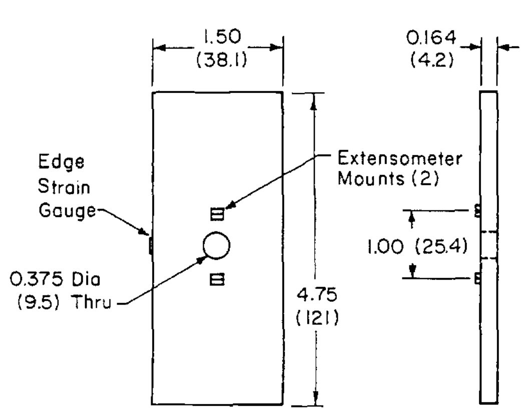

FIG. 1—*Test specimen dimensions in inches (mm). Load applied vertically.*

[2] All original measurements were recorded in U.S. customary units.

Mechanical loading of the specimens was performed in an ambient laboratory environment using a servo-controlled hydraulic testing machine in the load control mode. The specimens were accurately positioned in hydraulic grips with alignment plates as in Ref *12*. Utility cloth of 320 grit was placed between the specimen and the grip wedges to protect the laminate from grip-induced damage. The first ten cycles of fatigue loading were applied manually by the operator so that nondestructive evaluation of the material could be performed after the tenth cycle. Between 10 and 100 cycles, a function generator was used to apply a sinusoidal load at a frequency of 1 Hz. Such low frequencies for the first 100 cycles were necessary to minimize the effects of turn-on transients on the load history of the test specimen. After 100 cycles, fatigue tests were conducted at a frequency of 10 Hz.

Nondestructive evaluation (NDE) techniques used to monitor the growth of damage and its effects on global properties were penetrant-enhanced X-ray radiography, ultrasonic C-scan, and static secant modulus change, as detailed in Ref *14*. Zinc iodide has been shown to be an effective penetrant for highlighting damaged regions of composites for X-ray radiography [*15*]. A combination of radiographs taken at various angles of incidence proved valuable in determining the distribution of damage through the thickness. Three different angles were used: 0 deg (face, or through-the-thickness view), 15-deg rotation of the laminate plane from zero, and 90-deg rotation from zero (edge, or through-the-width view). The ultrasonic C-scan does not depend on penetration of an enhancing agent, but the particular device used in this investigation does not provide the resolution of X-ray radiography. For this reason it is used mainly to verify material integrity (voids, porosity, etc.) in regions inaccessible to the X-ray penetrant. The C-scan utilized tap water as a coupling medium between a 15-MHz transducer [6.4-mm diameter (0.25 in.) beam] and the specimen. A warm-temperature drying cycle [54°C (130°F) for several hours] in laboratory air after administering one of these NDE techniques ensures that detrimental moisture diffusion into the laminate is minimized [*16*].

Stiffness change has been used extensively as a means of evaluating damage accumulation in composite laminates [*14,17*]. To measure longitudinal stiffness change during fatigue cycling, the knife edges of a 25.4-mm (1 in.) extensometer were positioned in V-notches engraved in flat aluminum tabs centered on the hole (Fig. 1). The tabs were bonded to the specimen using a compliant silicone-type adhesive. The extensometer was held to the tabs with rubber bands. This arrangement enabled removal of the extensometer for other nondestructive material evaluation and accurate repositioning thereafter. Dynamic stiffness was monitored during tests by the operator using a peak-detector, but actual stiffness data were collected statically by applying monotonic tension and compression loads at appropriate cyclic intervals.

Residual tensile strength was measured on selected coupons after a predetermined static stiffness loss had been realized. A longitudinal strain gage was attached to the thin edge (Fig. 1) of specimens subjected to strength measurements for interspecimen comparison of strain-to-failure in a region of relatively little damage. Other coupons were selected to be deplied by partially pyrolizing the matrix material as in Ref *18*. With the aid of a penetrating marking agent (gold chloride), the deply technique enables detailed information on the location and extent of delamination to be documented and compared with the other investigative data, such as X-ray radiography, for specimens with approximately the same damage condition. For this study, "same damage condition" is defined as equal stiffness change [*19*].

Preliminary tests using specimens with different lengths were carried out to determine the effects of unsupported length (UNSL) on strength and life. While some of these tests were performed by the investigators at Virginia Tech, most were performed at NASA Langley under comparable testing conditions to verify the consistency of the data in different laboratories. In static compression tests, it was determined that UNSL's less than or equal to 63.5 mm (2.5 in.) caused crushing failure modes at about the same load (Fig. 2). The NASA data in Fig. 2 represent a mean and range based on the number of tests in parentheses, while the Virginia Tech (VPI) points each represent a single test. Fatigue test results suggested that an UNSL of greater than 63.5 mm (2.5 in.) allowed out-of-plane deflection effects to significantly shorten fatigue life, especially at higher load levels (Fig. 3). From these findings, a 60-mm (2.35 in.) UNSL was chosen for the remainder of the tests. Two load levels were chosen as representative of "low" and "high" fatigue loads. These were ±20.0 and ±24.5 kN (±4500 and ±5500 lb), respectively, or ±126 and ±154 MPa (±18.3 and ±22.4 ksi) based on the gross, unnotched area. These load levels correspond to remote longitudinal strains of ±2400 and±2900 $\mu\epsilon$.

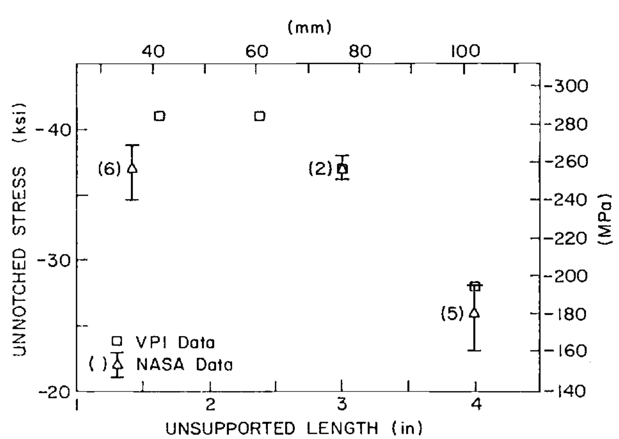

FIG. 2—*Compressive strength versus specimen unsupported length. NASA data include quantity, range and mean.*

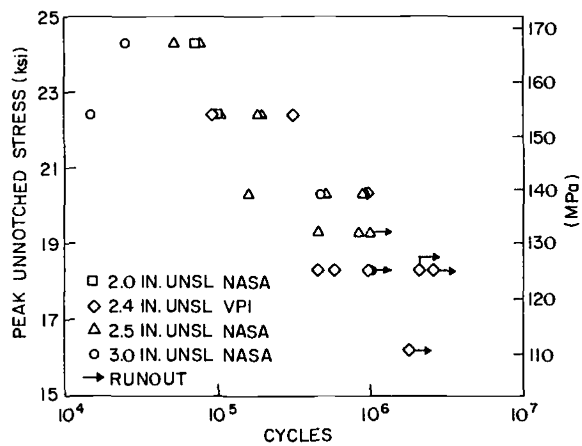

FIG. 3—*Stress-life relation for* R = −1 *loading. Each point represents one test.*

Results

Static Material Properties

Compressive strength measured with a single specimen having a UNSL of 60 mm was −45 kN (−10 kip), or −280 MPa (−41 ksi) based on the unnotched area (strength and stiffness data shown in Table 1), which is consistent with other compressive strengths shown in Fig. 2. Ultimate longitudinal compressive strains measured across the hole and at the straight edge were −7900 and −5000 $\mu\epsilon$, respectively. Visual examination of the compression fracture surface indicated a crushing mode of failure along a section transverse to the load axis and passing through the hole (Fig. 4*a*). Mean ultimate load in tension for seven specimens was 42 kN (9400 lb), or 260 MPa (38 ksi) based on the unnotched area. Longitudinal strain data were recorded for two of the tension tests, and are shown as mean values in Table 1. Mean tensile strains across the hole and on the edge were 7300 and 4600 $\mu\epsilon$, respectively. Visual observation of the tensile fracture surface revealed that many −45 deg plies through the thickness had no broken fibers. That is, these double plies sheared out of the surrounding 90-deg plies, creating a large delaminated surface in the process (Fig. 4*b*). Fibers in the near-surface +45-deg plies remained intact close to the hole. Farther in the interior and away from the hole, fibers in these plies failed along a transverse section to the load axis. Fibers in 0-deg plies failed along the underlying +45-deg transverse fracture line in the vicinity of the hole. Farther away from the hole, the 0-deg plies usually fractured more uniformly perpendicular to the load axis.

Mean ultimate load from the seven tension tests was used as a normalization factor for residual tensile strength tests to be performed on fatigue-damaged specimens. Ultimate longitudinal tensile strains from two tests were used to

TABLE 1—*Static and residual properties.*[a]

Fatigue Data					Residual Properties			
Specimen No.	Load History, $\frac{\text{min load}}{\text{max load}}$ to cycles (kN)	(k)	Extensometer Stiffness[b] T	C	Extensometer Strain, ϵ_1, $\mu\epsilon$	Edge Strain, ϵ_2, $\mu\epsilon$	$\frac{\epsilon_1}{\epsilon_2}$	Load, kN
6-11	static							
	compression	. . .	. . .	. . .	−7900	−5000	1.6	−45
	static tension	. . .	. . .	. . .	7300[c]	4600[c]	1.6[c]	42[d]
					[1.0]	[1.0]	[1.0]	[1.0]
2-8	−20.0/ +20.0	300			8800	5000	1.8	45
	(early Stage II)		[0.92]	[0.91]	[1.2]	[1.1]	[1.1]	[1.1]
2-11	−20.0/ +20.0	500			12000	6200	1.9	58
	(late Stage II)		[0.86]	[0.83]	[1.6]	[1.3]	[1.2]	[1.4]
1-8	−22.3/ +22.3	961			10300	5300	1.9	50
	(late Stage III)		[0.84]	[0.87][e]	[1.4]	[1.2]	[1.2]	[1.2]
2-14	−24.5/ +24.5	25			10300	5800	1.8	53
	(early Stage II)		[0.90]	[0.90]	[1.4]	[1.3]	[1.1]	[1.3]
2-5	−24.5/ +24.5	250			10800	5500	2.0	53
	(late Stage II)		[0.86]	[0.79]	[1.5]	[1.2]	[1.3]	[1.3]
1-11	−24.5/ +24.5	315			11300	5200	2.2	51
	(late Stage III)		[0.80]	[0.73]	[1.5]	[1.1]	[1.4]	[1.2]

[a] Numbers in square brackets are normalized to initial, undamaged values.
[b] T = tension, C = compression.
[c] Mean of two tests.
[d] Mean of seven tests.
[e] Increasing, due to out-of-plane deformation.
Unit conversion factors: 4.45N = 1 lb; 6.90 MPa = 1 ksi.

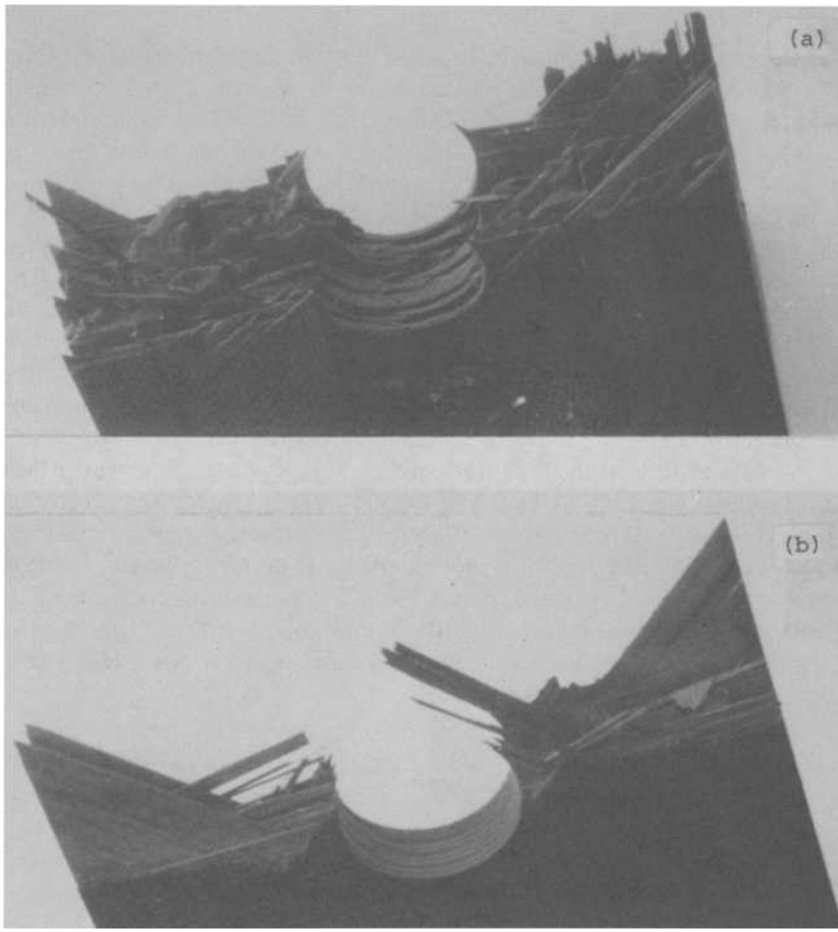

FIG. 4—*Fracture surfaces after monotonic loading:* (a) *Compression;* (b) *Tension.*

normalize strain data in the same manner. The ratio of strain across the hole to strain on the straight edge was computed for the undamaged specimens so that a comparison could be made with specimens damaged by fatigue loading. A change in this parameter reflects the redistribution of strain as fatigue damage accumulates. The mean ratios for monotonic compression and tension failure tests were both equal to 1.6.

Fatigue Life Data

Specimens cycled at the low load level (45% of compressive ultimate at $R = -1$) experienced lives of 451K cycles to runouts at 2.6M cycles. At the high load level (55% of compressive ultimate at $R = -1$), lives were between 93K and 315K cycles (Fig. 3).

Stiffness Response to T-C Fatigue

Three regions can be distinguished in a plot of static, secant, normalized tension and compression stiffness versus normalized life for high- and low-level fatigue tests at $R = -1$ (Figs. 5*a,b*). Here, stiffness is normalized to its initial value on the first cycle (E/E_0), while cycles are normalized to the number of cycles at failure (N/N_f). The tension and compression stiffnesses in Fig. 5 for a particular load level represent data from one test that was representative of typical specimen behavior. In each case, the first region spanning the first 10% of life is called Stage I and is distinguished by a rapid, but slowing, loss of stiffness. The compression stiffness decreases faster than tension stiffness during this stage. In the next 80% of life, called Stage II, stiffness loss rate is the slowest of any time in the fatigue life of the specimen, and is roughly linear with respect to the number of cycles. Compression and tension stiffnesses decrease at about the same rate. Stage III is a period of relatively rapid stiffness change that accelerates in the last 10% of life. At the high load level, Stage III was slightly shorter than at the low level, and displayed less stiffness drop. During the last stage, apparent compression stiffness may decrease, increase, or undergo some combination thereof, depending on the out-of-plane deformation of the highly damaged coupon relative to the strain measuring device. Tension stiffness does not change as much as compression stiffness during Stage III. The utility of stiffness degradation as an indicator of fatigue "age" in different specimens at various load levels is

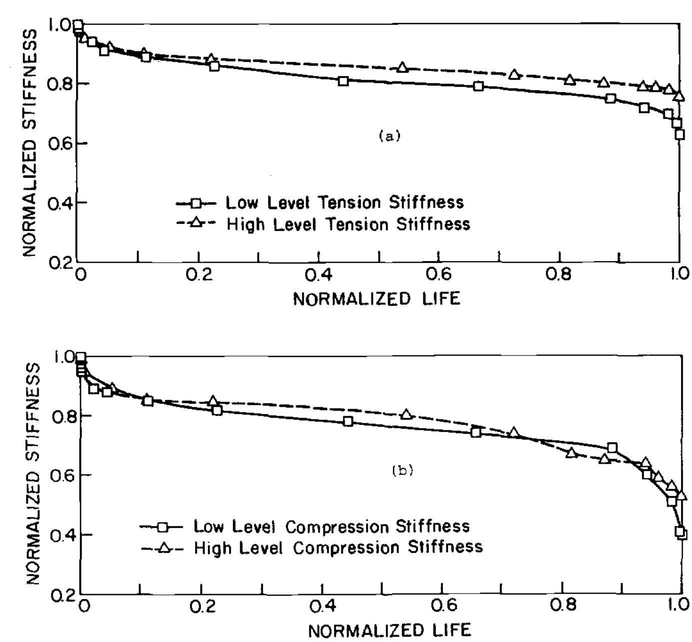

FIG. 5—*Stiffness-life relation:* (a) *Tension;* (b) *Compression.*

evident, as is the correspondence between tensile and compressive stiffness behavior. The similarities between the normalized tension and compression stiffness versus normalized life curves for two different load levels (corresponding to an order-of-magnitude difference in fatigue life) indicate that change in stiffness, rather than accumulated cycles, should be considered as a measure of the state of the material and its residual properties.

Fatigue Damage Mechanisms, Low Load Level (±20.0 kN)

Within the first ten load cycles, 0-deg ply cracks appear tangent to the hole. Cracks in all other off-axis plies form along the hole boundary by 100 cycles. All matrix cracking initiates randomly through the thickness, but within 1000 cycles is distributed rather uniformly in this respect. Tension and compression stiffnesses at this time are about 96% to 98% of their initial values, with compression generally being the lesser of the two.

At 1000 to 5000 cycles, interlaminar cracking begins to take place at the 45/90 interfaces closest to both surfaces (interface numbers 2 and 30), followed closely by cracking at 90/−45 interfaces (interface numbers 3 and 29). This means that at the point where a 90-deg matrix crack meets the neighboring +45- or −45-deg ply, the crack turns and follows that interface. The interlaminar cracking occurs at the 90-deg and 270-deg positions on the hole boundary and represents delamination initiation. The direction of growth is very consistent in that the delaminations on opposite sides of the 90-deg crack travel in opposite directions (Fig. 6).

There are other delamination initiation processes occurring along the hole boundary at the same time as those at the 45/90 and 90/−45 interfaces. At the first 0/45 interfaces under both surfaces (provided there was no drill-induced damage there initially), eight individual delaminations initiate in the densely cracked regions bounded by 0-deg tangent cracks and the hole boundary. Often, delamination at this interface occurs earlier in the second and fourth quadrants around the hole, where the 0 and +45-deg cracks overlap each other in adjacent plies. These surface delaminations grow away from the hole, but are arrested in lateral growth by the presence of the 0-deg tangent cracks. Within a few thousand cycles, the edge-view radiograph indicates delamination formation at each 0/45 interface through the thickness in the region bounded by 0-deg tangent cracks and the hole boundary. Figure 7*a* illustrates face and edge view radiographs at 5K cycles. The hole appears as a lighter region in the edge view. Note that the magnification of the edge view is greater than that of the face view. Stiffnesses measured with the extensometer during this delamination initiation period are 94% to 96% of their initial values.

Between 5K and 10K cycles, the second set of 45/90 and 90/−45 interfaces beneath the surface delaminate in a manner identical to the first, while all transverse matrix cracks extend in length. New delaminations initiate in the ligament area outside of the 0-deg tangents under the surface plies. This event can be

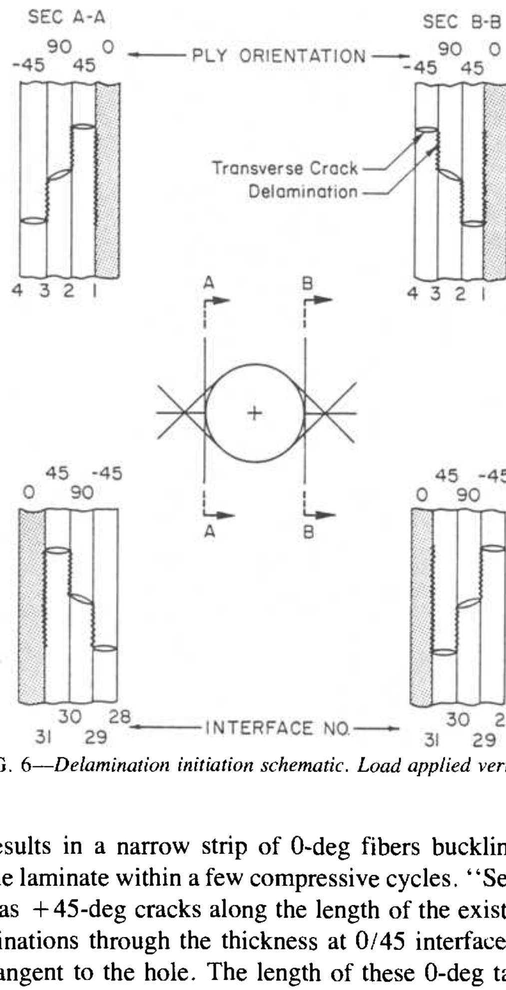

FIG. 6—*Delamination initiation schematic. Load applied vertically.*

sudden, and results in a narrow strip of 0-deg fibers buckling away from the remainder of the laminate within a few compressive cycles. "Second generation" cracks initiate as +45-deg cracks along the length of the existing 0-deg tangent cracks. Delaminations through the thickness at 0/45 interfaces extend with the 0-deg cracks tangent to the hole. The length of these 0-deg tangent cracks and delaminations are a function of distance from the surface, with those at the surface being longest. By 10K cycles, stiffnesses are between 91% and 93% of their initial values.

Between 10K and 40K cycles, the damage development process begins to gradually slow as all like interfaces through the thickness delaminate in similar sequential fashion (Fig. 7*b*). Note that in several of the radiographs, such as Fig. 7*b*, the extensometer tabs appear as dark, rectangular areas directly above and below the hole. These areas should not be confused with damage. "Third generation" cracks appear in the region between the 0-deg tangent cracks when 90-deg cracks initiate along the 45-deg cracks, which in turn initiated from the 0-deg cracks. Assuming that this phenomenon is not caused by a delayed infusion of zinc iodide into cracks formed earlier in the fatigue life (which could not be determined), the implication here is that the region above and below the hole

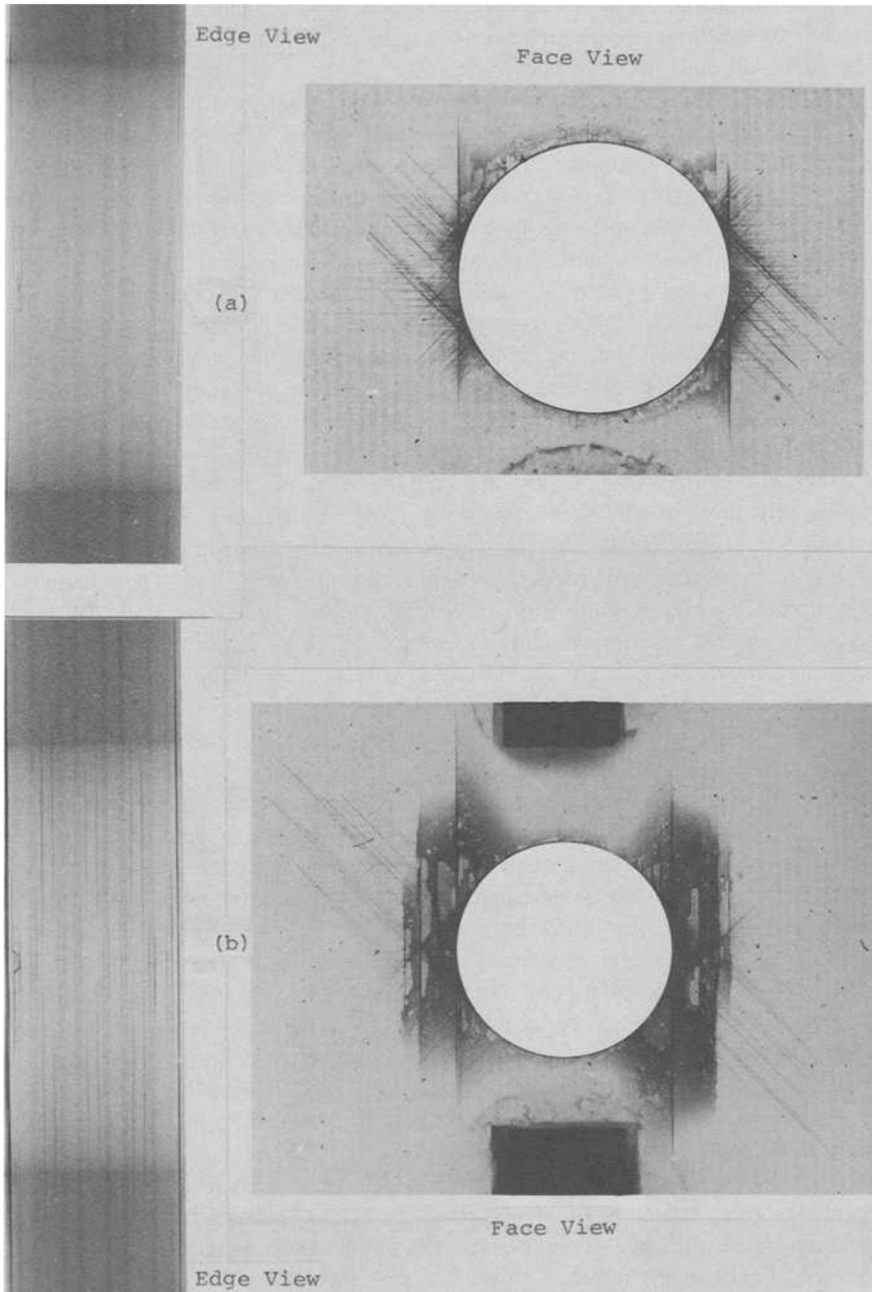

FIG. 7—*X-ray radiographs, low load level, Stage I, edge and face views:* (a) *5K cycles;* (b) *40K cycles. Load applied vertically.*

must still bear significant load, even though it is somewhat isolated by 0-deg cracks. At the straight edge, transverse matrix cracking initiates sequentially in the 90, −45, and +45-deg plies.

Stage I of damage development is usually completed by 40K to 60K cycles at the low load level. Continued lateral growth of the outermost 0/45 delaminations consists of widening strips of 0-deg fibers buckling away from the remainder of the laminate. This process usually initiates at the underlying +45-deg crack that is tangent to the hole and quickly spreads longitudinally in both directions. While 0/45 interface delaminations are larger at the surface of the laminate than in the interior, edge radiographs indicate that the delaminations on either side of the 90-deg plies through the thickness are of equal extent and that these particular delaminations remain confined to the triangular region formed by the +45- and −45-deg tangent cracks and the hole boundary. Stiffnesses at the end of Stage I are between 85% and 91% of their initial values, with compression being less than tension by about 5%.

Stage II of stiffness degradation and damage development is characterized by a relatively slow growth of matrix cracking and delamination. In the first half of Stage II, matrix cracks become denser and longer throughout the laminate, with most new crack initiation and growth occurring away from the hole boundary. Figure 8*a* is a magnification of +45-deg cracks initiating along 90-deg cracks in an area far from the hole (Specimen 2-2 at 100K cycles). Stiffnesses midway through Stage II are about 78% to 90% of their initial values (tension is approximately 5% greater than compression).

During the second half of Stage II, straight-edge delamination growth occurs in regions of dense transverse cracks, as shown in Fig. 8*b* for Specimen 6-2 at 90% of life. This type of delamination tends to grow along one of the prominent +45- or −45-deg transverse matrix cracks that originate tangent to the hole, and is frequently located on more than one interface near the laminate's surface. In the region between the 0-deg tangents above and below the hole, splits occur in the surface 0-deg ply, allowing the underlying 0/45 delamination to grow longitudinally. At the end of Stage II, normalized stiffnesses are typically 75% to 80% of initial values, with compression being 5% to 10% lower than tension.

Since stiffness correlated better with the observed damage state than a simple cycle count, tensile residual strength and deply data were obtained for specimens at stiffnesses corresponding to approximately 30% and 70% of life. One pair of specimens was matched in stiffness degradation for each of the two selected states of damage. Normalized stiffnesses of the first pair were about 90%, while those of the second pair were about 88% in tension and 81% in compression. Nondestructive inspection of these specimens with C-scanning and X-ray radiography supported the contention that a similar state of damage had been induced in each of the matched pairs. One specimen of each pair was deplied, and the other specimen was monotonically loaded in tension to failure. Tensile residual strength was also recorded at impending laminate fatigue failure.

Schematic reproductions of gold chloride tracings through one half of the

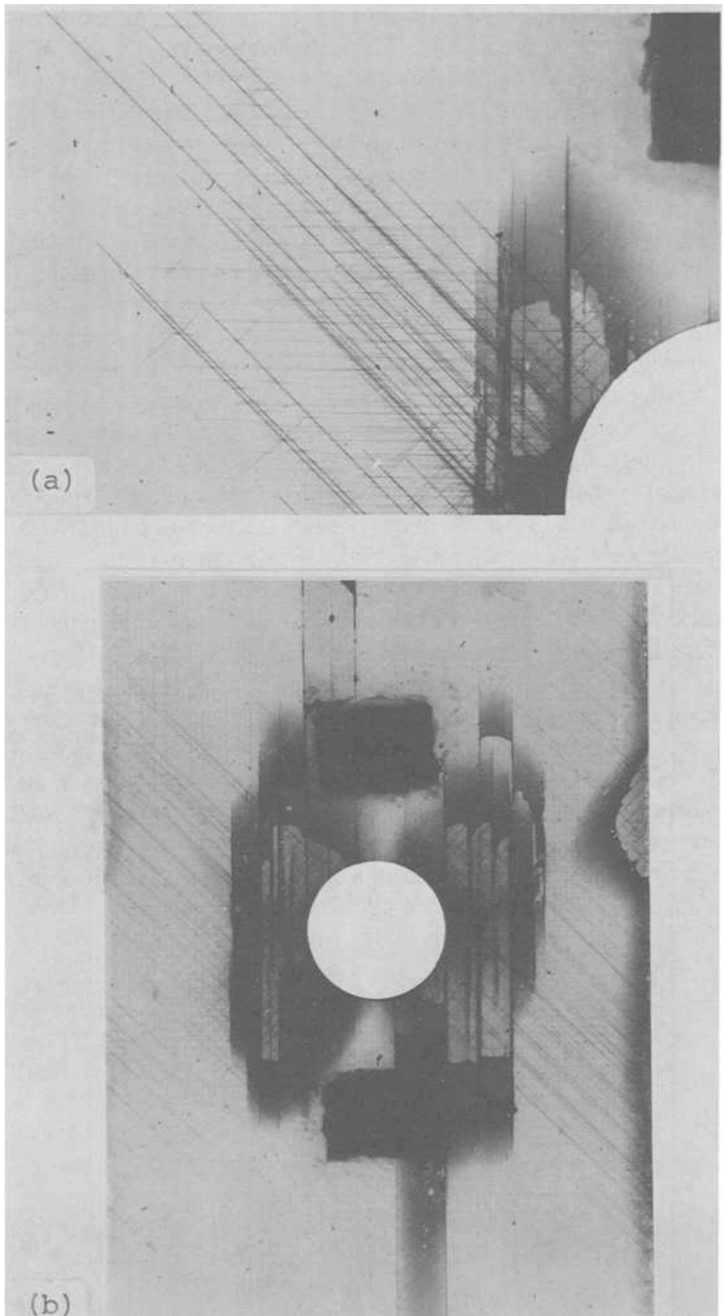

FIG. 8—*X-ray radiographs, low load level, Stage II:* (a) *Fourth quadrant matrix crack initiation;* (b) *End of Stage II.*

deplied, early Stage II laminate are illustrated in Fig. 9. Damage through the second half of the laminate was verified to be symmetric with that in the first half. Each diagram in this figure depicts the extent of damage at the interface of two plies of different orientations. The two crossed lines in the upper right corner of a diagram represent the orientations of the adjacent plies at the interface illustrated, and the numbers in the upper left corner are the interface identification numbers. Number 2, for example, is the second interface from the front surface, which separates 45-deg and 90-deg plies. Large shaded areas indicate large-scale delamination, whereas thin black lines represent matrix crack tracings from cracks common to that interface.

The effect of thickness on delamination is evidenced by noticing the much larger extent of the first interface delamination compared to the others in the interior. At interior 0/45 interfaces, delaminations follow the 0-deg tangent cracks in path. In the region outside of the 0-deg tangents, delaminations grow normal to the 0-deg tangent cracks and normal to prominent +45-deg cracks extending from the hole boundary. Delamination initiation at 0/45 interfaces seems to occur just above and below the 90- and 270-deg positions on the hole boundary, between the 0-deg tangents. The +45- and −45-deg cracks tangent to the hole form a well-defined boundary containing delamination growth along 90-deg plies. Dense cracks in any two adjoining plies often act as microdelamination initiation sites. These microdelaminations are not visible in Fig. 9, but they initiate as small web-shaped regions in the acute angles formed by the crack crossings. This phenomenon occurred most often along the 90-deg plies, and to a lesser extent along the 0-deg plies. A delamination's growth is suspected to be influenced by microdelamination coalescence along its frontier. However, as seen in the series of delamination schematics, large matrix cracks parallel to fibers could arrest delamination growth for a certain length of time. It should be kept in mind that the delamination growth sequence cannot be stated positively due to the non-continuous nature of damage monitoring via the deply technique.

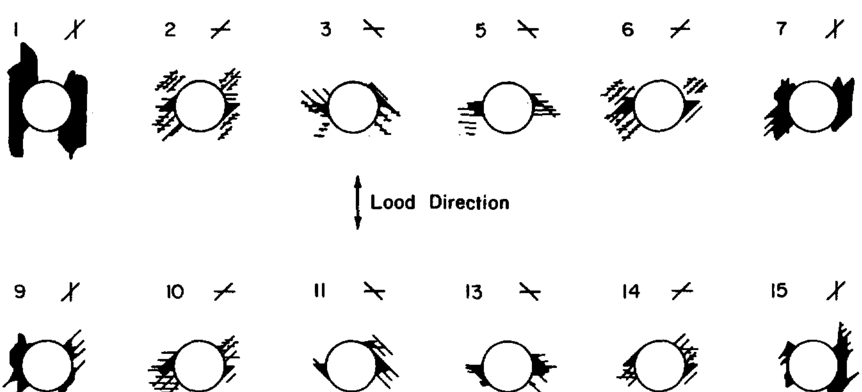

FIG. 9—*Gold chloride tracings between deplied laminae.*

As Stage II progresses, deply data indicate that most new delamination growth occurs at the first 0/45 interface beneath the surface. The 0/45 delaminations deeper in the interior of the laminate grow at a much slower rate, and the 45/90 and 90/−45 delaminations grow very little if at all. Large matrix cracks in +45, −45, and 90-deg plies effectively arrest delamination growth at their respective interfaces throughout this stage of damage development.

The residual tension test data for the laminates in Stage II are given in Table 1. The tensile strength increased to roughly 110% of mean initial strength in the first half of Stage II (within the scatterband of initial strength), and 140% in the second half. Therefore, Stage II is a period of tensile strength increase. During early Stage II, the ultimate longitudinal strains across the hole and on the edge were 120% and 110% of the mean initial values, respectively. The ratio of strain across the hole to that at the straight edge was 1.8, or 10% above the initial value. During late Stage II, the hole and edge strains had increased to 160% and 130% of initial values, respectively. The ratio of hole/edge strain had increased to 1.9, or 120% of the initial value, which reflects the effect of damage concentrated near the hole. Post-failure examination of a typical residual tension test specimen (Fig. 10*a*) reveals a fracture surface that resembles that of a tension test specimen with no cyclic load history. The fracture surface area increases with increasing damage, which may support the hypothesis that it is indeed a load redistribution (over a larger area) that causes notched laminates to undergo a residual strength increase. The double −45-deg plies through the thickness still show little evidence of fiber fractures. Aside from the surface 0-deg plies, which fractured over a highly irregular path, there is no significant difference in the appearance of fractured plies of similar orientation through the thickness.

Stage III comprises approximately the last 10% of finite fatigue life, but never occurs in runout fatigue tests. Tension stiffness declines nearly 10% of the initial stiffness, for a cumulative stiffness reduction of 20% to 40% of the initial value. Compression stiffness may change an additional 30% of the initial value in the positive or negative direction. A slight amount of nonlinearity may appear in the load-strain relation near the end of life.

In the early part of Stage III, delaminations in the laminate begin to spread rapidly in all directions. Just prior to the final failure event, one or more delaminations in any of the first few interfaces below the surface may extend continuously from the hole to the straight edge (Fig. 11). Matrix cracks do not increase significantly in density or extent during this stage. Visual observation of a specimen at the end of life reveals localized buckling of sublaminates near the surface of the laminate during the compression portion of the loading.

Due to difficulties in achieving a later Stage III damage state at the low [±20.0 kN (±4500 lb)] load level, the fatigue load was raised to ±22.3 kN (±5000 lb). This specimen showed signs of impending failure (rapid stiffness loss) at 961K cycles, and thus could be considered along with the other low-load-level tests that displayed a similar state of damage at over a half-million cycles. Tension and compression stiffnesses were 84% and 87% (increasing due to out of plane

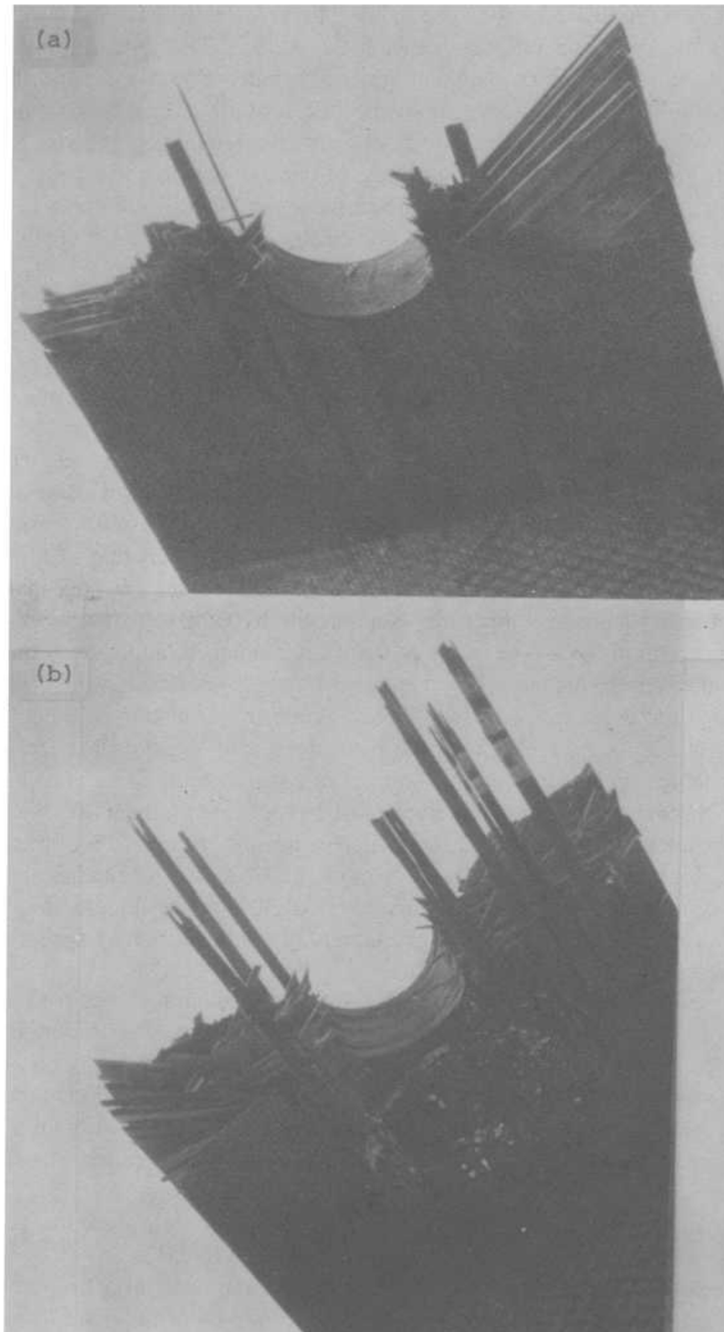

FIG. 10—*Fracture surfaces:* (a) *Residual tension test, low load level, late Stage II* (*rear view*); (b) *Fatigue failure, low load level.*

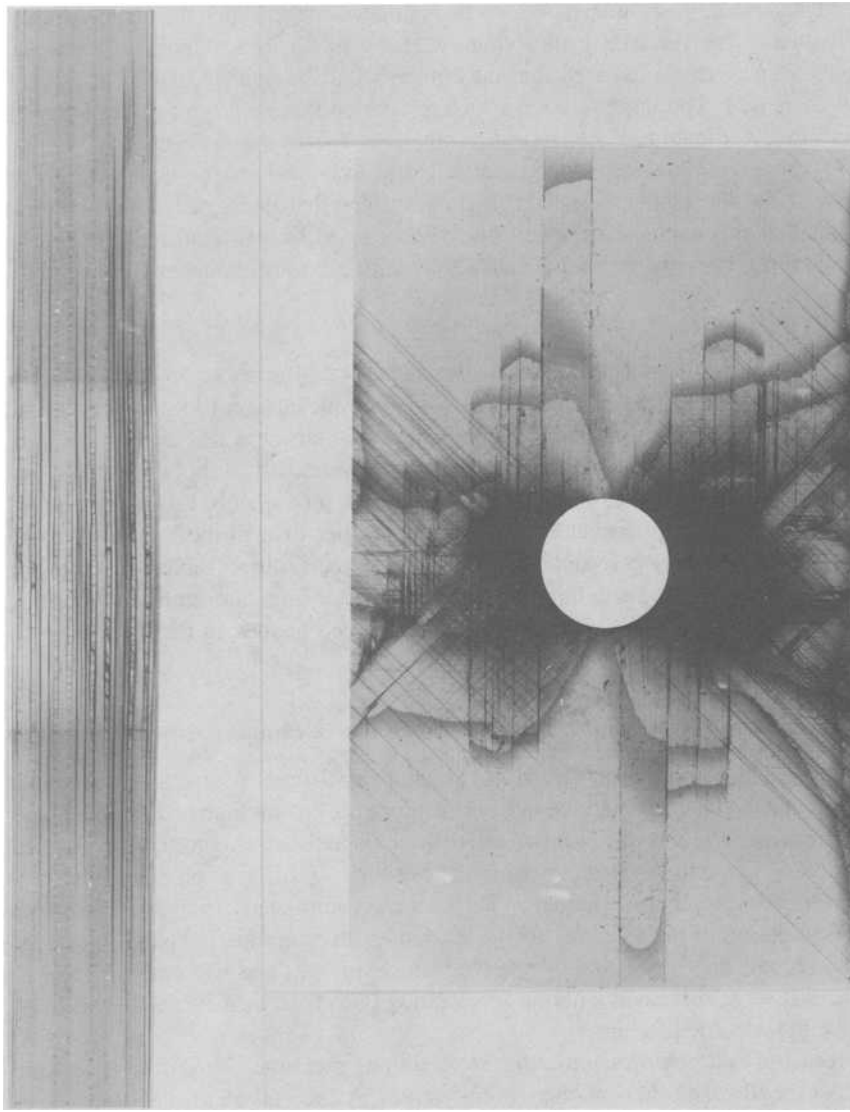

FIG. 11—*X-ray radiographs, low load level, end of life, edge and face views. Load applied vertically.*

deformation), respectively. Residual tensile strength was about 120% of its initial value, meaning that even at imminent failure, the tensile strength does not decrease significantly or enough to cause a tensile mode of failure. The ultimate strains at the hole and edge had increased to 140% and 120% of initial values, respectively (Table 1). The ratio of strain at the hole to that at the edge increased 20% to a value of 1.9. This information on ultimate load and strain change during progressive fatigue damage in a notched laminate suggests that the damage indeed "softens" the material in the vicinity of the notch in a manner that ultimate tensile strength is increased, but the compressive strength (or load at instability) is decreased. The large failure surface resembled that seen typically in Stage II, and involved many of the large delaminations visible via radiography.

A photograph of a specimen that failed in low-level fatigue is shown in Fig. 10*b*. Note the highly dispersed fracture surface that is characteristic of highly damaged specimens. Laminate failure was caused by the localized buckling of delaminated groups of laminae and the resulting loss of compressive stiffness.

Fatigue Damage Mechanisms, High Load Level (±24.5 kN)

Damage development at the high load level [±24.5 kN (±5500 lb)] is quite similar to that at the low load level when chronicled according to normalized stiffness. Figures 5*a* and 5*b* show that the static stiffness loss as a function of percentage of life is similar for the two load levels used in this study. Residual tensile strength achieves a steady-state value of approximately 130% of the initial mean value by approximately 30% of life (earlier than in the low-level tests), and remains nearly constant to impending fatigue failure (Table 1). As in the low load level, fatigue failure is caused by large delaminations and the resulting compressive instability. Additional details can be obtained in Ref *19*.

Discussion

Damage Mechanisms During Tension-Compression Fatigue (R = −*1*)

Excellent correlation between the amount of stiffness degradation, nature of the damage state, and fatigue age (or residual life) of the notched laminate was realized. Continuous monitoring of stiffness degradation suggested the classification of life into three stages which correspond to different phases of the progressive development of damage. The first stage consisted of rapid stiffness loss and initiation of most unique modes of damage through the laminate thickness. The second stage consisted of relatively slow stiffness loss and damage growth. The last stage coincided with the accelerating rate of damage events and stiffness loss that preceded failure.

Tension and compression stiffness retentions measured across the hole were between 40% and 80% of their initial values by the end of life. Stiffness degradation in compression was larger than that in tension, and was more sensitive to slight out-of-plane displacements of the locally delaminated test specimens.

Initial damage appeared in the form of transverse matrix cracks in off-axis plies around the hole, and 0-deg cracks tangent to the hole. Delamination initiation and growth were affected by the presence of prominent matrix cracks at the hole. Zero-degree cracks and their associated delaminations grew faster near the surface of the laminate. Delamination growth along the 90-deg plies was arrested by large cracks at the hole, and was not strongly affected by distance from the surface for much of the fatigue life.

At the two fatigue load levels considered in this investigation (45% and 55% of compressive ultimate load, $R = -1$), load level did not significantly affect the delamination initiation sequence. The typical specimen delaminated first at the outermost 0/45 interface in the second and fourth quadrants around the hole, and soon after at the outermost 45/90 near the 90- and 270-deg positions around the hole. Delaminations later filled in the first and third quadrants at 0/45 interfaces, and initiated in similar fashion at all interior interfaces. Toward the end of life, delamination growth accelerated, especially at interfaces near the surface and at the straight edges of the test specimen.

Microdelamination initiation was seen away from the hole at the crossing of transverse matrix cracks in adjacent plies, especially near the surface. The leading edge of a growing delamination was sometimes uniform and bounded by a large matrix crack. At other times it appeared irregular due to scattered microdelaminations.

Residual Tensile Strength

During T-C fatigue, tensile strength increased during the first 10% to 40% of life to a maximum of 140% of the undamaged strength. This increase was slower at the lower of two load levels. Residual tensile strength remained approximately constant to the end of life, when the coupons failed in a compressive mode.

Acknowledgment

This work was performed under NASA Langley Research Center Grant NAG-1-343, monitored by Dr. T. K. O'Brien.

References

[1] Ratwani, M. M. and Kan, H. P. in *Damage in Composite Materials, ASTM STP 775*, K. L. Reifsnider, Ed., American Society for Testing and Materials, Philadelphia, 1982, pp. 211–228.
[2] Whitcomb, J. D. in *Fatigue of Fibrous Composite Materials, ASTM STP 723*, American Society for Testing and Materials, Philadelphia, 1981, pp. 48–63.
[3] Reifsnider, K. L., Henneke, E. G. II, Stinchcomb, W. W., and Duke, J. C. in *Mechanics of Composite Materials*, Z. Hashin and C. T. Herakovich, Eds., *Proceedings* of the IUTAM Symposium on Mechanics of Composite Materials, Blacksburg, VA, 1982, pp. 399–420.
[4] Kress, G. R. and Stinchcomb W. W. in *Recent Advances in Composites in the United States and Japan, ASTM STP 864*, American Society for Testing and Materials, Philadelphia, 1985.
[5] Reifsnider, K. L., Schulte, K. and Duke, J. C. in *Long Term Behavior of Composites, ASTM STP 813*, T. K. O'Brien, Ed., American Society for Testing and Materials, Philadelphia, 1983, pp. 136–159.
[6] Saff, C. R., "Compression Fatigue Life Prediction Methodology for Composite Structures—Literature Survey," NADC-78203-60, Interim Report, Commander Naval Air Development Center, Warminster, PA, June 1980 (McDonnell Aircraft Co., St. Louis, MO).
[7] Phillips, E. P. in *Fatigue of Fibrous Composite Materials, ASTM STP 723*, American Society for Testing and Materials, Philadelphia, 1981, pp. 197–212.
[8] Miller, H. R., Ulman, D. A., Reifsnider, K. L., Bruner, R. D., Stinchcomb, W. W., and Liechti, K. M., "Cumulative Damage Model for Advanced Composite Materials," Final Technical Report (Phase II), AFWAL-TR-84-4007, Materials Laboratory, Air Force Wright Aero-

nautical Laboratories, Air Force Systems Command, Wright-Patterson AFB, OH, March 1984 (General Dynamics Corp., Fort Worth Division, Fort Worth, TX).

[9] Rosenfeld, M. S. and Gause, L. W. in *Fatigue of Fibrous Composite Materials, ASTM STP 723*, American Society for Testing and Materials, Philadelphia, 1981, pp. 174–196.

[10] Ryder, J. T. and Walker, E. K., "The Effect of Compressive Loading on the Fatigue Lifetime of Graphite/Epoxy Laminates," AFML-TR-79-4128, Final Technical Report, Air Force Materials Laboratory, Air Force Systems Command, Wright-Patterson AFB, OH, October 1979 (Lockheed-California Co., Burbank CA).

[11] Whitney, J. M. in *Long-Term Behavior of Composites, ASTM STP 813*, T. K. O'Brien, Ed., American Society for Testing and Materials, Philadelphia, 1983, pp. 225–245.

[12] Stinchcomb, W. W., Black, N. F., Reifsnider, K. L., and Henneke, E. G. II, "Damage Development Mechanisms in Notched Composite Laminates Under Compressive Fatigue Loading," Report No. 79055-60, Naval Air Development Center, Warminster, PA, May 1981.

[13] Harris, C. E. and Morris, D. H., "An Evaluation of the Effects of Stacking Sequence and Thickness on the Fatigue Life of Quasi-Isotropic Graphite/Epoxy Laminates," NASA Contractor Report 172169, Hampton, VA, April 1983.

[14] Jamison, R. D. and Reifsnider, K. L., "Advanced Fatigue Damage Development in Graphite Epoxy Laminates," AFWAL-TR-82-3103, Flight Dynamics Laboratory (FIBE), Air Force Wright Aeronautical Laboratories (AFSC), Wright-Patterson AFB, OH, Dec. 1982 (Virginia Polytechnic Institute and State University, Blacksburg, VA).

[15] Rummel, W. D., Tedrow, T., Brinkerhoff, H. D., "Enhanced X-Ray Stereoscopic NDE of Composite Materials," AFWAL-TR-80-3053, Final Report, Flight Dynamics Laboratory, AFSC, Air Force Wright Aeronautical Laboratories, Wright-Patterson AFB, OH, June 1980 (Martin Marietta Corp., Denver, CO).

[16] Kriz, R. D. and Stinchcomb, W. W. in *Damage in Composite Materials, ASTM STP 775*, K. L. Reifsnider, Ed., American Society for Testing and Materials, Philadelphia, 1982, pp. 63–80.

[17] Camponeschi, E. T. and Stinchcomb, W. W. in *Composite Materials: Testing and Design (Sixth Conference), ASTM STP 787*, I. M. Daniel, Ed., American Society for Testing and Materials, Philadelphia, 1982, pp. 225–246.

[18] Freeman, S. M. in *Composite Materials: Testing and Design (Sixth Conference), ASTM STP 787*, I. M. Daniel, Ed., American Society for Testing and Materials, Philadelphia, 1982, pp. 50–62.

[19] Bakis, C. E., "Fatigue Response of Notched Composite Laminates Subjected to Tension-Compression Loading," MS. thesis, Department of Engineering Science and Mechanics, Virginia Polytechnic Institute and State University, Blacksburg, VA, Dec. 1984.

Paul A. Lagace[1] *and Stephen C. Nolet*[1]

Effect of Ply Thickness on Longitudinal Splitting and Delamination in Graphite/Epoxy Under Compressive Cyclic Load

REFERENCE: Lagace, P. A. and Nolet, S. C., "**Effect of Ply Thickness on Longitudinal Splitting and Delamination in Graphite/Epoxy Under Compressive Cyclic Load,**" *Composite Materials: Fatigue and Fracture, ASTM STP 907*, H. T. Hahn, Ed., American Society for Testing and Materials, Philadelphia, 1986, pp. 335–360.

ABSTRACT: The initiation and growth of damage due to compressive cyclic loading was investigated in $[\pm 45_n/0_n]_s$ graphite/epoxy laminates where the "effective ply thickness" was varied by allowing n to take on the values 1, 2, and 3. A total of 35 axially loaded sandwich specimens with 6.35-mm-diameter holes were cycled at 7 Hz at peak stress levels of 52% to 72% of the static ultimate compressive stress of 425 MPa (which was experimentally determined to be independent of the value of n). Out-of-plane moiré interferometry and pulse-echo ultrasound techniques were used to nondestructively inspect the specimens and showed that three distinct modes of damage growth occur in these laminates. Delamination which initiates at the hole and grows in a radial or transverse fashion occurred only in 60% of the $[\pm 45/0]_s$ specimens. For these two types of damage, the growth was rapid and led to catastrophic failure of the specimen. The remainder of the $[\pm 45/0]_s$ specimens and all the laminates where the effective ply thickness was doubled and tripled, $[\pm 45_2/0_2]_s$ and $[\pm 45_3/0_3]_s$, exhibited delaminations which initiated at the hole edges and grew parallel to the load direction with the width of the delamination equal to the width of the hole. Catastrophic failure did not occur in these cases. There is a linear relationship between the delamination length and the logarithm of the number of applied load cycles in all these cases. However, the delamination initiated earlier and at lower stress levels for laminates with larger effective ply thicknesses. Specimen sectioning and microscopic examination show that this damage depends on the development of splitting in the 0-deg plies and subsequent delamination as a result of shear failure at the $-45°/0°$ ply interface in the region between the splits. Several $[0/\pm 45]_s$ and $[0_2/\pm 45_2]_s$ coupon specimens were cycled in tension and this splitting and subsequent delamination also developed. Residual tensile strength tests conducted on graphite/epoxy coupons debonded from the honeycomb after cycling showed a 50% increase in tensile strength over undamaged specimens with 6.35-mm-diameter holes. This is attributed to the redistribution of stress around the hole due to the relieving of stress concentration in the 0-deg plies by the splitting and delamination.

KEY WORDS: composite materials, cyclic load, damage growth, delamination, splitting, ply thickness, residual strength

[1] Assistant Professor of Aeronautics and Astronautics, Technology Laboratory for Advanced Composites, Massachusetts Institute of Technology, Cambridge, MA. Coauthor Nolet is currently 1st Lieutenant, USAF, McClellan AFB, Sacramento, CA.

The response of materials to repeated load is an important engineering concern. The damage which develops under cyclic load controls the usefulness and life of the material. In metals, fatigue damage is generally in the form of a single dominant through-crack and methods have been developed and are utilized to predict crack growth due to repeated loads. However, the multiplicity of damage modes in composite materials [*1–3*] makes the characterization of damage growth in composites a much more formidable task. The specific problem of delamination growth due to interlaminar stresses and localized buckling is unique to composite materials [*4–6*].

A number of factors affect the mode of damage and the growth rate in composites subjected to repeated loads. Among these are the type of loading, the orientation of the individual plies, the material used, and the stacking sequence of the laminate. The stacking sequence and ply orientations are especially important in terms of the interlaminar stress field generated at free edges. It has been shown that the interlaminar stresses at the free edge of a straight-edged specimen subjected to quasi-static tension load can cause failure due to delamination [*7*]. Recent work by several authors [*7–10*] has shown that an important parameter in determining when this delamination occurs is the thickness of the individual plies. As the layer thickness increases, the interlaminar stresses associated with the free edge will increase proportionally. Thus, the thicker the ply layer, the more likely that delamination will result due to these interlaminar stresses. O'Brien [*11*] has recently developed a technique using the strain energy release rate to account for this thickness dependence.

This out-of-plane damage mode is not limited to straight free edges of composite laminates, but can occur at other free edges such as at a hole [*12*]. Lucking et al [*13*] have shown that the interlaminar stress field in the vicinity of a hole is dependent upon the hole radius-to-thickness ratio. Their results of $[0/90]_s$ composite laminates with circular holes demonstrate that the maximum interlaminar normal stress increases with increasing radius-to-thickness ratio. This implies that the ply thickness effect found for straight free edges should also exist for notched laminates which delaminate.

Since interlaminar stresses are important in causing damage in composite laminates under cyclic load, it would seem likely that the ply thickness will have an important effect on the development of such damage since the interlaminar stress field will be altered. This is the subject of the current investigation.

Scope of Work

The main thrust of the current investigation is to examine the effect which ply thickness has on the development and propagation of damage in composite laminates subjected to compression-compression cyclic loading. The impact of ply thickness on the residual strength of these damaged laminates is also investigated.

The $[\pm 45/0]_s$ family of laminates was chosen for investigation since differing damage modes exist for this type of laminate. Previous authors have reported different damage modes for this laminate family due to a simple change in stacking sequence. Investigators who have looked at this laminate with the 0-deg plies on the surface [*14,15*], that is $[0/\pm45]_s$, under tension-tension fatigue report that the major damage mode is due to axial cracks which develop from the notch in the outer 0-deg layer and delamination of this layer between these cracks. Similar damage has been reported for this type of laminate when subjected to compression-compression loading [*16–18*]. Rosenfeld and Huang [*16*] have suggested that by placing other plies besides the 0-deg plies on the outside surface, this type of damage can be restricted. Fanucci and Mar [*19*] did this by testing $[\pm45/0]_s$ specimens in compression-compression and found that the damage mode was delamination which propagated in a radial fashion away from the hole.

In addition, several of these authors [*14,15,17*] have observed that the residual tensile strength increases after axial cracks develop in the $[0/\pm45]_s$ laminate. Therefore, this investigation also looks into the tensile residual strength of the specimens after they have been damaged by exposure to cyclic compressive load, and the effect that ply thickness has on this residual strength via the damage which is induced.

Experimental Procedure

Specimen Configuration

The specimen configuration used in testing is especially important in compression. The specimen and any associated supporting structure must minimize stresses due to specimen bending but not restrict failure modes of the material from developing due to local constraints. A number of jigs have been developed and used with varying success. In this program, it was necessary to not only load the specimen in compression but also to closely monitor damage development around the hole. Thus, any antibuckling jig would need to leave the area around the hole free for nondestructive inspection. Phillips [*20*] showed that the cyclic life of a composite specimen with a cutout was dependent upon the cutout size in the support plates. This problem is exacerbated in this case due to the fact that relatively thin laminates (six to eighteen plies) were investigated. In addition, antibuckling plates can restrict the development of delamination damage in compression via local ply buckling.

Success has been achieved in testing thin composite laminates in compression by using a sandwich beam [*18,21*]. This previous work was conducted on four-point bend specimens. This bending does introduce local stress concentrations in the material and also is not conducive to certain types of nondestructive investigation techniques (such as the moiré method).

For this work, the basic sandwich specimen was adopted but was tested as an axial column. A schematic of the specimen is shown in Fig. 1. The specimen consists of two 50-mm face sheets of graphite/epoxy of the same laminate configuration.

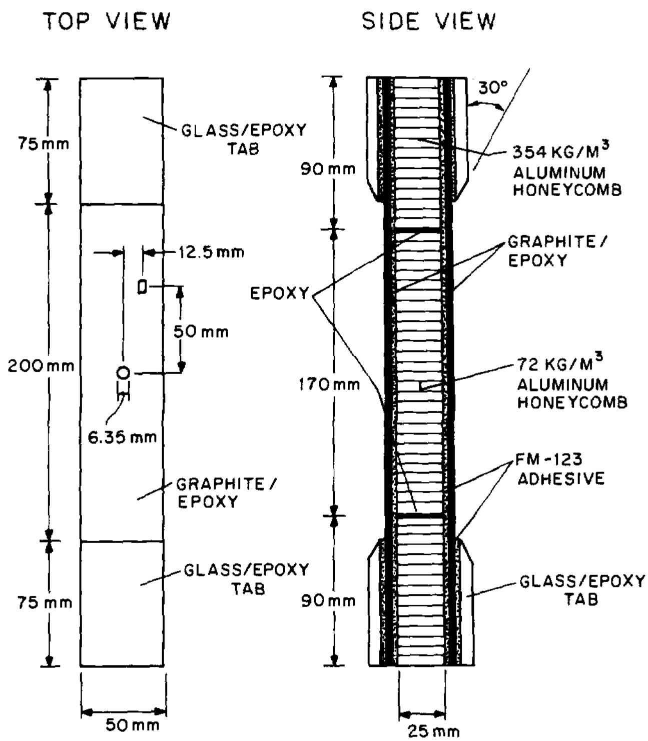

FIG. 1—*Physical characteristics of the sandwich specimen.*

The material used throughout the program was Hercules AS1/3501-6 graphite/epoxy unidirectional preimpregnated tape supplied in 300-mm-wide rolls and stored at temperatures below −18°C. The prepreg was cut using Stanley knives and laid up with the use of a jig to assure proper fiber angles from ply to ply. The material was cured as 300-mm by 350-mm plates in an autoclave under 0.59 MPa and 762-mm Hg vacuum in a two-step process: a one-hour hold at 116°C and a two-hour hold at 177°C. The cured plates were postcured in an oven at 177°C for eight hours. The complete laminates were cut into 50-mm-wide strips on a milling machine with a specially designed table using a water-cooled diamond wheel. All specimens had 6.35-mm-diameter holes drilled in them with the use of a diamond-coated drill and reamer set and a standard drill press. Water cooling was used in the drilling process. This process resulted in smooth-edged holes with no back-ply delaminations.

All specimens were inspected nondestructively using the pulse-echo ultrasound technique to locate any major flaws due to manufacturing. No delaminations were discovered using this process.

The completed graphite/epoxy face sheets were bonded onto a honeycomb support structure using film adhesive FM-123-2 supplied by American Cyanamid.

This process was conducted in an autoclave at 0.24 MPa and 107°C for two hours. The core consisted of two different types of aluminum honeycomb. The central part of the core in the test section had a low-density (72 kg/m^3) aluminum honeycomb while the end sections, 90 mm in length, had a high-density (354 kg/m^3) aluminum honeycomb. These three individual pieces of honeycomb were bonded end-to-end with a room-temperature cure epoxy before final bonding of the graphite/epoxy face sheets. The high-density aluminum honeycomb was chosen for the ends so that there was sufficient support to prevent crushing of the core when the specimens were gripped by the hydraulic grips. The low-density honeycomb was chosen for the test section so as to provide minimal restriction of the face sheets.

A test program was conducted to check the validity of this specimen and is reported by Nolet [22]. One important point which surfaced from this investigation was that the honeycomb should be aligned such that the ribbon direction runs parallel to load application for compression testing. It was found that such an arrangement least restricted Poisson's effect whereas placement of the honeycomb in the other orientation (ribbon direction perpendicular to compressive load application) restricted Poisson's contraction by 15 to 20%, thereby creating residual stresses in the face sheets.

A secondary bond was performed to place glass/epoxy loading tabs made of Scotchply Type 1002 on each end of the specimen using the FM-123-2 film adhesive. The tabs were of the $[0/90]_{ms}$ configuration with m equal to 2 (eight-ply tabs) for six-ply face sheets and m equal to 3 (eighteen-ply tabs) for 12-ply and 18-ply face sheets. These loading tabs were 75 mm in length. Thus the area of high-density honeycomb extended beyond the grip area. This was done to minimize local rotation and stress concentration which would occur if the low- to high-density honeycomb interface coincided with the tab end.

Longitudinal strain gages were bonded onto all specimens which were tested quasi-statically in order to obtain data to determine longitudinal moduli. This measurement was used as a means to check the quality control. Strain gage type EA-09-125AD-120 manufactured by Micro Measurements was used throughout. The gage was located away from the hole, as pictured in Fig. 1, in order to measure the far-field strain.

Test Matrix

As previously mentioned, the $[\pm 45/0]_s$ family of laminates was chosen for this investigation. The "effective ply thickness" of the graphite/epoxy was varied from 0.134 to 0.268 to 0.402 mm by sequentially laying up one, two, or three plies of the same lamination angle. This resulted in the three laminates $[\pm 45/0]_s$, $[\pm 45_2/0_2]_s$, and $[\pm 45_3/0_3]_s$. The nominal per-ply thickness of the AS1/3501-6 graphite/epoxy used throughout in reporting stresses is 0.134 mm. The manufacturing process yielded an average per-ply thickness of 0.133 mm with a coefficient of variation of 2.4%.

Both static and cyclic compression tests were conducted on the three laminates. Static tests were performed in order to experimentally obtain longitudinal modulus and the fracture stress to ascertain whether the effective ply thickness had an effect on the static fracture. Each of the three laminates was cycled at three maximum stress levels at a stress ratio of 10. The stress levels varied for the three different families and were, in part, dependent upon results obtained from previous tests.

A total of 56 specimens was tested in this program. Twenty-one of these were tested in static compression while the remaining 35 were tested under compression-compression cyclic loading. The entire test matrix is given in Table 1.

Test Procedure and Damage Detection

Testing was accomplished on an MTS 810 Material Test System with the aid of hydraulic grips. The static specimens were loaded at a constant stroke rate of 0.33 mm/min, yielding an approximate strain rate of 1800 microstrain/minute. Load and strain data were recorded through an automated data acquisition system using a PDP-11/34 computer. The tests were run monotonically to failure.

Cyclic testing was accomplished under load control with sinusoidal loading at a frequency of 7 Hz. A constant stress ratio of ten (minimum stress/maximum stress) was used for all tests.

Delamination growth was monitored during each cyclic test using one of two nondestructive inspection (NDI) methods. Since each specimen consisted of two graphite/epoxy face sheets, both sides were monitored and two sets of data were obtained for each specimen tested. The two NDI methods used are out-of-plane moiré interferometry and pulse-echo ultrasound.

Moiré out-of-plane interferometry has been successfully used to detect damage in graphite/epoxy laminates under compression-compression loading [*19*]. The moiré test setup used for this investigation consisted of 10-by-10-cm plates with

TABLE 1—*Experimental test program.*

Test Type	Peak Compressive Stress, MPa	Laminates[a]		
		$[\pm45/0]_s$	$[\pm45_2/0_2]_s$	$[\pm45_3/0_3]_s$
Monotonic to failure	failure stress	9[b]	8	5
Cyclic[c]	320	2	...	...
Cyclic	287	12	8	...
Cyclic	265	...	4	1
Cyclic	253	2	...	...
Cyclic	243	...	2	1
Cyclic	221	...	...	3

[a]All specimens have 6.35-mm-diameter holes.

[b]Number indicates number of specimens tested.

[c]All cyclic tests are compression-compression with a stress ratio ($\sigma_{min}/\sigma_{max}$) of 10 run at 7 Hz.

etched parallel lines (40 lines/cm) positioned parallel to both faces of the specimen. The plates were held by a set of three-degrees-of-freedom clamps that could align the glass within 0.5 mm of the composite. Collimated strobe lights were positioned at an angle of 45 deg and a distance of 50 cm to each composite face. The strobes were fired by a pulse from the function generator at the peak load of the cycle. This provided a stop-action view of the specimen during testing with the moiré pattern clearly displayed over both faces of the composite. The surface of the composite was spray painted with silver enamel to increase the contrast of the moiré patterns for photographs. This setup allows out-of-plane deflections to be picked up via the interference pattern created by the collimated light which shines through the grid. The smallest out-of-plane displacement that could be picked up with this system is 0.25 mm.

Moiré photographs were taken automatically at a preset frequency of 5000 cycles without halting the test. However, delaminations tended to grow quickly once initiated. When the growth rate of the delamination exceeded approximately 10 mm per 5000 cycles, the frequency of picture taking was increased to every 2000 cycles. This damage size is defined as the maximum linear distance of the damage area in any direction. The damage area was later measured from the negatives of the photographs projected onto a flat screen. The hole is used as a size reference.

The moiré interferometry was used for all the cyclic tests of the $[\pm 45/0]_s$ specimens and the first five tests of the $[\pm 45_2/0_2]_s$ specimens. In these latter five tests it was discovered that the out-of-plane deformation was insufficient to be detected by the moiré setup although a delamination did exist. This is due to the delaminated region being thicker than in the previous laminate and the local buckling causing a smaller out-of-plane delamination. For the remainder of these specimens and all the specimens of the $[\pm 45_3/0_3]_s$ laminate, delamination was monitored using the pulse-echo ultrasound technique. This inspection was accomplished with a Nova-Scope 2000 Digital Pulse-Echo Ultrasonic Thickness Gage with an NDT Instruments D1R transducer. The tests were stopped at 50 to 5000 cycle intervals to allow for manual inspection of the two face sheets. The frequency of inspection was chosen to ensure that the damage would not grow more than 10 mm in any direction between inspection intervals. Prior to the onset of delamination, the laminate was inspected at least every 1000 cycles. After the onset of delamination, this inspection interval was adjusted accordingly. A ruler was used to measure the length of the delamination as indicated by the ultrasonic technique, in terms of the maximum straight-line distance from the hole edge to the edge of the delamination as illustrated in Fig. 2. These measurements are accurate to 0.5 mm.

All cyclic tests were stopped when either failure occurred or damage grew to a size at which it was felt that failure would occur before the next inspection cycle. It was desirable to prevent failure of damaged cyclic specimens so that tensile residual strength tests could be run.

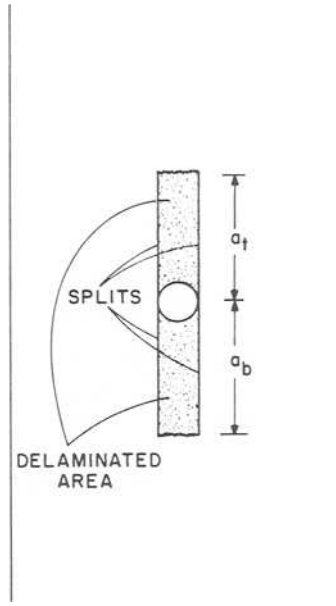

FIG. 2—*Definition of longitudinal delamination length.*

Experimental Results

Static Tests

The average compressive longitudinal moduli and failure stresses as well as the respective coefficient of variation (CV) are presented in Table 2. In all cases, the stress was determined based on the nominal thickness of the graphite/epoxy face sheets. The theoretical longitudinal modulus for these laminates is 57.7 GPa. This is calculated using classical laminated plate theory and the basic unidirectional ply elastic constants for Hercules AS1/3501-6 of

$$E_L = 130 \text{ GPa} \qquad E_T = 10.5 \text{ GPa}$$

$$G_{LT} = 6.0 \text{ GPa} \qquad \upsilon_{LT} = 0.28$$

TABLE 2—*Results of compressive monotonic to failure tests.*

	Longitudinal Moduli		Fracture Stresses	
Laminate[a]	E_L, GPa	CV	σ_F, MPa	CV
$[\pm45/0]_s$	56.3	4.4%	423	9.1%
$[\pm45_2/0_2]_s$	57.4	4.1%	421	7.7%
$[\pm45_3/0_3]_s$	57.0	5.8%	429	8.4%

[a] All specimens have 6.35-mm-diameter holes.

where the subscript L indicates the fiber direction and the subscript T the transverse direction. It can readily be seen that the measured moduli agree very well with the prediction. A typical stress-strain plot for these specimens shown in Fig. 3 indicates some softening behavior (that is, a reduction in modulus) but no strain discontinuities indicative of gross damage. This softening results in 10% reduction of the tangent modulus at failure.

The fracture stress results clearly show that the static failure is independent of ply thickness. This indicates that the static failure is not a result of interlaminar stresses but is an in-plane phenomenon as is indicated by the postmortem failure mode picture in Fig. 4. It is important to point out that the failure stress reported for these specimens is actually the failure stress of the weaker of the two face sheets of the specimen. When one face sheet fails, this induces gross bending resulting in failure of the remaining graphite/epoxy face. The average fracture stress will thus be slightly lower than if tests were conducted on the individual face sheets since the higher fracture stress of the stronger face sheet will not be attained.

Cyclic Test Results

Three distinct damage modes were observed in the cyclic tests. The first type of damage occurred only in the $[\pm 45/0]_s$ laminates and generally at relatively high stress levels. This damage mode is characterized by rapid growth perpendicular to the load direction which caused failure of the specimen within only a few cycles. This damage type was accompanied by loud clicking and popping sounds and was difficult to record through the moiré setup since the damage

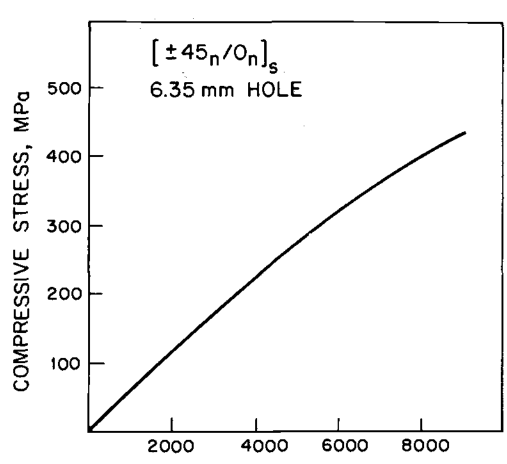

FIG. 3—*Compressive stress-strain behavior of* $[\pm 45_n/0_n]_s$ *laminate with a 6.35-mm hole.*

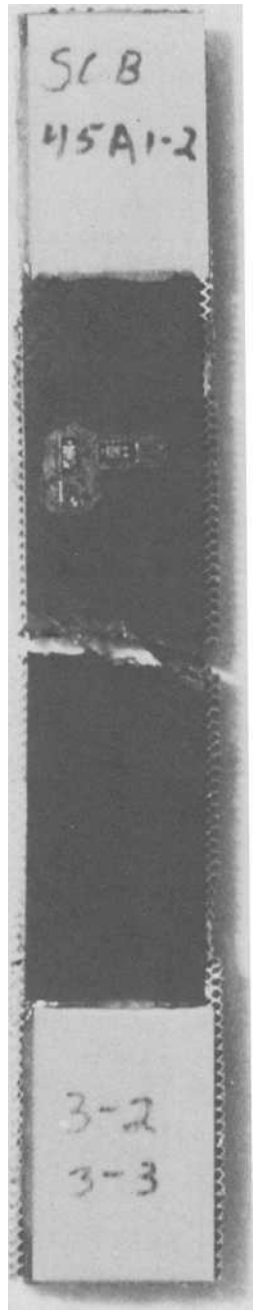

FIG. 4—*Postmortem failure mode of a* $[\pm 45_n/0_n]_s$ *laminate with a 6.35-mm hole loaded in static compression.*

grew to failure within only a few cycles. This type of damage occurred in five of the $[\pm 45/0]_s$ specimens and failure generally occurred nearly simultaneously with damage initiation. In these cases, the postmortem appearance of the specimen was similar to those tested under static load, indicating the existence of transverse cracks in the ±45-deg plies as well as general delamination.

The second type of damage again occurred only in the $[\pm 45/0]_s$ laminates. This damage mode is the same as that observed by Fanucci and Mar [19] in that delaminations formed along the edge of the hole at one or more locations and grew in a radial fashion away from the hole. This delamination growth was slow at first, but as the area of delamination increased, the growth became very rapid. A typical sequence of moiré photographs showing this growth is in Fig. 5. Seven of the $[\pm 45/0]_s$ specimens showed this type of damage. Two of these specimens were sectioned across the delaminated area using a water-cooled diamond wheel resulting in a smooth surface for inspection. The edges of the cut specimen were examined under a microscope at ×50 magnification. This inspection showed massive damage with delamination at all ply interfaces as well as transverse cracks throughout the thickness. The transverse cracks were prominent away from the delamination front, indicating that these cracks form after the delamination front moves by that region.

The remaining $[\pm 45/0]_s$ and all of the $[\pm 45_2/0_2]_s$ and $[\pm 45_3/0_3]_s$ specimens exhibited the third type of damage growth which extended along the longitudinal axis of the laminate parallel to the applied load. Moiré photographs of a damage sequence of this type are shown in Fig. 6. It is important to note that the width of this damage is the same as the diameter of the hole as the damage grew along two lines defined by the longitudinal lines tangent to the edges of the hole as illustrated in Fig. 2.

An inspection of several specimens with longitudinal delaminations was made to verify these NDI results. A transverse cut was made through the delaminated area, as previously described, and the edge of the cut specimen examined through a microscope at ×50 magnification. Figure 7 shows a photograph of a typical cross section. Two symmetric delaminations can clearly be seen at the −45°/0° ply interfaces. This delamination is centered in the laminate and is 6.35 mm in width as is the hole in the laminate. Close inspection of these photomicrographs also reveals that two matrix splits are located in the 0-deg plies at either end of the delamination.

A summary of all the results for the cyclic tests is presented in Tables 3 through 5 for the three different laminates. Of special interest in these three tables is the damage type which developed in each of the faces. The key used is:

NDD = no detectable damage,
TD = transverse damage (Type 1)
RD = radial delamination (Type 2), and
LD = longitudinal delamination (Type 3).

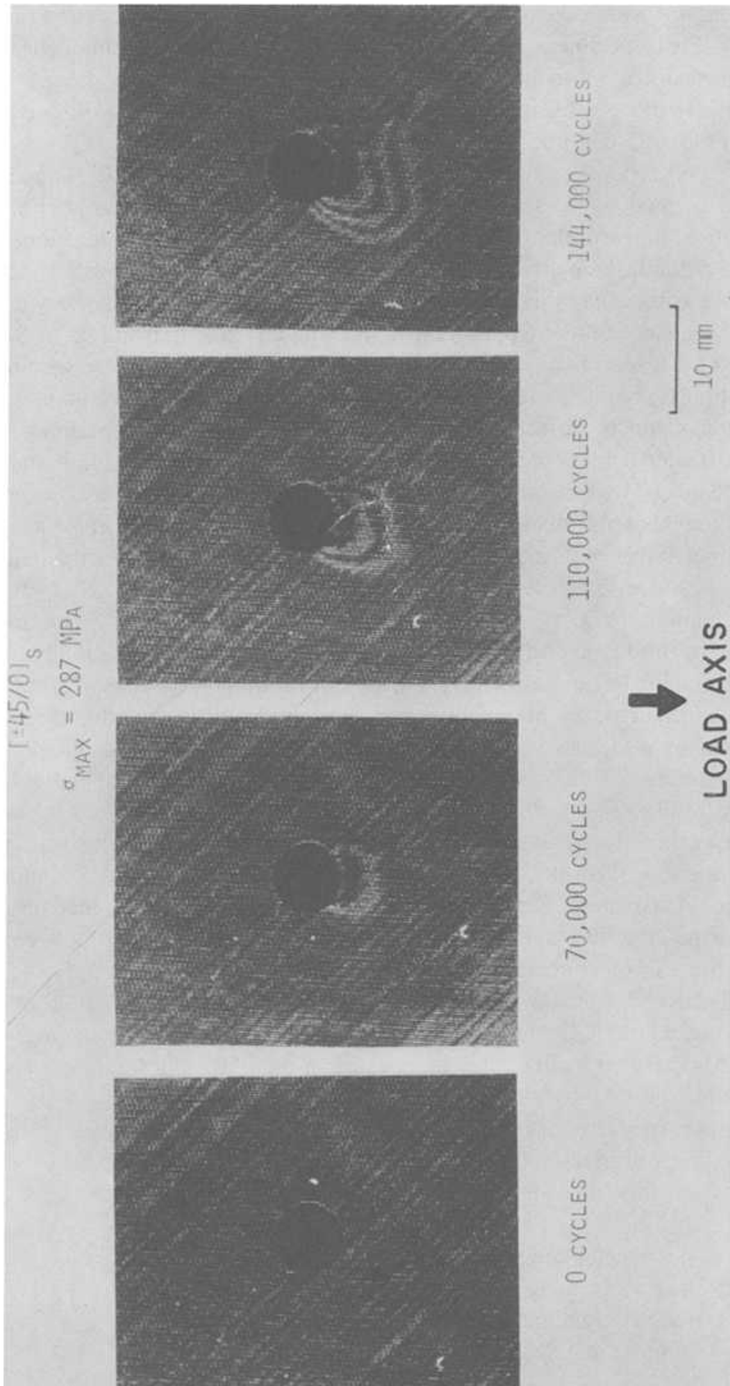

FIG. 5—*Radial delamination growth sequence.*

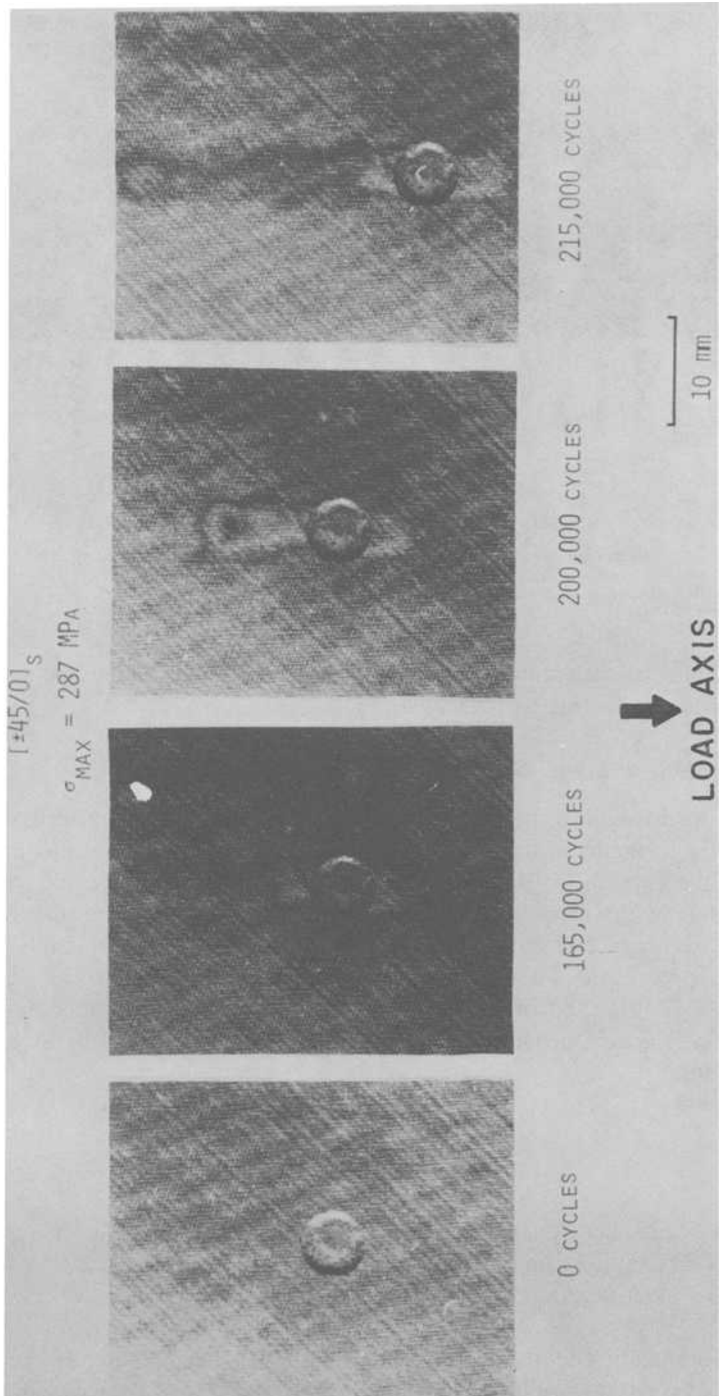

FIG. 6—*Longitudinal delamination growth sequence.*

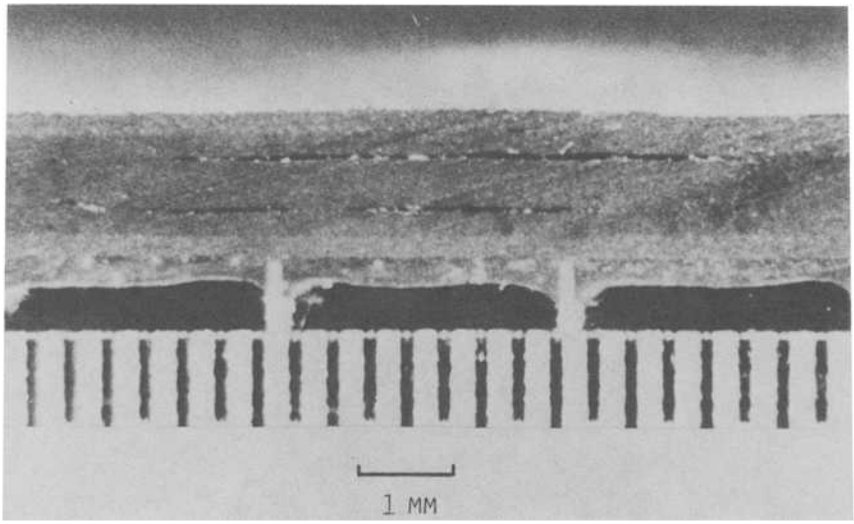

FIG. 7—*Photomicrograph of cross section through longitudinal delamination of* $[\pm 45_2/0_2]_s$ *specimen.*

The number of cycles to initiation is the experimental value of the first inspection interval when damage was detected.

Growth Rate of Longitudinal Delamination

The total length of the longitudinal delamination, $2a$, is characterized by the sum of the lengths of the two branches: one above the hole, a_t, and the other below the hole, a_b, as illustrated in Fig. 2. This length was plotted versus the logarithm of the number of applied load cycles for all the specimens which exhibited this type of damage. It was observed in these cases that this relation was nearly linear as illustrated in the typical experimental plot of Fig. 8.

Daken [*23*] has shown that the growth of splits from a notch in unidirectional composites under tension-tension cyclic load can be correlated by an equation of the form

$$2a = -A + B \log(N) \tag{1}$$

where

N = number of applied load cycles,
$2a$ = total delamination length, and
A, B = constants to be determined.

Daken originally used a natural logarithm correlation, but it seems more consistent to use a base-10 logarithm since it is more convenient to plot the data on a scale based on base-10 logarithms.

TABLE 3—*Cyclic test results for* $[\pm45/0]_s$ *specimens.*

Specimen No.	Face	Peak Compressive Stress, MPa	Damage Type	Cycles To Damage Initiation	Cycles At Test End
1	A	320	TD[a]	3 900	3 900[e]
	B		NDD[b]	. . .	
2	A	320	TD	800	800[e]
	B		NDD	. . .	
3	A	287	RD[c]	15 000	64 400
	B		NDD	. . .	
4	A	287	LD[d]	240 000	305 000
	B		LD	230 000	
5	A	287	NDD	. . .	10 100[e]
	B		TD	10 000	
6	A	287	LD	160 000	290 000
	B		NDD	. . .	
7	A	287	RD	145 000	239 000[e]
	B		NDD	. . .	
8	A	287	NDD	. . .	48 600[e]
	B		TD	48 600	
9	A	287	RD	60 000	144 000
	B		NDD	. . .	
10	A	287	RD	15 000	55 400[e]
	B		NDD	. . .	
11	A	287	LD	42 000	92 600
	B		NDD	. . .	
12	A	287	LD	120 000	161 000
	B		LD	100 000	
13	A	287	NDD	. . .	23 000
	B		RD	10 000	
14	A	287	TD	3 300	3 300[e]
	B		NDD	. . .	
15	A	253	NDD	. . .	400 000
	B		RD	155 000	
16	A	253	NDD	. . .	400 000
	B		RD	165 000	

[a]Transverse damage.
[b]No detectable delamination.
[c]Radial delamination.
[d]Longitudinal delamination.
[e]Test stopped due to failure.

Linear regressions were performed on the longitudinal delamination growth data for each graphite/epoxy face sheet in order to determine the values of the parameters A and B. Having determined the values of A and B, two important parameters can be calculated which characterize the delamination growth rate. These are the number of cycles to initiation, N_0, and the initial growth rate of delamination, $(2 \times da/dN)_0$. These are determined using the relations:

$$N_0 = 10^{A/B} \tag{2}$$

$$2\left(\frac{da}{dn}\right)_0 = 0.4343\,\frac{B}{N_0} \tag{3}$$

TABLE 4—*Cyclic test results for* $[\pm 45_2/0_2]_s$ *specimens.*

Specimen No.	Face	Peak Compressive Stress, MPa	Damage Type	Cycles To Damage Initiation	Cycles At Test End
1[a]	A	287	NDD[b]	...	110 000
	B		NDD	...	
2[a]	A	287	NDD	...	120 000
	B		NDD	...	
3[a]	A	287	NDD	...	83 000
	B		NDD	...	
4[a]	A	287	NDD	...	12 000
	B		LD[c]	[d]	
5[a]	A	287	NDD	...	84 000
	B		LD	[d]	
6	A	287	LD	2 000	9 500
	B		LD	6 000	
7	A	287	LD	1 500	12 000
	B		LD	1 000	
8	A	287	LD	1 500	14 000
	B		LD	3 500	
9	A	265	LD	11 000	48 000
	B		LD	7 000	
10	A	265	LD	7 000	60 000
	B		LD	12 000	
11	A	265	LD	4 000	13 000
	B		LD	1 000	
12	A	265	LD	3 000	20 000
	B		LD	6 000	
13	A	243	LD	10 000	50 000
	B		NDD	...	
14	A	243	LD	30 000	70 000
	B		NDD	...	

[a]Specimen monitored via moiré interferometry; all others monitored with ultrasound.
[b]No detectable delamination.
[c]Longitudinal delamination.
[d]*Unknown, longitudinal delamination found by sectioning coupon.*

TABLE 5—*Cyclic test results for* $[\pm 45_3/0_3]_s$ *specimen.*

Specimen No.	Face	Peak Compressive Stress, MPa	Damage Type	Cycles To Damage Initiation	Cycles At Test End
1	A	265	LD[a]	<500	3 000
	B		LD	<500	
2	A	243	LD	1 000	9 000
	B		LD	1 000	
3	A	221	LD	3 000	59 000
	B		LD	9 000	
4	A	221	LD	6 000	85 000
	B		LD	10 000	
5	A	221	LD	14 000	50 000
	B		LD	6 000	

[a]Longitudinal delamination.

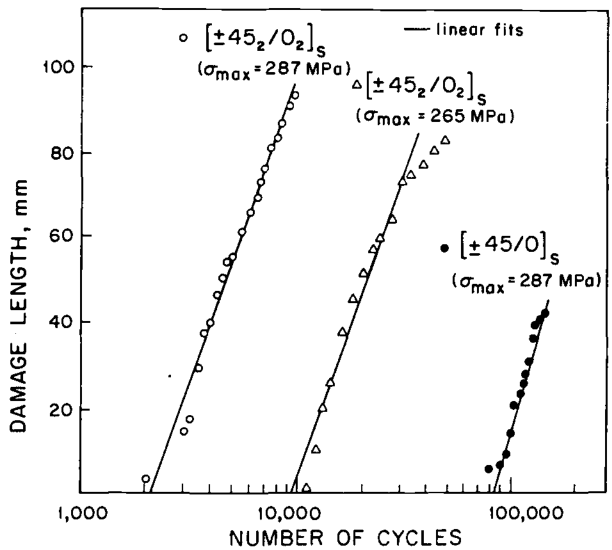

FIG. 8—*Typical plots of longitudinal delamination length versus logarithm of the number of applied load cycles.*

The average results for these calculations are listed in Table 6 for the three laminates tested. These results show that the initiation of this type of damage occurs considerably earlier for increased stress levels. The effective ply thickness has an even more dramatic effect on both the cycles to initiation and initial damage growth rate. A twofold increase in the effective ply thickness causes approximately a 40-fold decrease in the number of cycles to damage initiation. This twofold increase causes a 20-fold increase in the initial delamination growth rate.

The cycling of these specimens was halted before final failure. However, final failure would most likely not occur solely due to this longitudinal delamination

TABLE 6—*Average results of linear regressions on longitudinal delamination growth.*

Laminate	Peak Compressive Stress, MPa	N_0, cycles	CV	$\left(\frac{da}{dn}\right)_0$, mm/cycles
$[\pm 45/0]_s$	287	131 000	61%	5.7×10^{-4}
$[\pm 45_2/0_2]_s$	287	2 900	49%	1.0×10^{-2}
	265	5 300	51%	7.1×10^{-3}
	243	19 500	76%	1.8×10^{-3}
$[\pm 45_3/0_3]_s$	265	[a]		
	243	790	14%	2.4×10^{-2}
	221	8 200	57%	2.9×10^{-3}

[a] Damage grew from end to end of specimen before second inspection cycle.

mode. This damage mode is limited by the length of the test section. Once the delamination approaches the tabs, the effects of load introduction would become important and the results would no longer be valid.

Discussion

The existence of three distinct damage modes in the $[\pm 45/0]_s$ specimens indicates that there is a "competition" among various mechanisms to cause damage at a hole in these laminates. The transverse damage mode generally occurs at high stress levels and is a very rapid growth which causes final failure after relatively few applied load cycles. This may be related to the threshold stress level for cyclic loading reported by Black and Stinchcomb [*24*].

The radial delamination mode is also characterized by rapid growth, though not as rapid as the transverse mode. Once the delamination initiates, this latter mode can grow by a local buckling of the delaminated section. This local buckling can create large peel stresses at the delamination front which can cause further and more rapid growth. It therefore seems plausible that this damage mode may be attributable to tensile interlaminar normal stresses acting at the edge of the delamination front due to the local buckling which causes a Mode I type delamination growth. Wilkins et al [*25*] have shown that a Mode I growth in composites tends to be a very rapid phenomenon and may be treated as a static problem. Although no calculations were performed on the relative contributions of Modes I and II for this case, the experimental results seem to confirm this observation, especially in the fact that the relatively rapid delamination growth resulted in failure at a low number of applied load cycles. In addition, although transverse cracks did occur in the ± 45-deg plies, their location behind the delamination front indicates that they may be a secondary mode.

The third type of damage which occurred in the $[\pm 45/0]_s$ specimens and all of the specimens of the thicker two laminates involves a considerably different damage mechanism. The basic progress of damage appears to be splitting in the 0-deg plies from the point of maximum stress concentration at the edge of the hole and subsequent delamination of the two $-45°/0°$ interfaces betweeen the two longitudinal splits similar to that observed by Rosenfeld and Huang [*16*]. The fact that this damage growth obeys the same growth law as the growth of splits in unidirectional composites implies that the splitting process is the major controlling factor. However, the subsequent delamination plays an important role in this damage development as well.

Previous researchers (for example, Highsmith et al [*26*] and Law [*27*]) have shown that the local interlaminar stress fields around matrix cracks can cause delamination to initiate at the intersection of such cracks with ply interfaces. This does not, however, appear to be the mechanism observed in the case of longitudinal splits emanating from a hole. In the case where the local stress field due to the matrix crack causes delamination to initiate, the delamination is generally symmetric about the matrix crack [*26*]. In the current investigation, the delamination occurs only between the two longitudinal splits in the matrix in the

0-deg plies as shown schematically in Fig. 9. This delamination development is thus not symmetric about the matrix crack and cannot be attributed solely to the local interlaminar stress field at the crack tip.

A simple model can be devised to qualitatively explain this behavior. Once the longitudinal splits develop, load is transferred from the area between the 0-deg plies into the neighboring -45-deg plies by interlaminar shear stresses. The parts of the 0-deg plies which have delaminated can no longer carry any load and the delamination front grows. This model, as in Fig. 9, renders itself to a shear lag analysis to qualitatively determine the interlaminar shear stress in the matrix interlayer between the plies, σ_{xz}, as a function of the distance from the delamination front, x. The analysis results in an expression of the form (the details of this analysis can be found in Ref *22*)

$$\sigma_{xz}(x) = -\sqrt{\alpha}\, \sigma_{[0]}^{\infty}\, t_{[0]}\, e^{-\sqrt{\alpha}\,x} \tag{4}$$

This indicates how the far-field stress in the 0-deg layer, $\sigma_{[0]}^{\infty}$, is transferred into the ±45-deg sublaminates. The parameter is defined by

$$\alpha = \frac{G_m}{t_m}\left\{\frac{S_{[0]}}{t_{[0]}} + \frac{S_{[\pm45]}}{t_{[\pm45]}}\right\} \tag{5}$$

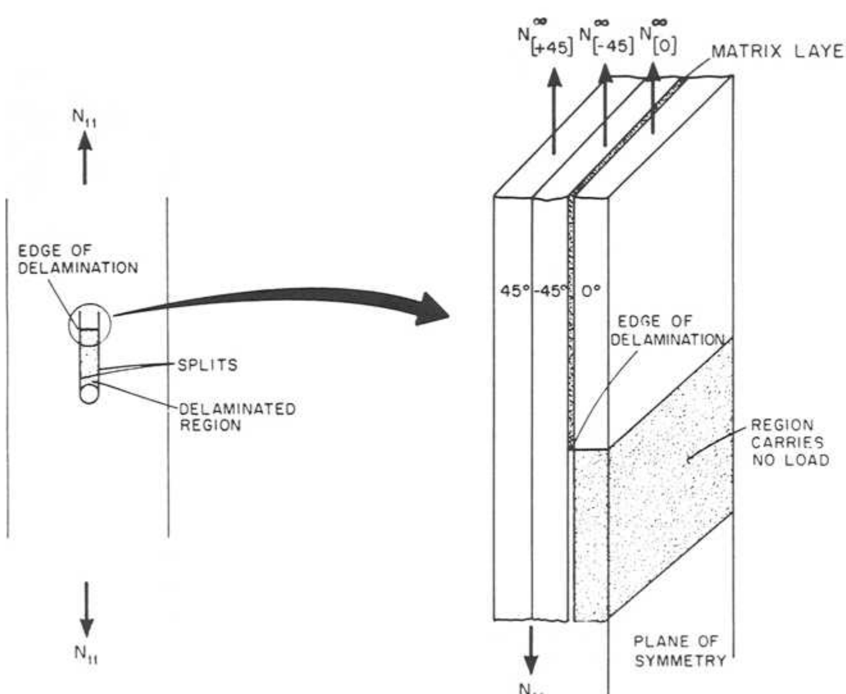

FIG. 9—*Schematic model of the progression of damage via longitudinal delamination.*

and is directly related to the shear modulus of the matrix, G_m, and the thickness of this layer, t_m, as well as the compliance (denoted by S) and thickness (denoted by t) of the 0-deg and ±45-deg sublaminates. This analysis qualitatively shows how the interlaminar shear stress at the delamination front between the axial splits increases with the thickness of the 0-deg layer.

A simple experiment was run to support the proposed mechanism of longitudinal delamination growth after splitting occurs. A $[\pm 45]_s$ laminate and a $[\pm 45_2]_s$ laminate were cured along with two [0] and $[0_2]$ laminates. Five 350-mm by 50-mm coupons were cut from each laminate and 6.35-mm holes drilled in the center of each coupon. A razor blade was used to cut two 50-mm-long 0-deg splits at the hole edge in the cured unidirectional laminates. These unidirectional coupons were then bonded with a room-temperature cure epoxy to the ±45-deg coupons, resulting in specimens of $[0_2//\pm 45_2]_s$ and $[0//\pm 45]_s$ configurations where the double slash, //, represents the room-temperature epoxy bondline. Loading tabs were bonded onto each end of the coupon resulting in the specimen depicted in Fig. 10.

These specimens were tested in static tension with the tests halted at 900 N increments to allow for inspection of the coupon via the ultrasonic technique. During application of load, each specimen exhibited delamination growth at the 0/45 interface between the splits in the 0-deg plies. The delamination initiated at a significantly lower stress level of 88 MPa in the $[0_2/\pm 45_2]_s$ coupons than the stress level of 132 MPa in the $[0/\pm 45]_s$ coupons. These tests clearly dem-

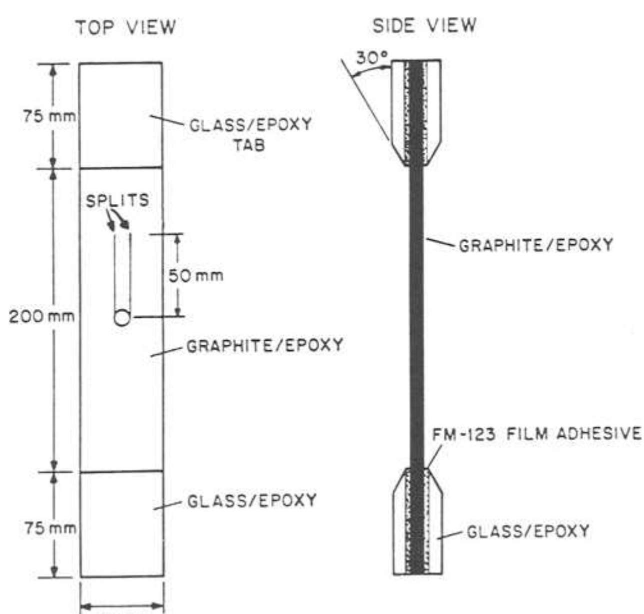

FIG. 10—*Physical characteristics of the special tensile coupon specimen with precut splits.*

onstrate that longitudinal delamination occurs as a result of interlaminar shear failure of the ply interface between the 0-deg ply and the neighboring angled ply in the regions between splits in the 0-deg ply.

Similarly constructed laminates without the premade splits were cycled in tension-tension. Splits originated at the edges of the hole and propagated longitudinally along with subsequent delamination. As the cycling continued, the delaminated 0-deg regions peeled away from the laminate as shown in Fig. 11.

The fact that the same damage occurs under tension indicates that it is not prompted by local buckling or peel stresses but by shear stresses. This suggests that this damage is a Mode II type damage propagation and, as suggested by Wilkins et al [*25*], is generally a slower damage propagation as found herein.

Equations 4 and 5 show that the relative elastic constants of the plies are important in determining the value of the shear stress at the ply interface. The elastic constraint of the neighboring plies is also important in determining when splitting will occur. Flaggs and Kural [*26*] have shown that the "in situ" strength, as determined by transverse cracking, depends upon the thickness of the ply layer. The elastic constraint of the neighboring angled plies induces stresses in the 0-deg plies which may help to restrict splitting. As the 0-deg layer becomes thicker, this constraint effect becomes less important and thus splitting is more likely to occur at lower applied loads. For the $[\pm 45/0]_s$ laminates, the elastic constraint of the neighboring plies may be enough to prevent splitting from occurring in the 0-deg layer and thus the other type of delamination damage eventually occurs. In the other two laminates with larger effective ply thicknesses, the development of splitting alters the stress distribution at the edge of the hole, which apparently prevents the peel stress induced delamination from occurring, thus increasing the life of the specimen.

Residual Strength Tests

Residual strength tests were conducted on the graphite/epoxy face sheets of the sandwich specimens which survived the cyclic loading and were not sectioned for microscopic inspection. The graphite/epoxy face sheets were debonded from the honeycomb by placing the specimens in a preheated oven at 150°C for ten minutes, at which point the face sheets were easily peeled away from the honeycomb. These face sheets then had four glass/epoxy loading tabs bonded onto them via the method previously described to result in the specimen depicted in Fig. 10 (minus the premade splits). A strain gage was installed to measure far-field longitudinal modulus.

A total of 46 such specimens were tested monotonically to failure in tension using the same procedure outlined for the static compression tests. The results are summarized in Table 7. Six $[\pm 45/0]_s$ coupon specimens were also manufactured and tested in static tension without being cycled to obtain the undamaged fracture stress of a coupon with a 6.35-mm hole. This value is 470 MPa.

The results for the $[\pm 45/0]_s$ laminates are delineated by the damage type found

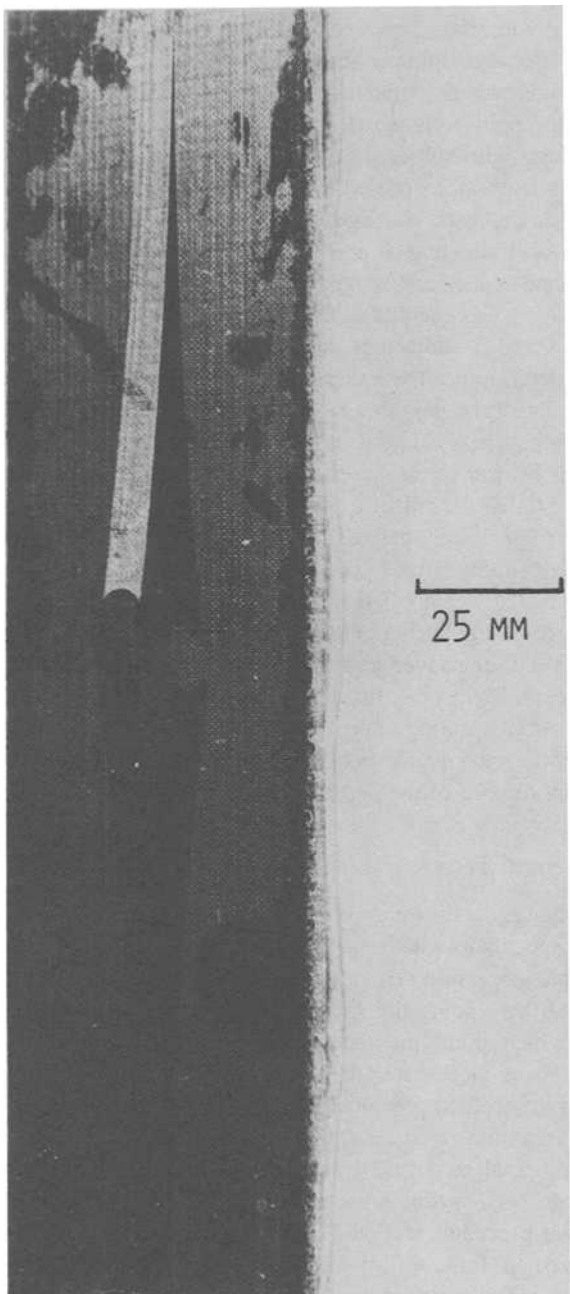

FIG. 11—*Photograph of special tensile coupon specimen after cyclic loading.*

TABLE 7—*Results of residual tensile strength tests.*

Laminate	Damage Type	Number of Specimens	Longitudinal Moduli		Tensile Strength	
			E_L, GPa	CV	σ_F, MPa	CV
$[\pm45/0]_s$	NDD[a]	6	59.3	6.2%	543	3.1%
	RD[b]	4	60.6	5.2%	496	17%
	LD[c]	5	57.0	5.3%	643	8.3%
$[\pm45_2/0_2]_s$	LD	21	54.9	10.3%	674	9.0%
$[\pm45_3/0_3]_s$	LD	10	54.8	9.5%	605	9.8%

[a]No detected damage.
[b]Radial delamination.
[c]Longitudinal delamination.

on that particular face sheet. The specimens with transverse or radial delamination show a slight increase in tensile fracture stress over the uncycled value. However, the specimens with longitudinal delamination have a considerable, on the order of 50%, increase in residual tensile stress. This trend holds true for the $[\pm45_2/0_2]_s$ and $[\pm45_3/0_3]_s$ specimens, which all had longitudinal delamination.

These results indicate that the longitudinal damage causes a stress redistribution around the hole such that the 0-deg plies no longer see the effect of the notch. The small strip of 0-deg ply between the splits which has delaminated also is no longer load-carrying. The residual strength is very near the unnotched strength of a $[\pm45/0]_s$ laminate in tension reported by Lagace [*12*]. Postmortem observation of the failed specimens confirms this hypothesis. A failed specimen pictured in Fig. 12 clearly shows the strip of 0-deg ply above the laminate which did not carry load while the remaining 0-deg fibers fractured across the width of the specimen.

By this longitudinal delamination, the laminate has become nearly notch-insensitive to longitudinal tensile load. It is important to point out, however, that other load types were not investigated: transverse tension, static compression, and shear. It would be dangerous to assume that the residual strength increase for this particular mode of loading would translate to increases in other modes. In fact, the delamination would most likely have a negative impact on several modes, especially transverse compression, where delamination could then propagate in the transverse direction parallel to the applied load.

The longitudinal moduli of these specimens show a very minor decrease on the order of 5%. However, this is more likely the result of the strain gage being affected by the split and delamination rather than a degradation of the material where the strain gage is located. This indicates that the damage is localized to the vicinity of the hole.

Conclusions

The results of this experimental program show that there is an important effect of the effective ply thickness on laminates of the $[\pm45_n/0_n]_s$ configuration. The

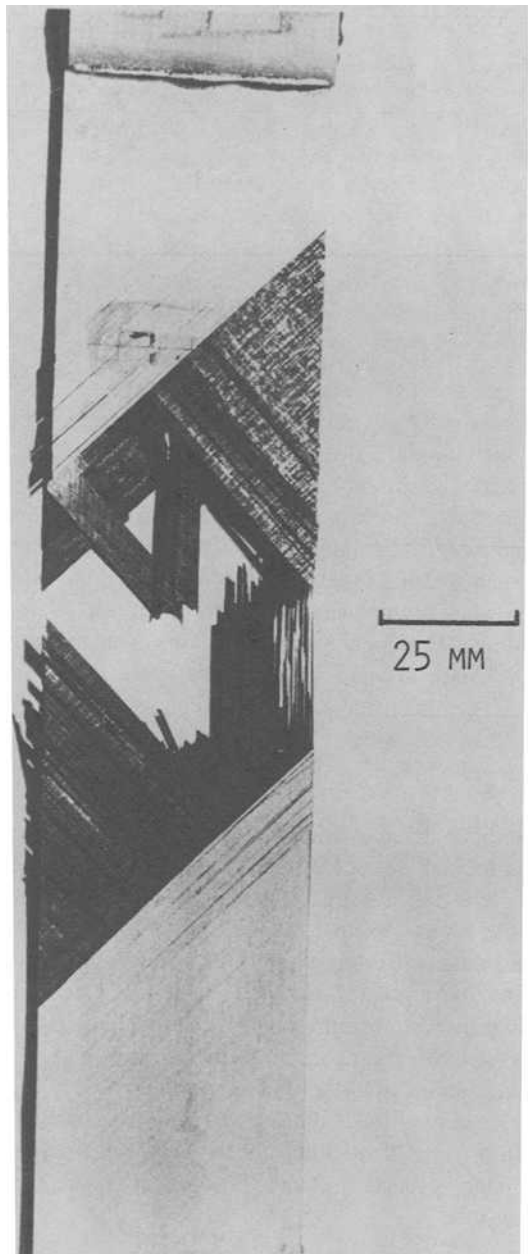

FIG. 12—*Postmortem failure mode of residual tensile strength specimen with longitudinal delamination.*

effective ply thickness does not change the compressive static fracture strength of 424 MPa for these graphite/epoxy specimens with 6.35-mm holes, but changes the mode of damage initiation and growth and the rate of such growth when the specimens are cycled in compression-compression. For the smallest ply thickness, the $[\pm 45/0]_s$ laminates, there is a competition among damage mechanisms to cause initial damage. The first two modes involved initiation and propagation of delamination, resulting in a rapid development of damage. The third type of damage development is more benign and involves the development of splits in the 0-deg plies at the edges of the holes and subsequent delamination of the two $-45/0$ interfaces between these two splits. This damage grows relatively slowly and at a rate which is linear with the logarithm of applied load cycles.

This longitudinal delamination mode occurs for all of the specimens with the thicker effective ply thicknesses, $[\pm 45_2/0_2]_s$ and $[\pm 45_3/0_3]_s$, due to the relaxation of elastic constraint from the neighboring plies. This mode of damage relieves the stress concentration at the edge of the hole and did not result in catastrophic failure in any of the specimens. Additionally, as the "effective ply thickness" is increased, damage initiation occurs earlier in the cycling and accumulates at a faster rate. This indicates the superiority of thin plies in suppressing certain modes of damage, specifically longitudinal splitting.

Residual tension tests conducted on these specimens showed a 50% increase in strength over uncycled specimens of the same configuration. This is again attributed to the relieving of the stress concentration at the hole edge. However, this fact demonstrates that using residual strength tests as an indication of the damage condition and tolerance of a composite part can be somewhat misleading. The longitudinal delamination increases the residual strength for the longitudinal tensile mode of loading but would most likely degrade transverse compression strength since delamination could then run via peel stresses generated by localized buckling. Tests should be run on these specimens with other load conditions to determine the effect of this damage on the residual strength in these other loading conditions.

Acknowledgments

This work was supported by the Air Force Office of Scientific Research under Grant No. AFOSR-82-0071 and Contract No. F49620-83-K-0015. Dr. Anthony K. Amos was the technical monitor.

References

[1] Salkind, M. J. in *Composite Materials: Testing and Design (Second Conference), ASTM STP 497*, American Society for Testing and Materials, Philadelphia, 1972, pp. 143–169.
[2] Hahn, H. T. in *Composite Materials: Testing and Design (Fifth Conference), ASTM STP 674*, American Society for Testing and Materials, Philadelphia, 1979, pp. 383–417.
[3] Talreja, R., *Proceedings of the Royal Society of London*, Series A378, 1981, pp. 461–475.

[4] Konishi, D. Y. and Johnston, W. R. in *Composite Materials: Testing and Design (Fifth Conference), ASTM STP 674,* American Society for Testing and Materials, Philadelphia, 1979, pp. 597–619.
[5] Ratwani, M. M. and Kan, H. P., *Journal of Aircraft,* Vol. 18, 1981, pp. 458–462.
[6] Ramkumar, R. L. in *Damage in Composite Materials, ASTM STP 775,* American Society for Testing and Materials, Philadelphia, 1982, pp. 184–210.
[7] Rodini, B. T., Jr., and Eisenmann, J. R. in *Proceedings,* Fourth Conference on Fibrous Composites, San Diego, CA, 1978, pp. 441–457.
[8] Herakovich, C. T., *Journal of Composite Materials,* Vol. 16, 1982, pp. 216–227.
[9] Kim, R. Y. and Soni, S. R. in *Proceedings,* United States–Japan Joint Conference on Experimental Analysis, Society for Experimental Stress Analysis, Hawaii, 1982, pp. 244–251.
[10] Kim, R. Y. and Soni, S. R., *Journal of Composite Materials,* Vol. 14, 1984, pp. 70–80.
[11] O'Brien, T. K. in *Damage in Composite Materials, ASTM STP 775,* American Society for Testing and Materials, Philadelphia, 1980, pp. 140–167.
[12] Lagace, P. A. in *Composite Materials: Testing and Design (Seventh Conference), ASTM STP 893,* American Society for Testing and Materials, Philadelphia, 1986.
[13] Lucking, W. M., Hoa, S. V., and Sankar, T. S., *Journal of Composite Materials,* Vol. 18, 1984, pp. 188–198.
[14] Kulkarni, S. V., McLaughlin, P. V., Jr., Pipes, R. B., and Rosen, B. W. in *Composite Materials: Testing and Design (Fourth Conference), ASTM STP 617,* American Society for Testing and Materials, Philadelphia, 1977, pp. 70–92.
[15] Ramani, S. V. and Williams, D. P. in *Fatigue of Filamentary Composite Materials, ASTM STP 636,* American Society for Testing and Materials, Philadelphia, 1977, pp. 27–46.
[16] Rosenfeld, S. M. and Huang, S. L., *Journal of Aircraft,* Vol. 15, 1978, pp. 264–268.
[17] Whitcomb, J. D. in *Fatigue of Composite Materials, ASTM STP 723,* American Society for Testing and Materials, Philadelphia, 1981, pp. 48–63.
[18] Mar, J. W., Graves, M. J., and Maass, D. P., *Journal of Aircraft,* Vol. 18, 1981, pp. 744–747.
[19] Fanucci, J. P. and Mar, J. W., *Journal of Composite Materials,* Vol. 16, 1982, pp. 94–102.
[20] Phillips, E. P. in *Fatigue of Fibrous Composite Materials, ASTM STP 723,* American Society for Testing and Materials, Philadelphia, 1981, pp. 197–212.
[21] Shuart, M. J. in *Test Methods and Design Allowables for Fibrous Composites, ASTM STP 734,* American Society for Testing and Materials, Philadelphia, 1979, pp. 152–165.
[22] Nolet, S. C., S. M. thesis, Massachusetts Institute of Technology, Cambridge, MA, Jan. 1984.
[23] Daken, M. H. M. H., S. M. thesis, Massachusetts Institute of Technology, Cambridge, MA, Feb. 1983.
[24] Black, N. F. and Stinchcomb, W. W. in *Long-Term Behavior of Composites, ASTM STP 813,* American Society for Testing and Materials, Philadelphia, 1983, pp. 95–115.
[25] Wilkins, D. J., Eisenmann, J. R., Camin, R. A., Margolis, W. S., and Benson, R. A. in *Damage in Composite Materials, ASTM STP 775,* American Society for Testing and Materials, Philadelphia, 1980, pp. 168–183.
[26] Highsmith, A. L., Stinchcomb, W. W., and Reifsnider, K. L. in *Effects of Defects in Composite Materials, ASTM STP 836,* American Society for Testing and Materials, Philadelphia, 1984, pp. 194–216.
[27] Law, G. E. in *Effects of Defects in Composite Materials, ASTM STP 836,* American Society for Testing and Materials, Philadelphia, 1984, pp. 143–160.
[28] Flaggs, D. L. and Kural, M. H., *Journal of Composite Materials,* Vol. 16, 1982, pp. 103–115.

Leif Carlsson,[1] *Curt Eidefeldt,*[2] *and Tommy Mohlin*[3]

Influence of Sublaminate Cracks on the Tension Fatigue Behavior of a Graphite/Epoxy Laminate

REFERENCE: Carlsson, L., Eidefeldt, C., and Mohlin, T., "**Influence of Sublaminate Cracks on the Tension Fatigue Behavior of a Graphite/Epoxy Laminate,**" *Composite Materials: Fatigue and Fracture, ASTM STP 907,* H. T. Hahn, Ed., American Society for Testing and Materials, Philadelphia, 1986, pp. 361–382.

ABSTRACT: Quasi-isotropic 32-ply graphite/epoxy specimens were tested in static tension and tension fatigue. Both dry specimens and specimens containing 1% moisture (by weight) were tested. The first type of damage observed under both static and cyclic loading was transverse matrix cracking in the 90-deg plies. Under continued static or cyclic loading the cracks propagated into the neighboring −45-deg plies. No delamination was observed under static loading. In fatigue the matrix cracks acted as initiators of delamination, which resulted in a marked reduction in stiffness and residual strength. For specimens which had been subjected to a tensile overload before fatigue cycling, delamination occurred earlier due to the formation of more transverse matrix cracks.

The major effect of moisture was to increase the stress level at which first-ply failure occurred and to delay damage development during fatigue at low stress levels. The leveling-off of the crack density at an approximately constant level during fatigue loading gives support to damage models which predict the occurrence of a characteristic damage state, independent of load history, before laminate failure.

KEY WORDS: composite materials, epoxy resin, fatigue (mechanics), fiber-reinforced composites, test methods

Composite materials and structures contain weak fracture paths parallel to the fibers. In multidirectional laminates matrix cracks are observed at load levels far below the ultimate failure load. In some cases these cracks may be beneficial in the sense that they may reduce stress concentrations around notches [*1*], but generally these cracks are detrimental since they provide initiation sites for delamination [*2*].

In fatigue, data for a unidirectional glass/epoxy composite [*3*] indicate a limiting tensile strain for matrix cracking as low as 0.1% in the 90-deg direction

[1] Section head, Materials, The Aeronautical Research Institute of Sweden (FFA), Bromma, Sweden. Present address: Center for Composite Materials, University of Delaware, Newark, DE 19716.

[2] The Defence Material Administration, Stockholm, Sweden.

[3] The Aeronautical Research Institute of Sweden (FFA), Bromma, Sweden. Present address: Du Pont de Nemours Nordiska AB, P.O. Box 501, Märsta, Sweden.

[4]. For a graphite/epoxy laminate, Harrison and Bader [5] found that the transverse matrix cracking strain under both static and fatigue loading is a strong function of the thickness of the 90-deg ply (or the number of adjacent 90-deg plies). The transverse matrix cracking strain was found to be lower in fatigue than under static loading.

This paper considers the interaction between sublaminate cracking and the fatigue properties of dry graphite/epoxy specimens and of graphite/epoxy specimens containing 1% moisture by weight. The axial stiffness change and the residual tensile strength is measured and related to the progression of matrix cracking studied by low-magnification light microscopy.

Experimental

Materials and Specimen Preparation

The laminate used in this study was made from Fiberite T300/1034E graphite/epoxy unidirectional prepeg that was vacuum-bagged and cured in an autoclave according to the manufacturer's recommendations.

Specimens used in the mechanical testing were unnotched quasi-isotropic 32-ply laminates with a $([0/\pm45/90]_s)_4$ layup, (E_x = 54 GPa). The specimens had a test section length of 30 mm and a width of 24 mm. End tabs were used to ensure a uniform distribution of load and to avoid damage to the outer layers in the gripping area.

Moisture Sorption

After curing and specimen fabrication, approximately half of specimens (about 30) were placed in an environmental chamber in which the temperature and the relative humidity (RH) were kept at 70°C and 95% RH, respectively. The specimens were kept in the environmental chamber until the weight gain reached 1%. The moisture distribution corresponding to this weight gain was calculated from the theory presented by Springer [6] and is presented in Fig. 1*a*. In order to obtain a more uniform moisture profile before the mechanical testing, the specimens were placed in a sealed plastic bag for about six months. The calculated [6] moisture profile is shown in Fig. 1*b*.

The remaining dry specimens were stored in laboratory air for about six months before testing. A check of the moisture content of the "dry" specimens revealed a weight gain of about 0.23%.

Static and Fatigue Testing, Nondestructive Examination

Static testing was performed in a 100-kN Amsler hydraulic testing machine with low mechanical noise to permit acoustic emission (AE) monitoring with a test setup described in Ref 7. The fatigue tests were performed in a 100-kN MTS servohydraulic testing machine operated under load control with a frequency of

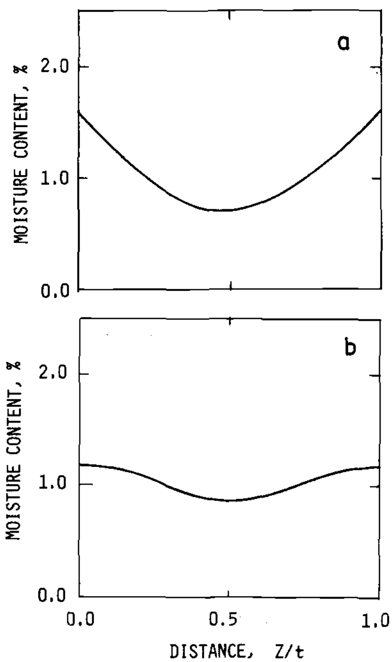

FIG. 1—*Moisture distribution inside the specimen:* (a) *after conditioning at 95% RH, 70°C, average moisture content ~1%;* (b) *after storage in a sealed plastic bag at 25°C for about six months, average moisture content ~1%.*

10 Hz. All cyclic tests were performed in pure tension at different constant-stress amplitudes with $R = 0$ ($R = \sigma_{min}/\sigma_{max}$).

The fatigue test programs for the dry and wet specimens are presented in Tables 1 and 2, respectively. It should be noted that the first-ply-failure stress, σ_{FPF}, differs for dry and wet specimens and since the same maximum cyclic stress, σ_{max}, was used for both the dry and wet specimens the ratios $\sigma_{max}/\sigma_{FPF}$ given in Tables 1 and 2 differ.

The axial stiffness was measured using a clip-gage technique reported in Ref *8*. Changes in axial stiffness were compared with the development of damage based on observations of the edges of the specimens. Earlier studies, for example, Ref *5*, indicate that damage in the form of matrix cracking and delamination initiate at the edges of a specimen. To nondestructively determine the extent of damage in the form of matrix cracking and delamination, one of the longitudinal edges of the specimens was polished and the test section was examined with a light microscope. The number of matrix cracks per centimeter counted along the free edge of the test section is here denoted "crack density" [*9*]. Since the layup, $([0/\pm45/90]_s)_4$, consists of four identical quasi-isotropic eight-ply sublaminates, the determination of the crack density becomes more accurate. Some specimens

TABLE 1—*Fatigue test program for dry specimens:* σ_{PRE} = *pre-stress;* σ_{FPF} = *first-ply-failure stress;* σ_{MAX} = *cyclic stress amplitude.* ρ *indicates measurement of crack density,* S *indicates measurement of stiffness,* R *indicates residual tensile strength determination, and an asterisk (*) indicates failure during fatigue loading.*

Specimen No.	σ_{PRE}, MPa	σ_{MAX}, MPa	$\frac{\sigma_{PRE}}{\sigma_{FPF}}$	$\frac{\sigma_{MAX}}{\sigma_{FPF}}$	No. of Load Cycles 10^0	10^2	10^4	10^5	10^6
1	0	225	0	0.87	ρ,*S*	ρ,*S*	ρ,*S*	ρ,*S*	ρ,*S*,*R*
2	0	225	0	0.87	ρ,*S*	ρ,*S*	ρ,*S*	. . .	ρ,*S*,*R*
3	0	225	0	0.87	ρ,*S*	ρ,*S*,*R*	. . .	. . .	. . .
4	0	225	0	0.87	ρ,*S*	ρ,*S*,*R*	. . .	. . .	. . .
5	0	225	0	0.87	ρ,*S*	ρ,*S*	ρ,*S*,*R*	. . .	. . .
6	0	225	0	0.87	ρ,*S*	ρ,*S*	ρ,*S*,*R*	. . .	. . .
7	440	225	1.69	0.87	ρ,*S*	ρ,*S*	ρ,*S*	. . .	ρ,*S*,*R*
8	440	225	1.69	0.87	ρ,*S*	ρ,*S*	ρ,*S*	. . .	ρ,*S*,*R*
9	0	287	0	1.10	ρ,*S*	ρ,*S*	ρ,*S*	. . .	ρ,*S*,*R*
10	0	287	0	1.10	ρ,*S*	ρ,*S*	ρ,*S*	. . .	ρ,*S*,*R*
11	0	318	0	1.22	ρ,*S*	ρ,*S*	ρ,*S*	ρ,*S*	ρ,*S*,*R*
12	0	318	0	1.22	ρ,*S*	ρ,*S*	ρ,*S*	ρ,*S*	ρ,*S*,*R*
13	0	348	0	1.34	ρ,*S*	ρ,*S*	ρ,*S*	ρ,*S*	ρ,*S*,*R*
14	0	348	0	1.34	ρ,*S*	ρ,*S*	ρ,*S*	ρ,*S*	ρ,*S*,*R*
15	0	348	0	1.34	ρ,*S*	ρ,*S*,*R*	. . .	. . .	. . .
16	0	348	0	1.34	ρ,*S*	ρ,*S*,*R*	. . .	. . .	. . .
17	0	348	0	1.34	ρ,*S*	ρ,*S*	ρ,*S*,*R*	. . .	. . .
18	0	348	0	1.34	ρ,*S*	ρ,*S*	ρ,*S*,*R*	. . .	. . .
19	0	400	0	1.54	ρ,*S*	ρ,*S*	ρ,*S**	. . .	. . .
20	0	400	0	1.54	ρ,*S*	ρ,*S*	ρ,*S**	. . .	. . .

TABLE 2—*Fatigue test program for wet specimens. Symbols are the same as in Table 1.*

Specimen No.	σ_{PRE}, MPa	σ_{MAX}, MPa	$\frac{\sigma_{PRE}}{\sigma_{FPF}}$	$\frac{\sigma_{MAX}}{\sigma_{FPF}}$	No. of Load Cycles 10^0	10^2	10^4	10^5	10^6
21	0	225	0	0.61	ρ,*S*	ρ,*S*	ρ,*S*	ρ,*S*	ρ,*S*,*R*
22	0	225	0	0.61	ρ,*S*	ρ,*S*	ρ,*S*	ρ,*S*	ρ,*S*,*R*
23	0	225	0	0.61	ρ,*S*	ρ,*S*,*R*	...	...	...
24	0	225	0	0.61	ρ,*S*	ρ,*S*,*R*	...	...	...
25	0	225	0	0.61	ρ,*S*	ρ,*S*	ρ,*S*,*R*	...	...
26	0	225	0	0.61	ρ,*S*	ρ,*S*	ρ,*S*,*R*	...	...
27	440	225	1.19	0.61	ρ,*S*	ρ,*S*	ρ,*S*	ρ,*S*	ρ,*S*,*R*
28	440	225	1.19	0.61	ρ,*S*	ρ,*S*	ρ,*S*	ρ,*S*	ρ,*S*,*R*
29	0	287	0	0.78	ρ,*S*	ρ,*S*	ρ,*S*	ρ,*S*	ρ,*S*,*R*
30	0	287	0	0.78	ρ,*S*	ρ,*S*	ρ,*S*	ρ,*S*	ρ,*S*,*R*
31	0	318	0	0.86	ρ,*S*	ρ,*S*	ρ,*S*	ρ,*S*	ρ,*S*,*R*
32	0	318	0	0.86	ρ,*S*	ρ,*S*	ρ,*S*	ρ,*S*	ρ,*S*,*R*
33	0	348	0	0.94	ρ,*S*	ρ,*S*	ρ,*S*	ρ,*S*	ρ,*S*,*R*
34	0	348	0	0.94	ρ,*S*	ρ,*S*	ρ,*S*	ρ,*S*	ρ,*S*,*R*
35	0	348	0	0.94	ρ,*S*	ρ,*S*,*R*	...	...	...
36	0	348	0	0.94	ρ,*S*	ρ,*S*,*R*	...	...	...
37	0	348	0	0.94	ρ,*S*	ρ,*S*	ρ,*S*,*R*	...	...
38	0	348	0	0.94	ρ,*S*	ρ,*S*	ρ,*S*,*R*	...	...
39	0	400	0	1.08	ρ,*S*	ρ,*S*	ρ,*S**	...	...
40	0	400	0	1.08	ρ,*S*	ρ,*S*	ρ,*S**	...	...

were also studied with the tetrabromoethane (TBE)-enhanced X-ray technique described in Ref *8*.

A short test section length, 30 mm, was decided upon since initially it had been planned to include in the study the effects of compression fatigue loading on damage initiation and growth. However, instability-related problems in compression clearly indicated that an unsupported specimen was not suitable, and thus only tension loading is considered in this study. Due to the short test section length, the results may be suspected as being influenced by the constraint due to the grips. However, as soon as damage in the form of transverse matrix cracking initiates, a redistribution of the stresses within the laminate will occur. As a consequence, the influence of external boundary conditions (clamping) on further damage development is expected to diminish. Experimental observations of the damage along the test section did not show any significant dependency on the location along the test section, or position in the thickness direction for plies with the same fiber orientation. Furthermore, a comparison with a previous study on a similar layup and material [*10*] gave similar results with regard to the damage state reached late in the fatigue life in the 90-deg and the neighboring −45-deg plies. Clamping is thus not considered to have a major influence on the test results reported here.

The dry specimens were tested in ambient laboratory air while the wet specimens were tested in a humid environment at room temperature using a specially developed moisture generator described in Ref *11*. In this way the moisture content was kept approximately constant at 1% during testing.

Results

Static Test Results

The stress at first-ply failure (FPF) was determined both by acoustic emission and by monitoring matrix cracks by light microscopy. Figure 2 shows a typical recording of axial strain and weighted cumulative AE as a function of axial stress. The strain shows an almost linear dependency on the applied stress up to final fracture for this fiber-dominated layup. On the other hand, the AE signal indicates that damage initiation starts at a stress level of approximately 270 MPa (±10%). Microscopic examination of the polished edges of the specimens and X-ray studies revealed that the major damage was matrix cracks across the width of the specimen in the 90-deg and −45-deg plies; see Fig. 3. Very few cracks were observed in the +45-deg plies. At no load level up to final fracture was there any indication of delamination except for a small amount of delamination at the 90/−45 interfaces bridging the cracks in the 90-deg and −45-deg plies.

Figure 4 shows the crack density, that is, the number of matrix cracks per centimeter, as a function of stress for the dry specimens. The points in the graph are average values of the measurements after the first cycle in the fatigue test program shown in Table 1 and some additional measurements on specimens subjected to stress levels close to the fracture stress. The measurements are

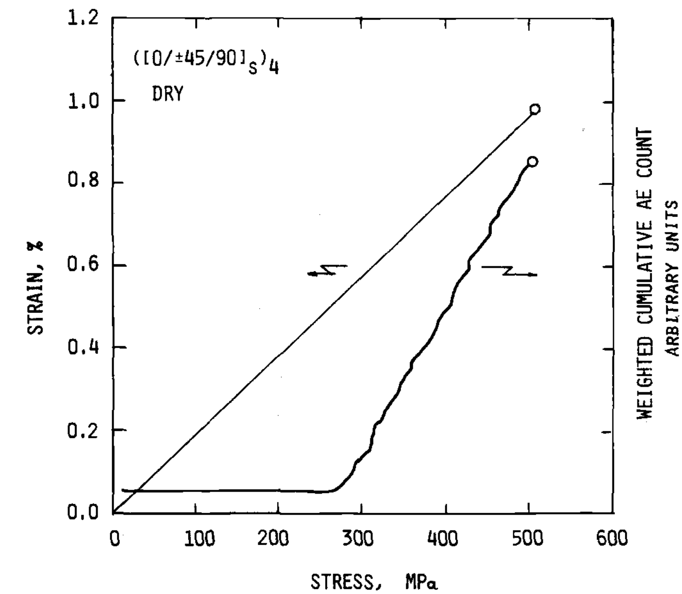

FIG. 2—*Axial strain and weighted cumulative AE count for a dry* ([0/±45/90]$_s$)$_4$ *laminate versus axial stress.*

consequently based on two to six specimens. The number of cracks in the 90-deg plies increased continuously with stress level from the occurrence of FPF at about 250 MPa. These cracks were initially arrested at the adjacent −45-deg plies (see Fig. 3*a*) until matrix cracks were initiated in the −45-deg plies close to the tips of the 90-deg cracks at about 350 MPa; see Fig. 3*b*. The number of 90-deg and −45-deg cracks increased continuously up to final fracture. Close to final fracture, approximately all 90-deg cracks had propagated into the neighboring −45-deg plies, resulting in about the same final crack densities in these plies. There was no leveling-off in the crack density as the applied load increased. It is therefore not possible here to define the saturation crack density or the "characteristic damage state" introduced by Reifsnider [*12*].

A typical AE recording for the wet laminate is shown in Fig. 5. The AE signal indicates that damage initiation starts at about 370 MPa (±10%), which is significantly higher than in the dry laminate, Fig. 2. As in the case of the dry laminate, microscopic examination of the polished edges of the specimens revealed that the major damage was matrix cracks in the 90-deg and −45-deg plies.

Figure 6 shows the development of matrix cracks in the 90-deg and the −45-deg plies during static loading. A comparison with the result for the dry laminate in Fig. 4 shows that the matrix cracks in the 90-deg plies are initiated at a higher stress in the wet laminate. Furthermore, the cracks in the −45-deg plies start at

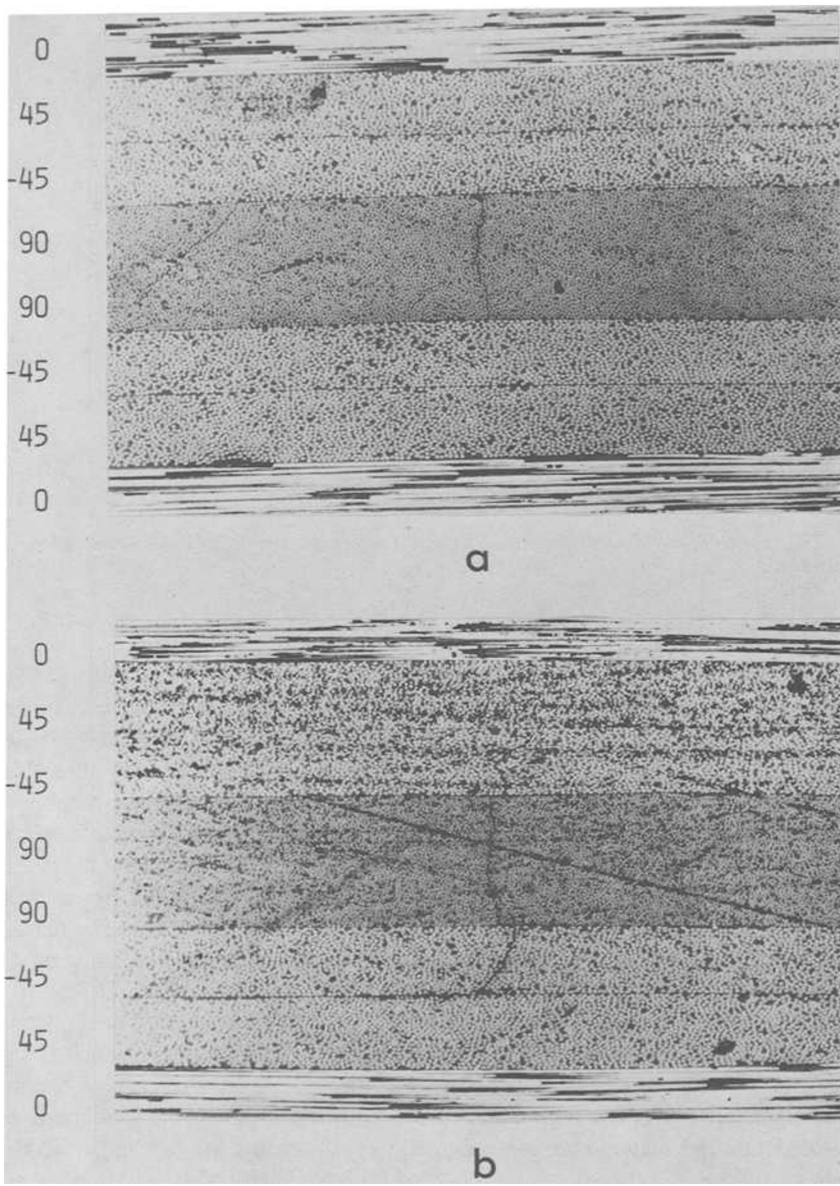

FIG. 3—*Matrix cracks in a portion of the dry laminate:* (a) *matrix crack in the 90-deg ply;* (b) *matrix cracks in the 90-deg and −45-deg plies.*

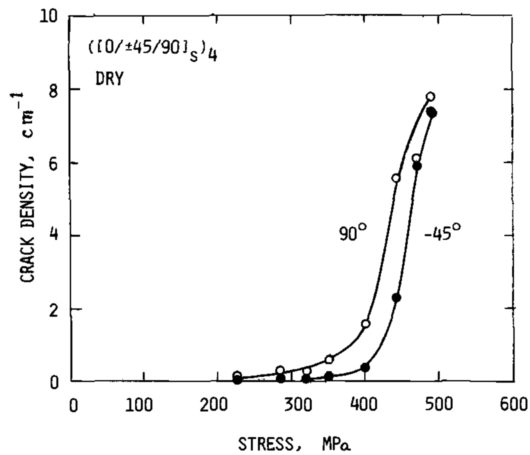

FIG. 4—*Crack density as a function of applied stress in a dry laminate.*

about the same stress level as the 90-deg cracks. No leveling-off in crack density was observed for the wet laminate. Consequently no "characteristic damage state" can be defined for the wet laminate subjected to static tensile loading.

Analysis of FPF

The constitutive relation for a ply in the laminate (temperature effects neglected) [13] is

$$\sigma_i = Q'_{ij}\,(\epsilon'_j - e'_j) \qquad (i,j = 1,2,6) \qquad (1)$$

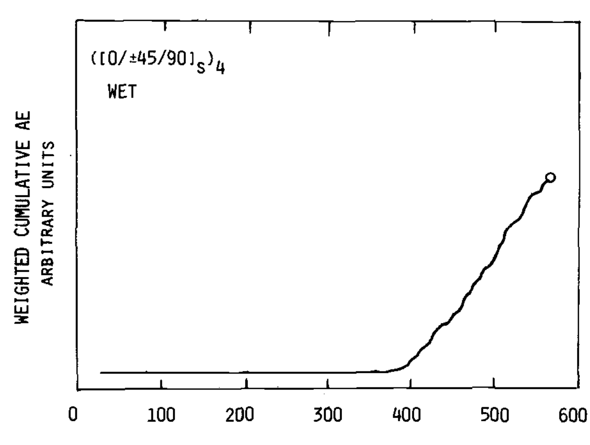

FIG. 5—*Weighted cumulative AE count for a wet laminate versus axial stress.*

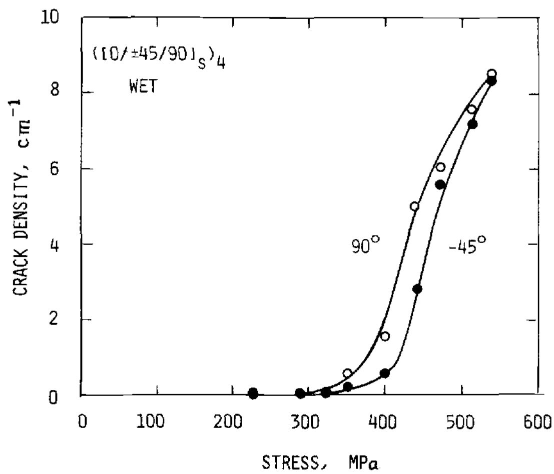

FIG. 6—*Crack density versus applied stress in a wet laminate.*

where

ϵ'_i = in-plane engineering strains (ϵ'_1 and ϵ'_2 are the strains in the longitudinal and transverse direction while ϵ'_6 is the in-plane shear strain),
Q'_{ij} = plane stress reduced stiffness matrix,
e'_j = expansional strains due to moisture absorption, and
σ'_i = in-plane stress components defined in a manner analogous to the strains.

The primed symbols refer to a nonprincipal coordinate system.

For a 90-deg ply in the laminate, Eq 1 leads to

$$\sigma_2 = Q_{12} (\epsilon_y{}^\circ - e_1) + Q_{22} (\epsilon_x{}^\circ - e_2) \tag{2}$$

in which $\epsilon_x{}^\circ$ and $\epsilon_y{}^\circ$ are the laminate strains in the longitudinal and transverse directions, respectively, and

$$\begin{aligned} e_1 &= \beta_1 M \\ e_2 &= \beta_2 M \end{aligned} \tag{3}$$

where β_1 and β_2 are the coefficients of hygroexpansion (in the fiber coordinate system) and M is the moisture content. Note that for the 90-deg ply the x- and 2-directions coincide.

The maximum stress criterion [*14*] may be used to predict first-ply failure in the 90-deg plies. Equations 2 and 3 with $\beta_1 \simeq 0$ give

$$Q_{12}\epsilon_y{}^\circ + Q_{22}\epsilon_x{}^\circ - Q_{22}\beta_2 M = \sigma_{2,\mathrm{Ult}} \tag{4}$$

Lamination theory [*14*] is used to obtain the laminate strains as a function of external load and moisture content. It leads to the following expression for the first-ply-failure stress:

$$\sigma_{FPF} = \frac{F_2(A_{12} - \nu_{12}A_{11}) + (A_{11}{}^2 - A_{12}{}^2)\,[\beta_2 M + \sigma_{2,\mathrm{Ult}}\,(1 - \nu_{12}\nu_{21})/E_{22}]}{(A_{11} - \nu_{12}A_{12})t} - \frac{F_1}{t} \tag{5}$$

where

A_{ij} $(i,j = 1,2)$ = laminate stiffness elements,
ν_{12},ν_{21} = Poisson's ratios of a ply,
E_{22} = transverse modulus of elasticity of a ply,
t = laminate thickness, and
F_1,F_2 = effective hygroscopic forces in the longitudinal and transverse directions of the laminate, respectively; see Ref *15*.

Experimental data analyzed in Ref *16* show that there is no measurable swelling until a threshold moisture content, M_t, is reached. For moisture contents, M, larger than M_t, M in Eqs 3–5 is thus replaced by $M - M_t$.

Properties measured on a unidirectional eight-ply laminate that was stored in the ambient laboratory environment are presented in Table 3. Using these properties in Eq 5, first-ply failure in the dry laminate is predicted to occur at 260 MPa. The good agreement with the experimental values 250 to 270 MPa in Figs. 2 and 4, despite the fact that thermal strains were neglected, indicates that stress relaxation combined with uptake of moisture during storage in laboratory air counter-balances the thermal stresses set up during cooling after the curing at an elevated temperature.

For the wet laminate, Ref *16* indicates the following reduction in the mechanical properties in Table 3 due to 1% moisture uptake:

$$\Delta E_{11} = 0,\quad \Delta E_{22} = -9\%,\quad \Delta\nu_{12} = 0,\quad \Delta G_{12} = -19\%,\quad \Delta\sigma_{2,\mathrm{Ult}} = -27\%$$

Using the wet mechanical properties and assuming the same moisture threshold $M_t = 0.4\%$ as in Ref *16*, Eq 5 predicts FPF to occur at 385 MPa, which is in relatively good agreement with the experimentally determined values.

Fatigue Test Results

The initial damage observed during fatigue loading took the form of matrix cracks in the 90-deg plies. These cracks are arrested initially at the adjacent −45-deg interfaces. After a larger number of load cycles more 90-deg cracks

TABLE 3—*Mechanical properties of a* $[0]_8$ *laminate.*

E_{11}, GPa	E_{22}, GPa	ν_{12}	G_{12}, GPa	β_2[a]	$\sigma_{2,Ult}$, MPa
143	11	0.35	4	0.0056	46.6

[a]From Ref *16*.

form and cracks are initiated in the adjacent −45-deg plies at the point of intersection of the transverse cracks and the 90/−45 interface.

A different feature in the development of damage in fatigue loading compared with static loading was the presence of delaminations in the later stages of fatigue loading. The first indication of delamination was observed at the 90/−45 interfaces where a small area of delamination bridged the transverse cracks in the 90-deg plies and the cracks in the −45-deg plies. Upon further cycling, a longer delamination crack formed at the +45/−45 interfaces between two −45-deg cracks. For large stress amplitudes, delamination also started between the 90-deg and −45-deg plies; see Fig. 7. Another feature that did not occur in static loading was the presence of a few cracks in the +45-deg plies close to the end of fatigue life. The number of these cracks was not counted since their location and occurrence were very scattered.

Figures 8 through 10 show the damage development in the dry specimens loaded in fatigue according to Table 1. Crack density, relative axial stiffness (stiffness at N load cycles/initial stiffness) and relative residual strength, defined in a manner analogous to relative stiffness, are reported as functions of the number

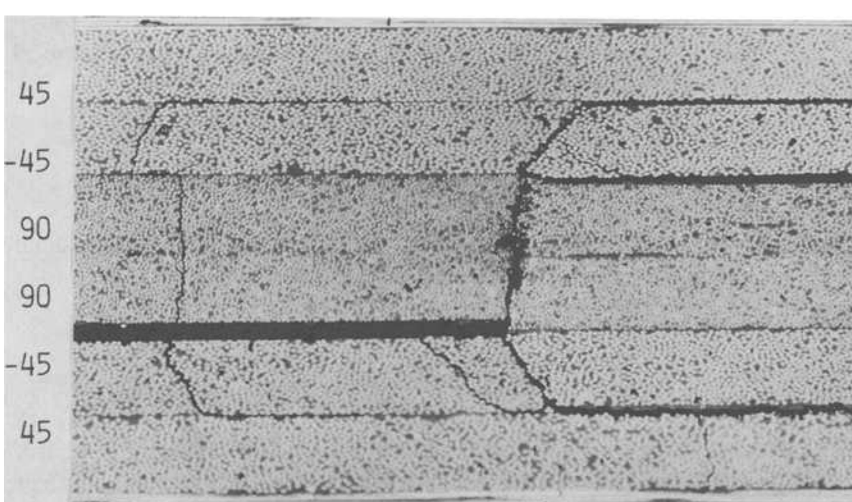

FIG. 7—*Damage in a fatigue-loaded dry laminate.*

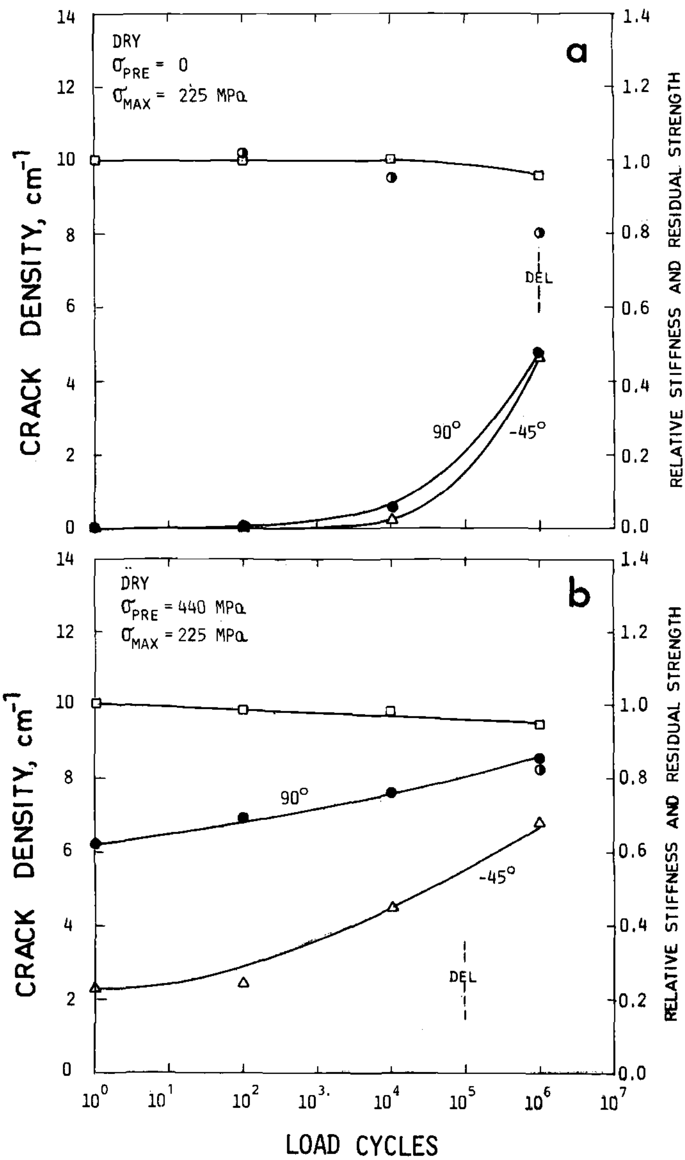

FIG. 8—*Crack density, relative stiffness, and relative residual strength during tension fatigue of dry laminates.* □ = *relative stiffness;* ◑ = *relative residual strength.* (a) σ_{PRE} = 0; σ_{MAX} = *225 MPa.* (b) σ_{PRE} = *440 MPa;* σ_{MAX} = *225 MPa.*

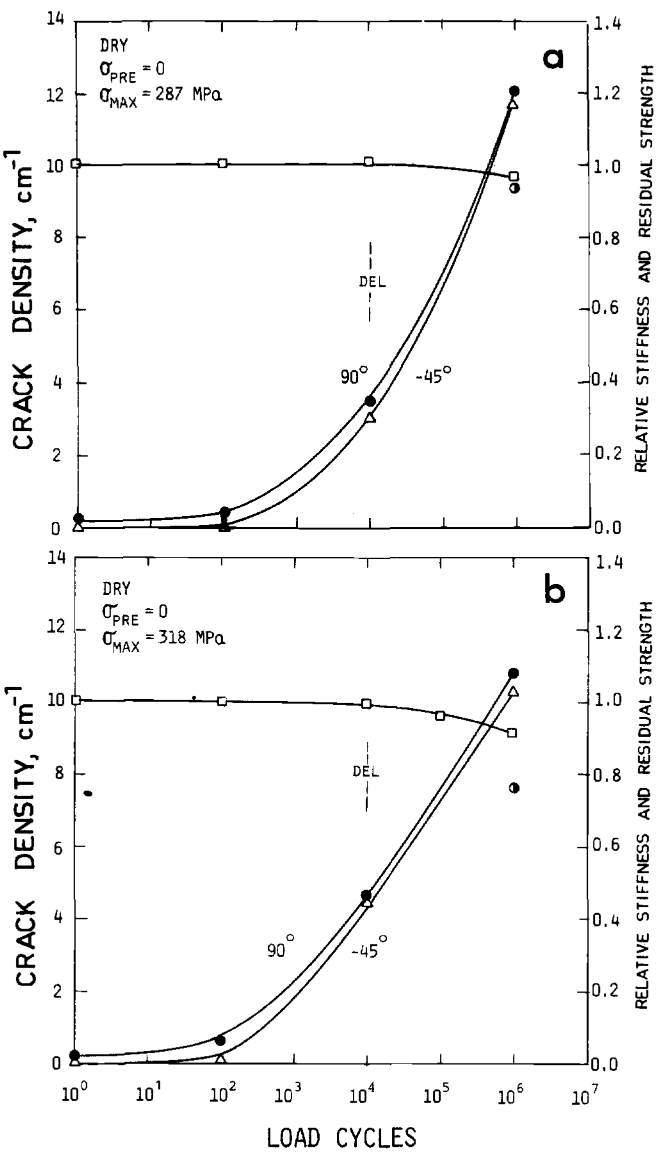

FIG. 9—*Crack density, relative stiffness, and relative residual strength during tension fatigue of dry laminates.* □ = *relative stiffness,* ◑ = *relative residual strength.* (a) $\sigma_{PRE} = 0$; $\sigma_{MAX} = 287$ *MPa.* (b) $\sigma_{PRE} = 0$; $\sigma_{MAX} = 318$ *MPa.*

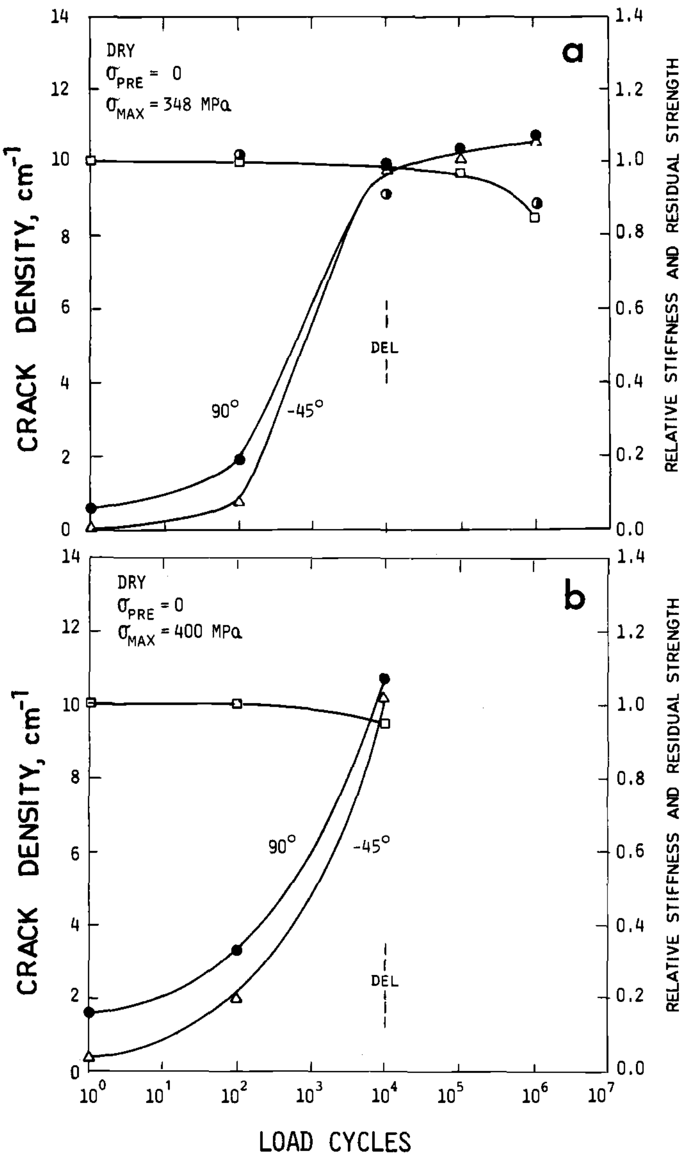

FIG. 10—*Crack density, relative stiffness, and relative residual strength during tension fatigue of dry laminates.* □ = *relative stiffness,* ◑ = *relative residual strength.* (a) σ_{PRE} = 0; σ_{MAX} = *348 MPa.* (b) σ_{PRE} = 0; σ_{MAX} = *400 MPa.*

of load cycles. The approximate number of load cycles for initiation of edge delamination is indicated with a vertical dotted line in each graph.

At a low stress amplitude and no prestress, Fig. 8*a*, matrix cracks begin in the 90-deg plies. Upon further cycling, the 90-deg cracks propagate into the adjacent -45-deg plies, leading to about the same crack density in the 90- and -45-deg plies. Close to 10^6 load cycles a small amount of delamination was observed at the $90/-45$ and $+45/-45$ interfaces at the tips of the matrix cracks. This delamination is apparently responsible for the observed reduction in stiffness and residual strength.

A high prestress leads to initial matrix cracks in the 90- and -45-deg plies before fatigue cycling, Fig. 8*b*. These cracks apparently act as initiators of delamination, so that this mode of damage was observed earlier in this case.

With increasing stress amplitudes, Figs. 9 and 10, the curves of crack density shift to a lower number of cycles, which shows that damage develops more rapidly. In Fig. 10*a* a plateau in crack density is reached after about 10^4 cycles. The leveling-off crack density is approximately 11 cm^{-1}. The specimens subjected to a very high stress amplitude, Fig. 10*b*, showed extensive damage development and failed between 10^4 and 10^5 load cycles. In all cases the maximum crack density is about 10 to 12 cracks/cm in both the 90-deg plies and the -45-deg plies. This supports the concept of a "characteristic damage state" (CDS) for fatigue loading as discussed by Reifsnider and Masters [*10,12*]. According to this concept, the crack patterns when fully developed are dependent on material properties, ply thicknesses, and stacking sequence, but are independent of load history.

Damage development in the wet specimens was somewhat different from that in the dry specimens. Besides the initially observed matrix cracks in the 90- and -45-deg plies and delamination at the $90/-45$ and ±45 interfaces after a larger number of load cycles, delamination was observed at the 90/90 interface and longitudinal cracks developed within the 90-deg plies in some specimens as shown in Fig. 11.

Figures 12 through 14 show the damage development in the wet specimens during fatigue cycling. With a low stress amplitude and no prestress, Fig. 12*a*, no matrix cracks or delamination were observed up to 10^6 load cycles. With a high prestress, Fig. 12*b*, the density of matrix cracks increased to constant levels in the 90- and -45-deg plies after about 10^4 cycles. Longitudinal cracks within the 90-deg ply (Fig. 11) were observed after about 10^2 cycles.

With increasing stress amplitude, Figs. 13 and 14, damage developed more rapidly. At the highest stress amplitude, Fig. 14, a crack density of about 10 cracks/cm was reached. A comparison with the damage development for the dry specimens reveals a significantly slower damage growth for the wet specimens at lower stress amplitudes. With increasing stress amplitudes the difference in damage growth behavior between the dry and wet specimens decreases. In fact, the damage growth at the largest stress amplitudes (348 and 400 MPa) is almost the same for dry and wet specimens. This means that the initial, internal stress

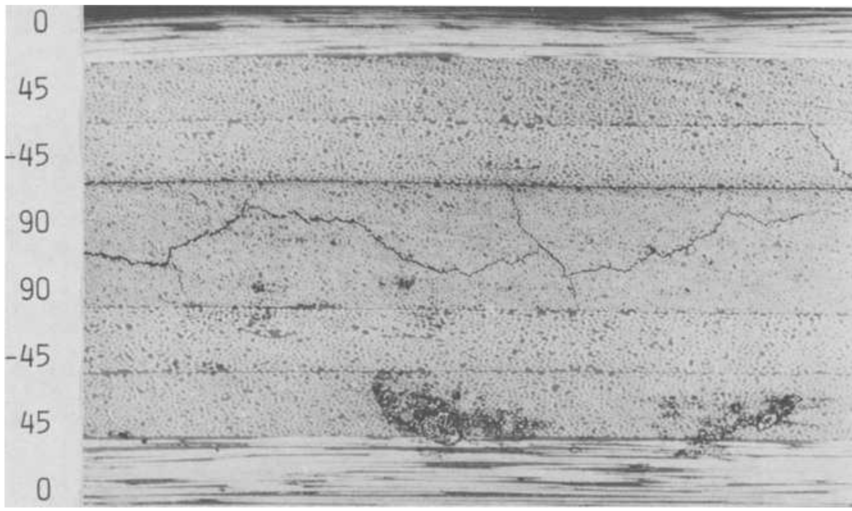

FIG. 11—*Longitudinal cracks within the 90-deg ply in a fatigue-loaded wet laminate.*

state becomes less important when a large amount of damage has occurred. This must be due to the redistribution of stresses due to damage progression.

The results presented here show that there is only a small difference in the characteristic damage state between the fatigue-loaded dry and wet specimens, the saturation density being approximately 11 and 10 cm^{-1} for dry and wet laminates, respectively. These values are higher than the largest crack density observed in static loading, which is about 8 cm^{-1} (Figs. 4 and 6).

It is interesting here to compare the saturation crack density with available theoretical predictions, namely, an approach based on fracture mechanics in conjunction with the finite-element method, proposed by Wang and Crossman [*17*], and a modified shear lag model proposed by Masters and Reifsnider [*10*]. The fracture mechanics approach yields a saturation density $\rho_s \simeq 1/(8d)$ for graphite/epoxy where d is the semi-thickness of the 90-deg layer. For the laminates in the present study this analysis yields $\rho_s \simeq 10$ cm^{-1}, in good agreement with the experimentally obtained values in the study. The shear lag analysis [*10*] was applied to both dry and wet 8-ply $[0/\pm45/90]_s$ laminates in Ref *16*. The predicted crack densities for dry and wet (1.2% weight gain) laminates were 14.4 and 13.2 cm^{-1}, respectively, which is somewhat higher than the experimental values obtained in this study.

Discussion and Conclusions

Data are presented here on damage growth during static and fatigue loading of a 32-ply quasi-isotropic laminate under ambient laboratory conditions and under humid room temperature conditions.

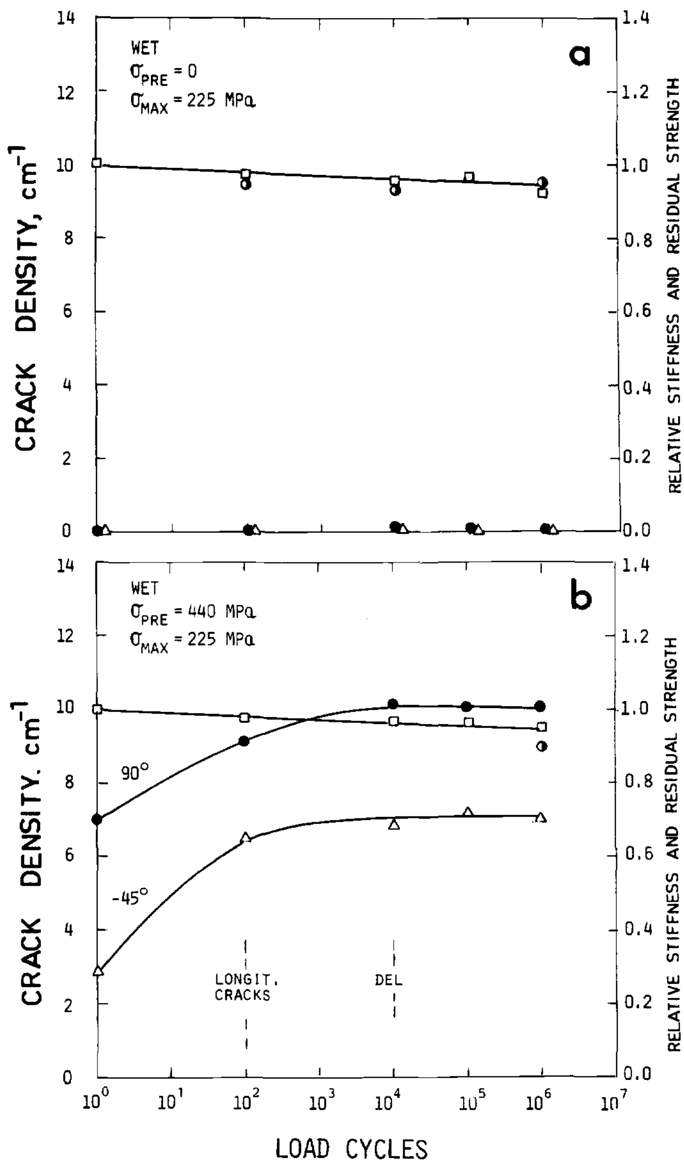

FIG. 12—*Crack density, relative stiffness, and relative residual strength during tension fatigue of wet laminates.* □ = *relative stiffness,* ◑ = *relative residual strength.* (a) $\sigma_{PRE} = 0$; $\sigma_{MAX} = 225$ *MPa.* (b) $\sigma_{PRE} = 440$ *MPa;* $\sigma_{MAX} = 225$ *MPa.*

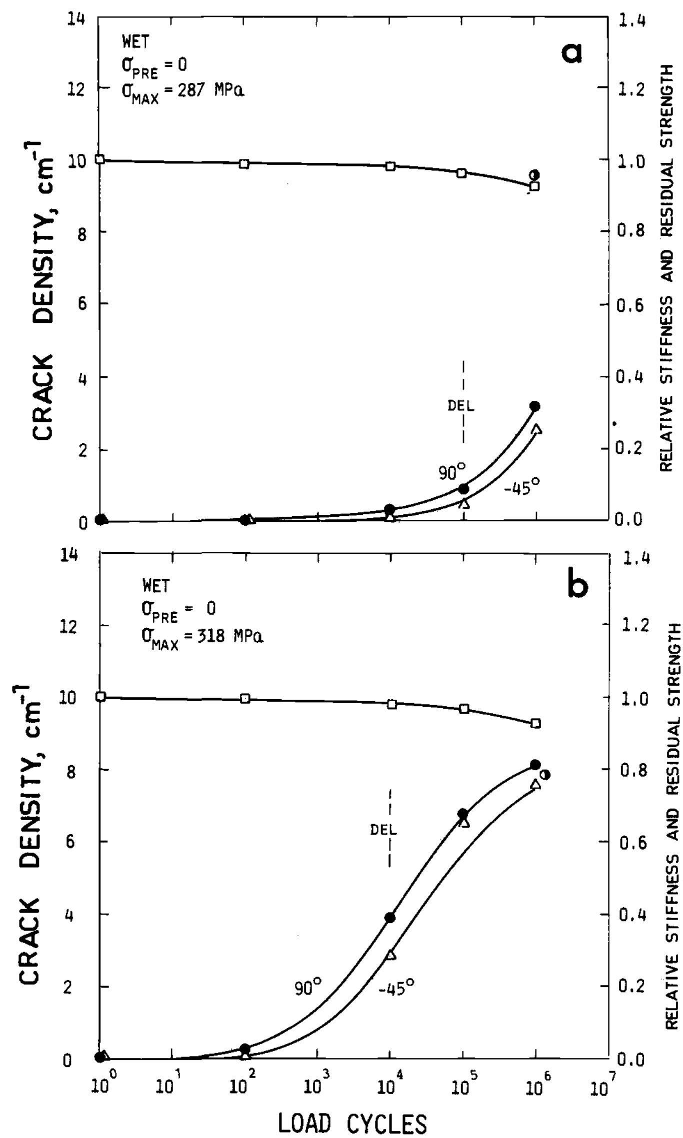

FIG. 13—*Crack density, relative stiffness, and relative residual strength during tension fatigue of wet laminates.* □ = *relative stiffness,* ◑ = *relative residual strength.* (a) $\sigma_{PRE} = 0$; $\sigma_{MAX} = 287$ *MPa.* (b) $\sigma_{PRE} = 0$; $\sigma_{MAX} = 318$ *MPa.*

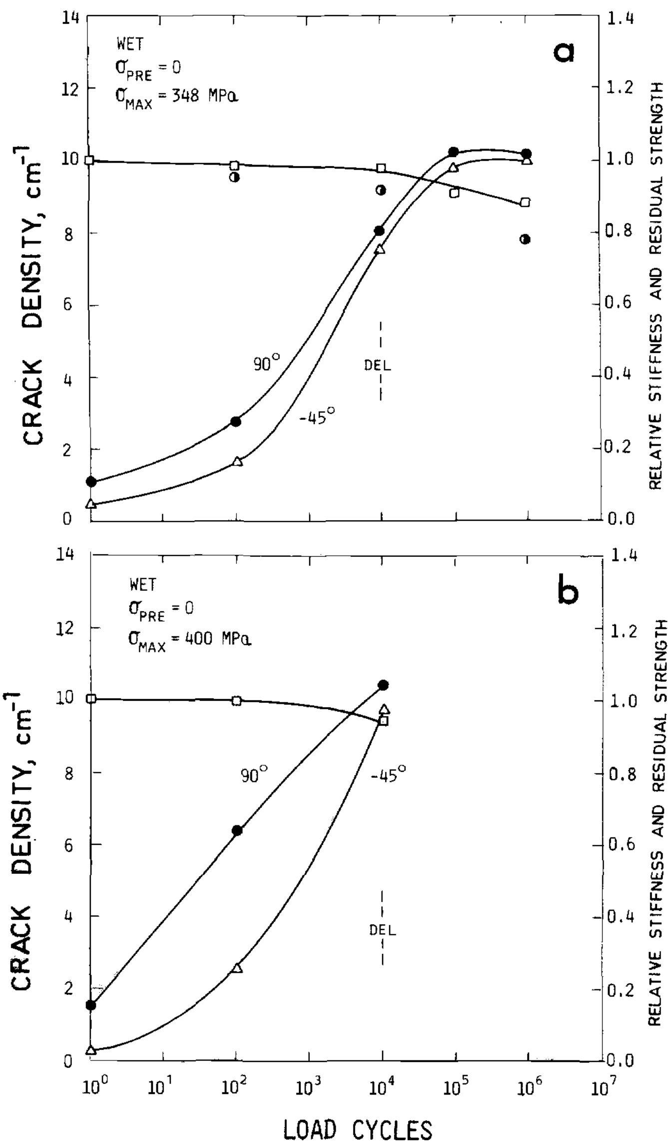

FIG. 14—*Crack density, relative stiffness, and relative residual strength during tension fatigue of wet laminates.* □ = *relative stiffness,* ◑ = *relative residual strength.* (a) $\sigma_{PRE} = 0$; $\sigma_{MAX} = 348$ *MPa.* (b) $\sigma_{PRE} = 0$; $\sigma_{MAX} = 400$ *MPa.*

The static test results show that the initial damage observed was transverse matrix cracks in the 90-deg plies. These cracks developed at a stress which was highly dependent on the moisture content in the laminate. The stress level at first-ply failure was significantly higher for the wet specimens than for the dry specimens, and could be predicted by the maximum stress criterion using classical lamination theory with moisture swelling included. At higher stress levels, further 90-deg ply cracking was observed. Almost all 90-deg cracks propagated into the adjacent −45-deg plies before final fracture of the laminate, which occurred at a higher stress for the wet specimens.

No leveling-off in the crack density was observed in static loading before final fracture. It is therefore not possible to define here the characteristic damage state in the static case. Acoustic Emission was found to be useful for monitoring damage during static loading. Under cyclic loading, however, the machine-generated noise precluded the use of AE for damage monitoring.

In tension fatigue loading, damage development similar to that found in static loading was observed. Edge delamination and a small number of +45-deg cracks were observed, however, in specimens subjected to a large number of load cycles, a high cyclic stress amplitude, or a high prestress before fatigue cycling. The delamination was observed to form between the tips of matrix cracks in the 90- and −45-deg plies; that is, the matrix cracks acted as initiators of delamination. Matrix cracks developed under fatigue loading at stress amplitudes as low as 78% of the static FPF stress.

Absorbed moisture was found to delay the damage development due to swelling of the matrix. It is also possible that the resin becomes more ductile in the swelled condition and hence less susceptible to crack initiation. In some of the wet specimens longitudinal cracks within the 90-deg ply developed during fatigue cycling.

The approximately constant value of the final crack density observed during fatigue loading indicates the occurrence of a characteristic damage state. The saturation crack density was somewhat higher for the dry specimens than for the wet specimens. There was good agreement between the experimental saturation crack density and the crack density predicted by the fracture mechanics approach of Wang and Crossman [*17*] and the shear lag analysis of Masters and Reifsnider [*10*]. The decrease in stiffness and residual strength during fatigue is attributed to delamination initiated by the matrix cracks.

Acknowledgments

The authors wish to thank Mr. Bo Norrbom for skillful experimental assistance. Thanks are also due to Dr. J. A. Bristow of STFI for linguistic revision.

References

[*1*] Bishop, S. M. and Dorey, G., "The Effect of Damage on the Tensile and Compressive Performance of Carbon Fiber Laminate" in *Proceedings*, Advisory Group for Aerospace Research and Development, Structures and Materials Meeting, London, 10–15 April 1983.

[2] Wilkins, D. J., "The Engineering Significance of Defects in Composite Structures" in *Proceedings*, Advisory Group for Aerospace Research and Development, Structures and Materials Meeting, London, 10–15 April 1983.
[3] Hashin, Z. and Rotem, A., *Journal of Composite Materials*, Vol. 7, 1973, p. 448.
[4] Talreja, R. in *Proceedings of the Royal Society of London*, Series A378, 1981, p. 461.
[5] Harrison, R. P. and Bader, M. G., *Fibre Science and Technology*, Vol. 18, 1983, p. 163.
[6] Springer, G. S. "*Environmental Effects on Composite Materials*," Technomic Publishing, Stamford, CT, 1981.
[7] Carlsson, L. and Norrbom, B., *Journal of Materials Science*, Vol. 18, 1983, p. 2503.
[8] Mohlin, T., Carlsson, L., and Blom, A. F., "An X-Ray Radiography Study of Delamination Growth in Notched Carbon/Epoxy Laminates" in *Proceedings*, TEQC 83, Testing, Evaluation and Quality Control of Composites, 13–14 Sept. 1983, University of Surrey, Guildford, U.K., 1983.
[9] Kim, R. Y. in *Advances in Composite Materials*, Vol. 2, Pergamon Press, Oxford, U.K., 1980, p. 1015.
[10] Masters, J. E. and Reifsnider, K. L. in *Damage in Composite Materials, ASTM STP 775*, Philadelphia, 1982, p. 40.
[11] Mohlin, T., Blom, A. F., Carlsson, L., and Gustavsson, A., in *Delamination and Debonding of Materials, ASTM STP 876*, American Society for Testing and Materials, Philadelphia, 1985, pp. 168–188.
[12] Reifsnider, K. L. and Masters, J. E., "Investigation of Characteristic Damage States in Composite Laminates," American Society for Mechanical Engineers Winter Annual Meeting, San Francisco, 1978.
[13] Halpin, J. C. and Pagano, N. J. in *Recent Advances in Engineering Science*," Gordon and Breach, New York, 1970, p. 3.
[14] Jones, R. M., *Mechanics of Composite Materials*, McGraw-Hill, New York, 1975.
[15] Carlsson, L., *Fiber Science and Technology*, Vol. 14, 1981, p. 201.
[16] Kriz, R. D. and Stinchcomb, W. W. in *Damage in Composite Materials, ASTM STP 775*, American Society for Testing and Materials, Philadelphia, 1982, p. 63.
[17] Wang, A. S. D. and Crossman, F. W., *Journal of Composite Materials, Supplement*, Vol. 14, 1980, p. 71.

Summary

Summary

Fracture

The papers in the fracture section covered both microscopic and macroscopic aspects of fracture of composites. The topics ranged from probabilistic fracture kinetics to laminate failure under bolt-bearing loads.

Krausz, Krausz, and Necsulescu proposed a probabilistic method of analyzing fracture expressing the environment-enhanced subcritical crack velocity as an appropriate kinetics combination of elementary rate constants. The rate constants were in turn given by equations of Arrhenius type in accordance with the assumption of a thermally activated process. Results of a computer simulation were shown for instantaneous crack velocities at various crack lengths.

The interface chemistry and failure modes of aluminum matrix composites were studied by Fu, Schmerling, and Marcus. They showed that an oxide in the form of γ-Al_2O_3 was present at some of the silicon carbide/aluminum (SiC/Al) interfaces while fine-grained γ-Al_2O_3 and coarse-grained Al_4C_3 were found in the interfaces of the as received graphite/aluminum (Gr/Al) composites. The fracture path in the discontinuous SiC/Al composite was not dominated by interfacial failure but primarily by matrix failure. The dominance of matrix failure increased with matrix ductility. During heat treatment of Gr/Al composites, some of the Al_4C_3 phase grew into and along the porous sites of the graphite fiber surface, thereby forming a mechanical locking which resulted in transverse strengthening.

Shirrell and Onachuck found that variations in mold coverage from 97.5% to 25% in R25 sheet molding compounds had virtually no effect on the critical hole size. Therefore, the spatial strength variability of this material did not appear to be related to mold coverage. Yet, a rubber toughening agent slightly reduced the notch sensitivity.

The remaining papers dealt with various aspects of fracture behavior of graphite/epoxy laminates. Peters used cracking of 90-deg plies in laminates to determine the *in situ* distribution of transverse strength. He showed that both the characteristic strength and the shape parameter decreased with increasing ply thickness. For quasi-isotropic T300/5208 laminates with part-through semi-elliptic surface flaws, Harris and Morris found that linear elastic fracture mechanics can predict the influence of the flaw shape and size on the notched strength. Quasi-isotropic laminates were also used by Aronsson and Bäcklund to study fracture of three-point bend specimens with a notch. They modeled the crack tip damage zone as a Dugdale-Barenblatt zone, and predicted fracture strengths as well as load-displacement curves. Similar laminates but under bolt-bearing loads were studied by Crews and Naik for failure modes, strengths, and failure energy. Typical damage sequences were found to be bearing damage onset at the hole boundary followed by growth of tension damage from the hole boundary. When the edge distance was small, shearout typified ultimate failure; however, in larger specimens ultimate failure involved bearing damage beyond the clampup washer. Extensive bearing damage dissipated more energy than tension damage. Ultimate failure was controlled by the maximum stress near the hole.

Grady and Sun used high-speed photography and a finite-element computer program to study propagation of an embedded delamination crack under impact. They found that if the delamination crack was placed near the top or bottom surface, local buckling of the sublaminate could cause the crack to become unstable. When the crack was in the midplane, however, there was no local buckling and the crack extension was dominated by the shear stress. The crack propagation and arrest depended on wave reflections from the boundaries as well as on wave propagation through the delaminated region. The complexity of the failure mechanisms defied analysis by the simplified finite-element method employed in the paper.

Fatigue

Most of the papers in the fatigue section addressed the mechanisms and modeling of damage growth in graphite/epoxy laminates. Yet, unidirectional composites and metal matrix composites were not completely left out.

Similar to polymer matrix composites, metal matrix composites also develop significant internal matrix cracking even when cycled below the fatigue limit, and hence exhibit stiffness loss. For silicon carbide/aluminum laminates of various layups, Johnson and Wallis applied Johnson's shakedown model to predict the fatigue-induced stiffness loss. Furthermore, they showed that for $[\pm 45]_{2s}$ laminate, the fatigue limit corresponded to the shakedown limit.

Failure mechanisms in unidirectional composites under longitudinal fatigue are difficult to identify because of the catastrophic nature of failure. To avoid this difficulty, Lorenzo and Hahn used a fiber bundle embedded in epoxy resin. In both glass and graphite bundles the omnipresent subcritical failure mechanism was matrix microcracking normal to the fibers. Yet, these microcracks were not deleterious in that they neither triggered fiber breaks nor grew bridging the fibers. A significant reduction in strength occurred in the glass bundle, indicating higher fatigue sensitivity of glass fibers compared with graphite fibers. The presence of a notch in a unidirectional composite invariably leads to longitudinal splitting from the notch tip under fatigue loading. This failure mode was confirmed by Mallick, Little, and Thomas in a notched pultruded E-glass/epoxy rod under rotating bend test. The longitudinal splitting before final failure was more extensive at lower stress amplitudes, and it resulted in a gradual increase in the dynamic deflection of the specimen.

Several papers discussed fatigue damage development and modeling of residual strength in multidirectional laminates. Charewicz and Daniel confirmed cracking of both longitudinal and transverse plies in cross-ply graphite/epoxy laminates, and proposed a cumulative damage model based on residual strength and the concept of equal damage curves. The ply cracking was shown to be delayed by absorbed moisture in a paper by Carlsson, Eidefeldt, and Mohlin. The absorbed moisture also retarded damage growth in quasi-isotropic laminates at low stress levels. Jamison showed that the transverse ply cracks enhanced fiber fracture in the load-bearing longitudinal plies. He further used acoustic emission to monitor failure events and concluded that fiber fracture was on average associated with a lower-amplitude emission than transverse ply cracking. The enhancement of fiber fracture by transverse cracks is the result of internal load redistribution after damage. Highsmith and Reifsnider showed through experiment and analysis significant strain redistributions in regions of highly localized damage such as ply cracks. Recognizing the importance of load redistribution, Reifsnider and Stinchcomb proposed a mechanistic approach to cumulative damage modeling based on the physics and mechanics of the details of the laminate response. The approach incorporates appropriate criteria for failure and degradation, and fully accounts for the change of stress state and damage modes.

Tough adhesive strips embedded in the interior of a laminate were shown by Chan to be effective in arresting and delaying delamination under tensile fatigue. Further, the Mode I component, not the total energy release rate, was suggested to be responsible for the initiation of delamination.

The role of thickness in fatigue of laminates with a hole was assessed in two papers. Lagace and Nolet showed that the delamination in $[\pm 45_n/0_n]_s$ laminates under compressive fatigue started earlier and at lower stress levels as n increased. Further, in thicker-ply laminates the delamination was only as wide as the hole and grew parallel to the load direction while most of the thinnest-ply specimens showed delamination growing radially from the hole, leading to catastrophic failure. Delamination growth from a hole can also be mostly transverse, as was shown by Bakis and Stinchcomb for a 32-ply quasi-isotropic laminate subjected to fully reversed tension-compression fatigue. As expected, the damage initiation and growth thus depend on the type of laminate as well as the type of loading. Also, both papers confirmed increase of tensile strength after fatigue as a result of stress relaxation induced by the damage at the hole boundary.

H. Thomas Hahn

Center for Composites Research, Washington University, St. Louis, MO; symposium chairman and editor.

Author Index

R

S

T

W

Subject Index

A

B

C

ISBN 0-8031-0470-7